Advances in Fatigue Lifetime Predictive Techniques

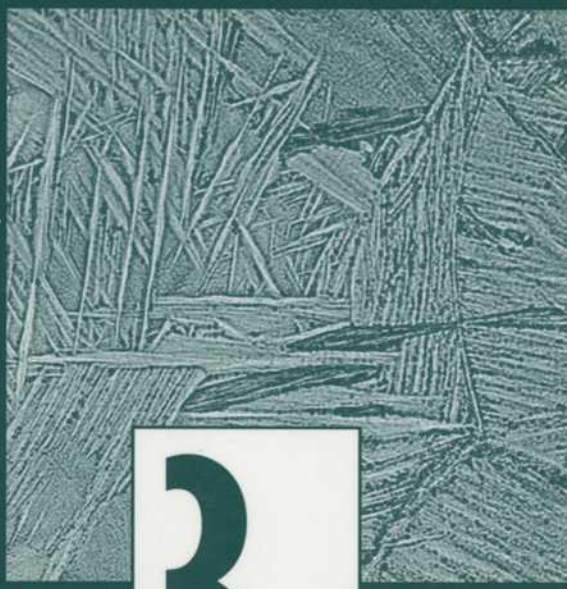

3rd volume

M. R. MITCHELL
R. W. LANDGRAF
editors

ASTM STP 1292

STP 1292

Advances in Fatigue Lifetime Predictive Techniques: 3rd Volume

M. R. Mitchell and R. W. Landgraf, editors

ASTM Publication Code Number (PCN):
04-012920-30

ASTM
100 Barr Harbor Drive
West Conshohocken, PA 19428-2959

Printed in the U.S.A.

Library of Congress Cataloging-in-Publication Data

ISSN: 1070-1079
ASTM Publication Code Number (PCN): 04-012920-30
ISBN: 0-8031-2029-X

Peer Review Policy

Each paper published in this volume was evaluated by three peer reviewers. The authors addressed all of the reviewers' comments to the satisfaction of both the technical editor(s) and the ASTM Committee on Publications.

The quality of the papers in this publication reflects not only the obvious efforts of the authors and the technical editor(s), but also the work of these peer reviewers. The ASTM Committee on Publications acknowledges with appreciation their dedication and contribution to time and effort on behalf of ASTM.

Printed in Ann Arbor, MI
January 1996

Foreword

This publication, *Advances in Fatigue Lifetime Predictive Techniques: 3rd Volume,* contains papers presented at the Third Symposium on Advances in Fatigue Lifetime Predictive Techniques, which was held in Montreal, Quebec on 16–17 May 1994. The symposium was sponsored by ASTM Committee E-08 on Fatigue and Fracture and by Subcommittee E08.05 on Cyclic Deformation and Fatigue Crack Formation. Symposium co-chairmen were M. R. Mitchell, Rockwell Science Center, Thousand Oaks, CA, and R. W. Landgraf, Virginia Polytechnic Institute and State University, Blacksburg, VA.

Contents

Overview

This volume, the third in a series on fatigue lifetime predictive techniques [see *ASTM STP 1122* (1991) and *STP 1211* (1993)], continues the tradition of providing a cross-disciplinary forum bringing together researchers and practitioners representing industry, universities, and government for the purpose of sharing knowledge and experiences associated with the important technological issue of understanding and controlling fatigue failures in components and structures. With the continuing trends toward structural weight reduction, performance optimization, and the application of tailored materials and structural elements, fatigue analysis has become an integral part of engineering design. Indeed, the availability of reliable life prediction methods can prove invaluable in developing durable products more quickly and at lower cost—issues of considerable concern for achieving global competitiveness.

As in past volumes, topical coverage among the 17 papers is broad and includes treatment of fundamental fatigue mechanisms as well as the development and application of fatigue design and analysis strategies. Composite materials continue to command the attention of researchers. The first two papers deal with the complexities of metal matrix composites exposed to combined mechanical and thermal environments. Neu and Nicholas present two analysis methods that account for multiple failure mechanisms as influenced by frequency, temperature, phasing, and environmental kinetics. Tamin and Ghonem discuss a combined analytical-experimental approach for studying cyclic and creep loading with emphasis on strain compatibility and the development and stability of thermal residual stresses.

The paper by Strait et al. explores thermo-mechanical fatigue in polymer matrix composites demonstrating the significant effect of level of constraint on system response and damage development. Elastomer composites are the subject of the paper by Liu and Lee in which a variety of nondestructive methods for detecting damage are evaluated.

Damage mechanics is another active area of research. Two papers deal with general computational fracture mechanics methods for life prediction. Chow and Wei extend a two-damage surface model in conjunction with finite element analysis to predict crack propagation in aluminum plates. Energy concepts are employed by Chang et al. to develop a general method for predicting crack initiation and growth using only uniaxial tensile data.

Crack initiation and growth at notches is the subject of papers by Hou and Lawrence, and Prakash et al. The first treatment involves a plasticity modified strip-yield model to account for the observed crack growth retardation following an overload. The second paper, employing fractographic and replication techniques to chart cracking behavior under spectrum loading, presents a growth model allowing for interaction of multiple cracks. In an experimental investigation of crack growth from a surface flaw under biaxial stress cycling, Zamrik and Ryan quantify the effect of biaxial ratio and a transition from Mode I to Mode II crack growth.

Microstructural effects on fatigue cracking behavior is the subject of the next two papers. Hardy investigates short crack behavior in a near α-titanium with emphasis on the early, microstructure-dependent behavior for which LEFM is not applicable and presents a two-stage empirical model that includes crack opening loads and identifies critical crack sizes above which fracture mechanics techniques do apply. Evans et al. likewise deal with a titanium alloy in developing a comprehensive database approach to component life estima-

tion that considers microstructural interactions and local plasticity in establishing an initial flaw size for calculations.

The final set of papers highlight the development and application of design methods for dealing with fatigue in components and structures. Bunch et al. detail the fatigue analysis methods used during the design and development of the B-2 bomber, while Sundar and Prakash consider lug joint performance under spectrum loading. Sheppard presents a continuation of her work on spot weld fatigue, extending the range of applicability to a variety of specimen types and notch profiles, including those subjected to post-weld treatments, and to the development of guidelines for selective thickening. Fatigue of coiled tubing, as used in oil drilling, is the subject of Tipton's paper in which he develops a damage parameter based on multiaxial plasticity analysis to predict combined pressurization and coiling events.

Reliability methods are employed by Kliman et al. to compute fatigue life distribution functions under time-varying loading sequences. Finally, the paper by Kalluri et al. addresses the often important influence of prestraining of components, as a result of manufacturing or service overstrains, on damage accumulation.

Taken as a whole, the papers in this volume provide ample evidence that important progress continues in our efforts to better understand and, hence, to control fatigue failure in a range of engineering structures. There is a clear trend among researchers toward confronting the many complexities of "real world" material systems, structural configurations, and service environments in arriving at more powerful tools for fatigue design and analysis. Further, the transfer of this new technology to engineering practice, long a challenge, appears to be proceeding in a timely manner. It is the derived practical benefits from past research efforts that provide an important impetus for further studies.

Michael R. Mitchell
Rockwell Science Center
Thousand Oaks, CA 91360
Symposium co-chairman and co-editor

Ronald W. Landgraf
Virginia Polytechnic Institute & State University
Blacksburg, VA 24061
Symposium co-chairman and co-editor

Richard W. Neu[1] *and Theodore Nicholas*[2]

Methodologies for Predicting the Thermomechanical Fatigue Life of Unidirectional Metal Matrix Composites

REFERENCE: Neu, R. W. and Nicholas, T., **"Methodologies for Predicting the Thermomechanical Fatigue Life of Unidirectional Metal Matrix Composites,"** *Advances in Fatigue Lifetime Predictive Techniques: 3rd Volume, ASTM STP 1292,* M. R. Mitchell and R. W. Landgraf, Eds., American Society for Testing and Materials, 1996, pp. 1–23.

ABSTRACT: Parameters and models to correlate the cycles to failure of a unidirectional metal matrix composite (SCS-6/Timetal 21S) undergoing thermal and mechanical loading are examined. Three different cycle types are considered: out-of-phase thermomechanical fatigue (TMF), in-phase TMF, and isothermal fatigue. A single parameter based on either the fiber or matrix behavior is shown not to correlate the cycles to failure of all the data. Two prediction methods are presented that assume that life may be dependent on at least two fatigue damage mechanisms and therefore consist of two terms. The first method, the linear life fraction model, shows that by using the response of the constituents, the life of these different cycle types are better correlated using two simple empirical relationships: one describing the fatigue damage in the matrix and the other fiber-dominated damage. The second method, the dominant damage model, is more complex but additionally brings in the effect of the environment. This latter method improves the predictions of the effects of the maximum temperature, temperature range, and frequency, especially under out-of-phase TMF and isothermal fatigue. The steady-state response of the constituents is determined using a 1-D micromechanics model with viscoplasticity. The residual stresses due to the CTE mismatch between the fiber and matrix during processing are included in the analysis.

KEYWORDS: metal matrix composites, titanium matrix, silicon carbide fibers, thermomechanical, fatigue, elevated temperature, micromechanics

One of the challenges of advanced metal matrix composites (MMCs) involves developing life prediction methodologies since most applications for these composites involve complex stress-temperature-time histories. The coefficient of thermal expansion (CTE) mismatch between the fiber and matrix and resulting thermal residual stresses from processing further add to the complexity. In general, a model that is capable of predicting life under different cycles and test conditions is desired. To simplify the present problem, three basic cycle types are identified: isothermal fatigue (IF), out-of-phase (OP) TMF, and in-phase (IP) TMF. The waveforms are triangular, and in OP TMF, the maximum stress and minimum temperature coincide, while in IP TMF, the maximum stress and maximum temperature coincide. The methodologies are evaluated under different test conditions, which include changes in the maximum temperature (T_{max}), temperature range (ΔT), and frequency. The aim of this investigation is to identify methodologies that are successful in correlating and predicting all three different cycle types under the various test conditions.

[1]Formerly, NRC associate, Wright Laboratory Materials Directorate, Wright-Patterson AFB, OH 45433-7817; currently, assistant professor, George W. Woodruft School of Mechanical Engineering, Georgia Institute of Technology; Atlanta, Ga 30332-0405.

[2]Senior scientist, Wright Laboratory Materials Directorate, Wright-Patterson AFB, OH 45433-7817.

Examination of the damage progression under OP TMF and IP TMF [*1–7*] clearly shows that the former is controlled by matrix fatigue and the latter is controlled by a progression of fiber failures. Under IF, a change in mechanisms from matrix fatigue to fiber-dominated failure is observed with an increase in maximum applied stress [*8–11*]. Two-term models that account for both matrix fatigue and fiber-dominated failure have been proposed as a method to consolidate data of different cycle types and account for the difference in observed damage mechanisms [*1,12*]. Since life is controlled by the local behavior, damage parameters and tools used for monolithics can be used to describe the degradation in each constituent. In addition, time-dependent and environmental effects may also affect fatigue life. The final failure involves the failure of both fibers and matrix, but for a given test condition one of the constituents generally controls the damage progression during the majority of life.

Two analyses are conducted to predict the life: (1) the constituent response is determined using micromechanics, and (2) the cycles to failure is determined using a parameter or expression that is dependent on the constituent response and environmental conditions, including temperature and time. This investigation focuses primarily on the second item by examining a number of single correlating parameters based on either the fiber or matrix behavior and two models consisting of two terms. For all cases the constituent response is calculated using the same micromechanics model to make the comparisons among the different parameters and life models consistent.

Experiments

The experimental data include OP TMF, IP TMF, and IF tests conducted on unnotched SCS-6/Timetal 21S $[0]_4$ composite under load control in laboratory air atmosphere with the load applied parallel to the fibers. The stress ratio (R = 0.1) and number of plies were constant for all tests. However, the fiber volume fraction (V_f) varied among the specimens and is accounted for in the micromechanics modeling. The baseline TMF tests were con-

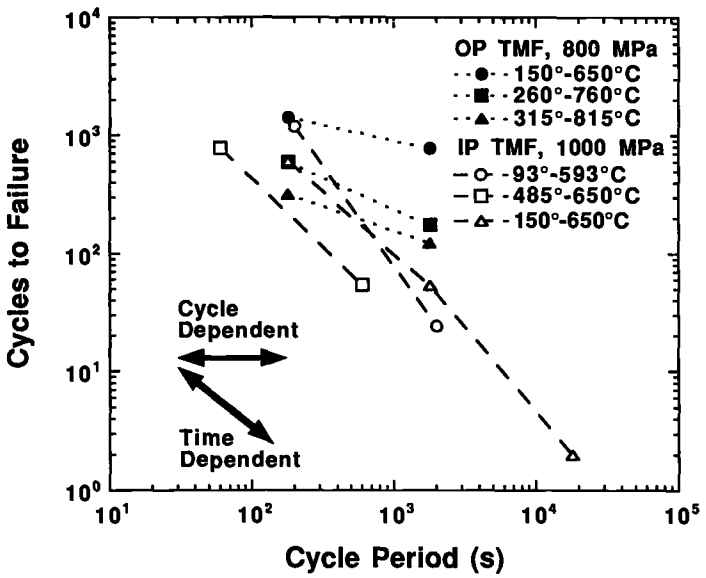

FIG. 1—*Effect of cycle period on OP and IP TMF life.*

ducted from 150 to 650°C at a frequency of 0.00556 Hz, and the baseline IF tests were conducted at 650°C at a similar frequency, 0.01 Hz. Cycles to failure is defined as the cycle when complete separation of the specimen occurs. The baseline data along with the details of the experiments are from Ref *6*. Further tests were then conducted to study how T_{max}, ΔT, and frequency affect the life compared to the baseline. Some of these results are summarized in Fig. 1. Increasing the cycle period (i.e., decreasing the frequency) decreases the life under both TMF phasings. However, the decrease under OP TMF ranges from a factor of 2 to 4, whereas the decrease under IP TMF is greater than a factor of 10. Thus OP TMF is both cycle and time dependent, whereas IP TMF is primarily time dependent. Additionally, under OP TMF an increase in T_{max} results in a decrease in life. Most of the OP TMF and IF data are reported in Ref *13*, although some of the IP TMF data are reported herein for the first time. All the experimental data are summarized in Tables 1 to 3.

Constituent Response

A 1-D micromechanics model (i.e., a rule of mixtures) with elastic fiber and viscoplastic matrix was used to determine the fiber and matrix response. Since this study involves tests conducted at different elevated temperatures and different frequencies, it is imperative that the micromechanics model accurately represents the time dependency of the composite behavior. To accomplish this, the matrix model was represented using the Bodner-Partom model [*14*] with constants given for Timetal 21S in Ref *15*. A good viscoplasticity model which represents the strain rate sensitivity of the matrix has been found to be more critical for obtaining the accurate axial response than a more complex geometric description [*16*].

TABLE 1—*Out-of-phase TMF tests.*

	Test Conditions					Computed Constituent Response					
Specimen ID	S_{max}, MPa	T_{min}, °C	T_{max}, °C	Frequency, Hz	V_f	σ^f_{max}, MPa	$\Delta\sigma^f$, MPa	σ^m_{max}, MPa	$\Delta\sigma^m$, MPa	$\Delta\epsilon^m$	N_f
Baseline											
92-179	1100	150	650	5.56E-03	0.32	1664	1503	835	750	0.00662	675
92-178	1000	150	650	5.56E-03	0.32	1455	1326	786	701	0.00617	919
92-177	900	150	650	5.56E-03	0.32	1246	1150	737	651	0.00572	1162
92-176	800	150	650	5.56E-03	0.32	1039	973	687	602	0.00527	1414
92-064	1100	150	650	5.56E-03	0.38	1572	1422	811	727	0.00641	911
92-065	900	150	650	5.56E-03	0.38	1193	1096	721	636	0.00558	1597
92-059	700	150	650	5.56E-03	0.37	820	775	630	546	0.00476	2112
92-060	600	150	650	5.56E-03	0.37	630	611	582	499	0.00434	3574
Others											
92-400	1000	150	815	4.18E-03	0.38	1520	1207	681	712	0.00704	198
92-398	800	150	815	4.18E-03	0.38	1118	868	605	630	0.00618	226
92-399	600	150	815	4.18E-03	0.38	708	524	534	550	0.00531	379
92-401	400	150	815	4.18E-03	0.38	302	180	460	470	0.00443	558
92-407	800	315	815	5.56E-03	0.38	1253	990	523	555	0.00582	316
92-408	800	260	760	5.56E-03	0.37	1201	952	565	584	0.00556	593
92-406	800	205	705	5.56E-03	0.38	1101	935	615	590	0.00535	1194
92-405	800	93	593	5.00E-03	0.38	944	945	712	582	0.00500	3573
92-410	800	650	815	1.67E-02	0.38	1751	1442	217	281	0.00510	732
92-411	800	485	650	1.67E-02	0.38	1386	1212	441	423	0.00431	4402
92-412	800	315	815	5.56E-04	0.38	1285	1037	503	532	0.00595	122
92-413	800	260	760	5.56E-04	0.38	1221	960	542	573	0.00558	175
93-118	800	150	650	5.56E-04	0.33	1092	976	656	595	0.00527	774

TABLE 2—*In-phase TMF tests.*

	Test Conditions					Computed Constituent Response					
Specimen ID	S_{max}, MPa	T_{min}, °C	T_{max}, °C	Frequency, Hz	V_f	σ^f_{max}, MPa	$\Delta\sigma^f$, MPa	σ^m_{max}, MPa	$\Delta\sigma^m$, MPa	$\Delta\epsilon^m$	N_f
Baseline											
92-173	900	150	650	5.56E-03	0.32	2496	2001	149	255	0.00270	229
92-172	800	150	650	5.56E-03	0.32	2186	1830	148	203	0.00222	1 097
92-175	700	150	650	5.56E-03	0.32	1877	1659	146	151	0.00175	6 251[a]
92-063	1100	150	650	5.56E-03	0.38	2656	2132	147	296	0.00306	208
92-061	1000	150	650	5.56E-03	0.38	2394	1973	146	248	0.00262	805
92-062	850	150	650	5.56E-03	0.38	2002	1735	144	175	0.00196	10 024[a]
Others											
93-115	1000	150	650	5.56E-03	0.34	2660	2100	145	287	0.00298	609
93-119	1000	93	593	5.00E-03	0.33	2408	2155	307	290	0.00325	1 189
93-116	1000	150	650	5.56E-04	0.34	2755	2077	96	296	0.00293	53
93-120	1000	93	593	5.00E-04	0.33	2650	2112	188	308	0.00317	24
93-122	1000	150	650	5.56E-05	0.33	2873	2100	78	310	0.00301	2
93-117	1000	485	650	1.67E-02	0.34	2626	1919	162	381	0.00413	780
93-121	1000	485	650	1.68E-03	0.33	2821	1932	103	394	0.00417	54

[a]Test was stopped before failure.

TABLE 3—*Isothermal fatigue tests.*

	Test Conditions				Computed Constituent Response					
Specimen ID	S_{max}, MPa	T, °C	Frequency, Hz	V_f	σ^f_{max}, MPa	$\Delta\sigma^f$, MPa	σ^m_{max}, MPa	$\Delta\sigma^m$, MPa	$\Delta\epsilon^m$	N_f
Baseline										
92-358	1000	650	1.00E−02	0.37	2385	1797	187	373	0.00486	1 848
92-360	900	650	1.00E−02	0.37	2145	1614	169	338	0.00436	2 343
92-357	800	650	1.00E−02	0.37	1904	1432	152	302	0.00387	5 177
92-359	700	650	1.00E−02	0.37	1659	1250	137	267	0.00338	9 990
Others										
92-208	1000	650	1.00E+00	0.34	2274	1823	344	427	0.00493	3 722
92-204	900	650	1.00E+00	0.35	1937	1616	342	379	0.00437	8 630
92-206	800	650	1.00E+00	0.34	1694	1459	339	342	0.00394	25 749
92-168	700	650	1.00E+00	0.35	1388	1257	330	295	0.00340	44 919
92-210	600	650	1.00E+00	0.34	1157	1093	313	256	0.00296	87 910
92-205	600	650	1.00E+00	0.34	1157	1093	313	256	0.00296	94 584
92-217	500	650	1.00E+00	0.34	919	911	284	213	0.00246	729 019
92-207	800	815	1.00E+00	0.34	2147	1706	106	212	0.00470	329
92-169	675	815	1.00E+00	0.34	1798	1412	97	193	0.00389	7 412
92-209	550	815	1.00E+00	0.34	1454	1131	84	168	0.00311	17 889
92-167	550	815	1.00E+00	0.34	1454	1131	84	168	0.00311	20 663
92-171	450	815	1.00E+00	0.34	1176	910	76	146	0.00251	53 196

The actual fiber volume fraction (V_f) for each experiment was used. A comparison between the 1-D model with a concentric cylinder model indicated that the average axial stress and strain values were similar when the composite was under an applied mechanical loading and varied by at most 15% when under a thermal loading only (i.e., when the applied stress was zero) [*17*]. Furthermore, the 1-D model ran about a factor of 10 faster than the concentric cylinder model. Since life prediction modeling tends to be highly empirical, small differ-

ences in the computed stress-strain response do not introduce inaccuracies in the life prediction as long as the same micromechanics model is used for all prediction analyses.

When a viscoplastic model is used, the constituent response is not initially stable and tends to ratchet toward some stabilized value. The ratchetting is caused by the stress relaxation of the matrix with the attendant increase in the fiber stress. Since the majority of the fatigue cycles occur under these stable conditions, the constituent response after stabilization is used in the prediction models. This is similar to using the strain or stress response at half life in low-cycle fatigue life prediction analyses. Similarly, Mirdamadi and Johnson ran VISCOPLY on a number of mission cycles until the response was stable [*4,18*].

The analysis of each test condition included a cooldown from 815°C that gives the thermal residual stresses, a ramp to the initial stress and temperature of the cycle, and ten thermal and mechanical cycles. A comparison of the model and experimental behavior at two frequencies under an IP TMF loading are given in Figs. 2 and 3. The model captures the inelastic strain on the first cycle as well as the ratchetting behavior with cycling. Since the model captures the composite behavior well, it provides confidence that the constituent behavior, which cannot be determined experimentally in the case of TMF, is also predicted well. The response of the constituents during processing and cycling for the two IP TMF cases are shown in Fig. 4. During the first nine cycles under IP TMF, the matrix stress relaxes, resulting in a 400-MPa increase in the fiber stress. The amount of increase in fiber stress is dependent on frequency, and for these two tests, the fiber stress is 250 MPa higher after nine cycles of a 30-min cycle compared to a 3-min cycle. In contrast, under OP TMF, the matrix relaxes very little and the response is nearly stable after the first cycle [*17,19*]. For OP TMF the maximum applied stress is at the low temperature of the cycle when the matrix is capable of carrying a greater portion of the load; consequently, the fiber stress is much lower under OP TMF. For illustration, the maximum fiber stresses at Cycle 10 under both IP and OP TMF with $V_f = 0.30$ and $T = 150$ to 650°C are shown in Fig. 5. The fiber stress under IP TMF is about twice as large. For this particular V_f, T_{max}, and ΔT, the increase in maximum fiber stress between a 3 and 30-min cycle is 150 MPa for IP TMF, whereas the frequency effect on fiber stress for OP TMF is somewhat less and decreases with decreasing maximum applied stress. The maximum fiber stress appears to be linearly related to the maximum stress applied to the composite. More details on the TMF response are given in Refs *17* and *19*. Since the constituent response is nearly stable after ten cycles, the response at Cycle 10 for each test condition is used in the life models. The response for each test is given in Tables 1 through 3.

Life Prediction Approaches

In this section a number of approaches are examined. First, approaches based solely on either the fiber response or matrix response are considered. However, these methods have limitations in predicting the general TMF response for many different stress-temperature-time histories. Two additional TMF models, the linear life fraction model (LLFM) and the dominant damage model (DDM), are considered that combine the effects of the fiber and matrix response to improve the TMF predictions over a wider range of test conditions. The DDM further incorporates environmental effects that help predict the T_{max}, ΔT, and frequency effects under TMF that are attributable to environment.

Based on Fiber Response

A number of researchers [*10,20–22*] have argued that since the fibers must fail to obtain composite failure, life is controlled by the fiber behavior. Therefore, the first parameter

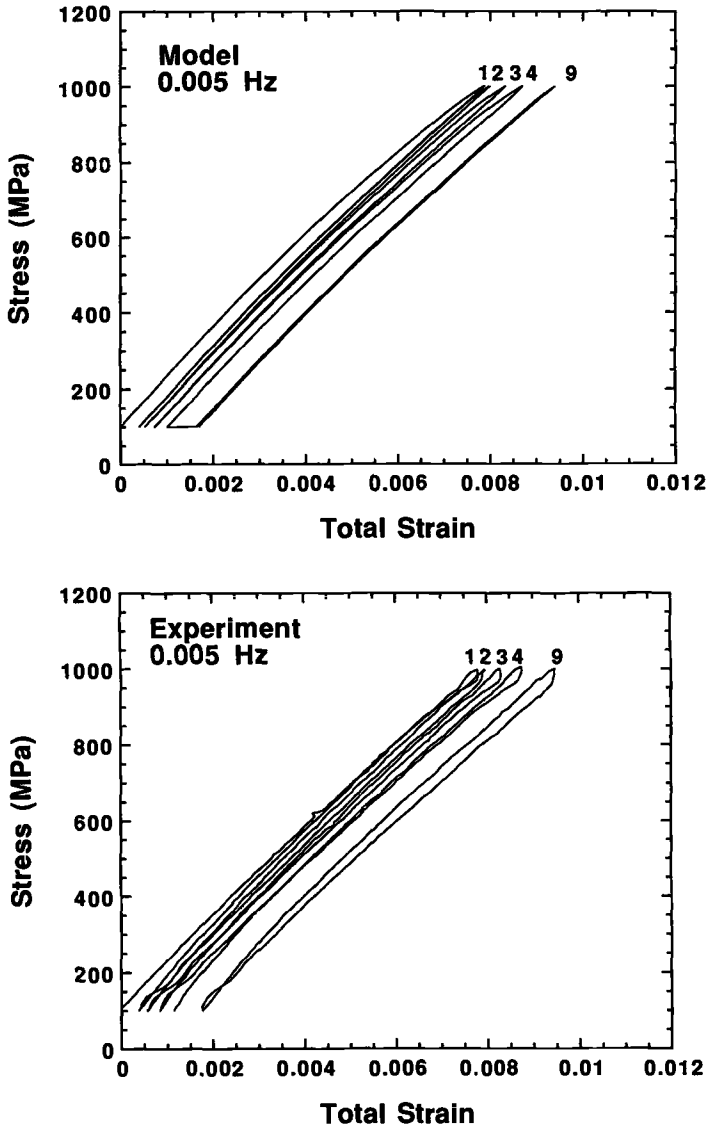

FIG. 2—*IP TMF response undergoing temperature cycle of 93 to 593°C at a frequency of 0.005 Hz* (V_f = *0.33):* (top) *model,* (bottom) *experiment.*

examined as a possible correlating parameter is the maximum fiber stress, σ^f_{max} (Fig. 6). The test data are separated by cycle types. The specific test conditions for each data point are given in Tables 1 through 3. The different cycle types tend to group together, with IP TMF and IF somewhat following a trend. For these tests an *S-N* curve for the fibers has been proposed [*21,23*]. Using σ^f_{max} assumes the strength of the fibers are degrading with number of cycles. In general, though, σ^f_{max} does not correlate all the data. If we say that σ^f_{max} correlates the IP TMF and IF data, the predictions for the OP TMF data are nonconservative

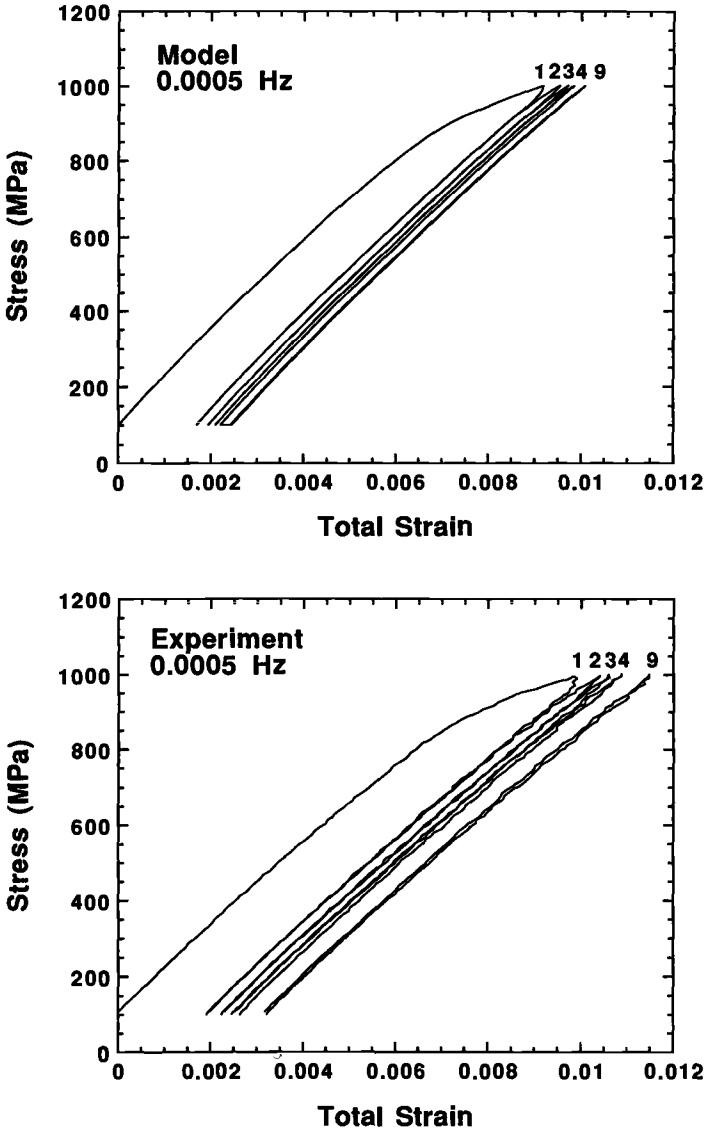

FIG. 3—*IP TMF response undergoing temperature cycle of 93 to 593°C at a frequency of 0.0005 Hz* (V_f = *0.33):* (top) *model,* (bottom) *experiment.*

and the error is more than a factor of 10. The plot of σ^{f}_{max} is similar to plotting ϵ_{max} of the composite at the computed stabilized value because fiber and matrix are both subjected to the same strain while the stresses vary depending on the V_f and modulus of the constituents. The fiber response is elastic, though the modulus varies a small amount with temperature [*24*]. No fiber fracture is assumed to occur before the stabilized (Cycle 10) behavior is reached. So simply using ϵ_{max} of the stabilized composite response does not correlate the data any better.

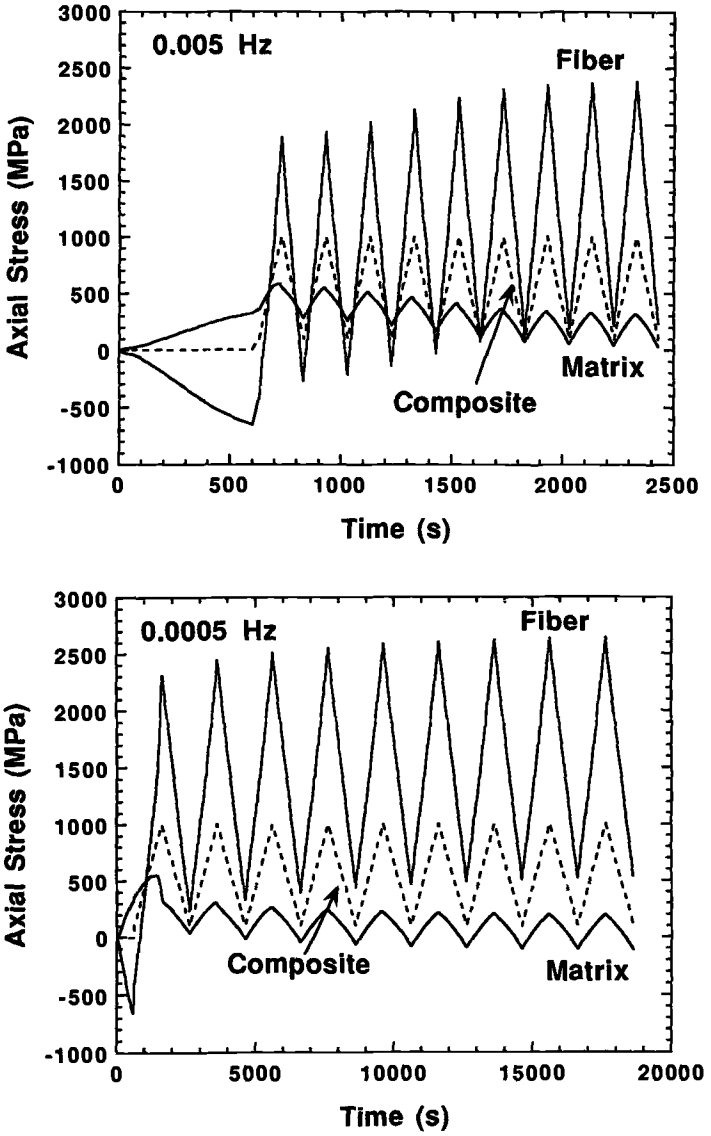

FIG. 4—*Fiber and matrix response for IP TMF undergoing temperature cycle of 93 to 593°C:* (top) *frequency of 0.005 Hz,* (bottom) *frequency of 0.0005 Hz.*

Others [*2,4,10,20*] have shown that fiber stress range ($\Delta\sigma^f$) can correlate the isothermal fatigue of different layups [*10,20*] as well as OP and IP TMF [*2,4*]. The fiber stress range has been successful in correlating tests of the same cycle type, but in general does not correlate different cycle types or variations in temperature and frequency [*4,25*]. Since $\Delta\sigma^f$ depends only on the range, it can be determined experimentally for isothermal fatigue by multiplying the composite strain range by the fiber modulus, eliminating the need to determine the thermal residual stress. For consistency though, the constituent behavior for

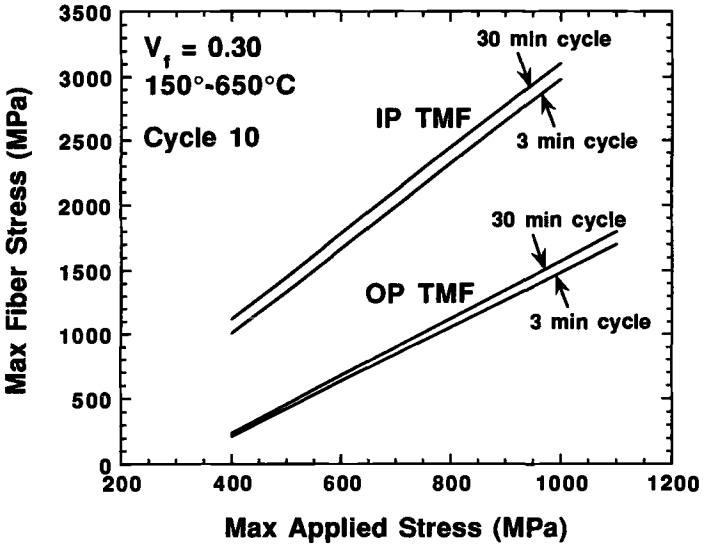

FIG. 5—*Computed maximum fiber stress for OP and IP TMF at cycle ten.*

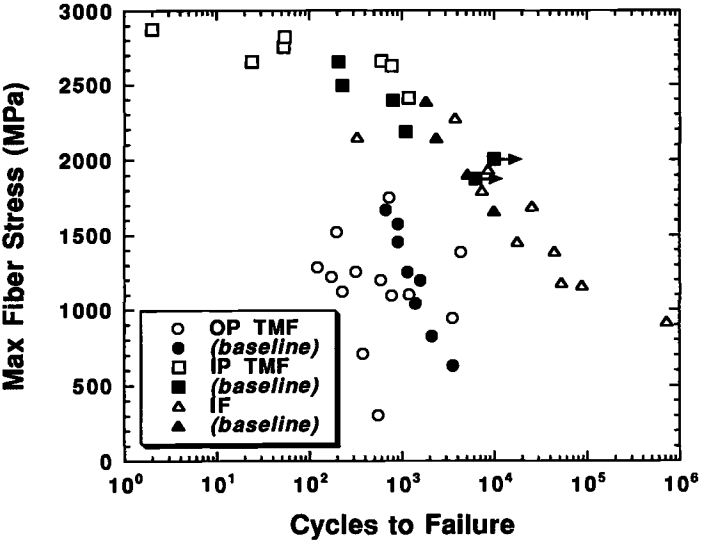

FIG. 6—*Correlation of all data based on maximum fiber stress.*

all cases was determined from the model. Plotting $\Delta\sigma^f$ seems to correlate all the data marginally better (Fig. 7), yet most of the OP TMF data still lie more than a factor of 10 away from IF and IP TMF data.

Recently Mirdamadi and Johnson [*18*] used $\sqrt{\Delta\sigma^f\sigma^f_{max}}$ as a correlating parameter and found it to work slightly better for their data. This parameter is motivated by the SWT parameter [*26*], which in this case accounts for both the cyclic effect as well as the mean stress effect on fiber degradation. However, no improvements in the correlation are realized for our data (Fig. 8). Mall et al. [*27*] introduced a term $\sigma^f_{max}\ (1 - R^f)^m$, $0 < m < 1$, to

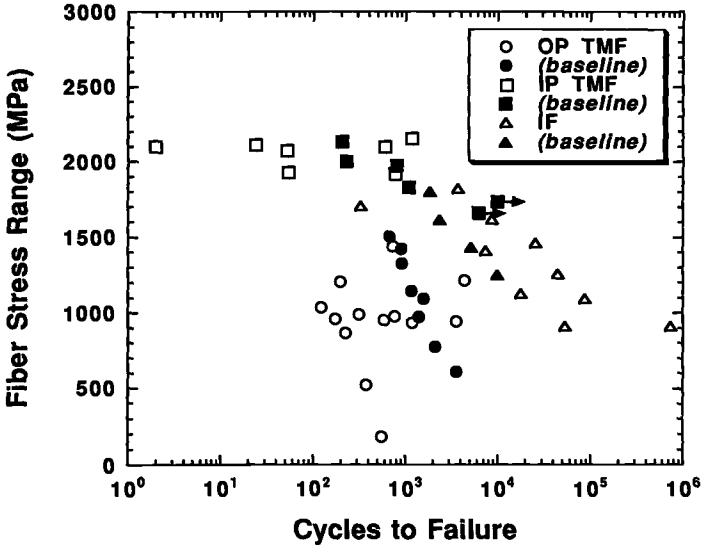

FIG. 7—*Correlation of all data based on fiber stress range.*

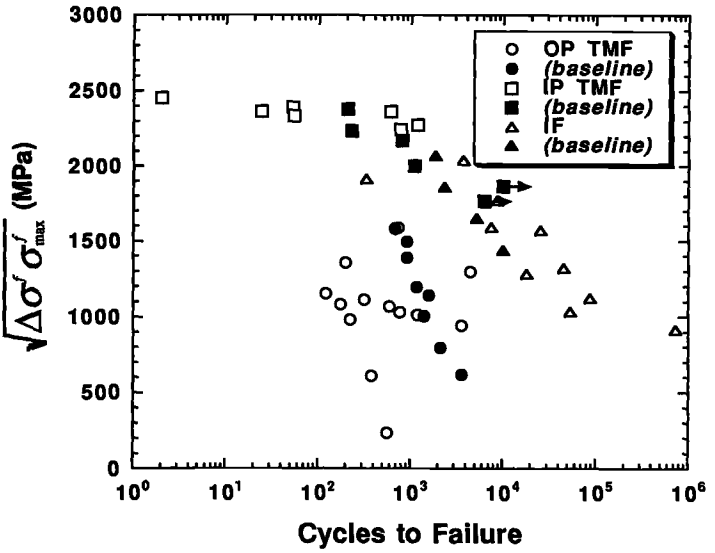

FIG. 8—*Correlation of all data based on maximum fiber stress and fiber stress range motivated by SWT parameter.*

account for any combination of stress range and mean stress, since $m = 0$ corresponds to σ^f_{max} and $m = 1$ to $\Delta\sigma^f$. Some small improvement in the ability to correlate TMF data was obtained.

Fiber behavior, in general, cannot correlate both IP and OP TMF data. It may correlate the data over a limited range of stresses or fatigue lives when the damage mechanism is controlled by the fiber stress only, such as IP TMF, but cannot correlate OP TMF, which is marked by matrix fatigue cracking. With matrix cracking, the fibers carry more of the load,

which may be included in the model to account for this effect [*18*]. However, once the matrix crack reaches the fibers during TMF or elevated temperature fatigue, accelerated fiber degradation occurs, mainly from the environmental attack of the carbon interface and notching of the silicon carbide fibers [*9,28*]. The fiber stress may remain well below the fiber strength, but the fiber strength may rapidly degrade after the matrix cracks reach the fibers.

Based on Matrix Response

Another approach is to assume that a crack initiates and grows in the matrix and therefore the damage progression is controlled by the matrix response [*9,23,29–31*]. First, matrix fatigue is assumed to be controlled by the matrix stress range, $\Delta\sigma^m$ (Fig. 9). Since OP TMF is matrix controlled, it would be expected that $\Delta\sigma^m$ correlates the OP TMF data; however, only the baseline data (i.e., one test condition) are correlated satisfactorily. Since locally the matrix undergoes low-cycle fatigue, matrix mechanical strain range, $\Delta\epsilon^m$, may be a more appropriate parameter for correlating the data (Fig. 10). This parameter seems to correlate the OP TMF and to some extent the IF data; however, the IP TMF predictions are non-conservative by more than a factor of 10. An SWT parameter (Fig. 11), which has been used to correlate room temperature fatigue [*29,30*] and elevated temperature fatigue of an MMC [*23*], does not improve the correlations.

Linear Life Fraction Model (LLFM)

None of the previous correlations using a single constituent response parameter could correlate all three distinct cycle types. In all cases the experiments from one of the cycle types could not be predicted within a factor of 10. Realizing this, Russ et al. [*1*] proposed a two-term model which assumes that a fraction of the life is controlled by the matrix and the remaining fraction is controlled by the fiber. They proposed empirical relationships that describe the cycles to failure for a fiber-dominated failure mode as

$$N_f = 10^{N_0}\left(1 - \frac{\sigma^f_{max}}{\sigma^*}\right) \tag{1}$$

and the cycles to failure for matrix-dominated failure mode as

$$N_m = B(\Delta\sigma^m)^{-n} \tag{2}$$

Assuming linear damage summation,

$$N = \frac{1}{\left(\frac{1}{N_f} + \frac{1}{N_m}\right)} \tag{3}$$

The constants were determined by fitting the baseline IP TMF and OP TMF data to Eqs 1 and 2, respectively (Fig. 12). From the fits, $N_0 = 8.8$, $\sigma^* = 3500$ MPa, $B = 2.4 \times 10^{14}$, and $n = 4.02$. The justification for a two-term model is the difference in the observed damage progression mechanisms. No matrix fatigue cracks are observed for loading types

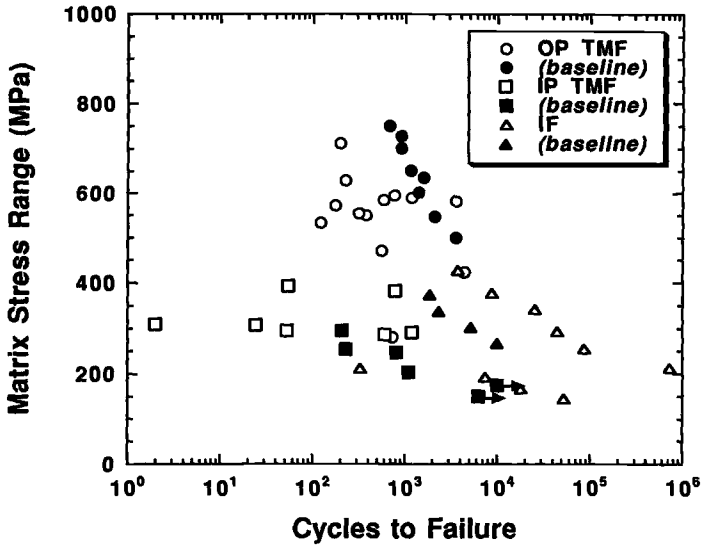

FIG. 9—*Correlation of all data based on matrix stress range.*

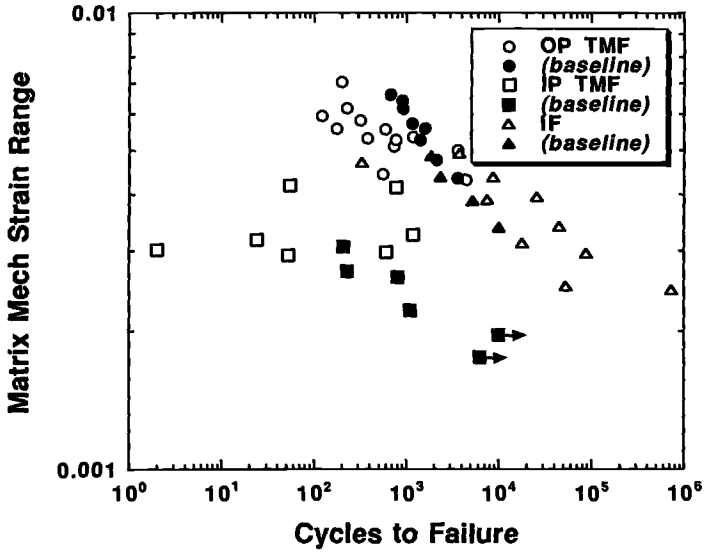

FIG. 10—*Correlation of all data based on matrix mechanical strain range.*

controlled completely by the fiber (i.e., IP TMF), whereas many matrix cracks are observed under matrix-dominated conditions (i.e., OP TMF) [*1–7*].

This version of the model correlates the baseline TMF data well since they were used to determine the constants (Fig. 13). It also predicts the IF baseline data within reason. Out of all the data, only four data (3 OP and 1 IP TMF) are not predicted with a factor of 10. However, the predictions of the nonbaseline data tended not to be as good as the correlated baseline data. Though not used in the present investigation, recent additions to this model

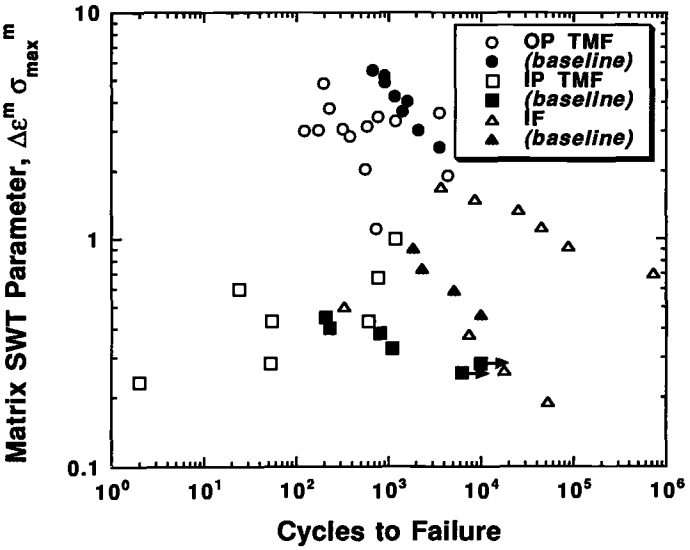

FIG. 11—*Correlation of all data based on matrix SWT parameter.*

include the effect of stress ratio on the fiber-dominated term as well as the decomposition of damage into cycle-dependent and time-dependent terms [*32*].

In the application of the LLFM, the consideration of damage resulting from two different mechanisms produces two independent terms and generally results in one term dominating over the other. In this situation, the model functions as a screening tool and computes life primarily from the dominant term. Through the introduction of temperature-dependent parameters, and by considering fiber-dominated, matrix-dominated, and time as well as cycle-dependent behavior, improvements in the ability to consolidate a large body of experimental data can be achieved.

Dominant Damage Model (DDM)

The final model examined also describes the damage using two terms, although more terms may be added [*12*]. The damage terms are motivated by the expected damage mechanisms for OP and IP TMF. Both temperature and time are incorporated to account for the kinetics of the environmental attack that have been observed to reduce life [*7,13,33,34*]. For unidirectional metal matrix composites, three damage mechanisms were identified [*12*]: (1) fatigue of the matrix, (2) surface-initiated fatigue-environment damage in the matrix, and (3) fiber-dominated damage. Each mechanism describes a series of events which may include synergistic interactions of fatigue and environment. The first mechanism describes the fatigue of the matrix in the absence of any environmental influence on the microcrack growth in the matrix. In this study none of the test cases are controlled by this mechanism, so it is not considered further. The second mechanism also describes matrix cracking, but in this case the environment plays a large role in the growth due to the synergistic fatigue-environment interaction, which is characteristic of an OP TMF test. The third mechanism describes the case when fibers fracture first, and it also includes an environmental factor which describes the gradual weakening of the fibers with time at temperature [*28*].

The damage per cycle, D, is the largest of the possible damage mechanisms (i.e., the dominant damage mechanism),

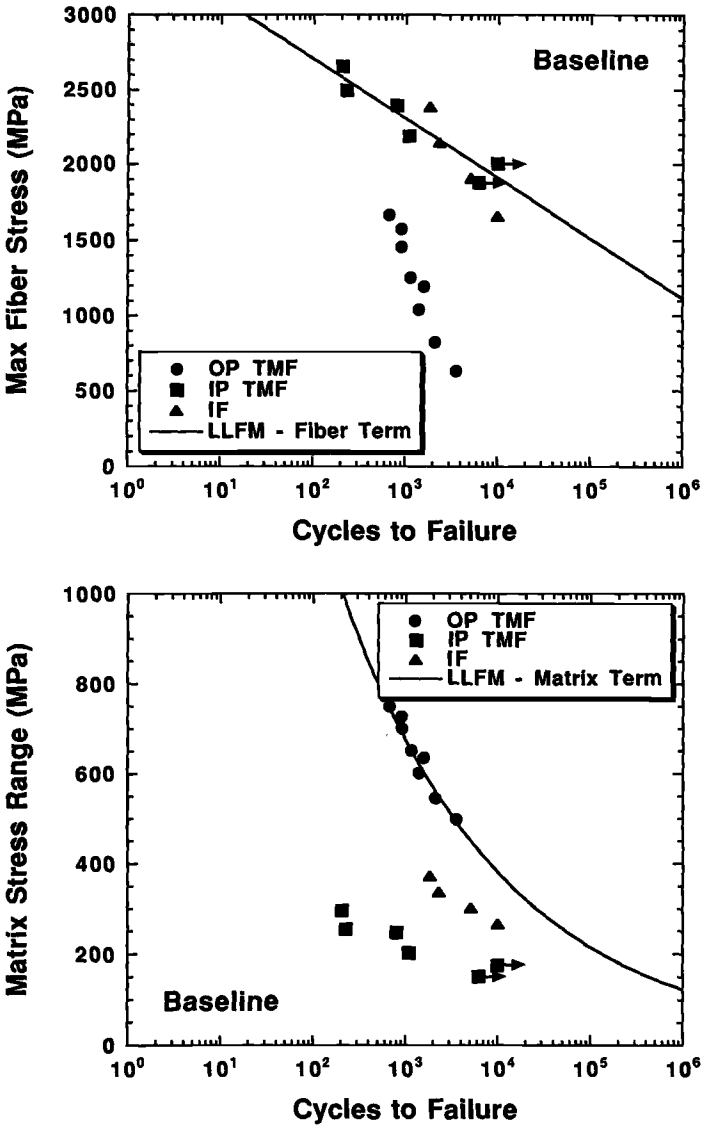

FIG. 12—*Correlation fits for LLFM:* (top) *fiber term,* (bottom) *matrix term.*

$$D = \max\left(D^{env}, D^{fib}\right) \tag{4}$$

where D^{env} is the surface-initiated fatigue-environment damage and D^{fib} is the fiber-dominated damage. If the damage mechanisms are completely independent, D can also be described as the sum of each damage mechanism as done in Refs *12* and *13*. The inverse of D is the number of cycles to failure,

$$N_f = 1/D \tag{5}$$

The surface-initiated fatigue-environment damage term is based on the fatigue-environ-

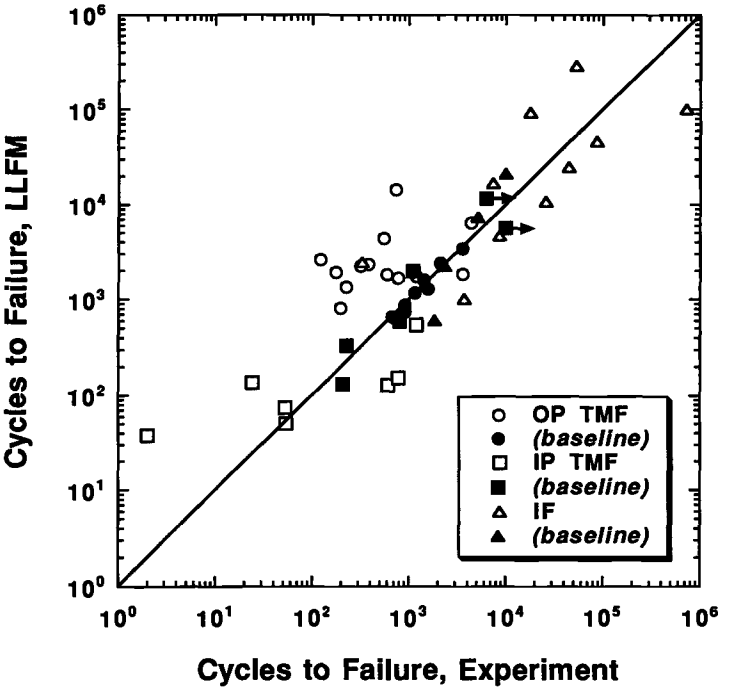

FIG. 13—*Comparison of experiments and LLFM for all data.*

ment interaction of cracks initiating at the surface and growing inward. Therefore, the damage term includes parameters that describe the environmental attack (time, temperature, kinetics of oxidation) as well as fatigue (matrix strain range). Synergistic effects due to the stress-temperature phasing are also incorporated. This damage term was derived in Ref *12*, thus only the resulting expression is given here,

$$D^{\text{env}} = \left[\frac{C_{\text{crit}}}{\Phi_{\text{ox}} D_{\text{eff}}}\right]^{-1/\beta} 2^{\alpha/\beta} t_c^{(1-\alpha/\beta)} (\Delta\epsilon^{\text{m}})^{(2+\alpha)/\beta} \tag{6}$$

where t_c is the period of a cycle, $\Delta\epsilon^{\text{m}}$ is the mechanical strain range in the matrix, and Φ_{ox} is the effective phasing of the cycle and is a function of the ratio of the thermal and mechanical strain rates,

$$\Phi_{\text{ox}} = \frac{1}{t_c}\int_0^{t_c} \exp\left[-\frac{1}{2}\left(\frac{(\dot{\epsilon}_{\text{th}}^{\text{m}}/\dot{\epsilon}^{\text{m}}) - M}{\xi_{\text{ox}}}\right)^2\right] dt \tag{7}$$

D_{eff} is the effective oxidation constant and is similar to an Arhennius-type expression averaged over a cycle,

$$D_{\text{eff}} = \frac{1}{t_c}\int_0^{t_c} D_0 \exp\left(-\frac{Q_{\text{ox}}}{RT}\right) dt \tag{8}$$

and the remaining symbols (C_{crit}, a, β, M, ξ_{ox}, D_0, Q_{ox}) are material parameters.

The fiber-dominated damage term describes the gradual weakening of the fibers with

time, temperature, and the kinetics of the degradation coupled with the stress in the fiber and the phasing of stress and temperature. This term indirectly includes the effects of environmental attack of the interface. The damage per cycle is given by

$$D^{fib} = \int_0^{t_c} A_{fib}\,\Phi_{fib} \exp\left(-\frac{Q_{fib}}{RT}\right)\left[\frac{\sigma^f}{\sigma_T}\right]^m dt \tag{9}$$

where Q_{fib} is the apparent activation energy for environmental attack of the fiber, σ^f is the axial stress in the fiber, σ_T is associated with the fiber strength, Φ_{fib} is the phasing factor which has a similar form as Eq 7 (see [*12*]), and the remaining symbols (m, A_{fib}) are material parameters.

The material parameters are determined from a limited number of key experiments, which include IF and baseline TMF tests. The remaining TMF tests under different T_{max}, ΔT, and frequency conditions are predictions. The material parameters for SCS-6/Timetal 21S are given in Table 4. More details on the determination of the parameters are given in Refs *12* and *13*.

All the data with the correlations and predictions are given in Fig. 14. In Fig. 14*a*, the 0.01 Hz IF curve shows a change in slope at 900 MPa. The dominant damage mechanism above this stress is fiber-dominated damage, whereas below this stress is surface-initiated fatigue-environment damage. A change in mechanism also occurs at 1 Hz, though it is a higher stress than those plotted in Fig. 14*a*. The highest stress experiment at 815°C is not correlated well and suggests it may be more controlled by the fiber-dominated mechanism. In Fig. 14*b*, the correlation to the IP TMF data captures the effect of V_f. OP TMF is nearly insensitive to V_f. The curve through the 150-815°C data is a true prediction. The temperature effect was captured from the IF tests conducted at 650 and 815°C. In all cases, IP TMF is controlled by the fiber-dominated damage mechanism, whereas OP TMF is controlled by the surface-initiated fatigue-environment damage mechanism. In Fig. 14*c*, the true predictions for OP TMF under different T_{max}, ΔT, and frequencies are all within a factor of 2 of the experimental life. This plot also shows that a change in T_{max} is much more detrimental to life

TABLE 4—*Material parameters for DDM.*

Material Parameters	
Surface-Initiated Fatigue-Environment Damage Constants	
D_0	1.2 $\mu m^2/s$
Q_{ox}	29.0 kJ/mol
a	0.4
β	0.54
M	−2.0
ξ_{ox}	1.25
C_{crit}	3.6×10^{-6} $\mu m^2 \cdot s^{-a}$
Fiber-Dominated Damage Constants	
Q_{fib}	112.9 kJ/mol
A_{fib}	3.81×10^5 1/s
m	16.6
M	1.0
ξ_{fib}	0.45
η	0.9
σ_T	3200 MPa

compared to an equivalent change in ΔT, similar to the conclusion by Gayda et al. [*34*]. In Fig. 14*d*, the predictions for IP TMF tests are not as good. The predictions capture both the large degradation in life due to frequency and the insensitivity of ΔT on the life; however, they overestimate the degradation in life with increasing T_{max}. The cycles to failure determined from the DDM are compared to experiments in Fig. 15. Modeling the environmental effects significantly improve the OP TMF and IF correlations and predictions.

Discussion

A single parameter suggesting that TMF life is controlled by either fiber or matrix alone is unable to correlate all the data of OP TMF, IP TMF, and IF within a factor of 10. Since more than one mechanism of damage progression occurs among these different cycle types and test conditions, these different damage mechanisms must be controlled by different parameters. Although both fiber and matrix must eventually break to get specimen failure, the events leading up to final failure control the life. A single parameter may correlate a limited amount of data if the damage mechanism remains unchanged over a narrow range of test conditions. However, the damage progressions under OP TMF and IP TMF are distinct, and therefore it is reasonable that one parameter does not correlate both cycle types.

Facilitating the comparison between the two-term models, a multiplying factor, M, quantifying the variation between the model and experimental life, is defined as

$$M = 10^{\sqrt{\frac{1}{n}\sum_{i=1}^{n}(\log N_{f_i}^{m} - \log N_{f_i}^{ex})^2}} \tag{10}$$

where n is the number of experiments, N_f^m is the cycles to failure from the model, and N_f^{ex} is the cycles to failure from experiments. Equation 10 is motivated by the standard deviation about a perfect correlation. For example, when M is 2, the standard deviation between the model and experimental lives is a factor of 2. The results are reported in Fig. 16. For all tests, the DDM fairs just a little better than the LLFM. The correlations and predictions for the DDM differ on average by about a factor of 3 from the experiments. The multiplying factor for each cycle type is also shown. The LLFM predicts all the different cycle types in about a factor of 3 to 4, which is an improvement over a single parameter correlation. Including the fatigue-environment effects in the DDM, the OP TMF data are all predicted within a factor of 2 with the average being just a factor of 1.3. Since IF is somewhat controlled by the fatigue-environment interaction, the IF predictions using the DDM are also better than the LLFM. However, the DDM is not as successful in predicting IP TMF. The LLFM, which does not incorporate time- and temperature-dependent environmental attack to the fiber, does a better job in predicting the IP TMF life. As shown in Fig. 14*d*, the DDM may be overpredicting the effect of the environment (i.e., T_{max}) on fiber degradation, and this may suggest that fiber degradation is more of a mechanical rubbing at the interface under IP TMF. It is also possible that applied stress, as opposed to fiber stress, has a greater influence on the environmental degradation of the fiber.

When the fiber-dominated damage mode operates, the stress-life curve has a relatively low slope which makes accurate prediction of the number of cycles to failure difficult since the life is so sensitive to the stress. Fortunately, when failure occurs under a fiber-dominated damage mechanism, the stress is always relatively high. When the stress is reduced, the predicted life from this mechanism becomes very large. For the baseline tests, no failure is reached by 10^4 cycles when the maximum stress applied to the composite is still about 0.6 of

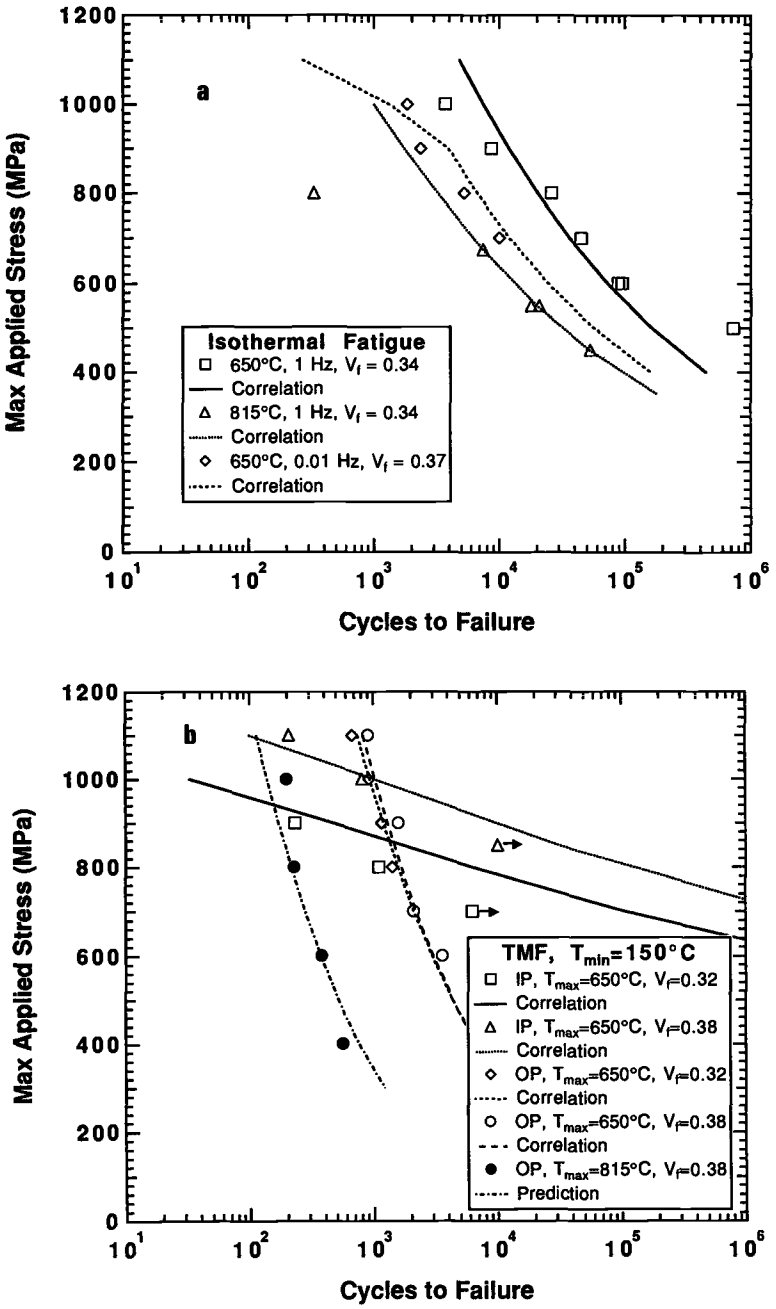

FIG. 14—*Correlations and predictions for DDM:* (a) *isothermal fatigue,* (b) *TMF,* T_{min} = *150°C,* (c) *OP TMF,* (d) *IP TMF.*

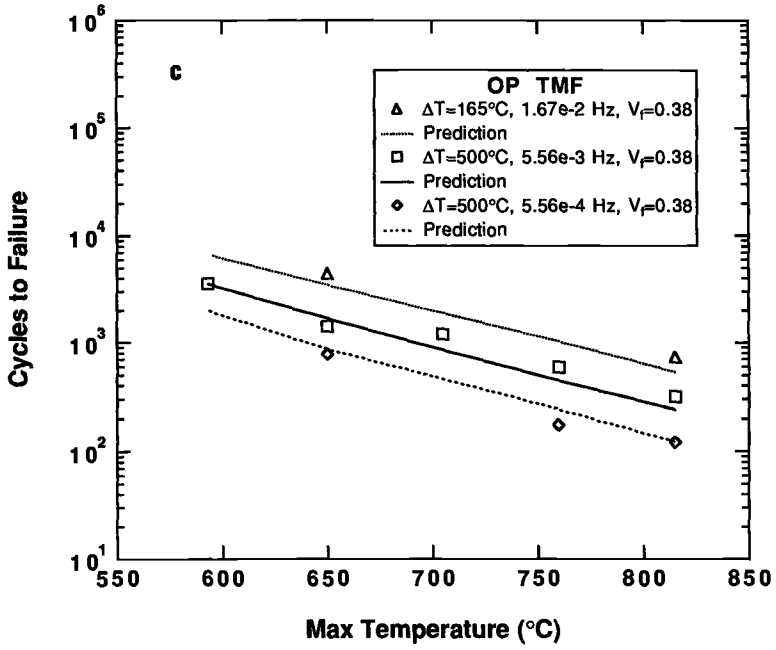

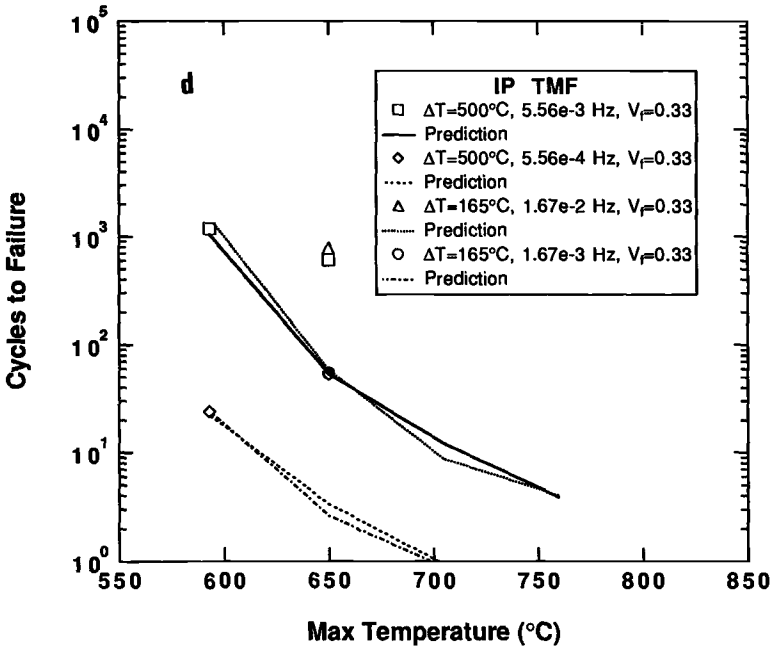

FIG. 14—(*Continued*).

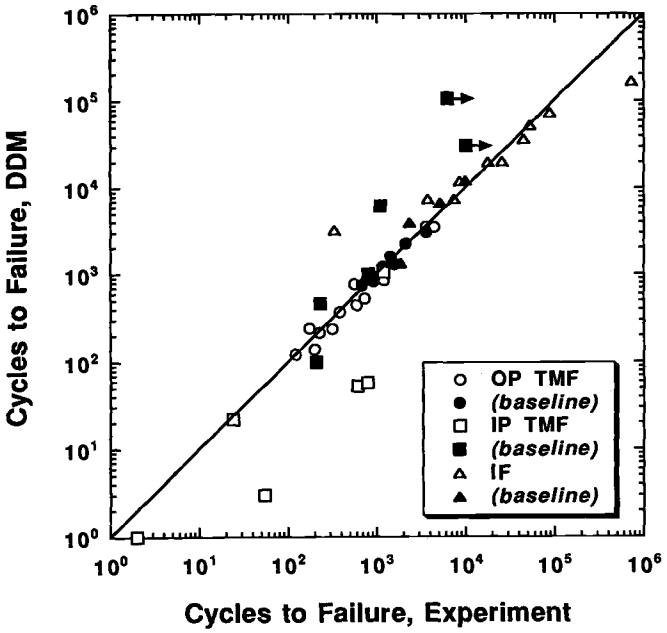

FIG. 15—*Comparison of experiments and DDM for all data.*

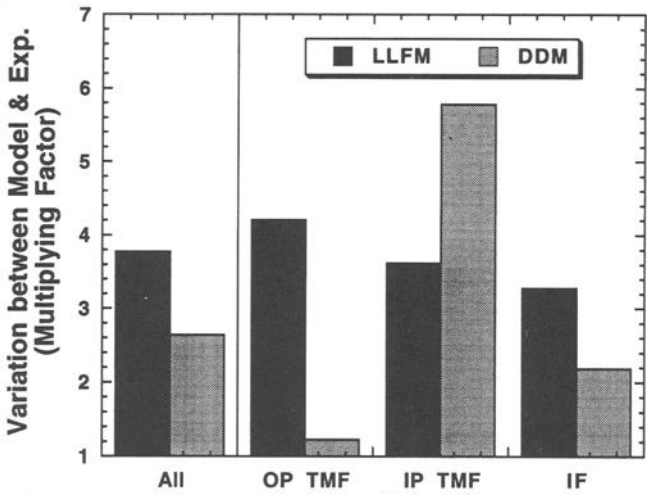

FIG. 16—*Multiplying factor describing the variation between each model and experiments.*

the ultimate tensile strength (UTS) at the maximum temperature of the cycle [*6*] (Fig. 14*b*). One would desire the design stress to be below this runout level if IP TMF conditions prevail. Therefore, even though the IP TMF predictions contain more error, they generally will not have to be used in design.

It turns out to be fortunate that OP TMF can be predicted with some confidence because failures under OP TMF can occur as low as 0.1 of the UTS [*6*]. Since the design stresses will most certainly be higher, it is critical that OP TMF is predicted well. Since adding fatigue-environment damage improves the prediction, a viscoplastic micromechanics model alone (i.e., without fatigue-environment damage) is not sufficient for predicting the T_{max}, ΔT, and frequency effects under OP TMF. In fact, using a time-independent elastic-bilinear plastic micromechanics model along with a fatigue-environment damage model is sufficient in predicting the OP TMF lives [*13*].

Conclusions

A general life prediction model for MMCs that is capable of predicting the cycles to failure of different cycle types requires at least two terms. The justification is that at least two distinct fatigue damage mechanisms occur depending on the cycle type. None of the single correlating parameters, which either describe the matrix or fiber behavior, correlate all cycle types within a factor of 10.

A linear life fraction model having both fiber and matrix failure mode terms is capable of predicting all the cycle types and test conditions on average within a factor of 4. Accounting for the fatigue-environment effects in the dominant damage model improves the OP TMF and IF predictions, and most of those tests are predicted within a factor of 2.

Under IP TMF, a fatigue limit (no failure to 10^4 cycles) is reached. For this cycle type, determining this limit is most relevant since the finite life predictions are less certain. Under OP TMF, there appears to be no fatigue limit, but the cycles to failure can be predicted within a factor of 2 when the fatigue-environment interaction is modeled.

Acknowledgments

Steve Russ of Wright Laboratory Materials Directorate, Wright-Patterson AFB, OH, conducted and gratefully provided the isothermal fatigue test data, and Demirkan Coker of the University of Dayton Research Institute, Dayton, OH, assisted with the micromechanics modeling. Support for the first author (RWN) was provided by the National Research Council (NRC), Washington, DC, through their Research Associateship Program.

References

[*1*] Russ, S. M., Nicholas, T., Bates, M., and Mall, S., "Thermomechanical Fatigue of SCS-6/Ti-24Al-11Nb Metal Matrix Composites," *Failure Mechanisms in High Temperature Composite Materials,* AD-Vol. 22/AMD-Vol. 122, G. K. Haritos, G. Newaz, and S. Mall, Eds., American Society of Mechanical Engineers, New York, 1991, pp. 37–43.

[*2*] Castelli, M. G., Bartolotta, P., and Ellis, J. R., "Thermomechanical Testing of High-Temperature Composites: Thermomechanical Fatigue (TMF) Behavior of SiC(SCS-6)/Ti-15-3," *Composites Materials: Testing and Design (Tenth Volume), ASTM STP 1120,* G. C. Grimes, Ed., American Society for Testing and Materials, West Conshohocken, PA, 1992, pp. 70–86.

[*3*] Castelli, M. G., "Characterization of Damage Progression in SCS-6/Timetal 21S [0]4 Under Thermomechanical Fatigue Loading," *Life Predictions Methodology for Titanium Matrix Composites,* ASTM STP 1253, American Society for Testing and Materials, West Conshohocken, PA, in press.

[*4*] Mirdamadi, M., Johnson, W. S., Bahei-El-Din, Y. A., and Castelli, M. G., "Analysis of Thermomechanical Fatigue of Unidirectional Titanium Metal Matrix Composites," *Composite*

Materials: Fatigue and Fracture, Fourth Volume, ASTM STP 1156, W. W. Stinchcomb and N. E. Ashbaugh, Eds., American Society for Testing and Materials, West Conshohocken, PA, 1993, pp. 591–607.

[5] Neu, R. W. and Roman, I., "Acoustic Emission Monitoring of Damage in Metal Matrix Composites Subjected to Thermomechanical Fatigue," *Composites Science and Technology,* Vol. 52, 1994, pp. 1–8.

[6] Neu, R. W. and Nicholas, T., "Effect of Laminate Orientation on the Thermomechanical Fatigue Behavior of a Titanium Matrix Composite," *Journal of Composites Technology and Research,* Vol. 16, No. 3, July 1994, pp. 214–224.

[7] Gabb, T. P. and Gayda, J., "Matrix Fatigue Cracking Mechanisms of α_2 TMC for Hypersonic Applications," NASA Technical Memorandum 106506, 1994, *Life Predictions Methodology for Titanium Matrix Composites, ASTM STP 1253,* American Society for Testing and Materials, West Conshohocken, PA, in press.

[8] El-Soudani, S. M. and Gambone, M. L., "Strain-Controlled Fatigue Testing of SCS-6/Ti-6Al-4V Metal-Matrix Composite," *Fundamental Relationships Between Microstructure and Mechanical Properties of Metal-Matrix Composites,* P. K. Liaw and M. N. Gungor, Eds., The Minerals, Metals & Materials Society, Warrendale, PA, 1990, pp. 669–704.

[9] Jeng, S. M., Yang, J. M., and Aksoy, S., "Damage Mechanisms of SCS-6/ Ti-6Al-4V Composites Under Thermal-Mechanical Fatigue," *Materials Science and Engineering,* Vol. A156, 1992, pp. 117–124.

[10] Pollock, W. D. and Johnson, W. S., "Characterization of Unnotched SCS-6/ Ti-15-3 Metal Matrix Composites at 650°C," *Composite Materials: Testing and Design (Tenth Volume), ASTM STP 1120,* G. C. Grimes, Ed., American Society for Testing and Materials, West Conshohocken, PA, 1992, pp. 175–191.

[11] Johnson, W. S., "Damage Development in Titanium Metal-Matrix Composites Subjected to Cyclic Loading," *Composites,* Vol. 24, No. 3, 1993, pp. 187–196.

[12] Neu, R. W., "A Mechanistic-based Thermomechanical Fatigue Life Prediction Model for Metal Matrix Composites," *Fatigue and Fracture of Engineering Materials and Structures,* Vol. 16, No. 8, 1993, pp. 811–828.

[13] Neu, R. W. and Nicholas, T., "Thermomechanical Fatigue of SCS-6/TIMETAL® 21S Under Out-of-Phase Loading," *Thermomechanical Behavior of Advanced Structural Materials,* W. F. Jones, Ed., AD-Vol. 34/AMD-Vol. 173, American Society of Mechanical Engineers, New York, 1993, pp. 97–111.

[14] Chan, K. S., Bodner, S. R., and Lindholm, U. S., "Phenomenological Modeling of Hardening and Thermal Recovery in Metals," *Journal of Engineering Materials and Technology,* Vol. 110, January 1988, pp. 1–8.

[15] Neu, R. W., "Nonisothermal Material Parameters for the Bodner-Partom Model," *Material Parameter Estimation for Modern Constitutive Equations,* L. A. Bertram, S. B. Brown, and A. D. Freed, Eds., MD-Vol. 43/AMD-Vol. 168, American Society of Mechanical Engineers, New York, 1993, pp. 211–226.

[16] Kroupa, J. L., Neu, R. W., Nicholas, T., Coker, D., Robertson, D. D., and Mall, S., "A Comparison of Analysis Tools for Predicting the Inelastic Cyclic Response of Cross-Ply Titanium Matrix Composites," *Life Predictions Methodology for Titanium Matrix Composites, ASTM STP 1253,* American Society for Testing and Materials, West Conshohocken, PA, in press.

[17] Neu, R. W., Coker, D., and Nicholas, T., "Cyclic Behavior of Unidirectional and Cross-ply Titanium Matrix Composites," submitted to *International Journal of Plasticity,* 1994.

[18] Mirdamadi, M. and Johnson, W. S., "Modeling and Life Predictions for TMC's Subjected to Mission Profiles," *Life Predictions Methodology for Titanium Matrix Composites, ASTM STP 1253,* American Society for Testing and Materials, West Conshohocken, PA, in press.

[19] Kroupa, J. L. and Neu, R. W., "The Nonisothermal Viscoplastic Behavior of a Titanium Matrix Composite," *Composites Engineering,* Vol. 4, No. 9, 1994, pp. 965–977.

[20] Johnson, W. S., Lubowinski, S. J., and Highsmith, A. L., "Mechanical Characterization of Unnotched SCS-6/Ti-15-3 Metal Matrix Composites at Room Temperature," *Thermal and Mechanical Behavior of Metal Matrix and Ceramic Matrix Composites, ASTM STP 1080,* J. M. Kennedy, H. H. Moeller, and W. S. Johnson, Eds., American Society for Testing and Materials, West Conshohocken, PA, 1990, pp. 193–218.

[21] Telesman, J., Kantzos, P., and Ghosn, L., "The Effect of the Environment and Temperature on Fiber Bridging in Titanium Based Composites," *Life Predictions Methodology for Titanium Matrix Composites, ASTM STP 1253,* American Society for Testing and Materials, West Conshohocken, PA, in press.

[22] Dvorak, G. J., Nigam, H., and Bahei-El-Din, Y. A., "Time and Temperature Dependent Behavior

of a SiC/Ti Composite," *Life Predictions Methodology for Titanium Matrix Composites, ASTM STP 1253*, American Society for Testing and Materials, West Conshohocken, PA, in press.

[*23*] Harmon, D. M., Finefield, M. A., Saff, C. R., and Harter, J. A., "Durability and Damage Tolerance Issues for Applications of Titanium Matrix Composites to Airframe Structures," *Life Predictions Methodology for Titanium Matrix Composites, ASTM STP 1253,* American Society for Testing and Materials, West Conshohocken, PA, in press.

[*24*] Coker, D., Ashbaugh, N. E., and Nicholas, T., "Analysis of the Thermomechanical Behavior of [0] and [0/90] SCS-6/Timetal 21S Composites," *Thermomechanical Behavior of Advanced Structural Materials,* W. F. Jones, Ed., AD-Vol. 34/AMD-Vol. 173, American Society of Mechanical Engineers, New York, 1993, pp. 1–16.

[*25*] Majumdar, B. S. and Newaz, G. M., "Thermomechanical Fatigue of a Quasi-isotropic Metal Matrix Composite," *Composite Materials: Fatigue and Fracture (Third Volume), ASTM STP 1110,* T. K. O'Brien, Ed., American Society for Testing and Materials, West Conshohocken, PA, 1991, pp. 732–752.

[*26*] Smith, K. N., Watson, P., and Topper, T. H., "A Stress-Strain Function for the Fatigue of Metals," *Journal of Materials,* Vol. 5, No. 4, December 1970, pp. 767–778.

[*27*] Mall, S., Hanson, D. G., Nicholas, T., and Russ, S. M., "Thermomechanical Fatigue Behavior of a Cross-Ply SCS-6/β21-S Metal Matrix Composite," *Constitutive Behavior of High Temperature Composites,* MD-Vol. 40, B. S. Majumdar, G. M. Newaz, and S. Mall, Eds., American Society of Mechanical Engineers, New York, 1992, pp. 91–106.

[*28*] Gambone, M. L. and Wawner, F. E., "The Effect of Elevated Temperature Exposure of Composites on the Strength Distribution of the Reinforcing Fibers," *Intermetallic Matrix Composites III,* Vol. 350, J. A. Graves, R. R. Bowman, and J. J. Lewandowski, Eds., MRS, Pittsburgh, PA, 1994, pp. 111–118.

[*29*] Herrmann, D. J., Ward, G. T., and Hillberry, B. M., "Prediction of Matrix Fatigue Crack Initiation from Notches in Titanium Matrix Composites," *Life Predictions Methodology for Titanium Matrix Composites, ASTM STP 1253,* American Society for Testing and Materials, West Conshohocken, PA, in press.

[*30*] Hillberry, B. M. and Johnson, W. S., "Prediction of Matrix Fatigue Crack Initiation in Notched SCS-6/Ti-15-3 Metal Matrix Composites," *Journal of Composites Technology and Research,* 1994.

[*31*] Halford, G. R., Lerch, B. A., and Saltsman, J. F., "Proposed Framework for Thermomechanical Life Modeling of Metal Matrix Composites," NASA Technical Paper 3320, July 1993.

[*32*] Nicholas, T., Russ, S. M., Neu, R. W., and Schehl, N., "Life Prediction of a [0/90] Metal Matrix Composite Under Isothermal and Thermomechanical Fatigue," *Life Predictions Methodology for Titanium Matrix Composites, ASTM STP 1253,* American Society for Testing and Materials, West Conshohocken, PA, in press.

[*33*] Brindley, P. K. and Draper, S. L., "Failure Mechanisms of 0° and 90° SiC/Ti-24Al-11Nb Composites Under Various Loading Conditions," *Structural Intermetallics,* R. Darolia, J. J. Lewandowski, C. T. Liu, P. L. Martin, D. B. Miracle, and M. V. Nathal, Eds., The Minerals, Metals & Materials Society, Warrendale, PA, 1993, pp. 727–737.

[*34*] Gayda, J., Gabb, T. P., and Lerch, B. A., "Fatigue-Environment Interactions in a SiC/Ti-15-3 Composite," *International Journal of Fatigue,* Vol. 15, No. 1, 1993, pp. 41–45.

M. N. Tamin[1] *and H. Ghonem*[1]

Evolution of Bridging Fiber Stress in Titanium Metal Matrix Composites at Elevated Temperature

REFERENCE: Tamin, M. N. and Ghonem, H., **"Evolution of Bridging Fiber Stress in Titanium Metal Matrix Composites at Elevated Temperature,"** *Advances in Fatigue Lifetime Predictive Techniques: 3rd Volume, ASTM STP 1292,* M. R. Mitchell and R. W. Landgraf, Eds., American Society for Testing and Materials, 1996, pp. 24–38.

ABSTRACT: This paper deals with the determination of stress evolution in bridging fibers during fatigue crack growth in a SM1240/Timetal-21S composite using the finite element method. Several parameters affecting this evolution were considered, namely, the process-induced residual stress, the creep characteristics of the matrix layer surrounding the fiber, the test temperature, and the loading frequency. In support of these calculations, a series of elevated temperature fatigue crack growth tests was conducted to identify the crack growth behavior of the composite when subjected to different temperatures at both high and low loading frequencies. Results of this numerical/experimental work were then utilized in conjunction with a postulated fiber fracture criterion based on the notion that a competition exists between the increase in the axial fiber stress and the continuous degradation of the fiber strength due to cyclic wear induced by the interface frictional shear stress. The conclusions of this study show that the axial stress in the bridging fibers increases with an increase in temperature and with a decrease in both the loading frequency and the matrix grain size. A combination of high-temperature, low-frequency, and small-matrix grain size would enhance creep deformation of the matrix, thus leading to an increase in the rate of the load transfer from the matrix to the bridging fibers. Furthermore, the presence of a compressive residual stress state in the bridging fibers retards the time-dependent increase of their axial stress. The fatigue strength of the bridging fibers was estimated to range from 720 to 870 MPa within the temperature range of 500 to 650°C. This strength was found to depend on both the temperature and the loading frequency.

KEYWORDS: fatigue crack growth rate, fiber bridging, bridging fiber stress, fiber strength, fracture, creep, load transfer, frictional shear stress, finite element analysis

Previous studies on several unidirectional fiber-reinforced metal matrix composites (MMCs) including SCS-6/Ti-6Al-4V, SCS-6/Ti-15V-3Al-3Cr-3Sn, SCS-6/Ti-24Al-11Nb, and SCS-6/Ti-25Al-10Nb-3Cr-1Mo indicated that fiber bridging is an operative damage mechanism under loading conditions of practical interest [*1–8*]. Fiber bridging occurs when the fiber strength is sufficiently high that a fatigue crack extends through the matrix, leaving unbroken fibers in the crack wake [*9–11*]. Bridging fibers can improve the fatigue crack growth properties by carrying part of the applied load, thus shielding the crack tip. Silicon carbide (SiC) fibers used as reinforcement in these composites have several carbon-rich coatings to accommodate fiber/matrix sliding and debonding [*12,13*]. Cyclic loading of the composites with SiC fibers causes debonding between the carbon-rich coating and the SiC

[1]Graduate student and professor, respectively, Mechanics of Materials Laboratory, Department of Mechanical Engineering, University of Rhode Island, Kingston, RI 02881.

part of the fiber, while the existence of the carbon-rich region permits slippage within the coating [*14*]. During fiber bridging, the crack tip driving force is modified by the presence of the crack tip shielding as the result of load transfer from the matrix to the fibers. Thermal residual stresses arising from the mismatch of the coefficients of thermal expansion (CTEs) of the composite constituents during initial cooldown may influence the load transfer characteristics by altering the fiber/matrix interfacial properties. The combination of chemical bonding and thermally induced clamping results in high interphase shear strength, especially at low temperatures. The transfer of load is further modified by various inelastic processes occurring at or in the vicinity of the fiber/matrix interface such as matrix plasticity, interfacial debonding, and frictional sliding. The stress experienced by a bridging fiber is a function of applied load, crack length, number of bridging fibers, the load partition between uncracked and cracked regions of the composite as well as the frictional shear stress present in the fiber/matrix interface region. The fiber surface frictional-related damage could result in a severe deterioration of the fiber strength and thus decrease its ability to carry the evolving load. The objective of this work is to determine the evolution characteristics of the stress in the bridging fibers as influenced by temperature, loading frequency, residual stress state, and material variables. A link will then be established between the fiber-bridging damage mechanisms and the fiber stress state for the purpose of determining the influence of the aforementioned parameters on the bridging fiber strength.

In the next section, the composite material used and the experimental procedures employed in fatigue crack growth tests are briefly outlined. This will be followed by a description of the resulting crack growth characteristics. The stress evolution of the bridging fiber will be calculated using the finite element method, and the results will be applied in a proposed fiber fracture criterion.

Material and Experimental Procedures

Fatigue crack growth tests were conducted on SM1240/Timetal-21S composite specimens. The chemical composition of the metastable β titanium alloy Timetal-21S is (in wt %): 0.1 Fe, 16.0 Mo, 3.06 Al, 2.9 Nb, 0.2 Si, 0.22 C, 0.12 O, 0.005 N with the balance being Ti. The SM1240 fiber with a diameter of 100 μm consists of chemically-vapor-deposited SiC on a 10-μm tungsten monofilament. A dual coating of carbon and titanium diboride, each layer having a thickness of 1 μm, is deposited on the surface. The consolidated, eight-ply, unidirectional composite ($[0°]_{(8)}$) has a nominal fiber volume fraction of 35%.

Center-hole rectangular specimens measuring 75 by 4 mm, with notches cut at opposite horizontal sides of the 1.577-mm-diameter hole, were used in fatigue crack growth tests. The tests were carried out at room temperature as well as at 500 and 650°C. The room temperature tests established the baseline crack growth behavior. The 500°C test, on the other hand, is the expected service temperature, while the 650°C test represents the near upper limit use of the matrix material. All tests were carried out under a constant applied stress range of 270 $\pm$ 5 MPa with the load ratio, R, of 0.1. The two loading frequencies considered in this study were 10 and 0.1 Hz. The selection of these frequencies is based on earlier work on Timetal-21S fiberless laminates, which showed that frequencies higher than 10 Hz produced an insignificant oxidation damage effect at temperatures below 650°C, while those lower than 10 Hz showed effects related to viscoplastic deformation and oxidation at temperatures up to 650°C [*15*].

Figure 1 shows a polished and chemically etched cross section of the as-fabricated composite. The fibers are aligned in a hexagonal array with an average center-to-center distance of 150 μm. The microstructure of the heat-treated matrix alloy consists of distinc-

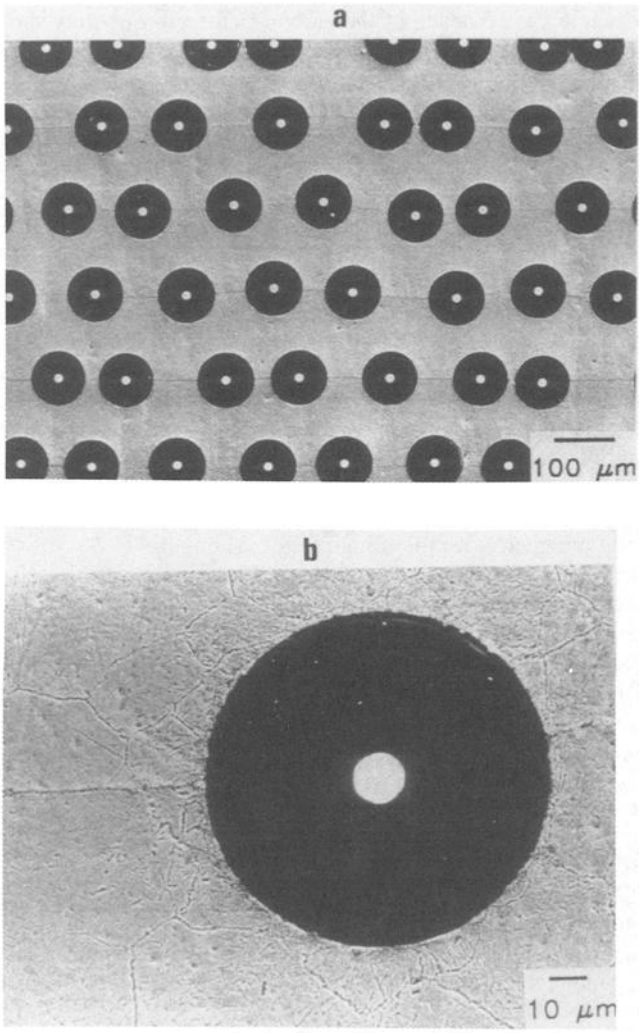

FIG. 1—*A polished and etched cross section of the as-received SM1240/Timetal-21S composite showing* (a) *the distribution of fibers, and* (b) *the region of fine matrix grains around the fiber.*

tive β grains with an average size of 80 μm containing Widmanstatten acicular α phase and a continuous grain boundary α material with a thickness of about 0.8 μm. The micrograph also reveals a distribution of small equiaxed grains immediately surrounding each fiber with an average grain diameter of 15 μm (see Fig. 1*b*). This fine-grain structure could have been the result of recrystallization during fabrication of the composite [*16*]. In high-temperature loadings, this zone with small grain size around the fibers will experience a creep deformation with a rate higher than that of the larger grain base matrix material. The effect of enhancement of creep deformation due to the existence of the duplex microstructure on the efficiency of load transfer to the fiber at elevated temperature loading is considered in this study.

The Crack Growth Process

In all the tests, the fatigue fracture process was seen to advance along a single dominant crack perpendicular to both the 0° fiber orientation and the direction of the applied load. The growth of the single crack was found to follow a trend in which the crack growth rate decreases continuously with an increasing applied stress intensity factor range (or crack length). The work in Ref *16* has associated this decrease in the crack growth rate with an increase in the number of fibers bridging the crack wake. The end of this stage is marked by the attainment of the minimum crack growth rate pertaining to the particular test condition. The first decelerated growth stage is followed by a transition to a stage that consists of repeated events of crack growth acceleration and retardation leading ultimately to crack instability and final failure of the specimen. The crack growth rate versus the applied stress intensity factor range curves limited to the first accelerated and decelerated stages in each test are shown in Fig. 2.

The 500°C/10-Hz test was repeated twice to establish the reproducibility of the observed behavior. Two additional 500°C/10-Hz tests were interrupted, one while in the initial crack growth deceleration stage and the other while in the following crack growth acceleration stage. A typical crack growth curve for this load case is shown in Fig. 2. The specimens were ground to the first layer of fibers and examined using optical microscopy to identify fractured fibers and the location of the fracture sites. Results of this work showed that all bridging fibers are intact while in the bridging stage. During the accelerated growth stage, however, several fibers at locations farthest away from the crack tip were broken along planes not coinciding with the matrix crack plane. These observations indicate that the crack growth transition from decelerated to accelerated growth is associated with the breakage of bridging fibers. In this, the fibers located near the crack mouth are the ones that have experienced the largest number of fatigue cycles, thus the greatest frictional surface wear, which in turn may result in extensive fiber strength degradation [*17*]. As the bridged crack propagates, a competition is set between the increase in the axial stress at a critical fiber cross section and the continuous decrease of the fiber strength. The failure of any of the bridging fibers would result in a decrease of the crack tip shielding, thus triggering a condition of crack growth acceleration. As will be discussed in the following section, the frictional shear stress, the component responsible for the surface wear damage of bridging fibers, is uniformly distributed along the fiber/matrix interface region. Emphasis will then be placed on estimating the stress evolution in the bridging fibers at a plane coinciding with the tip of the debonded interface since at this position bridging fibers experience the largest stress gradient due to the presence of large stresses at the crack tip.

Stress Distribution in Bridging Fibers

The stress distribution in the constituents of the composite and the evolution of fiber stress in the bridging fibers are predicted using the finite element method. Based on the fiber arrangement in this composite (see Fig. 1*a*), the fiber distribution is idealized as a hexagonal array architecture. A unit cell is then modeled as two concentric cylinders of a fiber with radius, r_f, and a matrix phase with an outer radius of $r_m = r_f/\sqrt{v_f}$, where $v_f = 0.35$ is the fiber volume fraction of the composite. A section of this axisymmetric cylinder is discretized into finite elements with the mesh shown in Fig. 3. The SiC fiber, SM1240, is assumed to behave elastically for all loading conditions, with elastic modulus, $E_f = 400$ GPa; Poisson ratio, $\nu = 0.22$; tensile strength, $\sigma_u = 3750$ MPa, and the temperature-dependent coefficient of thermal expansion (CTE) [*13,18*] (see Fig. 4). The elastic modulus, CTE, and yield limit of the Timetal-21S matrix alloy were also considered to be temperature-dependent [*15*], as

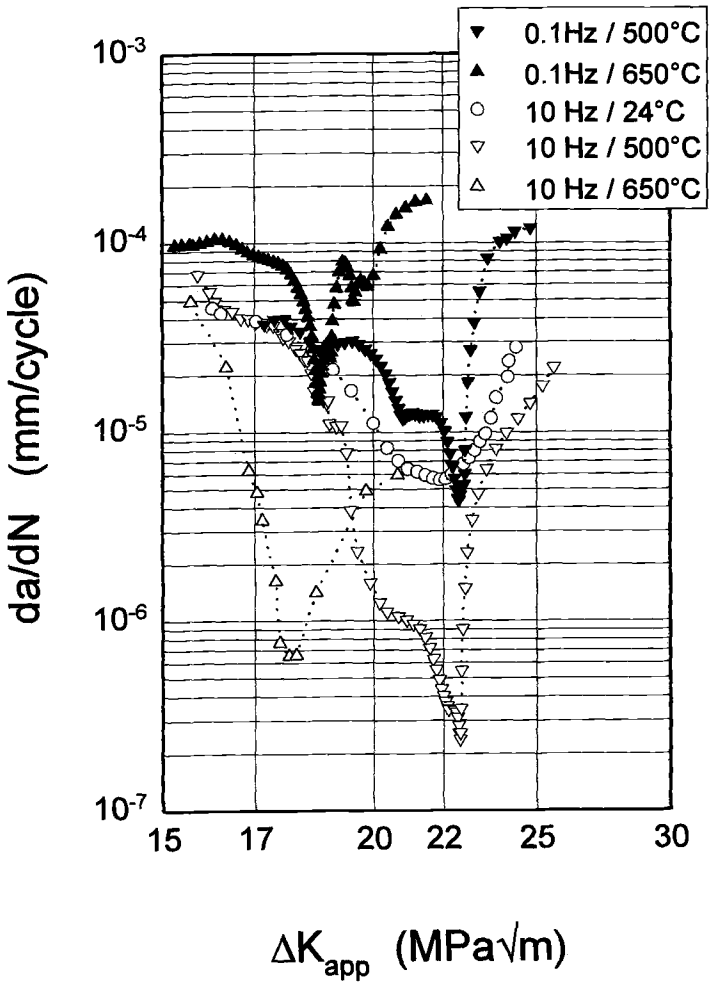

FIG. 2—*Fatigue crack growth rate,* da/dN, *versus the applied stress intensity factor range,* ΔK_{app}, *during the initial crack growth deceleration and acceleration stages.*

shown in Fig. 4. The creep properties of the matrix alloy are based on limited experimental data [*19,20*], and the creep behavior is represented by Bailey-Norton's equation in the transient and the steady-state stages of creep deformation [*21*]. The effect of duplex microstructure of the matrix phase is approximated by the assumption that the strain rate varies inversely proportional to the square of the grain diameter for self-diffusion creep [*22*].

The loading sequence of the present simulation includes cooldown from consolidation temperature to room temperature at a rate of 0.1°C/s, followed by reheating to the test temperature and the application of cyclic loading. The fiber/matrix interface is assumed to be perfectly bonded throughout cooldown from fabrication to room temperature and subsequent reheating to the test temperature. At the test temperature, the matrix crack and fiber/matrix interfacial debonding are introduced simultaneously. The outer surface of the matrix is maintained vertical in order to preserve the displacement compatibility of the unit cell

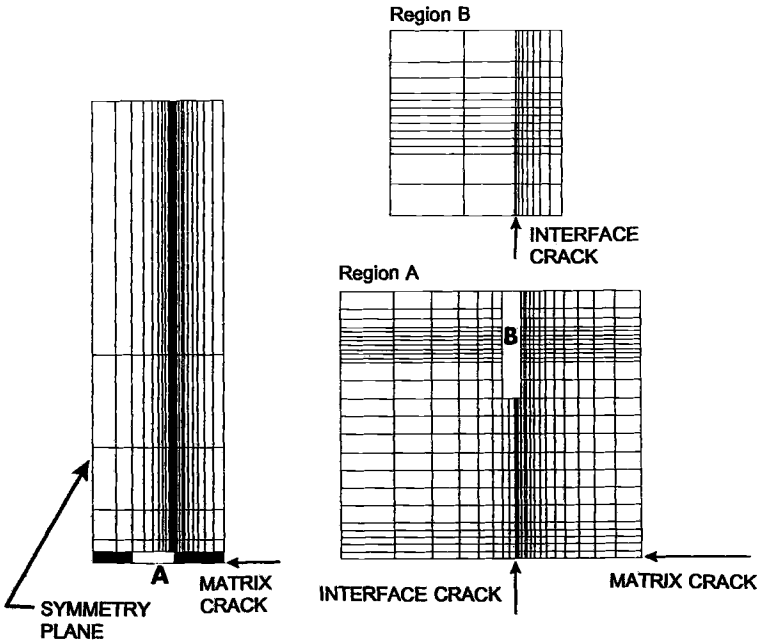

FIG. 3—*Finite element mesh employed in modeling the response of bridging fiber under cyclic loading.*

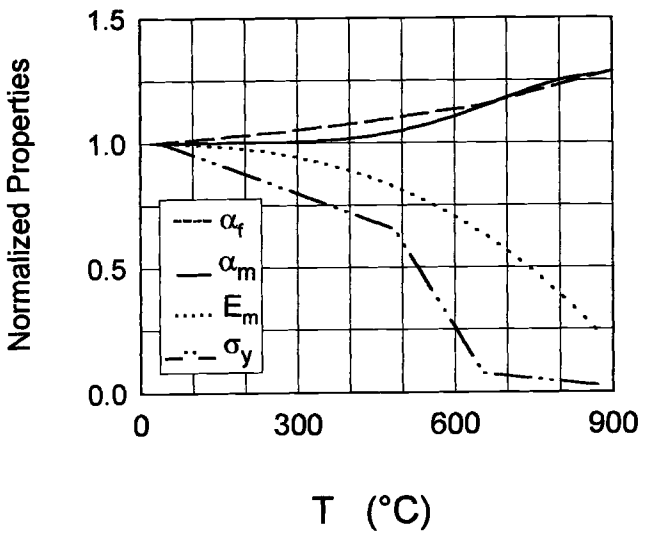

FIG. 4—*Young's modulus,* E, *yield strength,* σ_Y, *and coefficient of thermal expansion,* α_m, *for the Timetal-21S matrix alloy and the coefficient of thermal expansion,* α_f, *for the SM1240 fiber. The properties are normalized by their respective values at 24°C:* E_{RT} = *94 GPa,* $\sigma_{Y,RT}$ = *1040 MPa,* $\alpha_{m,RT}$ = *8.41* × 10^{-6}/°C, *and* $\alpha_{f,RT}$ = *4.72* × 10^{-6}/°C.

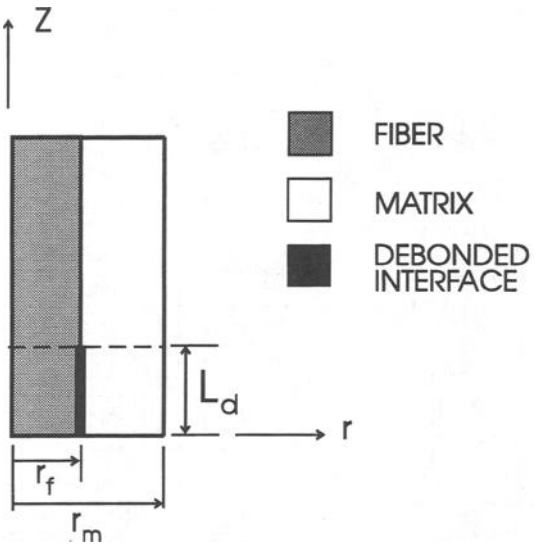

FIG. 5—*Cross section of the axisymmetric model showing the debonded length,* L_d, *radius of fiber,* r_f, *and radius of matrix cylinder,* r_m. z *and* r *are the axial and radial coordinate axes, respectively.*

with the surrounding composite. A schematic diagram of the model is illustrated in Fig. 5, defining the length of the debonded interface, L_d, and the distance, z, along the fiber measured from the plane coinciding with the matrix crack plane. These notations will be used in subsequent figures. Frictional effects are assumed to act along the fiber/matrix debonded length in the presence of compressive radial stress. The debonded length and the coefficient of friction required for use with the Coulomb law are selected so that the resulting crack opening displacement (COD) at a particular crack length matches that experimentally obtained [*14*]. This value of COD is assumed not to vary throughout the duration of the loading cycles. This assumption corresponds to the steady-state stage of the bridged crack growth where the debonded length is assumed to be stable [*23*].

Table 1 summarizes the test cases considered in this study. The variables being investigated are temperature, loading frequency, residual stress state, and the grain size of the fiber-surrounding matrix material. When the bridged crack reaches a length at which deceleration/acceleration crack growth transition occurs, the axial stress in the bridging fiber closest to the crack mouth is believed to have reached a maximum value. The finite element results show that the maximum axial stress in the bridging fiber is at the section coinciding with the matrix crack plane as illustrated in Fig. 6. However, fractographic analysis of SM1240/Timetal-21S composite specimens subjected to isothermal fatigue loadings showed that bridging fibers fractured at planes located above and below the matrix crack plane, as illustrated in Fig. 7. Studies on other MMCs such as SCS-6/Ti-6-4 and SCS-6/Ti-15-3-3 also reported a similar fracture feature of bridging fibers [*1,24*]. Furthermore, work by Thouless et al. [*25*] has suggested that the fracture plane of bridging fibers is at a distance from the matrix crack plane and that the location depends on the magnitude of the frictional shear stress along the fiber/matrix interface.

Typical distributions of radial and shear stress components along the fiber/matrix interface are illustrated in Figs. 8 and 9, respectively. It is noted that only a small variation of

TABLE 1—*Test parameters for the cases used in the finite element calculations.*

Test Case	Temperature, °C	Frequency, Hz	d^a
1A	500	10	1
1B	500	0.1	1
1C[b]	500	10	1
1D[b]	500	0.1	1
1E	500	10	0.3
1F	500	0.1	0.3
2A	650	10	1
2B	650	0.1	1
2C[b]	650	10	1
2D[b]	650	0.1	1
2E	650	10	0.3
2F	650	0.1	0.3

[a] $d = d_1/d_2$, where d_1 is grain size of the matrix layer in the immediate vicinity of the fiber and d_2 is the grain size of the basic matrix material.

[b] A case in which the process-induced residual stresses are not considered in the FE calculations.

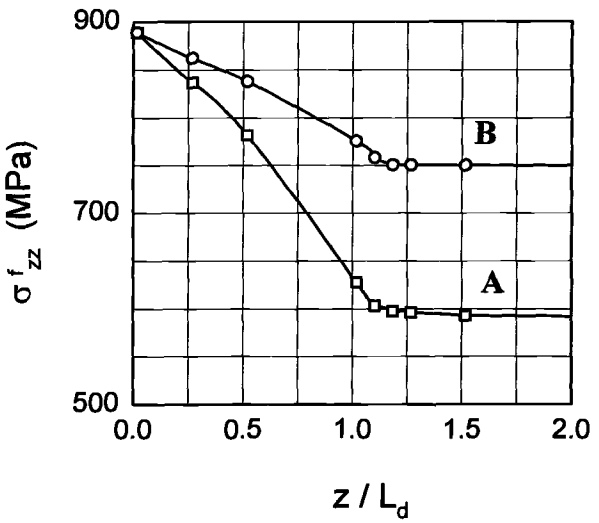

FIG. 6—*Variation of axial stress along the bridging fiber at different loading cycles. Curve A represents the stress variation after one load cycle, while curve B is the variation at the end of 500 load cycles. The debonded length,* $L_d = 1200$ *μm.*

frictional shear stress occurred along the slip length of the fiber/matrix interface, with an average value of 3.5 MPa. Consequently, it can be assumed that degradation of the fiber strength resulting from the frictional wear of the surface of the fiber is uniform, and the location of most probable failure site is determined from statistical consideration. In the crack tip region of the debonded length, the shear stress gradient is the highest due to the transition from the debonded region to the fully bonded region along the fiber/matrix interface. In addition, the evolution of the bridging fiber axial stress is most pronounced at cross sections in the vicinity of the Mode II crack tip because the residual stress state is less affected by the matrix crack and the debonding interface. Consequently, the evolution of

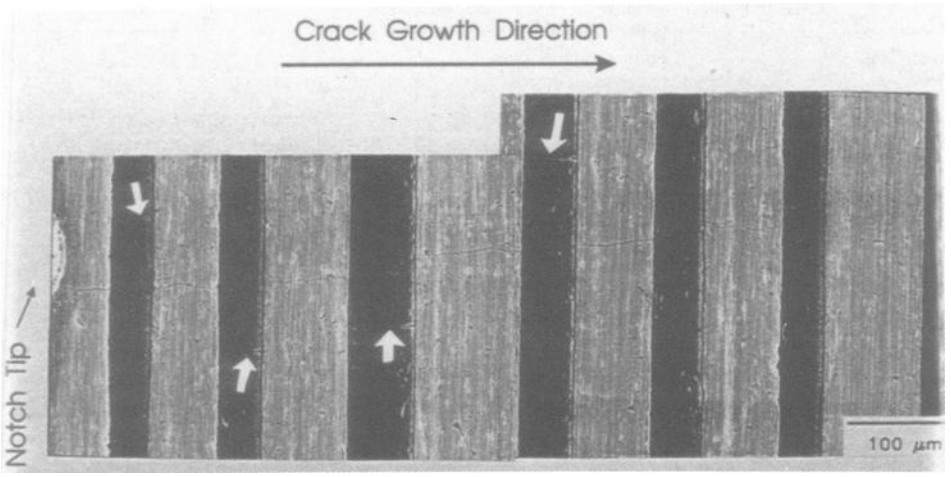

FIG. 7—*Fracture sites of bridging fibers for test condition 2B (see Table 1), marked with white arrows above and below the matrix crack plane. The dark areas are the fiber phase.*

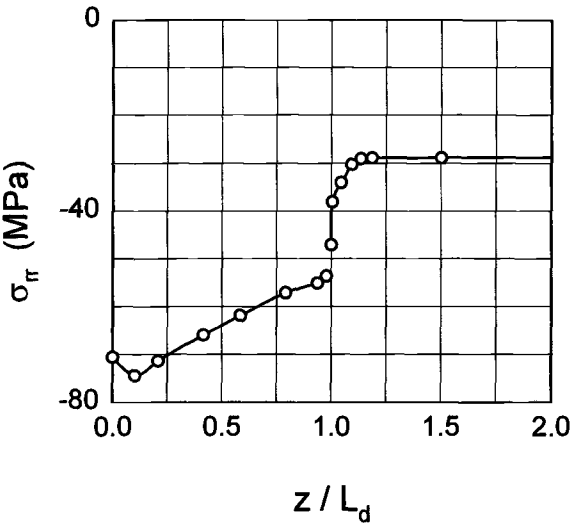

FIG. 8—*Variation of radial stress along the fiber/matrix interface at the peak of the first applied load cycle. The temperature is 650°C, and the debonded length,* L_d = *1200 μm.*

axial stress at a bridging fiber plane coinciding with the tip of the fiber/matrix interface is addressed in this study.

Stress Evolution in Bridging Fibers

The evolution of the axial bridging fiber stress at the cross section coinciding with the tip of the fiber/matrix debonded interface during fatigue loading for test cases listed in Table 1 is shown in Figs. 10*A* and 10*B* for loading frequencies of 0.1 and 10 Hz, respectively. As the

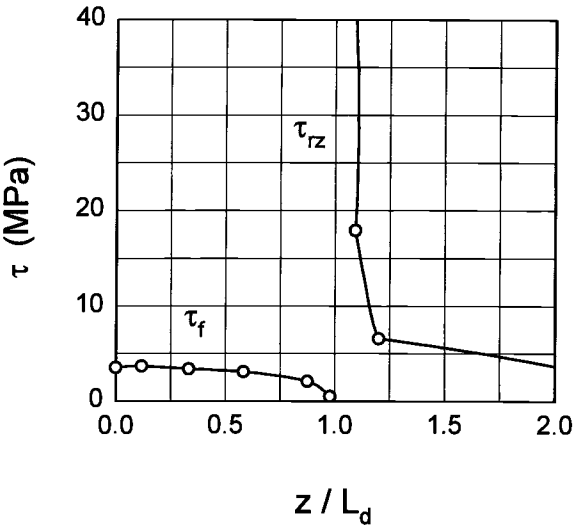

FIG. 9—*Variation of shear stress along the fiber/matrix interface. The frictional shear stress, τ_f, acts along the slip length, L_s = 950 μm, with the coefficient of friction, μ = 0.05, at test temperature 650°C. The debonded length, L_d = 1200 μm.*

loading cycles proceed, the matrix undergoes creep deformation and subsequent stress relaxation, resulting in a load transfer to the fiber. A higher level of axial fiber stress is predicted for a composite in which the fabrication-related compressive residual stress in the composite is not considered. Similarly, the fiber stress was found to increase when the layer of the matrix surrounding the fiber was assumed to consist of grain size smaller than that in the remaining of the matrix material. The presence of fine grains in the direct vicinity of the fiber enhances the stress relaxation of the matrix phase through creep deformation and thus increases the load being transferred to the bridging fiber.

Furthermore, comparison of the stress evolution curves for the 650 and 500°C tests indicates that the level of bridging fiber stress reached after the application of a certain number of load cycles is lower at lower temperature. This could be attributed to the rapid transfer of load from the matrix to the bridging fiber at a higher temperature level. For the same temperature, the material experienced the higher portion of the applied stress for a longer duration of time at a lower frequency, thus a greater contribution to matrix creep deformation, resulting in a higher level of bridging fiber stress. This contribution is also apparent in the higher slope of the evolution curve at lower frequency, which reflected a higher rate of load transfer to the bridging fiber due to stress relaxation of the matrix phase. The evolution of the fiber stress during isothermal fatigue is therefore dictated by the time-dependent deformation of the matrix, which is significant at lower frequencies.

Fatigue Strength of Bridging Fibers

As mentioned above, the transition from decelerated to accelerated crack growth is a result of the breakage of bridging fibers located near the crack mouth. The fracture of these fibers is assumed to occur when the evolving fiber stress level reached the value of the continuously decreasing fiber residual strength. This concept forms the basis for the fracture criterion of bridging fibers at elevated temperature [*26*]. The fatigue strength, S_f, is determined by locating along the fiber stress evolution curve the stress level corresponding to the

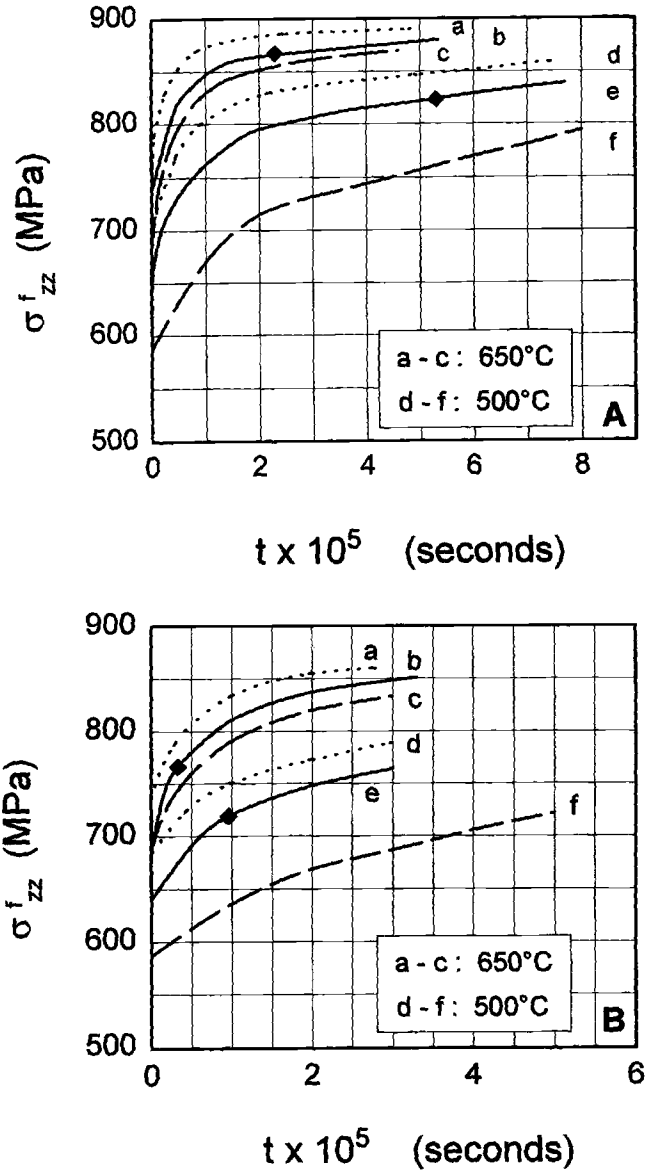

FIG. 10—*Evolution of axial stress in the bridging fiber at the loading frequencies of* (A) *0.1 Hz and* (B) *10 Hz.* ------ *without process-induced residual stress and with uniform large matrix grain size,* _____ *with residual stress and duplex microstructure of the matrix phase,* — — — — *with residual stress and uniform large-matrix grain size. The filled diamond symbols on Curves b and e represent the fatigue strength,* S_f, *of the bridging fibers.*

cycle number or the equivalent time at which the first transition to accelerated crack growth occurred, as indicated in Figs. 10*A* and 10*B* for 0.1 and 10 Hz test cases, respectively. The resulting fatigue strength, S_f, of the bridging fibers ranges from 720 to 870 MPa for the two temperature levels considered. It is further noted that the fatigue strength of the bridging fiber is both time and cycle dependent. The fiber strength at the test condition of 650°C, 10 Hz, for example, is determined as 760 MPa. As seen from Fig. 10*B*, assuming that this strength is unique for the particular briding fiber, it is then apparent that for a matrix with a uniform grain size, the presence of residual stresses due to consolidation could prolong the fatigue life of the bridging fibers. On the other hand, the absence of residual stresses would decrease the fiber life.

The influence of elevated temperatures and loading frequencies on the bridging fiber strength is summarized in Fig. 11. For the same temperature level, the bridging fiber strength increases as the frequency decreases. The decrease in frequency and the associated increase in the matrix creep rate permit the fiber stress to evolve to a higher level before the fiber surface wear generated by cyclic frictional sliding causes fiber failure. This type of competition between the fiber stress evolution and the fiber strength degradation due to frictional surface effects could also be used to interpret the observation that the number of loading cycles, and thus the fiber strength, decreases as the frequency increases, as indicated in Fig. 11. Experimental observation indicated that the number of fatigue cycles at the transition point for a loading frequency of 10 Hz is about two orders of magnitude higher than that for the low frequency of 0.1 Hz. At any frequency, the strength of the bridging fiber increases with an increasing temperature level. This is due to the fact that the frictional shear stress, which represents the degree of surface wear of the fiber, is lower at a higher temperature level. The temperature dependency of interfacial shear stress for several titanium MMC is reported elsewhere [*27,28*]. Based on the evolution characteristics of the bridging fiber stress and its postulated strength degradation during the fiber-bridging process, it is noted that the evolution of the bridging fiber stress is time dependent in nature, while the bridging fiber strength is primarily cycle dependent.

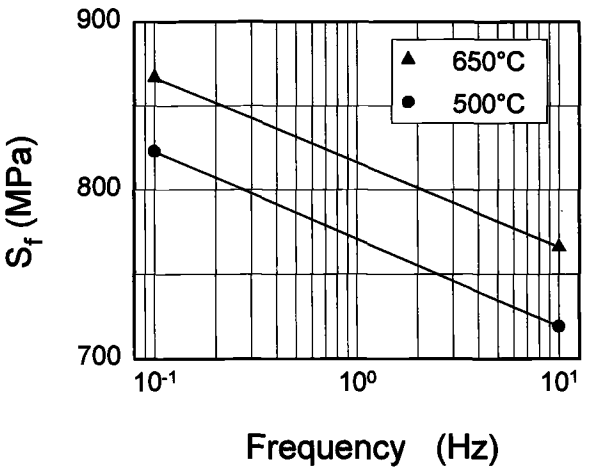

FIG. 11—*The influence of temperature and loading frequency on the fatigue strength of bridging fiber in the SM1240/Timetal-21S composite.*

Conclusions

An attempt was made to determine the evolution of stress in bridging fibers during the fatigue crack growth in a SM1240/Timetal-21S composite using the finite element method. Several parameters affecting this evolution were considered; namely, the presence of the process-induced residual stress, the creep behavior of the matrix layer surrounding the fiber, the test temperature, and the loading frequency. In support of these calculations, a series of elevated temperature fatigue crack growth tests was conducted in order to identify the crack growth behavior of the composite when subjected to different temperatures at both high and low loading frequencies. Results of this numerical/experimental work were then utilized in conjunction with a postulated bridging fiber fracture criterion based on the notion that a competition exists between an increase in the axial fiber stress and the continuous degradation of fiber strength due to cyclic wear induced by the interface frictional shear stress. The conclusions of this study are summarized as follows:

1. The stress in the bridging fibers increases with increasing temperature level and with the decrease of both the loading frequency and the fiber-surrounding matrix grain size. The rate of increase in the stress is proportional to the temperature but inversely proportional to the loading frequency and the matrix grain size. A combination of high temperature, low frequency, and small matrix grain size enhances creep deformation of the matrix, thus leading to an increase in the load being transferred to the bridging fiber. The evolution of the bridging fiber stress is basically time dependent.
2. The fiber compressive residual stress state induced during consolidation of the composite retards the time-dependent increase of the axial stress in the bridging fiber. This residual stress state decreases with increasing temperature level and number of fatigue cycles.
3. The fatigue strength of bridging fibers ranges from 720 to 870 MPa within the temperature range from 500 to 650°C, and the strength depends on both the temperature and loading frequency.

Acknowledgment

The composite material used in this study was manufactured by United Technologies, Pratt & Whitney, East Hartford, CT, as part of a joint research program between P&W, Wright-Patterson AFB Materials Laboratory and the University of Rhode Island. The authors acknowledge the contribution of Dr. M. Thompson of UTRC and Dr. T. Nicholas of WPAFB towards this program. This research was supported by USAF Office of Scientific Research under grant F49620. Dr. W. Jones is the program manager.

References

[1] Davidson, D. L., "The Micromechanics of Fatigue Crack Growth at 25 C in Ti-6Al-4V Reinforced with SCS-6 Fibers," *Metallurgical Transactions A,* Vol. 23A, March 1992, pp. 865–879.
[2] Telesman, J., Ghosn, L. J., and Kantzos, P., "Methodology for Prediction of Fiber Bridging Effects in Composites," *Journal of Composites Technology and Research,* Vol. 15, No. 3, Fall 1993, pp. 234–241.
[3] Bakuckas, J. G. and Johnson, W. S., "Application of Fiber Bridging Model in Fatigue Crack Growth in Unidirectional Titanium Matrix Composites," *Journal of Composite Technology and Research,* Vol. 15, No. 3, Fall 1993, pp. 242–255.
[4] Jeng, S. M., Allassoeur, P., and Yang, J.-M., "Fracture Mechanisms of Fiber-reinforced Titanium Alloy Matrix Composites, V: Fatigue Crack Propagation," *Materials Science and Engineering,* Vol. A154, 1992, pp. 11–19.
[5] Sensmeier, M. D. and Wright, P. K., "The Effect of Fiber Bridging on Fatigue Crack Growth in

Titanium Matrix Composites," in *Fundamental Relationships Between Microstructure and Mechanical Properties of Metal-Matrix Composites,* P. K. Liaw and M. N. Gungor, Eds., The Minerals, Metals & Materials Society, Warrendale, PA, 1990, pp. 441–457.

[6] Bowen, P., Ibbotson, A. R., and Beevers, C. J., "Characterization of Crack Growth in Continuous Fiber Reinforced Titanium Based Composites Under Cyclic Loading," *Fatigue of Advanced Materials,* R. O. Ritchie, R. H. Dauskardt, and B. N. Cox, Eds., Materials and Component Engineering Publications Ltd., PO Box 1550, Edgbaston, Birmingham B15 2JZ, UK, 1991, pp. 379–393.

[7] Ibbotson, A. R., Bowen, P., and Beevers, C. J., "Cyclic Fatigue Resistance of Fiber Reinforced Titanium Metal Matrix Composites at Ambient and Elevated Temperature," *Proceedings,* 7th Titanium Conference, San Diego, July, 1992.

[8] Brindley, P. K., Draper, S. L., Eldridge, J. I., Nathal, M. V., and Arnold, S. M., "The Effect of Temperature on the Deformation and Fracture of SiC/Ti-24Al-11Nb," *Metallurgical Transactions,* Vol. 23A, 1992, pp. 2527–2540.

[9] Evans, A. G. and He, M. Y., "Interface Debonding and Fiber Cracking in Brittle Matrix Composites," *Journal of the American Ceramics Society,* Vol. 72, No. 12, 1989, pp. 2300–2303.

[10] Marshall, D. B., Cox, B. N., and Evans, A. G., "The Mechanics of Matrix Cracking in Brittle-Matrix Fiber Composites," *Acta Metallurgica,* Vol. 33, No. 11, 1985, pp. 2013–2021.

[11] Cox, B. N. and Lo, C. S., "Load Ratio, Notch, and Scale Effects for Bridged Cracks in Fibrous Composites," *Acta Metallurgica,* Vol. 40, No. 1, 1992, pp. 69–80.

[12] Lerch, B. A., Hull, D. R., and Leonhardt, T. A., "Microstructure of a SiC/Ti-15-3 Composites," *Composites,* Vol. 21, No. 3, May 1990, pp. 216–224.

[13] Petitcorp, Y. L., Lahaye, M., Pailler, R., and Naslain, R., "Modern Boron and SiC CVD Filaments: A Comparative Study," *Composites Science and Technology,* Vol. 32, 1988, pp. 31–55.

[14] Zheng, D. and Ghonem, H., "High Temperature/High Frequency Fatigue Crack Growth Damage Mechanisms in Titanium Metal Matrix Composites," *Life Prediction Methodology for Titanium Matrix Composites, ASTM STP 1253,* W. S. Johnson, J. M. Lareon, and B. N. Cox, Eds., ASTM, Philadelphia.

[15] Ghonem, H., Wen, Y., Zheng, D., Thompson, M., and Linsey, G., "Effects of Temperature and Frequency on Fatigue Crack Growth in Ti-β21S Monolithic Laminate," *Materials Science and Engineering,* Vol. 161, 1993, pp. 45–53.

[16] Zheng, D. and Ghonem, H., "Fatigue Crack Growth of SM-1240/TIMETAL-21S Metal Matrix Composites at Elevated Temperatures," *Metallurgical Transactions A,* Vol. 26A, No. 9, 1995, pp. 2469–2478.

[17] Chan, K. S., "Effects of Interface Degradation on Fiber Bridging of Composite Fatigue Cracks," *Acta Metallurgica,* Vol. 41, No. 3, 1993, pp. 761–768.

[18] SIGMA Monofilament Products, Information Sheets, BP Metal Composites Limited, RAE Road, Farnborough, Hampshire GU14 6XE, UK.

[19] Khobaib, M. and Ashbaugh, N., University of Dayton Research Institute, Dayton, OH, October 1991, unpublished work.

[20] Martin, P. L., Bingel, W. H., and Mahoney, M. W., "SiC-Reinforced β-21S Creep Properties," *Workshop Proceedings on Titanium Matrix Components,* P. R. Smith and W. C. Revelos, Eds., April 1992, WL-TR-92-4035, Wright Patterson Air Force Base, OH, pp. 277–291.

[21] Tamin, M. N., Zheng, D., and Ghonem, H., "Time-Dependent Behavior of Continuous-Fiber-Reinforced Metal Matrix Composites: Modeling and Applications," *Journal of Composites Technology and Research,* Vol. 16, No. 4, October 1994, pp. 314–322.

[22] Reed-Hill, E. E., *Physical Metallurgy Principles,* Van Nostrand and Co., New York and London, 1964.

[23] Su, Z. and Ghonem, H., "Fatigue Crack Tip Shielding Effects in Metal Matrix Composites," Mechanics of Materials Laboratory, University of Rhode Island, Kingston, RI, Report: MML-95-2, 1995.

[24] Jeng, S. M., Nguyen, T. H. B., Dana, O., and Yang, J. M., "Fatigue Cracking of Fiber Reinforced Titanium Matrix Composites," *Journal of Composite Technology and Research,* Vol. 15, No. 3, Fall 1993, pp. 217–224.

[25] Thouless, M. D., Sbaizero, O., Sigl, L. S., and Evans, A. G., "Effect of Interface Mechanical Properties on Pullout in a SiC-Fiber-Reinforced Lithium Aluminum Silicate Glass Ceramic," *Journal of the American Ceramic Society,* Vol. 72, No. 4, 1989, pp. 525–532.

[26] Tamin, M. N. and Ghonem, H., "A Fracture Criterion for Bridging Fibers in Titanium Metal Matrix Composites at Elevated Temperature," *Proceedings,* Symposium on Durability of

Composite Materials, R. C. Wetherhold, Ed., ASME Winter Annual Meeting, Chicago, IL, 6–11 Nov. 1994, American Society of Mechanical Engineers, New York, MD-Vol. 51, pp. 51–58.

[27] Eldridge, J. I. and Ebihara, B. T., "Fiber Push-out Testing Apparatus for Elevated Temperatures," *Journal of Materials Research,* Vol. 9, No. 4, April 1994, pp. 1035–1042.

[28] Osborne, D. and Ghonem, H., "Determination of Frictional Shear Stress of SM1240/Timetal-21S at Elevated Temperature," internal report, Mechanics of Materials Laboratory, University of Rhode Island, 1994.

Larry H. Strait,[1] *Kevin L. Koudela,*[2] *Mark L. Karasek,*[1] *Maurice F. Amateau,*[3] *and James P. Runt*[3]

Thermomechanical Fatigue of Polymer Matrix Composites

REFERENCE: Strait, L. H., Koudela, K. L., Karasek, M. L., Amateau, M. F., and Runt, J. P., **"Thermomechanical Fatigue of Polymer Matrix Composites,"** *Advances in Fatigue Lifetime Predictive Techniques: 3rd Volume, ASTM STP 1292,* M. R. Mitchell and R. W. Landgraf, Eds., American Society for Testing and Materials, 1996, pp. 39–66.

ABSTRACT: The present research was undertaken to evaluate the effects of mechanical constraint on the response of polymer matrix composites during thermal cycling. Analytical and experimental techniques were used to characterize the response of carbon-fiber-reinforced cyanate ester and bismaleimide composites. Cross-ply laminates were subjected to thermal cycles from 24 to 177°C in the unconstrained, fully constrained, and overconstrained conditions. Laminate response, damage mechanisms, and residual compressive properties were characterized for each material and degree of constraint. The results of this research indicate that the level of constraint can have a significant effect on the response of polymer matrix composites during thermal cycling. However, longer-term testing is required to determine if the observed changes in response will ultimately affect the final failure mode and fatigue endurance of the materials.

KEYWORDS: bismaleimide, composites, cyanate ester, thermomechanical fatigue

Thermomechanical fatigue occurs when a structural component is subjected to thermal cycling under mechanical constraint and/or superimposed mechanical loading. Structural components subject to thermomechanical loading include aircraft engine components and support structure, heat exchangers, piping, etc. Traditionally, such components have been fabricated from metals or metal alloys, and the behavior of these materials under thermomechanical loading has been extensively investigated. However, the performance requirements for the next generation of aircraft can only be satisfied if substantial reductions in weight are realized. One means of achieving these reductions is through the use of fiber-reinforced polymer composites utilizing high-temperature matrix materials. Considerable work has been performed to characterize the effects of temperature on the physical and mechanical properties of these materials, and the effects of unconstrained thermal cycling have been documented in the literature [*1–7*]. Unfortunately, little or no information is currently available regarding the effects of thermomechanical fatigue, i.e., constrained thermal cycling, on polymer matrix composites. The present research examines the effects of mechanical constraint on the behavior of carbon-fiber-reinforced cyanate ester and bismaleimide composites subjected to thermal cycling.

Defining the degree of constraint is considerably more complicated for composite materi-

[1]Research associate, Applied Research Laboratory, P.O. Box 30, State College, PA 16804-0030.
[2]Research assistant, Applied Research Laboratory, P.O. Box 30, State College, PA 16804-0030.
[3]Professor of engineering science and mechanics and professor of polymer science, respectively, The Pennsylvania State University, University Park, PA 16802.

als relative to metals or alloys. Varying degrees of constraint may exist within composite materials at the constituent (fiber and matrix) and ply levels. Varying degrees of external constraint may also be applied at the laminate level. Throughout this document, all references to degree of constraint refer to external constraint on the laminate unless otherwise specified. Thermal cycling without external constraint is referred to as unconstrained cycling in spite of the fact that constraint may be present at the constituent and ply levels within the laminate. Thermal cycling with rigid external constraint is referred to as fully constrained thermal cycling. Finally, thermal cycling with a superimposed mechanical strain is referred to as overconstrained thermal cycling. A more detailed discussion of degrees of constraint in composite materials is available elsewhere [*8*].

Materials and Methods

Prepreg consisting of Hercules IM6 carbon fiber tows in a cyanate ester resin produced by Mitsubishi Gas Chemical Company, Inc. (IM6/BT3008) was fabricated by wet filament winding. Unidirectional and cross-ply laminates of IM6/BT3008 were layed up and molded in an autoclave. Prepreg consisting of Hercules IM7 carbon fibers in a bismaleimide resin (IM7/5250-4) was purchased from BASF Structural Materials, Inc. Cross-ply laminates of IM7/5250-4 were layed up and molded in an autoclave. Lamina physical and mechanical properties were generated for IM6/BT3008 as a function of temperature from 24 to 177°C. Details of the materials, fabrication techniques, and lamina-property testing are available elsewhere [*8*].

Thermomechanical Analysis

Limited analytical work was performed to predict the response of IM6/BT3008 $[0/90]_{3S}$ laminates during unconstrained, fully constrained, and overconstrained thermal cycling from 24 to 177°C. Predicted quantities include the laminate strain, constraining force, and ply stresses as a function of temperature. Ply stresses are used to explain laminate response and damage mechanisms observed experimentally. Laminate strain and constraining force are compared with experimental data to validate the analysis. The analysis accounts for changes in lamina physical and mechanical properties with temperature and for nonlinear stress-strain response where applicable. However, the analysis does not account for time-dependent deformation (creep and stress relaxation), matrix yielding, microcracking, or other damage that may accumulate during the first or subsequent cycles. Results of parametric studies are presented to demonstrate the sensitivity of the analysis with respect to the temperature dependence of the lamina properties, the nonlinear stress-strain response, and the laminate stress-free temperature.

Computer Code Generation

A computer code was generated to perform the analysis. The code is based on classical laminate theory, and its structure is similar to that of GENLAM [*9*]. However, the program has been modified to include temperature-dependent lamina physical and mechanical properties and nonlinear stress-strain response [*8*]. Input to the program includes the degree of constraint, the upper (T_{MAX}) and lower (T_{MIN}) bounds of the thermal cycle, the laminate stress-free temperature (T_{SFT}), the laminate stacking sequence or layup, the temperature-dependent lamina physical and mechanical properties, and the nonlinear stress-strain response, where applicable.

The code begins its calculations at T_{SFT} and steps the temperature down to T_{MIN} in 5.6°C increments. This imparts the correct residual stress distribution in the laminate at the start of

the thermal cycle. In the presented study, the laminate is unconstrained during this portion of the analysis. The temperature-dependent lamina physical and mechanical properties are determined at the midpoint of each temperature interval. The properties dependent on nonlinear stress-strain response are determined at the midpoint of each temperature interval and at the corresponding lamina strain. For each temperature step in the unconstrained condition, the code outputs the laminate strains in the reference coordinate system (ϵ_{XX} and ϵ_{YY}) and the ply stresses in the principal material directions (σ_{11}, σ_{22}, and τ_{12}). In the present study, the X-direction is parallel to the 0° plies in the laminate and the 1-direction is parallel to the fibers in the plies. Upon reaching the constraint temperature (T_{CON}), the code applies the appropriate boundary conditions to the laminate. In the present study, T_{CON} corresponds to T_{MIN}, and the constraint is applied by fixing the laminate strain in the X-direction (i.e., $\epsilon_{XX} = 0$ for full constraint). After the temperature reaches T_{MIN}, the code steps the temperature up to T_{MAX} in 5.6°C increments. Lamina physical and mechanical properties are determined as described previously. For each temperature step in the constrained condition, the code outputs the laminate strains (ϵ_{XX} and ϵ_{YY}), constraining force per unit width (N_{XX}), and ply stresses (σ_{11}, σ_{22}, and τ_{12}).

Baseline Analysis

The baseline analysis was performed for an IM6/BT3008 $[0/90]_{3S}$ laminate (T_{SFT} = 124°C) subject to unconstrained and fully constrained thermal cycling from 24 to 177°C. For the fully constrained condition, the following boundary condition was imposed on the laminate at the constraint temperature (T_{CON} = 24°C)

$$\epsilon_{XX} = 0$$

where ϵ_{XX} is the laminate strain in the X-direction. The 0° ply stresses in the X-direction are given as a function of temperature in Fig. 1 for both the unconstrained and fully constrained cases. The 90° ply stresses in the X-direction are given in Fig. 2. As expected, the effects of full constraint are greater for the 0° plies, which carry a larger portion of the load. The Y-

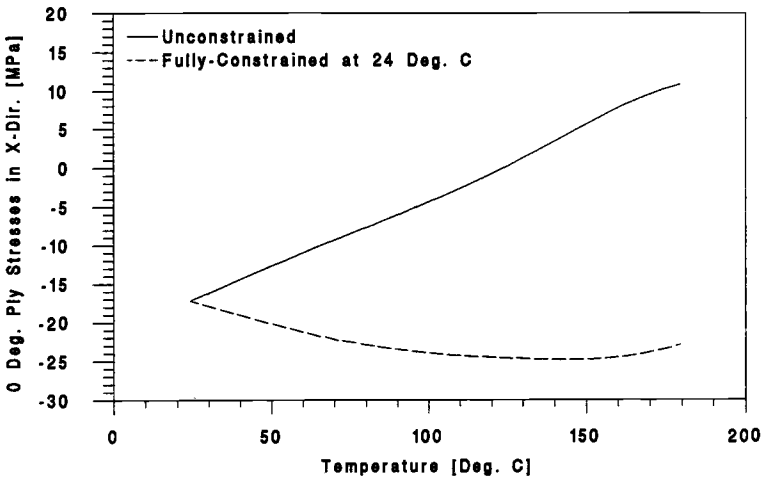

FIG. 1—*0° ply stresses in X-direction during unconstrained and fully constrained thermal cycling of IM6/BT3008* $[0/90]_{3S}$.

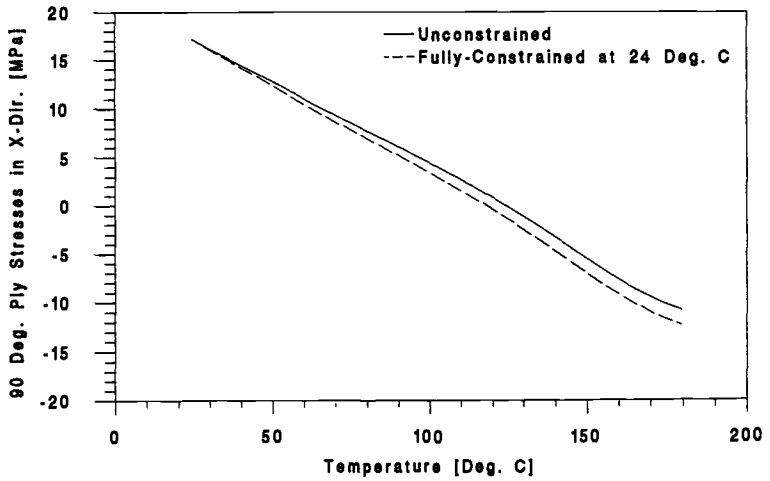

FIG. 2—*90° ply stresses in X-direction during unconstrained and fully constrained thermal cycling of IM6/BT3008 [0/90]$_{3S}$.*

direction ply stresses in the fully constrained laminate are within 4% of those in the unconstrained laminate. The small difference can be attributed to Poisson effects.

At first glance, the changes in the X-direction ply stresses with full constraint may appear insignificant. The 0° ply stress in the constrained laminate at 177°C is −23.2 MPa versus a 0° compressive strength of −317 MPa [*8*]. The 90° ply stress in the constrained laminate at 177°C is −12.0 MPa versus a 90° compressive strength of −53.1 MPa [*8*]. However, three additional points should be considered. First, it is not a static failure that is of concern here but rather the development of fatigue damage in the material over an extended service life. Second, the effects of time-dependent deformation may lead to changes in the ply stress distribution over time. These effects are of particular concern for the 90° plies in the constrained laminate where the stress level at 177°C is approximately 23% of the strength. Finally, the ply stresses presented here do not take into account any external service loads applied to the laminate. Superposition of stresses resulting from such loads could further reduce the safety factors for ply failure.

Parametric Studies

After the baseline analysis was completed, a series of parametric studies were performed to determine the sensitivity of the analysis with respect to the temperature dependence of the lamina properties, the nonlinear stress-strain response, and the laminate stress-free temperature. The temperature dependence of the lamina properties and laminate stress-free temperature were expected to have a significant impact on the ply stress predictions. The nonlinear stress-strain response was expected to have a relatively minor effect on the ply stress predictions for the $[0/90]_{3S}$ laminate due to the absence of shear strains in the plies. However, nonlinear stress-strain response was expected to play a greater role in determining the ply stresses in laminates containing a large percentage of off-axis plies in which shear strains are present.

Nonlinear Stress-Strain Response—To illustrate the effects of nonlinear stress-strain response, the baseline analysis was repeated without introducing the strain dependence of the lamina transverse and shear moduli. The effects of nonlinear stress-strain response are

minimal for the $[0/90]_{3S}$ laminate in the unconstrained and fully constrained conditions. The error in the ply stress predictions introduced by omitting the nonlinear stress-strain response is less than 5% for both the unconstrained and fully constrained laminates.

Temperature-Dependent Properties—To demonstrate the effects of temperature-dependent lamina mechanical properties, the baseline analysis was repeated using only the lamina mechanical property data generated at 24°C. Temperature-dependent lamina CTEs were utilized, and the nonlinear stress-strain response, while minimal, was considered in the determination of the transverse and shear moduli at 24°C. The 0 and 90° ply stresses in the X-direction calculated with and without the temperature-dependent lamina properties are given as a function of temperature in Figs. 3 and 4, respectively. As expected, the tempera-

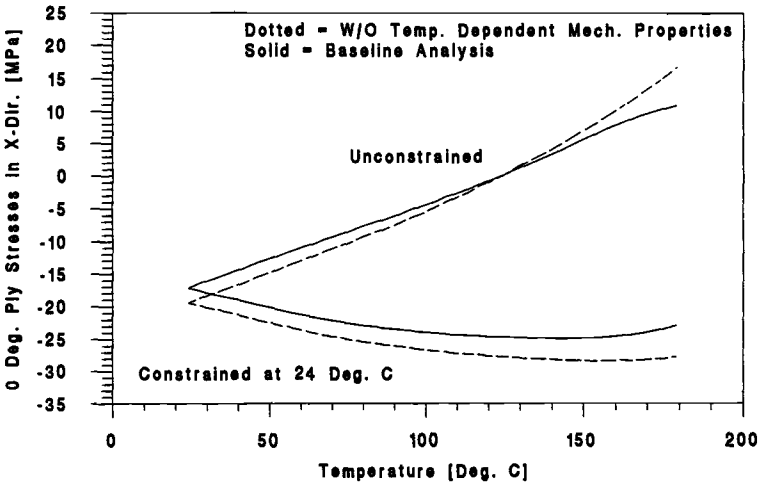

FIG. 3—*Effects of temperature-dependent properties on 0° ply stresses in X-direction during thermal cycling.*

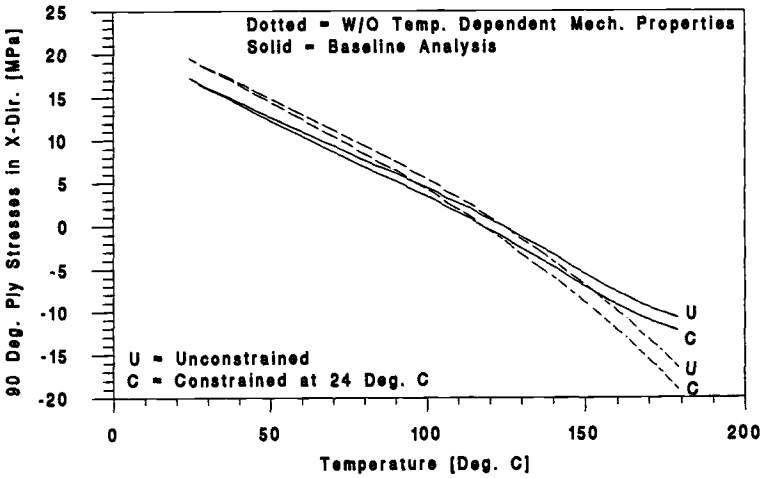

FIG. 4—*Effects of temperature-dependent properties on 90° ply stresses in X-direction during thermal cycling.*

ture dependence of the lamina properties has a significant impact on the ply stress predictions. Errors resulting from omitting temperature dependence are conservative and result in overprediction of the ply stresses.

Stress-Free Temperature—To illustrate the effects of laminate stress-free temperature (T_{SFT}), the baseline analysis was repeated with T_{SFT} set at 179°C rather than 124°C. All other parameters were consistent with the original baseline analysis. It should be noted that the choice of 179°C was not arbitrary. Initially, the maximum cure temperature (T_{CURE}) was to be used for this calculation since it is often assumed that $T_{SFT} = T_{CURE}$. However, for the IM6/BT3008 material, T_{CURE} was 200°C, while mechanical property data were determined only up to 177°C. A lower value of T_{SFT} (179°C) was chosen to avoid errors resulting from extrapolating the mechanical property data beyond the upper bound of the available test results. The 0 and 90° ply stresses in the X-direction calculated with T_{SFT} set at 124 and 179°C are given as a function of temperature in Figs. 5 and 6, respectively. As expected, T_{SFT} has a significant impact on the ply stress predictions. Assuming a higher T_{SFT} can result in a substantial overprediction of the tensile stresses present in the 90° plies at 24°C. Increasing T_{SFT} from 124 to 179°C increases the predicted value of the 90° ply stress at 24°C from 17.2 to 27.4 MPa. The 90° tensile strength of IM6/BT3008 is 39 MPa at 24°C [*8*]. Thus the 55°C increase in T_{SFT} increases the 90° ply stress from 44 to 70% of the static strength. Had T_{SFT} been set at the cure temperature (200°C) as is often the case when T_{SFT} is not known, the predicted value of the 90° ply stress would have been even higher.

Overconstrained Cycling

The baseline analysis examined the fully constrained case with the constraint temperature (T_{CON}) set at 24°C. This case is representative of a structure for which the composite subcomponents are manufactured separately and attached in a secondary operation that takes place at ambient temperature and provides a precise fit-up with no gaps or prestress. The composite subcomponents exhibit residual stresses imposed during cool down from the processing temperature due to the mismatch in CTE between the constituents and between plies of different orientations. No external constraint is present at ambient temperature. On

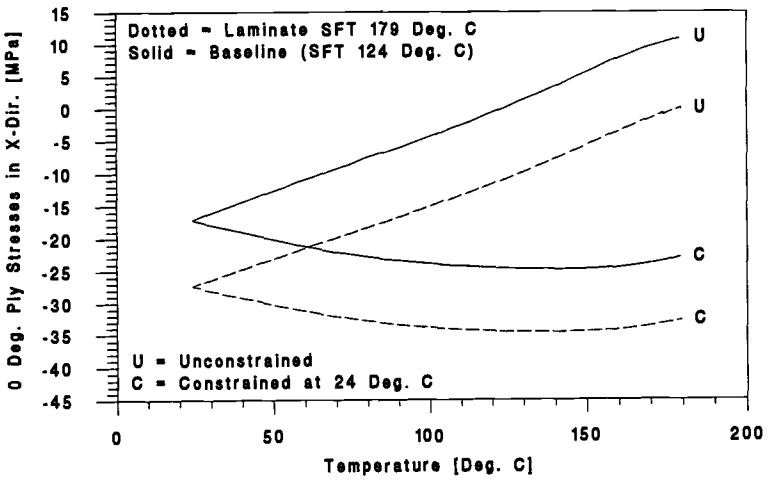

FIG. 5—*Effects of stress-free temperature on 0° ply stresses in X-direction during thermal cycling.*

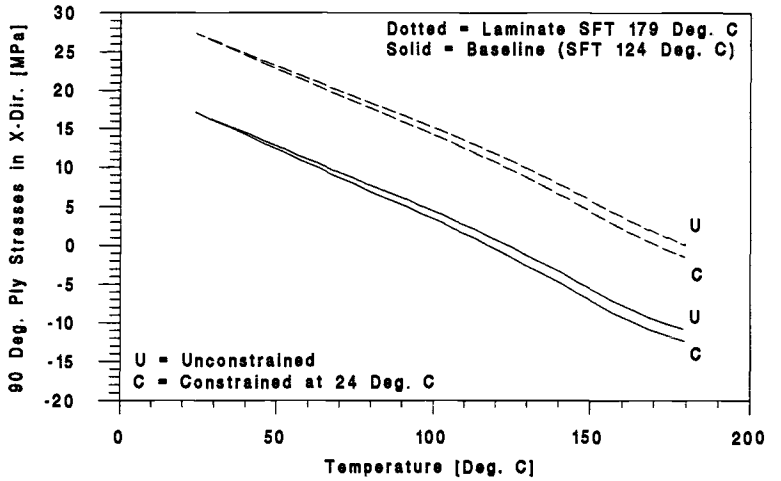

FIG. 6—*Effects of stress-free temperature on 90° ply stresses in X-direction during thermal cycling.*

heating, the composite expands/contracts against the surrounding structure, which remains fixed due to large thermal mass or active cooling systems. The resulting stresses are superimposed on the residual stresses, which are locked in by the constraint. An alternative case of practical importance is the overconstrained case with T_{CON} set at 24°C. This case is representative of structures similar to those of the fully constrained case but lacking large thermal mass or active cooling systems. In such cases, the composite subcomponents are forced to expand/contract by the surrounding structure, which is typically composed of a metal alloy with a relatively large CTE.

To illustrate the effects of overconstrained thermal cycling, an analysis was performed for an IM6/BT3008 $[0/90]_{3S}$ laminate subject to overconstrained thermal cycling from 24 to 177°C. The parameters used in the analysis were similar to those used for the baseline case including T_{CON}, which remained at 24°C. However, the full-constraint condition ($\epsilon_{XX} = 0$) imposed at T_{CON} in the baseline analysis was replaced by an overconstrained condition defined as follows

$$\epsilon_{XX} = \alpha_{CON}(T - T_{CON})$$

where ϵ_{XX} is the laminate strain in the X-direction, α_{CON} is the CTE of the material applying the constraint, and T is the temperature at the midpoint of the current temperature interval. It should be emphasized that this constraint condition assumes that the structure imposing the constraint is much stiffer than the composite subcomponent due to a larger cross section and/or higher modulus material. Two variations of this case are presented, one for a Ti-6Al-4V structure with a composite subcomponent and one for a 6061-T6 Al structure with a composite subcomponent. CTE data for these materials relative to the IM6/BT3008 composite are given in Table 1.

The 0 and 90° ply stress predictions for the $[0/90]_{3S}$ layup subject to thermal cycling in the unconstrained, fully constrained, and overconstrained conditions are presented in Figs. 7 and 8, respectively. As expected, the ply stresses developed with a 6061-T6 Al constraint are more severe than those with a Ti-6Al-4V constraint due to the higher coefficient of thermal expansion of 6061-T6 Al. For the 6061-T6 Al constraint, the 90° ply stress at 177°C is 77%

TABLE 1—*Coefficient of thermal expansion (CTE) data for various materials* [8].

Material	CTE, μ/°C	
	24°C	177°C
6061-T6 aluminum	23.6	23.6
Titanium-6% aluminum-4% vanadium (Ti-6Al-4V)	9.5	9.5
IM6/BT3008 $[90]_n$	23.93	45.82
IM6/BT3008 $[0]_n$	0.404	−1.149

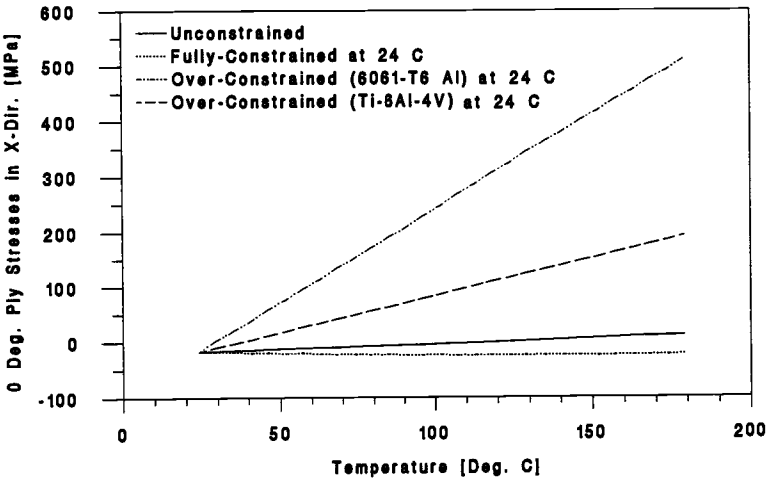

FIG. 7—*0° ply stresses in X-direction during overconstrained thermal cycling of IM6/BT3008 [0/90]$_{3S}$.*

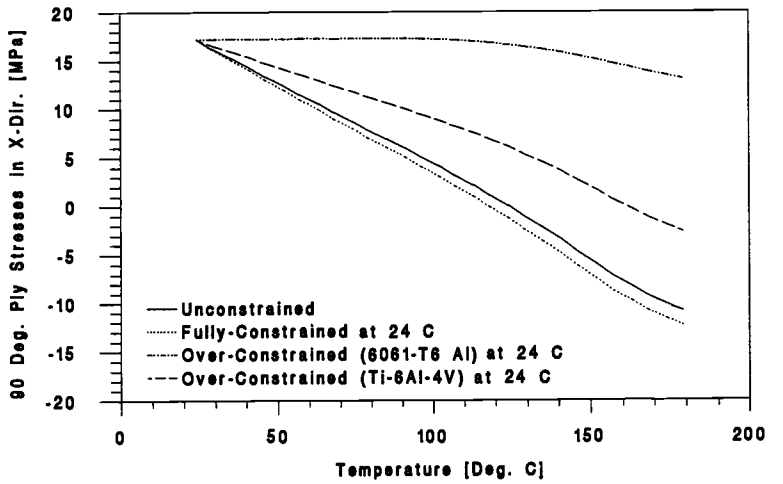

FIG. 8—*90° ply stresses in X-direction during overconstrained thermal cycling of IM6/BT3008 [0/90]$_{3S}$.*

of the transverse tensile strength [*8*]. Difficulties were encountered measuring the longitudinal tensile strength IM6/BT3008 at 177°C [*8*]. However, available data indicate that the 0° ply stress at 177°C may be as much as 35% of the longitudinal tensile strength. These results indicate that overconstrained cycling with a 6061-T6 Al constraint (T_{CON} = 24°C) represents a very severe service condition relative to unconstrained or fully constrained cycling. Fortunately, the ply stresses developed during thermal cycling in the overconstrained condition can be reduced by increasing T_{CON} to the stress-free temperature of the laminate [*8*]. In actual structures, this can be achieved by in situ curing of the composite subcomponents.

Thermomechanical Fatigue Testing

IM6/BT3008 $[0/90]_{3S}$ and IM7/5250-4 $[0/90]_{5S}$ laminates were subjected to thermal cycles from 24 to 177°C in the unconstrained, fully constrained, and overconstrained conditions. Details of the test methods and test results are provided below.

Experimental Methods

Specimen Preparation—The specimen utilized for the thermomechanical fatigue tests was based on the compression specimen described in the ASTM Test Method for Compressive Properties of Unidirectional or Crossply Fiber-Resin Composites (ASTM D 3410). A schematic of the specimen is provided in Fig. 9. This specimen was selected for its ability to accommodate tensile or compressive loads.

Coupons measuring 13.97 by 1.27 cm were machined from IM6/BT3008 $[0/90]_{3S}$ and IM7/5250-4 $[0/90]_{5S}$ laminates with the long dimension at 0°. End tabs were machined from an IM6/5250-4 $[0/90)_3/0]_S$ laminate with the long dimension at 0°. Details of the machining procedure are available elsewhere [*8*]. End tabs were bonded to the specimens with American Cyanamid HT 424 film adhesive. After end tab bonding, one edge of each specimen was polished using 220 to 4000-grit Al_2O_3 papers and 1-μm Al_2O_3 suspension on polishing cloth. Polishing was necessary to permit examination of the gage section with an optical microscope prior to and following thermomechanical cycling. After polishing, the length and width of each specimen were measured at the center of the gage section. A Type J thermocouple was bonded to each specimen at the center of the gage section. Bonding was accomplished in two steps. First, two plies of American Cyanamid FM 87-1 film adhesive were applied to the specimen and fully cured. These plies were necessary to electrically isolate the thermocouple from the conductive composite. Next, the thermocouple was bonded to the specimen using two additional plies of FM 87-1.

Test Equipment—Thermomechanical fatigue tests were conducted on a servohydraulic test frame equipped with hydraulic grips and a dynamic extensometer. Heating of the sample gage section was accomplished using 120-VAC, 7.75-kW/m^2, silicone rubber heating tapes. Cooling was accomplished with 69 kPa forced air. Data acquisition and control of the temperature, load, and strain set points were accomplished with a personal computer equipped with a data acquisition and control board. A schematic showing a sample loaded in the test fixture is given in Fig. 10.

To start the test, the operator inputs the level of constraint, constraint temperature (T_{CON}), the number of cycles to complete (N_{CYC}), the maximum temperature for the cycle (T_{MAX}), and the minimum temperature for the cycle (T_{MIN}). The thermal cycle begins at T_{MIN}. The computer closes the heating relay and begins to monitor the heat tape temperature (T_{TAPE}), sample temperature (T_{SAM}), load (P), and strain (ϵ). The load (unconstrained cycling) or strain (constrained cycling) is compared with the set point, and a feedback signal is output to the Instron to adjust the reading. T_{TAPE}, T_{SAM}, P, and ϵ readings are written to an output file

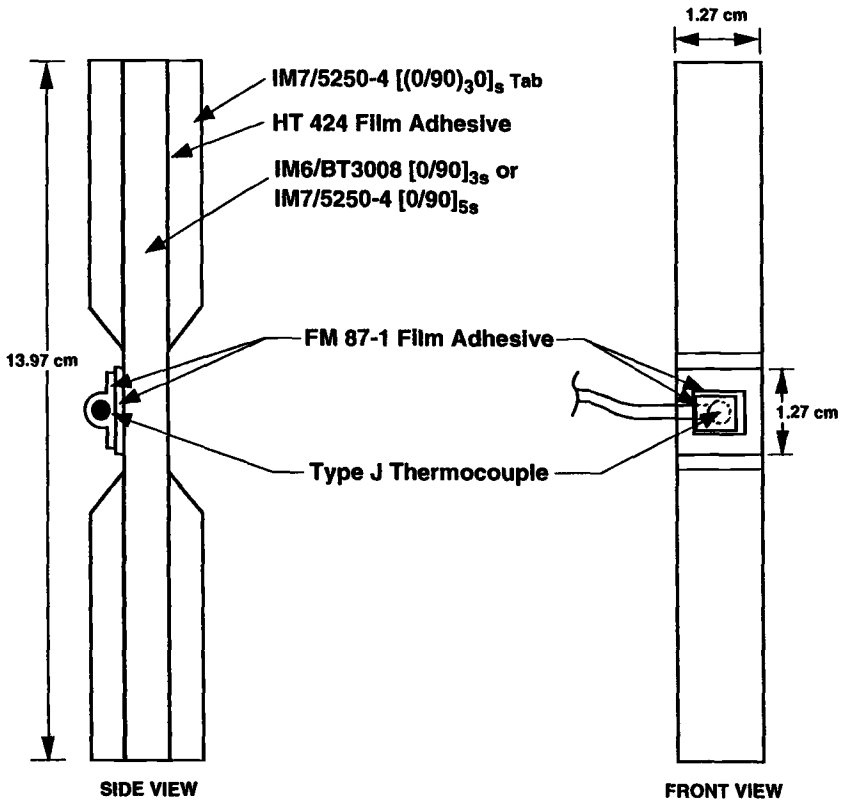

FIG. 9—*Thermomechanical fatigue specimen.*

when $T_{SAM} = T_{MIN}$ and at 5°F (2.8°C) increments on T_{SAM} thereafter. When $T_{SAM} > T_{MAX}$, the heating relay opens and the cooling relay closes. Data continue to be written to the output file at 5°F (2.8°C) increments on T_{SAM}.

Preliminary Tests—A series of preliminary tests were performed to verify the specimen design and test equipment and to establish detailed procedures for performing unconstrained, fully constrained and overconstrained tests. The resulting test methods are discussed individually in the next section.

A preliminary test was also performed to characterize the temperature gradient in the sample and to verify that the location selected for bonding the thermocouple was appropriate. An IM6/BT3008 sample was selected, and several Type J thermocouples were bonded to the surface and embedded within the sample. The sample was loaded into the test fixture and subjected to ten thermal cycles from 24 to 177°C. Readings from all thermocouples were recorded at 15-s intervals. Readings for thermocouples in the gage section were within a ±2.8°C range over the 24 to 177°C interval for all cycles. Readings for thermocouples outside the gage section lagged by approximately 28°C. These results indicated that the temperature variation in the gage section was minimal, and that a single thermocouple bonded to the surface at the center of the gage section was adequate to determine the sample temperature.

Three additional tests were performed to ensure that the temperature cycle was consistent throughout each test and between tests. A different sample was used for each test to evaluate the effects of small variations in the test setup. Data from the three tests (*A*, *B*, and *C*) are

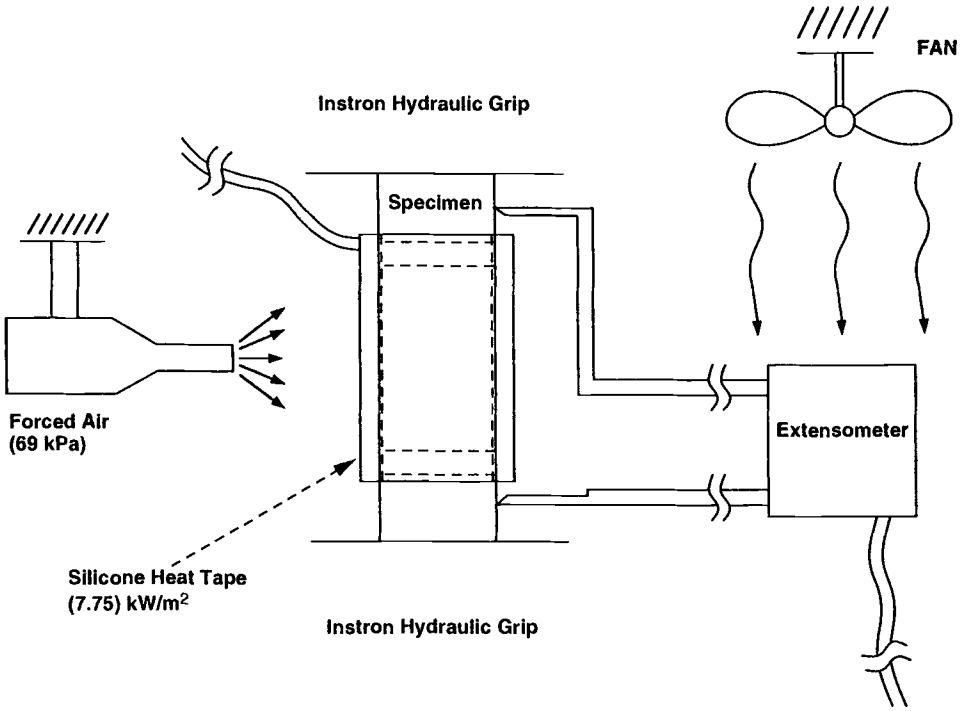

FIG. 10—*Thermomechanical fatigue test fixture.*

given in Fig. 11. Little or no variation in the temperature cycle was apparent between cycles in a given test. However, small but significant variations in the temperature cycle were observed between tests. These were attributed to slight differences in the clearance between the heat tape and the individual samples. The most important aspect of the temperature cycle is the asymmetry in the heating and cooling rates. In all cases, the heating rate is significantly lower than the cooling rate, particularly at the upper end of the thermal cycle. The effect of the asymmetry in the heating and cooling rates on the test results is discussed in detail in the section on experimental results.

Test Procedures

Unconstrained Thermal Cycling—Unconstrained thermal cycling was performed in load control. A load set point of 0 kN was maintained while the sample temperature was cycled between 24 and 177°C. The laminate strain was monitored as a function of sample temperature for comparison with analytical predictions.

Fully-Constrained Thermal Cycling—Fully constrained thermal cycling was performed in strain control. A strain set point of 0 microstrain (μ) was maintained while the sample temperature was cycled between 24 and 177°C. The load on the laminate was monitored as a function of sample temperature for comparison with analytical predictions.

Overconstrained Thermal Cycling—Overconstrained thermal cycling was performed in strain control. A strain set point of

$$\epsilon_{xx} = 23.6\text{E-}6(T - 24)$$

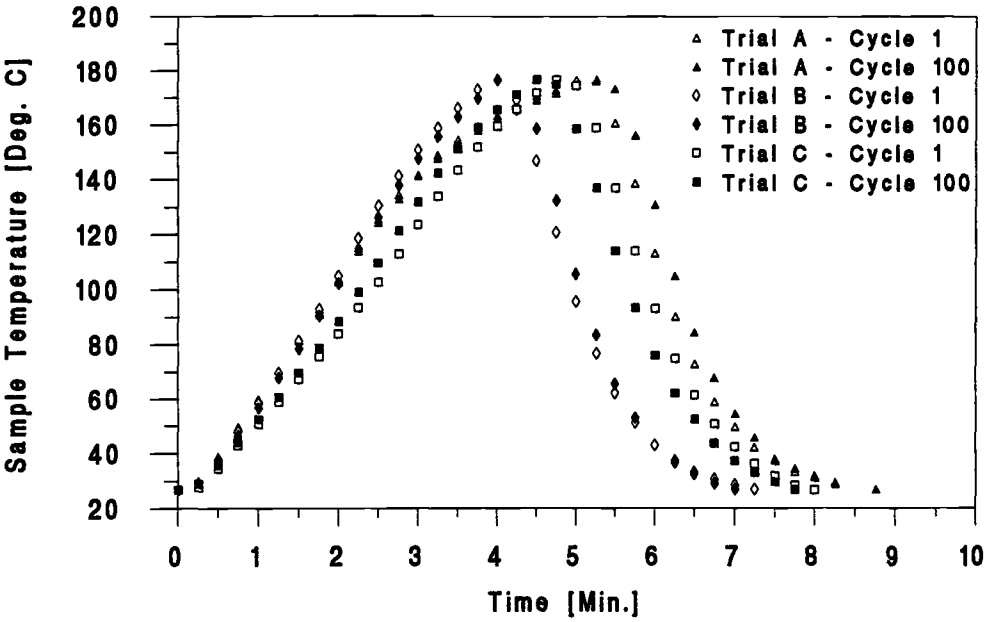

FIG. 11—*Sample temperature versus time for Trials A, B, and C (Cycles 1 and 100).*

was maintained while the sample temperature was cycled between 24 and 177°C. This corresponds to a case in which the constraining material is 6061-T6 Al. The load on the laminate was monitored as a function of sample temperature for comparison with analytical predictions.

Damage Characterization—After cycling, the polished edge of each coupon was cleaned by wiping with 1,1,1-trichloroethane and was examined using an optical microscope. The presence of matrix cracks, fiber/matrix disbonds, delaminations, and other damage was recorded.

Residual Mechanical Properties—After damage characterization, the residual compressive strength and modulus of each coupon was measured. The compression tests were performed in a Wyoming-modified IITRI test fixture. Strain measurement was accomplished with bonded strain gages. The method of attachment of the thermocouple precluded the use of back-to-back strain gages. A single gage was bonded to the surface of each coupon at the center of the gage section on the face opposite the thermocouple. Results of preliminary tests performed on coupons without thermocouples indicated that bending effects were negligible below 0.5% strain. All modulus measurements were performed using a chord from 0.1 to 0.3% strain.

Experimental Results

IM6/BT3008

Unconstrained Thermal Cycling—Experimental values of laminate strain as a function of sample temperature (Cycle 1) are given in Fig. 12 for a typical IM6/BT3008 sample in the unconstrained condition. The data are compared with the prediction from the baseline analysis. The correlation between the predicted and experimental laminate strains is good during heating to approximately 121°C, at which point the strain begins to drop off from the

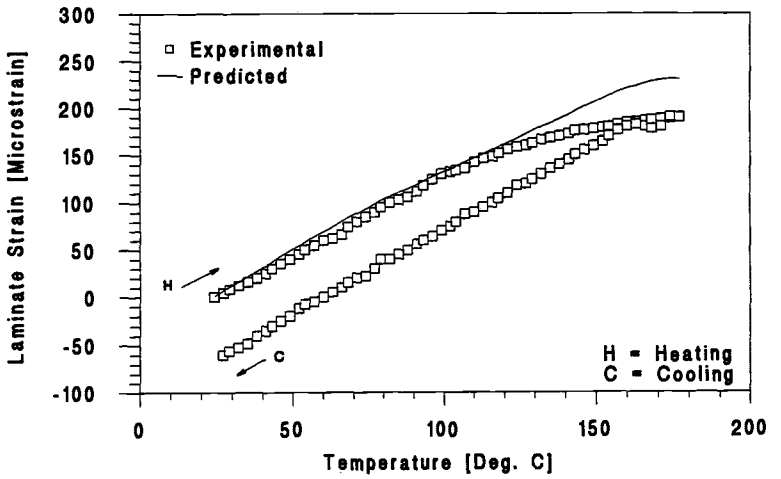

FIG. 12—*Predicted versus experimental laminate strain as a function of temperature (Cycle 1) for IM6/BT3008 $[0/90]_{3S}$ in the unconstrained condition.*

predicted values. The deviation between the predicted and experimental strain increases with temperature to the upper limit of the cycle (177°C). On cooling, hysteresis is apparent in the strain-temperature response, indicating the presence of permanent deformation in the sample. The hysteresis is attributed to time-dependent deformation in the 90° plies of the laminate. The effects of time-dependent deformation are more pronounced during heating due to the asymmetry in the heating and cooling rates at elevated temperature. Time-dependent deformation was not accounted for in the analytical model that was used to predict the laminate response. Compressive stresses develop in the 90° plies when the laminate is heated above the stress-free temperature (124°C) due to the higher coefficient of thermal expansion of the 90° plies relative to the 0° plies. Relaxation of the compressive stresses appears to occur over time at the higher temperatures, thereby releasing some of the constraint on the 0° plies and allowing them to contract. This results in a net decrease in laminate strain relative to that predicted without accounting for time-dependent deformation.

It is important to emphasize that the time-dependent deformation in the IM6/BT3008 laminate influences the ply stress distribution as well as the net laminate strain. Stress relaxation results in lower compressive stresses in the 90° plies at temperatures above 121°C than those predicted in the baseline analysis. As a result, the tensile stresses developed in the 90° plies during cooling will be higher than those predicted in the baseline analysis. The baseline analysis predicts a 90° ply stress of 17.2 MPa on cooling to 24°C. This value corresponds to 44% of the transverse tensile strength of IM6/BT3008 at that temperature. For the sample shown in Fig. 12, the hysteresis in Cycle 1 resulted in a net decrease in laminate strain of approximately 60 μ at 24°C. This corresponds to an increase of approximately 0.5 MPa in the 90° ply stress at 24°C, bringing the value to approximately 17.7 MPa or 45% of the transverse tensile strength. This increase, while small, does represent an increase in the potential for microcracking in the 90° plies.

The progression of hysteresis in the laminate strain versus temperature response for the IM6/BT3008 sample in the unconstrained condition is shown in Figs. 13 and 14. During Cycles 2 through 40, the degree of hysteresis per cycle decreases, but the net laminate strain at 24°C continues to decrease. At the end of Cycle 40, the progressive hysteresis has reduced the laminate strain by approximately 150 μ relative to the start of Cycle 1. This corresponds

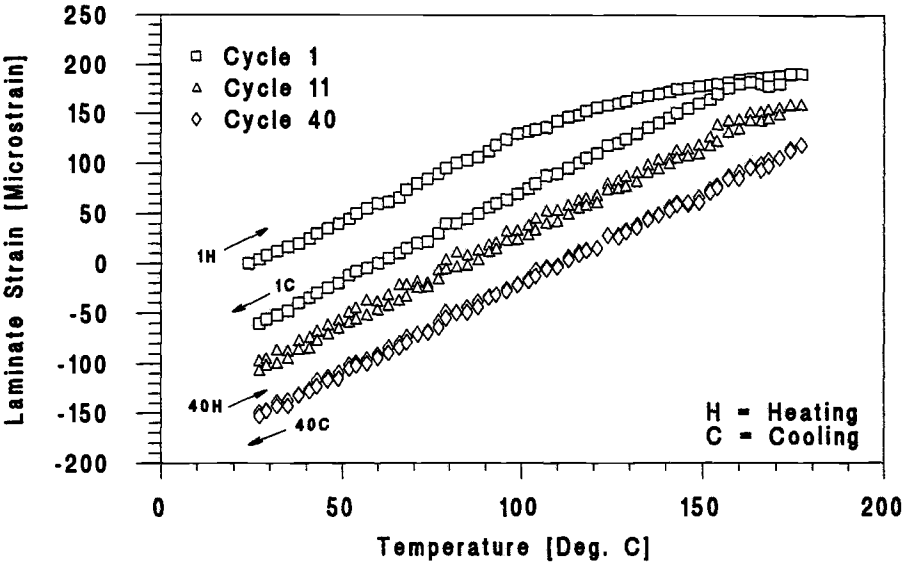

FIG. 13—*Experimental laminate strain as a function of temperature (Cycles 1, 11, and 40) for IM6/BT3008 [0/90]$_{3S}$ in the unconstrained condition.*

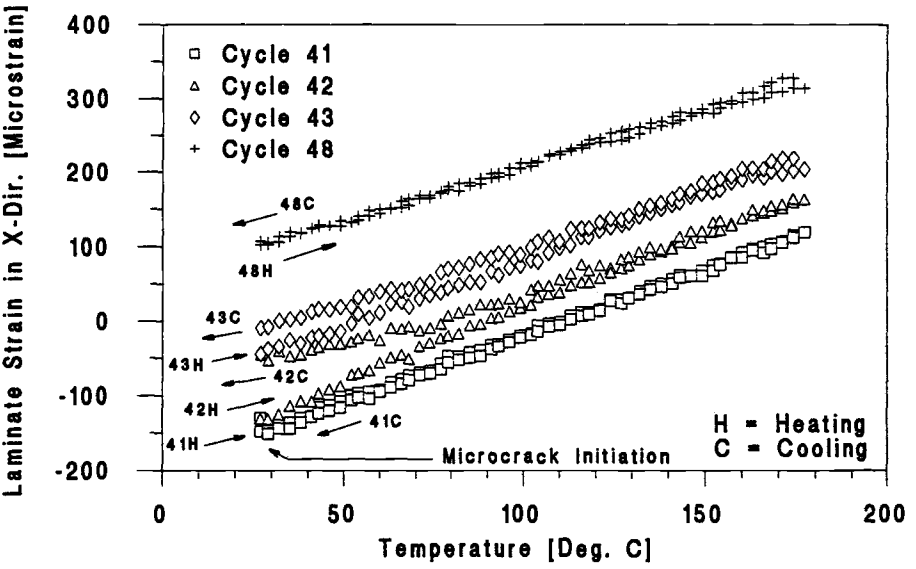

FIG. 14—*Experimental laminate strain as a function of temperature (Cycles 41, 42, 43, and 48) for IM6/BT3008 [0/90]$_{3S}$ in the unconstrained condition.*

to an increase of approximately 1.3 MPa in the 90° ply stress at 24°C, bringing the value to approximately 18.5 MPa or 47% of the transverse tensile strength. At the end of Cycle 41, there is a sharp increase in laminate strain of approximately 15 μ as the sample temperature approaches 24°C. The increase in laminate strain is attributed to the initiation of microcracks in the 90° plies. Initiation of microcracks relieves some of the tensile stress in the 90° plies, thereby reducing the constraint on the 0° plies and allowing them to expand. This, in turn, results in an increase in the laminate strain.

The data for Cycle 42 show a larger increase in laminate strain than expected for the initial heating portion of the cycle. This result suggests that the microcracks continue to propagate as long as a significant level of tensile stress is present in the 90° plies. As the temperature rises and the tensile stresses in the 90° plies are reduced, the microcracks arrest and the slope of the laminate strain versus temperature curve returns to the previous value. Microcrack propagation resumes during the latter portion of the cooling cycle as the tensile stresses in the 90° plies increase once again. The propagation of microcracks in Cycle 42 produces an increase in laminate strain of approximately 85 μ. This process is repeated in Cycles 43 through 48. With each cycle, the increase in laminate strain is reduced since the tensile stresses in the 90° plies are relieved by propagation of the microcracks. At the end of Cycle 48, the laminate strain has been increased by approximately 260 μ relative to the end of Cycle 40. This corresponds to a decrease of approximately 2.3 MPa in the 90° ply stress at 24°C, bringing the value to approximately 16.2 MPa or 42% of the transverse tensile strength.

After Cycle 48, the response of the laminate stabilizes for several cycles possibly due to the microcracks arresting at the adjacent 0° plies. Subsequently, signs of time-dependent deformation reappear at the upper end of the heating cycle, and hysteresis becomes apparent on cooling. The degree of hysteresis per cycle is considerably less than the early cycles, but results in a steady decrease in laminate strain until the initiation of additional microcracks and the corresponding increase in laminate strain. This process is repeated throughout the test as shown in Figs. 15 and 16. The maximum test duration for the present study was 1000 cycles. For the samples tested in the unconstrained condition, there were no signs of reaching a saturation crack density within 1000 cycles.

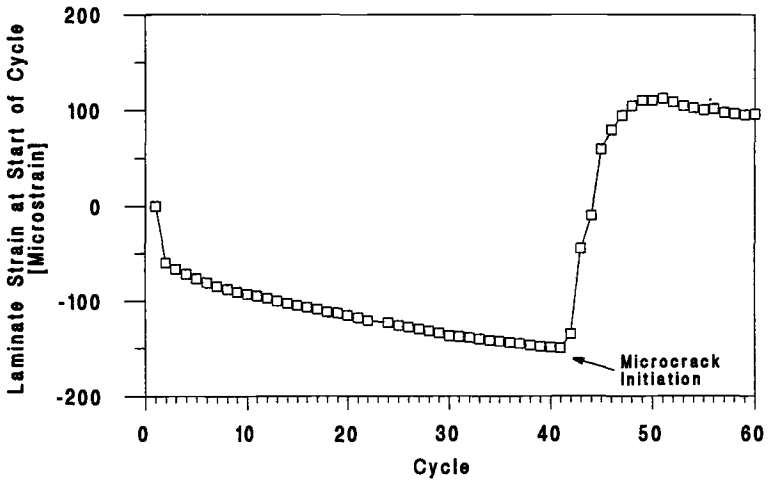

FIG. 15—*Experimental laminate strain at start of cycle (24°C) for IM6/BT3008 [0/90]$_{3S}$ in the unconstrained condition (Cycles 1 to 60).*

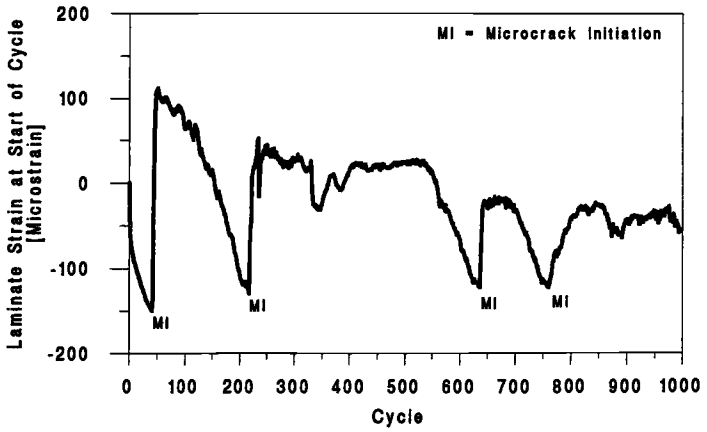

FIG. 16—*Experimental laminate strain at start of cycle (24°C) for IM6/BT3008 $[0/90]_{3S}$ in the unconstrained condition (Cycles 1 to 1000).*

The observed changes in the laminate strain versus temperature response of the IM6/BT3008 samples during unconstrained thermal cycling have been attributed to time-dependent deformation in the 90° plies, which leads to an increase in ply stress and ultimately to microcracking. This explanation is consistent with the damage observed in the IM6/BT3008 samples after cycling (Table 2). After 1000 cycles in the unconstrained condition, the samples exhibit an average transverse crack density of 23 ± 4 cracks/cm. No reduction in compressive modulus or strength is apparent relative to as-molded samples (Tables 3 and 4). This is not surprising, as the effects of microcracking on compressive properties are minimized by crack closure. Had the test duration been extended and delaminations initiated at junctions between microcracks in adjacent plies, it is likely that significant reductions in compressive properties would have been observed.

TABLE 2—*Transverse crack density in IM6/BT3008 and IM7/5250-4 laminates.*

	Transverse Crack Density, cracks/cm			
		1000 Cycles from 24 to 177°C		
Material	As-Molded	Unconstrained	Fully Constrained	Overconstrained
IM6/BT3008	0.0	23 ± 4	15 ± 4	20 ± 6[a]
IM7/5250-4	0.0	0.0	0.0	1 ± 0

[a]Significant fiber/matrix debonding observed in these coupons.

TABLE 3—*Residual compressive modulus of IM6/BT3008 and IM7/5250-4 laminates.*

	Compressive Modulus, GPa			
		1000 Cycles from 24 to 177°C		
Material	As-Molded	Unconstrained	Fully Constrained	Overconstrained
IM6/BT3008	74.5 ± 1.3	73.0 ± 2.7	73.6 ± 2.1	73.9 ± 11.3
IM7/5250-4	77.9 ± 8.6	73.8 ± 6.2	69.4 ± 0.9	81.9 ± 5.7

TABLE 4—*Residual compressive strength of IM6/BT3008 and IM7/5250-4 laminates.*

	Compressive Strength, MPa			
		1000 Cycles from 24 to 177°C		
Material	As-Molded	Unconstrained	Fully Constrained	Overconstrained
IM6/BT3008	820 ± 54	792 ± 40	798 ± 14	758 ± 11
IM7/5250-4	935 ± 99	930 ± 107	817 ± 7	873 ± 38

Fully-Constrained Thermal Cycling—Experimental values of constraining force as a function of sample temperature (Cycle 1) are given in Fig. 17 for a typical IM6/BT3008 sample in the fully constrained condition. The data are compared with the prediction from the baseline analysis. The prediction fits the data well up to approximately 110°C. The slight difference in slope is attributed to overprediction of the laminate modulus by the analytical model, which is based on classical laminate theory. Above 110°C, the load begins to drop off from the predicted values. The deviation between the predicted and experimental load increases with temperature to the upper limit of the cycle (177°C). On cooling, hysteresis is apparent in the load-temperature response, indicating the presence of permanent deformation in the sample. As in the unconstrained case, the hysteresis is attributed to time-dependent deformation in the 90° plies of the laminate. The appearance of time-dependent deformation at lower temperature in the fully constrained sample relative to the unconstrained sample is consistent with the 90° ply stress predictions from the baseline analysis. Compressive stresses develop more rapidly in the 90° plies of the fully constrained laminate relative to the unconstrained laminate. This is due to the application of a compressive constraining force that is applied to prevent expansion of the laminate and maintain the zero strain condition. As in the unconstrained laminate, relaxation of the compressive stresses appears to occur over time at the higher temperatures, thereby releasing some of the constraint on the 0° plies and allowing them to contract. This results in a net decrease in

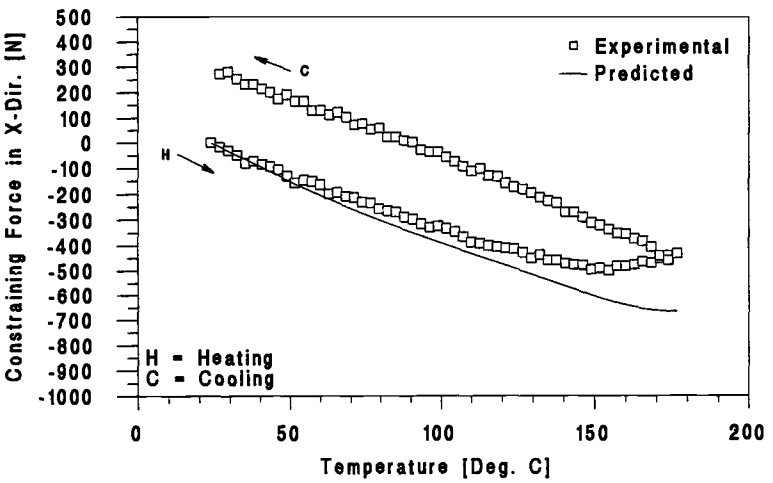

FIG. 17—*Predicted versus experimental constraining force as a function of temperature (Cycle 1) for IM6/BT3008 $[0/90]_{3S}$ in the fully constrained condition.*

laminate strain. In order to maintain the zero strain condition, the compressive constraining force must be reduced to compensate for the decrease in laminate strain resulting from time-dependent deformation. As in the unconstrained case, the effects of time-dependent deformation are more pronounced during heating due to the asymmetry in the heating and cooling rates at elevated temperature.

The time-dependent deformation in the IM6/BT3008 laminate influences the ply stress distribution as well as the constraining force. Stress relaxation results in lower compressive stresses in the 90° plies during heating than those predicted in the baseline analysis. As a result, the tensile stresses developed in the 90° plies during cooling will be higher than those predicted in the baseline analysis. The baseline analysis predicts a 90° ply stress of 17.2 MPa on cooling to 24°C. This is the same value predicted for the unconstrained laminate since the constraining force is applied at 24°C. It represents 44% of the transverse tensile strength of IM6/BT3008 at that temperature. For the fully constrained sample shown in Fig. 17, the hysteresis in Cycle 1 resulted in a net increase in the constraining force of approximately 275 N at 24°C. This corresponds to an increase of approximately 0.8 MPa in the 90° ply stress at 24°C, bringing the value to approximately 18.0 MPa or 46% of the transverse tensile strength. Recall that, for the unconstrained sample, the 90° ply stress increased to approximately 17.7 MPa or 45% of the transverse tensile strength on Cycle 1. This result suggests that the onset of microcracking should occur at a lower cycle count for the fully constrained laminate relative to the unconstrained laminate.

The progression of hysteresis in the constraining force versus temperature response for the IM6/BT3008 sample in the fully constrained condition is shown in Figs. 18 and 19. During Cycles 1 through 7, the degree of hysteresis per cycle decreases, but the constraining force at 24°C continues to increase. At the end of Cycle 7, the progressive hysteresis has increased the constraining force by approximately 460 N relative to the start of Cycle 1. This corresponds to an increase of approximately 1.4 MPa in the 90° ply stress at 24°C, bringing the value to approximately 18.6 MPa or 48% of the transverse tensile strength. At the end of

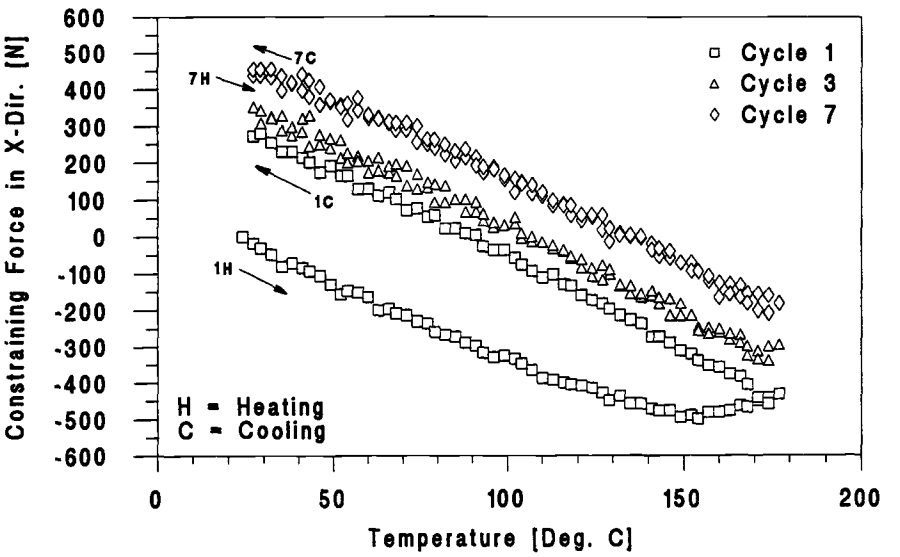

FIG. 18—*Experimental constraining force as a function of temperature (Cycles 1, 3, and 7) for IM6/BT3008 $[0/90]_{3S}$ in the fully constrained condition.*

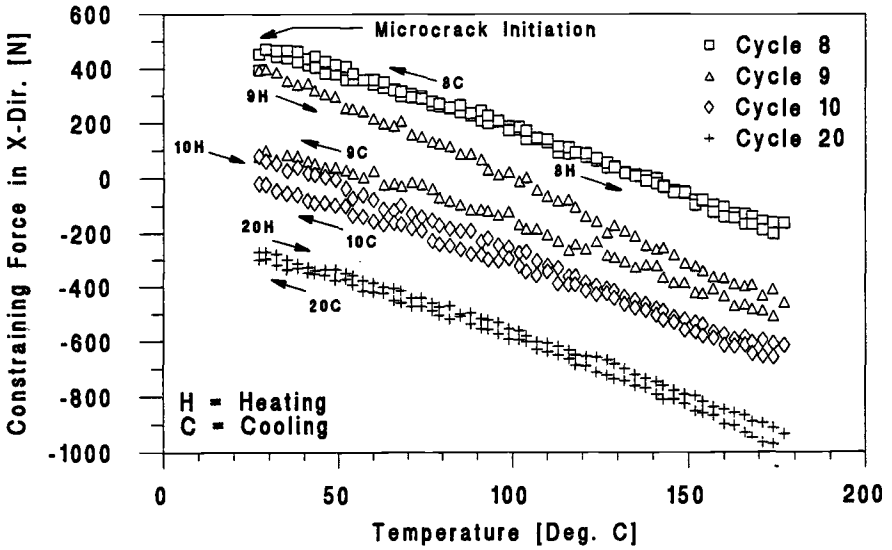

FIG. 19—*Experimental constraining force as a function of temperature (Cycles 8, 9, 10, and 20) for IM6/BT3008 $[0/90]_{3S}$ in the fully constrained condition.*

Cycle 8, there is a sharp decrease in constraining force of approximately 70 N as the sample temperature approaches 24°C. The decrease in constraining force is attributed to the initiation of microcracks in the 90° plies. Initiation of microcracks relieves some of the tensile stress in the 90° plies, thereby reducing the constraint on the 0° plies and allowing them to expand. This, in turn, results in an increase in the laminate strain and a corresponding decrease in the tensile constraining force to maintain the zero strain condition. This explanation is supported by the fact that microcrack initiation appeared to occur at approximately the same level of 90° ply stress for both the unconstrained (18.5 MPa) and fully constrained (18.6 MPa) samples. The more rapid initiation of microcracks in the fully constrained sample (8 cycles) relative to the unconstrained sample (41 cycles) is expected, considering the higher 90° ply stresses developed during heating, which result in higher hysteresis per cycle.

During Cycles 9 through 20, microcrack propagation occurs in the 90° plies of the fully constrained sample in much the same manner as described previously for the unconstrained sample. With each cycle, the decrease in constraining force is reduced because the tensile stresses in the 90° plies are relieved by propagation of the microcracks. At the end of Cycle 20, the constraining force has been reduced by approximately 760 N relative to the end of Cycle 7. This corresponds to a decrease of approximately 2.3 MPa in the 90° ply stress at 24°C, bringing the value to approximately 16.3 MPa or 42% of the transverse tensile strength. After Cycle 20, the response of the laminate stabilizes for several cycles, possibly due to the microcracks arresting at the adjacent 0° plies. It is interesting to note that stabilization of the laminate response occurred at approximately the same level of 90° ply stress for both the unconstrained (16.2 MPa) and fully constrained (16.3 MPa) laminates. As in the unconstrained case, signs of time-dependent deformation subsequently reappear at the upper end of the heating cycle, and hysteresis becomes apparent on cooling. The degree of hysteresis per cycle is considerably less than the early cycles, but results in a steady increase in constraining force until the initiation of additional microcracks and the corresponding

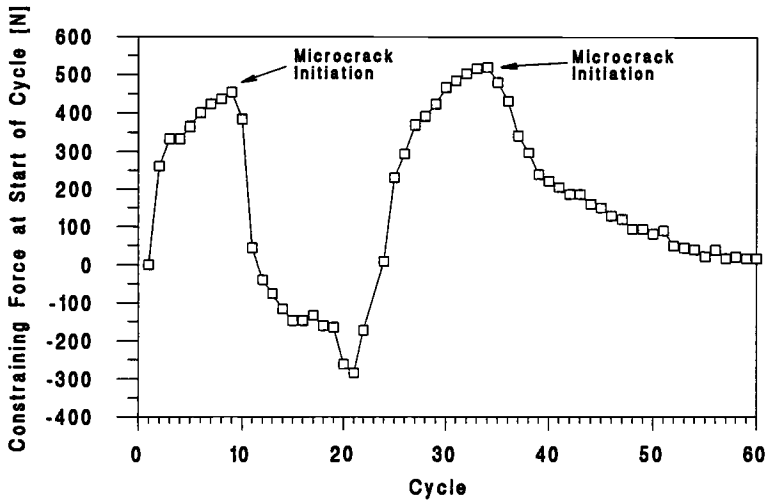

FIG. 20—*Experimental constraining force at start of cycle (24°C) for IM6/BT3008 $[0/90]_{3S}$ in the fully constrained condition (Cycles 1 to 60).*

decrease in constraining force. This process is repeated throughout the test as shown in Figs. 20 and 21. The maximum test duration for the present study was 1000 cycles. For the samples tested in the fully constrained condition, there were no signs of reaching a saturation crack density within 1000 cycles.

The observed changes in the constraining force versus temperature response of the IM6/BT3008 samples during fully constrained thermal cycling have been attributed to time-dependent deformation in the 90° plies, which leads to an increase in ply stress and ultimately to microcracking. Transverse ply cracking appears to initiate more rapidly for fully constrained samples (8 cycles) relative to unconstrained samples (41 cycles) due to the

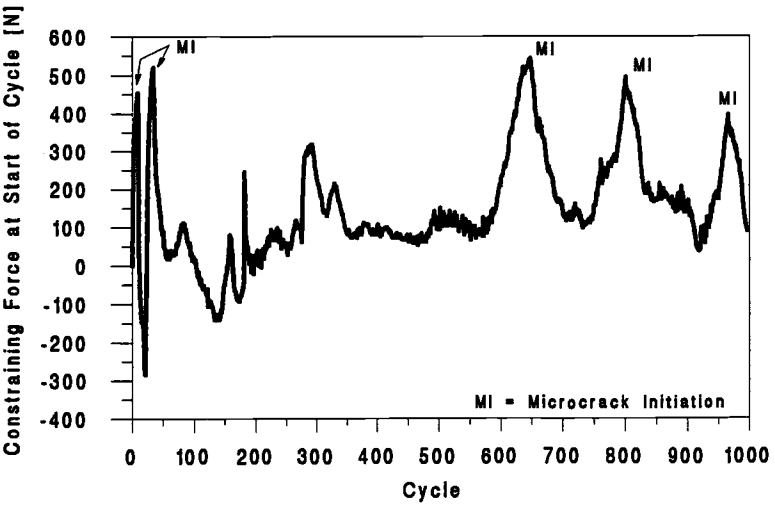

FIG. 21—*Experimental constraining force at start of cycle (24°C) for IM6/BT3008 $[0/90]_{3S}$ in the fully constrained condition (Cycles 1 to 1000).*

higher 90° ply stresses developed during heating, which result in more time-dependent deformation per cycle. However, crack density measurements performed on IM6/BT3008 samples indicate that the number of microcracks is statistically equivalent in the unconstrained and fully constrained samples after 1000 cycles (Table 2). Residual compressive properties are also equivalent for the unconstrained and fully constrained samples after 1000 cycles (Table 3). The compressive properties show no reduction relative to results for as-molded samples. This is likely the result of crack closure effects as discussed previously.

Overconstrained Thermal Cycling—Experimental values of constraining force as a function of sample temperature (Cycle 1) are given in Fig. 22 for a typical IM6/BT3008 sample in the overconstrained condition. In this case, the material applying the constraint is 6061-T6 aluminum (CTE = 23.6 μ/°C). The data are compared with the prediction from the overconstrained analysis. The prediction fits the data to within 6% over the entire temperature interval. The small deviation between the predicted and experimental values is attributed to overprediction of the laminate modulus by the analytical model, which is based on classical laminate theory. It is interesting to note that the overconstrained laminate exhibits no sign of hysteresis as observed in the unconstrained and fully constrained laminates. However, time-dependent deformation is expected based on the ply stress predictions which indicate that the 90° ply stress is 77% of the transverse tensile strength at 177°C. The lack of hysteresis in the constraining force versus temperature response can be explained in terms of the ply stress distribution. In the overconstrained samples, both the 0 and 90° plies are in tension once the temperature exceeds 30°C. Relaxation of the tensile stresses in the 90° plies over time at the higher temperatures may cause the 0° plies to carry additional tensile load, but the increase in stress is very small relative to the longitudinal tensile strength of the material. Therefore, time-dependent deformation in the 90° plies is expected to result in little or no change in the net laminate strain for the overconstrained case. Since the net laminate strain is unaffected by the time-dependent deformation, no adjustment of the constraining force is required to maintain the overconstrained condition.

In Fig. 23, constraining force versus temperature data for an overconstrained IM6/BT3008 sample during Cycle 1 are compared with similar data for Cycle 1000. Small

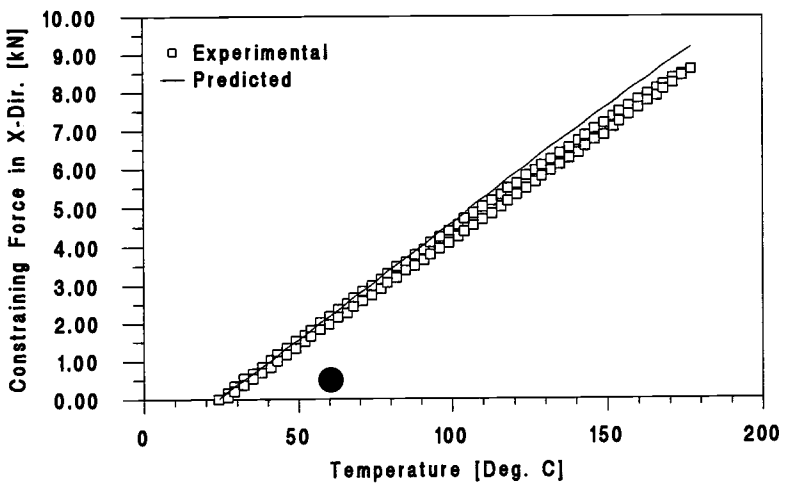

FIG. 22—*Predicted versus experimental constraining force as a function of temperature (Cycle 1) for IM6/BT3008 $[0/90]_{3S}$ in the overconstrained condition.*

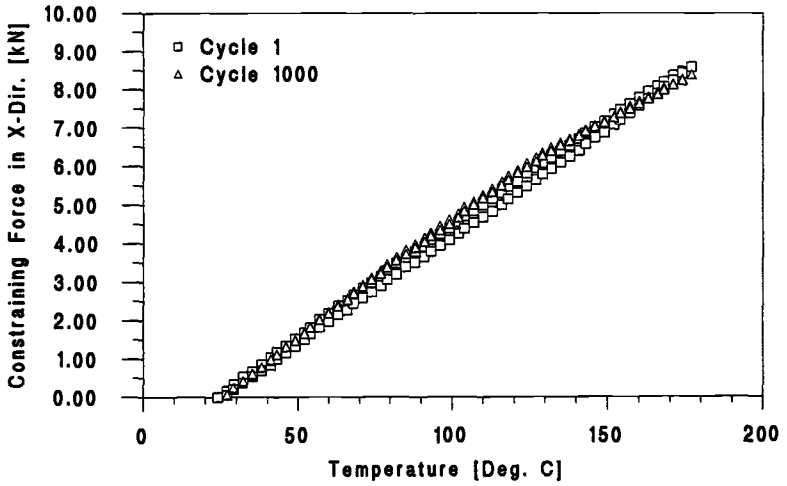

FIG. 23—*Experimental constraining force as a function of temperature (Cycles 1 and 1000) for IM6/BT3008 [0/90]$_{3S}$ in the overconstrained condition.*

but significant changes are apparent in the constraining force versus temperature response. The changes occur gradually throughout the test and are attributed to slight changes in laminate CTE and laminate modulus resulting from microcracking in the 90° plies. Crack initiation could not be traced to a specific cycle as in the unconstrained and fully constrained samples. This was due to the ply stress distribution in the overconstrained laminate (see previous paragraph). Transverse crack density measurements performed on IM6/BT3008 samples indicate that the number of microcracks in the overconstrained samples is statistically equivalent to that in the unconstrained and fully constrained samples after 1000 cycles (Table 2). However, extensive fiber/matrix debonding was observed in the overconstrained samples that was not apparent in the unconstrained or fully constrained samples. This additional damage is accompanied by a small but significant reduction in laminate compressive strength (Table 4), which suggests that failure is initiated by matrix shear failure in the 90° plies. In cases involving transverse compressive loading, it has been suggested that matrix shear failure is precipitated by failure of the fiber/matrix interfacial bond [*10*]. Thus, the presence of fiber/matrix debonding in the 90° plies of the overconstrained samples would be expected to reduce the laminate compressive strength by initiating matrix shear failure in the 90° plies at lower stress levels. The laminate compressive strength for the overconstrained samples is 8% lower than that of the as-molded samples. No significant reduction was apparent for the unconstrained or fully constrained samples where fiber/matrix debonding was not present. The residual compressive modulus for the overconstrained samples showed no reduction relative to the as-molded samples. This is probably due to crack closure effects as discussed previously.

IM7/5250-4

Unconstrained Thermal Cycling—Experimental values of laminate strain as a function of sample temperature (Cycle 1) are given in Fig. 24 for a typical IM7/5250-4 sample in the unconstrained condition. The data are compared with similar data for IM6/BT3008 discussed previously. The IM7/5250-4 laminate exhibits significantly less thermal expansion over the temperature range from 24 to 177°C. This result is consistent with the lamina

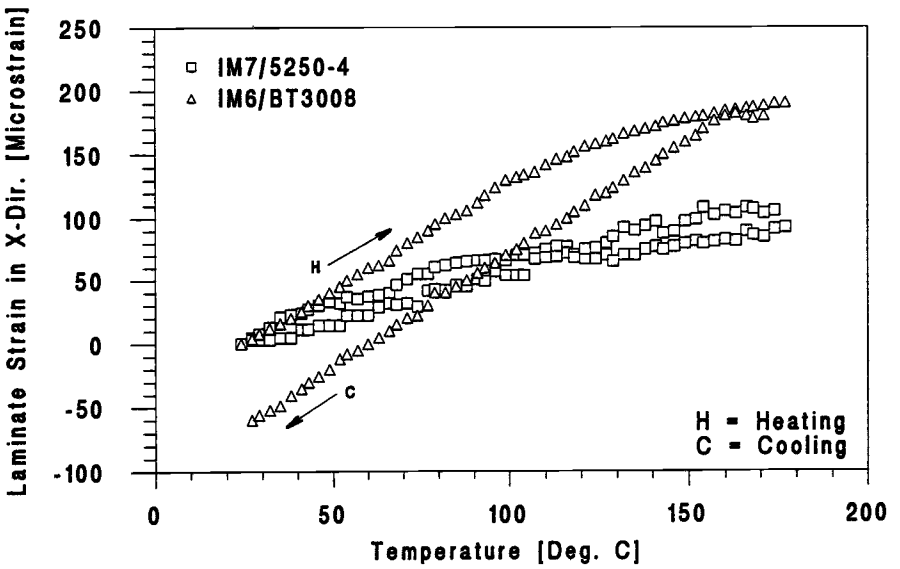

FIG. 24—*Experimental laminate strain as a function of temperature (Cycle 1) for IM7/5250-4 $[0/90]_{5S}$ and IM6/BT3008 $[0/90]_{3S}$ in the unconstrained condition.*

coefficient of thermal expansion (CTE) data for the two materials [*8*]. Temperature-dependent CTE data were unavailable for IM7/5250-4. Single values were reported without specification of the temperature range over which they were measured. The longitudinal (0°) CTE reported for IM7/5250-4 was well below the range calculated for IM6/BT3008 over the 24 to 177°C interval. The transverse (90°) CTE reported for IM7/5250-4 was at the lower end of the range calculated for IM6/BT3008. Based on this data, a significantly lower laminate CTE would be expected for IM7/5250-4.

In addition to its lower thermal expansion, the IM7/5250-4 laminate also differs from the IM6/BT3008 laminate in that it exhibits no signs of time-dependent deformation. In Fig. 25, laminate strain versus temperature data for IM7/5250-4 during Cycle 1 are compared with similar data for Cycle 1000. No hysteresis is observed in the laminate strain versus temperature response for IM7/5250-4 at any point during the test. The lack of time-dependent deformation in the IM7/5250-4 laminate is attributed to the higher T_g of the 5250-4 bismaleimide resin (300°C) relative to that of the BT3008 cyanate ester resin (221°C).

The lack of hysteresis in the IM7/5250-4 samples subjected to unconstrained thermal cycling is consistent with the observed transverse crack densities (Table 2) and residual mechanical properties (Tables 3 and 4). After 1000 cycles, no microcracking was observed in the samples, and no change in compressive modulus or strength was apparent.

Fully Constrained Thermal Cycling—Experimental values of constraining force as a function of sample temperature (Cycle 1) are given in Fig. 26 for a typical IM7/5250-4 sample in the fully constrained condition. The data are compared with similar data for IM6/BT3008 discussed previously. As discussed in the previous section, the IM7/5250-4 laminate exhibits significantly less thermal expansion over the temperature range from 24 to 177°C, which results in significantly lower values of constraining force. The IM7/5250-4 laminate also differs from the IM6/BT3008 laminate in that it exhibits no signs of time-dependent deformation. In Fig. 27, constraining force versus temperature data for IM7/5250-4 during Cycle 1 are compared with similar data for Cycle 1000. As in the

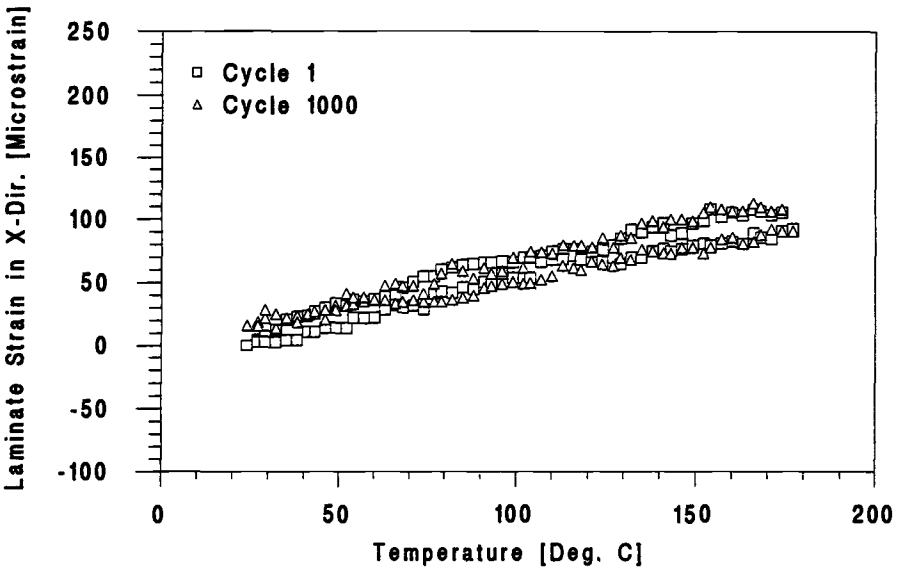

FIG. 25—*Experimental laminate strain as a function of temperature (Cycles 1 and 1000) for IM7/5250-4 $[0/90]_{5S}$ in the unconstrained condition.*

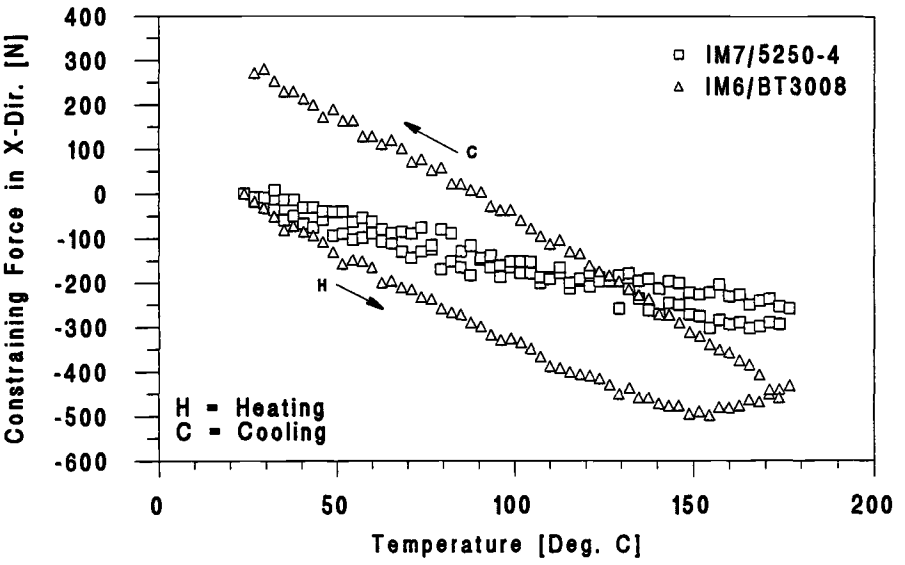

FIG. 26—*Experimental constraining force as a function of temperature (Cycle 1) for IM7/5250-4 $[0/90]_{5S}$ and IM6/BT3008 $[0/90]_{3S}$ in the fully constrained condition.*

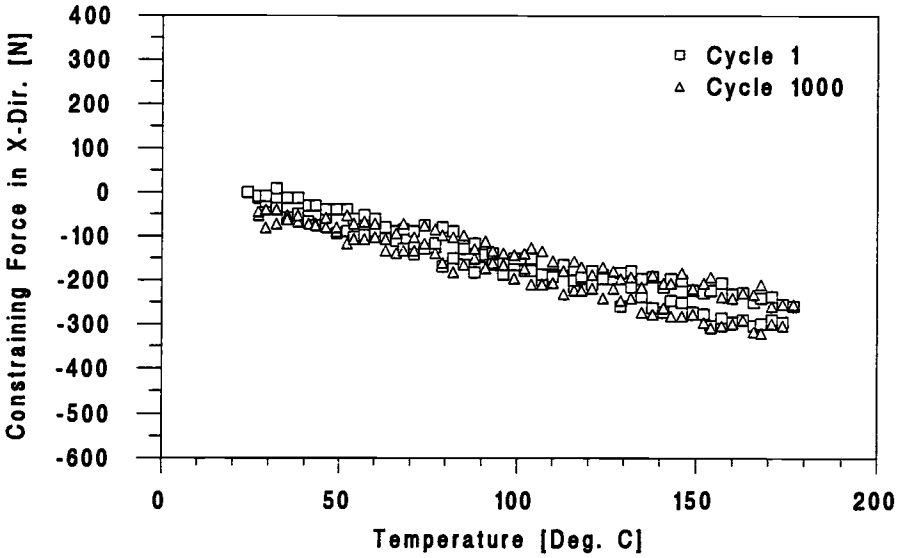

FIG. 27—*Experimental constraining force as a function of temperature (Cycles 1 and 1000) for IM7/5250-4 [0/90]$_{5S}$ in the fully constrained condition.*

unconstrained case, no hysteresis is observed in the laminate response for IM7/5250-4 at any point during the test.

The lack of hysteresis in the IM7/5250-4 samples subjected to fully constrained thermal cycling is consistent with the observed transverse crack densities (Table 2). After 1000 cycles in the fully constrained condition, no microcracking was observed in the samples. A reduction in compressive modulus was noted but was within one standard deviation in the data (Table 3). However, a reduction in compressive strength was apparent that was significant to one standard deviation (Table 4). This decrease may be due to the presence of damage not detectable using optical microscopy and not extensive enough to influence the laminate response during thermal cycling, or it may simply be an anomaly in the data. More testing will be required to make this determination.

Overconstrained Thermal Cycling—Experimental values of constraining force as a function of sample temperature (Cycle 1) are given in Fig. 28 for a typical IM7/5250-4 sample in the overconstrained condition. In this case, the material applying the constraint is 6061-T6 aluminum (CTE = 23.6 μ/°C). The data are compared with similar data for IM6/BT3008 discussed previously. Although the IM7/5250-4 laminate exhibits significantly less thermal expansion than the IM6/BT3008 laminate, its response in the overconstrained condition is nearly identical to that of the IM6/BT3008 laminate. This is attributed to the large mechanical strain applied to the laminates in the overconstrained condition, which overshadows the differences in thermal strain. Since the cross-ply layups utilized in this study include a significant number of 0° plies, the large mechanical strain results in a fiber-dominated response for both the IM7/5250-4 and IM6/BT3008 laminates. Given the similar mechanical properties of IM6 and IM7 carbon fibers, a nearly equivalent response is expected for the two materials in the overconstrained condition. The slightly higher slope of the constraining force versus temperature curve for the IM7/5250-4 laminate above 150°C is consistent with the higher T_g of the 5250-4 resin. Had the thermal cycle been extended above 177°C, it is likely that this difference would have increased with temperature.

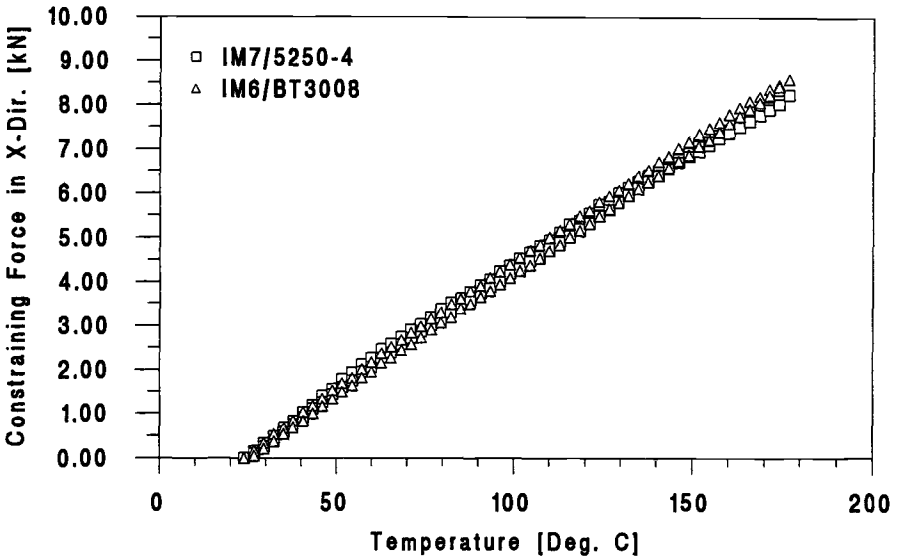

FIG. 28—*Experimental constraining force as a function of temperature (Cycle 1) for IM7/5250-4 $[0/90]_{5S}$ and IM6/BT3008 $[0/90]_{3S}$ in the overconstrained condition.*

In Fig. 29, constraining force versus temperature data for an overconstrained IM7/5250-4 sample during Cycle 1 are compared with similar data for Cycle 1000. Small but significant changes are apparent in the constraining force versus temperature response. The changes occur gradually throughout the test and are attributed to slight changes in laminate CTE and

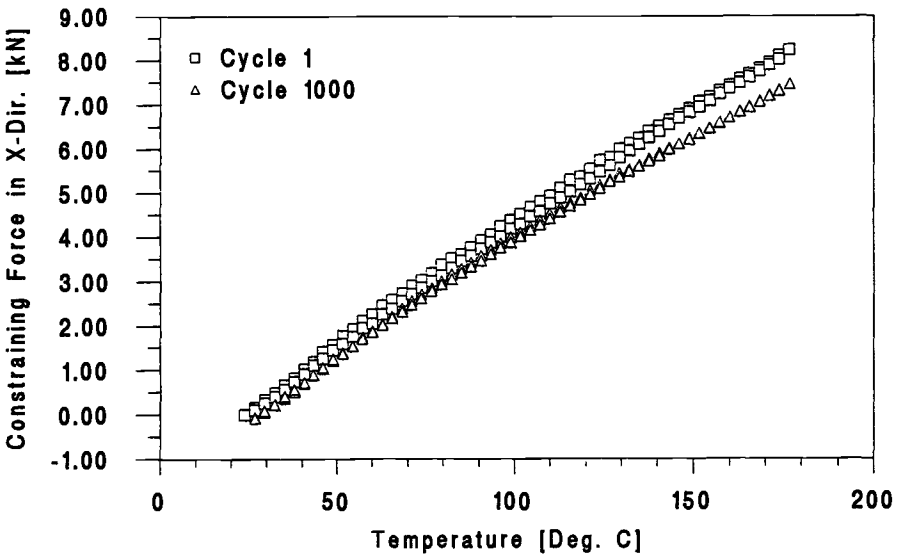

FIG. 29—*Experimental constraining force as a function of temperature (Cycles 1 and 1000) for IM7/5250-4 $[0/90]_{5S}$ in the overconstrained condition.*

laminate modulus resulting from microcracking in the 90° plies. Crack initiation could not be traced to a specific cycle. This is thought to be due to the ply stress distribution (see discussion for IM6/BT3008 in overconstrained condition). Transverse crack density measurements indicate that a small amount of microcracking did occur in the IM7/5250-4 samples cycled in the overconstrained condition (Table 2). However, this damage did not result in statistically significant reductions in compressive properties relative to as-molded material (Tables 3 and 4). This is probably due to the low crack density as well as crack closure effects.

Summary and Conclusions

The present research was undertaken to evaluate the effects of mechanical constraint on the response of carbon-fiber-reinforced cyanate ester (IM6/BT3008) and bismaleimide (IM7/5250-4) laminates during thermal cycling. Analytical and experimental techniques were used to characterize the response of cross-ply laminates subjected to thermal cycles from 24 to 177°C in the unconstrained, fully constrained, and overconstrained conditions.

Predicted ply stress distributions are significantly different for the various degrees of constraint and are highly sensitive to temperature-dependent lamina properties and laminate stress-free temperature. Predictions of laminate response correlate well with experimental results. However, deviations are apparent at elevated temperature that are attributed to the effects of time-dependent deformation. Time-dependent deformation is not considered in the present analytical model.

Changes in laminate response are observed during thermal cycling of IM6/BT3008 laminates in the unconstrained and fully constrained conditions. The changes are attributed to time-dependent deformation in the 90° plies, which leads to changes in the ply stress distribution and ultimately to transverse microcracking. Microcracking initiates more rapidly for fully constrained laminates due to higher 90° ply stresses that result in more time-dependent deformation per cycle. With continued cycling, microcrack densities for unconstrained and fully constrained laminates appear to converge and become equivalent after 1000 cycles. The ply stress distribution in overconstrained laminates is substantially different. Time-dependent deformation in the 90° plies results in changes in the ply stress distribution but does not significantly alter the laminate response. Therefore, the initiation of microcracks is not traceable to a specific point in the test. The microcrack density in overconstrained laminates is equivalent to that in unconstrained and fully constrained laminates after 1000 cycles. However, extensive fiber/matrix debonding is observed in the overconstrained laminates. This additional damage is accompanied by a small but significant reduction in compressive strength.

IM7/5250-4 laminates are unaffected by 1000 thermal cycles in the unconstrained and fully constrained conditions. A small amount of transverse ply microcracking is observed after 1000 thermal cycles in the overconstrained condition. However, this damage does not result in a statistically significant reduction in compressive strength. The superior performance of IM7/5250-4 is attributed to the higher glass transition temperature of the bismaleimide resin.

The results of this research indicate that the level of constraint can have a significant effect on the response of polymer matrix composites during thermal cycling. However, longer-term testing is required to determine if the observed changes in response will ultimately affect the final failure mode and fatigue endurance of the materials.

References

[1] Adams, D. S. and Herakovich, C. T., "Influence of Damage on the Thermal Response of Graphite-Epoxy Laminates," *Journal of Thermal Stresses,* Vol. 7, 1984, p. 91.
[2] Bowles, D. E., "Effects of Microcracks on the Thermal Expansion of Composite Laminates," *Journal of Composite Materials,* Vol. 17, 1984, p. 273.
[3] Adams, D. S., Bowles, D. E., and Herakovich, C. T., "Thermally Induced Transverse Cracking in Graphite-Epoxy Cross-Ply Laminates," *Journal of Reinforced Plastics and Composites,* Vol. 5, 1986, p. 152.
[4] Mazzio, V. F. and Mehan, R. L., "Effects of Thermal Cycling on the Properties of Graphite-Epoxy Composites," *Composite Materials: Testing and Design, ASTM STP 617,* American Society for Testing and Materials, West Conshohocken, PA, 1977.
[5] Tomkins, S. S. and Williams, S. L., "Effects of Thermal Cycling on Mechanical Properties of Graphite Polyimide," *Journal of Spacecraft,* Vol. 21, No. 3, 1984, p. 274.
[6] Owens, G. A. and Schofield, S. E., "Thermal Cycling and Mechanical Property Assessment of Carbon Fibre Fabric Reinforced PMR-15 Polyimide Laminates," *Composite Science and Technology,* Vol. 33, 1988, p. 177.
[7] Camahort, J. L., Rennhack, E. H., and Coons, W. C., "Effects of Thermal Cycling Environment on Graphite/Epoxy Composites," *Environmental Effects on Advanced Composite Materials, ASTM STP 602,* American Society for Testing and Materials, West Conshohocken, PA, 1976.
[8] Strait, L. H., "Thermo-Mechanical Fatigue of Polymer Matrix Composites," Ph.D. thesis, The Pennsylvania State University, University Park, PA, May 1994.
[9] Tsai, S. W., *Composites Design—4th Edition,* Think Composites Inc., Dayton, OH, 1988.
[10] Collins, T. A., "Transverse Compressive Behavior of Unidirectional Carbon Fiber Reinforced Plastics," *Composites,* Vol. 5, No. 3, 1974, p. 108.

D. S. Liu[1] *and B. L. Lee*[1]

Cumulative Fatigue Damage of Angle-Plied Fiber-Reinforced Elastomer Composites and Its Dependence on Minimum Stress

REFERENCE: Liu, D. S. and Lee, B. L., **"Cumulative Fatigue Damage of Angle-Plied Fiber-Reinforced Elastomer Composites and Its Dependence on Minimum Stress,"** *Advances in Fatigue Lifetime Predictive Techniques: 3rd Volume, ASTM STP 1292,* M. R. Mitchell and R. W. Landgraf, Eds., American Society for Testing and Materials, 1996, pp. 67–85.

ABSTRACT: The effects of minimum stress on cumulative damage and fatigue lifetime were assessed for an angle-plied nylon-cord-reinforced elastomer composite that represents the bias aircraft tire carcass. The *S-N* curves were established under constant minimum stress rather than constant *R*-ratio. The trends of *longer* fatigue life at a given stress range and higher fatigue endurance limit of the composite were clearly observed with a *higher* level of minimum stress. These trends stem from the fact that the stress and strain are *not* linearly related to each other. The stress-strain curve of the elastomer matrix composite exhibits strain stiffening. As a result, in a stress-controlled fatigue test, a shorter strain range or a smaller amount of strain energy is experienced for the same stress range when the level of minimum stress is raised. However, it should be noted that the levels of minimum stress used in the study happened to be safely below a critical level for the initiation of fiber-matrix debonding under static tension. As in other structural materials, the increase of applied stress level in elastomers can be regarded as an increase of the damage potential. Therefore, when the minimum stress exceeds a critical level, the damage potential effect may become dominant and a shorter fatigue life at a given stress range could be observed with a higher level of minimum stress in *S-N* curves. In the stress-controlled fatigue tests, the role of damage potential could be assessed more clearly when the fatigue life data were plotted directly against the damage parameters, such as strain range, dynamic creep rate, dissipated strain energy, and stored strain energy. The fatigue life curves based on the damage parameters at midlife showed a clear trend of a *shorter* fatigue life with a *higher* level of minimum stress. This trend could be established at a given strain range, dynamic creep rate, or dissipated strain energy. The results are in striking contrast to the trend of the *S-N* curves. The trend of a shorter fatigue life with a higher level of minimum stress was less obvious at a given stored strain energy. The values of dynamic creep rate, dissipated strain energy, and stored strain energy at midlife were found to have a power law relationship with the fatigue life of aircraft tire carcass composite.

KEYWORDS: cord-rubber composites, aircraft tires, elastomers, life prediction, fatigue damage, delamination, minimum stress

As described in previous papers [*1–3*], the angle-plied cord-reinforced elastomer composite specimens, which represent the material elements of the bias aircraft tire carcass, exhibit a large interply shear strain under uniaxial tension. Interply shear strain develops in angle-ply laminates when the constituent plies exhibit in-plane shear deformation of opposite direction but the action is prevented by mutual constraint due to interply bonding [*1,2,4–9*].

[1]Research assistant and associate professor, respectively, Department of Engineering Science and Mechanics, The Pennsylvania State University, University Park, PA 16802.

Fiber-reinforced elastomer composites exhibit unusually high levels of interply shear strain that result from the load-induced change of reinforcement angle allowed by the extreme compliance of an elastomer matrix. Above a critical value of interply shear strain, these composite specimens undergo localized failure initiated in the form of fiber-matrix debonding around the cut ends of fibrous cord reinforcements at the edge of the finite width coupons. It was found that the described critical load for the onset of fiber-matrix debonding constitutes a threshold level for infinite fatigue life, i.e., fatigue endurance limit, of the composites [*1,2*]. Under cyclic tensile stresses exceeding the endurance limit, fiber-matrix debonding was found to propagate and develop into the matrix cracking and delamination leading to gross failure of the composites.

The phenomena of debonding, matrix cracking, and delamination of elastomer matrix composites has been studied by a number of investigators [*9–22*]. Lake et al. [*9–11*] and Kawamoto and Mandell [*12*] tried to correlate delimination growth rate of angle-plied composite laminate with crack propagation characteristics of matrix elastomer (with no cord reinforcement). Pullout of fibrous cord reinforcement from the elastomer matrix and the resulting failure modes were examined in detail by Gent et al. [*13–15*]. Also related to the issue of debonding, Kendall et al. [*16–18*] studied the bonding strength and interfacial cracking of elastomer composites. Huang and Yeoh's work [*19,20*] confirmed the formation of penny-shaped cracks under cyclic tension at the edges of the laminate specimen, which was covered with strips of matrix elastomer. The growth rate of penny-shaped cracks at the cord ends could be correlated with the crack propagation characteristics of matrix elastomer. Related to the issue, there exists a considerable amount of information on elastomer fracture [*11,23–31*].

In examining the modes of damage accumulation and establishing the fatigue lifetime profile of tire materials, the authors of this paper [*1,2*] utilized specimens of steel wire cable-reinforced model composite as well as a nylon-cord-reinforced composite representing typical bias aircraft tire carcass. For both material systems, the *S-N* data were obtained under cyclic tension with constant amplitude of stress, which allows more realistic representation of footprint loading for tires. Under cyclic loading with constant amplitude of stress, the damage accumulation was accompanied by a steady increase in temperature and local strain. At a given cyclic stress range (i.e., 2 times amplitude), the use of higher frequency was found to significantly affect strain response and heat build-up characteristics of composites, thereby reducing the fatigue lifetime [*3*]. Aside from the frequency effect, another interesting observation was that with a higher level of minimum cyclic stress, the model composite with steel cable reinforcement exhibits a *longer* fatigue life at a given stress range [*2*]. This puzzling result has provoked current investigation on the effect of minimum stress on the fatigue behavior of nylon-cord-reinforced elastomer composites.

For metals, plastics, and fiber-reinforced composites with rigid matrices, the effects of minimum-stress-to-maximum-stress ratios (*R*-ratio) or mean stress on the fatigue behavior have been the subject of numerous investigations. Normally, the *R*-ratio or mean stress is kept constant in each set of experimental evaluation. As a result, the minimum stress will not be the same in each *S-N* curve for tension-tension fatigue. However, it should be noted that, in real fatigue-loading sequences for a given footprint area of tire, the minimum stress is constant due to the presence of inflation pressure. The minimum stress in fatigue is basically a static stress and therefore may be considered as a creep stress. For the case of metal, the creep effect is normally small and negligible. On the other hand, for materials with distinct viscoelastic properties, such as elastomers and elastomer matrix composites, the creep effect may not be negligible. Surprisingly few studies have been documented for the effect of minimum stress on the fatigue behavior of elastomers or elastomer matrix composites.

Although the *S-N* curves presented previously [*1–3*] were based on a fixed value of minimum stress, the level of minimum stress was chosen rather arbitrarily. In this study, the question of the creep effect on the fatigue damage and lifetime of the elastomer composites was investigated in detail by generating a series of *S-N* curves with the minimum stresses kept constant at various levels. Three different levels of minimum stress utilized were up to 20% of static tensile strength of angle-plied, nylon-cord-reinforced composite laminate. In addition to the measurement of fatigue life, the following parameters were monitored: strain range, the rate of increase in cyclic strain, dissipated strain energy, stored strain energy, and gross failure strain.

Experiments

Materials and Specimen Preparation

Flat laminate panels of a cord-reinforced elastomer composite representing bias KC-135 aircraft tire carcass were supplied by the Goodyear Tire and Rubber Co. (Akron, OH). The composite laminate was made of carbon-black-filled proprietary compound matrix and 1260/2 nylon cord reinforcement laid at an angle of $\pm 38°$ (Table 1). To avoid tension-bending coupling, the laminates were constructed with a symmetric ply layup. Coupon specimens 19 mm in width were cut from these panels, and edges were polished on a sand-belt machine. The specimen had free edges, with the cut ends of reinforcing cords exposed.

Mechanical Testing

To establish the *S-N* data, fatigue testing of composite specimens was carried out under a broad range of stress amplitude but with fixed values of minimum stress. Three different levels of minimum stress were employed: 1.38, 3.45, and 5.17 MPa. A low frequency of 1 Hz was used to minimize hysteretic heating [*3*]. Cyclic loading mode was based on a sine wave function. Fatigue life was defined at the catastrophic failure of the specimen in the form of gross delamination. Throughout the testing, the force-displacement data were recorded and the hysteresis loops were generated. The areas inside and under the hysteresis loop were measured to define dissipated strain energy and stored strain energy, respectively.

TABLE 1—*Specifications of aircraft tire carcass composite specimen; reinforcement 1260/2 nylon cord; matrix—proprietary elastomer compound.*

Composite Specimen Specifications	
Reinforcement angle	$+38°$, $-38°$, $-38°$, $+38°$
Cord modulus	2.07 GPa (300×10^3 psi)
Matrix modulus	5.51 MPa (800 psi)
Cross-sectional area of cord	0.342 mm^2 (5.3×10^{-4} in.^{2})
Specimen width	19.05 mm (0.75 in.)
Specimen thickness	6.35 mm (0.25 in.)

Results and Discussion

Minimum Stress Effects on the S-N *Relationship*

Confirming previous observations [*1–3*], the angle-plied laminate of nylon cord-reinforced elastomer composite used in this study exhibited a normal failure sequence of cord-matrix debonding developing into delamination under cyclic tension. Debonding was initiated around the cut ends of reinforcing cords at the edge of the coupons. Although debonding was observed in the very early stage of fatigue life, the extent of debonding was found to increase gradually. In the meantime, some matrix cracks formed around the debonded area, apparently due to the stress concentration. Matrix cracks widened and eventually developed into the delamination, leading to gross failure of the specimen. One unique feature of the aircraft tire carcass composite was a relatively long lifetime sustained after the onset of delamination. This tendency was more pronounced at lower stress ranges.

The *S-N* curves generated under three different levels of minimum cyclic stress (1.38, 3.45, and 5.17 MPa) were found to be linear on a logarithm scale, allowing the determination of a power law relationship (Fig. 1). A trend of *longer* fatigue life was clearly observed at a given stress range with a *higher* level of minimum stress, although the difference between the data sets for the two highest levels of minimum stress tested, 3.45 and 5.17 MPa, was relatively small (Figs. 1 and 2). As shown in the semi-log plot of Fig. 2, the use of a higher level of minimum stress also raised the fatigue endurance limit of the composite. The occurrence of a longer fatigue life for a given stress range with a higher level of minimum stress was previously observed in the case of model composites [*2*]. The current

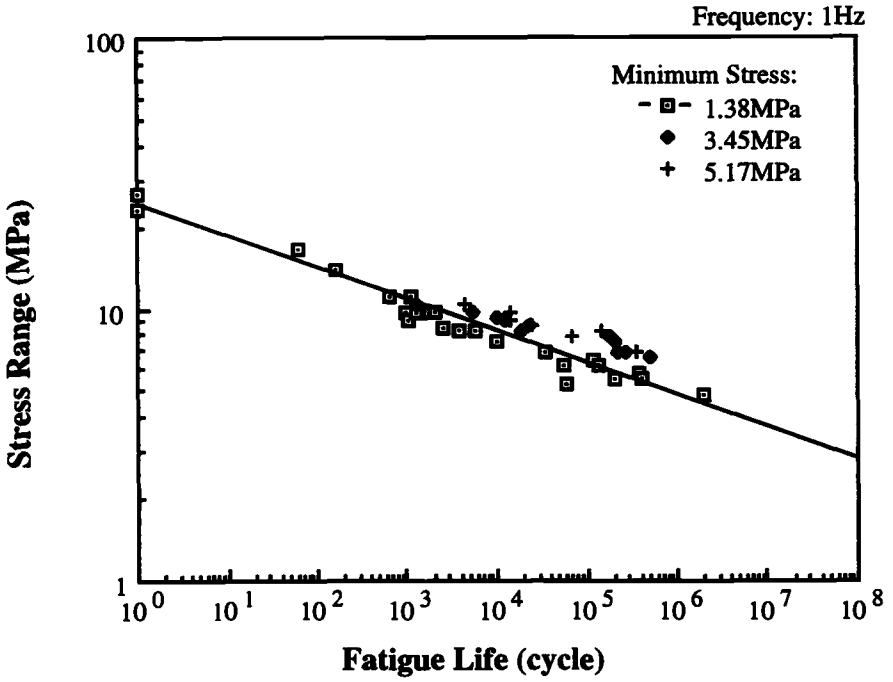

FIG. 1—*Stress range versus fatigue life for nylon-cord-reinforced elastomer composite on a logarithm scale (minimum stress: 1.38, 3.45, and 5.17 MPa; frequency: 1 Hz).*

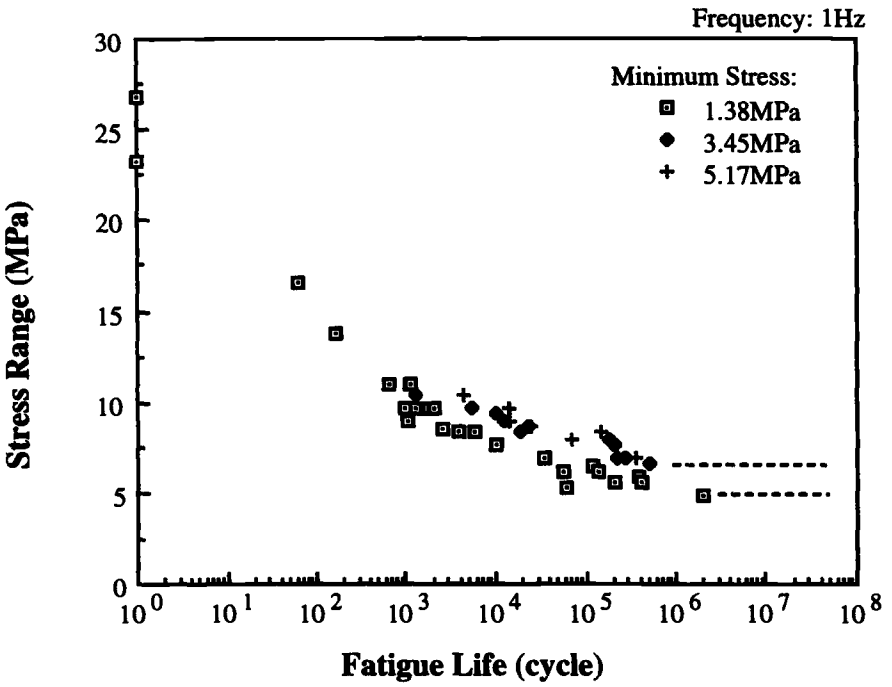

FIG. 2—*Stress range versus fatigue life for nylon-cord-reinforced elastomer composite on a semi-logarithm scale (minimum stress: 1.38, 3.45, and 5.17 MPa; frequency: 1 Hz).*

investigation indicates that the following two factors are involved in the effect of minimum stress on the fatigue life of nylon-cord-reinforced elastomer composite: (a) the nonlinear stress-strain relationship, and (b) the change of damage potential.

Stress and strain are mutually dependent variables. The change of the stress in a material therefore involves change of the strain. For the case in which the stress and strain are *not* linearly related to each other as in elastomers or elastomer composites, the problem may not be well described by using stress or strain only. As shown in Fig. 3, a typical cyclic stress-strain curve of nylon-cord-reinforced elastomer composite has a tendency of strain stiffening. The slope of the curve will continuously increase as the strain increases. Under this type of stress-strain curve that reflects general characteristics of rubber-like material, one can readily see that a shorter strain range is always generated for the same stress range placed on a higher level of the stress-strain curve (Fig. 3). Thus, in stress-controlled fatigue testing, a shorter strain range is experienced for the same stress range applied when the level of minimum stress is raised (Fig. 4). This could also mean a smaller amount of strain energy to be generated under the higher level of minimum stress. In fact, a smaller amount of dissipated energy (the area inside the hysteresis loop) under the higher level of minimum stress has been observed in this research (Fig. 5).

As discussed so far, the trend of a longer fatigue life of elastomer matrix composite with a higher level of minimum stress stems clearly from the fact that a shorter strain range or smaller amount of strain energy is experienced for the same stress range tested at the higher level of minimum stress. However, it should be noted that the test results reported so far are restricted to minimum stress levels up to 20% of static tensile strength of aircraft tire carcass

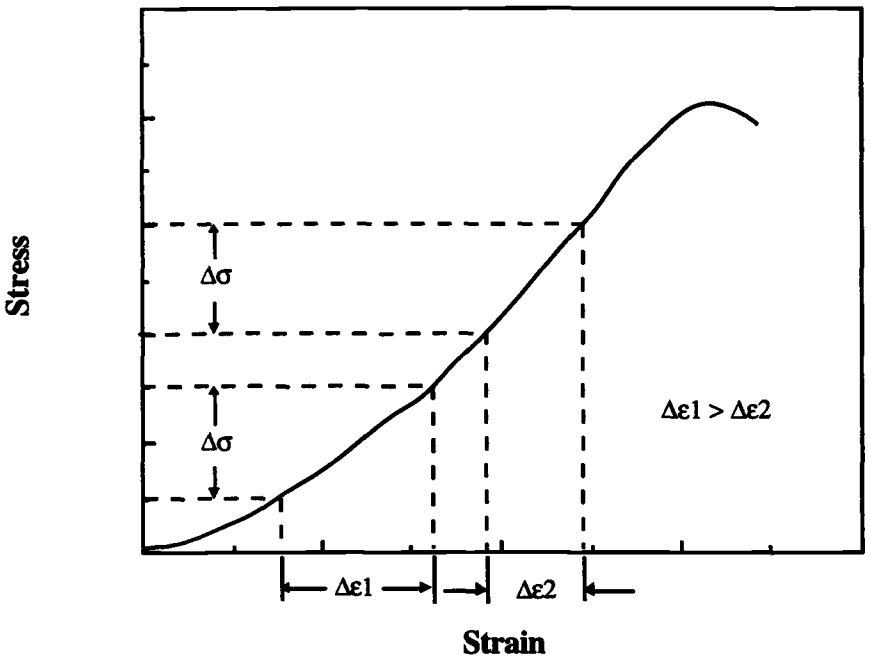

FIG. 3—*Typical tensile stress-strain curve for nylon-cord-reinforced elastomer composite with expected strain response at a given stress strange.*

composite. These levels of minimum stress are safely below a critical level for the initiation of fiber-matrix debonding under static tension [*1,2*]. When the minimum stress exceeds the critical level, its effect on the fatigue life of elastomer matrix composite could be quite different. As in other structural materials, the increase of applied stress level in elastomers leads to an increase of stored energy (the increase of the area under the stress-strain curve). Since the stored energy will act as a damage parameter in a potential form, the increase of stress level can be regarded as an increase of damage potential. Therefore, when the minimum stress reaches a critical level, this damage potential effect may become dominant and a shorter fatigue life at a given stress range could be observed with a higher level of minimum stress. One can think about an extreme case as the minimum stress reaches the ultimate tensile strength of the material.

As a result of the combination of these two contradicting factors, the *S-N* curve is expected to move gradually to the longer life region up to a certain point but eventually will shift back to the shorter life region with the increase of minimum cyclic stress. Further fatigue testing of aircraft tire carcass composite with even higher levels of minimum stress is planned to confirm this speculation. The existence of these two contradicting trends was partly confirmed in the preliminary results of model composite that will be published elsewhere. Related to this issue, it can also be foreseen that, for the *strain-controlled* fatigue testing, consistently shorter fatigue life can always be expected with the increase of minimum strain at a given strain amplitude. This is due to the following two factors. First of all, again due to the strain-stiffening response, a larger stress range will always be generated for the same strain range tested at a higher level of minimum strain (Fig. 6). As a consequence, more strain energy can be generated with the increase of minimum strain. Secondly, the increase of minimum strain also means the increase of damage potential.

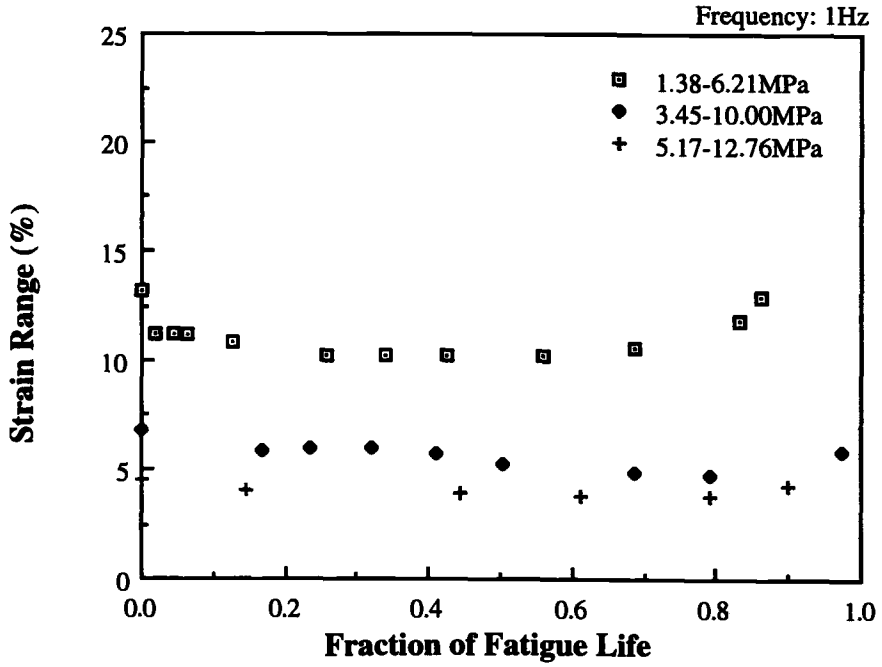

FIG. 4—*Strain range versus the fraction of fatigue life for nylon-cord-reinforced elastomer composite (stress range: 1.38 to 6.21, 3.45 to 10.0, and 5.17 to 12.76 MPa).*

Back to the current issue of minimum stress effect in *stress-controlled* fatigue loading, the role of damage potential can be assessed more clearly when the fatigue life data are plotted directly against damage parameters such as strain range, strain increase rate, dissipated strain energy, or stored strain energy. Since the fatigue process involves the change of both stress and strain, which are not linearly related, the damage parameters based on the strain energy may be able to describe the cause-effect relationship more accurately. Within this context, the effect of minimum stress on the damage parameters was first examined in stress-controlled fatigue tests, and then the fatigue life curves were reconstructed based on the damage parameters. The results are described in the ensuing two sections.

Minimum Stress Effects on Damage Parameters

The stress-controlled fatigue testing of elastomer matrix composites normally involves a distinct change of cyclic strain. Consequently, the strain-related damage parameters become obvious variables from which the cumulative damage of the composites may be estimated. As in the case of model composites [*1,2*], the process of damage accumulation in the aircraft tire carcass composite was accompanied by a continuous increase of cyclic strain. The change of cyclic strain (either maximum or minimum) was found to undergo three stages after an initial stepwise increase (Fig. 7). At first, the strain increased rapidly but at a progressively lower rate. In the second region, the strain increased at a constant rate (steady-state). Throughout the first and second regions, which consumed a major part of the fatigue life, the damage occurred in the forms of cord-matrix debonding and matrix cracking. Towards the end of the second region, partial delamination appeared at the specimen edge. In the final third region, the cyclic strain increased rapidly at a progressively higher rate with the delamination growth eventually leading to catastrophic failure.

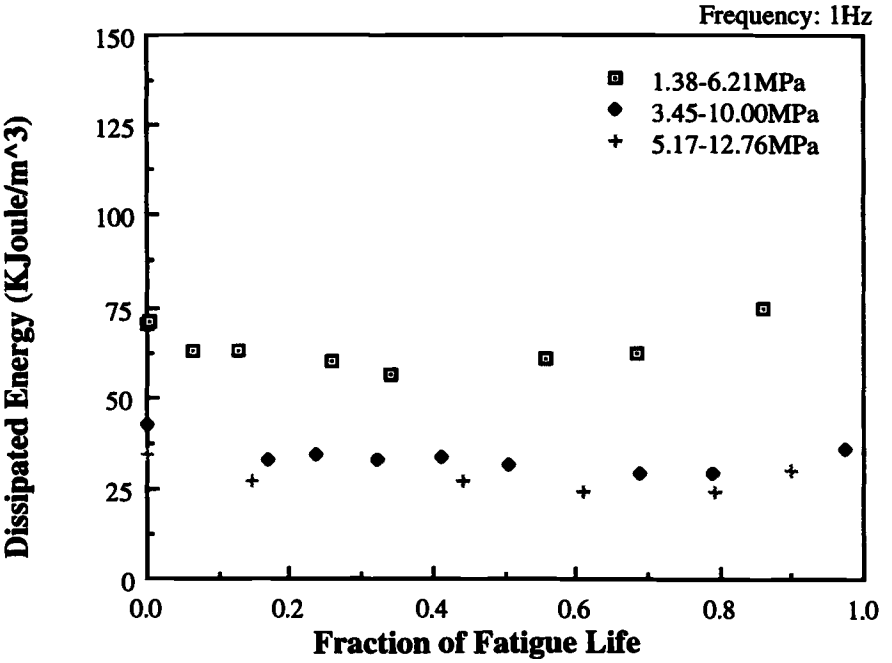

FIG. 5—*Dissipated strain energy versus the fraction of fatigue life for nylon-cord-reinforced elastomer composite (stress range: 1.38 to 6.21, 3.45 to 10.0, and 5.17 to 12.76 MPa).*

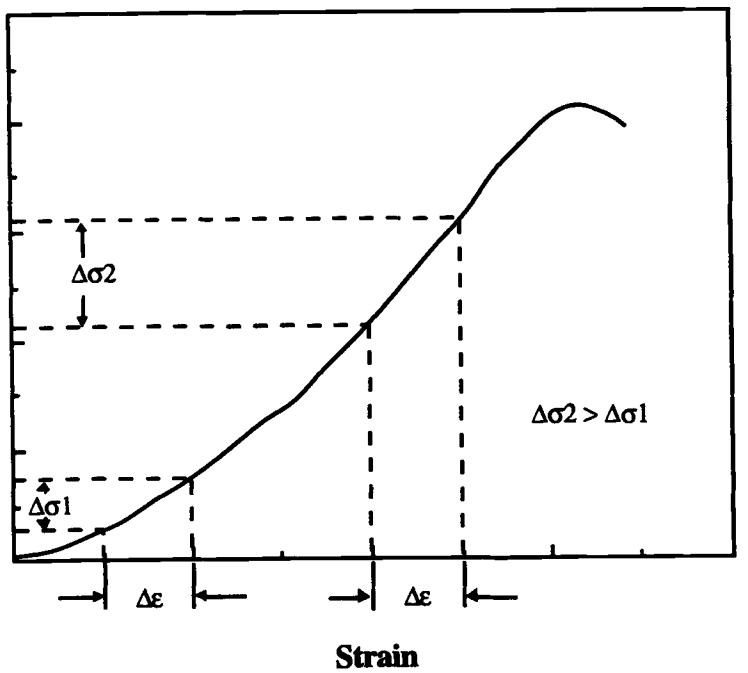

FIG. 6—*Typical tensile stress-strain curve for nylon-cord-reinforced elastomer composite with expected stress response at a given strain range.*

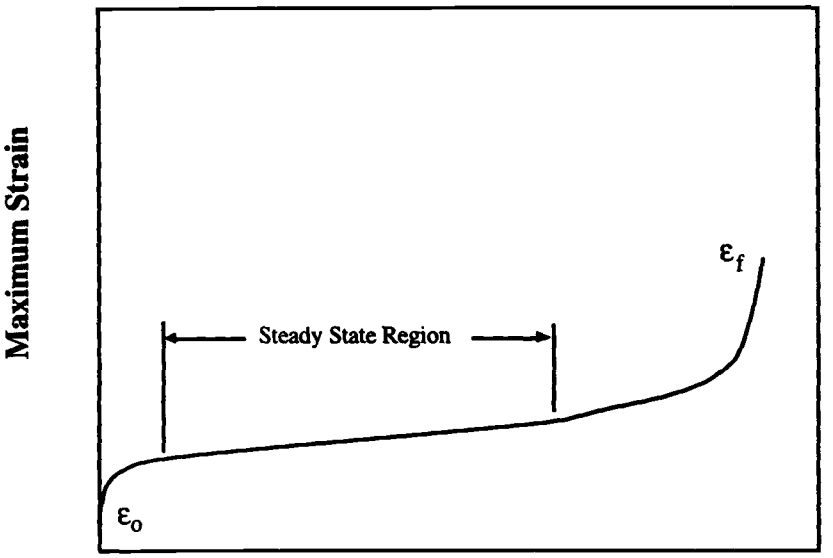

FIG. 7—*Relationship between the resultant maximum strain and the number of cycles for nylon-cord-reinforced elastomer composite.*

Along with the observed change of cyclic strain as a function of time, the cyclic stress-strain relationship in the form of a hysteresis loop provided insightful damage parameters. Cyclic stress-strain data were used to define the levels of strain energy throughout the fatigue life. As stated earlier, the following two energy-related variables were examined: the dissipated strain energy defined as the area inside the hysteresis loop and the stored strain energy as the area under the hysteresis loop (Fig. 8). Since most of the fatigue life of elastomer composite was spent in the steady-state region of maximum strain versus time curve (Fig. 7), the midlife (approximately one-half of the fatigue life) values of the damage parameters such as strain range, dissipated strain energy, and stored strain energy were found to be more reliable damage parameters than the values at the beginning or unstable final region. Thus, the effect of minimum stress on these damage parameters were examined in detail in the current study. The rate of increase in maximum strain (so-called "dynamic creep rate") in the steady-state region and the gross failure strain of the composite specimens were also measured to assess the cumulative fatigue damage at each combination of stress range and minimum stress.

As shown in Fig. 9, a linear relationship between the strain range at midlife and the applied stress range was observed for all three levels of minimum stress tested. Also apparent was the influence of minimum stress on the midlife strain range. At a given stress range, a clear trend of shorter strain range at midlife was associated with a higher level of minimum stress, which is consistent with the previous observation of strain-hardening behavior of elastomer composites (Fig. 3). The dynamic creep rate in the steady-state region was found to exhibit a power law relationship with the applied stress range (Fig. 10). Although the difference between the data sets for the two highest levels of minimum stress (3.45 and 5.17 MPa) was small, a trend of lower dynamic creep rate at a given stress range could be observed with a higher level of minimum stress. On the other hand, there was no obvious difference in the gross failure strain (initial maximum strain plus total dynamic

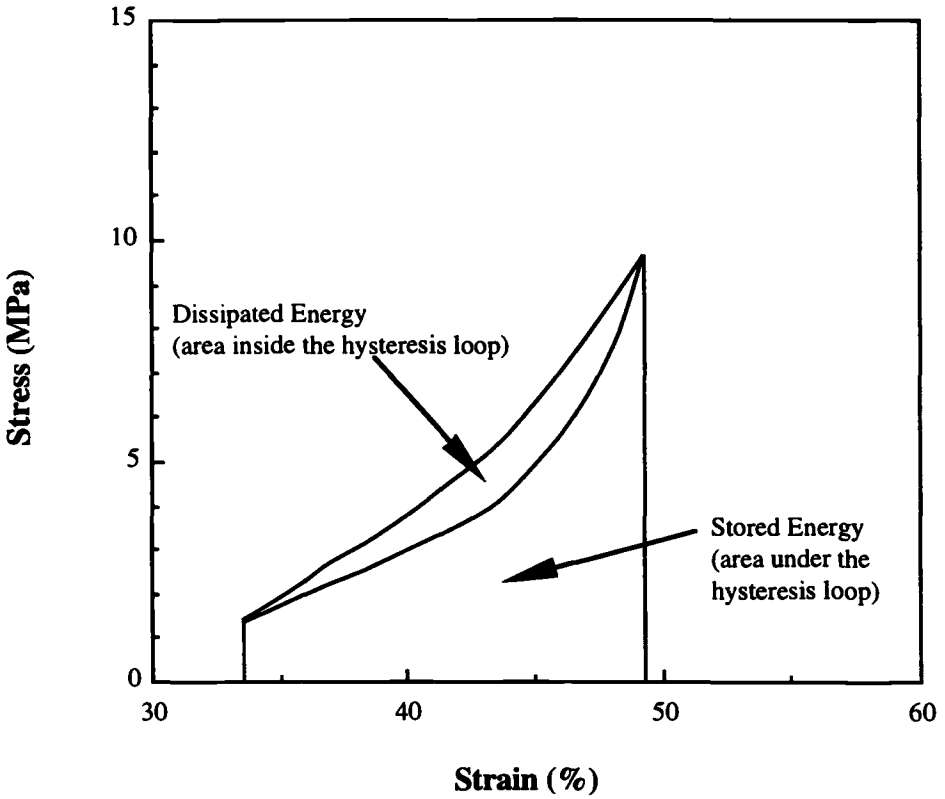

FIG. 8—*Typical hysteresis curve for nylon-cord-reinforced elastomer composite under cyclic tension.*

creep) for the three levels of minimum stress tested so far (Fig. 11). The failure strains under the minimum stresses of 1.38, 3.45, and 5.17 MPa all averaged around 70%.

In addition to the midlife strain range and dynamic creep rate, the strain energy values at midlife were clearly affected by the level of minimum stress at a given stress range. As shown in Fig. 12, a linear relationship was found to exist between the dissipated strain energy at midlife and the applied stress range. A trend of a smaller amount of dissipated strain energy at a given stress range was clearly observed with a higher level of minimum stress. Figure 12 also shows that the dissipated strain energy became relatively small when the level of minimum stress was high. At a given stress range, the dissipated strain energy for the lowest level of minimum stress tested so far (1.38 MPa) was about four times that for the highest level of minimum stress (5.17 MPa). The relationship between the stored strain energy at midlife and the applied stress range is shown in Fig. 13. A linear relationship could be observed between the two variables. The stored strain energy at a given stress range became smaller with the increase of minimum stress. However, the differences between these sets of data were not so obvious as in the case of the dissipated strain energy.

Fatigue Life Curves Based on Damage Parameters

As discussed in the previous sections, the midlife values of the damage parameters, such as strain range, dynamic creep rate, dissipated strain energy, and stored strain energy, were all found to decrease with the higher minimum stress at a given stress range. The results

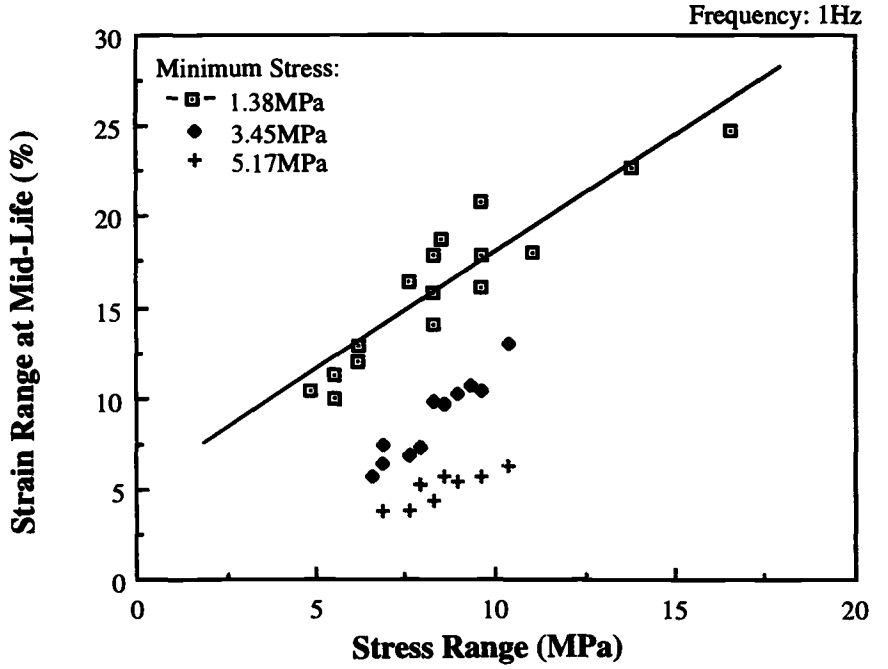

FIG. 9—*Strain range at mid-life versus stress range for nylon-cord-reinforced elastomer composite (minimum stress: 1.38, 3.45, and 5.17 MPa).*

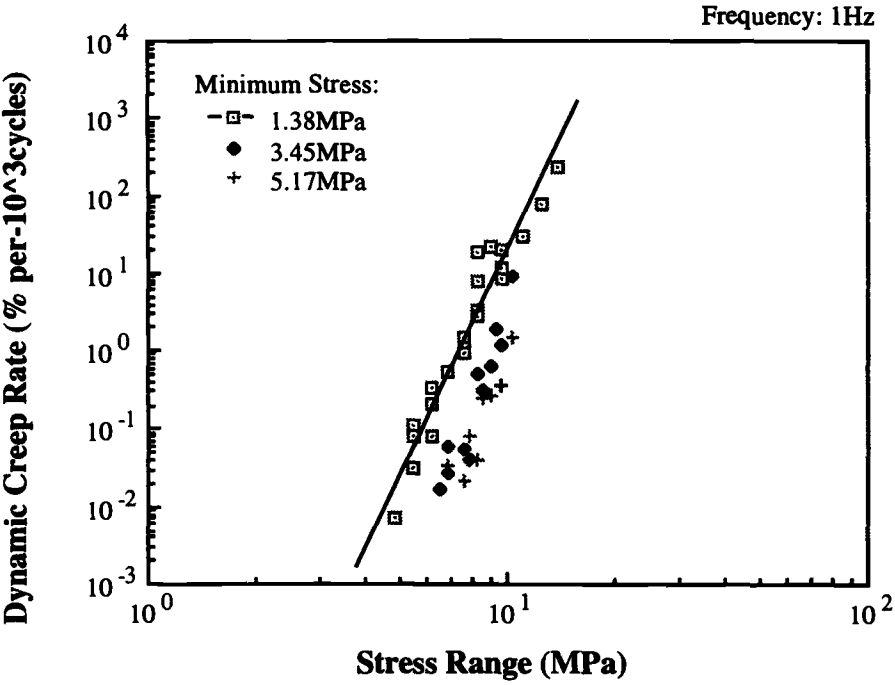

FIG. 10—*Dynamic creep rate in steady-state region versus stress range for nylon-cord-reinforced elastomer composite (minimum stress: 1.38, 3.45, and 5.17 MPa).*

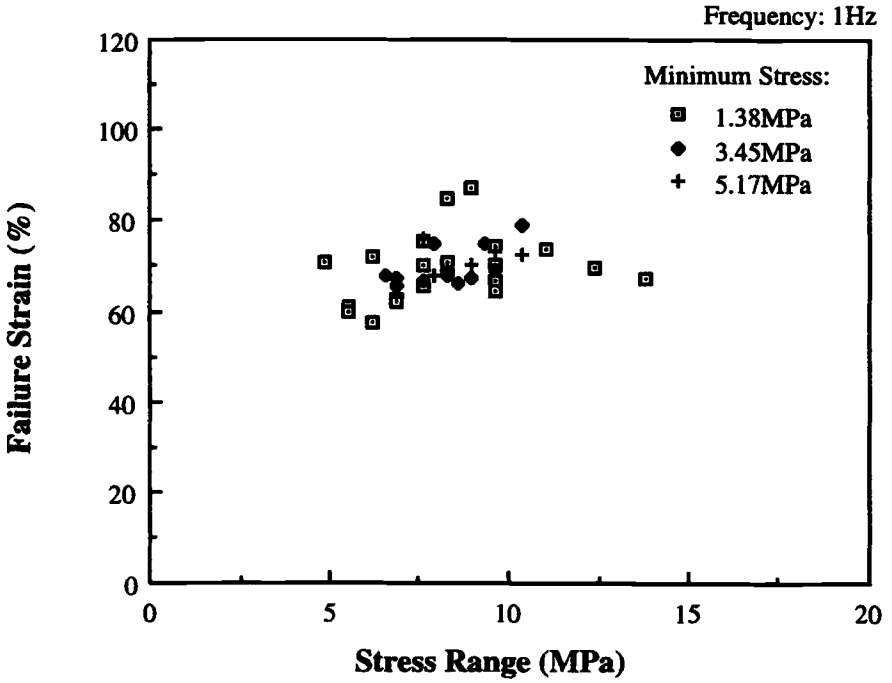

FIG. 11—*Gross failure strain versus stress range for nylon-cord-reinforced elastomer composite (minimum stress: 1.38, 3.45, and 5.17 MPa).*

were consistent with the observed trend of longer fatigue life of elastomer matrix composite with higher level of minimum stress. Therefore, the fatigue life data were plotted directly against the above-listed damage parameters to clarify the role of damage potential. Figure 14 shows the fatigue life curves based on the strain range at midlife. An obvious trend of shorter fatigue life with a higher level of minimum stress could be established at a given strain range. The result is in striking contrast to the trend of the *S-N* curves in Figs. 1 or 2. As shown in a semi-log plot of Fig. 14, the midlife strain range had a linear relationship with the fatigue life in a log value. The fatigue life data plotted against the dynamic creep rate is shown in Fig. 15. Interestingly, the data fell into a power law relationship. A trend of shorter fatigue life with a higher level of minimum stress was also observed at a given dynamic creep rate, although the difference between the data sets for the two highest levels of minimum stress (3.45 and 5.17 MPa) was relatively small.

When the fatigue life data were plotted against the dissipated strain energy at midlife, the same trend of shorter fatigue life was observed with a higher level of minimum stress (Fig. 16). A power law relationship could be established between the dissipated strain energy and fatigue life. The identical data in a semi-log plot (Fig. 17) indicated the presence of an endurance limit. The endurance limit of the dissipated strain energy decreased with an increase of minimum stress. Again it should be noted that the results reported here were from the fatigue tests in which the level of minimum stress was below 20% of the ultimate tensile strength of the composite. As mentioned before, an increase of the minimum stress can be considered as an increase of damage potential. When the minimum stress reaches a critical level, the effect of the damage potential may become dominant. The material will fail at any stress range. In this case, there will be no fatigue endurance limit for the applied

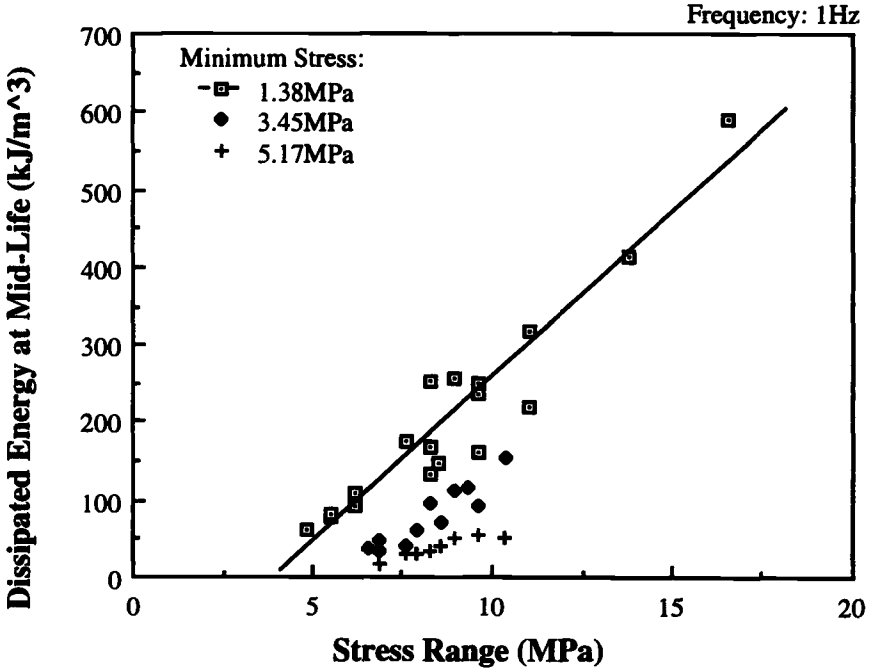

FIG. 12—*Dissipated strain energy at midlife versus stress range for nylon-cord-reinforced elastomer composite (minimum stress: 1.38, 3.45, and 5.17 MPa).*

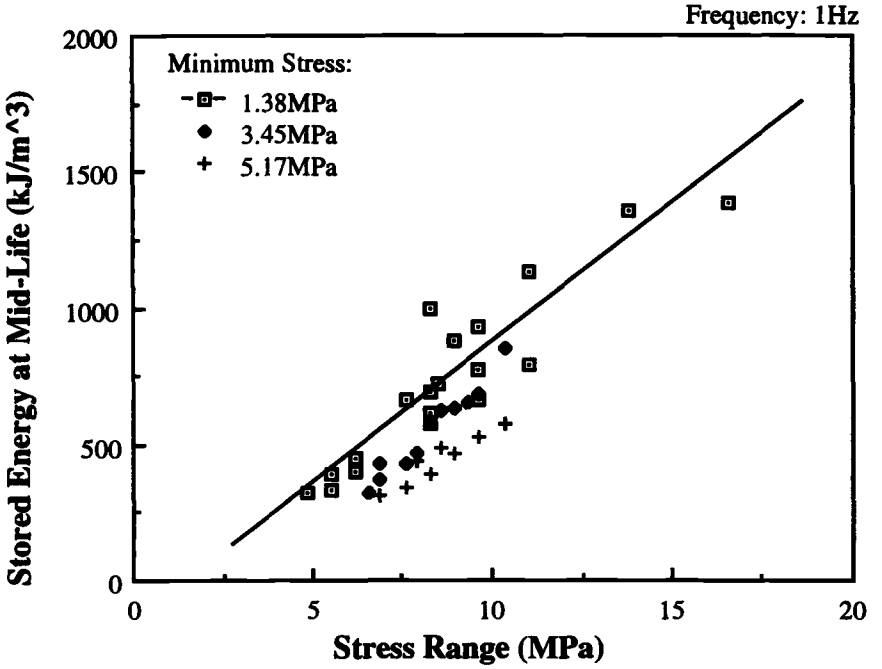

FIG. 13—*Stored strain energy at midlife versus stress range for nylon-cord-reinforced elastomer composite (minimum stress: 1.38, 3.45, and 5.17 MPa).*

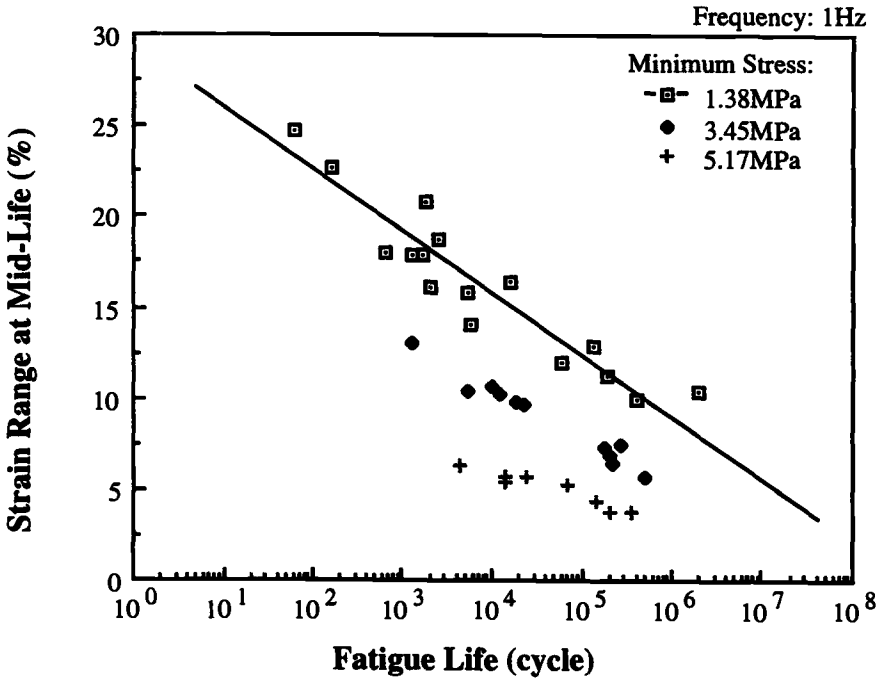

FIG. 14—*Strain range at midlife versus fatigue life for nylon-cord-reinforced elastomer composite (minimum stress: 1.38, 3.45, and 5.17 MPa).*

stress range or for the dissipated strain energy. Finally, the fatigue life curves based on the stored strain energy at midlife are shown in Fig. 18. A power law relationship could be established between the stored strain energy and fatigue life. However, a trend of shorter fatigue life with a higher level of minimum stress was less obvious at a given stored strain energy.

The damage parameters discussed so far, including the strain range, dynamic creep rate, dissipated strain energy, and stored strain energy, appear to be major variables that control the fatigue life of aircraft tire carcass composite. Their dependence on minimum stress at a given stress range is not straightforward due to the strain-hardening behavior of elastomeric materials. However, at a given level of these damage parameters, shorter fatigue life of elastomer composite can be associated with higher minimum stress. This observation indirectly demonstrates the increase of damage potential at a higher level of minimum stress.

Concluding Remarks

The effects of minimum stress on the cumulative damage and fatigue lifetime were assessed for an angle-plied nylon cord-reinforced elastomer composite that represents the bias aircraft tire carcass. The composite laminate specimens exhibited a normal failure sequence of fiber-matrix debonding developing into the delamination under cyclic tension. The *S-N* curves were established under constant minimum stress rather than constant *R*-ratio. The trends of longer fatigue life at a given stress range and higher fatigue endurance limit of the composite were clearly observed with a higher level of minimum stress. These trends stem from the fact that the stress and strain are not linearly related to each other. The

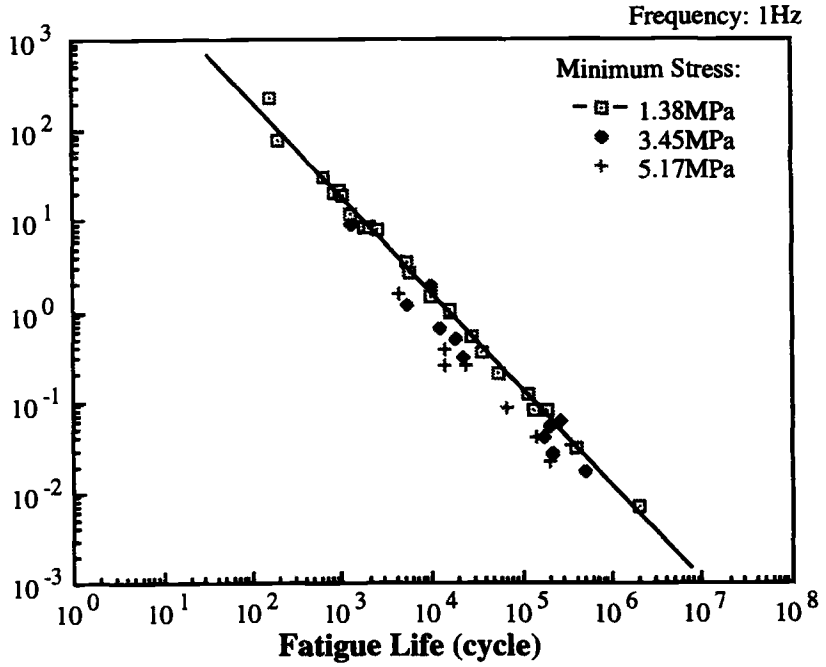

FIG. 15—*Dynamic creep rate in steady-state region versus fatigue life for nylon-cord-reinforced elastomer composite (minimum stress: 1.38, 3.45, and 5.17 MPa).*

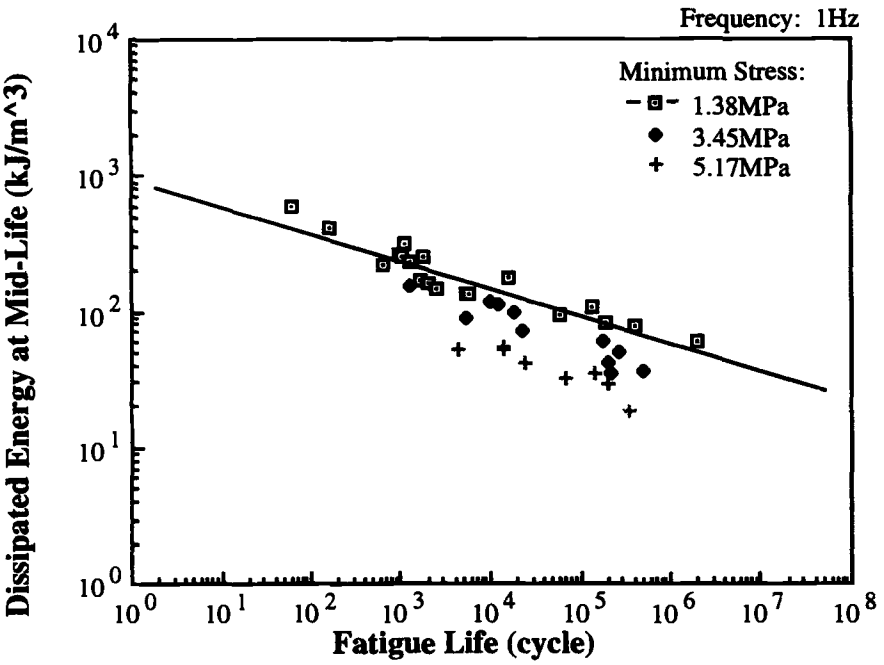

FIG. 16—*Dissipated strain energy at midlife versus fatigue life for nylon-cord-reinforced elastomer composite on a logarithm scale (minimum stress: 1.38, 3.45, and 5.17 MPa).*

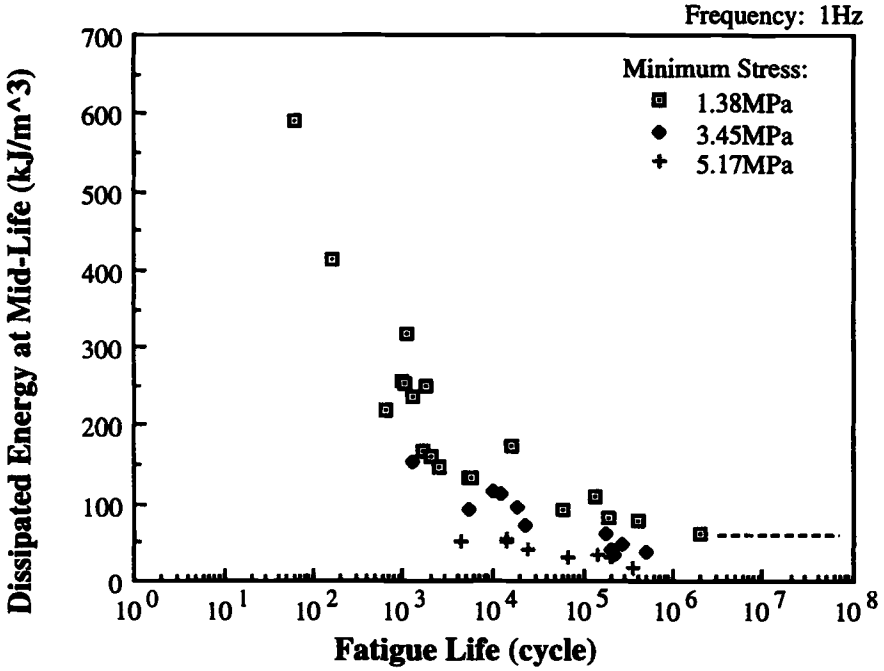

FIG. 17—*Dissipated strain energy at midlife versus fatigue life for nylon-cord-reinforced elastomer composite on a semi-logarithm scale (minimum stress: 1.38, 3.45, and 5.17 MPa).*

stress-strain curve of the elastomer matrix composite exhibits strain stiffening. As a result, in a stress-controlled fatigue test, a shorter strain range or a smaller amount of strain energy is experienced for the same stress range when the level of minimum stress is raised.

However, it should be noted that the current test results are restricted to the case of having minimum stress up to 20% of static tensile strength of aircraft tire carcass composite. The levels of minimum stress happened to be safely below a critical level for the initiation of fiber-matrix debonding under static tension. As in other structural materials, the increase of applied stress level in elastomers can be regarded as an increase of the damage potential. Therefore, when the minimum stress exceeds a critical level, the damage potential effect may become dominant, and a shorter fatigue life at a given stress range could be observed with a higher level of minimum stress in *S-N* curves. Related to this issue, it can also be foreseen that, for the strain-controlled fatigue testing, consistently shorter fatigue life can always be expected with the increase of minimum strain at a given strain amplitude. Here a larger stress range will always be generated for the same strain range tested at a higher level of minimum strain. In addition, the increase of minimum strain means the increase of damage potential.

In the stress-controlled fatigue tests, the role of damage potential could be assessed more clearly when the fatigue life data were plotted directly against the damage parameters, such as strain range, dynamic creep rate, dissipated strain energy, and stored strain energy. The fatigue life curves based on the damage parameters at midlife showed a clear trend of a shorter fatigue life with a higher level of minimum stress. This trend could be established at a given strain range, dynamic creep rate, or dissipated strain energy. The results are in striking contrast to the trend of the *S-N* curves. The trend of a shorter fatigue life with a

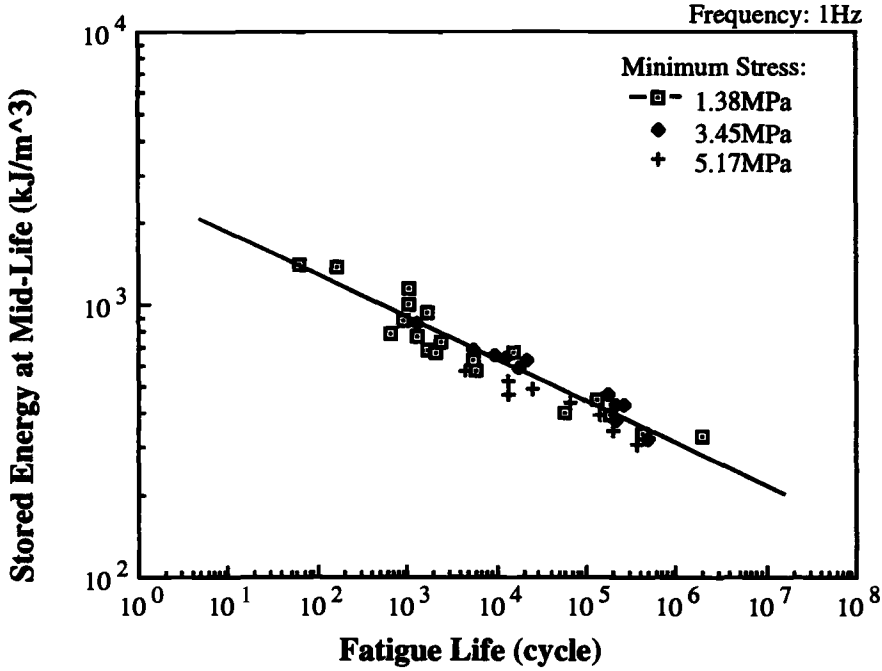

FIG. 18—*Stored strain energy at midlife versus fatigue life for nylon-cord-reinforced elastomer composite (minimum stress: 1.38, 3.45, and 5.17 MPa).*

higher level of minimum stress was less obvious at a given stored strain energy. The values of dynamic creep rate, dissipated strain energy, and stored strain energy were found to have a power law relationship with the fatigue life of elastomer matrix composite. At a given minimum stress, the strain range, dissipated strain energy, and stored strain energy exhibited a linear relationship with the applied stress range.

Acknowledgments

We are grateful to the Flight Dynamics Directorate of Air Force Wright Laboratory for sponsorship of this research. We sincerely appreciate continuing support and encouragement for our research program from M. Chawla, A. H. Mayer, P. C. Ulrich, and A. V. Petersons at the Vehicle Subsystems Division of Flight Dynamics Directorate. We would also like to thank our colleagues at the Landing Gear Systems Group of Vehicle Subsystems Division, J. P. Medzorian and P. M. Wagner, for the discussion of this research work. Finally, our sincere thanks should go to A. G. Causa, Y. M. Huang, and R. Burgan at The Goodyear Tire and Rubber Company for providing composite specimens.

References

[*1*] Lee, B. L., Medzorian, J. P., Fourspring, P. M., Migut, G. J., and Ulrich, P. C., "Study of Fracture Behavior of Cord-Rubber Composites for Laboratory Prediction of Aircraft Tire Durability," Paper 901907, *Proceedings,* SAE International Aerospace Technology Conference, Society of Automotive Engineers, Warrendale, PA, 1990.

[*2*] Lee, B. L., Medzorian, J. P., Hippo, P. K., Liu, D. S., and Ulrich, P. C., "Fatigue Lifetime Prediction of Angle-Plied Fiber-Reinforced Elastomer Composites as Pneumatic Tire Materials,"

Advances in Fatigue Lifetime Predictive Techniques (2nd Conference), ASTM STP 1211, American Society for Testing and Materials, West Conshohocken, PA, 1993, p. 203.

[3] Lee, B. L., Smith, J. A., Medzorian, J. P., Chawla, M., and Ulrich, P. C., "Fracture Behavior of Fiber-Reinforced Elastomer Composites under Fatigue Loading," *Proceedings,* 9th International Conference on Composite Materials, Vol. 2, University of Zaragoza, Spain & Woodhead Publishers, Cambridge, England, 1993, p. 821.

[4] Walter, J. D., "Cord-Reinforced Rubber," *Mechanics of Pneumatic Tires,* S. K. Clark, Ed., U.S. Department of Transportation, Washington, DC, 1982.

[5] Stalnaker, D. O., Kennedy, R. H., and Ford, J. L., "Interlaminar Shear Strain in a Two-Ply Balanced Cord-Rubber Composites," *Experimental Mechanics,* Vol. 20, 1980, p. 87.

[6] Ford, J. L., Patel, H. P., and Turner, J. L., "Interlaminar Shear Effects in Cord-Rubber Composites," *Fiber Science and Technology,* Vol. 17, 1982, p. 255.

[7] Rothert, H., Nguyen, B., and Gall, R., "Comparative Study on the Incorporation of Composite Material for Tyre Computation," *Composite Structures,* Proceedings of 2nd International Conference on Composite Structures, Applied Science Publishers, London, 1983, p. 549.

[8] Cembrola, R. J. and Dudek, T. J., "Cord/Rubber Material Properties," *Rubber Chemistry and Technology,* Vol. 58, 1985, p. 830.

[9] Breidenbach, R. F. and Lake, G. J., "Mechanics of Fracture in Two-Ply Laminates," *Rubber Chemistry and Technology,* Vol. 52, 1979, p. 96.

[10] Breidenbach, R. F. and Lake, G. J., "Application of Fracture Mechanics to Rubber Articles Including Tyres," *Philosophical Transactions of the Royal Society of London,* Vol. A299, 1981, p. 189.

[11] Lake, G. J., "Application of an Energetics Approach to Fatigue and Fracture in Elastomers," Paper A, *Proceedings,* 145th Spring Technical Meeting of Rubber Division, American Chemical Society, Chicago, IL, 1994.

[12] Kawamoto, J., "Fatigue of Rubber Composites," Ph.D. thesis (Advisor: J. F. Mandell), Massachusetts Institute of Technology, Cambridge, MA, 1988.

[13] Gent, A. N., "Detachment of an Elastic Matrix from a Rigid Spherical Inclusion," *Journal of Materials Science,* Vol. 15, 1980, p. 2884.

[14] Gent, A. N., "Failure of Cord-Rubber Composites by Pull-Out or Transverse Fracture," *Journal of Materials Science,* Vol. 16, 1981, p. 949.

[15] Gent, A. N. and Lai, S. M., "Interfacial Bonding, Energy Dissipation and Strength," Paper D, *Proceedings,* 145th Spring Technical Meeting of Rubber Division, American Chemical Society, Chicago, IL, 1994.

[16] Kendall, K., "The Adhesion and Surface Energy of Elastic Solids," *Journal of Physics D: Applied Physics,* Vol. 4, 1971, p. 1186.

[17] Kendall, K., "Crack Propagation in Lap Shear Joints," *Journal of Physics D: Applied Physics,* Vol. 8, 1975, p. 512.

[18] Kendall, K., "Interfacial Cracking of a Composite—Part 1. Interlaminar Shear and Tension," *Journal of Materials Science,* Vol. 11, 1976, p. 638.

[19] Huang, Y. S. and Yeoh, O. H., "Crack Initiation and Propagation in Model Cord-Rubber Composites," *Rubber Chemistry and Technology,* Vol. 62, No. 4, 1989, p. 709.

[20] Yeoh, O. H., "Model Studies of Failure Phenomena in Tires," Paper C, *Proceedings,* 145th Spring Technical Meeting of Rubber Division, American Chemical Society, Chicago, IL, 1994.

[21] Schijve, J., "Prediction Methods for Fatigue Crack Growth in Aircraft Material," *Fracture Mechanics, ASTM STP 700,* American Society for Testing and Materials, West Conshohocken, PA, 1979, p. 3.

[22] Clark, S. K., "Loss of Adhesion of Cord-Rubber Composites in Aircraft Tires," *Tire Science and Technology,* Vol. 14, No. 1, 1986, p. 33.

[23] Rivlin, R. S. and Thomas, A. G., "Rupture of Rubber—I. Characteristic Energy for Tearing," *Journal of Polymer Science,* Vol. 10, 1953, p. 291.

[24] Gent, A. N., Lindley, P. B., and Thomas, A. G., "Cut Growth and Fatigue of Rubbers—I. The Relationship between Cut Growth and Fatigue," *Journal of Applied Polymer Science,* Vol. 8, 1964, p. 455.

[25] Lake, G. J. and Lindley, P. B., "The Mechanical Fatigue Limit for Rubber," *Journal of Applied Polymer Science,* Vol. 9, 1965, p. 1233.

[26] Lake, G. J. and Thomas, A. G., "The Strength of Highly Elastic Materials," *Proceedings of the Royal Society of London,* Vol. A300, 1967, p. 108.

[27] Gent, A. N., "Strength of Elastomers," Chapter 10, *Science of Technology of Rubber,* F. R. Eirich, Ed., Academic Press, New York, 1978.

[28] Stacer, R. G., Yanyo, L. C., and Kelley, F. N., "Observations on the Tearing of Elastomers," *Rubber Chemistry and Technology*, Vol. 58, 1985, p. 421.

[29] Young, D. G., "Fatigue Crack Propagation in Elastomer Compounds: Effects of Strain Rate, Temperature, Strain Level, and Oxidation," *Rubber Chemistry and Technology*, Vol. 59, 1986, p. 809.

[30] Lee, R. F. and Donovan, J. A., "J-Integral and Crack Opening Displacement as Crack Initiation Criteria in Natural Rubber in Pure Shear and Tensile Specimens," *Rubber Chemistry and Technology*, Vol. 60, 1987, p. 674.

[31] Stevenson, A., "Fatigue and Fracture of Rubber in Engineering Applications," Paper B, *Proceedings*, 145th Spring Technical Meeting of Rubber Division, American Chemical Society, Chicago, IL, 1994.

Chi L. Chow[1] *and Yong Wei*[2]

A Fatigue Damage Model for Crack Propagation

REFERENCE: Chow, C. L. and Wei, Y., **"A Fatigue Damage Model for Crack Propagation,"** *Advances in Fatigue Lifetime Predictive Techniques, 3rd Volume, ASTM STP 1292,* M. R. Mitchell and R. W. Landgraf, Eds., American Society for Testing and Materials, 1996, pp. 86–99.

ABSTRACT: This paper presents a fatigue damage model for crack propagation in characterizing the fatigue crack growth behavior of cracked structures. Special emphasis is placed on the numerical simulation of cyclic loading and the dependence of the numerical results on the finite element mesh discretization. A practical method for predicting fatigue crack propagation in engineering structures is proposed. The predicted results are compared favorably with those measured experimentally from fatigue testing a center cracked panel of 2024-T3(Alclad) aluminum plates.

KEYWORDS: damage mechanics, fatigue, crack propagation, aluminum alloy, finite element analysis

Nomenclature

a	Crack length
$\mathbf{A}$	Damage compliance tensor
$\mathbf{B}$	Transformation matrix
B_0	Initial plastic damage threshold
B, $B(w_p)$	Increment of plastic damage threshold
$\mathbf{C}$	Elastic compliance tensor of virgin material
$\bar{\mathbf{C}}$	Effective elastic tensor of damaged material
$\bar{\mathbf{C}}^{ep}$	Effective instantaneous tangent modulus tensor
$\mathbf{C}^s$	Symmetric form of $\bar{\mathbf{C}}^{ep}$
d	Independent component of damage tensor
d_f	Independent component of fatigue damage
d_p	Independent component of plastic damage
$\mathbf{D}$	Damage tensor
$\mathbf{D}_f$	Fatigue damage tensor
$\mathbf{D}_p$	Plastic damage tensor
E	Young's modulus
F_{fd}	Fatigue damage surface
F_{pd}	Plastic damage surface
$\mathbf{K}$	Finite element stiffness
K_{Ic}	Critical stress intensity factor

[1]Department of Mechanical Engineering, University of Michigan-Dearborn, Dearborn, MI 48128-1491.
[2]Pacific Technique Development Co. Ltd., Balaklavsky Prosp. 5, KV 287, 113639 Moscow, Russia.

ΔK Stress intensity range
K_0 Fatigue constant
$K(w)$ Fatigue coefficient as function of overall damage
J_{Ic} Critical J-integral
ΔJ J-integral range
$\mathbf{M}$ Damage effect tensor
N Number of cycles
w Overall fatigue damage
w_c Critical overall fatigue damage
w_f Overall fatigue damage
w_p Overall plastic damage
$\mathbf{Y}$ Damage energy release rate
Y_d, Y_μ Independent components of $\mathbf{Y}$
Y_{fd} Defined in Eq 5
Y_{pd} Defined in Eq 4
α Material constant varying between 0 and 1
μ Independent component of damage tensor
ν Poisson's ratio
γ Damage evolution coefficient
σ Stress
σ_y Yield stress
σ_{max} Maximum stress corresponding to Y_{pd}
σ_{min} Minimum stress
$\Delta\sigma$ Stress range
σ_0 Minimum stress corresponding to minimum Y_{pd}
σ_{act} Defined in Eq 19
σ^+ Positive part of stress tensor
σ^- Negative part of stress tensor
$\Delta\sigma^+$ Positive part of stress range in a cycle
$\Delta\sigma^-$ Negative part of stress range in a cycle

Introduction

Since the inception of the Paris law for fatigue crack propagation (FCP) based on the application of fracture mechanics, this global approach has become popular among engineers for the prediction of fatigue failure in engineering structures [*1,2*]. Generally, the fatigue crack propagation rate is governed by a crack tip parameter such as the stress intensity factor, the crack tip opening displacement, or the J-integral. Thus, a generalized law is expressed as

$$\frac{da}{dN} = f(P) \tag{1}$$

where P is a general crack tip parameter. By integrating Eq 1 from the initial to a certain crack length, we can compute the resulting number of cycles. Therefore, it is important to establish a proper function $f(P)$ under complex loading conditions. A large number of FCP models have been proposed empirically to describe the crack behavior in their respective crack growth phases [*3–10*]. Due to the complex nature of fatigue damage, the process of

fatigue crack growth is artificially divided into several phases, such as microcracks, short macrocracks, and long macrocracks. Consequently, many experimental tests need to be carried out to determine the material constants for each FCP formulation. Furthermore, there often exist ambiguities in the transition between the phases due to restricted applicability of each formulation. Another anomaly in the FCP formulation is the expression of $f(P)$ in Eq 1 in terms of ΔK or ΔJ. Unlike K_{Ic} and J_{Ic}, both ΔK and ΔJ are not intrinsic material properties. Consequently, Eq 1 is simply a form of fatigue data reduction exercise and should not therefore be used indiscriminately for structural fatigue design analysis. In addition, the most severe drawback of the conventional fracture mechanics approaches is their inability to take into account the microcracks/voids in a real-life material. From the physical point of view, fatigue damage is caused by material degradation due to the nucleation, growth, and coalescence of the inherent microcracks/voids under cyclic loading. Any design conclusions drawn from a fatigue analysis without the consideration of these inherent material imperfections would therefore be suspect.

A method to overcome these difficulties and therefore a simpler design methodology for engineers can be provided by the emerging theory of damage mechanics. The application of this local approach to fracture has made significant progress in the design of engineering components and structures [*11–16*]. By combining the damage mechanics theory with the finite element method, we can analyze the whole process from the threshold condition of material degradation and damage evolution to the formulation of a macrocrack and then final failure.

This paper applies a fatigue damage model proposed recently by the authors [*17,18*] to the characterization of the fatigue crack growth process in a 2024-T3 Alclad plate containing a center crack. The model is in essence based on the theory of damage mechanics, which takes into account the presence of microcracks/voids in real-life materials. The distribution of these microdefects is introduced through a set of internal state variables known as damage variables such that the constitutive equations of elasticity and plasticity are developed coupled with damage effects. The nucleation, growth, and coalescence of the microdefects under cyclic loading are introduced in the model through a set of damage evolution equations. A material element is postulated to have been ruptured after the accumulated damage within the element reaches a critical value, which is considered an intrinsic material property and determined experimentally. The model has been applied successfully to characterize fatigue damage process not only in smooth but also notched specimens [*16–18*]. This paper applies the fatigue model to crack growth process at the crack tip, which extends incrementally after damage accumulation due to load application as depicted in Fig. 1. Methods of simulating cyclic loading and the dependence of the numerical results on the

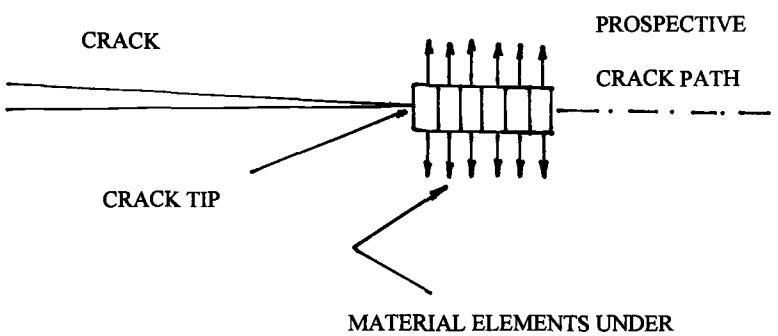

FIG. 1—*Material elements at the crack tip under fatigue damage.*

finite element mesh discretization are investigated, and a simplified predictive procedure is proposed for the fatigue damage analysis. Finally, the accuracy of the predicted results is discussed and found to be satisfactory in comparison with the measured fatigue data.

Fatigue Damage Model

During the fatigue loading, the microstructure of a material element changes due to nucleation and growth of microcracks or defects. It is difficult to describe this change in fine detail by a mathematical model in view of the complexity of the random distribution and size of the microcracks and the irreversible physically induced fatigue microcracking processes. To establish a damage model that can be used to predict fatigue failure in engineering structures, it is necessary to introduce a set of proper internal state variables for characterizing the averaging effect of gradual material deterioration under cyclic load application. The averaging process is assumed to be carried out on a material element that is small enough to be taken as a "mathematical point" to define mechanical variables, such as stress, strain, damage, etc., but large enough so that the elementary mechanisms of the material are well represented by the continuous state variables within the context of classical continuum mechanics theory [*13*].

According to the fatigue damage model [*16–18*], the damage accumulation under cyclic loading $\mathbf{D}$ is divided into two processes, fatigue damage $\mathbf{D}_f$ and plastic damage $\mathbf{D}_p$, or $\mathbf{D} = \mathbf{D}_f + \mathbf{D}_p$. The plastic damage refers to the damage that occurs during the first quarter cycle when the material is stressed beyond elastic limit or during a plastic overload condition in fatigue spectrum loading. These two damage processes are identified by two damage surfaces, a fatigue damage surface corresponding to the fatigue endurance limit, and a plastic damage surface corresponding to the initiation of plastic damage, as follows

$$\mathbf{F}_{fd}(Y_{fd,1}, Y_{pd}^{min}) = 0 \tag{2}$$

$$F_{pd}(\mathbf{Y}, B) = Y_{pd}^{1/2} - [B_0 + B(w_p)] = 0 \tag{3}$$

where Y_{pd}, Y_{fd} are defined as

$$Y_{pd} = \tfrac{1}{2}(Y_d^2 + 2\gamma Y_d Y_\mu + Y_\mu^2) \tag{4}$$

$$Y_{fd} = \tfrac{1}{2}(Y_{d,f}^2 + 2\gamma Y_{d,f} Y_{\mu,f} + Y_{\mu,f}^2) \tag{5}$$

where $Y_{fd,1}$ is the critical value of Y_{fd} on the fatigue damage surface, Y_{pd}^{min} is the minimum value of Y_{pd} over a cycle, B_0 is the initial plastic damage threshold, B is the increment of plastic damage threshold, w_p is the overall plastic damage, and γ is the damage evolution coefficient. Y_d and Y_μ are two independent components of plastic damage energy release rate, $\mathbf{Y}$. $Y_{d,f}$ and $Y_{\mu,f}$ are two independent components of fatigue damage energy release rate, $\mathbf{Y}_f$. These components of the damage energy release rate are expressed as [*18*]

$$Y_d = -\frac{1}{1-d}\sigma^T : \bar{\mathbf{C}}^{-1} : \sigma \qquad Y_\mu = -\frac{1}{1-d}\sigma^T : \mathbf{A}^{-1} : \sigma \tag{6}$$

$$Y_{d,f}(\sigma, \mathbf{D}) = Y_d(\sigma_{act}, \mathbf{D}) \qquad Y_{\mu,f}(\sigma, \mathbf{D}) = Y_\mu(\sigma_{act}, \mathbf{D}) \tag{7}$$

where $\mathbf{C}^{-1}$ is the elastic compliance tensor of virgin material, and $\mathbf{A}^{-1}$ is expressed in the matrix form as

$$\mathbf{A}^{-1} = \frac{1}{E(1-d)} \begin{bmatrix} A_1 & A_2 & A_2 & 0 & 0 & 0 \\ A_2 & A_1 & A_2 & 0 & 0 & 0 \\ A_2 & A_2 & A_1 & 0 & 0 & 0 \\ 0 & 0 & 0 & 2(A_1 - A_2) & 0 & 0 \\ 0 & 0 & 0 & 0 & 2(A_1 - A_2) & 0 \\ 0 & 0 & 0 & 0 & 0 & 2(A_1 - A_2) \end{bmatrix} \tag{8}$$

$$A_1 = 2\mu(1-\nu) - 2\nu \qquad A_2 = (1+\mu)(1-\nu) - 2\mu\nu$$

where d and μ are two independent components of damage variable $\mathbf{D}$, respectively, in x and y directions; E is Young's modulus of virgin material; ν is Poisson's ratio of virgin material; and σ is the true stress tensor. σ_{act} as defined in Eq 19 is the active stress, which is designed to account for the difference between the fatigue damage accumulation under tension and compression. Therefore, there may be three cases of damage accumulation under any complex loading condition:

1. If the stress state is inside the fatigue damage surface, there is no damage accumulation.
2. If the stress state is between two damage surfaces, the resulting damage is defined as fatigue damage.
3. If the stress state is outside the plastic damage surface, the resulting damage is defined as plastic damage.

The total damage ($\mathbf{D}$) is postulated to be the linear summation of fatigue damage ($\mathbf{D}_f$) and plastic damage ($\mathbf{D}_p$). It can be written as

$$\mathbf{D} = \mathbf{D}_f + \mathbf{D}_p \tag{9}$$

or equivalently as

$$w = w_f + w_p \tag{10}$$

where w is the total overall damage, w_f is the overall fatigue damage, and w_p is the overall plastic damage. When the total overall damage w reaches a critical value w_c, the element of material is said to be ruptured. Therefore, the entire process of damage initiation, damage evolution, crack initiation, and propagation leading to final rupture can be simulated by this local approach, which would not otherwise be possible using the fracture mechanics approach.

By postulating that the damage state in an element of material can be characterized by a macroscopic state variable $\mathbf{M}(\mathbf{D})$,

$$\mathbf{M} = \frac{1}{1-d} \begin{bmatrix} 1 & \mu & \mu & 0 & 0 & 0 \\ \mu & 1 & \mu & 0 & 0 & 0 \\ \mu & \mu & 1 & 0 & 0 & 0 \\ 0 & 0 & 0 & 1-\mu & 0 & 0 \\ 0 & 0 & 0 & 0 & 1-\mu & 0 \\ 0 & 0 & 0 & 0 & 0 & 1-\mu \end{bmatrix} \tag{11}$$

the evolution equation of damage is expressed based on the damage mechanics theory as follows [*18*]

$$\dot{d}_f = -\frac{\lambda_{fd}(Y_{d,f} + \gamma Y_{\mu,f})}{2Y_{fd}^{1/2}} \qquad \dot{\mu}_f = -\frac{\lambda_{fd}(\gamma Y_{d,f} + Y_{\mu,f})}{2Y_{fd}^{1/2}} \tag{12}$$

$$\dot{w}_f = \lambda_{fd} = \frac{Y_{d,f}\dot{Y}_{d,f} + \gamma Y_{d,f}\dot{Y}_{\mu,f} + \gamma Y_{\mu,f}\dot{Y}_{d,f} + Y_{\mu,f}\dot{Y}_{\mu,f}}{2Y_{fd}^{1/2}K(w)} \tag{13}$$

$$\dot{d}_p = -\frac{\lambda_{pd}(Y_d + \gamma Y_\mu)}{2Y_{pd}^{1/2}} \qquad \dot{\mu}_p = -\frac{\lambda_{pd}(\gamma Y_d + Y_\mu)}{2Y_{pd}^{1/2}} \tag{14}$$

$$\dot{w}_p = \lambda_{pd} = \frac{Y_d\dot{Y}_d + \gamma Y_d\dot{Y}_\mu + \gamma Y_\mu\dot{Y}_d + Y_\mu\dot{Y}_\mu}{2Y_{pd}^{1/2}\dfrac{dB}{dw_p}} \tag{15}$$

where the function $K(w)$ may be expressed to a first approximation as

$$K(w) = K_0\left(1 - \frac{w}{w_c}\right) \tag{16}$$

where d_f and μ_f are two independent components of fatigue damage $\mathbf{D}_f$, d_p and μ_p are two independent components of plastic damage $\mathbf{D}_p$, λ_{fd} and λ_{pd} are Lagrange multipliers, w_c is the critical value of w, and K_0 is a material constant.

In order to consider the difference between the damaging process under tensile and compressive loading condition, the effective stress range is introduced in the fatigue damage model and has been successfully used to predict the effect of mean stress on the fatigue life of a smooth specimen [*18*]. The stress range in a cycle may be decomposed into two parts as follows:

$$\Delta\sigma^+ = \sigma_{max} - \sigma_0 \qquad \Delta\sigma^- = \sigma_0 - \sigma_{min} \tag{17}$$

where σ_{max} and σ_0 are the stress tensors corresponding to the maximum and minimum value of Y_{pd} in a cycle, respectively, and σ_{min} is the stress tensor at the instant half a cycle after (or before) σ_{max} appears. Under uniaxial cyclic loading, there are two distinct phases of damage:

1. For tension-compression loading, the minimum stress is negative. The minimum value of Y_{pd} is zero so that σ_0 equals 0. That means the positive part is the tensile stress, and the negative part is the absolute value of the compressive stress.
2. For tension-tension loading, the minimum stress is positive. So the value of Y_{pd} increases monotonically as the loading increases, and the value of σ_0 is equal to the minimum stress. Therefore, the positive part is the total stress range, and the negative part is zero.

Accordingly, the effective stress range may be written as a first approximation as follows

$$\Delta\sigma_{eff} = \Delta\sigma^+ + \alpha\Delta\sigma^- \tag{18}$$

and the active stress σ_{act} is introduced as [*18*]

$$\sigma_{act} = \begin{cases} \sigma - \sigma_0 + \alpha(\sigma_0 - \sigma_{min}), & \text{if } Y_{pd}(\sigma_0) > Y_{pd}(\sigma_{max}) \\ \alpha(\sigma - \sigma_{min}), & \text{if } Y_{pd}(\sigma_{min}) < Y_{pd}(\sigma_0) \end{cases} \tag{19}$$

where α is a material constant and varies usually from 0 to 1. If α is zero, there is no contribution from the negative part to the damage accumulation. Otherwise, the effect of the negative part is the same as that of the positive part when α is 1.

Finite Element Analysis

Due to damage accumulation, the local rigidity in a material element decreases during the loading process. This change should be included in the numerical analysis to achieve an accurate assessment of stress distribution near the crack tip. Although the constitutive equations of damaged material are more complex than that of undamaged material [*18*], the conventional finite element method can be conveniently modified to include the effect of deterioration of material properties. By deriving a new effective instantaneous tangent modulus matrix, $\bar{\mathbf{C}}^{ep}$, which includes the effect of damage, the element stiffness matrix can be computed as [*16*]

$$[K_{ij}] = \int_V^2 [B_{ij}]^T : [c_{ij}^s] : [B_{ij}]\, dV \qquad \mathbf{C}^s = \frac{1}{2}(\bar{\mathbf{C}}^{ep} + \bar{\mathbf{C}}^{epT}) \tag{20}$$

where $[B_{ij}]$ is the transformation matrix, and $\mathbf{C}^s$, a symmetric matrix, is used to evaluate the element stiffness in an iteration procedure to overcome the difficulties caused by the asymmetric matrix $\bar{\mathbf{C}}^{ep}$. It should be emphasized that $\mathbf{C}^s$ is only used to evaluate the element stiffness matrix in an iteration procedure, as the relationship between the incremental true stress and strain is ultimately determined by $\bar{\mathbf{C}}^{ep}$. Consequently, the accuracy of the results obtained by this approach is the same as that by the conventional FEM analysis.

The following numerical analysis was performed using a general purpose finite element program known as NFAP, which was modified to incorporate the fatigue damage model. The overall damage at each integration point is calculated by integrating Eqs 11 to 14. It is postulated that rupture of an integration point takes place when the total overall damage in a particular material element reaches its critical value, w_c. This rupture state is simulated in the FEM analysis by reducing the rigidity and strength of this point to zero. The aggregation of ruptured points is interpreted as a part of the global crack. In order to simulate the crack closure, the ruptured points may recover the capability of sustaining the stress to the value it has attained at its critical state whenever the strain component perpendicular to the crack propagation direction at these points are found to be negative. Therefore, the whole process of fatigue crack propagation from the initiation of damage, damage evolution, and formation of a macrocrack to the final failure of a component can be analyzed by the proposed unified method of fatigue damage analysis.

Crack Growth Analysis

The behavior of a fatigue crack growing in a cracked plate is studied in this paper in order to demonstrate the applicability of the damage model discussed above. The material chosen for the investigation is an as-received Al alloy 2024-T3 Alclad plate with a thickness of 3.175 mm. The true stress-strain curve and the increment of plastic damage threshold–overall plastic damage curve $B(w_p)$ are shown in Fig. 2 and Fig. 3, respectively.

The dimensions of the specimen used for fatigue damage analysis are shown in Fig. 4. The experimental tests were carried out on an AMSLER high-frequency vibrophore machine. The loading was 45 ± 16.5 MPa with the loading direction normal to the specimen's rolling direction at about 100 Hz. A total of five specimens was used to measure the crack growth results under the specified loading. The material constants in the fatigue damage model were measured by a series of uniaxial tension tests and uniaxial fatigue tests on smooth specimens described in Ref *18* as follows

$$\gamma = 0.7 \quad B_0 = 0.7413\,\text{MPa} \quad w_c = 0.245 \quad E = 74\,300\,\text{MPa}$$
$$\nu = 0.33 \quad \sigma_y = 330\,\text{MPa} \quad \alpha = 0.45 \quad K_0 = 423\,500\,\text{MPa}$$

The plate is assumed to be in a state of plane stress in the numerical analysis. Only a quarter of the specimen needs to be analyzed due to the symmetry of the geometry and the loading condition. The first computational question to be examined relates to the choice of cycle numbers used to compute the damage accumulation in a loading process. It is impracticable to calculate the damage accumulation every cycle, especially for constant amplitude high-cycle fatigue. A step-wise procedure needs to be devised to reduce the computing time within a practical limit [*16*]. Consequently, the whole loading process is divided into several steps. The damage accumulation in a cycle is assumed within each computational step to remain the same. To check the effect of the number of cycles ΔN chosen for a step on the convergence of the numerical results, a numerical experiment was

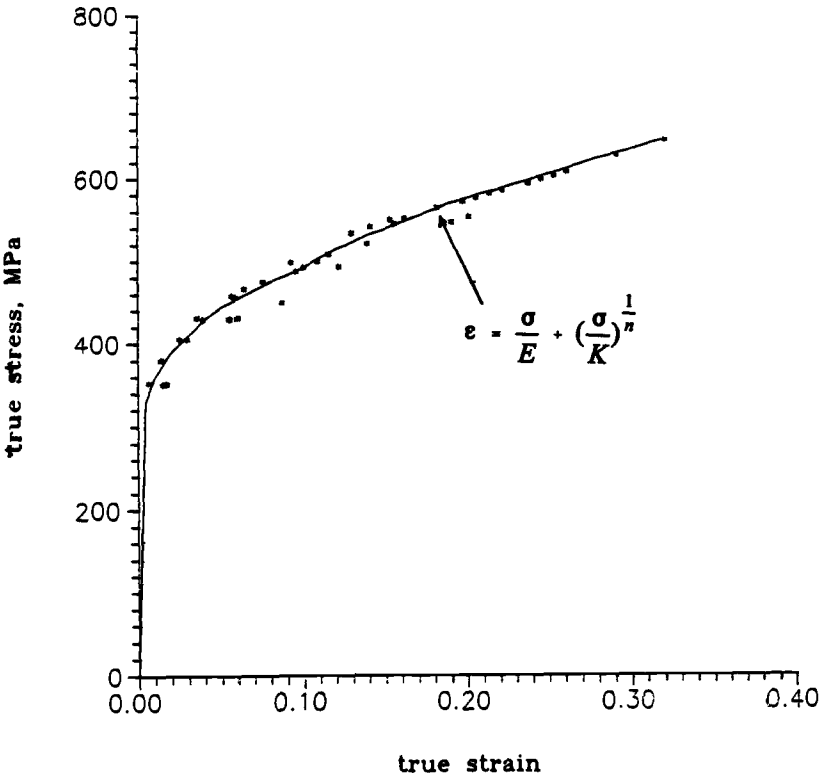

FIG. 2—*Relationship between true stress and true strain.*

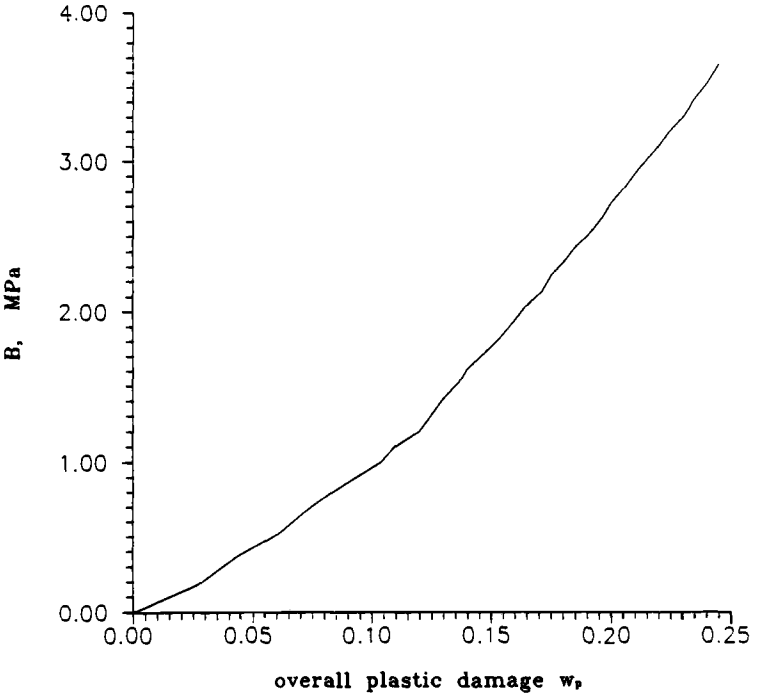

FIG. 3—*Relationship between* B *and* W_p.

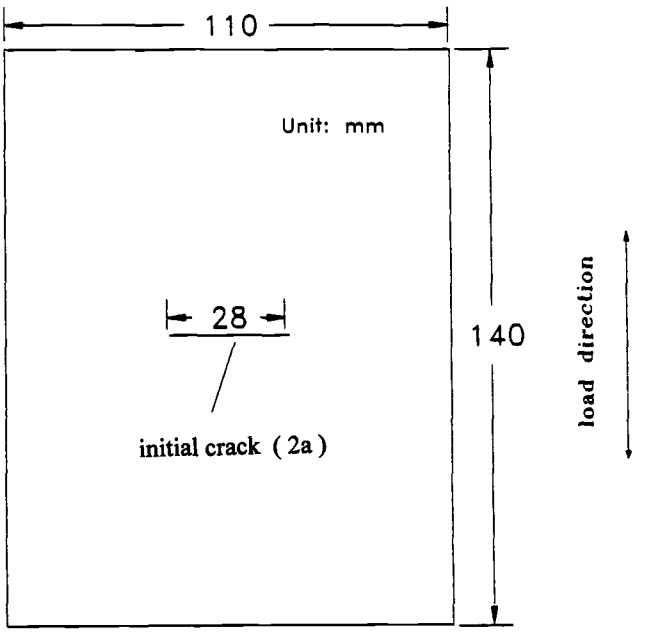

FIG. 4—*Center cracked plate.*

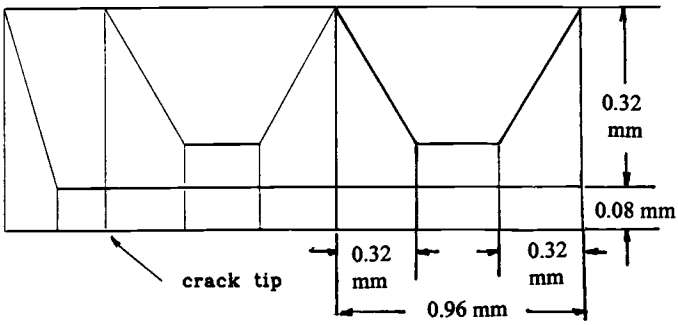

FIG. 5—*Finite element mesh construction at the crack tip.*

performed. A total of 90 eight-noded isoparametric plane stress elements with 306 nodes was used. The element area integrations were performed with a two-by-two Gaussian numerical integration scheme. The finite element mesh near the crack tip is shown in Fig. 5. The dimensions of the elements ahead of the macrocrack are 0.08 mm (height) by 0.32 mm (length). Three different cyclic increments, i.e., ΔN of 1000 cycles, 500 cycles, and 250 cycles, in each step were selected for the investigation. The cycles predicted for the crack growth process for each ΔN are shown in Fig. 6. No sign of convergence can be observed from the figure. A larger number of steps should be taken to attain a consistent result. However, if we first calculate the damage accumulation with a larger ΔN until the overall damage at the integration point near the crack tip has attained its critical value and then choose a smaller $\Delta N_r = 50$ cycles for the release of rigidity and strength at this point, more

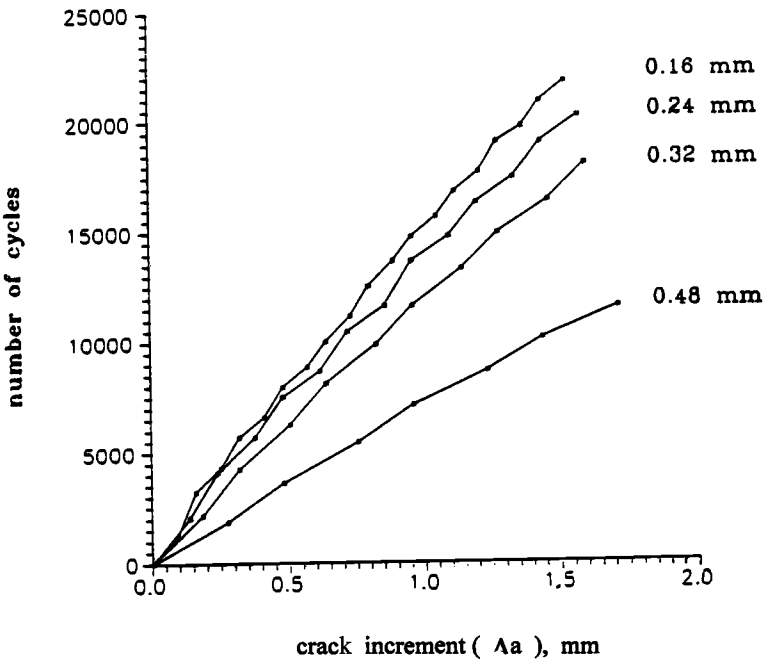

FIG. 6—*Effect of constant* ΔN *on solution convergence.*

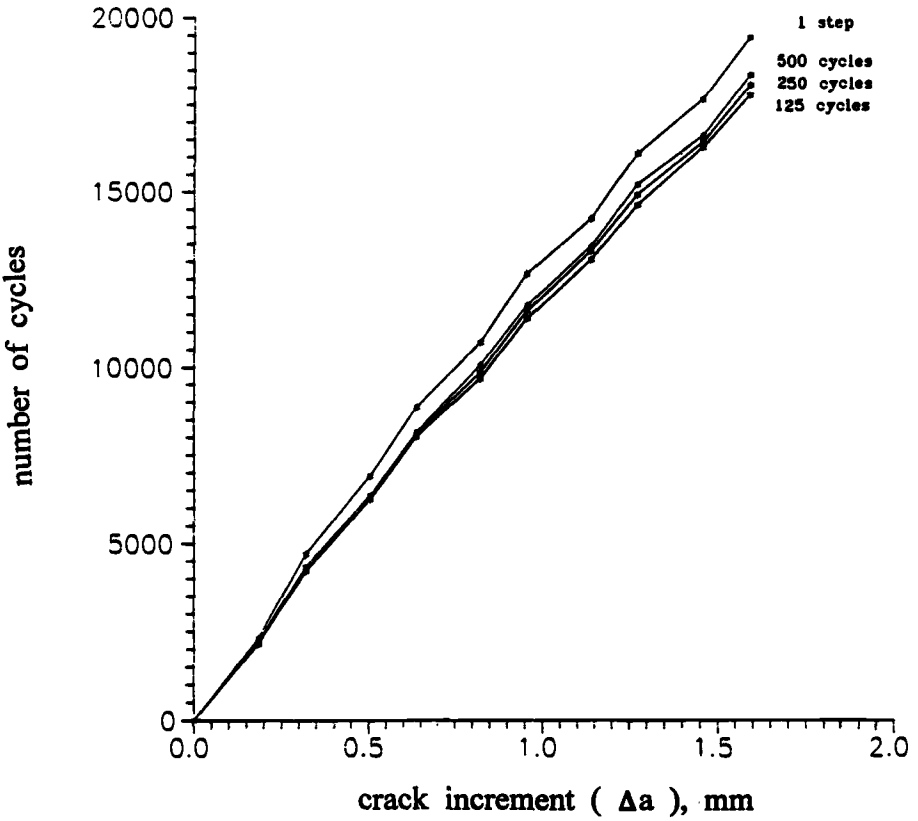

FIG. 7—*Effect of variable* ΔN *on solution convergence.*

accurate results can be obtained as shown in Fig. 7. It can be observed from the figure that there is almost no difference to the choice of ΔN less than 500 cycles. For the problem under investigation, it has been found from the computed numerical results that the number of cycles to cause a crack to propagate from one integration point to its ensuing point is about 1500 to 2000 cycles.

It may be concluded from the numerical experiments that it is appropriate to divide a loading process into three computational procedures, i.e., ΔN to attain the overall damage close to its critical value, ΔN_r to cause rupture of an integration point, and then ΔN to yield crack incremental growth. It is of interest to note that there is only about 10% discrepancy even if the procedure adopting a constant ΔN throughout the entire loading process is employed. This is evident by comparing the results shown in Figs. 6 and 7 using $\Delta N = 250$ cycles from which a discrepancy of about 10% can be observed. Therefore, for the rupture of second integration point after the first one, this particular loading process should be divided into at least six steps in order to achieve a satisfactory result when ΔN in each step is kept constant.

Another computational question to be resolved in this paper is the dependence of numerical results on the finite element size. Four different dimensions of finite element mesh shown in Fig. 5 ahead of the crack tip along the crack propagation direction are selected. The horizontal lengths of 0.16, 0.24, 0.32, and 0.48 mm were selected, while the element

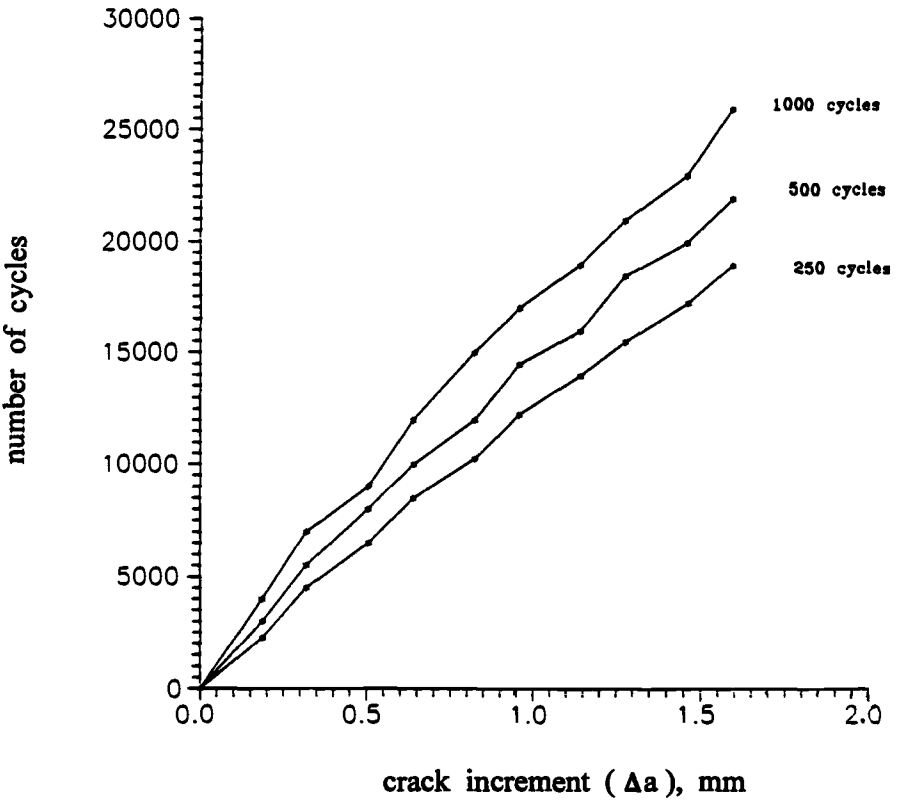

FIG. 8—*Effect of finite element mesh size.*

height remained constant at 0.08 mm. The computational procedure with $\Delta N = 500$ cycles and $\Delta N_r = 50$ cycles discussed above to simulate a loading process was adopted. It can be observed from Fig. 8 that there is no marked difference on the choice of element sizes except for the case of the horizontal element length of 0.48 mm. The maximum difference in the predicted fatigue life between the first three cases is about 22%.

It can be concluded from the above numerical experiments that satisfactory predictions can be achieved using the computational procedures described above in comparison with the data scatter normally observed in fatigue testing. The dependence of numerical results on finite element mesh size remains, however, an open problem [*19*].

To check the accuracy of the predicted results, a numerical analysis was performed for an incremental crack growth of 15 mm. A total of 171 elements with 541 nodes was chosen. The mesh discretization near the crack tip is shown in Fig. 5 employing several 0.08 by 0.32-mm elements along the crack growth direction. The cyclic loading simulation was carried out by employing a constant $\Delta N = 250$ cycles for the entire loading process. Comparison between the experimental results and the predicted ones is found to be satisfactory as shown in Fig. 9.

Conclusions

The application of a fatigue damage model to predict constant amplitude fatigue crack growth in a 2024-T3 Alclad plate containing a center crack under uniaxial constant ampli-

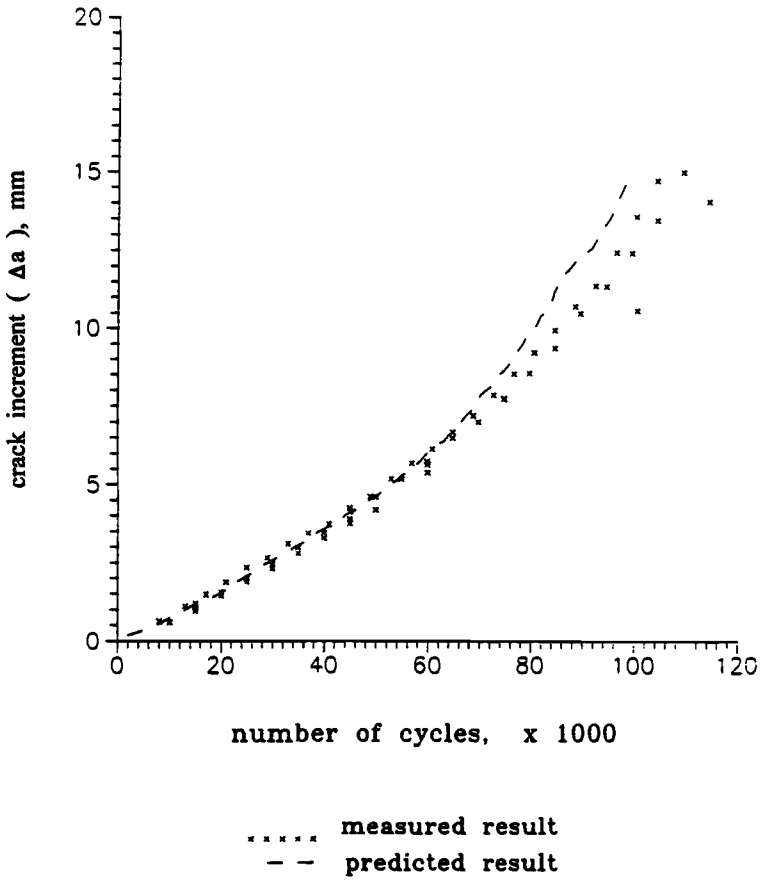

FIG. 9—*Fatigue crack growth under cyclic loading of 45 ± 16.5 MPa.*

tude loading is presented. The analysis on fatigue crack propagation was carried out both experimentally and numerically. Two main computational questions are examined and discussed:

1. The simulation of cyclic loading is performed in a step-wise procedure rather than cycle by cycle to reduce the computing time within a practical limit for engineering design analysis. The effect of the number of cycles chosen for each step on the accuracy of the numerical results is examined, and a simple computational procedure is recommended to achieve satisfactory convergence and accuracy in the numerical solution.
2. The dependence of the numerical results on the finite element mesh size is investigated. Satisfactory results have been obtained in comparison with the data scatter normally observed in fatigue testing if an appropriate choice of mesh size is made.

Acknowledgment

The research described in this paper has been sponsored by the Croucher Foundation whose support is gratefully acknowledged.

References

[1] Paris, P. C., Gomez, M. P., and Anderson, W. P., "A Rational Analytic Theory of Fatigue," *The Trend in Engineering*, Vol. 13, 1961, pp. 281–285.

[2] Paris, P. C., "Twenty Years of Reflection on Questions Involving Fatigue Crack Growth. Part I: Historical Observations and Perspectives," *Fatigue Thresholds*, 1981, pp. 3–10.

[3] Nowack, H. and Marissen, R., "Fatigue Crack Propagation of Short and Long Cracks: Physics Basis, Prediction Methods and Engineering Significance," *Fatigue '87*, 1987, pp. 207–222.

[4] McEvily, A. J., "On the Growth of Small/Short Fatigue Cracks," *JSME International Journal Series*, Vol. 32, No. 2, 1989, pp. 181–198.

[5] Nishitani, H. and Kawagoishi, N., "Fatigue Crack Growth Laws in Small and Large Cracks and their Physical Background," *JSME International Journal Series I*, Vol. 35, No. 1, 1992, pp. 1–12.

[6] Tanaka, K., "Mechanics and Micromechanics of Fatigue Crack Propagation," *Fracture Mechanics: Perspectives and Directions, ASTM STP 1020*, American Society for Testing and Materials, West Conshohocken, PA, 1989, pp. 151–165.

[7] Liu, H. W., "A Review of Fatigue Crack Growth Analyses," *Theoretical Applied Fracture Mechanics*, Vol. 16, 1991, pp. 91–116.

[8] Saxena, A. and Hudak, S. J., Jr., "Role of Crack Tip Stress Relaxation in Fatigue Crack Growth," *Fracture Mechanics (11th Conference), ASTM STP 677*, American Society for Testing and Materials, West Conshohocken, PA, 1979, pp. 215–232.

[9] Mowbray, D. F., "Derivation of a Low-Cycle Fatigue Relationship Employing the J-integral Approach to Crack Growth," *Cracks and Fracture (9th Conference), ASTM STP 601*, American Society for Testing and Materials, West Conshohocken, PA, 1976, pp. 33–46.

[10] Majumdar, S. and Morrow, J. D., "Correction Between Fatigue Crack Propagation and Low Cycle Fatigue Properties," *ASTM STP 559*, American Society for Testing and Materials, West Conshohocken, PA, 1974, pp. 158–182.

[11] Chaboche, J. L., "Continuous Damage Mechanics—A Tool to Describe Phenomena Before Crack Initiation," *Nuclear Engineering and Design*, Vol. 64, 1981, pp. 233–247.

[12] Chaboche, J. L., "Continuum Damage Mechanics: Present State and Future Trends," *Nuclear Engineering and Design*, Vol. 105, 1987, pp. 19–23.

[13] Lemaitre, J., "Local Approach of Fracture," *Engineering Fracture Mechanics*, Vol. 25, No. 5, 1986, pp. 523–537.

[14] Chaboche, J. L. and Lesne, P. M., "A Non-linear Continuous Fatigue Damage Model," *Fatigue Fracture Engineering Materials and Structures*, Vol. 11, 1988, pp. 1–17.

[15] Murakami, S., "A Continuum Mechanics Theory of Anisotropic Damage," *Yielding, Damage, and Failure of Anisotropic Solids, EGF5*, 1990, pp. 465–478.

[16] Chow, C. L. and Wei, Y., "A Damage Mechanics Model of Fatigue Crack Initiation in Notched Plates," *Theoretical Applied Fracture Mechanics*, Vol. 16, 1991, pp. 123–133.

[17] Chow, C. L. and Wei, Y., "A Model of Continuum Damage Mechanics for Fatigue Failure," *International Journal of Fracture*, Vol. 50, 1991, pp. 301–316.

[18] Wei, Y., Chow, C. L., and Duggan, B. J., "A Damage Model of Fatigue Analysis for AL Alloy 2024-T3," *Advances in Engineering Plasticity and its Application*, 1992, pp. 325–332.

[19] Bazant, Z. P., "Mechanics of Distributed Cracking," *Applied Mechanics Reviews*, Vol. 39, 1986, pp. 675–685.

Anthony T. Chang,[1] *Norman W. Nelson,*[1] *Jennifer A. Cordes,*[1] *and Yung-Joon Kim*[1]

Fatigue Prediction Based on Computational Fracture Mechanics

REFERENCE: Chang, A. T., Nelson, N. W., Cordes, J. A., and Kim, Y.-J., **"Fatigue Prediction Based on Computational Fracture Mechanics,"** *Advances in Fatigue Lifetime Predictive Techniques: 3rd Volume, ASTM STP 1292,* M. R. Mitchell and R. W. Landgraf, Eds., American Society for Testing and Materials, 1996, pp. 100–115.

ABSTRACT: A general numerical method has been developed to predict fatigue crack initiation and fatigue crack propagation under cyclic loads. Finite element technique is employed to model specimen geometry. The method requires uniaxial stress/strain material data only; empirical fatigue constants are not required. It determines the number of load cycles for crack initiation or for crack propagation based on fracture energy, W, and dissipated energy per cycle, E. Fracture energy is the plastic-strain energy contained in a Dugdale-type cohesive stress zone located near an initial defect. The size of the cohesive zone of a specimen is established by a computational procedure that simulates elastic-plastic fracture under static loading. Dissipated energy per cycle is the plastic-strain energy in a hysteresis loop that exhibits cyclically stable behavior after "shake-down." The number of cycles to initiate a crack or to propagate a crack to a finite amount is obtained by dividing the fracture energy, W, by the dissipated energy per cycle, E.

Verification examples showing stress amplitude versus number of cycles (S-N diagram) are compared with experimental results. Also, experimental crack growth rate as a function of stress intensity factor (Paris-type equation) is compared with calculated results based on this method. Fatigue constants based on experimental data were not required in the computations. Limited comparison of predicted cycles to experimental results indicates good correlation. This work is significant in that it suggests a new and improved approach to problems of fatigue. Since fatigue behavior can be predicted using only uniaxial material tensile data, it holds out the promise of a reduced need for experimental work in the future.

KEYWORDS: fatigue prediction, fracture mechanics, testing

Introduction

Background

Fatigue failure is the consequence of cumulative cyclic damage induced by repeated fluctuating loads. Fatigue crack initiation or fatigue crack propagation occurs only when there is plastic strain or yielding. For constant amplitude cyclic loadings, fatigue life can be represented by the number of load cycles, N. After a certain number of load cycles, the accumulated cyclic damage in the form of irreversible plastic-strain energy causes the initiation and subsequent propagation of a crack. Crack initiation life for cyclic loadings can be represented by the number of cycles, N_i, required to initiate a crack. The number of cycles, N_p, required to propagate a crack to component failure may be considered as the

[1]Department of Mechanical Engineering, Stevens Institute of Technology, Hoboken, NJ 07030.

fatigue propagation life. Total fatigue life, N, is the sum of the fatigue initiation and fatigue propagation lives.

Specimen fatigue behavior is often represented by a diagram of fluctuating stress amplitude, S, versus load cycles, N. A typical S-N diagram, as shown in Fig. 1, may be divided into three regions. Above a certain cyclic stress amplitude, the number of cycles to reach component failure is very small. This region may be considered as the low-cycle region. Region II is classified as the crack propagation region. In this region the number of load cycles, N, is a function of applied stress amplitude, S. The fatigue behavior in the third region exhibits an applied cyclic amplitude threshold below which cracks do not initiate. The proposed method in this paper may be employed to study fatigue behavior in all three regions.

A widely used method to study fatigue behavior is the strain-life method, which is based on the observation that the response of components with notches depends on the strain and deformation history near the notch. Experimentally generated parameters are required to represent material fatigue properties. Applications [*1,2*] of this method are mostly for low-cycle fatigue problems. The proposed computational method in this paper, like the strain-life method, predicts fatigue behavior based on strain history near a crack or notch. Unlike the strain-life method, the present approach is based on fracture mechanics considerations and may be applied to both high-cycle and low-cycle fatigue problems.

For crack propagation, Paris and Erdogan [*3*] proposed a semi-empirical power-law equation to represent fatigue behavior for metals. In the governing equation, the change of crack length with respect to number of cycles (da/dN) is assumed to be a function of the difference in the stress intensity factors (ΔK) evaluated at the maximum and minimum applied cyclic loads. Material fatigue data are required with this approach.

To explain differences in fatigue behavior due to the ratio between fluctuating maximum load and minimum load, Elber [*4*] introduced the concept of crack closure. The prediction of crack growth is based on a correlation of crack growth rate data with the "effective" stress-intensity factor at the crack tip similar to a Paris-type equation. Newman [*5*] developed a

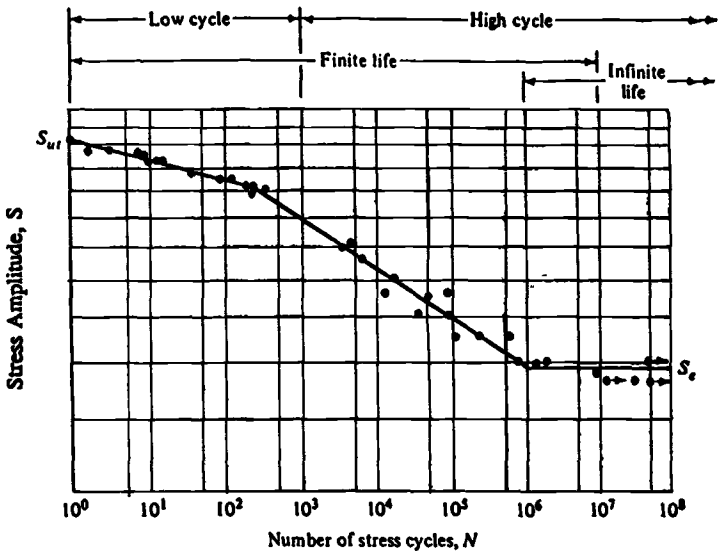

FIG. 1—*A typical* S-N *diagram.*

computational procedure based on finite element technique to simulate crack closure. The method has been shown by Newman [*6*] to be particularly useful for predicting crack growth behavior under spectrum loadings. Drew [*7*] and Dexter [*8*] have demonstrated that the method can be applied to cases with overload and underload. Dowling and Begley [*9*] used the *J*-integral value and applied the concept to cases with small-scale plasticity. Recent applications of the concept were provided by de Koning [*10*], Keyvanfar [*11*], Dawicke [*12*], Ranganathan [*13*], and Kumar [*14*]. All these applications require a known power-law equation that has at least two experimentally determined material fatigue properties.

Overview of Proposed Method

In this paper a computational method is proposed to predict component fatigue life without prior knowledge of its fatigue behavior. The only material data required in the computational procedure is the uniaxial stress/strain diagram. Geometric dependencies such as thickness, specimen size, and initial crack length are automatically incorporated into a finite element model. The computational method may be used to predict threshold load cycles to crack initiation as well as the number of cycles for crack propagation. The number of fluctuating load cycles is determined by the fracture energy, W, and the dissipated energy per cycle, E. Fracture energies that cause crack initiation, W_i, or crack propagation, W_p, are contained in a cohesive stress zone located in front of a crack or flaw. The amount of dissipated energy per cycle, E, under fluctuating loading is determined by a method similar to the "shake-down" concept [*15*]. Component fatigue lives are determined by dividing the combined energies (W_i and W_p) by the dissipated energy per cycle, E.

Major Assumptions of Proposed Method

1. An initial sharp defect such as a crack exists. This means plastic strain is always present in the component.
2. Material cyclic compressive yield strength is the same as the cyclic tensile strength.
3. The dissipated energy per cycle, E, is a function of the plastic dissipation in a fatigue process zone created by cyclic loading.
4. If there is a material cyclic hardening or softening effect, a number of cycles are required to achieve a stable "shake-down" hysteresis loop. It is assumed that this number of cycles is small compared to the total number of cycles to failure.
5. The fracture energy, W, may be determined by an elastic/plastic static fracture analysis performed by a computational procedure [*16*]. The procedure simulates the size of the cohesive stress zone in front of the crack and the stable crack growth as a function of monotonically increasing applied load.
6. The number of cycles to initiate a crack or advance a crack may be found by dividing the fracture energy, W, by the dissipated energy per cycle, E.
7. The amplitude of the cyclic load is constant. Different cyclic loads must be studied separately and their effects combined.

Limitations of Proposed Method

1. Material properties should be represented by cyclic stress/strain data. If there is substantial strain hardening or softening during cyclic loading, different stress/strain data should be employed depending on the range of the cyclic loadings.
2. If the specimen is subjected to only a few cycles with a very high strain range, the transition effects from one cyclic stress/strain curve to another cyclic stress/strain

curve may not be neglected. This could have an effect on the accuracy of the dissipated energy per cycle, E.

3. If the plastic strain developed at the crack tip is very low, it is difficult to refine the finite element mesh sufficiently so that the dissipated energy per cycle, E, may be calculated accurately.
4. Examples studied so far involve two-dimensional specimens modeled by plane-stress or plane-strain finite elements. A change in thickness (necking) due to high strain at the crack tip may require three-dimensional analysis.

Computational Procedure for Elastic/Plastic Fracture

The computational procedure for elastic-plastic fracture predicts load versus stable crack growth behavior and is employed to determine the required fracture energy, W, for fatigue crack growth. Finite element technique is employed to represent the specimen. Planar elements are used to model flat panel specimens. Material stress/strain data and material strain hardening are included. The finite element mesh has duplicate grid-point pairs along the free crack surfaces and along the direction where damaged surfaces develop. The duplicate grid-point pairs operate under one of the following three modes:

1. They are constrained to have the same displacement before the flow stress, defined as the average between yield strength and ultimate strength, is reached.
2. They are used to model relative displacement between grid-point pairs once the flow stress is reached and an equivalent cohesive force, F_c, is inserted between the grid-point pairs.
3. They are used to model crack growth when critical crack tip opening displacement (CTOD) values are reached.

When grid-point pairs are in the second mode, they create a Dugdale-type cohesive stress zone in front of the crack. For computational convenience, the cohesive stress is equated to the flow stress so that strain-hardening effects are included in an approximated manner. This cohesive stress zone serves three purposes: (1) to represent the crack front stress distribution without special crack tip finite elements, (2) to indicate the size of the cohesive zone, and (3) to provide nodal displacements in the cohesive stress zone.

Two assumptions are introduced to simulate static fracture: one for crack initiation and another one for crack propagation. The first assumption is that crack initiation occurs when the load versus crack mouth opening displacement (CMOD) curve deviates by 5% from its linear elastic slope. This assumption is consistent with the ASTM Test Method for Plane-Strain Fracture Toughness of Metallic Materials (E 399-83) for testing of plane-strain stress intensity factor K_{Ic} under brittle fracture conditions. Figure 2*a* illustrates the ASTM testing procedure. This can be compared with Fig. 2*b*, which shows the load versus the CMOD curve of a simulated example and the crack initiation criterion. Deviation from the initial tangent line in both curves is proportional to the amount of plastic strain near the crack tip. At the 5% deviation point, a sufficient amount of irreversible plastic strain has been introduced into the specimen to cause crack initiation. The size of the associated cohesive zone is the critical value, r_p, and the corresponding CTOD is the critical CTOD, V_i. At crack initiation, the crack advances a distance equal to half of the distance to the next finite element node.

For subsequent crack growth, it is assumed that the governing fracture parameter is the critical CTOD value that is generated during the computational process. A one-element size crack growth occurs when the CTOD at any nodal location "j" reaches its critical value,

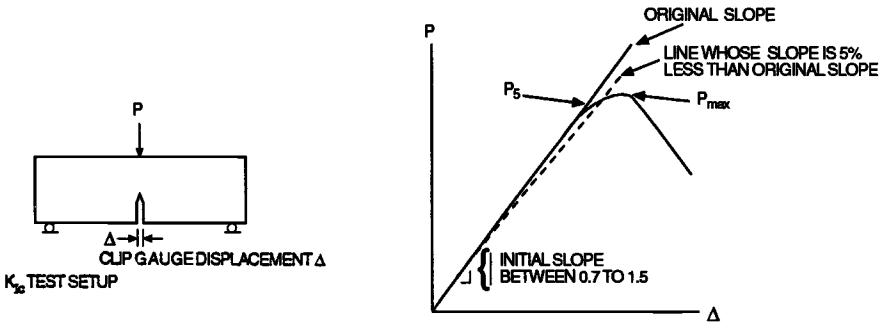

(a) ASTM Specification E-399-83.

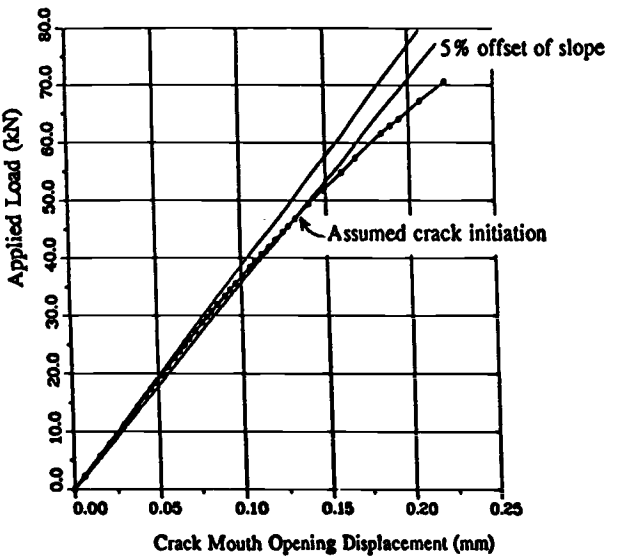

(b) Simulated Case (Example 1)

FIG. 2—*Crack initiation.*

V_{Rj}. The critical V_{Rj} value is determined from the CTOD at crack initiation, V_i, and the CTOD of node "j" immediately after the crack advanced past the last node, "$j - 1$." By designating this plastic-wake CTOD as $V_{pw,j}$, the critical CTOD of node "j" may be calculated by

$$V_{R,j} = V_i + V_{pw,j} \tag{1}$$

In the above equation, V_i represents the CTOD at crack initiation, and the other term, $V_{pw,j}$, may be considered as the effect of plastic wake on the critical CTOD. In most cases, the

effect of plastic wake, $V_{pw,j}$, gradually dominates the critical CTOD value as the crack advances. Equation 1 may be used to generate a critical CTOD curve as a function of crack growth.

The computational process consists of a series of load step increases and changes in cohesive stress zone size. At each load step, nodal forces are compared with the equivalent flow force and CTOD is checked against critical $V_{R,j}$. The computational steps are repeated until the cohesive zone extends through the component ligament (stable crack growth followed by plastic collapse) or until critical $V_{R,j}$ values are reached simultaneously at all grid-point pairs in the damage zone (stable crack growth followed by unstable crack growth).

Fatigue Prediction

Fatigue prediction relies on the assumptions that the number of load cycles required for crack initiation can be obtained from

$$N_i = W_i/E \tag{2}$$

and the number of cycles for crack propagation is

$$N_p = W_p/E \tag{3}$$

where E represents the dissipated energy of each fluctuating cycle, and W_i and W_p are the fracture energies obtained from the plastic-strain energies in the cohesive stress zone.

The static fracture simulation procedure is used to establish the size of the cohesive stress zone and nodal displacements within this zone. The fracture energy, W_i, at crack initiation is calculated by

$$W_i = \int \sigma_0 \, 3 \, dA \tag{4}$$

where σ_0 is the flow stress, and 3 represents displacements in the cohesive zone at crack initiation. This integration is performed along the critical cohesive stress zone, r_p, and is the plastic-strain energy generated within the zone by the static crack initiation load. In a similar manner as Eq 4, the fracture energy, W_p, required to reach a certain crack growth size is computed based on its corresponding cohesive stress zone.

If W_1 and W_2 are fracture energies required to reach two different crack sizes a_1 and a_2, the number of propagation cycles, N_p, to advance a crack from a_1 to a_2 under an applied fluctuating load with dissipated energy per cycle, E, is

$$N_p = (W_2 - W_1)/E \tag{5}$$

When a crack grows from an initial size, a_i, to a crack length of a_2, the strain energy, W_1, in the above equation is the W_i of Eq 4. The total number of cycles to reach a_2 can then be simplified as

$$N = W_2/E \tag{6}$$

If the crack length a_2 is much larger than a_i, the computation of the above equation should be divided into a number of smaller steps with different crack growths because the growing crack length affects the value of the dissipated energy, E.

The dissipated energy per cycle, E, is caused by a cyclic load fluctuating between maximum load level, L_{max}, and minimum load level, L_{min}. It is calculated in two steps. First, the number of nodes, n, in the cohesive stress zone that contributes to energy E is determined from an elastic-plastic analysis of the specimen without cohesive zone. The specimen is initially loaded to load level L_{max}, and a damaged plastic zone, demonstrated in Fig. 3*a*, develops. The specimen is then unloaded to load level L_{min}. Under this load level, elastic

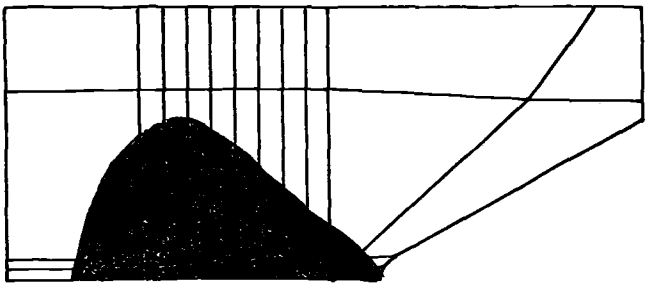

(a) Under Maximum Load 20 ksi
(positive yielding in dark area)

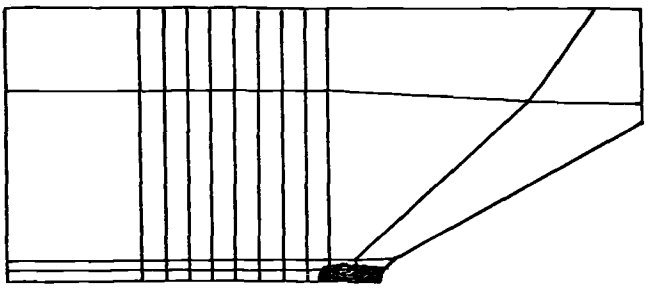

(b) After Restart with Minimum Load, zero
(negative yielding in dark area)

FIG. 3—*Fatigue fracture process zone.*

material surrounding the damaged zone forces material in some portion of the plastic damage zone into compressive yield. The length of this portion represented by n number of nodes may be considered as a fatigue fracture process zone as shown in Fig. 3*b*. In this fatigue process zone, nodal strains had gone from plastic tensile strain under maximum load, L_{max}, to plastic compressive strain under minimum load, L_{min}. During subsequent cyclic actions, work at these nodes produces cyclic plastic strain that generates fatigue crack growth. Only nodes in the fatigue process zone contribute to the strain energy per cycle, E. Nodal strains ϵ_{max} at load level L_{max} and ϵ_{min} at load level L_{min} in the fatigue process zone are used to determine the value of E.

Once the size and nodal strains of the fatigue process zone are determined, the second step is to find the value of the dissipated energy per cycle, E. E is the summation of nodal dissipated energies, e_i, in the fatigue fracture process zone. The load-displacement relationship at each node between load level L_{max} and load level L_{min} can be idealized in the form as shown in Fig. 4. Displacement, d_{max}, of a node in the fatigue fracture process zone under load level L_{max} is calculated by the elastic-plastic fracture simulation. The nodal displacement, d_{min}, under load, L_{min}, is approximated by

$$d_{min} = d_{max}(\epsilon_{min}/\epsilon_{max}) \tag{7}$$

where ϵ_{max} and ϵ_{min} are nodal strains under load levels L_{max} and L_{min} obtained in the "shakedown" analysis. This leads to a nodal dissipated energy in the form

$$e_i = 2F_c d_{max}(1 - \epsilon_{min}/\epsilon_{max}) \tag{8}$$

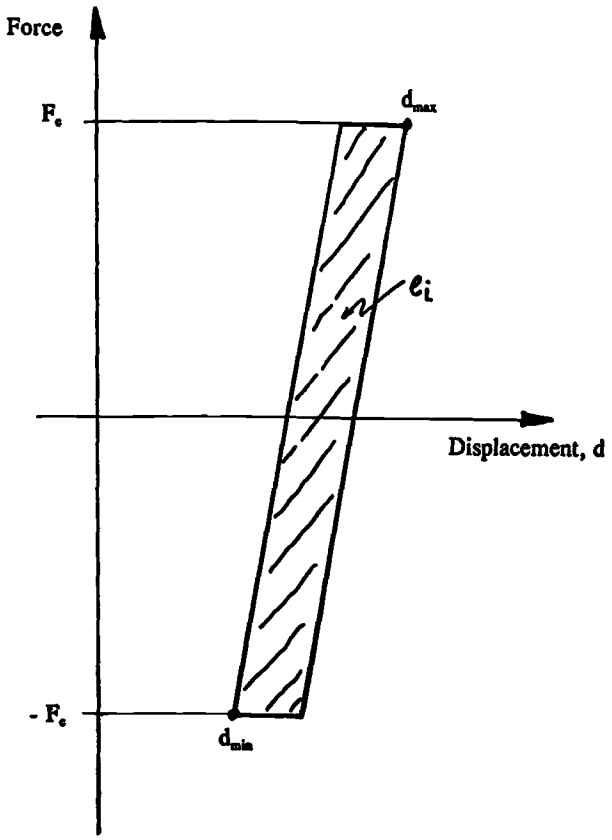

FIG. 4—*Schematic of dissipated energy of a node.*

where F_c is the nodal force corresponding to the flow stress. Summation of dissipated energies of all n nodes in the fatigue fracture process zone leads to the dissipated energy per cycle

$$E = \Sigma e_i \tag{9}$$

Since the determination of dissipated energy per cycle depends on the size of the fatigue fracture process zone that is a fraction of the cohesive stress zone, there has to be a large number of finite element nodes in the cohesive stress zone to achieve acceptable accuracy.

Validation Examples

Three experimental examples from the literature are presented and compared with computational results. In the first example, the total number of cycles for crack initiation and for crack growth were compared with measured data for specimens with sharp cracks. The second example demonstrates the application of the fatigue prediction method in cases with notched flaws. Again, the total numbers of cycles were compared. In the third example, the fatigue prediction method was applied to a specimen with known fatigue propagation properties. These results were computed using material data from a monotonically loaded tension specimen. Cyclic stress-strain data, if available, would have been preferred.

As mentioned before, a fine mesh is needed in front of a crack tip in order to have sufficient nodes to properly represent the fatigue fracture process zone. To minimize the need for small-sized elements, flow stress was replaced by yield strength as the material failure criteria in the computed examples. This resulted in larger cohesive stress zones and larger fatigue fracture process zones than would have occurred using the flow stress. To be consistent, both dissipated energy per cycle, E, and fracture energy, W, were calculated based on yield strength. All numerical computations were performed using the general purpose finite element program ABAQUS [*17*].

Example 1: Predicting Crack Initiation Cycles

Jack and Price [*18*] performed fatigue tests on edge-notched mild steel specimens and measured electrical potential drop to determine crack initiation under load cycles. The mild steel had a yield strength of 239 MPa and ultimate strength of 420 MPa. The form and dimensions of the specimen are shown in Fig. 5. The specimen has a uniform thickness of 5.1 mm. All fatigue tests were done under zero-tension load condition (load ratio $R = 0$). It was estimated that the specimen thickness was not sufficient for the plane-strain condition to dominate fracture behavior, therefore the specimen was modeled by plane-stress elements. The smallest element size was 0.051 mm. Two different notch depths were studied by the

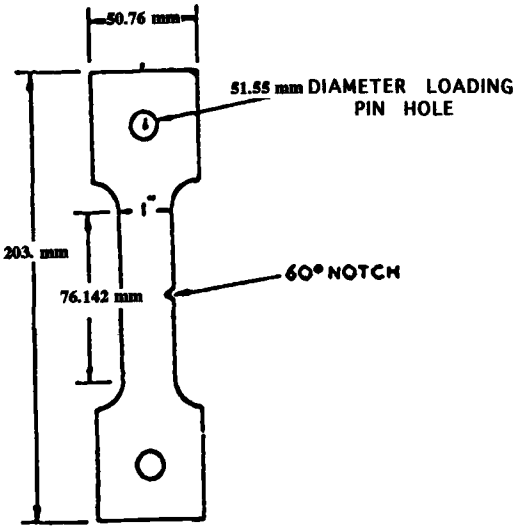

Material : Mild Steel
Yield Stress : 239 MPa
Ultimate Stress : 420 MPa
Thickness : 5mm
Notch root radius : .05 mm
Two notch depths studied : 1.27 mm and 3.81 mm

FIG. 5—*Example 1.*

present prediction method: 1.27 and 3.81 mm. For the case with 3.81-mm notch depth, the load versus the crack-mouth-opening-displacement curve was generated and is shown in Fig. 2*b*. Although there is a notch root radius given as 0.051 mm, it was assumed to be small enough to be considered as a sharp tip in the finite element model. The critical CTOD at crack initiation was found to be 1.48×10^{-3} mm, and the corresponding critical cohesive zone size was 1.83 mm.

The dissipated energy per cycle, E, was calculated according to the procedure given. Under some load amplitudes, crack growth is predicted. Effects of crack growth were neglected in the calculation of dissipated energy per cycle, E. Results are summarized in Table 1.

The fracture energy, W_i, required for crack initiation of the two selected cases was determined by Eq 4. Numbers of cycles to reach crack initiation according to Eq 2 were found to be much smaller than measured results. It was concluded that minute quantities of crack growth associated with theoretically declared crack initiation cannot be observed experimentally. Therefore, the measured cycles for crack initiation must be associated with a specific amount of crack growth that is experimentally measurable. Since Ref *18* did not state the criteria for crack initiation, it was assumed that the crack initiation is associated with crack growth sizes in the range of 0.28 to 0.33 mm, consistent with experimental equipment for measuring crack growth at the time these experiments were conducted.

Based on these initial crack growth assumptions, the fracture energies, W, were calculated, and numbers of cycles depending on load amplitudes were determined. The resulting load versus number of cycles is shown in Fig. 6. Measured data were found to be between results obtained from the two assumed crack growth sizes. Also, cyclic behavior of the 1.27-mm notch depth case with 0.28-mm crack growth is given in Fig. 6. Not knowing the exact amount of crack growth of the experimental results, it is difficult to assess the quality of the calculated predictions. However, they do reflect the dependency between load amplitudes and number of cycles.

Example 2: Generating S-N Diagram

Extensive fatigue crack tests of double-edged-notched specimens are described in Ref *19*. Specimens were machined from 25.4-mm-thick HY-130 steel plate and tested over a range of fluctuating stresses between zero and a maximum amplitude. Nine starting crack-tip radii ranging from zero to infinity were studied. The number of cycles required to generate a 0.25-mm crack was recorded. The specimen configuration is shown in Fig. 7.

The prediction of crack initiation in the present method relies on the 5% criteria, which is

TABLE 1—*Dissipated energy per cycle.*

Notch Depth, mm	Load Amplitude, MPa	Dissipated Energy per Cycle, E, N/mm
1.27	0.0689	8.27×10^{-3}
1.27	0.1034	5.05×10^{-2}
1.27	0.1379	9.82×10^{-2}
1.27	0.1724	2.29×10^{-1}
1.27	0.2069	4.53×10^{-1}
3.81	0.1034	3.94×10^{-1}
3.81	0.1379	8.09×10^{-1}
3.81	0.1724	1.7289

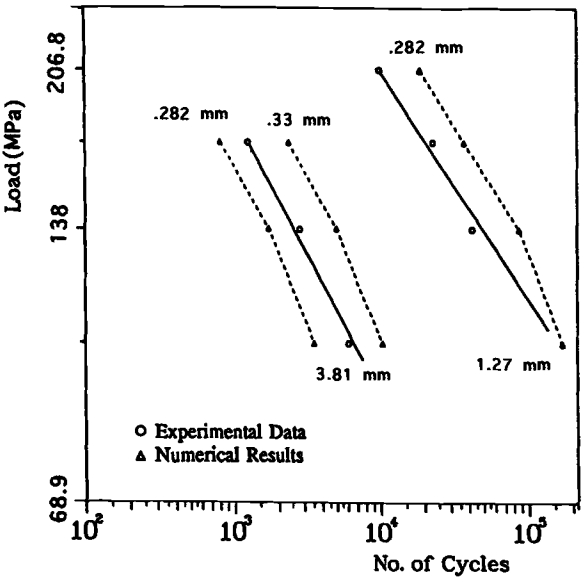

FIG. 6—*Comparison with experimental data.*

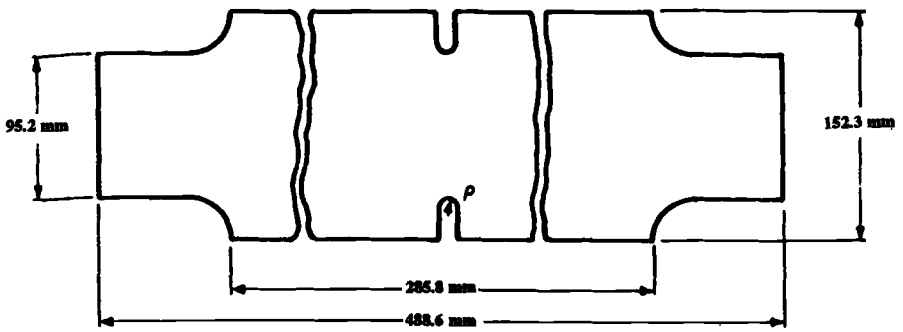

Material : HY130
Yield Stress : 1006 MPa
Ultimate Stress : 1054 MPa
Thickness : 3.17 mm
Two notch depths studied : 4 mm and 1.6 mm

FIG. 7—*Example 2.*

valid only when a sharp crack tip exists. In this example with finite notch root radius, there are two possible modified approaches. In the first approach, crack initiation is determined by a specimen of the same configuration but with the notch assumed to have a sharp crack tip. Crack initiation of the specimen with finite notch radius is thus assumed to take place when the cohesive stress zone size matches the one obtained by the sharp crack tip specimen. Once the crack has initiated, the procedure to simulate crack growth remains the same. The second modified approach assumes a certain amount of surface imperfection at the notch root radius. The imperfection reflects the quality of the surface finish and can be represented by the ratio a/r, where a is the length of the maximum surface crack and r the notch root radius. Specimens with different a/r ratios have different cohesive stress zone sizes at crack initiation. Both approaches lead to similar results in terms of the total number of cycles to reach a certain crack size. For this example, the first approach was selected.

Starting with an elastic-plastic fracture analysis of the specimen, sizes of the cohesive stress zone and their fracture energies were determined for different load amplitudes. The associated fracture process zone and dissipated strain energy per cycle were calculated according to the procedure given above. The total number of cycles required to reach a crack growth of 0.025 mm was found by Eq 6. Results for two notch-tip radii are compared to experimental data in Fig. 8. For both cases, the computer prediction did not do well at lower load amplitudes. The cause of the inaccuracy is the need for very fine meshes to accurately calculate the size of a small fatigue fracture process zone. This is particularly noticeable in the case with the larger root radius.

Example 3: Generating the da/dN *Curve*

According to Paris and Erdogan [*3*], crack propagation may be represented by a power-law equation in the form

$$da/dN = A(\Delta K)^m \tag{10}$$

where a is the crack length, N is the number of cycles, and ΔK is the stress intensity factor fluctuation. The constants A and m are parameters determined by curve-fitting of material test data. In Fig. 9, a typical set of experimental material data [*20*] is shown. The fatigue crack growth rate, da/dN, is plotted as function of the difference between the maximum and minimum stress intensity factor ΔK for six aluminum alloys. The yield strength of these alloys ranges from 234.4 to 379.2 MPa.

To demonstrate the application of the present fatigue prediction method to crack propagation problems, an arbitrary specimen configuration shown in Fig. 10 was chosen. The mesh distribution for one quarter of the specimen is also shown in Fig. 10. The initial crack length was 25.4 mm, and the fracture energy, ΔW, to reach a crack growth of 0.51 mm was found to be 0.045 N/m. Using two different maximum load amplitudes (zero to tension), L_1 and L_2, two different dissipated energies per cycle, E_1 and E_2, were calculated. Employing Eq 6, two cyclic lives, ΔN_1 and ΔN_2, were determined for the same amount of crack growth. The stress intensity factor, ΔK, under the two loads, L_1 and L_2, were calculated by standard linear elastic fracture mechanics. Results are given in Table 2.

The computed results that plot as a straight line are also shown in Fig. 9. Notice that the computed results fall close to the scatter band of the experimental data. If desired, the constants A and m in Eq 10 may be determined. In such a case the constants A and m will, in general, depend on the specimen geometry chosen to do the simulation. In other words, since elastic-plastic fracture is, in general, geometry dependent, so will the fatigue constants A and m be specimen geometry dependent.

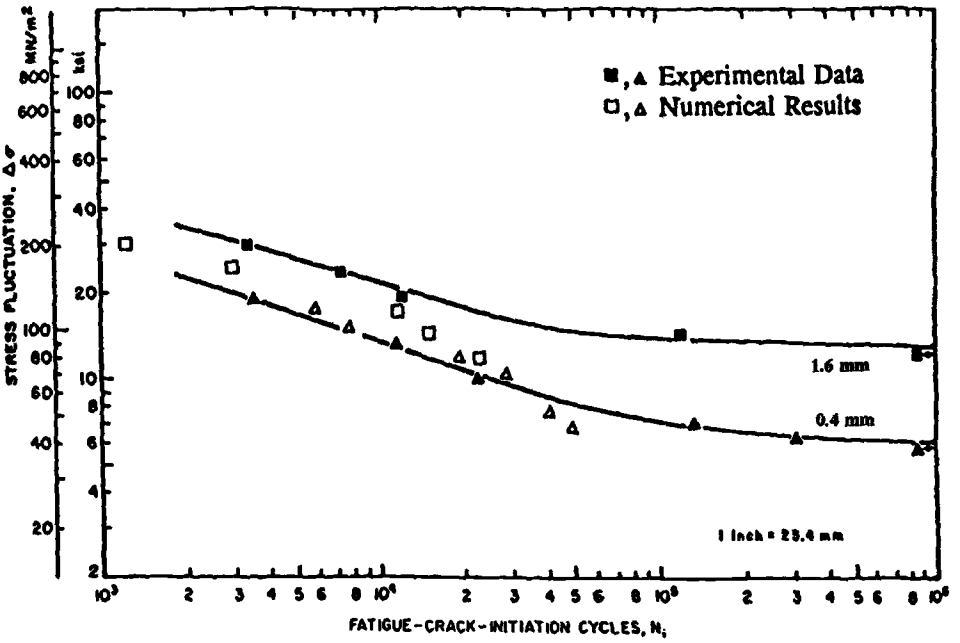

FIG. 8—*Comparison with experimental data.*

Conclusions

The fatigue prediction method presented in this paper is designed to simulate fatigue behavior from crack initiation through crack propagation to ultimate rupture. Although not enough examples have been studied, the proposed method has the basic mechanisms for being consistent with experimental observations. Reasons for the different fatigue behavior in the three regions of a typical *S-N* diagram can be explained by parameters used in the present method. With high-cycle loadings, fatigue behavior is mostly governed by load amplitudes. With the proposed method, the calculation of number of cycles at high-cycle fatigue is dominated by the dissipated energy per cycle, E, which depends on load amplitude. In an extreme case where the fatigue process zone is very small under fluctuating maximum and minimum load levels, the value of E approaches zero, resulting in essentially infinite fatigue life. At low-cycle fatigue, with larger load amplitudes, fatigue behavior according to the proposed method is governed largely by fracture energy, W, for both crack initiation and crack propagation. This is consistent with expectation because both fracture energy and low-cycle fatigue behavior depend on static fracture behavior.

Another indication that the basic approach of the present method is correct can be found in the following observation. Under large load amplitudes (low-cycle fatigue), the crack growth rate per cycle, da/dN, becomes very high. Experimental data indicate that this phase of accelerated crack-growth rate occurs at a constant value of crack-tip opening displacement (CTOD). This is consistent with the present approach, which determines the fatigue behavior in this region of high-load amplitude by the maximum fracture energy, W, value associated with a constant CTOD.

The proposed method also reflects the mean load (R ratio) effects of the loading. This effect is represented in the dissipated energy per cycle, E. When calculating this energy, the maximum load level determines the size of the damage zone near the crack. Upon unload-

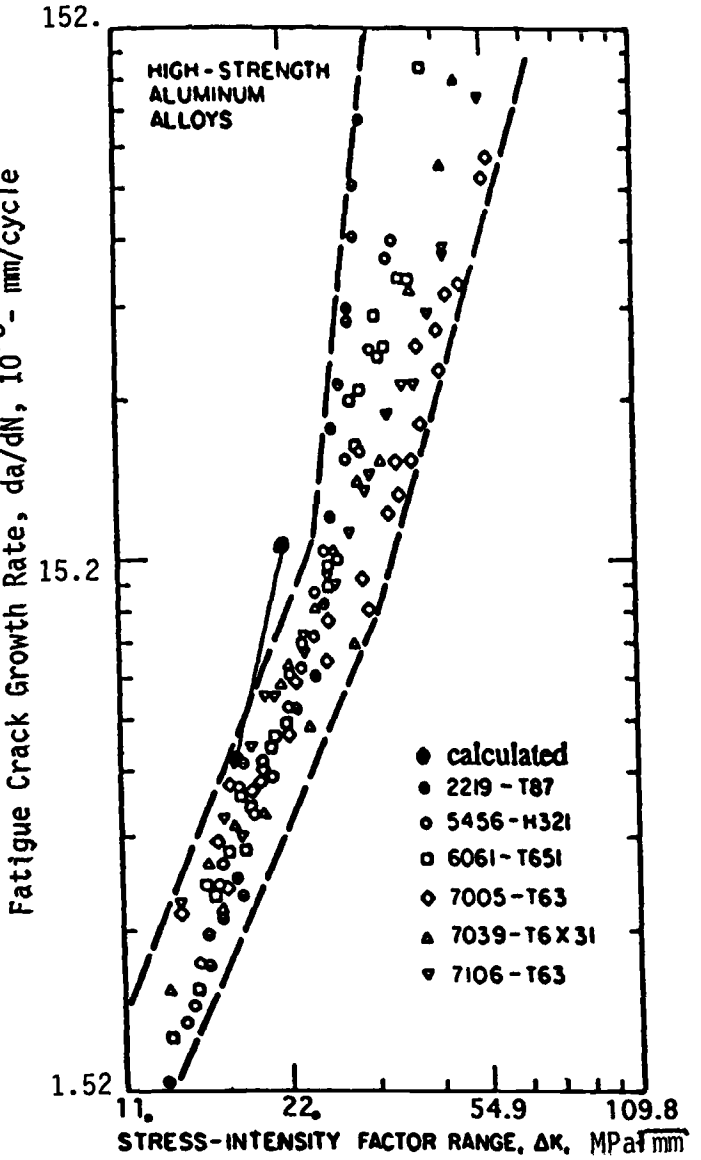

FIG. 9—*Plot of* da/dN *versus* ΔK *for six aluminum alloys.*

ing, the size of the fatigue process zone depends on the amount of unloading associated with the minimum load level. With a lower minimum load level, more of the damage zone will be forced into compressive yield by the surrounding elastic stresses. This leads to a larger E value or a less number of load cycles, which is consistent with expectations.

A commercial finite element code, ABAQUS, was employed to perform all computations. In the calculation of fracture energy, W, progressive nodal damage or release (crack growth) due to increased loading was tracked manually. At the occurrence of an event, boundary conditions of the finite element model were altered to reflect either nodal damage or node

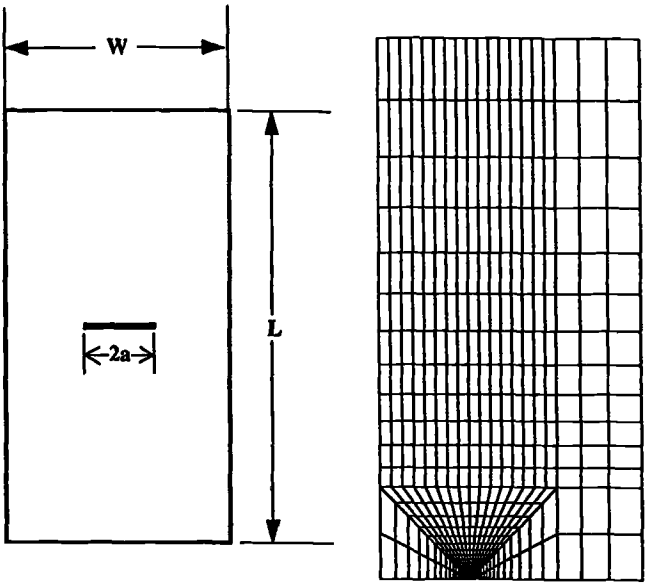

Material : 6061-T651 Aluminum
Yield Stress : 268.95 MPa
Ultimate Stress : 317.00 MPa
W = 76.1 mm, L = 149.7 mm, 2a = 25.4 mm
Thickness : .50 mm

FIG. 10—*Example 3.*

release. After inserting the changes into the finite element model, the program was restarted including the strain distribution generated by the previous load step. Load steps between restarts were held small. For each restart, typically one to four equilibrium iterations were required. ABAQUS default tolerance, which requires the residual force vector to be less than 0.5% of the force vector, was employed. Numerical iteration problems were not encountered.

In summary, a computational procedure to predict cyclic fatigue behavior using only uniaxial tensile stress/strain data has been developed. Comparison with experimental results shows acceptable correlation. Like most finite element solutions, the quality of the computer simulation depends on the refinement of the finite element mesh. This is particularly critical for the determination of the fatigue fracture process zone and the associated dissipated energy per cycle, E, for small load amplitudes. The implication in terms of accuracy requires future investigation. Another important effect that must be studied is the implication of using noncyclic stress/strain data. Other work not discussed here shows wider applicability

TABLE 2—*Stress intensity factor.*

Load, MPa	ΔK, MPa$\sqrt{\text{m}}$	*da/dN*, mm/cycle
78.6	16.48	1.09×10^{-3}
104.8	21.98	2.79×10^{-3}

of the proposed approach, including problems of corrosion fatigue and high-temperature creep fatigue.

References

[1] Androv, V., "A New Damage Parameter for Fatigue Life Predictions under Local Strain Analysis," *International Journal of Fatigue,* Vol. 15, November 1993, No. 6, pp. 451–454.

[2] Zhang, A., Bui-Quoc, T., and Gomuc, R., "A Procedure for Low-cycle Fatigue Life Prediction for Various Temperatures and Strain Rates," *Transactions of the ASME, Journal of Engineering,* Vol. 112, October 1990, No. 4, pp. 422–425.

[3] Paris, P. C. and Erdogan, F., "A Critical Analysis of Crack Propagation Laws," *Journal of Basic Engineering, ASME Transactions,* Series D, American Society of Mechanical Engineers, New York, 1963, pp. 528–534.

[4] Elber, W., "Fatigue Crack Closure under Cyclic Tension," *Engineering Fracture Mechanics,* Vol. 2, 1970, pp. 37–45.

[5] Newman, J. C., Jr., "A Finite-Element Analysis of Fatigue Crack Closure," *Mechanics of Crack Growth, ASTM STP 590,* American Society for Testing and Materials, West Conshohocken, PA, 1976, pp. 281–301.

[6] Newman, J. C., Jr., "A Crack-Closure Model for Predicting Fatigue Crack Growth under Aircraft Spectrum Loading," *Methods and Models for Predicting Fatigue Crack Growth under Random Loading, ASTM STP 748,* American Society for Testing and Materials, West Conshohocken, PA, 1981, pp. 53–84.

[7] Drew, M. W. and Thompson, K. R. L., "The Effect of Overload Cycles on Fatigue Crack Propagation in Two Structural Steels," *Engineering Fracture Mechanics,* Vol. 30, 1988, pp. 579–593.

[8] Dexter, R. J., Hudak Jr., S. J., and Davidson, D. L., "Modeling and Measurement of Crack Closure and Crack Growth Following Overloads and Underloads," *Engineering Fracture Mechanics,* Vol. 33, No. 6, 1989, pp. 855–870.

[9] Dowling, N. E. and Begley, J. A., "Mechanics of Crack Growth," *Mechanics of Crack Growth, ASTM STP 590,* American Society for Testing and Materials, West Conshohocken, PA, 1976, pp. 82–103.

[10] de Koning, A. U. and Liefting, G., "Analysis of Crack Opening Behavior by Application of a Discretized Strip Yield Model," *Mechanics of Fatigue Crack Closure, ASTM STP 982,* J. C. Newman, Jr. and W. Elber, Eds., American Society for Testing and Materials, West Conshohocken, PA, 1988, pp. 437–458.

[11] Keyvanfar, F. and Nelson, D. V., "Predictions of Fatigue Crack Growth Behavior Using a Crack Closure Ligament Model," *Mechanics of Fatigue Crack Closure, ASTM STP 982,* J. C. Newman, Jr. and W. Elber, Eds., American Society for Testing and Materials, West Conshohocken, PA, 1988, pp. 437–458.

[12] Dawicke, D. S., Grandt, A. F. Jr., and Newman, J. C. Jr., "Three-dimensional Crack Closure Behavior," *Engineering Fracture Mechanics,* Vol. 36, No. 1, 1990, pp. 111–121.

[13] Ranganathan, N., Benguediab, M., Nicolas, C., Henaff, G., and Petit, J., "Fatigue Crack Propagation Under Block Loading Analyzed in Terms of Equivalent Loading Concept," *Engineering Fracture Mechanics,* Vol. 42, 1992, pp. 59–71.

[14] Kumar, R., "Review on Crack Closure for Constant Amplitude Loading in Fatigue," *Engineering Fracture Mechanics,* Vol. 42, 1992, pp. 389–400.

[15] Chen, W. F. and Han, D. J., *Plasticity for Structural Engineers,* Springer Verlag, New York, 1988, pp. 205–207.

[16] Cordes, J., Chang, A., Nelson, N., and Kim, Y., "A Computational Procedure to Predict Elastic/Plastic Fracture," *Engineering Fracture Mechanics Journal,* Vol. 51, No. 1, 1995, pp. 151–159.

[17] *ABAQUS,* Hibbit, Karlson and Sorensen, Inc. Pawtucket, RI.

[18] Jack, A. R. and Price, A. T., "The Initiation of Fatigue Cracks from Notches in Mild Steel Plates," *International Journal of Fracture Mechanics,* Vol. 6, No. 4, December 1970, pp. 401–409.

[19] Barsom, J. M. and McNicol, R. C., "Effect of Stress Concentration on Fatigue-Crack Initiation in HY-130 Steel," *Fracture Toughness and Slow-Stable Cracking (8th Conf.), ASTM STP 559,* American Society for Testing and Materials, West Conshohocken, PA, 1974, pp. 183–204.

[20] Crooker, J. M., "Crack Propagation in Aluminum Alloys Under High-amplitude Cyclic Load," Naval Research Laboratory Report 7286, Washington, DC, 12 July 1971.

Chien-Yung Hou[1] *and Frederick V. Lawrence*[2]

A Crack-Closure Model for the Fatigue Behavior of Notched Components

REFERENCE: Hou, C.-Y. and Lawrence, F. V., **"A Crack-Closure Model for the Fatigue Behavior of Notched Components,"** *Advances in Fatigue Lifetime Predictive Techniques: 3rd Volume, ASTM STP 1292,* M. R. Mitchell and R. W. Landgraf, Eds., American Society for Testing and Materials, 1996, pp. 116–135.

ABSTRACT: Newman's Dugdale strip-yield model for crack closure was used to estimate the crack-closure behavior of cracks emanating from notches. The estimated effective stress-intensity ratio $U(a) = \Delta K_{eff}(a)/\Delta K(a)$ obtained using Newman's model did not exhibit the frequently observed "dip" presumably caused by the notch plasticity. To incorporate the effects of notch plasticity into the Newman model, the plastic stretches caused by the notch were superposed on the plastic stretches caused by the crack tip. A finite element procedure was used to calculate the magnitude of the notch plastic stretches. It was found that the magnitude of the notch plastic stretches was much larger than that of the crack-tip plastic stretches and that the notch plastic stretches were the main source of the plastic wake when the crack tip was within the notch plastic zone. The validity of the proposed modification of Newman's Dugdale strip-yield model was verified by comparing the predicted results with the published experimental data for various notched components. The effects of the notch-plastic zone on $U(a)$ were found to be significant for stress ratio $R \geq 0$ but to be unimportant for $R \leq -1$.

KEYWORDS: plasticity-induced crack closure, notches, crack propagation, Newman's modified Dugdale strip-yield model

Nomenclature

a	Crack length
C', m	Material constants for modified Paris law
D	Notch depth
da/dN	Crack growth rate
h	Weight function
K_r	Stress-intensity factor of the reference crack system
K_S, K_σ	Stress-intensity factor caused by remote stress and strip-yield load
K_t	Stress concentration factor
l_t	Transition crack length
R	Stress ratio
r	Notch radius
ρ_c, ρ_n	Crack-tip and notch plastic zone size
S_{max}, S_{min}	Maximum and minimum remote stress
S_{open}, K_{open}	Crack opening stress and stress-intensity factor
$\sigma(x)$	Elastic notch-stress distribution
σ_c	Crack-face contact stresses

[1]Research assistant, Department of Civil Engineering, University of Illinois at Urbana-Champaign, IL 61801.

[2]Professor, Department of Civil Engineering and Material Science and Engineering, University of Illinois at Urbana-Champaign, IL 61801.

σ_0 Flow stress
t Plate thickness
U Effective stress-intensity factor ratio
u_{nA}, u_{nB} Crack-face displacement of the two notched plates
u_r Elastic crack-face displacement of the reference crack system
u_1 Elastic crack-face displacement caused by remote stress
u_2 Elastic crack-face displacement caused by strip-yield load
W Plate width
x_c Distance from the crack tip
ΔK, ΔK_{eff} Stress-intensity range and effective stress-intensity range
S_y, S_u Yield and ultimate strength of material

Introduction

Linear elastic fracture mechanics (LEFM) and the Paris power law are commonly used to predict the growth of fatigue cracks. However, these simple models do not always successfully model short crack behavior. Recently, the concepts of crack closure, the effective stress intensity factor, K_{eff}, and the stress intensity ratio, $U(a)$, have been used to rationalize the behavior of (mechanically) short cracks and to improve the modeling of crack growth

$$U(a) = \frac{\Delta K_{eff}(a)}{\Delta K(a)} = \frac{S_{max} - S_{open}(a)}{S_{max} - S_{min}} \tag{1}$$

In the past, FEA has been used to simulate plasticity-induced crack closure (PICC) [*1*]. The advantage of FEA is that it can be applied to any crack geometry and loading condition. However, it is difficult to apply FEA to short cracks propagating under plane strain conditions because the element size has to be small enough to capture the very small crack-tip plastic zone. Moreover, the calculated crack-opening stresses are affected by the mesh element size and the crack-tip node-releasing scheme used [2]. Therefore, for the problem at hand, FEA methods are laborious, costly, and too slow. Thus, one must find a more efficient method of estimating the stress intensity ratio as a function of crack length $U(a)$ in order to include the growth of small cracks in fatigue life simulation models for notched components.

An alternative and potentially rapid numerical method for estimating $U(a)$ is Newman's Dugdale strip-yield model [*3,4*]. Newman's model estimates the crack-face contact stresses by calculating the magnitude of the plastic wake left behind the crack tip, and allows one to estimate the crack-opening stress (S_{open}) and $U(a)$ from this information. However, as will be seen, Newman's model does not capture *all* the subtleties of crack closure behavior for a crack emanating from a notch. In the present study, a variation of Newman's model was developed that simulates the development of PICC for cracks emanating from notches and includes the effects of notch root plastic deformation on the crack closure of small cracks located within the notch's plastic zone.

Newman's Modified Dugdale Strip-Yield Model for Crack Closure of Notched Components

Dugdale-Type Crack

As shown in Fig. 1*a*, a Dugdale-type crack in a plate subjected to remote load contains two regions: plastically deformed material ahead of the crack tip (darkly shaded area), and regions other than this region that remain elastic. The crack-tip plastic zone size, ρ_c, which

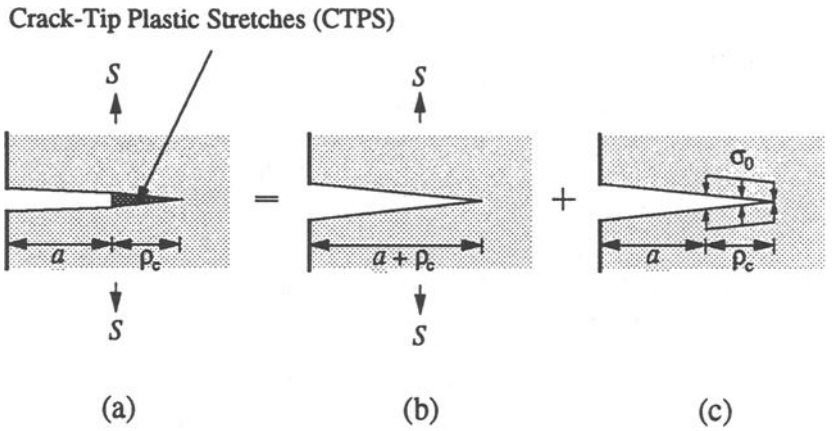

FIG. 1—*A Dugdale-type crack and the crack-tip plastic stretches.*

controls the crack-closure phenomenon, can be calculated by assuming a fictitious crack of length $a + \rho_c$ loaded by two load systems: the remote load S (Fig. 1*b*) and the uniformly distributed flow stress, σ_0, extending from a to $a + \rho_c$ (Fig. 1*c*). These two loading conditions produce stress-intensity factors K_S and K_σ at the fictitious crack tip. Because the stress intensity experienced at the fictitious crack tip must be zero, the value of ρ_c can be obtained from the relation

$$K_S + K_\sigma = 0 \tag{2}$$

The permanent deformations (parallel to the loading direction) produced by the crack-tip stress field are termed the "crack-tip plastic stretches" (or CTPS, see Fig. 1*a*). During the fatigue process, fatigue cracks propagate and sever small regions ahead of the crack tip. These severed regions become a part of the "plastic wake" behind the crack tip, and the magnitude of that region's CTPS determines the nature of their (new) contribution to the plastic wake and the intensity of the contact stresses that develop if the crack closes when the remote stress is minimum. These contact stresses are related to the crack-opening stress of next load cycle (Fig. 2). Newman [*3*] estimated the crack-opening stress and thus simulated PICC by calculating the magnitude of CTPS, the height of plastic wake (at any time), and, finally, the contact stresses along crack faces at minimum load.

Figure 3 shows the calculated crack-closure levels for cracks emanating from various radii circular notches using Newman's method. All the predicted closure levels reach the same stable state after cracks grow a sufficient distance. This distance increases as the notch size increases. This notch size effect results from the fact that the (elastic) notch-induced stresses extend greater distances for larger notches.

Difficulties with the Newman's Model When Applied to Notched Components

Experimental studies of $U(a)$ (as will be seen, particularly those carried out with $R = 0$) frequently show a "dip" (Fig. 4). Many researchers suggest that this dip is due to the plasticity *induced by the notch.*

Shin and Smith [*5*] measured the S_{open} of high-stress concentration specimens using the compliance method with a crack-tip clip gauge. Significant dips were found in the measured U values. Verreman et al. [*6*] measured the S_{open} of stress-relieved cruciform joints using

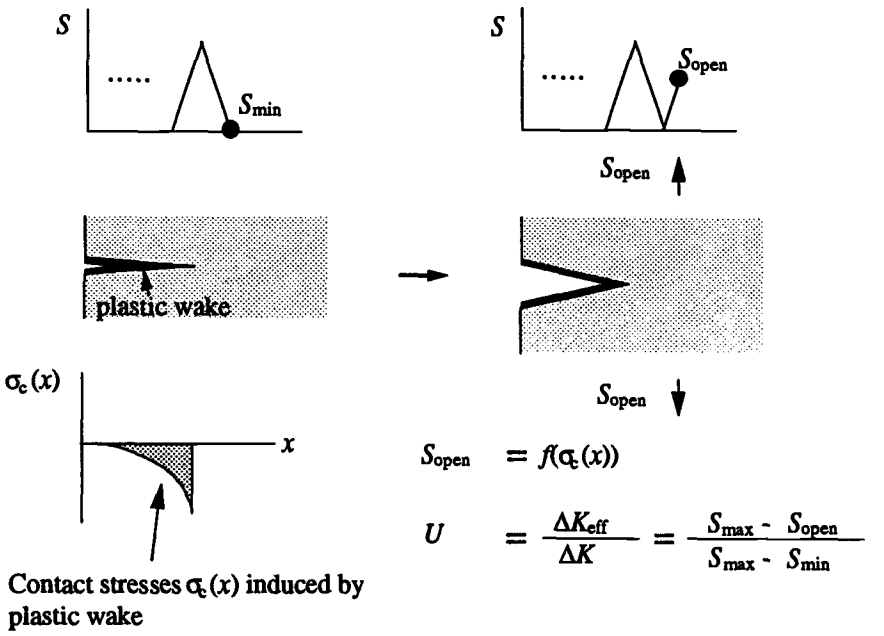

FIG. 2—*An illustration of the strip-yield model for crack closure.*

strain gauges. They claimed that the error of the measured S_{open} was ± 6 MPa with the crack opening level monitoring system they used. This value was approximately 3 to 6% of the S_{max} they applied on the specimens. They reported that through-width cracks were systematically observed. Their data also showed dips for $R = 0$ cases. They stated that the increase of the U values from the minimum location of the dip was due to the monotonic notch plasticity. Tao et al. [*7*] measured S_{open} emanating from circular notches. A mild dip could also be found if their reported S_{open} values were converted to U values.

McClung and Sehitoglu [*8*] used finite element techniques to study the opening stresses of

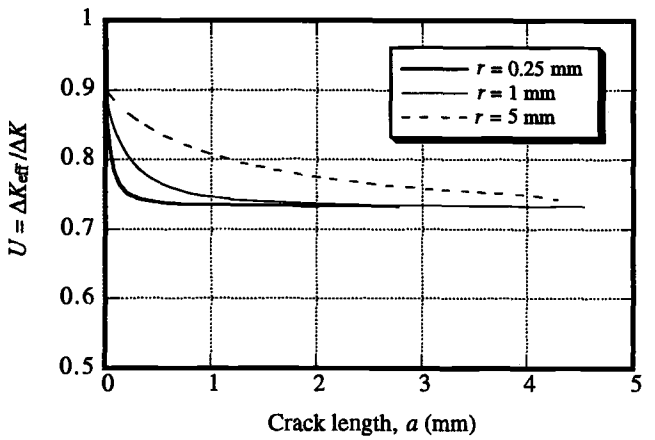

FIG. 3—*The calculated* U(a) *of various notch radii using Newman's strip-yield model:* ($S_{max}/\sigma_0 = 0.5$, R = 0, E = 200 GPa, $\sigma_0 = 400$ MPa).

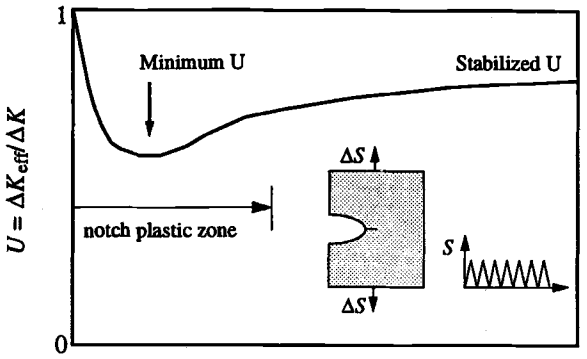

FIG. 4—*The effects of the notch plastic zone on crack-closure behavior.*

notches with $K_t = 3$ and 5. No significant dips were found when the S_{open} values were converted to U values. An explanation for this discrepancy is that when FEA is used for crack closure analysis, the load is applied step by step from S_{min} to S_{max} during a load cycle. The crack opening stresses are determined by observing the conditions of the crack faces. For instance, if the load is 0.2 S_{max} and the calculated crack faces are found to be fully open, the S_{open} is 0.2 S_{max}. If the load increment is 10% of S_{max}, the calculated S_{open} would be 0.3 S_{max} even if the correct S_{open} is 0.21 S_{max}, that is, the calculated U values would have 9% of error for $R = 0$ cases. This error is close to the difference between the minimum U value of the dip and the stabilized U value for a mild stress concentration (see Fig. 4). Hence, the error might obscure the dip.

Finally, it is well known that a fatigue crack is retarded when it propagates in an overload plastic zone. The measured U values always show a significant dip. It is reasonable to expect that a similar phenomenon should result when a crack propagates in a notch plastic zone.

The above mentioned "dip" in $U(a)$ is not and cannot be predicted by Newman's strip-yield model in its original form.[3] This inability arises because the strip-yield model accounts for *crack-tip* plasticity but does not consider the plastic deformation contributed by the *notch itself* during first application of load. This notch plasticity must be added to the crack-tip plasticity, and hence it must affect the closure levels for cracks propagating within the notch plastic zone. As will be discussed below, Newman's model was modified to include the plastic deformation contributed by the notch during the first load application in an attempt to simulate more realistically the growth of cracks emanating from notches.

Modification of Newman's Model to Include the Effects of the Notch Plasticity

Notch Plastic Stretches

Since the crack-tip plastic deformations parallel to the loading direction (CTPS) are the key concept of Newman's model, a crude but simple way of including the effects of the notch plastic zone is to calculate the notch plastic stretches (NPS) generated during the first application of load and linearly add these to the crack-tip plastic stretches (CTPS), that is, to superpose the NPS on the CTPS.

[3]See Appendix for details of the formulations of the strip-yield model for notched components in this study.

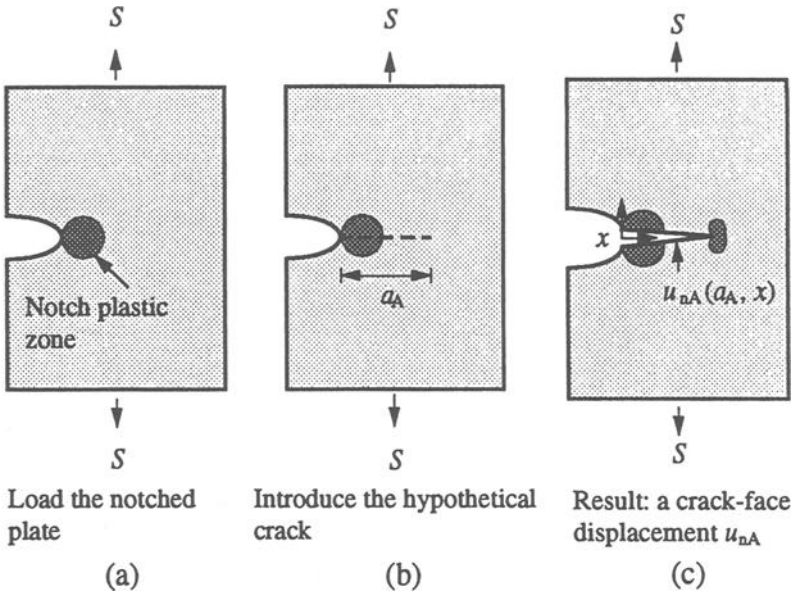

FIG. 5—*The notched plate for* u_{nA} (a_A,x).

The procedure developed in this study for estimating the NPS is as follows: First consider a hypothetical notched plate loaded by a remote load S that produces a notch plastic zone (Fig. 5*a*). A crack of length a_A is introduced into the loaded plate (Fig. 5*b*). The introduction of this crack results in crack-face displacements $u_{nA}(a_A,x)$ (Fig. 5*c*). Second, consider a hypothetical notched plate having a *preexisting* crack of the same length as the crack in the previous notched plate (Fig. 6*a*). This second notched plate is *then* loaded by a remote stress, S, and a second, different set of crack-face displacements, $u_{nB}(a_A,x)$, will result (Fig. 6*b*). FEA[4] was used to calculate $u_{nA}(a_A,x)$ and $u_{nB}(a_A,x)$ (Fig. 7). Figure 8 shows typical crack-face displacements $u_{nA}(a_A,x)$ and $u_{nB}(a_A,x)$ obtained from FEA.

The one half of the difference between $u_{nA}(a_A,x)$ and $u_{nB}(a_A,x)$ is taken to be the notch tip plastic stretch (NPS) generated during the first application of the remote load in a notched component

$$\frac{\text{NPS}(x)}{2} = u_{nB}(a_A,x) - u_{nA}(a_A,x) \tag{3}$$

[4]The commercial software PATRAN was used to generate the finite element mesh, and the ABAQUS was used for the elastic-plastic FEA. The plate was 100 mm wide, having a circular notch with radius $r = 5$ mm. The constant strain triangle element was chosen, and the mesh around the notch is shown in Fig. 7. The material was assumed to have an elastic-perfectly-plastic stress-strain relationship with a flow stress $\sigma_0 = 400$ MPa. Young's modulus was 200 GPa. The isotropic hardening rule and the Von Mises criteria were employed in the calculations. The crack-face displacements $u_{nA}(a_A, x)$ and $u_{nB}(a_A, x)$ were calculated at load levels of $S/\sigma_0 = 0.38$, 0.5, and 0.63 for the plane stress condition. Since the hypothetical crack coincided with the boundary conditions (no displacement in the loading direction), which were located at the symmetrical line of the plate, the hypothetical crack in the first plate was introduced by releasing the constrained nodes up to an arbitrary chosen node that was located beyond the monotonic notch plastic zone.

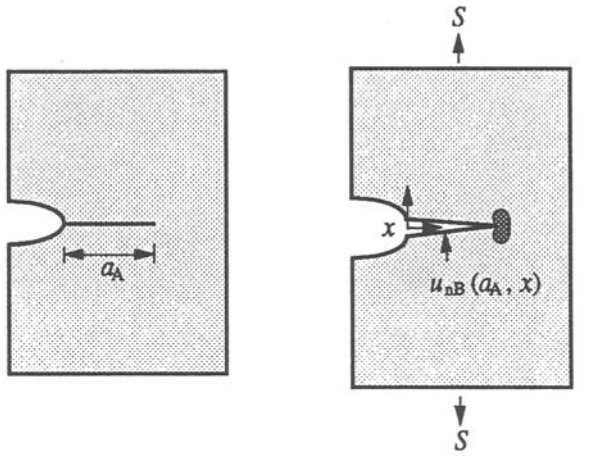

FIG. 6—*The notched plate for* $u_{nB}(a_A,x)$.

The key idea is that *both* the NPS and the CTPS are the sources of the plastic wake left on the crack faces as cracks propagate from notches. As seen in Fig. 9, the size of the CTPS is dependent on the crack length, but the size of the NPS is not dependent on crack length.

To assess the relative contribution of the NPS and CTPS to the plastic wake, the size of the CTPS at any crack length, a, was compared with that of the NPS at a corresponding distance, x, from the notch root NPS ($x = a$). Consider a moving coordinate system with its origin located at the crack tip. The magnitude of the CTPS at any distance, x_c, from the crack

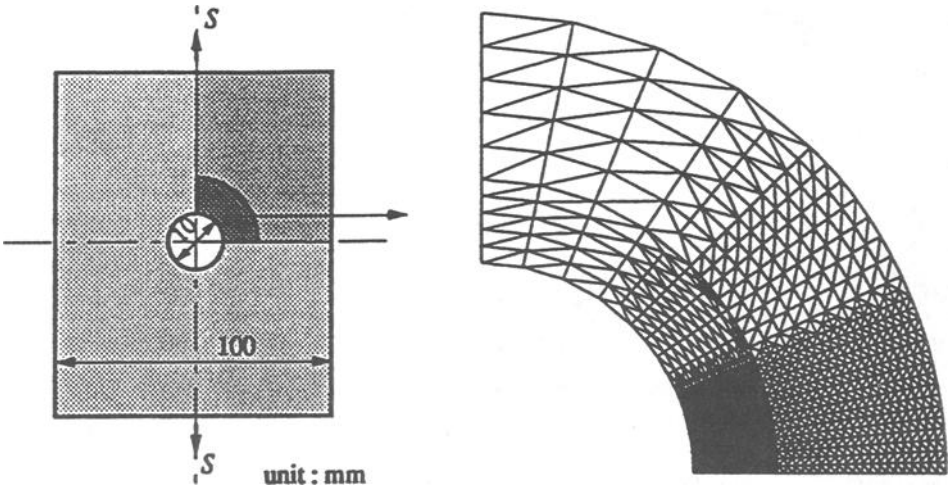

FIG. 7—*The plate and the notch geometry considered and the mesh around the notch in FEA.*

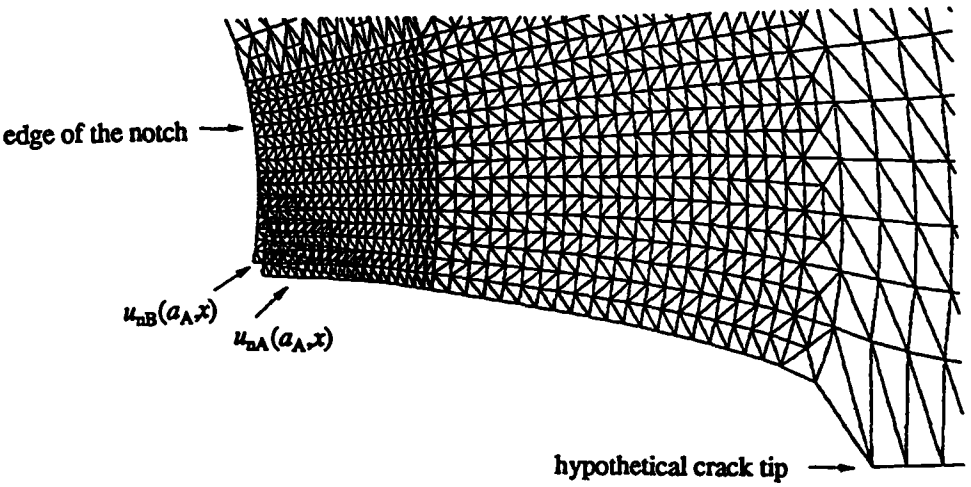

FIG. 8—*The exaggerated crack-face displacements of the two notch plates.*

tip is CTPS (x_c). Figure 9*a* shows the CTPS as a function of *distance from the crack tip.* The NPS as a function of *distance from the notch root* is also shown in Fig. 9*a*. The CTPS ($x_c = 0$) was chosen as an index of the size of CTPS for a crack of length a and is compared with the value of the NPS at $x = a$, that is, NPS ($x = a$).

The strip-yield model was used to calculate the values of CTPS (x_c) for a crack emanating from the 5-mm-radius circular notch previously considered in Fig. 3. The ratios of CTPS ($x_c = 0$) to NPS ($x = a$), that is, CTPS/NPS, are plotted versus the ratio of the crack length to the notch plastic zone size, a/ρ_n, in Fig. 10. The results show a similar trend at various load levels. The values of the ratio CTPS/NPS vary from 10^{-2} at $a/\rho_n \approx 0$ to over[5] 10 at $a/\rho_n = 1$. The value of the ratio CTPS/NPS becomes unity for crack lengths about 15 to 30% of the notch plastic zone size. When the crack length is less 10% of the notch plastic zone size, the ratio decreases drastically and the NPS becomes dominant.

These results suggest that for very small cracks ($a/\rho_n < 0.05$) the entire crack-tip plastic zone is embedded within the notch plastic zone and the CTPS are much smaller than the NPS. Hence, at this stage, the plastic wake left behind the crack tip is controlled mainly by the NPS. As the crack becomes larger, the size of CTPS becomes comparable to that of the NPS, and the CTPS contributes an important part to the plastic wake. Finally, when the crack propagates beyond the notch plastic zone, the plastic wake left behind the crack tip is controlled solely by the CTPS.

Incorporating the NPS into Newman's Model

To apply the strip-yield model for the crack closure in a notch plastic zone, the total plastic stretches (TPS) ahead of the crack tip caused by the interactions of the CTPS and the NPS must be estimated. However, the TPS cannot be calculated directly from a relationship like Eq 2 in the strip-yield model since the NPS cannot be collapsed into an infinitesimally narrow strip on the crack plane as in the Dugdale model, that is, the Dugdale-type crack cannot be placed in a notch plastic zone.

In spite of the fact that Newman's model was based on a Dugdale-type crack, his model

[5]The values of the ratio CTPS/NPS should be infinite when $a/\rho_n = 1$, but the numerical errors in the FEA have yielded finite values.

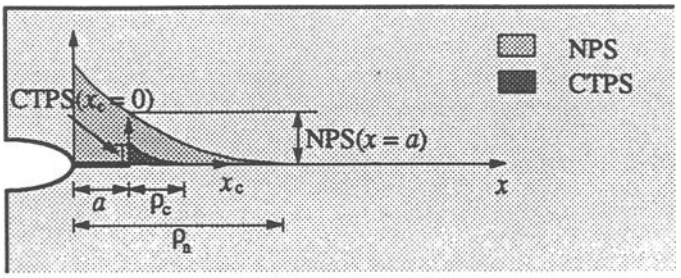

(a) $a + \rho_c < \rho_n$

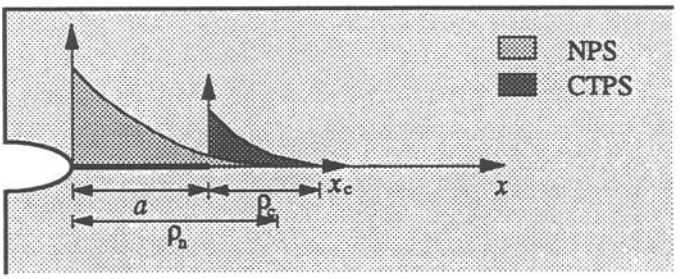

(b) $a + \rho_c > \rho_n$, and $a < \rho_n$

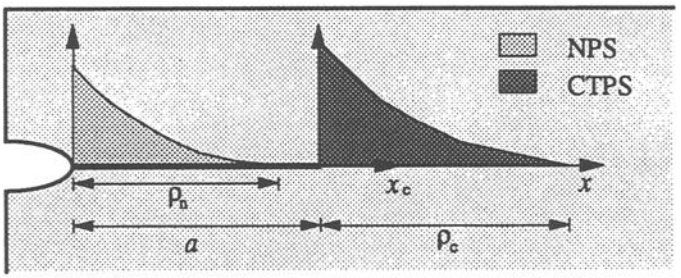

(c) $a + \rho_c > \rho_n$, and $a > \rho_n$

FIG. 9—*The CTPS and the NPS.*

calculates the crack-opening stresses if the plastic zone size and the magnitude of plastic stretches are given. It is not important that the stretches be calculated using the theory of a Dugdale-type crack: the NPS calculated from FEA may be used with the CTPS calculated from a Dugdale-type crack to estimate the TPS in a notch plastic zone and to calculate crack closure using the strip-yield model.

Thus, the effects of the NPS were incorporated into Newman's Model by simply superposing the calculated CTPS and NPS to obtain a *total* plastic stretch (TPS) for each location in the plastic zone (ahead of the crack tip at any time)[6]

$$\text{TPS}(x_c) = \text{NPS}(a + x_c) + \text{CTPS}(x_c) \tag{4}$$

[6]Note that the NPS shown in Eq 4 is calculated based on the coordinate system located at the notch root, and the TPS and the CTPS are based on the moving crack-tip coordinate system.

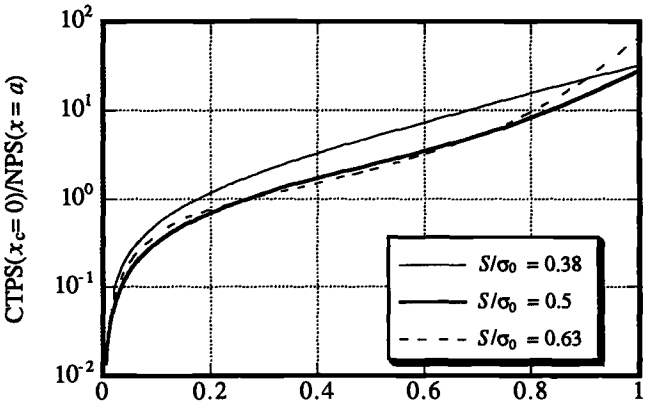

FIG. 10—*Comparison of the CTPS with the NPS.*

This approach for incorporating the NPS into the strip-yield model will hereafter be referred to as the strip-yield model for notched components or SYMNC model.

Figure 9 shows three cases encountered in the strip-yield model for a crack propagating in a notch plastic zone. Figure 9*a* is the case in which the calculated crack-tip plastic zone, ρ_c, is fully embedded in the notch plastic zone, ρ_n. The NPS and the CTPS located behind the crack tip have become the plastic wake; hence, the plastic zone size should be $\rho_n - a$. Figure 9*b* shows a case when the notch and crack-tip plastic zones overlap. Since the boundary of the crack-tip plastic zone is located beyond the notch plastic zone, the proper plastic zone size for this case is ρ_c. Figure 9*c* shows the case when the crack has propagated well out of the notch plastic zone. In this case, the plastic zone size is ρ_c and the TPS(x_c) = CTPS(x_c) because the NPS($a + x_c$) equals zero.

Comparison of Predicted Results of the SYMNC Model with Experimental Data

Two sets of notch crack closure data reported in the literature were compared with the analytical results of the SYMNC model. The crack growth rate was predicted using the Paris power law written in terms of the effective stress intensity factor

$$da/dN = C'(\Delta K_{eff})^m = C'(U\Delta K)^m \tag{5}$$

The $U(a)$ was calculated from an initial crack length of 0.01 mm. All the calculations were performed using HP-UX workstations. The CPU time was 5 to 25 min for an entire $U(a)$ curve excluding the separate FEA analysis of the NPS.

Sharp, Single-Edge Notch in a BS4360 50B Steel Plate

Shin and Smith [5] measured the crack closure behavior of cracks emanating from two types of edge-notched BS4360 50B steel specimens (see Fig. 11 and Table 1). The two types of specimens had a notch depth, D, of 35 mm, notch radii, r, of 0.4 and 1.4 mm, and stress concentration factors of 29 and 16.8, respectively. A remote stress range of 90 MPa was applied at stress ratio $R = 0.05$. Because large plastic zones were produced at the notch root of such high-stress concentration notches, the crack-closure behavior was largely affected by notch plasticity. An unnotched specimen having an initial crack length of 35 mm was also tested. It is obvious in Fig. 12 that the crack closure behavior of the unnotched specimen

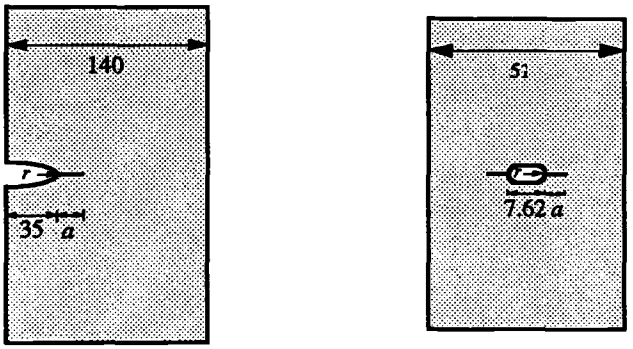

Single, sharp-edge notch
$r = 0.4, 1.4, \quad K_t = 29, 16.8$
$t = 2$
BS4360 50B Steel

Blunt center notch
$r = 3.81, \quad K_t = 4$
$t = 5.7$
1020 Steel

units: mm

FIG. 11—*The plastic strains in the crack-tip plastic zone and in the notch plastic zone.*

TABLE 1—*Material properties for model predictions.*

Material	Flow Stress, σ_0, MPa	C' *	m
BS4360 50B steel [5]	436	3.88×10^{-8}	2.6
1020 steel [10]	325	8.03×10^{-9}	3.2

*These C' values are appropriate for *da/dN* in mm/cycle.

(which was influenced only by crack-tip plasticity) was different from the behavior of the notched specimens.

The results of FEA based on the plane stress condition gave the notch plastic zone sizes approximately 5.2 mm for both notches. For both notched specimens, the calculated S_{open} values started from 0, gradually increased to maximum values of approximate 0.2 S_{max}, and then decreased. Figure 12*a* shows the measured U values and the predicted results of converting S_{open} to U using Eq 1. The tested data of the radius 1.4-mm notch and those of the notch-free crack cluster together and were given by a scatter band. The test data of the smaller root radius notch (r = 0.4 mm) showed a significant "dip" but merged with the scatter band at a crack length of approximately 8 mm, implying that the NPS no longer exert any influence at crack lengths greater than 8 mm.

Smith et al. [9] estimated the transition crack length,[7] (l_t), as $0.13\sqrt{Dr}$. The transition crack lengths of the two notches using Smith's estimation were approximately 0.9 and 0.5 mm for a notch radius of 1.4 and 0.4 mm, respectively. If one adopts Smith's transition crack length as the furthest spatial extent of notch influence, the behavior of the notched and unnotched specimens should converge when $a > 0.9$ mm. In Fig. 12*a*, it is obvious that the $U(a)$ curves converge at a distance greater than 0.9 mm and at approximately the distance of

[7]The crack length at which the stress-intensity factor is not affected by the notch-stress field.

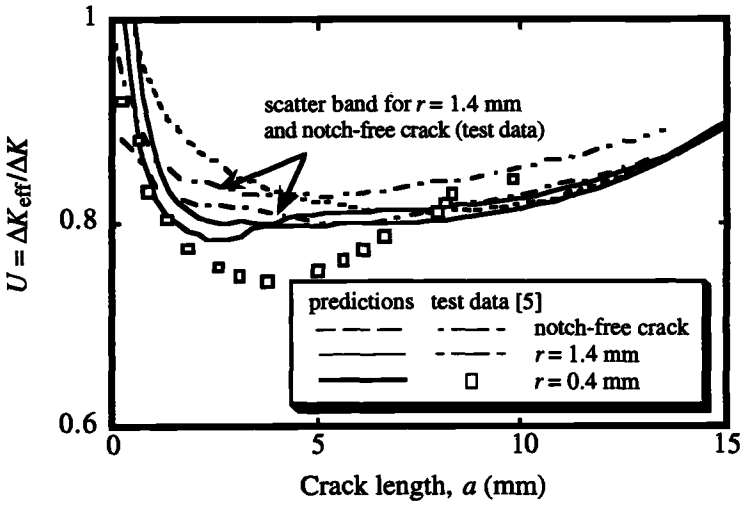

(a)

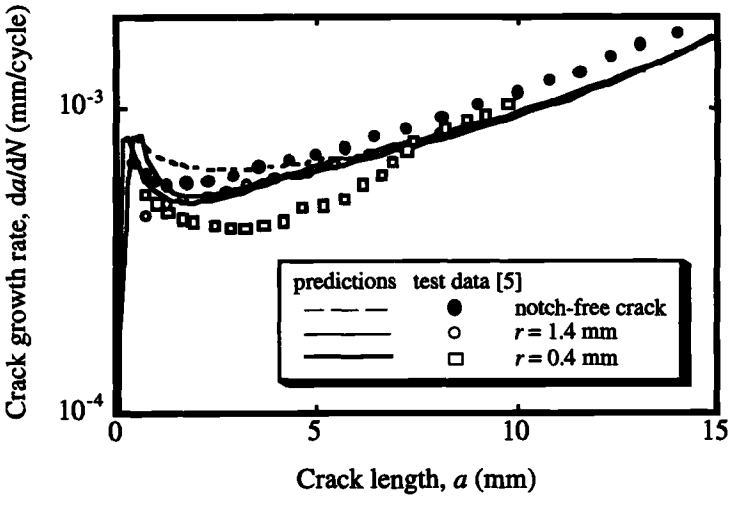

(b)

FIG. 12—*The specimens and the material considered in the model predictions.*

the plastic zone size, as is the expectation based on the results of the SYMNC model. Figure 12*b* shows the measured and predicted crack growth rates using the SYMNC model.

Blunt Center Notch in a 1020 Steel Plate

Sehitoglu [*10*] studied the behavior of cracks emanating from center-notched panels containing a blunt notch ($K_t = 4$, see Fig. 11). The material considered was 1020 steel $S_y = 325$ MPa. Predictions made using the SYMNC model were compared with Sehitoglu's results at four stress levels ($S_{max} = 96$, 117, 146, and 166 MPa). The stress ratio in Sehitoglu's tests was $R = -1$.

For simplicity, the plane-stress condition was used in the FEA despite the fact that the plate thickness was 5.7 mm. The results showed that no notch plastic zone was developed at the notch root for the cases of $S_{max} = 96$ and 117 MPa. The notch plastic zone sizes were 0.7 and 1.2 mm for the other two stress levels.

The calculated S_{open} values developed from S_{min}, i.e., $-S_{max}$ to a maximum value of approximately 0.2 S_{max} for $S_{max} = 96$ MPa and of 0 for $S_{max} = 166$ MPa. This predicted crack-opening behavior confirmed Newman's results [*4*] that S_{open} developed from negative values for $R = -1$ cases. When the S_{open} values were converted to U values using Eq 1, because the denominator $S_{max} - S_{min} = 2S_{max}$, the calculated minimum U values reduced to approximately 0.4 to 0.5 despite the fact that calculated maximum S_{open} values were close to those in the previous $R = 0.05$ cases.

The predicted $U(a)$ curves are shown in Fig. 13*a*. For all load levels, the $U(a)$ curves first decreased and then increased as crack length became longer. It seems that this trend is a notch plastic zone induced dip. However, there are two reasons to reject this proposition: (1) the minimum values of $U(a)$ of all load levels take place beyond the notch plastic zones, and (2) if an infinite plate ($W = \infty$) was used in the calculations, the $U(a)$ would stabilize. Since the predicted U curves showed no "dip" attributable to the notch plastic zone, it seems that the crack closure levels are not affected by the notch plastic zone for the cases considered. Figure 13*b* shows the predicted crack growth rate, which compared favorably with the test data.

Discussion

Validity of the Method of Estimating the Total Plastic Stretches

The interaction of crack-tip plasticity with the plastic field of a notch must certainly be a nonlinear process, and thus the simple superposition of NPS and CTPS to obtain the TPS (Eq 4) is open to question. As shown in Fig. 14, a crack-tip plastic zone is created in the plastic zone of a preexisting notch. At any location, x,y, the plastic strain parallel to the loading direction caused by the notch stress is denoted as $\epsilon_{pn}(x,y)$. The plastic strain caused by the crack-tip stress without the effects of the original notch plasticity is denoted as $\epsilon_{pc}(x,y)$. According to plasticity theory, if a crack-tip stress field is introduced that is more severe than that of the existing notch, the yield surface at (x,y), which was activated by the original notch plasticity, would be moved to a new state, and the new state of the yield surface would be identical to the state in which the material is yielded solely by the crack-tip stress without the effects of original notch plasticity. In other words, the plastic strain at (x,y), i.e., $\epsilon_p(x,y)$ is either $\epsilon_{pn}(x,y)$ or $\epsilon_{pc}(x,y)$.

When a crack-tip plastic zone is fully embedded in a notch plastic zone (see Fig. 14), the NPS, CTPS, and the NPS can be calculated by

$$\text{NPS}(x) = 2\int_0^{y_2} \epsilon_{pn}(x, y)\, dy \tag{6}$$

$$\text{CTPS}(x) = 2\int_0^{y_1} \epsilon_{pc}(x, y)\, dy \tag{7}$$

$$\text{TPS}(x) = 2\int_0^{y_1} \epsilon_{pc}(x, y)\, dy + 2\int_{y_1}^{y_2} \epsilon_{pn}(x, y)\, dy = \text{CTPS}(x) + \text{NPS}(x)\Big|_{y_1}^{y_2} \tag{8}$$

$$\text{Error} = 100\% \left(\frac{(\text{NPS})_0^{y_1}}{\text{CTPS}(x) + \text{NPS}(x)\Big|_{y_1}^{y_2}} \right) \tag{9}$$

The plastic stretches at the crack tip are used to discuss the error of Eq 4 since the magnitude of the plastic stretches ahead of the crack tip is largest at this location; furthermore, that plastic stretch will become plastic wake after the next crack growth increment and will affect the calculated crack closure.

In comparing the results of NPS + CTPS with the TPS, it is found that the difference is the integration of the $\epsilon_{pn}(x,y)$ from 0 to the boundary of the crack-tip plastic zone. Hence, it is evident that the accuracy of Eq 4 depends on the relative size of the crack-tip plastic zone to the notch plastic zone. The smaller the crack-tip plastic zone is, the more accurate are the estimates made using Eq 4. This condition occurs when the crack begins growing from a notch root.

As the crack grows, the value of the $\text{NPS}(x)\Big|_0^{y_1}$ increases and that of the $\text{NPS}(x)\Big|_{y_1}^{y_2}$ decreases; thus, the error predicted by Eq 9 would increase. If part of the crack-tip plastic zone boundary is coincident with that of the notch plastic zone, that is, $y_1 = y_2$, the value of the crack-tip plastic zone should be zero; and $\text{NPS}(x)\Big|_0^{y_1} = \text{NPS}(x)$. When the crack length is 0.3 ρ_n, the magnitude of the CTPS ($x_c = 0$) is comparable with that of the NPS(x) (see Fig. 10), and the error would be close to 100% since CTPS ($x_c = 0$) $\approx$ NPS(x). When the crack becomes longer, the numerator in Eq 9 becomes less important than the denominator since the CTPS are larger than both the $\text{NPS}(x)\Big|_0^{y_1}$ and $\text{NPS}(x)\Big|_{y_1}^{y_2}$. Hence Eq 4 might result in large errors for certain values of crack length. The largest difference between the NPS + CTPS and the correct TPS probably would be the order of NPS. However, when one considers the complex theoretical stress analysis or the amount of elastic-plastic FEA work required to calculate the TPS, it would seem that Eq 4 is an attractive and adequate simplification.

Lack of Sensitivity to NPS When R = −1

For the cases of the blunt center-notched specimens, it was seen that the experimentally observed crack-closure "dip" in a notch was not predicted by the SYMNC model for $R = -1$ (see Fig. 13*a*). Studies were made to understand the reason for this unexpected result, and the findings are discussed below.

As illustrated in Fig. 2, the strip-yield model predicts the crack-closure effects from the contact stresses along the crack faces at the minimum load of a loading cycle. The sharp single-edge-notched specimens with a notch radius of 0.4 mm was used to compare the contact stresses calculated from the model with and without the NPS incorporated. Figure 15 shows the contact stress distribution[8] on crack faces at minimum stress for the case of $R = 0.05$. The contact stresses at a distance away from the crack tip are higher for the case with the NPS incorporated. This increase is a result of the fact that the addition of the NPS to the CTPS produces a larger size plastic wake. Since larger contact stresses result, the calculated

[8]These results correspond to a crack length of 2.33 mm (entirely embedded in the monotonic notch plastic zone).

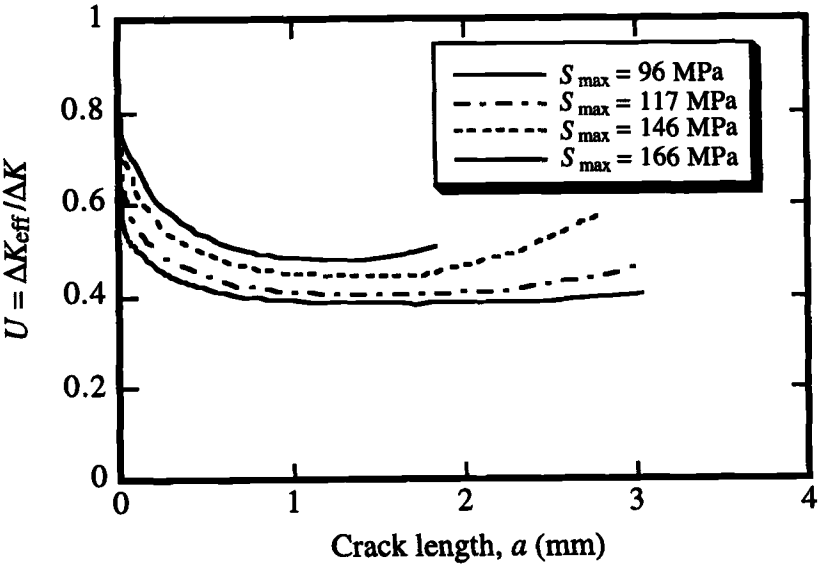

(a)

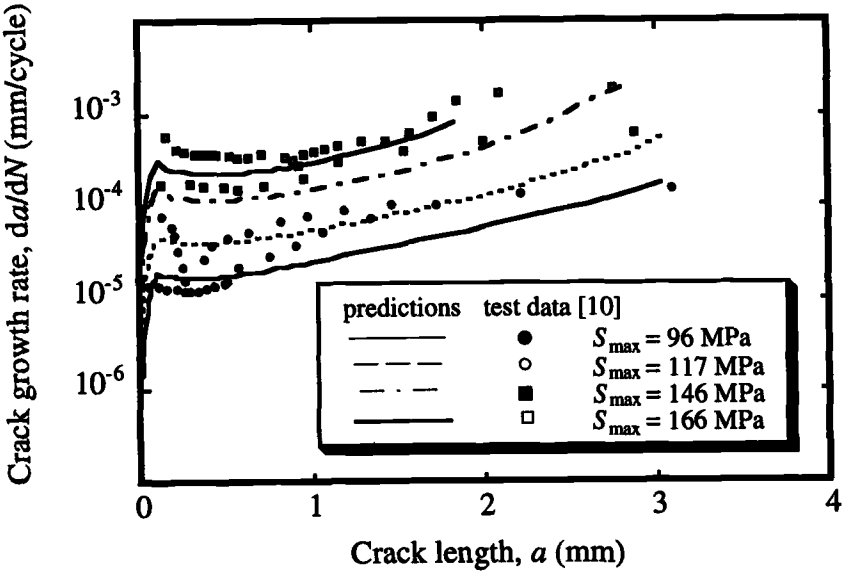

(b)

FIG. 13—*The test and the predicted results for the sharp, single-edge notch:* (a) *the* U(a) *curves;* (b) *the crack growth rate.*

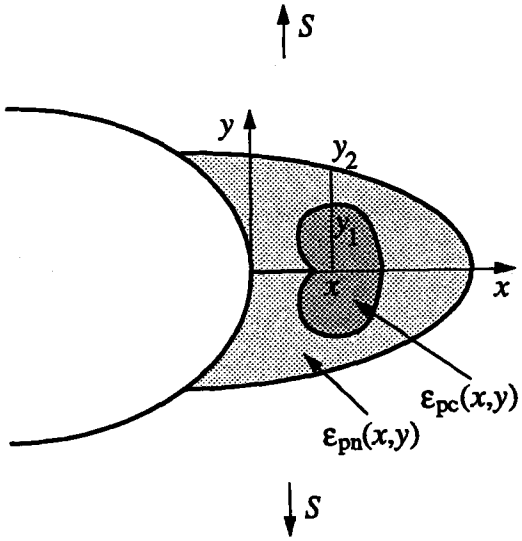

FIG. 14—*The predicted results for the center blunt notch:* (a) *the* U(a) *curves;* (b) *the test and predicted crack growth rate.*

$U(a)$ curve in Fig. 12*a* indicates a value of U at that crack length of 0.78. Recalculation of the $U(a)$ curve without the NPS incorporated gives a value of U is 0.86 at that crack length. Since the value of U is smaller when the NPS is incorporated, the "dip" appears in the predicted $U(a)$ curve.

For the case of $R = -1$, the calculated results of both the strip-yield model and the SYMNC model show that the plastic wake always yields at minimum load. Because elastic-perfectly-plastic material properties are assumed, the contact stress distributions calculated by both Newman's and the SYMNC models are the same, i.e., $\sigma_{c,wNPS}(x) = \sigma_{c,w/oNPS}(x) = -\sigma_0$. Therefore, the calculated $U(a)$ curve of the strip-yield model curves are not influenced

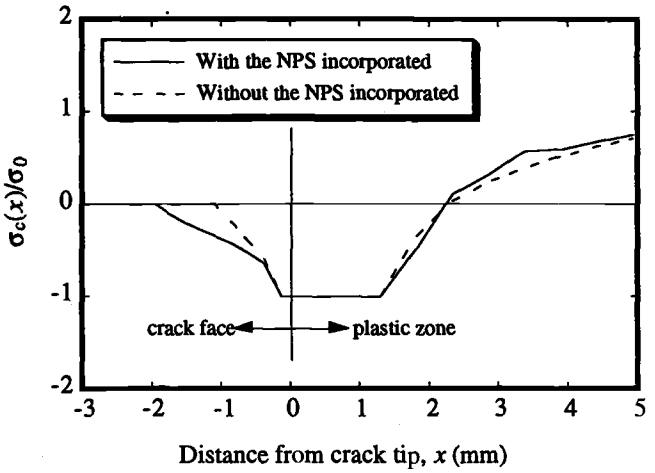

FIG. 15—*The calculated contact stresses with and without incorporating the NPS.*

by incorporating the NPS in calculations, and hence the "dip" of the $U(a)$ curve predicted in $R = 0.05$ cases will not occur in the $R = -1$ case.

The above discussion leads to the conclusion that the notch plastic deformations should not increase crack-closure effects for $R = -1$ or more negative values. Many researchers have measured the U values for cracks emanating from notches. Those measured U values that show significant "dip" are always those tests performed at $R \geq 0$ [*5–7*]. There are also measured data that show no "dip." However, when one checks the loading conditions of these latter experiments, it is not surprising that the applied stress ratios are always $R = -1$ or more negative values [*6,11,12*].

Obviously, the effects of load ratio on the crack-closure behavior in notch plastic zones are similar to the crack-growth retardation caused by a tensile single overload. Most research work on the overload effects was performed for an overload followed by $R = 0$ constant amplitude loading. This condition is similar to the discussed notch components subjected to $R = 0$ loading, and the "dip" of $U(a)$ curves is related. However, when a single, tensile overload is followed by constant amplitude loads with $R \leq -1$, the dip of the $U(a)$ would be diminished since the condition is similar to the notched components that are subjected to $R \leq -1$ loading. Hence, crack-growth retardation effects should be insignificant for this condition. This observation may explain the experimental results of Stephens et al. [*13*], which showed that negative stress ratios reduce crack retardation effects.

Concluding Remarks

Analyses of notch and crack-tip plastic stretches suggest that notch plasticity is the main source of the plastic wake when the crack length is small compared with the notch plastic zone. As the crack length increases, crack-tip plasticity increasingly contributes to the plastic wake and thus to crack-closure behavior. A model termed the Strip-Yield Model for Notched Components (SYMNC) was developed that considers the effects of notch plastic deformations on the crack-closure behavior in the vicinity of a notch. When the notch plastic deformations were considered, the predicted results showed different crack-closure behavior from those predicted by Newman's original strip-yield model for $R \geq 0$ cases. The SYMNC model predicted the dip of $U(a)$ curves that were observed in some experimental data for $R \geq 0$.

Acknowledgments

This investigation was supported by the Fracture Control Program at the University of Illinois at Urbana-Champaign and the Cooperative Research Program at Edison Welding Institute. The authors wish to thank Dr. J. C. Newman, Jr. and Prof. H. Sehitoglu for many useful discussions.

APPENDIX

Mathematical Formulation of the Strip-Yield Model for Notched Components

The equations below outline the adaptation of Newman's original strip-yield model to notched components. Newman's original formulation is only for cracks in smooth specimens or cracks in circular notches. Because the following equations are used, the model can

be applied to various notched components if the elastic notch stresses are known. The details of the model and the significance of these equations are discussed in Ref *3*.

The weight function derived by Petroski et al. [*14*] for a single-edge crack was used to calculate notch stress-intensity factor $K(a)$

$$K(a) = \frac{H}{K_r(a)} \int_0^a \sigma(x) \frac{\partial u_r(a, x)}{\partial a} dx \tag{A.1}$$

A single-edge crack in a smooth-plate-subjected remote stress S was the arbitrarily chosen reference system (Fig. A.1*a*). Because the corresponding $u_r(a,x)$ is not readily available from stress-intensity factor handbooks, an approximate equation for $u_r(a,x)$ given in Ref *14* was used. The $u_r(a,x)$ was calculated by the approximate equation

$$u_r(a,x) = \frac{S}{H\sqrt{2}} \left[4F_r\left(\frac{a}{W}\right) a^{1/2}(a - x)^{1/2} + G_r\left(\frac{a}{W}\right) a^{-1/2}(a - x)^{3/2} \right] \tag{A.2}$$

where

$$F_r\left(\frac{a}{W}\right) = 1.12 - 0.231\left(\frac{a}{W}\right) + 10.55\left(\frac{a}{W}\right)^2 - 21.72\left(\frac{a}{W}\right)^3 + 30.39\left(\frac{a}{W}\right)^4 \tag{A.3}$$

$$G_r\left(\frac{a}{W}\right) = \left[I_1(a) - 4F_r\left(\frac{a}{W}\right) a^{1/2} I_2(a) \right] a^{1/2}/I_3(a) \tag{A.4}$$

$$I_1(a) = \sqrt{2}\pi S \int_0^a F_r\left(\frac{a}{W}\right)^2 ada \tag{A.5}$$

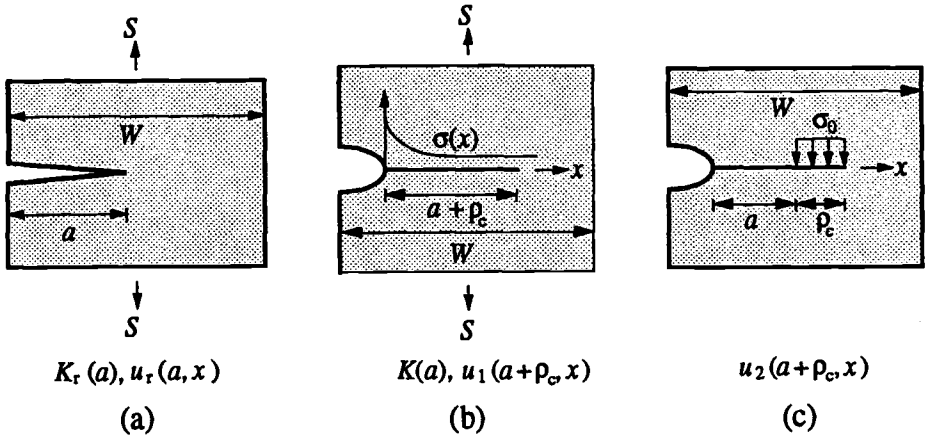

FIG. A.1—*The required information in the strip-yield model for crack closure:* (a) *the arbitrarily chosen single-edge crack system;* (b) *the notch-stress intensity and the crack-face displacement caused by remote load;* (c) *the crack-face displacement caused by the strip-yield load.*

$$I_2(a) = \int_0^a \sigma(x)(a - x)^{1/2}\,dx \tag{A.6}$$

$$I_3(a) = \int_0^a \sigma(x)(a - x)^{3/2}\,dx \tag{A.7}$$

In a Dugdale-type crack, the CTPS are calculated from two sets of elastic crack-face displacement of the fictitious crack: (1) the crack-face displacement caused by remote load S, i.e., $u_1(a + \rho_c, x)$ (Fig. A.1*b*) and (2) the crack-face displacement caused by the uniformly distributed flow stress, σ_0, extending from a to $a + \rho_c$, i.e., $u_2(a + \rho_c, x)$ (Fig. A.1*c*).

The required notch-elastic, crack-face displacement functions were obtained using the following procedure: Since $u_r(a,x)$ was calculated based on $K_r(a)$ using Eq A.2, the same procedure can be applied to calculate the notch crack-face displacement (caused by remote stress, see Fig. A.1*b*) $u_1(a,x)$. Therefore, after the notch stress-intensity factor $K(a)$ is calculated, the $u_1(a,x)$ was obtained using Eq A.2 and Eq A.3 through A.7 with the $F_r(a/W)$ and $G_r(a/W)$ replaced by $F(a/W)$ and $G(a/W)$. The $F(a/W)$ was calculated

$$F\left(\frac{a}{W}\right) = \frac{K(a)}{S\sqrt{\pi a}} \tag{A.8}$$

Note that $K(a)$ was obtained by Eq A.1 using the notch stress distribution $\sigma(x)$. It is important to replace the crack length a by $a + \rho_c$ in Eq A.2 through A.8 during calculations because all the equations are applied to the fictitious crack of crack length $a + \rho_c$. Since erroneous results were reported [*15*] for crack-face displacement caused by yield-strip load using Eq A.2, the $u_2(a + \rho_c, x)$ (caused by the strip-yield load ahead of the crack tip, see Fig. A.1*c*) was calculated using a double integral equation

$$u_2(a + \rho_c, x) = \sigma_0 \int_0^{a+\rho_c} \int_{a_1}^{a+\rho_c} h(c, a')h(x, a')da'\,dc \tag{A.9}$$

$$a_1 = \max(c, x)$$

where $h(c,a')$ and $h(x,a')$ are the weight functions derived by Bueckner for single-edge cracks [*16*]

$$h(a,x) = \sqrt{\frac{2}{\pi a}} \frac{1}{\sqrt{1 - \frac{x}{a}}} \left[1 + m_1\left(1 - \frac{x}{a}\right) + m_2\left(1 - \frac{x}{a}\right)^2\right] \tag{A.10}$$

$$m_1 = 0.6147 + 17.1844\left(\frac{a}{W}\right)^2 + 8.7822\left(\frac{a}{W}\right)^6 \tag{A.11}$$

$$m_2 = 0.2502 + 3.2889\left(\frac{a}{W}\right)^2 + 70.0444\left(\frac{a}{W}\right)^6 \tag{A.12}$$

According to Newman's strip-yield model, the crack-tip plastic zone (from $x = a$ to $x = a + \rho_c$) is divided into ten elements. The magnitude of CTPS at the center of the element is calculated by

$$\text{CTPS}(x_i)/2 = u_1(a + \rho_c, x_i) - u_2(a + \rho_c, x_i) \qquad a < x_i < a + \rho_c \tag{A.13}$$

In the SYMNC model, the value of $a + \rho_c$ is compared with that of ρ_n. If $a + \rho_c$ is larger than ρ_n, the magnitudes of CTPS, NPS are calculated at the center of the elements following Newman's approach. If $a + \rho_c$ is smaller than ρ_n, which indicates that the crack-tip plastic zone is entirely embedded in the notch plastic zone, the range from $x = a$ to $x = \rho_n$ is divided into ten elements. The CTPS(x_i) and the NPS(x_i) are then calculated at these elements, and the TPS(x_i) are calculated using Eq 4.

When the TPS are calculated, the remaining algorithm to calculate crack closure is identical to Newman's approach.

References

[1] Newman, J. C., Jr., "A Finite-Element Analysis of Fatigue Crack Closure," *Mechanics of Crack Growth, ASTM STP 590,* American Society for Testing and Materials, Philadelphia, 1976, pp. 281–301.

[2] McClung, R. C. and Sehitoglu, H., "On the Finite Element Analysis of Fatigue Crack Closure—1. Basic Modeling Issues," *Engineering Fracture Mechanics,* Vol. 33, 1989, pp. 237–252.

[3] Newman, J. C., Jr., "A Crack-Closure Model for Predicting Fatigue Crack Growth Under Aircraft Spectrum Loading," *Methods and Models for Predicting Fatigue Crack Growth Under Random Loading, ASTM STP 748,* American Society for Testing and Materials, Philadelphia, 1983, pp. 53–84.

[4] Newman, J. C., Jr., "A Nonlinear Fracture Mechanics Approach to the Growth of Small Cracks," *AGARD Report 328,* 1983, pp. 6.1–6.26.

[5] Shin, C. S. and Smith, R. A., "Fatigue Crack Growth at Stress Concentrations—The Role of Notch Plasticity and Crack Closure," *Engineering Fracture Mechanics,* Vol. 29, 1988, pp. 301–315.

[6] Verreman, Y., Ballon, J.-P., and Masounave, J., "Closure and Propagation Behavior of Short Fatigue Cracks at Different R-Ratios," *Fatigue 87,* 1987, Emos, Worley, U.K., pp. 371–380.

[7] Tao, Y., He, J., and Hu, N., "Effect of Notch Stress Field and Crack Closure on Short Fatigue Crack Growth," *Fatigue and Fracture of Engineering Materials and Structures,* Vol. 13, 1990, pp. 423–430.

[8] McClung, R. C. and Sehitoglu, H., "Closure and Growth of Fatigue Cracks at Notches," *Journal of Engineering Materials and Technology,* Vol. 114, 1992, pp. 1–7.

[9] Smith, R. A. and Miller, K. J., "Fatigue Cracks at Notches," *International Journal of Mechanical Science,* Vol. 19, 1977, pp. 11–22.

[10] Sehitoglu, H., "Characterization of Crack Closure," *Fracture Mechanics, ASTM STP 868,* American Society for Testing and Materials, Philadelphia, 1985, pp. 361–380.

[11] Ogura, K., Miyoshi, Y., and Nishikawa, I., "Fatigue Crack Growth and Closure of Small Cracks at Notch Roof," *Current Japanese Materials Research,* MRS, Society of Material Science, Japan, Vol. I, 1987, pp. 41–65.

[12] Jono, M. and Song, J., "Growth and Closure of Short Fatigue Cracks," *Current Japanese Materials Research,* MRS, Vol. I, Society of Material Science, Japan, 1987, pp. 67–91.

[13] Stephens, R. I., Sheets, E. C., and Njus, G. O., "Fatigue Crack Growth and Life Predictions in Man-Ten Steel Subjected to Single and Intermittent Tensile Overloads," *Cyclic Stress-Strain Behavior—Analysis, Experimentation, and Failure Prediction, ASTM STP 519,* American Society for Testing and Materials, Philadelphia, 1973, pp. 176–191.

[14] Petroski, H. J. and Achenbach, J. D., "Computation of the Weight Function from a Stress Intensity Factor," *Engineering Fracture Mechanics,* Vol. 10, 1978, pp. 257–266.

[15] Görner, F., Mattheck, C., Morawietz, P., and Munz, D., "Limitations of the Petroski-Achenbach Crack Opening Displacement Approximation for the Calculation of Weight Functions," *Engineering Fracture Mechanics,* Vol. 22, 1985, pp. 269–277.

[16] Bueckner, H. F., "Field Singularities and Related Integral Representations," *Mechanics of Fracture 1—Methods of Analysis and Solution of Crack Problems,* G. C. Sih, Ed., Noordhoff, Leyden, 1973.

Raghu V. Prakash,[1] *R. Sunder,*[2] *and E. I. Mitchenko*[3]

A Study of Naturally Initiating Notch Root Fatigue Cracks Under Spectrum Loading

REFERENCE: Prakash, R. V., Sunder, R., and Mitchenko, E. I., **"A Study of Naturally Initiating Notch Root Fatigue Cracks Under Spectrum Loading,"** *Advances in Fatigue Lifetime Predictive Techniques: 3rd Volume, ASTM STP 1292,* M. R. Mitchell and R. W. Landgraf, Eds., American Society for Testing and Materials, 1996, pp. 136–160.

ABSTRACT: The kinetics of short cracks at notches were studied in 2014-T6511 Al-Cu alloy extruded bar stock under modified versions of FALSTAFF and TWIST load spectra. Experiments were conducted on test coupons of different thickness and at different stress levels. The effects of these and other parameters on the density and growth rate patterns of multiple cracks were investigated. The quality of fractographic crack growth rate measurements was found to be superior to surface replica technique. It was also observed that artificially initiated fatigue cracks grow slower than naturally initiated ones. Interaction of naturally initiating multiple cracks was quantified.

KEYWORDS: short cracks, notch root fatigue, spectrum loading, multiple cracks, thickness effect, replica, fractography

The so-called "short crack effect" attracted much attention in view of apparent deviations from well-established fracture mechanics concepts that relate crack growth rate uniquely with the stress intensity factor. Most research on the short crack effect has been restricted to constant amplitude loading and near-threshold loading conditions, which accentuate the effect of microstructure, residual stresses, crack extension mode, etc. Most fatigue failures, on the other hand, occur under random service load conditions and are initiated at stress raisers like holes, fillets, and fasteners. Recent research suggests that provided notch root inelasticity and short crack closure effects are accounted for, fracture mechanics (FM) can be extended to cover cracks as small as 10 to 50 μm [*1*]. Reference *2* considers the possibility of FM-based endurance prediction by integrating the progress of initial defects from Cycle 1 to failure.

This paper attempts to summarize observations made in the course of a three-year research program dedicated to notch root short crack growth under spectrum loading. The work was performed on L168 (equivalent of 2014-T6511) Al-Cu alloy extruded bar stock, which is used to fabricate primary airframe load-carrying components. Early work was under a modified FALSTAFF load spectrum using 6-mm-thick coupons with a 6-mm central hole to study the growth of naturally initiating short fatigue cracks [*3*]. This was followed by experiments on additional thicknesses and also using a different load spectrum. The goal was to investigate the influence on short crack kinetics of a number of variables including stress level, material thickness, multiple crack interaction, and natural versus artificial crack

[1]Structural Integrity Division, National Aerospace Laboratories, Bangalore 560 017, India.
[2]Presently with Biss Research, 99, 14A Cross, Malleswaram, Bangalore 560017, India.
[3]Visiting scientist from Kiev Institute for Strength Problems, Timiryazevskaya, 2, Kiev 252 014, Ukraine.

initiation. The research was motivated by the possibility that one or more of these variables are likely to affect the mechanics of crack growth in a way that may not be significant in the case of long cracks.

Experimental Procedure

Specimens

The material used was L168 (2014-T6511) extruded bar stock of a 70 by 200-mm section. Figure 1 shows the different specimen geometries used in testing. Initial tests were conducted on 6-mm-thick specimens with a central hole. Later, the single edge hole specimens of 12.5 and 3.5-mm thickness were included in testing. These specimens provided access for replica application to track the formation and growth of notch surface cracks. A single test was conducted on a 12.5-mm edge-notched coupon with artificial crack initiators introduced through electrical discharge machining (EDM). This test was aimed at studying the interaction of two coplanar cracks. All other tests involved naturally initiating cracks. A total of twelve specimens were tested as part of the experimental program. All the test coupons were cut along the extrusion direction from the same batch to ensure similarity of mechanical properties. These were determined through standard laboratory coupon testing for tensile, low-cycle fatigue, and fatigue crack growth properties [*1*]. A summary of these properties appears in Table 1.

Load Sequences

The testing was performed under modified versions of the FALSTAFF [*4,5*] and TWIST [*6*] load spectra (Fig. 2). The modifications were required to ensure the possibility of determining crack growth rates through fractography of the fatigue failures, which was the main goal of the study. No other technique is available to investigate the formation and growth of part-through cracks of small dimensions. The results reported in this paper were obtained under the programmed sequence FalstaffUp, which was arranged with smaller load cycles arranged to fall on the rising half of larger cycles. Reference *5* describes how modified FALSTAFF was derived and validated for similarity to the original randomized FALSTAFF in terms of identical fatigue crack growth rates. It also shows that fractographically determined (long) crack growth rates correspond with surface as well as computerized compliance-based estimates.

The modified TWIST sequence was derived in the same way as FALSTAFF [*5*]. No validation tests were performed to demonstrate its equivalence to the original randomized version. The modified FALSTAFF spectrum had been validated against the original randomized version [*3*].

The majority of tests were performed under the FALSTAFF spectrum. The volume of testing under TWIST was restricted. The bulk of damage in TWIST is caused by the smaller cycles [*7*]. As a consequence, duration of testing at a given reference stress is about 15 times longer than in the case of FALSTAFF.

Testing

Testing was performed on 50 and 100-kN computer-controlled servohydraulic load frames equipped with hydraulic grips to hold the specimens. Average test frequency was about 15 Hz. During tests on edge notch specimens, loading was held periodically at about 50% of maximum load to apply the replication tape. This process required a few minutes for the acetone-soaked cellulose acetate tape to dry completely. No effect by way of discontinu-

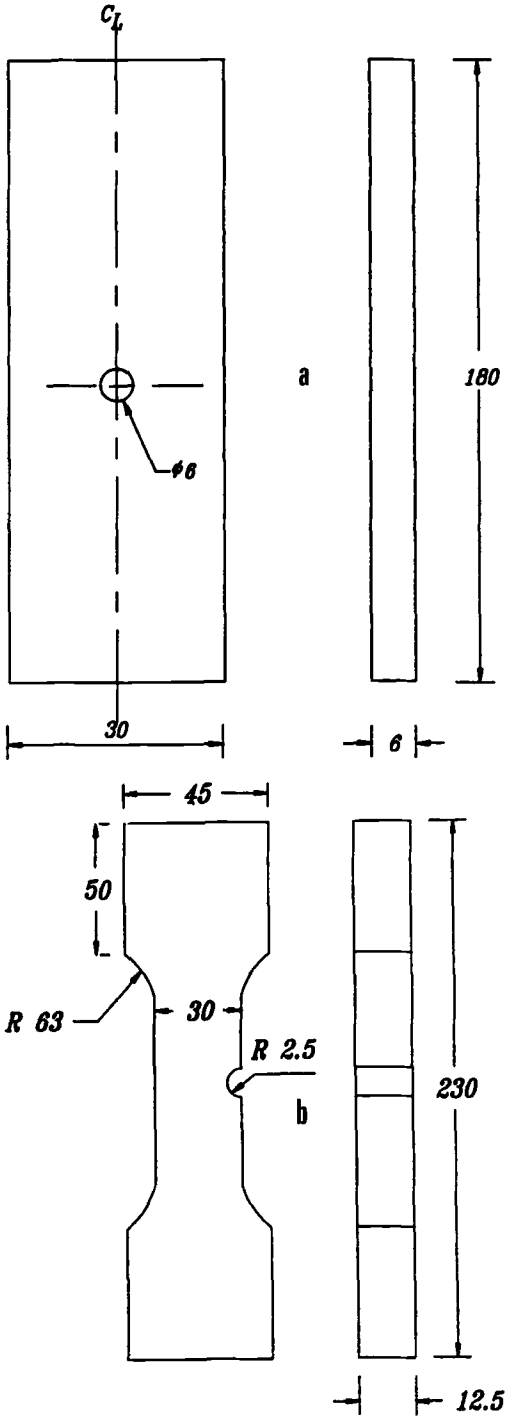

FIG. 1—*Specimen geometries:* (a) *coupon with central hole,* (b) *edge-notched coupon, 12.5 mm thick,* (c) *hourglass coupon with edge notch, and* (d) *edge-notched coupon with two electrical discharge machined crack initiators.*

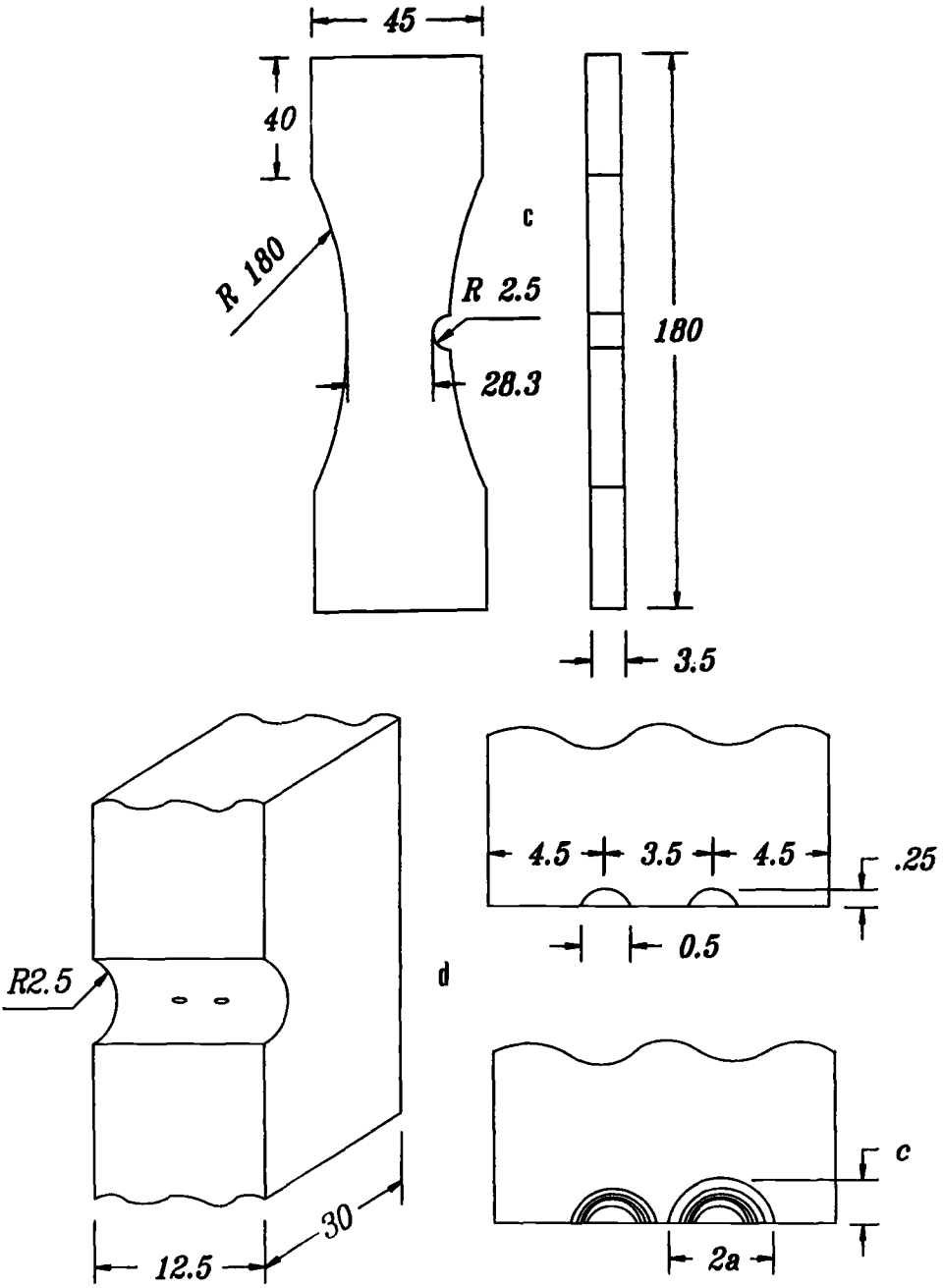

FIG. 1—*Continued.*

TABLE 1—*Material properties of L168 (2014-T6511).*

(a) Mechanical Properties			
0.2% Yield Stress, MPa	UTS, MPa	E, GPa	% Elongation
420	480	73.65	10.0

(b) Low-Cycle Fatigue Constants			
K', MPa	n'	σ_f', MPa	ϵ_f'
602.32	0.0526	850	0.28

(c) Fracture Mechanics Constants		
C, mm/MPa$\sqrt{m}$	m	Kc, MPa$\sqrt{m}$
1.0×10^{-7}	3.27	60.0

ity in crack growth kinetics was detected, however, that could have been attributed to the test interruption.

Stress Levels

Three stress levels were used in the tests: S_{ref} = 275, 225, and 190-MPa gross reference stress. The reference stress corresponds to the highest load level in the spectrum. Other levels are proportionately scaled as defined in the Rainflow count table for the load spectrum. Gross stress was computed over the plane of expected crack growth assuming absence of the notch. For the material studied, S_{ref} = 275 MPa causes cyclic yield at the notch root, while 225 and 190 MPa cause monotonic yield. These conditions apply to both the FALSTAFF and TWIST spectra. However, testing at 190 MPa under the TWIST load spectrum did not result in fatigue failure even after 100 million cycles, and this case had to be discarded from the study.

Fractography

Fatigue crack growth rates were measured through optical fractography of the fatigue failures. Reference *3* provides details on the procedures used. The fractographic technique provided clear pictures of programmed load striation formation down to a crack size of 10 to 20 μm. Initial fractography was carried out on a Neophot-2 microscope. Subsequently, an Olympus BH2 microscope with digital imaging capability was used. Software on the latter also assisted in the determination of striation spacing. The notch surface replicas collected during testing were also observed under the optical microscope. These revealed crack formation sites and their progress including merger after intervals of cycling. In the course of the study, the quality of surface-replica-based growth rate estimates was compared with fractographic evidence.

Data Processing

Average growth rate from replica records was estimated as the ratio of crack increment to cycle interval. Growth rates obtained from optical fractography were not processed in any manner because striation spacing by itself represents crack growth rate. Short crack growth rate data obtained in this fashion showed remarkable consistency in continuity, much like long crack growth rates. However, growth rates of multiple cracks were seldom similar in

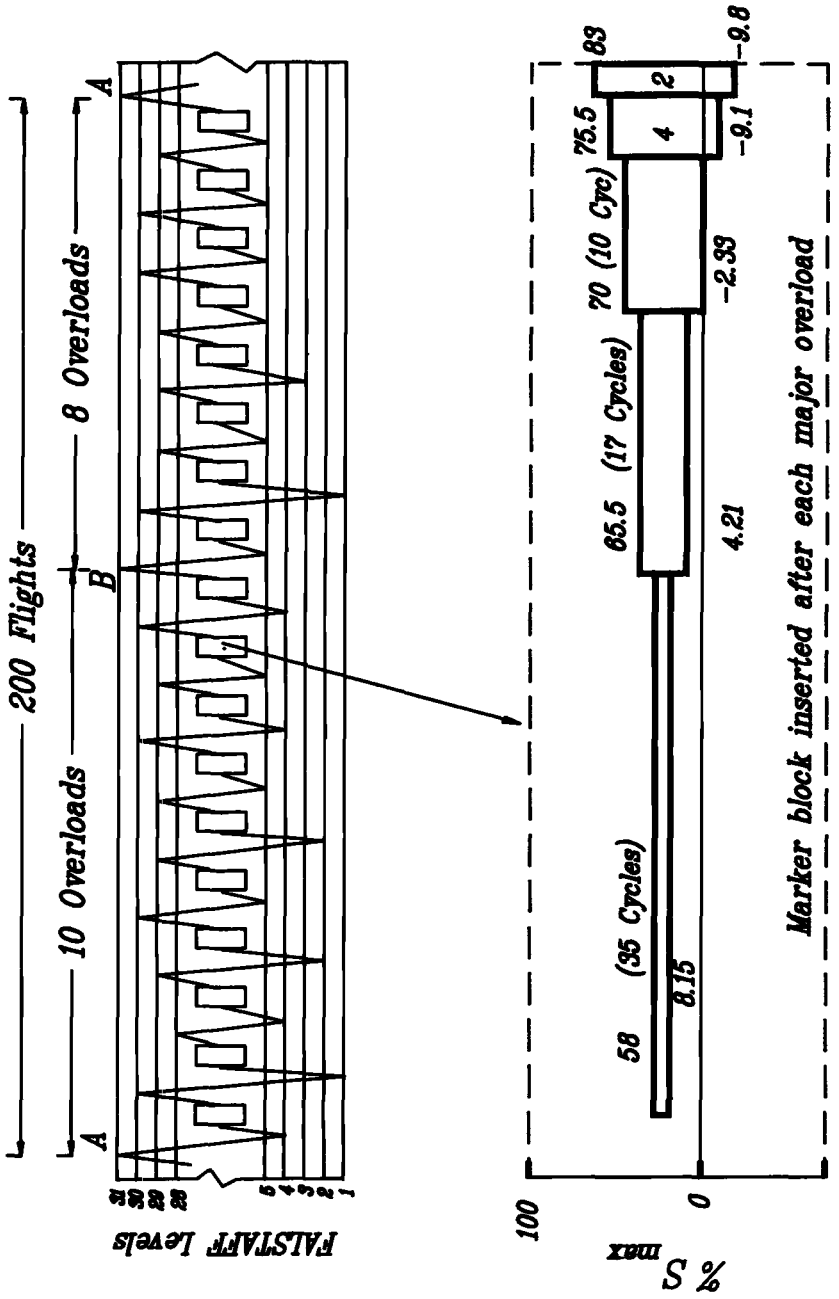

FIG. 2—*Modified FALSTAFF and TWIST load spectra.*

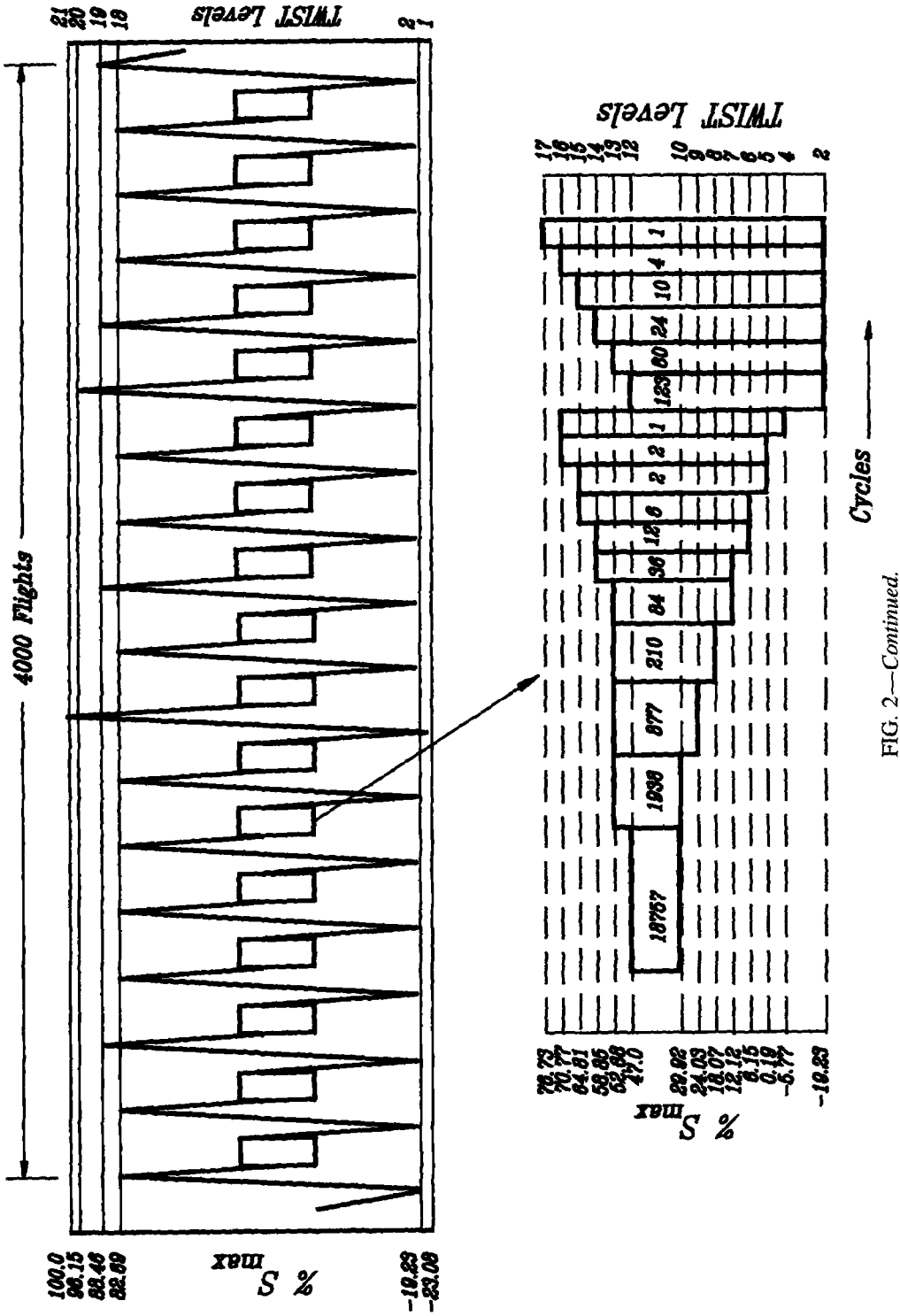

FIG. 2—*Continued.*

view of their interaction. To avoid data cluttering when multiple cracks were tracked, growth rates for individual cracks were approximated by a least square fit straight line. The correlation coefficient in most cases exceeded 0.97. Replica-based growth rate measurements, however, did not show this consistency. They yielded correlation coefficients ranging from 0.6 to 0.8, which are not adequate to justify a least square fit.

To reconstruct the interaction of multiple cracks from fractographic evidence, growth rates were integrated "backward from failure" in the direction of individual crack formation sites on the notch surface. The integration is based on the premise that the crack was never arrested at any point, which would have been revealed by rubbing marks and retarded crack growth immediately preceding and following the crack arrest point.

For consistency, growth rates were computed as mm/flight. The FALSTAFF spectrum covers 200 flights, while the TWIST spectrum covers 4000 flights. Though flight duration in terms of both number of cycles as well as damage content varied significantly in the original spectrum, it was assumed for the convenience of data comparison that crack growth per flight can be estimated as crack growth over a full block (spectrum duration) divided by number of flights in the spectrum.

Fractographic Versus Surface Measurements of Crack Growth Rate

The empirical results presented below appear to suggest that surface measurements of crack growth may be responsible for the perceived scatter in short crack growth rates.

Short Crack Growth Rates Do Not Exhibit More Scatter Than Long Cracks

This was observed in the early stages of this program [*3*] and appears to be confirmed by fractographic measurements on all subsequent failures. The consistency in the evolution of crack shape by way of its even progress across the entire front was in fact useful in obtaining growth rate estimates for regions that did not provide clear pictures because of local damage to the failure surface. This is illustrated by the data in Fig. 3 for a quarter elliptical corner crack on a 3.5-mm-thick edge-notched specimen subject to the FalstaffUp sequence at a stress level of 190 MPa. A schematic of the crack front progress appears on the figure with lines showing two different radials from the crack origin. The fractographic growth rate estimates for the two directions fall into a single narrow band. Similar observations were made on other failures and are in contrast to surface-replica-based crack-growth-rate measurements that suggest considerable scatter in data [*8*].

Surface-Replica-Based Measurements of Fatigue Crack Growth Exaggerate Scatter in Fatigue Crack Growth Rate

This is illustrated by data in Figs. 4*a* through 4*f*. Figures 4*a* and 4*b* show crack growth rate under FalstaffUp versus (surface) crack length at 275 and 225 MPa, respectively, measured on the 3.5-mm-thick coupons using optical fractography (symbols) and surface replication (lines). Figures 4*c* and 4*d* show similar data obtained on the 12.5-mm-thick specimens. The data are for multiple naturally initiating cracks (shown as different symbols and lines), down in depth to 20 to 40 μm. Figure 4*e* compares crack growth rate estimates from the 12.5-mm-thick specimen with two artificial crack initiators 250 μm deep. These data were obtained at a stress level of 225 MPa.

In all the cases shown in Fig. 4, the replica-based data exhibit considerable "scatter," that is, of the same order as reported in the literature [*8*]. On the other hand, fractographic measurements appear to indicate the same scatter as for long cracks at similar crack growth rate [*3*].

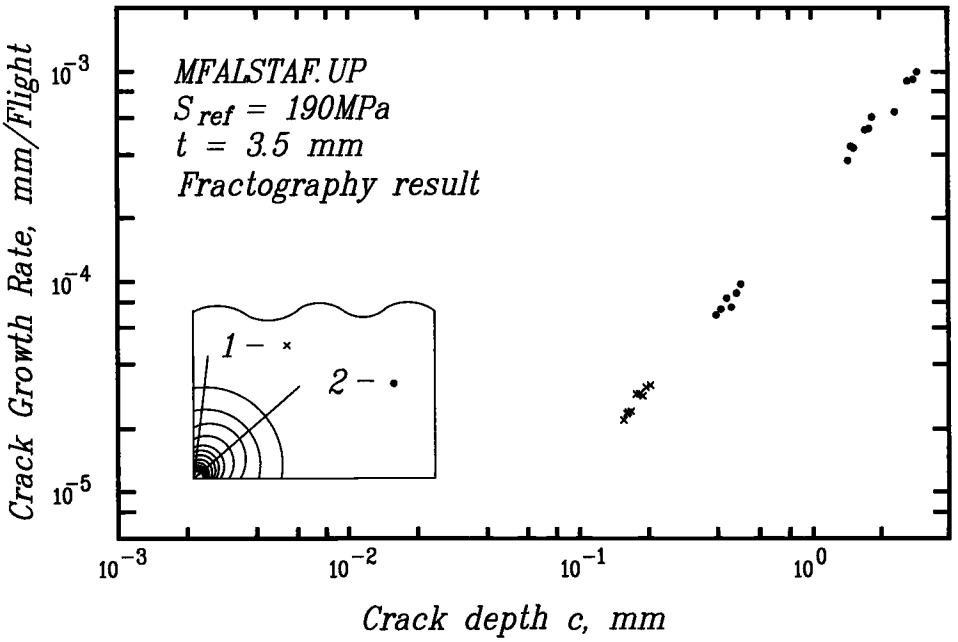

FIG. 3—*Crack growth rate data from two different locations on the crack front.*

Clearly, surface replica technique appears to introduce error into measurements that creates an impression of scatter in crack growth rate. A number of factors may contribute to errors. The human element involved in replication of the notch surface may contribute to errors in crack size estimation as the extent to which true crack length is transferred will depend on the pressure applied. The notch surface experiences plane stress conditions that allow considerable cyclic deformation at the crack tip. Under these conditions, it is difficult to identify the tip of the fatigue crack due to the transverse contraction of the plastic zone, which can be misinterpreted as an extended crack. Finally, while inner points on the crack front are forced by crack tip opening constraints to move "in step" with each other, such a constraint does not exist on the notch surface that can actually behave as a stretchable ligament subject to extensive deformation and tear. The fatigue crack as observed on the surface may thus appear to grow discontinuously, a phenomenon often observed through a traveling microscope during experiments. These observations point to fractographic measurements as a preferred choice where practical. However, many materials may not exhibit the clear striation patterns obtained in our experiments. Besides, it may not be always possible to engineer load sequences suitable for fractography. Finally, the replication technique provides vital information on (multisite) crack formation over the entire fatigue critical notch surface. Fractographic measurements only cover the plane over which fatigue failure finally occurred. Fatigue cracks that initiated on other planes are not accessible for examination.

In summary, the fractographic technique offers distinct advantages by way of consistency in measurements and the possibility of tracking subsurface multiple crack kinetics along the primary fracture surface. The test data described further in this paper refer only to fractographic crack growth rate measurements.

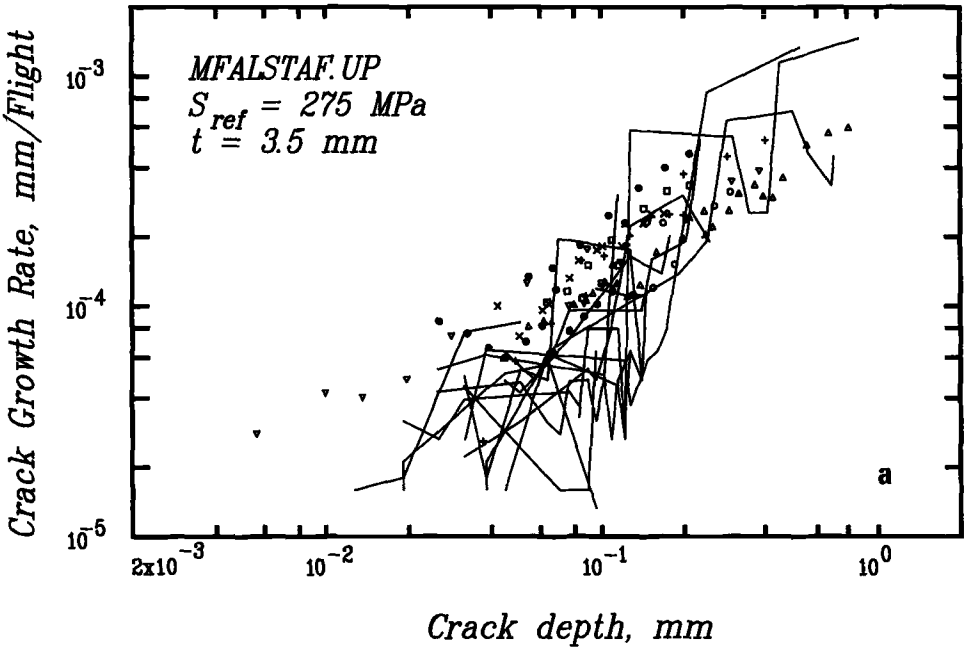

FIG. 4—*Crack growth rates obtained using replica technique and from optical fractography under modified FALSTAFF:* (a) −275 *MPa*, t = 3.5 *mm*, (b) −225 *MPa*, t = 3.5 *mm*, (c) −275 *MPa*, t = 12.5 *mm*, (d) −225 *MPa*, t = 12.5 *mm*, (e) −225 *MPa*, t = 12.5 *mm, specimen with artificial initiators.*

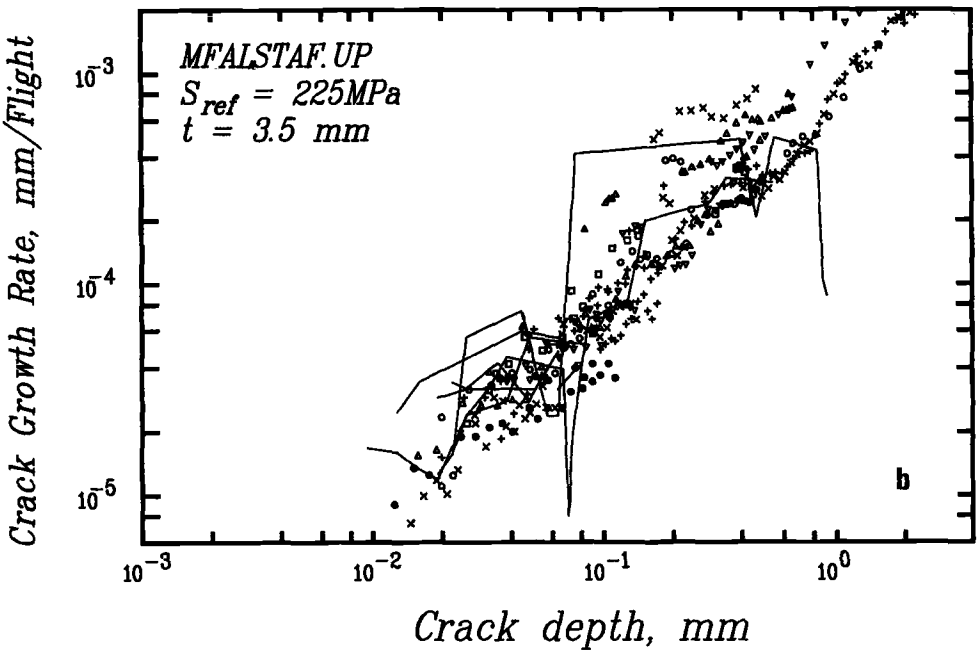

FIG. 4—*Continued.*

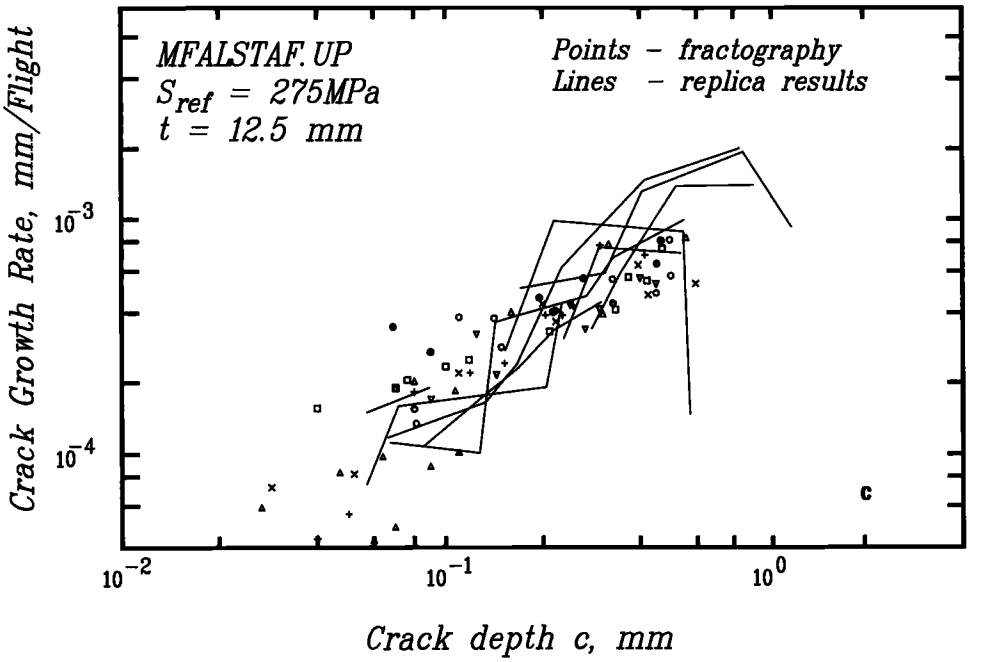

FIG. 4—*Continued.*

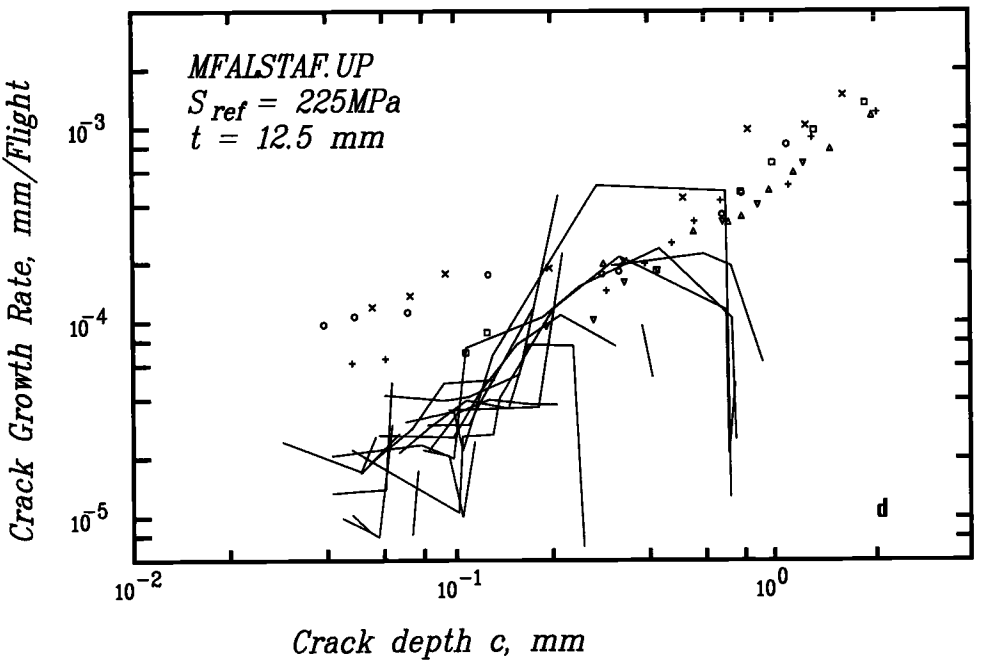

FIG. 4—*Continued.*

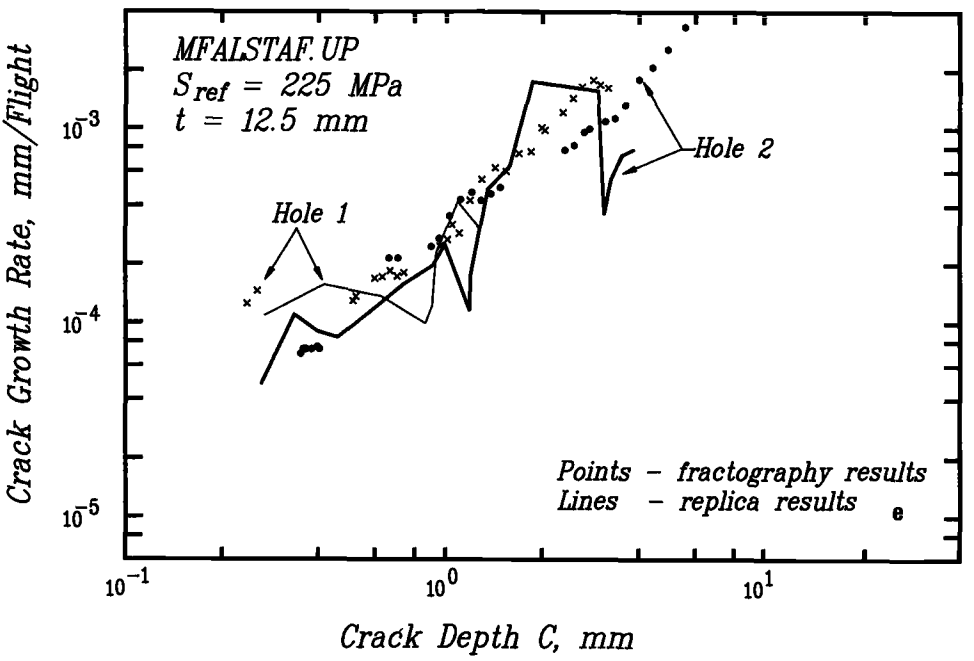

FIG. 4—*Continued.*

Mechanics of Multiple Crack Formation and Growth

The Stress Intensity for Artificially Initiated Fatigue Cracks Can Be Different from That for Naturally Initiating Ones

Figure 5 shows growth rate data (lines) for the two artificially initiated cracks under FalstaffUp loading at S_{ref} = 225 MPa. Figure 1*d* shows the specimen and crack starter details. Data obtained at the same stress level for naturally initiating cracks are shown as symbols. Different symbols are used to designate individual cracks that formed on the notch surface.

The naturally initiating cracks show a wide variation in growth rates (almost over an order of magnitude). This is attributed to the influence of existing crack(s) on the accelerated formation and growth of new cracks. Obviously, a large part-through crack at the notch will significantly increase stress levels over the uncracked section of the notch root, leading to early formation of new cracks and their accelerated growth to merge with the existing one(s).

The two artificially initiated cracks started growing simultaneously and more or less at the same rate. At a depth of about 1.7 mm, the two merged as indicated by the same line beyond this depth. As no rapid acceleration follows the merger, one may be led to believe that the two cracks grew relatively independent of each other. A similar conclusion was reached in Ref *9* in experiments on a pair of coplanar cracks. This conclusion is questionable because it can be argued that the two cracks did influence each other. But because they did so in equal proportion, the effect was unnoticed. One may suggest that the influence of the two cracks on one another increased gradually to the point of merger, explaining why there was no apparent acceleration after merger. It may also be noted that the initial growth rate of the

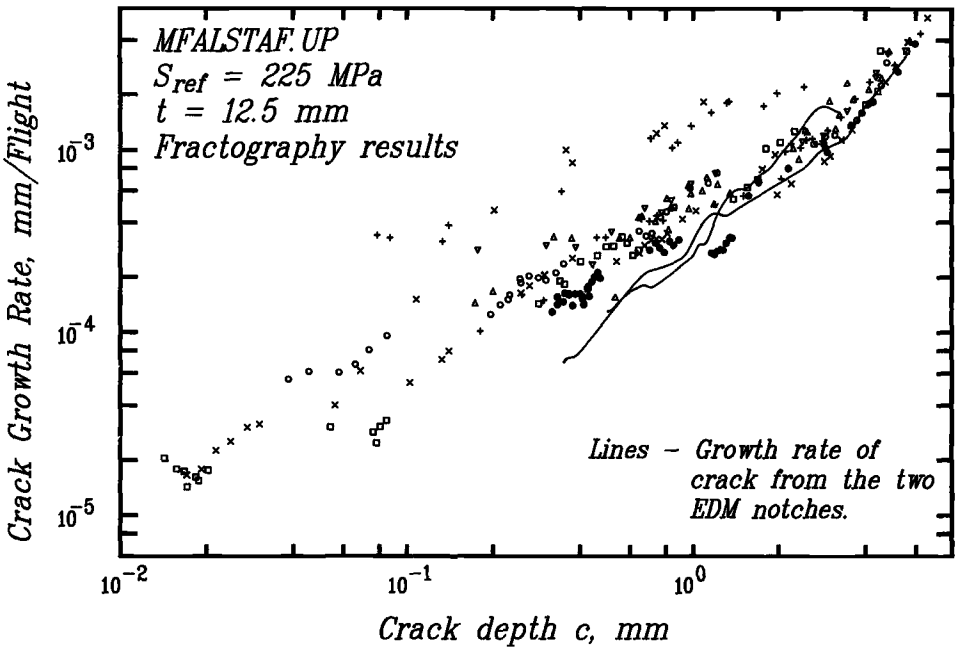

FIG. 5—*Comparison of growth rate of artificially initiated cracks with data for multiple naturally initiating cracks.*

artificially initiated cracks is lower by a factor of two than that of the slowest naturally initialized crack. Obviously, the EDM crack starter behaves as a "notch-in-a-notch."Small cracks growing from it will no doubt see a much greater stress concentration than the semicircular edge. However, their initial size will be effectively reduced by the EDM notch depth. This effect is schematically described in Fig. 6. One may conclude that to be of practical value, experiments on short, part-through cracks must involve naturally initiating cracks. Alternately, an FEM analysis of the "notch-in-a-notch" may be required.

Number of Naturally Initializing Fatigue Cracks Increases with Stress Level

Figure 7 shows a bar chart summary of observed crack initiation sites as a function of stress level. Crack origins were detected by retracing the crack path at different points along the specimen thickness. The normal to the crack front leads to its origin. All observed origins were on the notch surface. At S_{ref} = 275 MPa under FalstaffUp, as many as 31 initiation sites were detected on the fracture from the 12.5-mm-thick specimen. On the 3.5-mm-thick specimen, fewer sites were observed. Though there appears to be no strict correlation between thickness and number of sites, the density of sites on the thinner coupons appears to be consistently higher. This may be related to the domination of plane stress conditions on the thinner coupon, which enhances cyclic slip activity and associated fatigue crack formation.

As shown in Fig. 7, a combination of the type of load spectrum, stress level, as well as material thickness appear to affect the density of naturally forming cracks. Further study of these effects is likely to enhance residual life prediction capability through a more precise definition of crack-driving force.

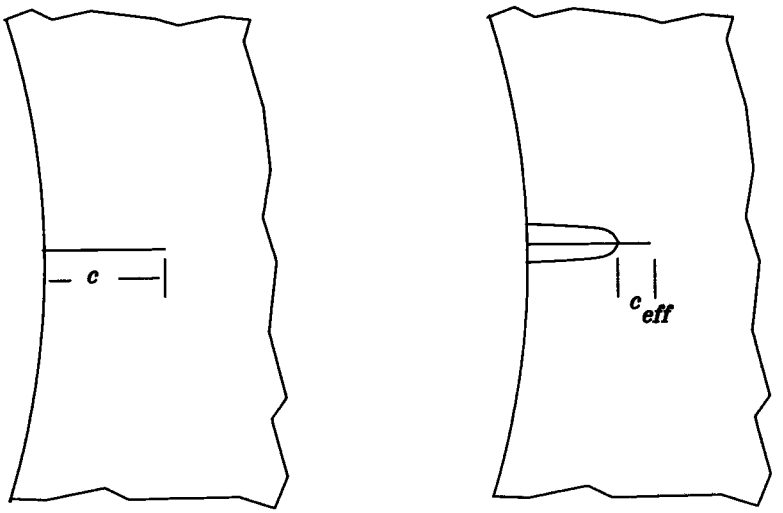

FIG. 6—*Schematic of the "notch-within-notch" effect in the case of artificially initialized cracks.*

Natural Cracks Do Not Initiate Simultaneously

The dominant crack that formed first accelerates the formation and growth of subsequent cracks. During the modeling effort, it was noted that predicting the growth of the dominant crack alone (ignoring the effect of newly forming cracks) would provide a fairly accurate estimate of residual fatigue life [2]. It was also noted [1] that when non-coplanar cracks merge, there is no sudden acceleration in crack growth. In this study, acceleration was noticed at the merger of coplanar cracks, but is restricted to the transition region for crack shape to settle from two semicircles into one. Figure 8 shows typical fractographs from testing under the TWIST spectrum at S_{ref} = 275 MPa. Four of the 22 detected crack origins are shown. Figures 8*a* and 8*b* show a semielliptical and quarter elliptical crack in their early

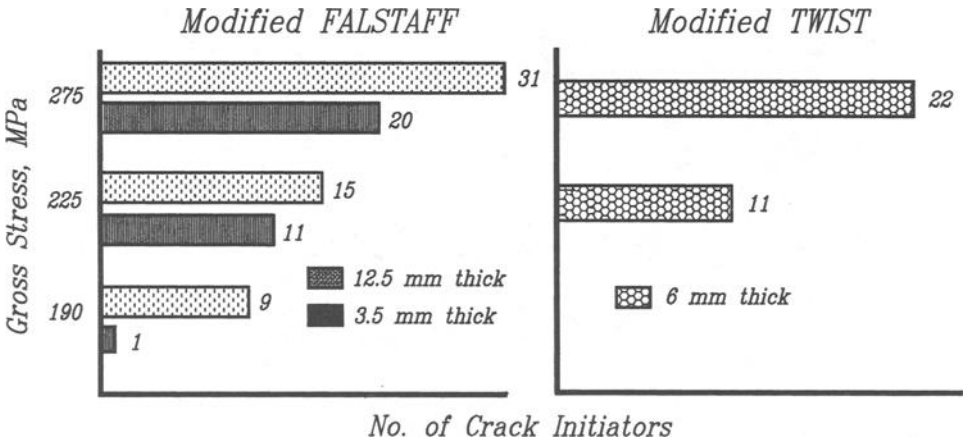

FIG. 7—*Summary of number of observed crack initiation sites versus stress level.*

stage of growth. A steady acceleration is noticed with the application of a new spectrum block. Striations show crack extension in a single step of the spectrum. Spectrum duration is covered by 18 steps. As the severe overloads that control growth rate through crack closure are extremely rare (occurring only a few times over the 400 000 cycle block), striation spacing shows a stepwise increase after each block. This increase is marginal compared to the acceleration that is noticed at the merger of two cracks (Fig. 8*c*). Growth rate versus crack depth for these two cracks appears on Fig. 8*d*. Once the cracks merge into a single front, crack growth rate stabilizes with the formation of the new semielliptical front. In the intermediate points preceding this, crack growth is clearly accelerated. Clearly, in this region, the two crack fronts actually move towards each other, rapidly cracking the highly stressed ligament between them. This is analogous to acceleration observed along the surface ligament when a part-through crack turns into a through crack.

The Influence of Larger Cracks on the Stress Intensity of Smaller Cracks Is Noticeable

This was established by retracing the growth process of individual cracks backwards from the point of failure—a procedure often used in failure analysis [*10*]. The study was performed on a failure under the FALSTAFF load spectrum at S_{ref} = 275 MPa. The growth rates for individual cracks appear in Fig. 9 [*11*]. Figure 10 shows crack formation maps reconstructed for different load block intervals. For simplicity, all cracks were assumed to be semicircular. Ignoring variations in crack closure stress between the different stress, a unique relationship was assumed between crack growth rate, *da/dF*, and reference stress intensity, K_{ref}. Using the slope of this relationship for the dominant crack as a reference (and ignoring the effect on the dominant crack of newer cracks), an equivalent K_{ref} was estimated for the other cracks and appears as an "F_i" multicrack "influence" factor versus crack depth for individual cracks in Fig. 11.

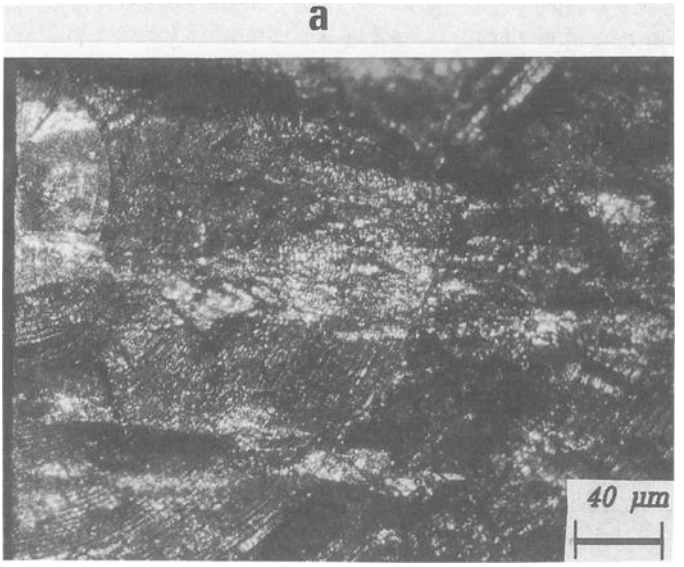

FIG. 8—(a,b) *Optical fractographs of naturally formed semielliptical and quarter elliptical cracks under TWIST at* S_{ref} = *275 MPa;* (c) *two semielliptical cracks merging;* (d) *pre and post merger crack growth rate transition for the two cracks in* (c).

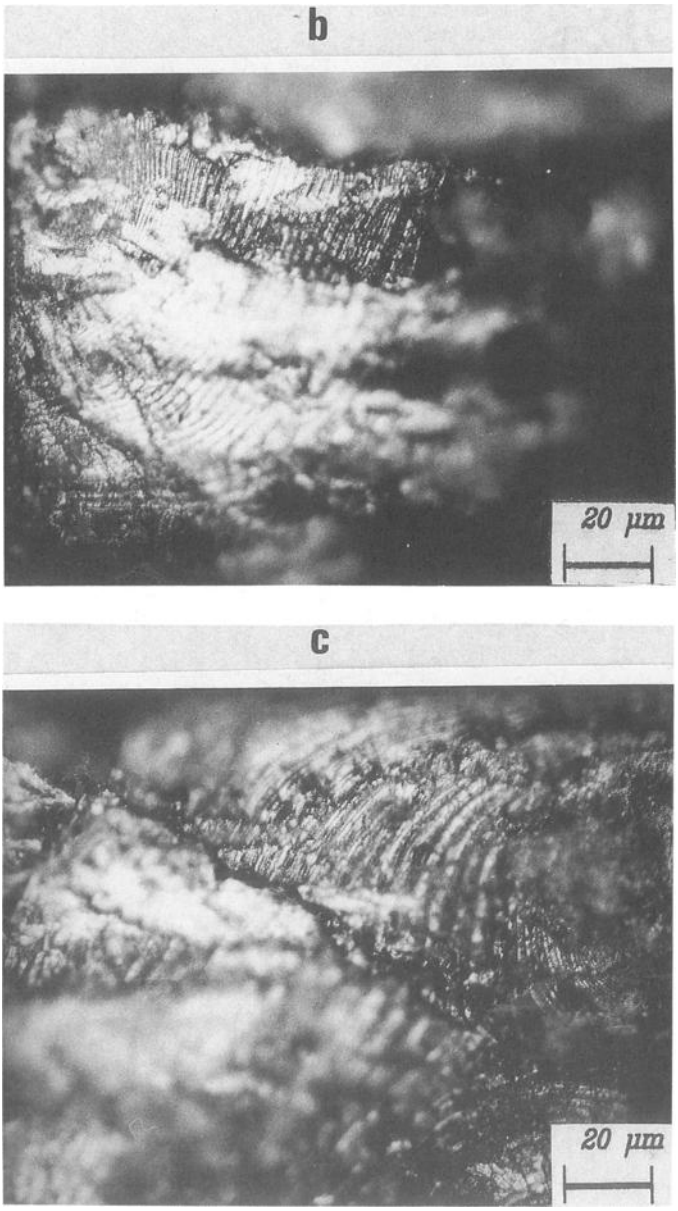

FIG. 8—*Continued.*

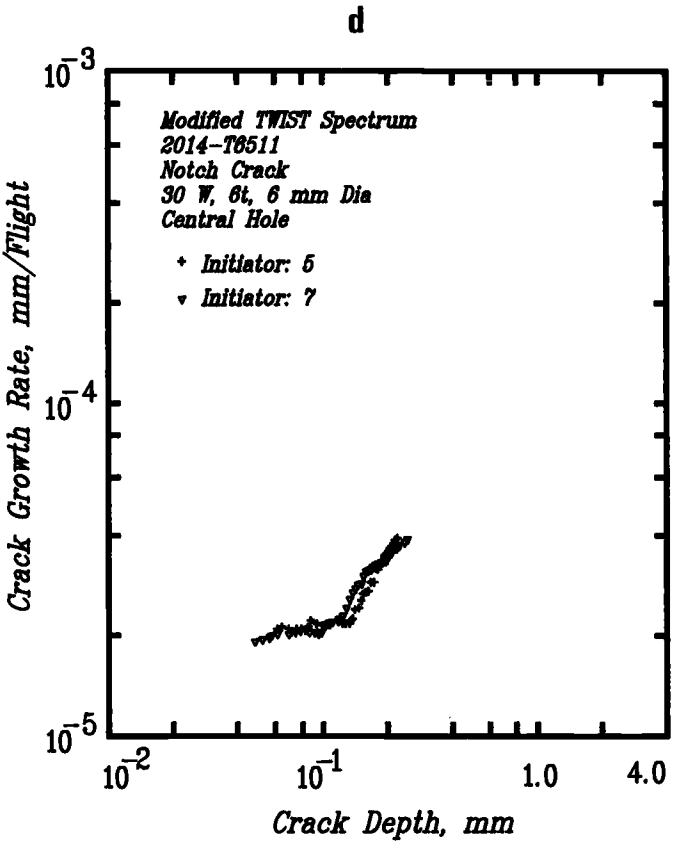

FIG. 8—*Continued.*

The data in Fig. 11 present only a qualitative picture and cannot be used readily in engineering practice for lack of an explicit relationship accounting for the influence of number and size of preexisting flaws.

As shown by the values for F_i inserted at individual crack fronts in Fig. 11, this factor can in some cases exceed the ratio of through-crack to part-through-crack stress intensity. While noting that there is much scope for analytical simulation of multiple crack interaction, it may be observed that future work in this area should be directed at simulating the interaction of dissimilar cracks so that real conditions are taken into account. For purposes of predicting residual life of a component, consideration of a single dominant crack may be adequate. The F_i factor becomes significant when assessing residual life for the purpose of assigning inspection periods where access for inspection is limited. This may, for example, be a load-carrying member that is exposed on one side only or a lug joint with a bush fitting that covers the entire notch surface. In such cases, while considering that a small crack can be detected at the point of access, it may have to be assumed that one or more cracks of larger noninspectable size is already present elsewhere. Thereby, the crack subject to detection is likely to grow much faster than if it had been the dominant one.

From the viewpoint of design approach, the dominant crack determines safe life. It also determines inspection interval if accessibility for inspection is assured. In the event of

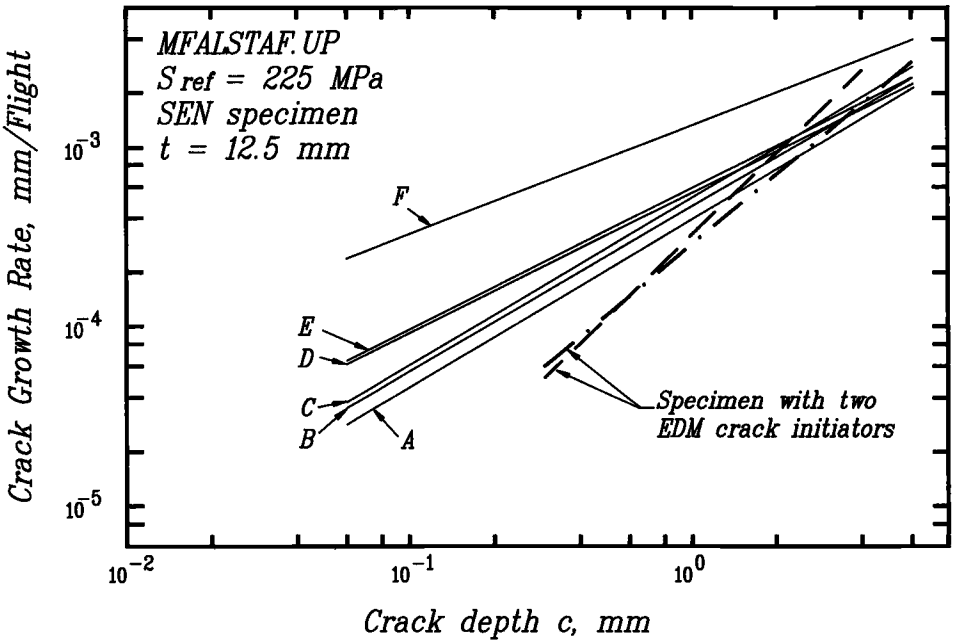

FIG. 9—*Summary of growth rates for multiple cracks* [11]. *Data for FALSTAFF spectrum from a 12.5-mm-thick specimen at 275 MPa.*

restricted access for inspection, the crack subject to detection will determine inspection interval. In this case, the possibility of accelerated growth cannot be discounted, and, as shown in Fig. 11, assumption of a through crack may not be conservative enough.

Thickness Variation Between 3.5 and 12.5 mm Does Not Appear to Significantly Influence the Envelope of Short Crack Growth Rates

Figures 12*a*, 12*b*, and 12*c* show the envelope of crack growth rates for multiple cracks under FalstaffUp at S_{ref} = (*a*) 275, (*b*) 225, and (*c*) 190 MPa. In all three figures, it is clear that the lower bound growth rates differ very little, indicating that dominant cracks in the two thicknesses grew at the same rate. This is significant from the modeling angle as it would follow that a short crack prediction model validated for one thickness is likely to give good predictions for other thicknesses. It had been suggested earlier that plane stress conditions in thinner specimens contribute to early crack formation due to enhanced cyclic slip. Similar growth rates for dominant cracks in Figs. 12*a*, 12*b*, and 12*c* appear to suggest that the crack tip cyclic stress state for short cracks may not be affected by specimen thickness.

In case of the data for 275 and 225 MPa, it is clearly seen that the upper bound tends towards the lower bound with an increase in crack depth as crack merger progresses. The two bounds are, however, parallel in case of lower stress of 190 MPa, indicating that disparity in growth rates will continue to greater crack depth. At lower stress levels, more cycling (and more crack extension) is required before an existing (dominant) crack can force the formation of a new crack at the notch root. For the same reason, the density of cracks at S_{ref} = 190 MPa was about 10 to 30% of that at S_{ref} = 225 and 275 MPa (see Fig. 7).

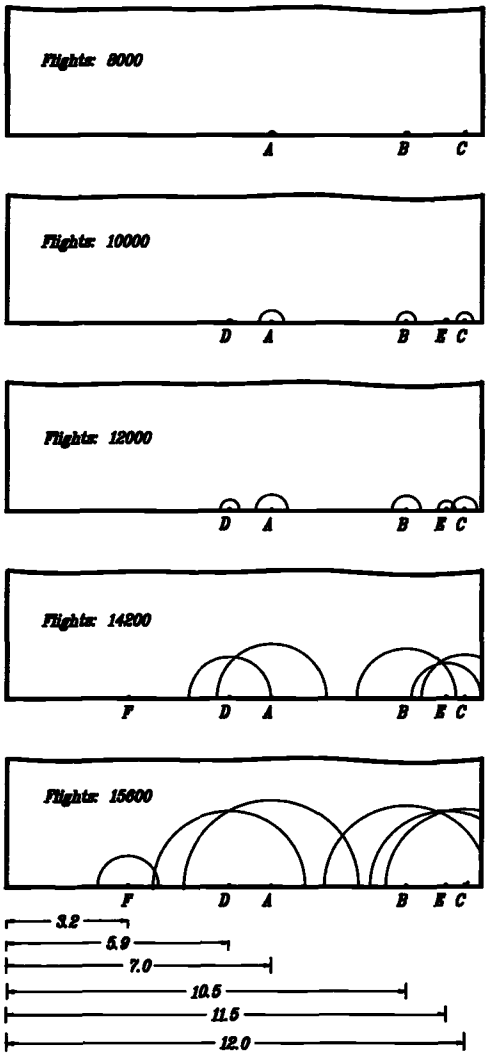

FIG. 10—*Crack formation maps reconstructed from fractography and data in Fig. 9.*

Consequently, even as the dominant crack approaches a large size, the density of smaller coplanar cracks on the notch surface is not sufficiently large to force early merger, thereby extending the envelope of accelerated growth rates.

The data in Figs. 12*a* through 12*c* for the three stress levels are combined in Fig. 12*d* to provide an interesting summary. To avoid clutter, the data are restricted to 12.5-mm thickness. In the case of the lower bound growth rates that represent dominant crack behavior, there is a consistent stress level effect related to higher stress intensity at a given crack depth. The three lines are parallel and spaced in proportion to stress increment as would be estimated by an analytical model. The upper bounds, however, are not proportionately spaced because of the effect of crack density noted previously. In fact, the three curves

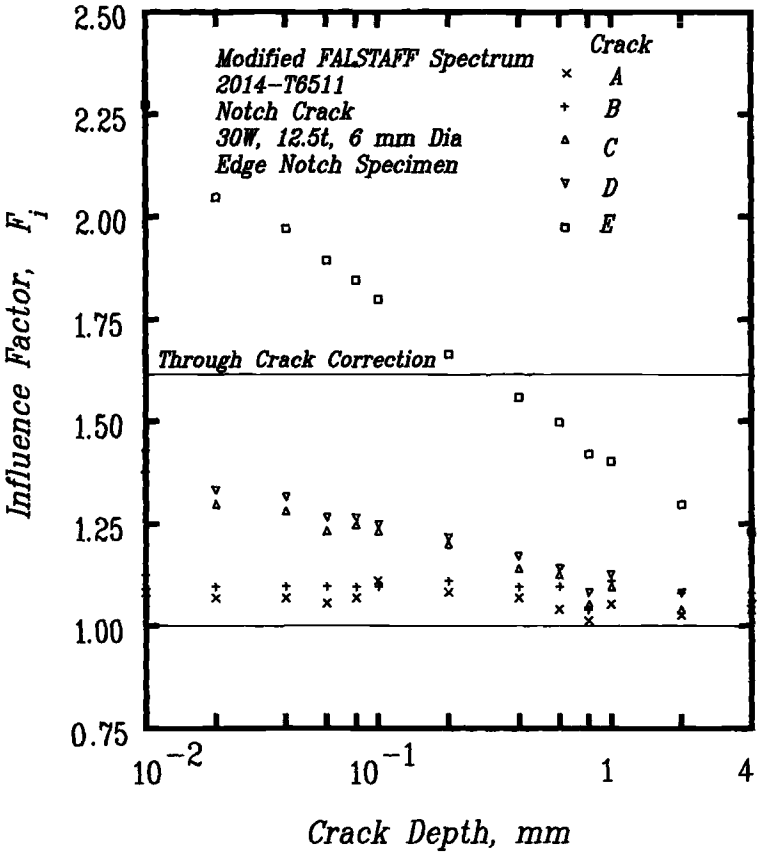

FIG. 11—*Empirically determined influence factor, F_i, for multiple cracks using data from Figs. 9 and 10.*

appear to merge at the right, misleadingly suggesting that upper bound growth rates did not depend on stress level (while, in fact, the phenomeon was caused by the difference in crack density).

Summary

The availability of a wide variety of data for a single batch of material provided a unique opportunity to characterize the influence of a number of variables on short crack growth under aircraft spectrum loading. While some of the observations made may not apply to other materials, the empirical evidence suggests that fracture mechanics can be extended to spectrum-load notch-root short-crack-growth analysis. As indicated in previous work on the same material, reasonable predictions of short crack growth behavior can be made down to a crack size around 50 μm [*1,2*]. Empirical evidence provided in this study and others shows that cracks down to 10 μm in size behave in a consistent and repeatable manner that can be modeled. Two additional inputs are required to extend long crack laboratory test data to notch root short cracks [*1*]: the influence of notch root cyclic inelasticity on crack driving

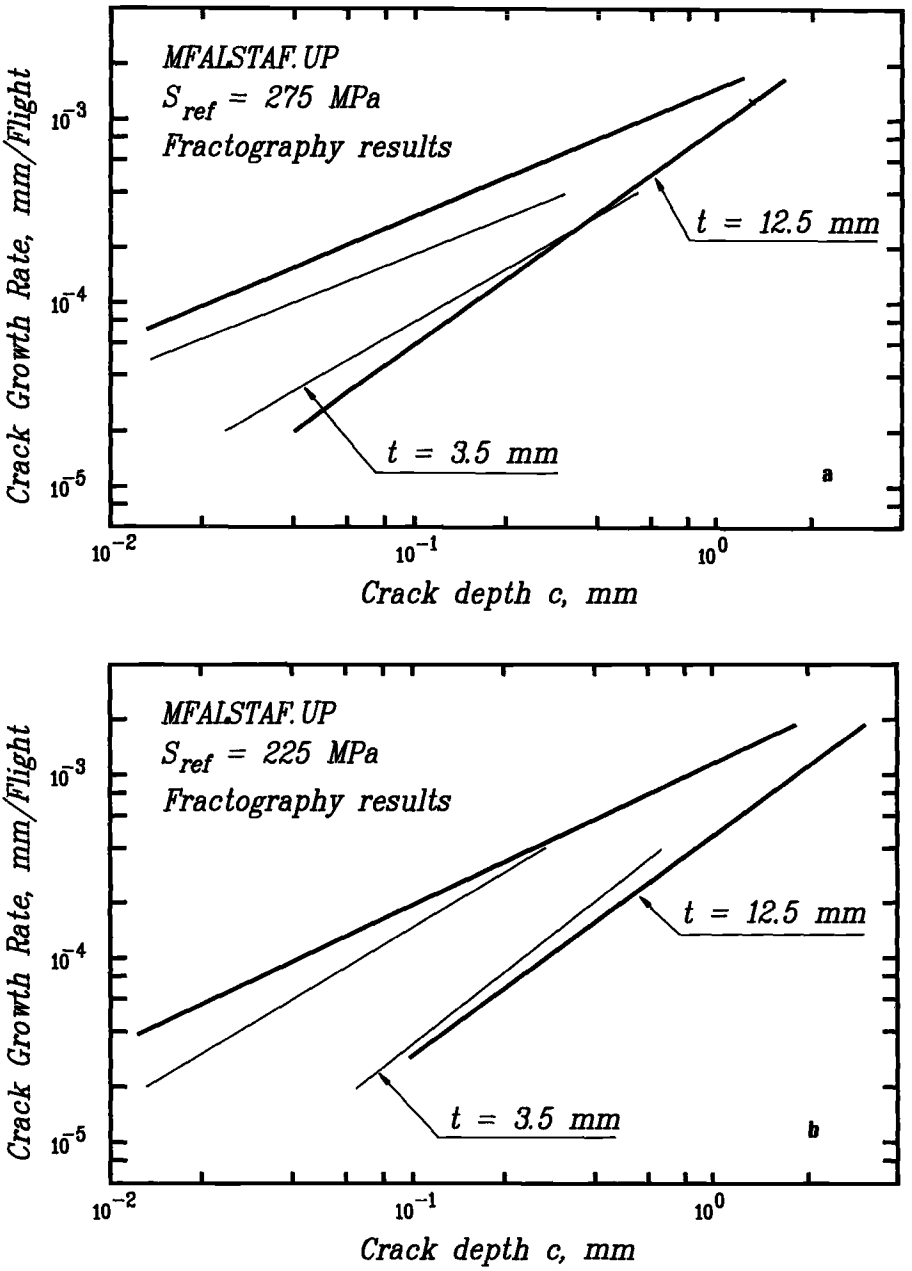

FIG. 12—*Thickness effect on crack growth rate envelope:* (a,b,c) *upper and lower bound growth rates at 275, 225, and 190 MPa, respectively, for* t = *12.5 and 3.5 mm;* (d) *effect of stress level on upper and lower bound growth rates. Data for* t = *12.5 mm.*

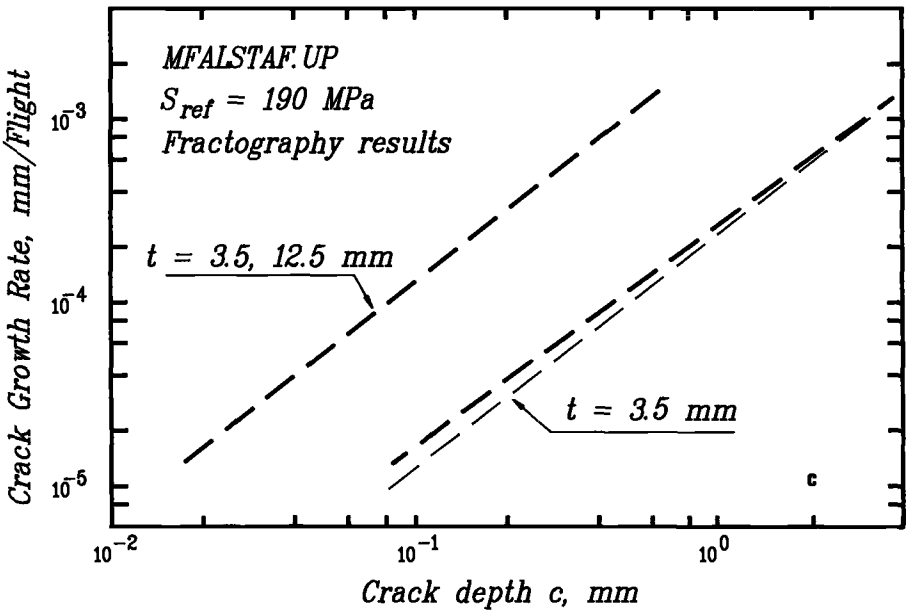

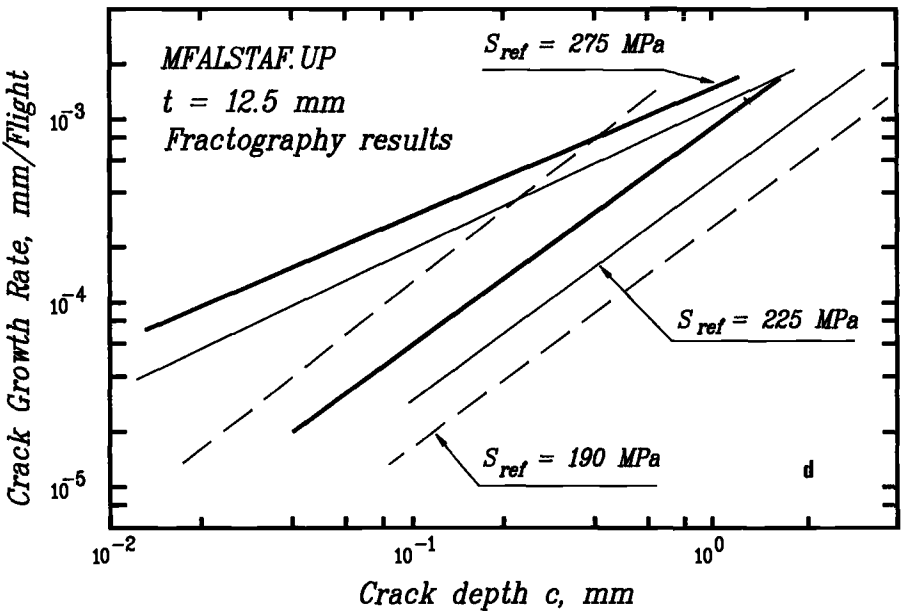

FIG. 12—*Continued.*

force and hysteretic crack closure behavior, whose significance also increases with notch root inelasticity.

The significance of the "short crack" effect under spectrum loading can be judged from a comparison of crack growth rates versus reference stress intensity for long and short cracks made in Fig. 13. The short crack effect appears to have substantial influence on crack growth rates and obviously cannot be disregarded. As the short crack extends, its growth rate falls into a single scatter band with data for other stress levels including the low elastic stress levels for long cracks. Considering that short cracks grow faster than long cracks at a given stress intensity, their consideration may be essential in design. MilSpec 83444A on airframe damage tolerance and durability call for consideration of an initial defect size of 125 μm for fracture-mechanics-based endurance estimates. The empirical evidence collected in the course of this study covers much smaller crack sizes and appears to confirm the possibility of performing the required analysis. At the same time, it may also be noted that analysis for life between inspections involves much larger crack sizes that may be handled adequately by long crack relationships. The exception may be the case of multiple crack formation, which is likely to require estimates of influence factor, F_i. While much work has been devoted to the development of analytical techniques to handle coplanar and non-coplanar multiple cracks of identical size [*12–14*], the interaction of cracks of unequal size appears to be of greater practical significance.

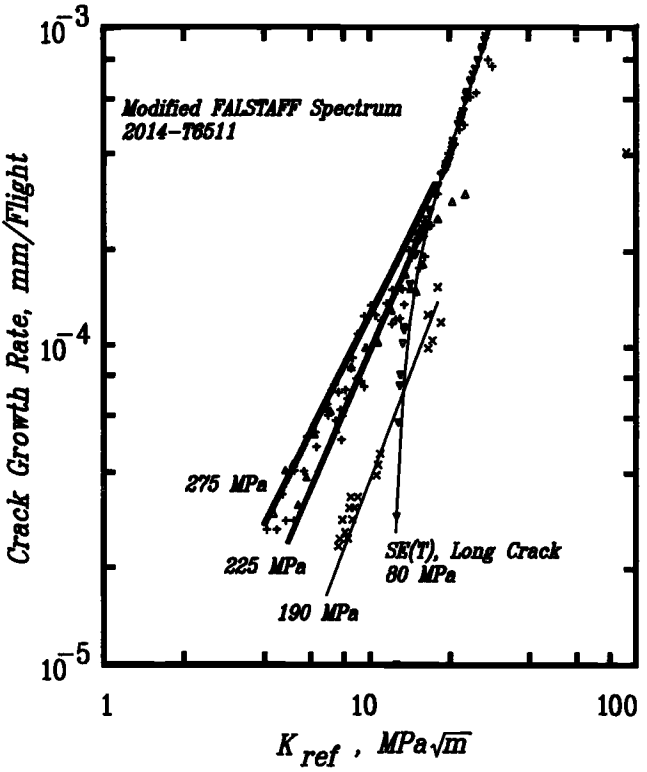

FIG. 13—*Comparison of crack growth rate trends for short and long cracks.*

Conclusions

The following conclusions may be drawn from the study of short crack formation and growth in notched coupons from L168 (2014-T6511) extruded bar stock under modified FALSTAFF and TWIST load spectra:

1. Fractographic measurements of crack growth rate show considerably less scatter than surface replica measurements of crack extension.
2. Artificially initiated notch root cracks grow at a rate slower than naturally initiated cracks of the same size. Growth rate appears to stabilize after some crack extension, whose magnitude may exceed the interval of short crack behavior. To be of practical value, experiments on short, part-through cracks must involve naturally initiating cracks.
3. The interaction of multiple cracks can be substantial if they are allowed to initiate naturally with inherent random variation in life to formation of a crack of particular size. This interaction is reflected in the accelerated growth of cracks that form later. The associated influence factor on stress intensity can exceed a factor of two, and the assumption of a through crack in design applications may therefore not always be conservative.
4. The density of naturally initiating multiple cracks depends on spectrum type and increases with stress level. It affects the envelope of crack growth rates for multiple cracks. However, the (lower bound) growth rate for the dominant crack appears to be thickness independent.
5. Available empirical evidence suggests that fracture mechanics can handle the growth of naturally initiating notch root small cracks.

Acknowledgment

This work was performed with support from the Aeronautical Development Agency and the Department of Science and Technology. Optical microscopy assistance of Ms. Tashina Kariappa and Mr. H. M. Girish of COMAT Services is gratefully acknowledged.

References

[1] Sunder, R., Prakash, R. V., and Mitchenko, E. I., "Calculation of Spectrum Load Notch Root Crack Growth Rate Under Elastic and Inelastic Conditions," *Advances in Fatigue Lifetime Predictive Techniques, Second Volume, ASTM STP 1211,* M. R. Mitchell and R. W. Landgraf, Eds., American Society for Testing and Materials, West Conshohocken, PA, 1993, pp. 30–44.

[2] Newman, J. C., Jr., Phillips, E. P., Swain, M. H., and Everett, R. A., Jr., "Fatigue Mechanics: An Assessment of a Unified Approach to Life Prediction," *Advances in Fatigue Lifetime Predictive Techniques, ASTM STP 1122,* M. R. Mitchell and R. W. Landgraf, Eds., American Society for Testing and Materials, West Conshohocken, PA, 1992, pp. 5–27.

[3] Sunder, R., Prakash, R. V., and Mitchenko, E. I., "Fractographic Study of Notch Fatigue Crack Closure and Growth Rates," *Fractography of Modern Engineering Materials: Composites and Metals, Second Volume, ASTM STP 1203,* J. E. Masters and L. N. Gilbertson, Eds., American Society for Testing and Materials, West Conshohocken, PA, 1993, pp. 113–131.

[4] Van Dijk, G. M. and de Jonge, J. B. in *Proceedings,* 8th ICAF Symposium, International Committee on Aeronautical Fatigue, Lausanne, Switzerland, 1975, pp. 3.61/1-3.61/39.

[5] Mitchenko, E. I., Prakash, R. V., and Sunder, R., "Fatigue Crack Growth Under Programmed Equivalent of FALSTAFF Spectrum," NAL Project Document PDST 9233, National Aeronautical Laboratory, Bangalore, August 1992 (to appear in *Fatigue and Fracture of Engineering Materials and Structures,* 1995).

[6] Schuetz, D. in *Proceedings,* Seventh ICAF Symposium, A. M. Stagg, Ed., International Committee on Aeronautical Fatigue, London, Vol. 2, 1973, pp. 3.4/1–3.4/34.

[7] Sunder, R., "Contribution of Individual Spectrum Load Cycles to Damage in Notch Root Crack Initiation, Short and Long Crack Growth," *Advances in Fatigue Lifetime Predictive Techniques:*

Second Volume, ASTM STP 1211, M. R. Mitchell and R. W. Landgraf, Eds., American Society for Testing and Materials, West Conshohocken, PA, 1993, pp. 19–29.

[*8*] Newman, J. C. and Edwards, P. R., "Short-Crack Growth Behaviour in an Aluminium Alloy—An AGARD Cooperative Test Programme," AGARD Report No. 732, 1988.

[*9*] Soboyejo, W. O., "On the Prediction of the Fatigue Propagation of Semi-Elliptical Defects," *Advances in Fatigue Lifetime Predictive Techniques, ASTM STP 1122,* M. R. Mitchell and R. W. Landgraf, Eds., American Society for Testing and Materials, West Conshohocken, PA, 1992, pp. 435–448.

[*10*] Forsyth, P. J. E., "The Determination of Fatigue Crack History from Fracture Surface Analysis," *Advances in Crack Length Measurement,* C. J. Beevers, Ed., Engineering Materials Advisory Services Ltd., West Midlands, UK, 1982, pp. 3–40.

[*11*] Sunder, R., Prakash, R. V., and Mitchenko, E. I., "Growth of Artificially and Naturally Initiating Notch Root Cracks Under FALSTAFF Spectrum Loading," NAL Project Document PDSN 9305, National Aerospace Laboratories, Bangalore, September 1993 (also, paper 10, AGARD Report 797, "An Assessment of Fatigue Damage and Crack Growth Prediction Techniques," AGARD, Paris, March 1994).

[*12*] Isida, M., "Analysis of Stress Intensity Factors for Plates Containing Random Array of Cracks," *Bulletin of the Society of Mechanical Engineers,* Vol. 13, 1970, pp. 635–642.

[*13*] Chang, R., "On Crack-Crack Interaction and Coalescence in Fatigue," *Engineering Fracture Mechanics,* Vol. 16, No. 5, 1982, pp. 683–693.

[*14*] Soboyejo, A. F., Thakker, A. B., and Tritsch, D. E., "An Experimental and Numerical Investigation of the Growth and Coalescence of Multiple Cracks at Notches," *Fracture Mechanics: Seventeenth Volume, ASTM STP 905,* J. H. Underwood, R. Chait, C. W. Smith, D. P. Wilhem, W. A. Andrews, and J. C. Newman, Eds., American Society for Testing and Materials, West Conshohocken, PA, 1986, pp. 239–252.

S. Y. Zamrik[1] *and R. E. Ryan*[1]

Fatigue Crack Propagation in IN-718 Material under Biaxial Stress Bending

REFERENCE: Zamrik, S. Y. and Ryan, R. E., **"Fatigue Crack Propagation in IN-718 Material under Biaxial Stress Bending,"** *Advances in Fatigue Lifetime Predictive Techniques: 3rd Volume, ASTM STP 1292,* M. R. Mitchell and R. W. Landgraf, Eds., American Society for Testing and Materials, 1996, pp. 161–187.

ABSTRACT: The effect of biaxial stress cycling on the crack growth process in IN-718 plate specimens was investigated using a semielliptical surface flaw as a crack starter. The method of anticlastic bending was used to generate the biaxial stress field. This bending method generates two bending stresses: a tensile stress normal to the crack surface and a compressive stress transverse to the tensile stress at the tip of the crack. In a biaxial stress field, the linear elastic fracture mechanics (LEFM) theory predicts that the stress parallel to the crack direction has no effect on crack growth rate. However, in the past two decades, experimental studies have shown that a stress parallel (transverse) to the crack tip influences crack growth rate. In this investigation, the effect of biaxial stress ratio ($\beta = -\sigma_2/\sigma_1$) of -1 on fatigue crack growth is presented. At a constant cyclic load, a crack growth transition from Mode I to Mode II was observed to take place when ΔK reached the value of 17.5 ksi $\sqrt{\text{in.}}$ (19.2 MPa $\sqrt{\text{m}}$). Also, an acceleration in the fatigue crack growth rate was observed due to the compressive transverse stress.

KEYWORDS: fatigue, crack growth, anticlastic bending, biaxial stress cycling

Nomenclature

A, B_i	Material constants
a	Fatigue crack depth
b	One-half diagonal length of plate specimen
c	Fatigue crack half length
D	Plate stiffness
E	Young's modulus of elasticity
F	Total load on plate under anticlastic bending
F_0	Load required to initiate yielding
I	Moment of inertia
K	Stress intensity factor
ΔK	Stress intensity factor range
L	Length of section taken through plate specimen parallel to diagonal
M_L	Bending moment per unit length
M_x, M_y	Bending moment per unit length about referenced axes
N	Number of cycles
n	Number of test data points
P	Load applied at each corner of plate under anticlastic bending
p, q, m	Numerical exponents

[1]Department of Engineering Science and Mechanics, The Pennsylvania State University, University Park, PA 16802.

Q Flaw shape parameter
t Plate thickness
w Displacement of neutral plane of plate from unloaded middle plane
x, y, z Cartesian coordinates
α Semielliptical surface crack aspect ratio: crack depth divided by crack length
γ Angle measured from minor axis of semielliptical surface crack in the plane of the crack
δ Maximum displacement between adjacent corners of the plate perpendicular to the plane of the plane of the plate
δ_0 Deflection required to initiate yielding
ϵ Strain
ϵ_0 Tensile yield strain
η Dimensionless magnification factor which accounts for crack geometry and type of loading on stress intensity factor
μ Poisson's ratio
σ Normal stress
σ_e Effective stress
σ_0 Tensile yield stress
σ_x, σ_y Stresses along reference axis
σ_{max} Maximum stress at crack tip
σ_1, σ_2 Principal stresses
Φ Elliptical integral of the second kind

A number of experimental techniques are used to generate data under multiaxial stress cycling: combinations of axial load and torsion, reversed bending of wide plate specimens, and pressurized thin-walled tubes. From an academic point of view, combined axial and torsion fatigue loading of thin-walled tubes has the advantage since the occurrence of stress and strain gradients are practically eliminated. However, from the standpoint of simplicity and economy, reversed bending of plate specimens seems to be a more practical method to use in biaxial fatigue experimental studies. In particular, the reverse bending technique requires less complicated test equipment because good alignment of the test apparatus is not as critical as for axial-torsion tests. Also, since fatigue cracks are generally initiated on the surface of the plate specimen, they can be easily detected and observed as the cracks grow.

Several types of reversed plate bending methods have been developed, including cantilever bending of wide specimens [*1*], pulsating hydrostatic pressure applied to the surface of the plate [*2*], and anticlastic bending [*3*]. Anticlastic bending is a case of pure biaxial bending of a plate in which two principal curvatures are opposite in signs. The state of stress on the surface of the specimen is biaxial tension-compression. When a simple beam theory is used as a first approximation [*4*] of anticlastic bending, it is found that the square plate constitutes beams of uniform strength along its two diagonals, giving a distribution of uniform stress and strain over all the specimen surface. Thus, any effect of an area or volume of highly stressed or strained material in the specimen is eliminated. This feature is the main advantage of this type of reversed bending testing over others and was the basis for developing the anticlastic testing procedure for fatigue as well as for crack propagation studies.

For crack propagation studies, a semielliptical crack starter slot was induced at the center of the plate. Experience gained from service failures indicates that a semielliptical-shaped crack with a length-to-depth ratio of 3 to 5 reasonably characterizes the type of flaw found in failed components.

The material selected for crack growth analysis was IN-718, a turbine blade material where biaxial fatigue failures have been found to occur in actual application. Turbine blades in gas turbines experience a tension-compression biaxial stress field at the blade root due to the action of high bending, shear, and centrifugal forces. IN-718 is a high-strength nickel base superalloy used primarily in a high-temperature environment.

Analysis of Anticlastic Bending Method

In the experimental program, theoretical relationships between the parameters of load, deflection, stress, and strain were needed to assess crack growth. A schematic of a rhombic plate under anticlastic bending is shown in Fig. 1. The middle plane of the plate, before bending, is taken as the x-y neutral plane. The deflection of the plate surface, w, is measured from the middle plane. The displacement, δ, is designated as maximum displacement between adjacent corners of the plate perpendicular to the plane of the plate. The bending moments, M_x and M_y, are defined as moments per unit length. For the special case of bending a square plate, the moments about the principal axes are equal and opposite ($M_x = M_y = M_L$), resulting in the following expression for deflection, w

$$w(x,y) = -M_L(x^2 - y^2)/2D(1 - \mu) \tag{1}$$

where D and μ are the plate stiffness and Poisson's ratio, respectively, and M_L, shown in Fig. 2, is transmitted along section L, which is cut at a distance x from the diagonal BC and can be expressed in terms of the applied load as

$$M_L = P(b - x)/L \tag{2}$$

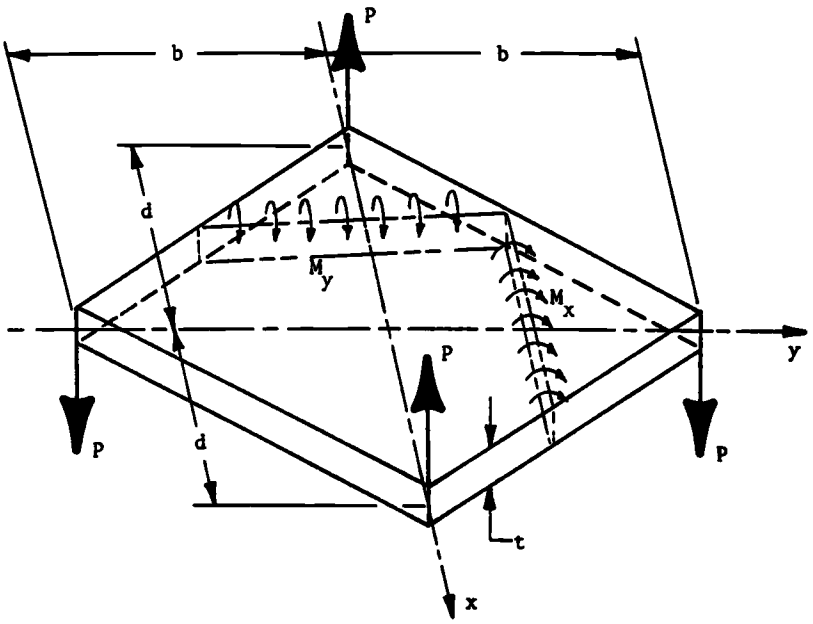

FIG. 1—*Rhombic plate under anticlastic bending.*

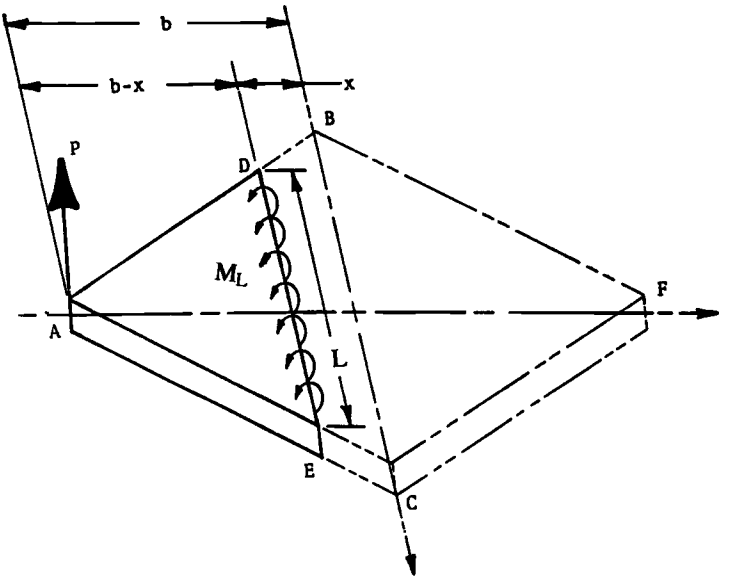

FIG. 2—*Square plate under anticlastic bending. Moment* M_L *is generated by concentrated loads at corners.*

where P is the applied load at each corner of the square plate, and b is one half of the diagonal length of the plate. Since the diagonals are equal, using similar triangles a relation between x, b, and L is obtained as

$$(b - x)/L = b/2b = \tfrac{1}{2} \tag{3}$$

$$L = 2(b - x) \tag{4}$$

Therefore, the moment per unit length at any section parallel to diagonal BC in terms of the external applied load, F, is

$$M_L = F/4 \tag{5}$$

The total load of the plate F is used since this is the quantity measured. By symmetry, Eq 5 is also the moment at any section parallel to diagonal AF.

The deflection at any point of the plate surface can then be expressed in terms of applied load F as

$$w(x,y) = -F(x^2 - y^2)/8\,D(1 - \mu) \tag{6}$$

The displacement, δ, between the adjacent corners of the square plate is equal to twice the maximum deflection, w

$$\delta = 2w_{\max} = Fb^2/4D(1 - \mu) \tag{7}$$

or

$$\delta = 3(1 + \mu)b^2F/Et^3 \tag{8}$$

The strain across the surface of the plate for a strain ratio of $\epsilon_x/\epsilon_y = -1$ can be expressed as

$$\epsilon = (1 + \mu)\sigma/E = 3(1 + \mu)F/2Et^2 \tag{9}$$

resulting in

$$\epsilon = \delta t/2b^2 \tag{10}$$

The von Mises yield condition was used as the basis for establishing the maximum allowable load, given as

$$\sigma_x^2 + \sigma_y^2 - \sigma_x\sigma_y = \sigma_0^2 \tag{11}$$

where σ_0 is the yield stress. For anticlastic bending of a square plate $\sigma_x = \sigma_y$ results in

$$\sigma_x = \sigma_0/\sqrt{3} \tag{12}$$

or in terms of the maximum allowable load, F_0

$$F_0 = 2t^2\sigma_0/3\sqrt{3} \tag{13}$$

Theoretical values of critical deflection and strain can be obtained as

$$\delta_0 = 2(1 + \mu)b^2\sigma_0/\sqrt{3}Et \tag{14}$$

$$\epsilon_0 = 3(1 + \mu)\sigma_0/2\sqrt{3}E \tag{15}$$

Stress Intensity Factor for Surface Flaw in Bending

The semielliptical surface flaw has long been recognized as a close approximation to an actual flaw that may initiate the fatigue and fracture process. The stress intensity factor expressed as

$$K = \eta\sigma\sqrt{\frac{\pi a}{Q}} \tag{16}$$

will be used for the biaxial fatigue crack growth where η is a coefficient that reflects the correction factors required to account for crack geometry and type of loading on the surface flaw. Q, the flaw shape parameter, is defined as

$$Q = \Phi^2 - 0.212(\sigma/\sigma_0)^2 \tag{17}$$

and the elliptical integral, Φ, is defined by

$$\Phi = \int_0^{\pi/2}\left[1 - \left(\frac{c^2 - a^2}{c^2}\right)\sin^2\phi\right]^{1/2} d\phi \tag{18}$$

The dependence of the elliptical integral on the crack geometry is shown in Fig. 3. The stress parameter in Eq 16 was controlled in the fatigue test and maintained at a constant

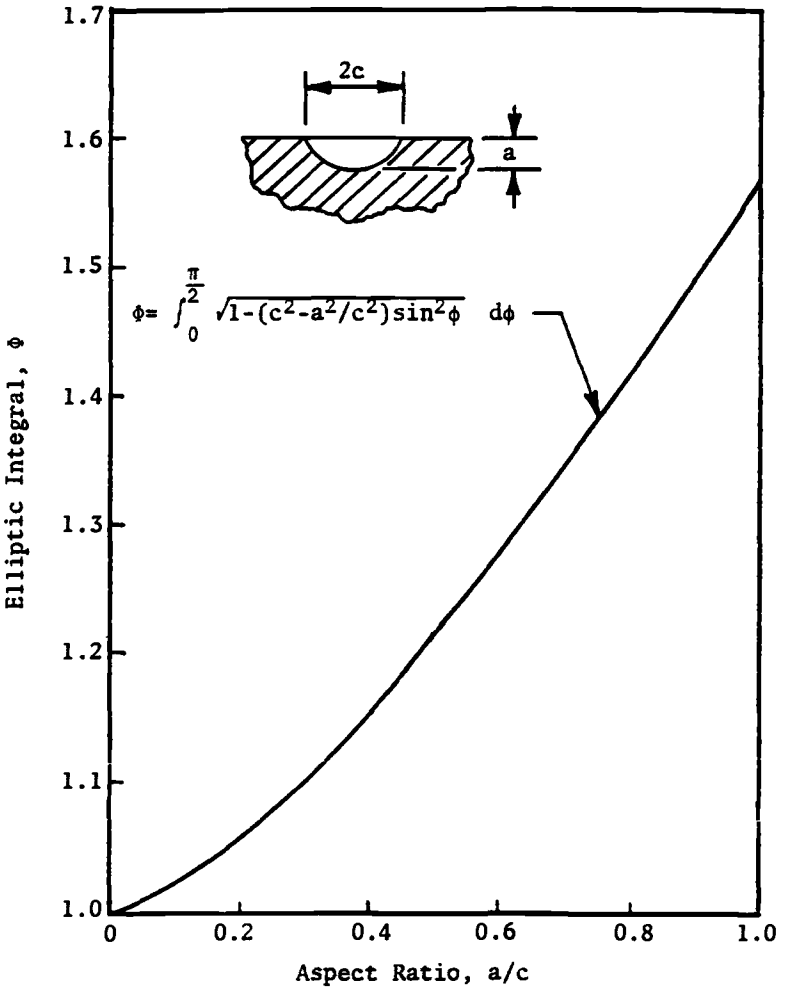

FIG. 3—*Elliptical integral of the second kind as a function of aspect ratio.*

value. The correction factor, Q, is expressed as a function of the surface crack aspect ratio of $a/2c$, the material yield stress and the outer fiber bending stress, all of which are known quantities. However, the coefficient η was determined from Grandt and Sinclair's results [5] on surface cracks in bending for various aspect ratios and crack depth-to-plate thickness ratios (a/t) for positions on both the major and minor axes of the semielliptical surface flaw. Figure 4, used in the experimental study, is an illustrative example for η at the tip of a surface crack with an aspect ratio of $a/2c = 0.3$.

Assuming a constant aspect ratio throughout the fatigue test, K (used in Eq 16) was related to the crack length as

$$K = \eta\sigma\sqrt{\frac{\pi(2c)\alpha}{Q}} \tag{19}$$

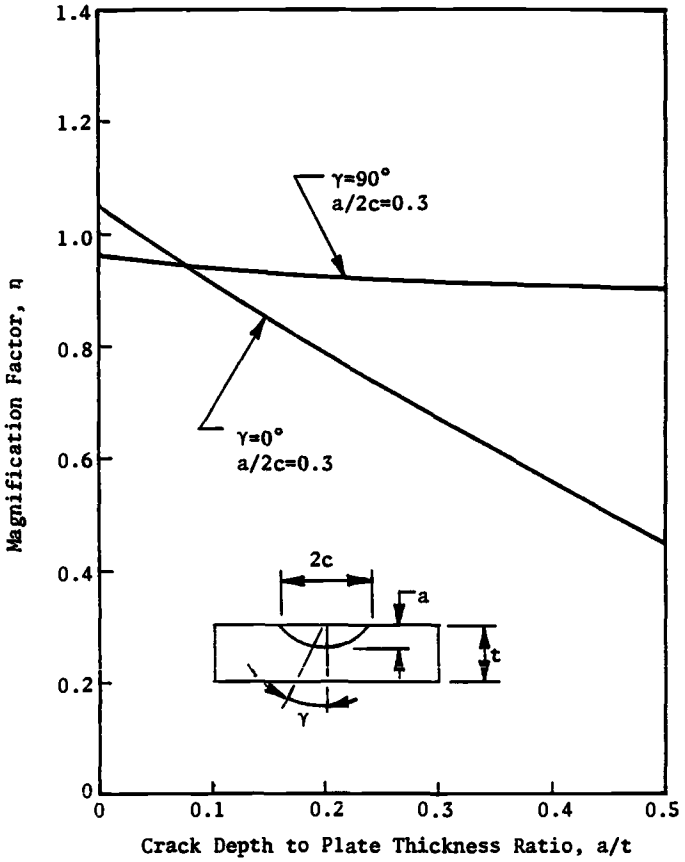

FIG. 4—*Correlation of dimensionless magnification factors for semielliptical surface flaws in bending* [5].

where $\alpha = a/2c_0$ is constant. This assumption is consistent with the Grandt and Sinclair findings that, under load control tests, although crack growth into the plate lagged behind the growth along the plate surface, the difference in rates was only on the order of 2 to 3%. Since no practical method of detecting fatigue crack growth through the thickness of the biaxial plate specimens exists, results rely on surface crack measurements that are easily obtained.

Test Procedure

Anticlastic bending method [7] was used in the experimental study of biaxial fatigue crack propagation. When a rhombic plate is subjected to this type of bending, the diagonals of the plate are the principal curvatures that are equal for a square plate but with opposite signs. The resulting elastic stress and strain distributions are uniform all across the plate surface with a principal stress and principal strain ratio of $1: -1$.

The testing program was divided into two series. The first series was performed to determine strain and loading data for various values of static displacement. This series was necessary to verify the theoretical analysis of a rhombic plate under anticlastic bending, to

show the validity of a constant biaxial strain distribution across the surface of the plate, and to provide reference data to show any variation in the load-deflection relationship during the cyclic test. The second series of testing determined the fatigue crack propagation characteristics of IN-718 plate specimens in a biaxial stress field. Crack growth data were obtained from the specimen that had a small slot machined in the surface at the center of one side of the specimen. The slot represented the initial crack size in the plate, and the total crack length was measured optically as the fatigue crack propagated from each side of the slot under cyclic loading. All tests were conducted at room temperature.

Specimen Configuration and Apparatus

The material used was IN-718 rolled plate with a nominal thickness of 0.25 in. (6.35 mm). Mechanical properties are presented in Table 1. All of the plate specimens tested were square shaped, having diagonal lengths of 3.0 in. (76.2 mm) as shown in Fig. 5. The specimen diagonals were oriented longitudinally and transversely to the rolling direction. The plate specimen corners were widened and extended to provide for the attachment of a 0.5-in. (12.7-mm)-diameter cylindrical roller at each corner. Ideal anticlastic bending is done by applying concentrated forces at the four corners, perpendicular to the plane of the plate. Rollers were required so that the forces could be applied to the plate without causing unnecessary stress concentration and to avoid applying a mean strain in the specimen (which could be caused by a more rigid connection between the plate and the loading mechanism).

The surface flaw (slot) was induced into the plate surface by an electro discharge machining (EDM) process, sometimes referred to as "electrospark" machining, that removes metal through the action of high-energy electric sparks upon the surface of the workpiece). The semielliptical EDM slot had dimensions 0.017 in. (0.432 mm) deep by 0.0528 in. (1.341 mm) long by 0.004 in. (0.102 mm) wide with the plane of the slot parallel to the plate rolling direction. The specimen surface was polished to a mirror luster image so that fatigue cracks would be distinguished easily when viewed under a microscope. All polishing strokes were made perpendicular to the slot (and plate rolling direction).

Measuring Instruments

Measurements of all fatigue cracks were done optically. The length of the fatigue crack was measured by a linear optical comparator. A high-intensity lamp was used in conjunction with the comparator to illuminate the specimen surface. The lamp was equipped with a filter and an adjustable lens that could focus the filtered light at any desired focal distance. The lamp was positioned so that the angle of incidence of the light beam on the crack was approximately 60°. Another microscope was also used when measurements of the propagating crack were required in an x-y coordinate frame of reference.

TABLE 1—*Mechanical properties of IN 718.*

	IN 718
Yield strength (0.02%)	132 ksi (910 MPa)
Yield strength (0.2%)	145 ksi (1000 MPa)
Ultimate stress	187 ksi (1290 MPa)
Modulus of elasticity	30.4×10^3 ksi (210 GPa)
Poisson's ratio, μ	0.29
Tensile elongation	20%

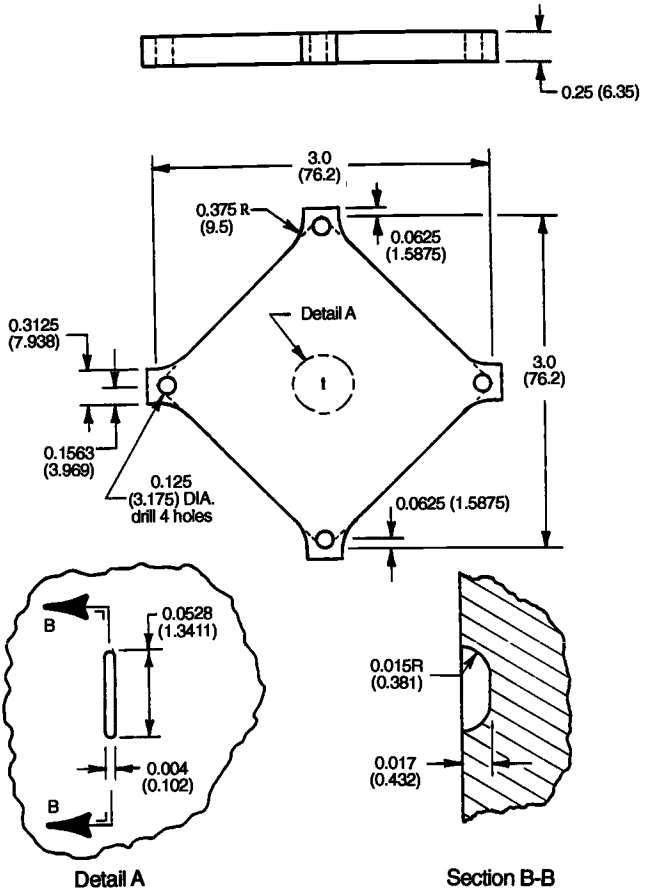

FIG. 5—*Dimensions of a square plate biaxial fatigue specimen, in. (mm).*

Calibration Tests

Calibration tests were carried out to establish the null (zero) position of the specimen loading fixture and to obtain specimen load-deflection calibration, specimen load-strain calibration, and specimen deflection-strain calibration.

A deflection-controlled test system was employed. The controlling parameter in the crack propagation tests was the stress intensity factor at the root of the EDM slot. Since the stress intensity factor was load dependent, the relation between load and deflection was required so the stress intensity factor could be determined for any corresponding loading mechanism deflection setting. The specimen loading fixture was placed in a monotonic compression machine, and, by applying incremental load values to the notched specimen, the corresponding deflection was recorded. The resulting load-deflection curve is shown in Fig. 6. The linear relationship between the applied load and resulting deflection was fitted to

$$F = 52\,174\,\delta$$

where F is measured in pounds and δ in inches (N, mm).

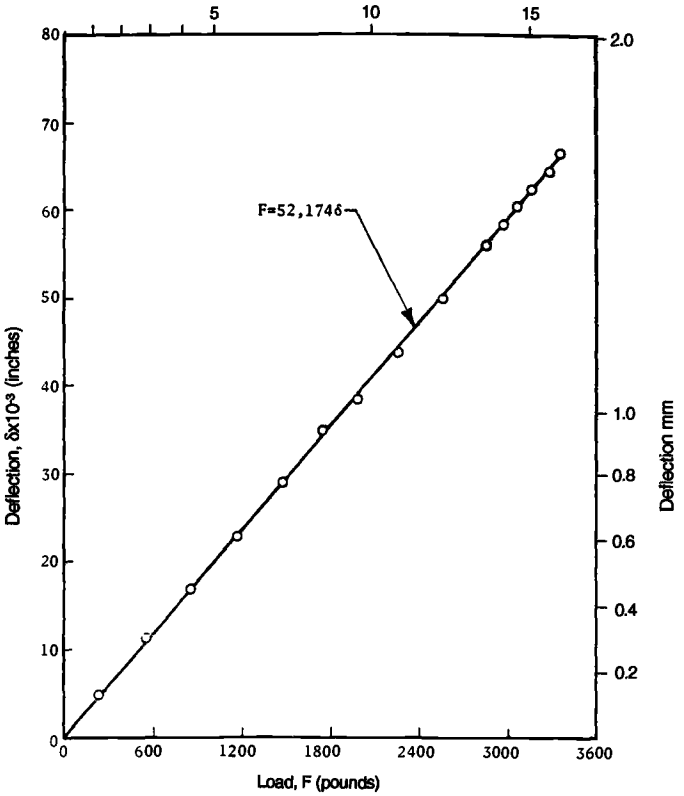

FIG. 6—*Load versus deflection for notched fatigue specimen.*

From this curve, the initial stress intensity factor for the cyclic tests could be determined for any deflection by finding the corresponding load and using the relationship between load and linear elastic stress intensity factor for the particular slot and stress field.

The relationship between the stress intensity factor and load can be found by using the bending stress in the rhombic plate in terms of the applied load F and plate thickness t as

$$\sigma = 3F/2t^2 \tag{20}$$

Substituting this expression into Q and the elliptical integral relations

$$K = \frac{1.5\eta F}{t^2}\left[\frac{\pi(2c)\alpha}{\Phi^2 - \left(\frac{0.477F^2}{\sigma_0^2 t^4}\right)}\right]^{1/2} \tag{21}$$

Using the EDM slot dimensions, and with the aspect ratio as $a/2c_0 = 0.321$, the corresponding Φ from Fig. 3 is 1.31. The dimensionless magnification factor, η, is obtained from Fig. 4 as $\eta = 0.95$. Therefore, K is calculated as

$$K = 22.8F\left[\frac{0.0534}{1.716 - 5.81 \times 10^{-9}F^2}\right]^{1/2} \tag{22}$$

The stress intensity factor can also be expressed in terms of the measured experimental deflection from the load-deflection relation

$$K = 1.19 \times 10^6 \delta \left[\frac{0.0534}{1.716 - 15.8\delta^2} \right]^{1/2} \tag{23}$$

A plot of the theoretical stress intensity factor versus deflection is shown in Fig. 7.

The relation between both the load and deflection to strain on the specimen surface was determined so that during the test program, when either of these parameters were measured, the resulting applied strain would be known. It was important to establish the upper limits of both the applied load and resulting deflection as the applied strain approached its yield value. Strain measurements were obtained in the load-strain and deflection-strain calibration test by using foil strain gage rosettes mounted on the surface of the specimens at the center

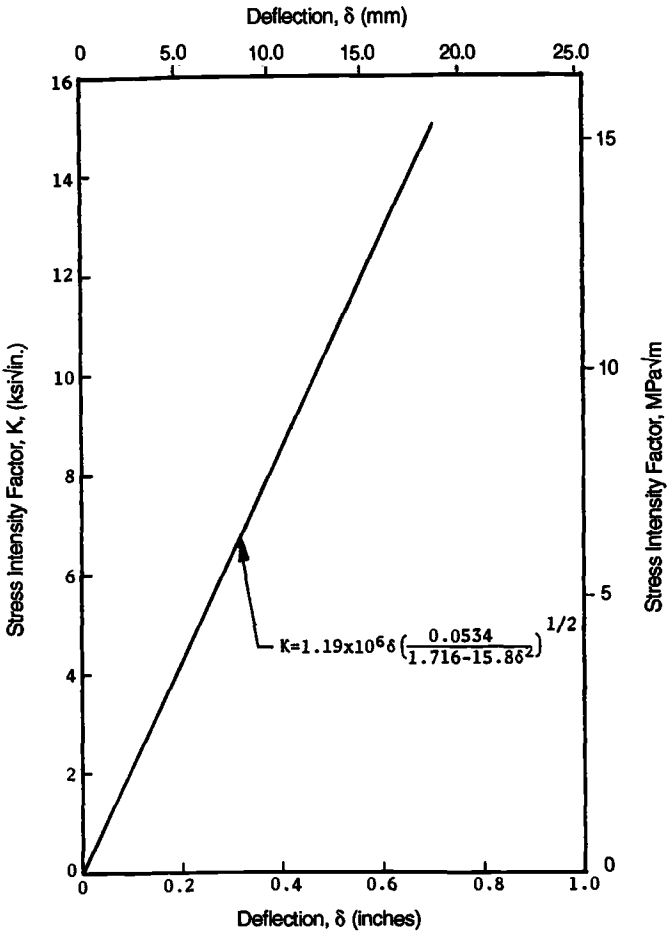

FIG. 7—*Stress intensity at tip of EDM slot versus plate deflection.*

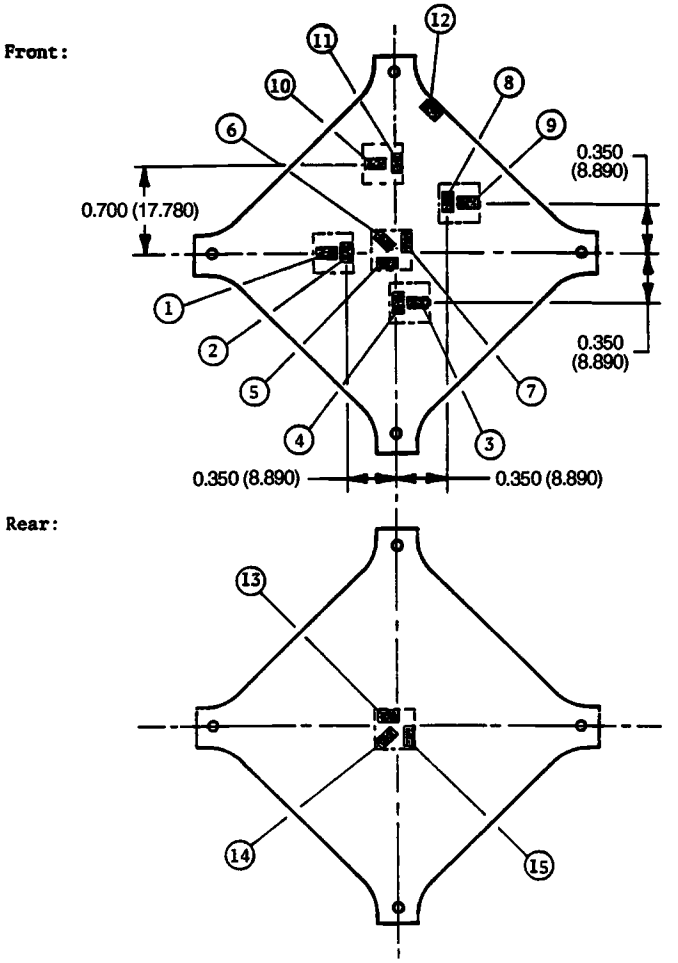

FIG. 8—*Location of strain gages mounted on specimen used for static deflection tests, in. (mm).*

of each plate. Two of the gage elements were aligned with the diagonals and one oriented 45° to the diagonals, as shown in Fig. 8. Calibration curves are shown in Figs. 9 and 10, respectively. The calibration tests verified that the strains along the specimen diagonals were nearly equal in magnitude but opposite in sign, and that these were the principal strains since the strains at a 45° angle to the diagonal were nearly zero. Strain distribution across specimen surface versus plate deflection is shown in Fig. 11. The strains in directions parallel to the plate diagonals at various points across the surface were approximately constant. The strain readings were quite close to one another at low deflections with increasing variance as the deflection was increased. The maximum discrepancy occurred at the largest deflection and was less than 8%. Based on data shown in Fig. 11, it is reasonable to assume that uniform distribution of stresses and strains exists across the surface of the plate. Figure 12 shows the experimental values for deflection versus strain using Eq 10.

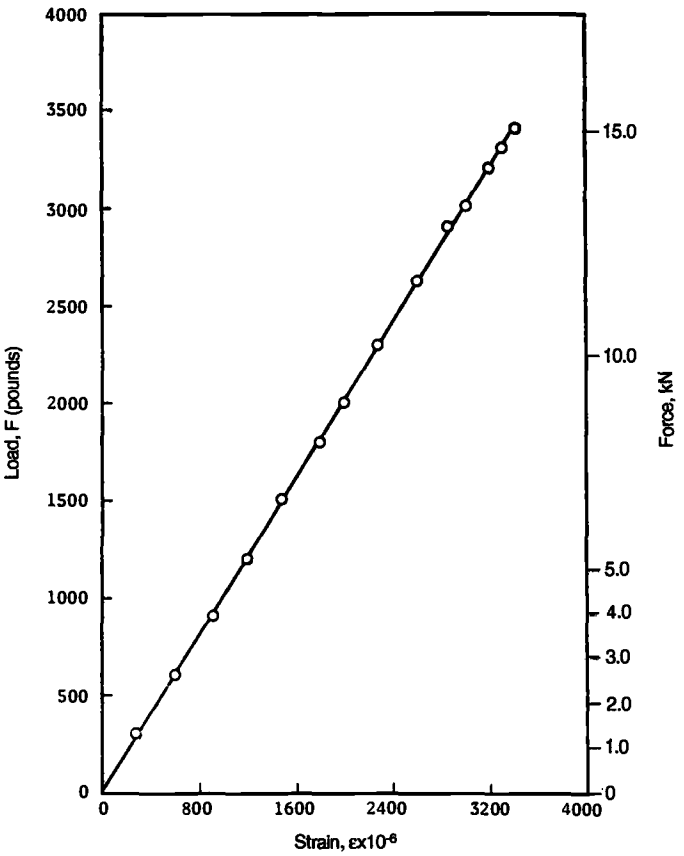

FIG. 9—*Load versus strain for notched fatigue specimen.*

A final series of static tests were made to determine the effect of the EDM slot and fatigue crack on the load-deflection relationship of the specimen. Static load and deflection data were obtained both prior to and at intermittent intervals during cyclic tests. The results are shown in Figs. 13, 14, and 15. The data plotted in Fig. 13 were taken from the initial loading of two square IN-718 plate specimens of the same size and thickness with one plate having the EDM slot. The notched specimen deflected more than the solid specimen under the same load. Also, Fig. 14 shows the load deflection characteristics of the notch specimen as a function of cyclic life. Once the fatigue crack began to propagate from the ends of the EDM slot, a static load-deflection test was run about every 30 000 cycles. This set of curves shows that at a constant deflection the load-carrying capacity of the plate was reduced as the crack increased in size. For this reason, the deflection amplitude was continually increased during the fatigue test so that the load on the specimen could be considered constant. It was necessary to compensate for the permanent deformation that occurred with increasing crack length and cyclic life. Figure 15 shows the amount of permanent deformation experienced by the specimen as a function of cyclic life. Intermittent adjustments were made by using the calibration tests to ensure constant load throughout the fatigue tests.

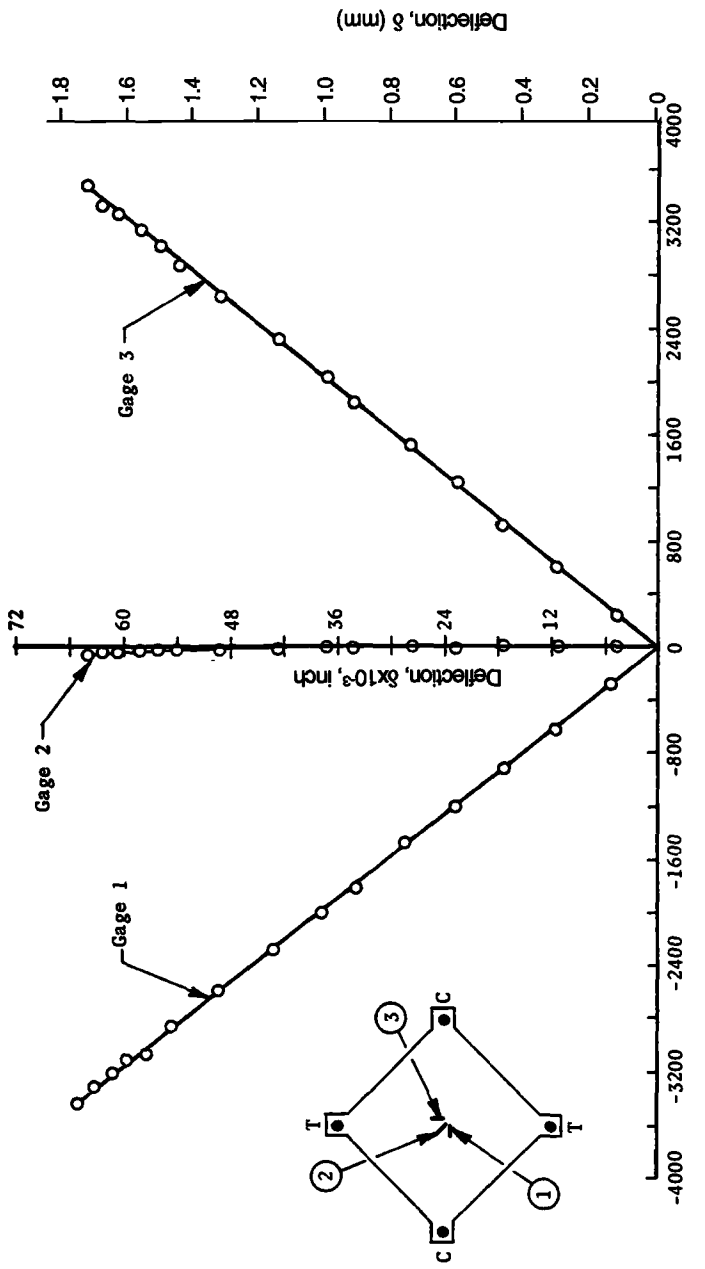

FIG. 10—*Deflection versus strain for notched fatigue specimen.*

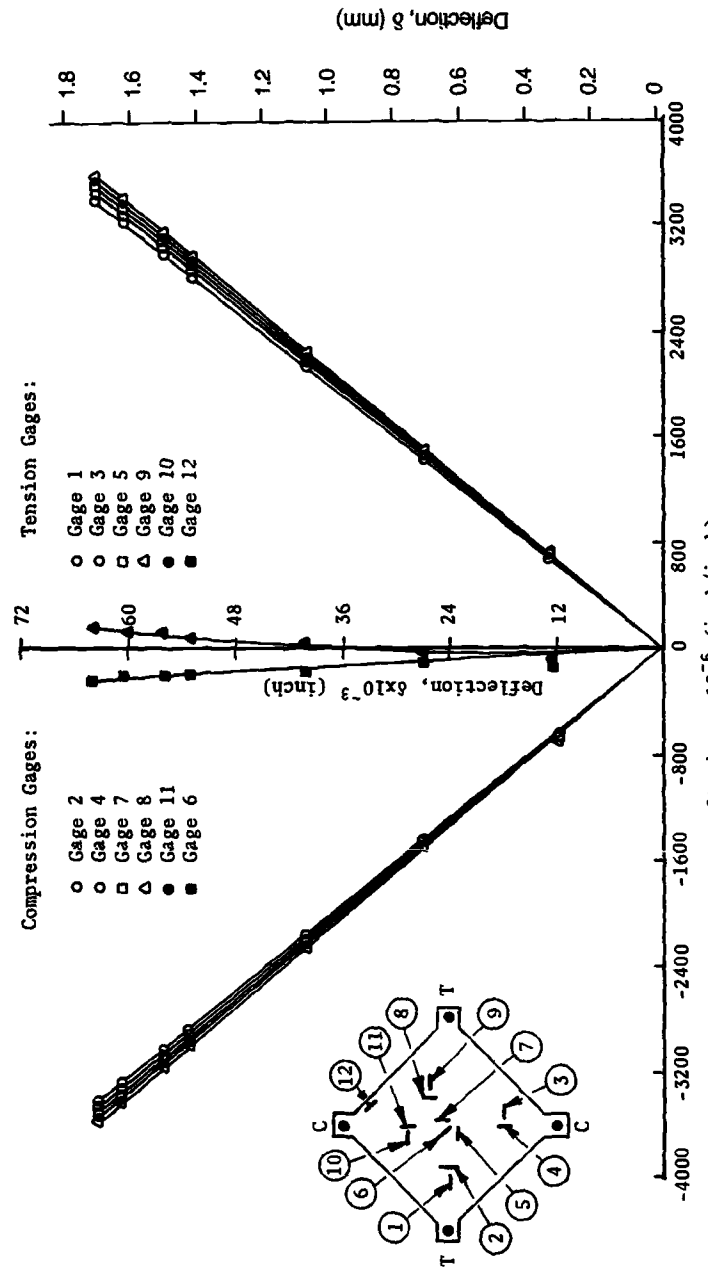

FIG. 11—*Strain distribution across specimen surface versus plate deflection.*

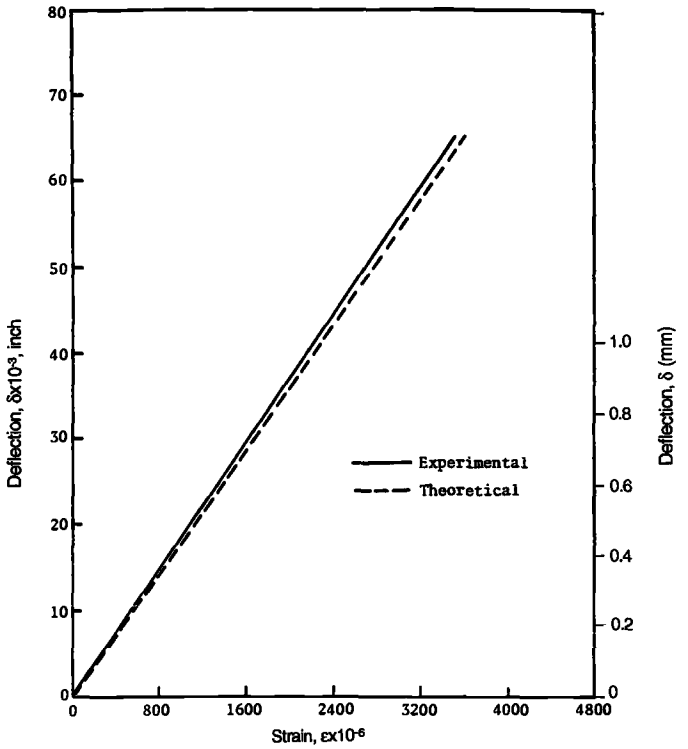

FIG. 12—*Comparison of experimental and theoretical results (deflection versus strain).*

Test Results and Discussion

Crack Propagation Tests

The general objective of this portion of the test program was to observe the fatigue crack growth characteristics in a biaxial stress field and to correlate the growth rate to an analytically derived stress field parameter in terms of K by using the general form of

$$dc/dN = B_0(\Delta K)^m \tag{24}$$

The initial load applied to the specimen was chosen to be 3000 lbs (13 350 N). This value was an estimate of the load required to be above the threshold value needed to initiate crack growth from the starter slot and yet low enough to be below the yield load. The threshold value was unknown, but the upper limit was determined from Eq 13, expressed as

$$F_0 = 2\sigma_0 t^2/3\sqrt{3} = 2(145\,000)(0.25)^2/(3\sqrt{3}) = 3490\text{ lb}\,(15\,500\text{ N})$$

Knowing the applied load, the initial stress intensity factor can be calculated using Eq 22, resulting in

$$K = 12.25\text{ ksi}\sqrt{\text{in.}}(13.47\text{ MPa}\sqrt{\text{m}})$$

The initial load was maintained for the first 41 500 cycles of the test. However, when no fatigue crack was observed at either tip of the EDM slot, the load was increased to 3300 lb

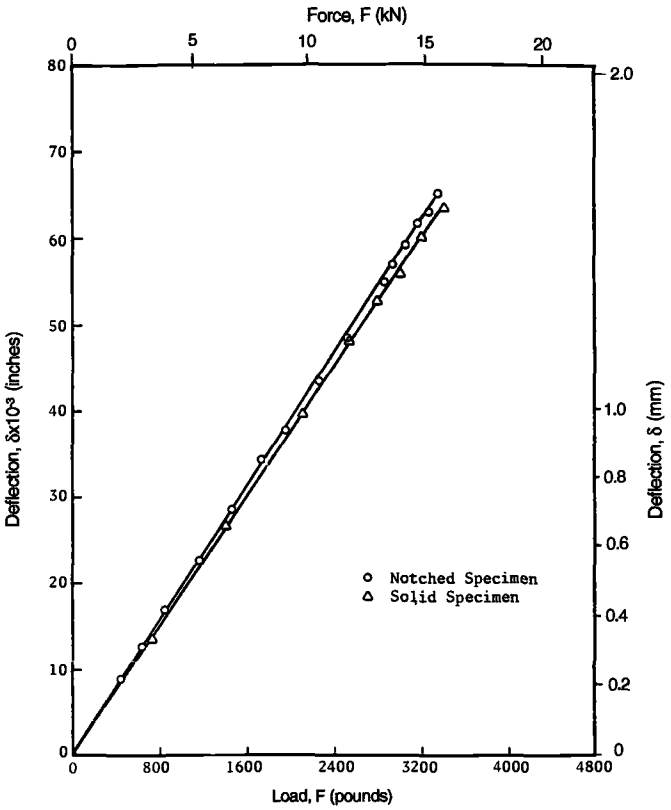

FIG. 13—*Effect of EDM slot on load-deflection relationship of plate specimen.*

(14 700 N). The outer fiber stress and stress intensity factor calculated for the increased load were 79.2 ksi (550 MPa) and 13.5 ksi$\sqrt{\text{in.}}$ (14.9 MPa $\sqrt{\text{m}}$), respectively. The testing was resumed, and after an additional 21 100 cycles were applied, a 0.006-in. (0.152 mm) crack was observed at each tip of the EDM slot. The crack propagated in the plane of the EDM slot, which was perpendicular to the applied tensile stress. The load was maintained at 3300 lb (14 700 N) from 41 500 cycles until testing was terminated at 206 000 cycles. At 86 000 cycles the fatigue crack propagating from one end of the slot began to deviate from plane growth, and at 92 000 cycles the crack end of the slot began to deviate from plane growth, and at 92 000 cycles the crack propagating from the opposite end began to grow out of the plane of the slot in a similar manner. When it was determined that this type of growth was steady state and not just a small excursion from plane growth, the method of measurement was revised.

Rather than measuring the total length of the curvilinear crack, the location of each crack tip was recorded in an x-y coordinate frame of reference. The initial fatigue crack is shown in Fig. 16. Figure 17 shows the history of the fatigue crack propagation by showing the positions of the advancing crack fronts identified with their corresponding number of cycles. Also shown is the final crack configuration at the time the fatigue test was stopped at 206 000 cycles. It should be noted that crack growth rates are based on changes in the total crack lengths. Since the same conditions should exist at both crack tips, it would be expected that the cracks propagate in a similar manner. However, this was not necessarily

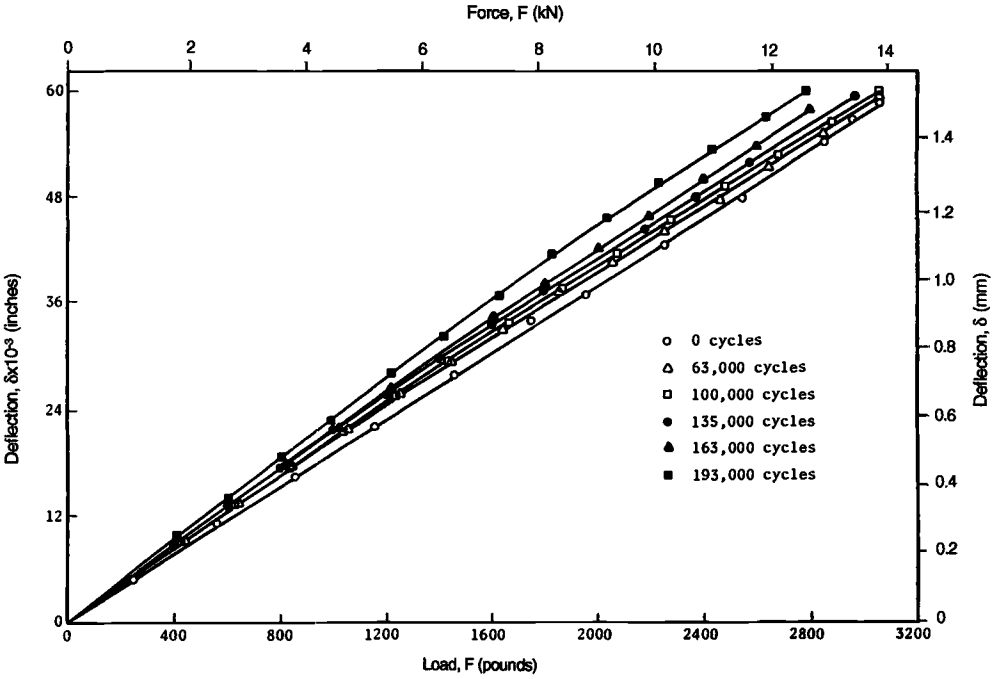

FIG. 14—*Load versus deflection for plate specimen as a function of cyclic life.*

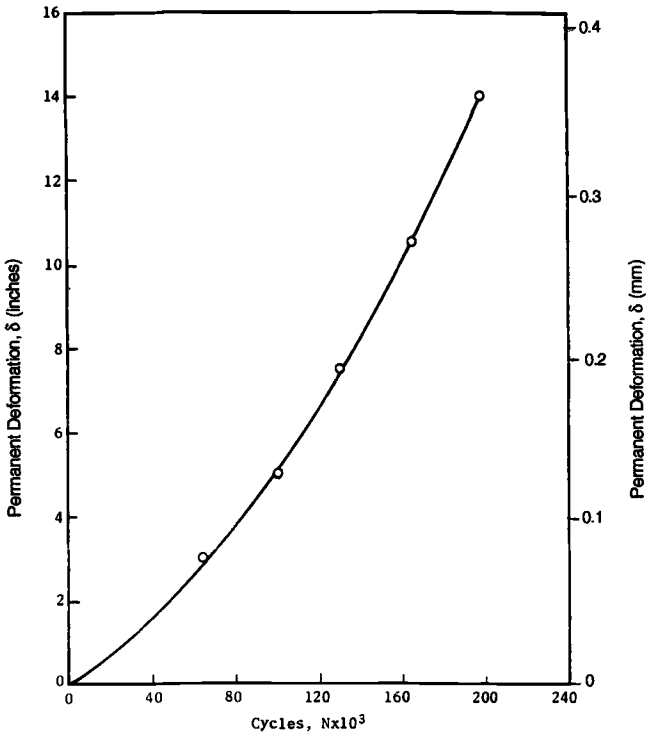

FIG. 15—*Permanent deformation of fatigue specimen versus number of cycles.*

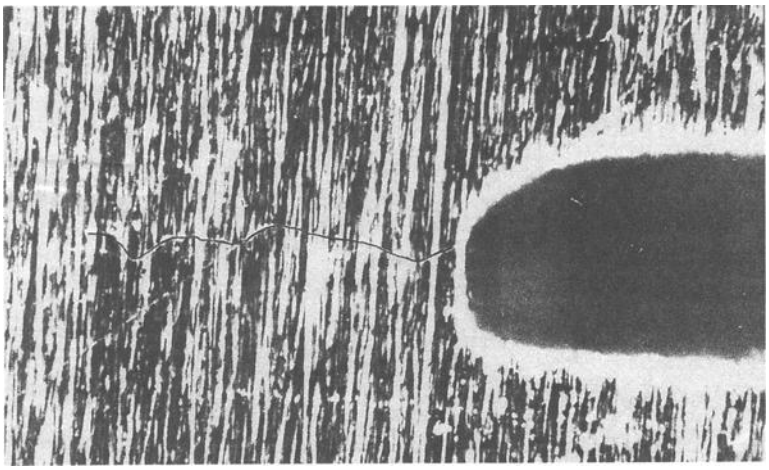

FIG. 16—*Fatigue crack at tip of EDM slot at 62 600 cycles.*

the case, as seen in Fig. 17. Figure 18 shows a comparison of the crack growth from each end. The crack at the top deviated from plane growth earlier and grew to a greater length; however, once the cracks turned, both grew at approximately a 45° angle to the plate diagonals, indicating that they were propagating along the direction of maximum shear stress.

Figure 19 presents the experimental results of crack length versus number of cycles. It is from these data that crack growth rates and stress intensity factors were determined. The data show that fatigue cracks began growing slowly from the tips of the slot and that total crack length increased at an increasing rate up to 115 000 cycles. After that point, the crack length increased in a linear fashion with the number of cycles. The rate of growth was dependent on the instantaneous length of the crack until the cracks turned and began growing along the plane of maximum shear, where it then became independent of crack length.

Figure 20 shows the individual growth rates at each end of the slot despite the fact that both crack tips in the plate specimen experienced the same stress intensity factor. The specimen exhibited the peculiar behavior within one crack first grew at a slower rate than the other and subsequently propagated at a rate somewhat faster. Further, it can be noted from the two curves that one crack tip counterbalances the behavior of its companion crack tip by propagating rapidly when the latter moved slowly and then slowed down when the latter accelerated. Consequently, the overall average crack growth rate tended to remain constant. This behavior of crack growth might be attributed to possible changes in local microstructure such as grain orientation or other forms of anisotropy.

The data plotted in Fig. 19 are examined more closely in Figs. 21 and 22. Figure 21 shows the crack length versus number of cycles for the initial portion of the curve up to and during the fracture mode transition from failure perpendicular to the applied tensile stress to shear fracture at 45° to the applied stress. Figure 22 shows the remainder of the growth, which is completely by shear failure. The discontinuity in the initial portion of the curve was due to a change in the method of measuring crack length. Originally, the length measurements were made linearly and then changed to the curvilinear method.

The fracture mode transition began at about 85 000 cycles, but it was 115 000 before the method of measurement was revised. This left a range of 20 000 cycles where the curvilinear crack was being measured with a linear device. The actual crack length is estimated in

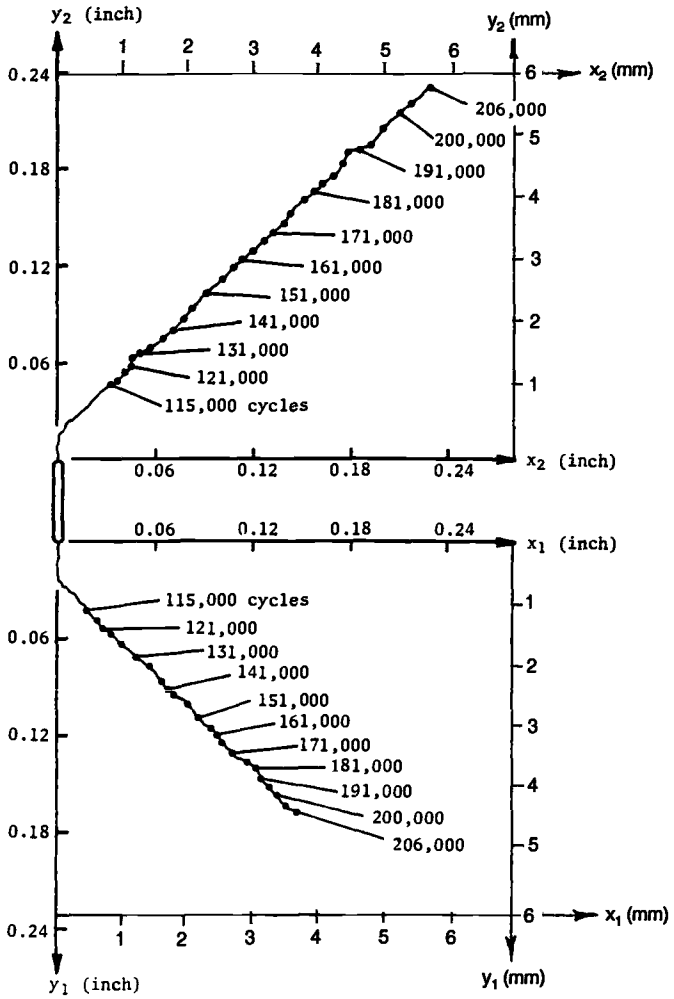

FIG. 17—*Experimentally measured crack tip positions during fatigue testing.*

Fig. 21 by a smooth fit curve between the data prior to 85 000 cycles and after 115 000 cycles. The estimated values of the crack lengths were used in calculating crack growth rates. The crack growth rate from 115 000 cycles to the conclusion of the test indicates that the mean growth rate is $d(2c)/dN = 4.9 \times 10^{-6}$ in. per cycle (1.245×10^{-7} m/cycle). It can therefore be concluded that, after the mode of failure had transformed to that of pure shear, the crack growth rate was constant and the stress intensities at the tips of the fatigue crack were not a function of the increasing crack length. This is due to the fact that the crack growth is now a function of the state of stress where the crack grew along the maximum shear plane. The original aspect ratio of $a/2c_0 = 0.321$ was assumed to be constant during the growth of the fatigue crack in Mode I. This assumption is made at least for the range of data up to the point where fracture mode transition had been completed. The crack growth rates $d(2c)/dN$, dc/dN, and da/dN are therefore interchangeable and have the relationships

$$d(2c)/dN = 2\,dc/dN = (1/0.321)(da/dN)$$

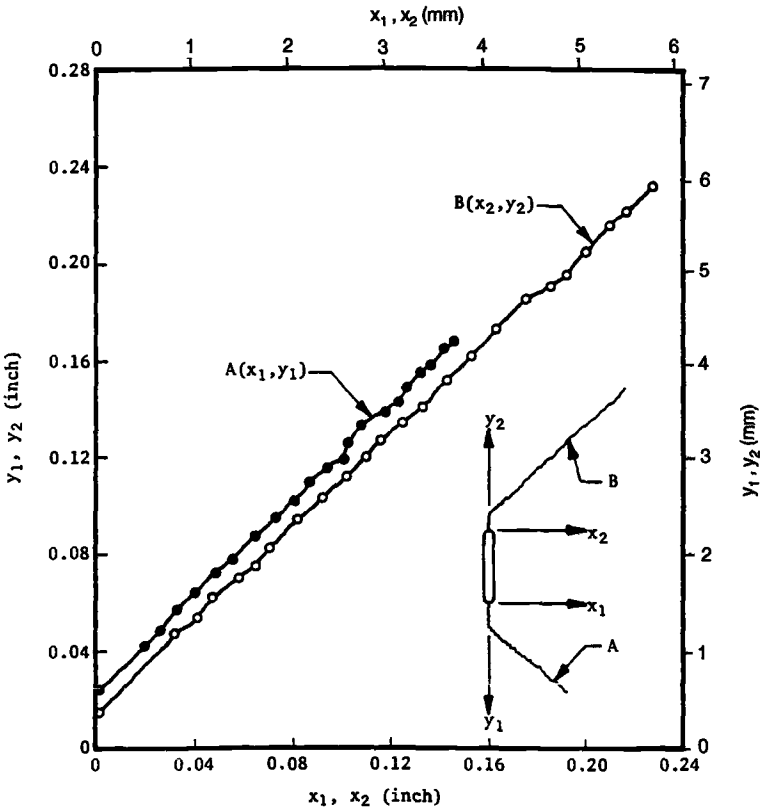

FIG. 18—*Comparison of fatigue crack growth from each end of EDM slot, crack tip coordinates.*

The corresponding ΔK values are computed from the applied load, F, and respective crack lengths using the stress intensity expression given by Eq 21 where the parameters are $\eta = 0.95$, $\sigma_0 = 145$ ksi (1000 MPa), and $\Phi = 1.31$. Figure 23 shows the correlation on the basis of

$$\Delta K = 58\,756\sqrt{2c} \tag{25}$$

Since the value of ΔK is associated with zero to maximum loading, the stress intensity range used in the test was numerically equal to the maximum stress intensity factor.

Fracture mode transition, indicated on Fig. 23, began at about 85 000 cycles. At this point the fatigue crack was 0.0886 in. (2.25 mm) long, and the corresponding stress intensity factor from Eq 25 was $\Delta K = 17.5$ ksi$\sqrt{\text{in.}}$ (19.2 MPa$\sqrt{\text{m}}$). Values of *dc/dN* were plotted against corresponding ΔK values up to the point at which the fracture mode transition had been completed. This occurred at about 115 000 cycles when the crack was 0.1639 in. (4.163 mm) long with a corresponding $\Delta K = 23.8$ ksi$\sqrt{\text{in.}}$ (26.2 MPa$\sqrt{\text{m}}$). After the transition, Fig. 22 shows that crack length is a linear function of the number of cycles and hence the growth rate is independent of the instantaneous values of the crack length and is

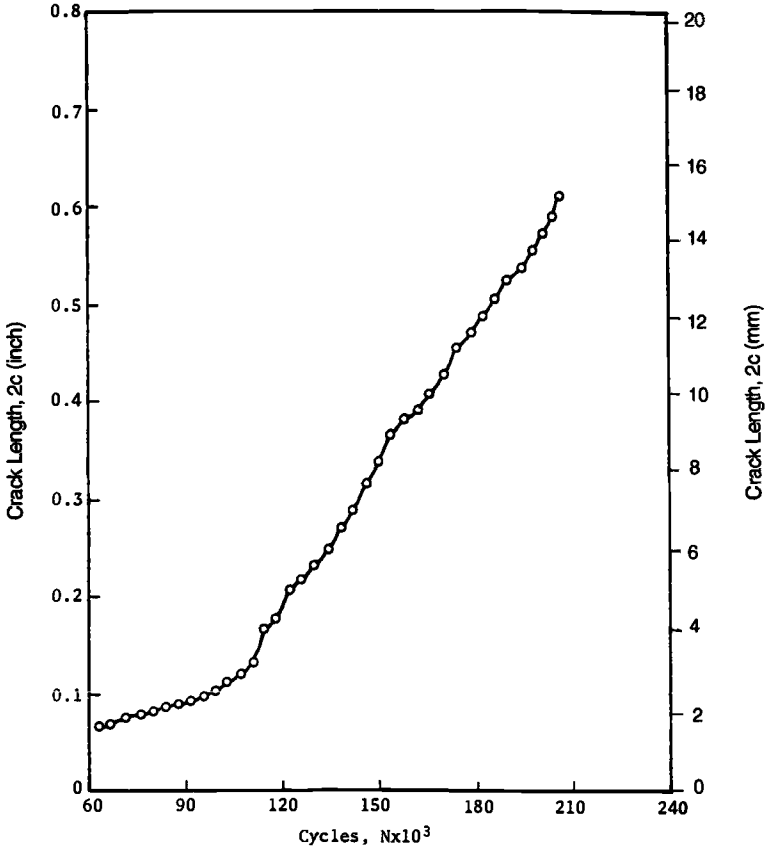

FIG. 19—*Total fatigue crack length versus number of cycles.*

constant. This is shown in Fig. 23 as a straight line parallel to the abscissa at a crack growth rate of $dc/dN = 2.45 \times 10^{-6}$ in. per cycle (0.62×10^{-7} m/cycle).

The data prior to and during the transition to failure along the maximum shear plane indicate that there is also a linear relationship between log dc/dN and log ΔK values in this range. Using a least-squares linear regression analysis of the data, the slope was found to be $m = 4.76$. Once the slope was known, the constant B_0 was determined from the best fit straight line passed through the mean values of the n number of data points defined by

$$\log \frac{dc}{dN} = \frac{1}{N} \sum_n \log \frac{dc}{dN} = -6.164 \tag{26}$$

$$\log \Delta K = \frac{1}{n} \sum_n \log \Delta K = 4.253 \tag{27}$$

These mean values can therefore be used to solve for B_0 from

$$B_0 = \frac{dc/dN}{(\Delta K)^{4.76}} = \frac{6.85 \times 10^{-7}}{(17\,907)^{4.76}} = 3.94 \times 10^{-27}$$

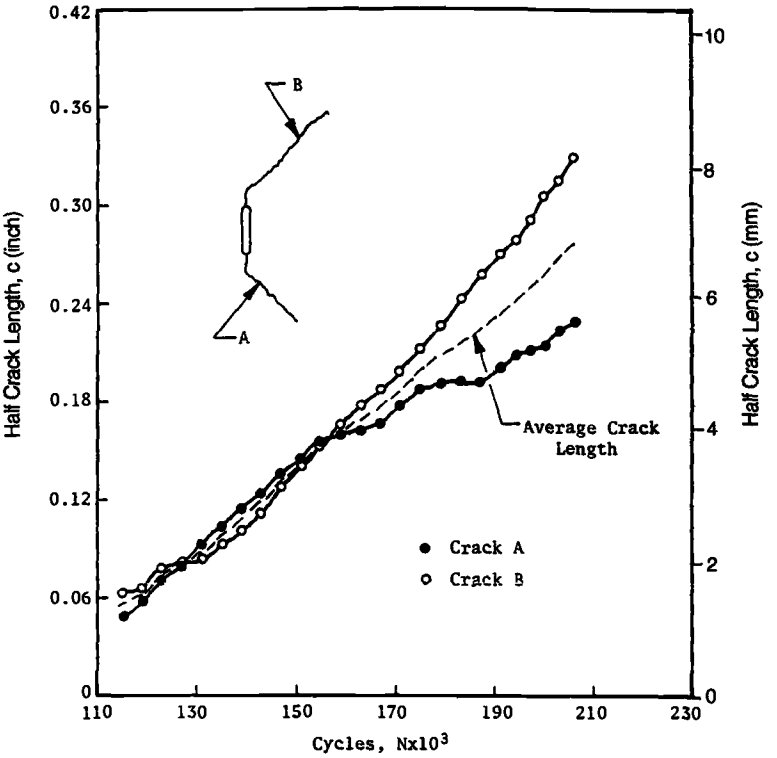

FIG. 20—*Comparison of fatigue crack growth from each end of EDM slot, crack length versus number of cycles.*

Fracture Mode Transition

During the biaxial fatigue test, the crack propagation showed that there were two separate modes of fatigue crack growth with a transition range of growth between the two. The first mode consisted of a crack propagating along a plane normal to the applied tensile stress and occurred until ΔK reached a value of 17.5 ksi$\sqrt{\text{in.}}$ (19.2 MPa$\sqrt{\text{m}}$). The second mode was initiated when ΔK reached a value of 23.8 ksi$\sqrt{\text{in.}}$ (26.2 MPa$\sqrt{\text{m}}$) and was characterized by crack growth along the maximum shear plane.

Based on the Irwin analysis [6], the fracture mode transition may be a function of the size of the plastic zone ahead of the crack. When the plastic zone size was small relative to the specimen thickness, the crack progressed along a plane normal to the loading direction. For a small plastic zone, the tensile stress perpendicular to the crack surface is zero at the specimen surface but approaches $\mu(\sigma_x + \sigma_y)$ in the interior. This is due to the constraints caused by the restriction of strain in the specimen thickness direction leading to a plane strain condition. When a large plastic zone occurs at the tip of the crack, the fracture path shifts to a plane oriented 45° to the loading direction and through the thickness direction. For a large plastic zone, the restriction of strain in the thickness direction is removed, the stress in this direction is approximately zero, and crack growth along the inclined plane is considered to be a plane stress crack propagation. Therefore, it is reasoned that when the plastic zone at the advancing fatigue crack reaches a critical size, the transition from flat to shear failure would occur.

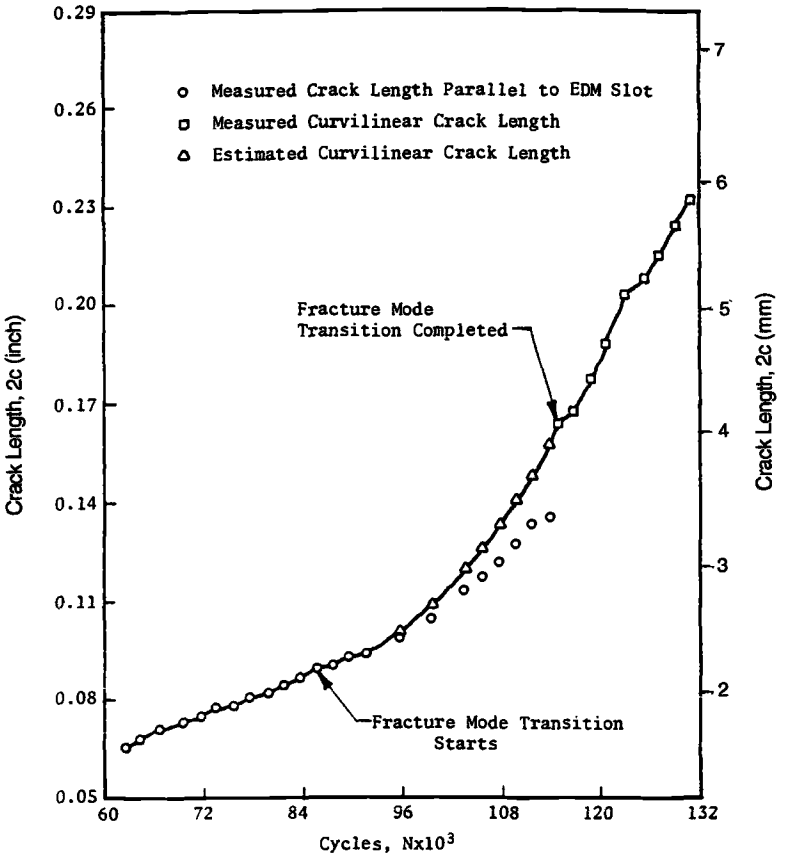

FIG. 21—*Fatigue crack length versus number of cycles showing fracture mode transition.*

Wilhem [*8*] established the transition point for many materials including IN-718. His results show that the transition to shear fracture occurred at ΔK = 14 ksi$\sqrt{\text{in.}}$ ± 5 ksi$\sqrt{\text{in.}}$ (15.46 ± 5.5) MPa$\sqrt{\text{m}}$. In comparison with the biaxial crack growth study, the initial stress intensity factor, based on the EDM slot dimensions and initial loading of 3300 lb (14 700 N), was ΔK = 13.53 ksi$\sqrt{\text{in.}}$ (14.9 MPa $\sqrt{\text{m}}$). Thus, the fatigue crack had only to grow a small distance from each tip of the starter slot to increase the stress intensity to the critical point required for mode transition at ΔK = 17.5 ksi$\sqrt{\text{in.}}$ (19.2 MPa $\sqrt{\text{m}}$) and to be completed at ΔK = 23.8 ksi$\sqrt{\text{in.}}$ (26.2 MPa $\sqrt{\text{m}}$.

If the initial stress intensity for the starter slot placed the crack tip stress intensity value above the transition value, the crack growth would occur as shear mode cracking throughout the fatigue life. This has been found to be true in other biaxial fatigue tests under anticlastic bending [*8*].

Summary and Conclusions

Fatigue crack propagation characteristics of a high-strength nickel base alloy were investigated under a biaxial stress field. Anticlastic bending of square plate specimens was used to impose the biaxial stress field across the surface of the plate specimen with a principal

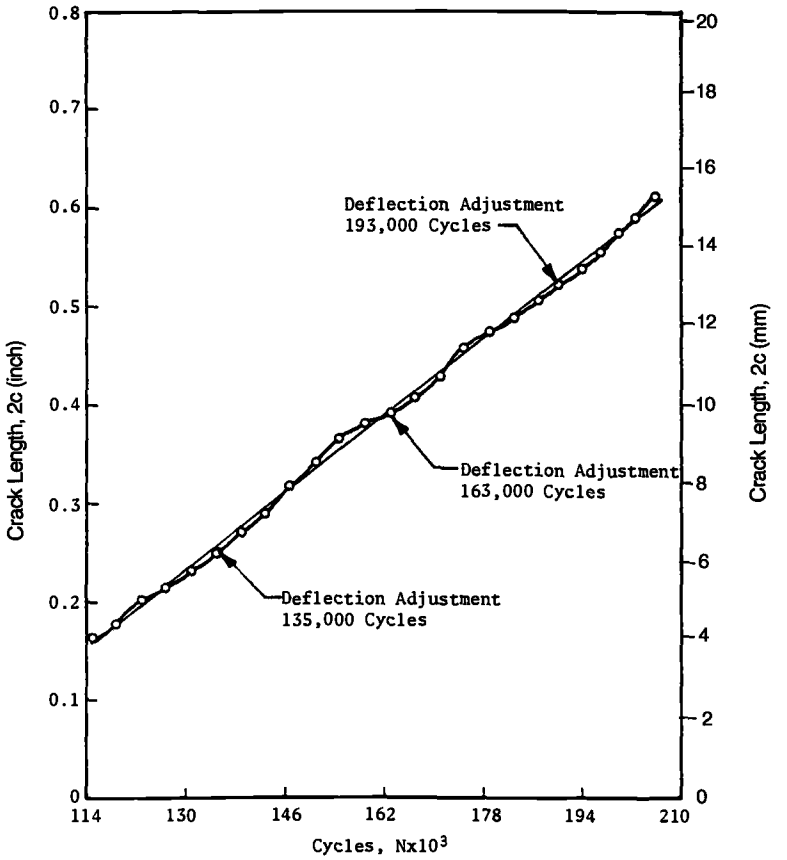

FIG. 22—*Fatigue crack length versus number of cycles showing remainder of crack growth by shear failure.*

stress ratio of 1: −1. A semielliptical EDM crack starter was induced at the center of the specimen surface. Several types of calibration tests were conducted to ensure proper data interpretation.

During the biaxial fatigue test, the length of the propagating fatigue crack was measured at intervals of 2000 cycles of applied load. Initially, the crack grew along the plate diagonal perpendicular to the applied tensile stress and parallel to the applied compressive stress.

The fatigue crack growth occurred in three separate stages. The first stage of crack growth consisted of propagation along a plane normal to the applied tensile load and occurred until the stress intensity factor reached a value of 17.5 ksi$\sqrt{\text{in.}}$ (19.2 MPa $\sqrt{\text{m}}$). The second stage was a transition stage in the crack growth that was characterized by continuous change in the orientation of the plane of crack growth until steady-state growth occurred along the maximum shear plane, which was 45° to the principal stresses. The stress intensity factor had a value of 23.8 ksi$\sqrt{\text{in.}}$ (26.2 MPa $\sqrt{\text{m}}$) upon completion of the transition growth. Once the steady crack growth in the second mode of fatigue crack propagation along the maximum shear plane was achieved, the crack growth rate was found to no longer be a function of the stress intensity factor, but rather a function of the state of stress that existed on the plate surface. The crack growth rate became constant under load control.

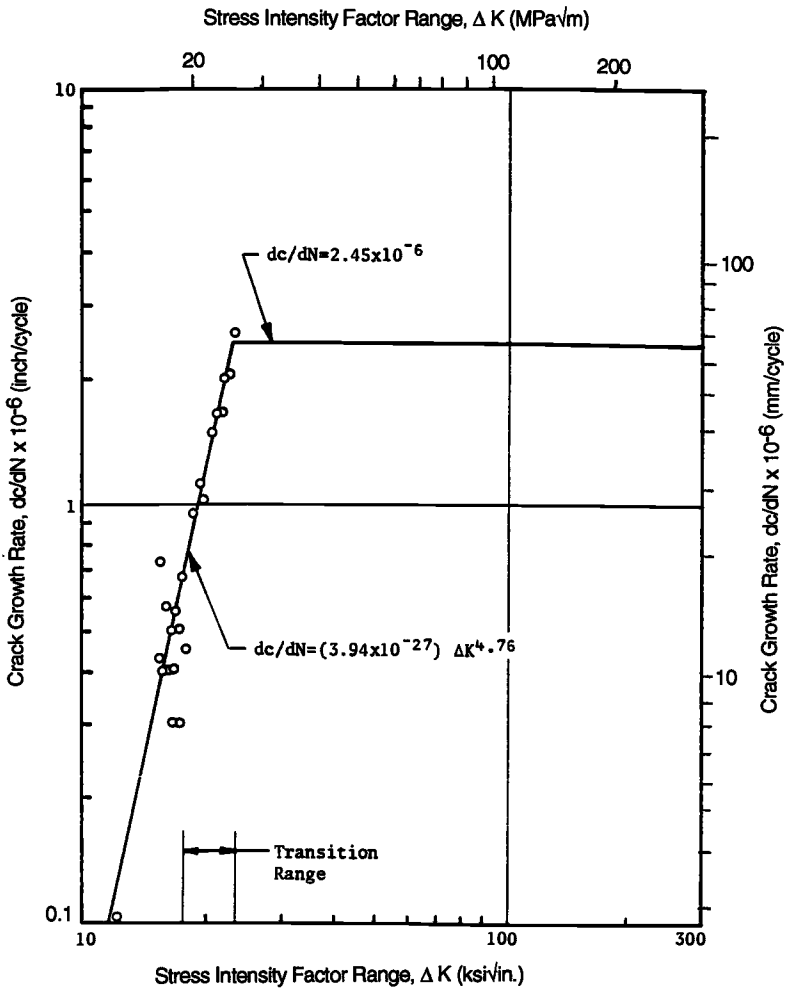

FIG. 23—*Fatigue crack growth rate versus stress intensity factor range.*

References

[1] Weiss, V., Sessler, J., and Packman, P., "Effect of Several Parameters on Low Cycle Fatigue Behavior," *Acta Metallurgica,* Vol. 11, No. 7, 1963, pp. 809–816.

[2] Shewchuk, J. and Joshi, S. R., "Fatigue Crack Propagation in a Biaxial Stress Field," *Experimental Mechanics,* Vol. 10, No. 12, 1970, pp. 529–533.

[3] Zamrik, S. Y. and Shabara, M., "The Effect of Stress Ratio on Fatigue Crack Growth in a Biaxial Stress Field," *ASME Transactions, Journal of Pressure Vessel Technology,* Vol. 99, Series J, No. 1, 1977, pp. 137–143.

[4] Lui, H. W., "Fatigue Crack Propagation and Applied Stress Range—An Energy Approach," *ASME Transactions, Journal of Basic Engineering,* Vol. 85, 1963, pp. 116–122.

[5] Grandt, Jr., A. F. and Sinclair, G. M., "Stress Intensity Factors for Surface Cracks in Bending," *Stress Analysis and Growth of Cracks, ASTM STP 513,* American Society for Testing and Materials, West Conshohocken, PA, 1972, pp. 37–58.

[6] Irwin, G. R., "Fracture Mode Transition for a Crack Transversing a Plate," *ASME Transactions, Journal of Basic Engineering,* Vol. 28, 1960, pp. 417–425.

[7] Zamrik, S. Y. and Davis, D. C., "A Novel Test Method and Apparatus for Multiaxial Fatigue Studies," *Advances in Multiaxial Fatigue, ASTM STP 1191,* D. L. McDowell and R. Ellis, Eds., American Society for Testing and Materials, West Conshohocken, PA, 1993, pp. 204–219.

[8] Wilheim, D. P., "Investigation of Cyclic Crack Growth Transition Behavior," *Fatigue Crack Propagation, ASTM STP 415,* American Society for Testing and Materials, West Conshohocken, PA, 1967, pp. 363–383.

Mark C. Hardy[1]

Modeling the Behavior of Short Fatigue Cracks in a Near-α Titanium Alloy

REFERENCE: Hardy, M. C., **"Modeling the Behavior of Short Fatigue Cracks in a Near-α Titanium Alloy,"** *Advances in Fatigue Lifetime Predictive Techniques: 3rd Volume, ASTM STP 1292,* M. R. Mitchell and R. W. Landgraf, Eds., American Society for Testing and Materials, 1996, pp. 188–201.

ABSTRACT: Low-cycle fatigue is the greatest potential cause of failure in critical aero-engine components. To prevent premature failure, the fatigue life of these components needs to be predicted accurately. This requires knowledge of crack nucleation and growth under fatigue loading. Initial crack propagation is not continuous as a result of obstacles such as grain boundaries. Laboratory observation has shown that cracks decelerate rapidly as they approach these boundaries. Further growth may be impeded for a considerable number of cycles if there is a significant difference in orientation between the cracked and adjacent grains. This behavior effectively disappears at longer crack sizes. A detailed quantitative appraisal of crack growth rates is vital for component life predictions based on fracture mechanics. Cracks that nucleate during engine operation experience very high stresses that may exceed the material yield stress. Established linear elastic fracture mechanics may not be applicable due to loss of similitude caused by violation of the small-scale yielding criterion. These concepts are also based on continuum fracture mechanics and therefore cannot describe the early stages of crack growth. This paper considers an empirical model for short crack growth in a β heat-treated near-α titanium alloy at room temperature. Crack growth rate equations are expressed in terms of crack length and effective stress range and were derived from experimental crack length versus cycles data. These data were generated at constant peak stress and various stress ratios. The expressions are shown to give an excellent representation of experimental crack growth rate versus crack length data. In producing the model, procedures have been established to determine crack opening loads and critical crack sizes above which continuum fracture mechanics apply.

KEYWORDS: low-cycle fatigue, fracture mechanics, short fatigue cracks, titanium alloys

Nomenclature

a	Crack length
a_0	Initial crack size
a_{crit}	Crack growth sensitive to microstructure at crack lengths $< a_{crit}$
a_f	Crack size leading to component or specimen failure
a_s	Size of a flaw required for crack growth after Cycle 1
A	Constant in Eq 11
B	Parameter in Eq 9
C, m	Parameters in Eq 1
C_i	Parameter in Eq 6
CFM	Continuum fracture mechanics
d	Slip band distance from crack nucleation site to microstructural obstacle

[1]Higher scientific officer, Defence Research Agency (Pyestock), Farnborough, Hampshire, GU14 0LS, UK.

da/dN	Crack growth rate
$\Delta\epsilon$	Strain range
$\Delta\epsilon_e$, $\Delta\epsilon_p$	Elastic and plastic strain range
K_{max}	Maximum stress intensity factor
ΔK	Stress intensity factor range
LEFM	Linear elastic fracture mechanics
M	Microstructural unit size, i.e., in this case, α-colony size
MCG	Microstructural crack growth, i.e., crack growth sensitive to microstructure
N	Cycles
N_{MCG}, N_{CFM}	Crack propagation life in MCG and CFM regimes
R	Stress ratio defined as $\sigma_{min}/\sigma_{max}$
r_p	Monotonic crack tip plastic zone size
σ_{min}, σ_{max}	Minimum and maximum stress
σ_{op}	Crack opening stress
σ_y	Material yield stress
$\Delta\sigma$	Stress range defined as $\sigma_{max} - \sigma_{min}$
$\Delta\sigma_{eff}$	Stress range defined as $\sigma_{max} - \sigma_{op}$
U	$\Delta\sigma_{eff}/\Delta\sigma$

Introduction

Low-cycle fatigue is the greatest potential cause of failure in critical aero-engine components. To prevent catastrophic failure in-service, the fatigue life of these components must be predicted accurately. Fatigue life can be calculated by integration of fracture mechanics expressions from an initial flaw size to a crack size responsible for burst. This procedure relies on the accuracy of crack growth models and requires a detailed characterization of crack growth rates. At present, the stress intensity factor range (ΔK) is used to describe crack growth rates (da/dN) via the following power law expression proposed by Paris [*1*]

$$da/dN = C\Delta K^m \tag{1}$$

where C and m are experimentally determined parameters. This expression is applicable to conditions of linear elastic fracture mechanics (LEFM) [*2,3*], i.e., to long cracks growing under low alternating stress. However, long cracks and low loads are not typical of many aero-engine components. Cracks that nucleate in compressor and turbine disks between inspection intervals must be physically small and are certainly shorter than 0.75 mm in size. Such cracks experience very high stresses as operating conditions in current aero-engines subject components to stresses approaching the material yield stress so that local plasticity does occur [*4*]. The crack sizes and stresses involved are therefore likely to violate the small-scale yielding criterion [*5*] necessary for LEFM.

The power law expression also assumes continuum mechanics. This assumption is inappropriate, however, for the initial stages of crack growth due to microstructural obstacles such as grain boundaries or inclusions. Observation has shown that crack growth drastically decelerates as crack tips approach these obstacles [*6*]. It has been argued that this occurs in response to diminishing plasticity [*7*]. Further crack propagation may be impeded for a significant number of cycles if there is a significant difference in orientation between the cracked and adjacent grains. This discontinuous behavior effectively disappears at longer crack sizes.

The intention of this work is to empirically model the behavior of artificially initiated

short fatigue cracks in a β heat-treated near-α titanium alloy at room temperature under high stresses.

Material

IMI 829 (Ti-5.5Al-3.5Sn-3Zr-1Nb-0.25Mo-0.3Si) [*8*] is a β heat-treated near-α titanium alloy used for rotating components in the hotter compressor stages of aero-engines [*9*]. Blanks, 22 mm in diameter and 100 mm long, were cut from extruded bar 50 mm in diameter and solution treated in the β phase field at 1050°C for 45 min. Once removed from the furnace, they were air cooled and then annealed at 625°C for 2 h before a final air cool. Figure 1 shows the resulting microstructure that consists of aligned α-colonies in large prior β grains. There are also regions of coarse basketweave, α. This microstructure will be found in thicker component sections [*9*] and is likely to offer the least resistance to crack nucleation and growth [*10*].

The distribution of α-colony sizes in Fig. 2 was produced from over 1000 α-colony measurements [*11*]. It shows that most of the colonies are between 25 to 125 μm.

Experimental Procedure

Cracks were grown from a 250-μm starter slit in 10 by 10-mm square section corner crack specimens [*12*]. All tests were performed at room temperature in laboratory air under constant amplitude cyclic loading at a frequency of 1 Hz using a closed loop servohydraulic machine. A triangular waveform was used throughout. The test program was designed to investigate the effect of stress ratio on short crack growth at a peak stress of 650 MPa, which is above the material cyclic yield stress and is 74% of the 0.2% proof stress [*13*]. Stress ratios, R, of 0.05, 0.3, 0.5, 0.6 and 0.7 were examined.

The growth of cracks was monitored using an automated pulsed d-c potential drop system [*14*]. Fine platinum wires, 63 μm in diameter, served as electrical probes that were spot

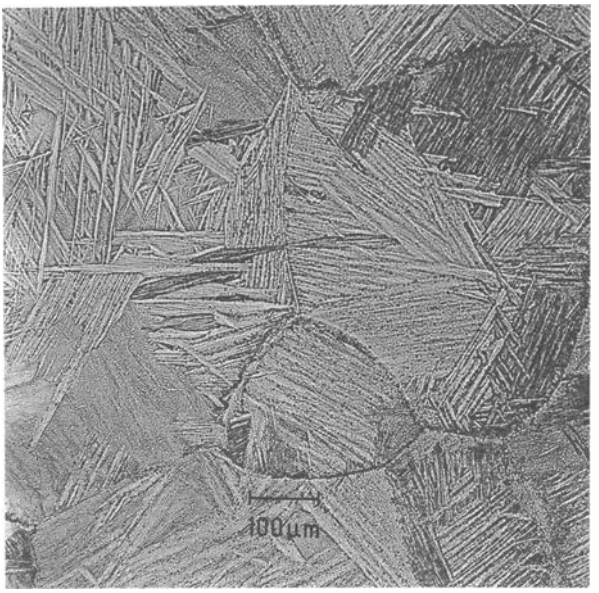

FIG. 1—*Microstructure of IMI 829 after heat treatment.*

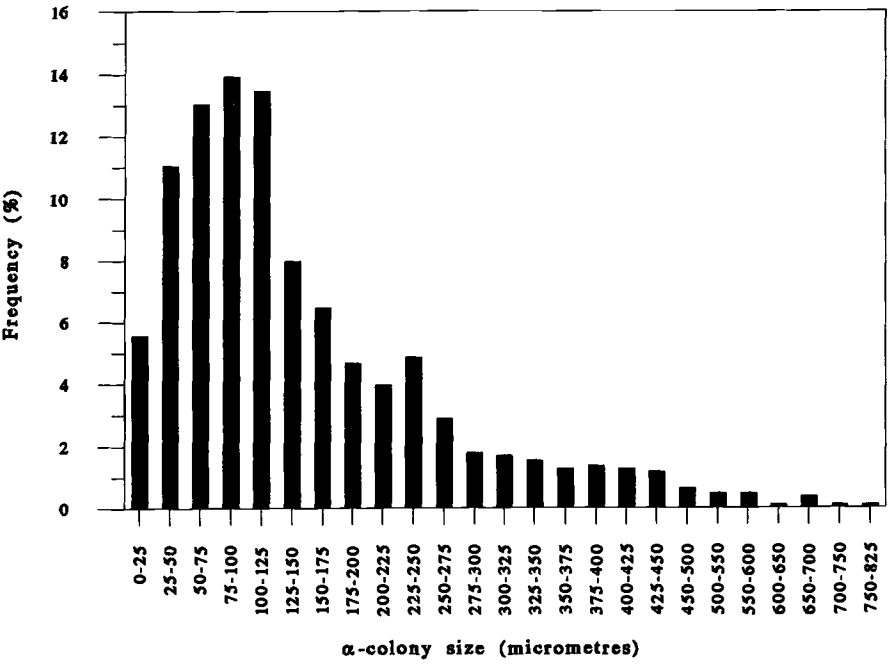

FIG. 2—*Distribution of α-colony sizes in the heat-treated IMI 829 examined in this study.*

welded to the specimens following AGARD guidelines [*12*]. An expression for crack length from the measured potential is given elsewhere [*14*]. Crack growth at the surface was also recorded by two 35-mm cameras attached to microscopes placed perpendicular to two adjacent specimen surfaces. These surfaces were carefully polished and etched to examine the influence of microstructure on crack growth. The camera system is linked to the computer data collection routine so that a frame is taken during each voltage measurement. Actual surface crack lengths were measured from magnified images projected onto paper.

Results

Test data are presented in Fig. 3 as applied stress range versus crack propagation lives for crack growth of 0.25 to 3.0 mm beyond the starter slit. As different stress ratios were used at a constant peak stress, a series of *S-N* curves is produced. A Basquin expression has been shown to describe the *S-N* behavior of IMI 829 at room temperature for the range of lives given in Fig. 3 [*13*]. However, the *R* of 0.05 and 0.3 data in Fig. 3 do not obey the Basquin relationship of high *R* data. This suggests that, at low *R* ratio, cracks grow only for a fraction of the applied stress range as a result of crack closure. The reduced stress range, $\Delta\sigma_{eff}$, and therefore the crack opening stress, σ_{op}, can be determined in these tests by forcing data onto the line defined by high *R* points. The crack opening stress values are plotted as a proportion of the maximum stress (σ_{op}/σ_{max}) in Fig. 4. It must be assumed from these data that crack opening stress does not vary with crack size. The mean σ_{op}/σ_{max} and $\Delta\sigma_{eff}$ values for the *R* of 0.05 and 0.3 tests are 0.32, 438 MPa, and 0.48, 338 MPa, respectively.

The above procedure used crack-length data obtained from the potential drop system. These data relate to the whole crack front and as such are less affected by local variations in

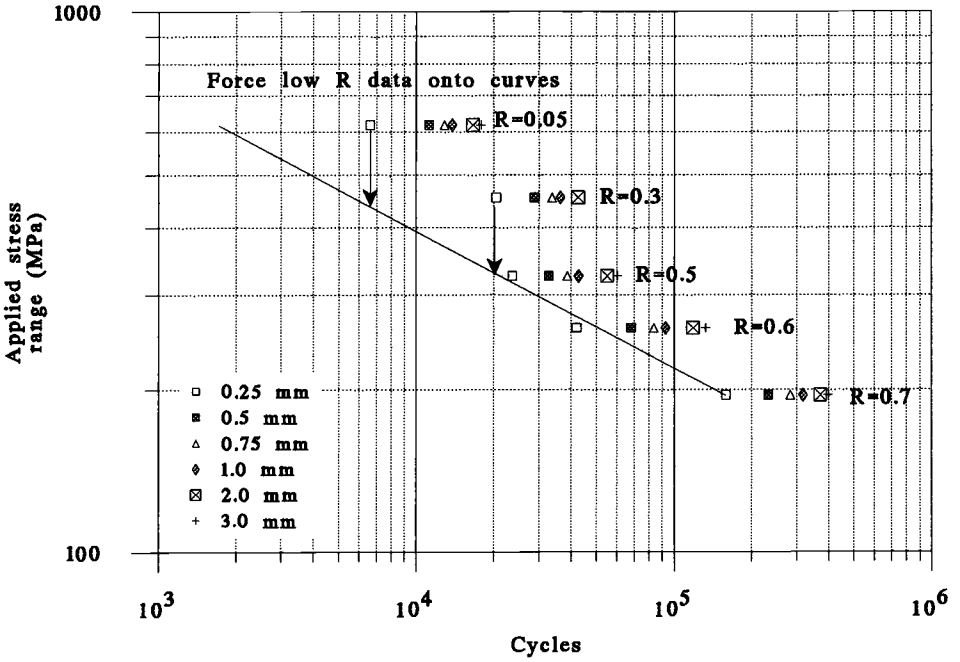

FIG. 3—*Effect of stress range on crack propagation lives for potential drop derived crack sizes of 0.25 to 3.0 mm beyond the starter slit.*

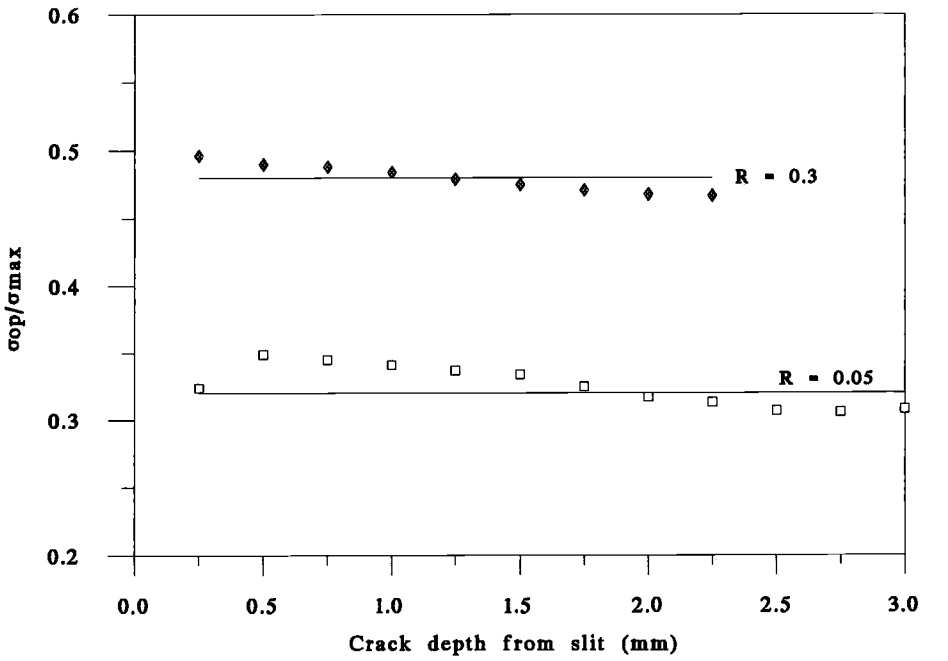

FIG. 4—*Ratio of crack opening stress to maximum applied stress (σ_{op}/σ_{max}) versus crack size data.*

growth due to material microstructure. Optical crack length measurements are better able to detect such variations and are therefore more appropriate for modeling short crack behavior.

The influence of microstructure on crack growth can be illustrated on a plot showing the natural logarithm of actual surface crack length versus cycles (Fig. 5). For cracks smaller than a critical crack size a_{crit}, crack growth periodically accelerates and decelerates. Close inspection of etched specimen faces with these data has shown that the growth rate of a crack decreases as it approaches an α-colony boundary. Beyond a_{crit}, crack growth appears to be more continuous.

Modeling the Behavior of Short Fatigue Cracks

The modified Kitagawa-Takahashi diagram [*2,15*] in Fig. 6 suggests that the growth of cracks in highly stressed aero-engine components predominantly falls into two short crack growth regimes [*16*]. The first, for crack lengths below a_{crit}, is microstructure dependent and can be termed microstructural crack growth (MCG). The second regime, for cracks greater in size than a_{crit}, can be modeled using elastic-plastic continuum fracture mechanics (CFM). The two lines that separate propagating cracks into MCG, CFM, and LEFM regimes were derived from Lankford's two criteria for rapid short crack growth

$$\frac{r_p}{a} \geq 0.05 \tag{2}$$

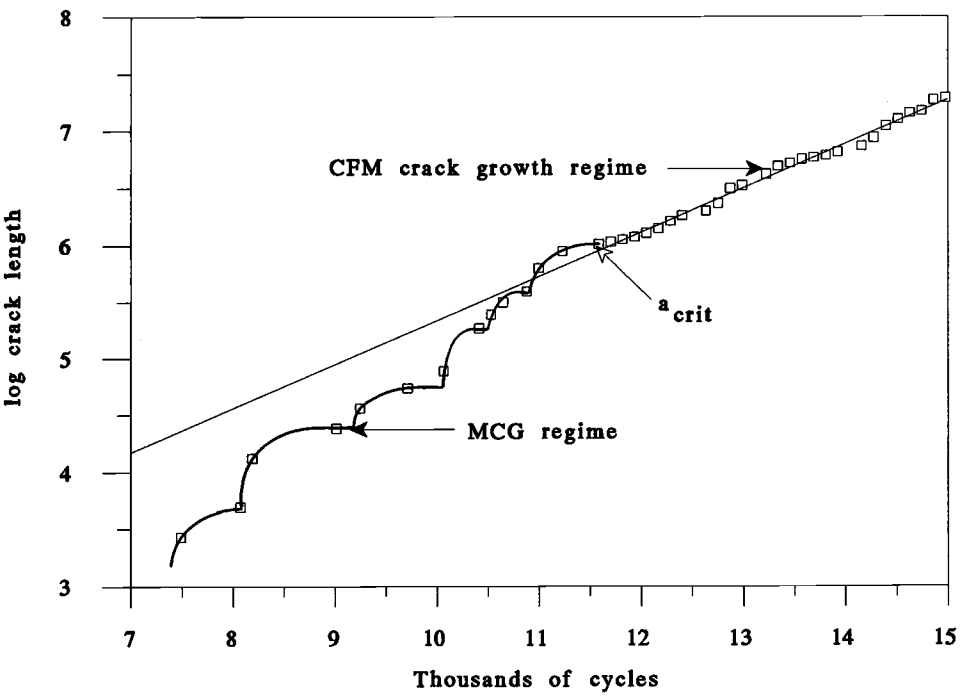

FIG. 5—*Natural logarithm of crack length versus cycles data from* R *of 0.05 test. Data are separated by* a_{crit} *into microstructural (MCG) and continuum fracture mechanics (CFM) crack growth regimes.*

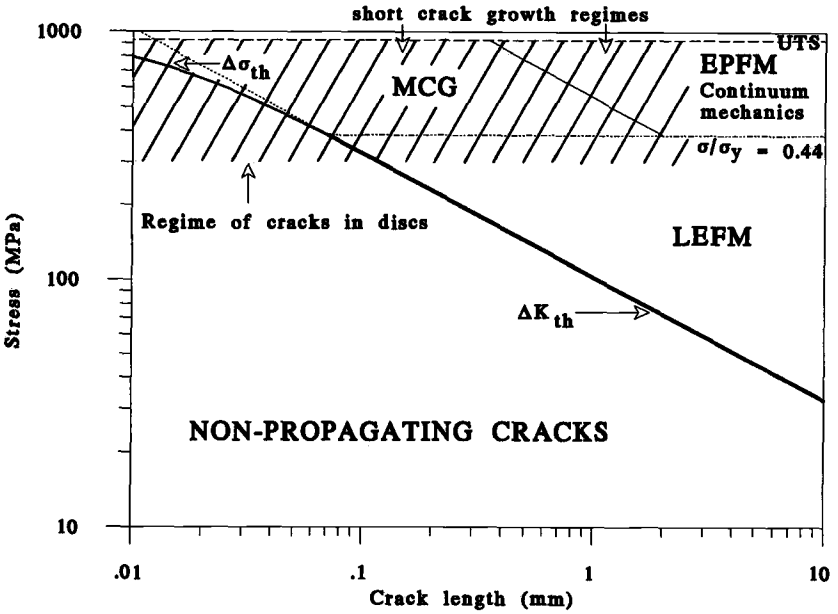

FIG. 6—*Kitagawa-Takahashi diagram for IMI 829 at room temperature showing that cracks nucleating in disks during engine operation lie in short crack regimes.*

$$\frac{r_p}{M} \leq 1 \tag{3}$$

where r_p is the monotonic crack tip plastic zone size ($\sim 0.15(K_{max}/\sigma_y)^2$), a is the crack size, and M is the microstructural unit size [*17*]. Larsen et al. [*18*] expressed both equations in terms of the peak cyclic stress and the material yield stress by substituting in expressions for r_p and K. A simplified version of Pickard's stress intensity factor solution for cracks with circular and elliptical fronts [*19*] has been substituted into the expression for r_p so that Eqs 2 and 3 become

$$\frac{\sigma_{max}}{\sigma_y} \geq 0.44 \tag{4}$$

$$\sigma_{max} \leq \frac{\sigma_y}{2.32}\sqrt{\frac{M\pi}{0.15a}} \tag{5}$$

where M is the α-colony size in β heat-treated near-α titanium alloys.

The second criterion suggests that the MCG regime is dependent on peak stress, crack length, and α-colony size. Determination of a_{crit} from $\log_e a$ versus N data has shown that the critical crack length is not constant for a peak stress of 650 MPa [*11*]. This was attributed to the variation in α-colony sizes and was not due to the difference in stress range. Good agreement with a_{crit} was found when appropriate M values were used in Eq 5.

Microstructural Crack Growth

As demonstrated in Fig. 5, the growth rate of a crack smaller than a_{crit} decreases as it approaches an α-colony boundary. Hobson [*20,21*] empirically derived the following expression for this behavior

$$da/dN = C_i(d - a) \tag{6}$$

where d is the distance from the nucleation point to the first microstructural obstacle, and C_i is a function of alternating stress or strain. The model assumes that slip, responsible for Stage I crack growth, extends across the microstructural unit but is blocked by the obstacle. These ideas were originally proposed by Morris et al. [*7,22*] to explain discontinuous short crack behavior. The terms d and $(d - a)$ represent the slip band length and the remaining slip band plastic zone size, respectively. It follows, therefore, that crack arrest ($da/dN = 0$) occurs when $a = d$.

Since more than one microstructural barrier is encountered before the crack grows to the critical size a_{crit}, several expressions are required, each specific to growth within an α-colony. The approach has been used successfully by Yates and Grabowski [*23*] for modeling Stage I crack growth in a nickel base superalloy. In the present study, MCG expressions were derived by fitting curves to groups of $\log_e a$ versus N data corresponding to crack growth within individual α-colonies. Colony boundaries were defined on these plots through examination of surface crack photographs and specimen fracture surfaces. Curves were then used to produce da/dN versus $d - a$ data such as those in Fig. 7.

Figure 7 illustrates that Eq 6 does describe the behavior of microstructure-dependent short cracks. It also shows that there is a large variation in C_i that appears to be independent of colony size. This may result from the differences in crack length, stress range, and α-colony orientation. The influence of a pseudo crack length, given by the cumulative microstructural unit sizes d on C_i is shown in Fig. 8. There is significant scatter in C_i that increases with R and decreasing stress range. Scatter in C_i for high R data will influence fatigue life predictions, but variations in fatigue life for low stress ranges is expected as the majority of life is spent in crack nucleation. Despite the varying degrees of scatter, C_i shows a power

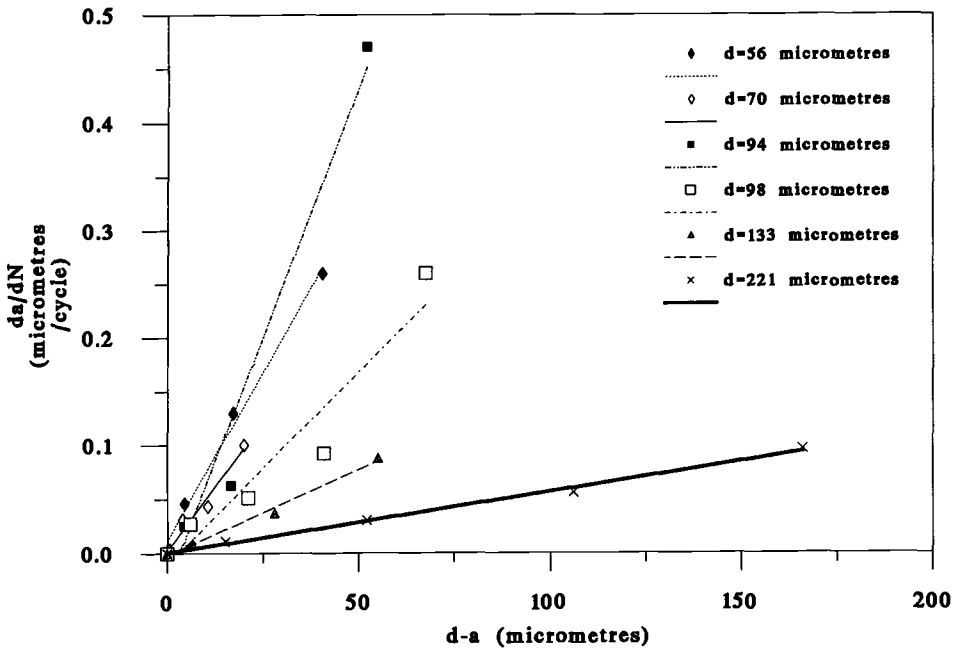

FIG. 7—*Crack growth rate* (da/dN) *versus* d − a *data from* R *of 0.5 test. The plot shows a large variation in gradient* C_i.

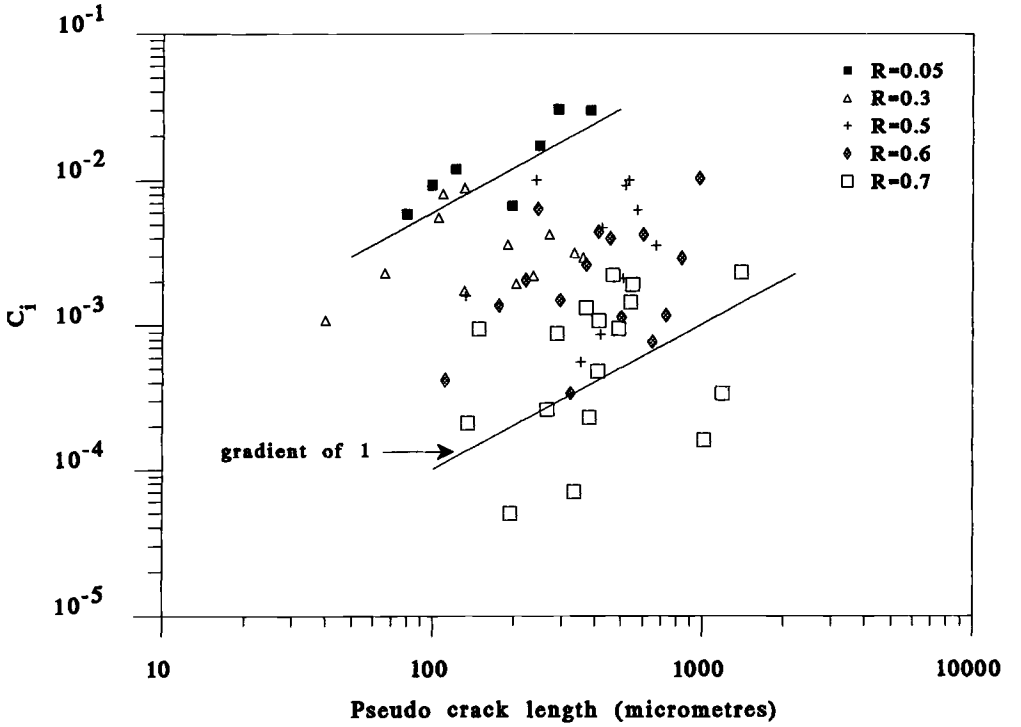

FIG. 8—*Effect of pseudo crack size* (Σd) *on parameter* C_i.

law increase with crack length. The exponent of this relationship is given by the gradients of lines through the various R data in Fig. 8. These were found to lie between 0.2 and 1. Similarly, Fig. 9 shows that for approximately constant pseudo crack sizes, C_i is dependent on effective stress range, $\Delta\sigma_{eff}$. Curves fitted to various crack size data in Fig. 9 show that the $\Delta\sigma_{eff}$ exponent lies between 1 and 5.

It is likely that the orientation of an α-colony will determine its resistance to slip, crack nucleation, and growth [*24,10*]. This resistance will be reflected in the crack length and stress range exponents controlling C_i. Consequently, α-colonies with the least resistance to crack growth may be expected to have C_i values determined by the most pessimistic exponents, i.e.

$$C_i = 4 \times 10^{-18} \Delta\sigma_{eff}^5 a \tag{7}$$

The constant, 4×10^{-18}, was obtained from a least squares curve fit on C_i versus $\Delta\sigma_{eff}^5 a$ data. Substituting Eq 7 into Eq 6 gives the following expression for microstructural crack growth in IMI 829 at room temperature (all length dimensions in μm, stress range in MPa, and crack growth rate in μm/cycle)

$$da/dN = 4 \times 10^{-18} \Delta\sigma_{eff}^5 a(d - a) \tag{8}$$

where $a < a_{crit}$ and d is the size of α-colonies encountered by cracks smaller than a_{crit}. The variation in α-colony sizes may hinder the application of the crack growth rate formula for life prediction of IMI 829 components. A random d generator, based on the distribution of α-colony sizes (Fig. 2), is required for further progress to be made.

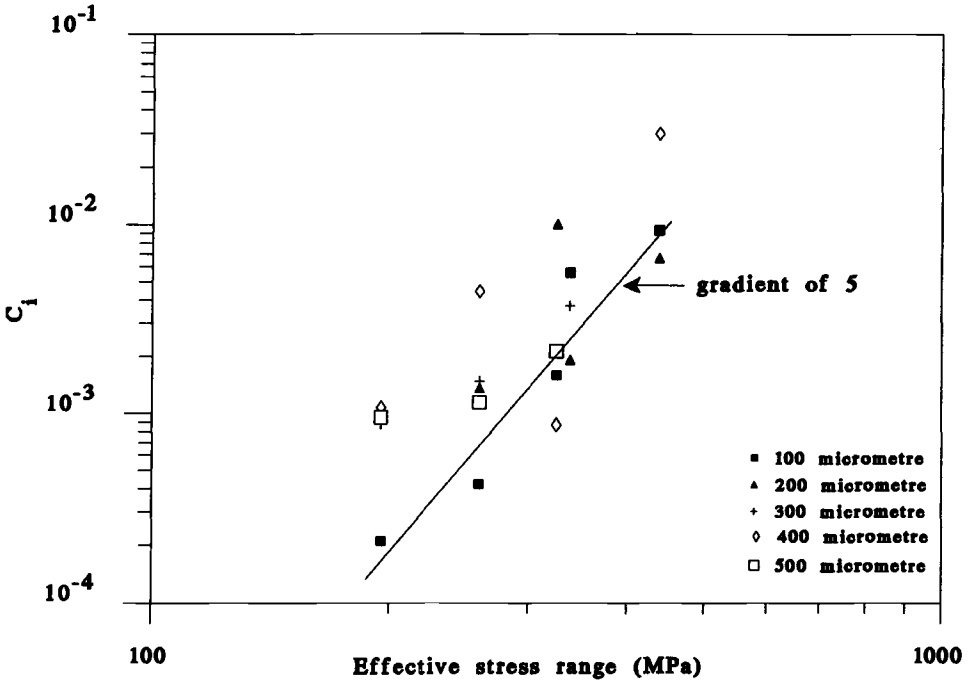

FIG. 9—*Effect of effective stress range on parameter* C_i.

Continuum Fracture Mechanics

The following expression was initially proposed to describe crack propagation under high strain fatigue [*25,26*]

$$da/dN = Ba \tag{9}$$

where B is a function of strain range $\Delta\epsilon$ or $\Delta\sigma$. It has since been used to model the behavior of short fatigue cracks for both LEFM and EPFM conditions [*21*]. The choice of using $\Delta\epsilon$ or $\Delta\sigma$ in Eq 9 depends on the testing conditions. For stresses (given in MPa) above the cyclic yield in IMI 829 at room temperature [*13*]

$$\Delta\sigma \simeq 3217\Delta\epsilon_p^{0.31} \tag{10}$$

where $\Delta\epsilon_p$ is the plastic strain range given in percent. The results of strain control tests on plain LCF specimens suggest that the macroscopic $\Delta\epsilon_p$ is less than 1% of the elastic strain, $\Delta\epsilon_e$, for a peak shakedown stress of 650 MPa [*13*]. Stress range is therefore an appropriate parameter to describe the experimental crack growth rate data in this study. Integration of Eq 9 yields

$$\log_e a = BN + A \tag{11}$$

where A is a constant. This shows that B can be determined from the gradient of lines fitted to CFM crack growth data in $\log_e a$ versus N plots (Fig. 5). The stress dependence of B is illustrated in Fig. 10 and is described by

$$B = 3.2 \times 10^{-16}[\Delta\sigma_{eff}]^{4.5} \tag{12}$$

Substituting Eq 12 into Eq 9 yields the following crack growth rate expression (all length dimensions in μm, stress range in MPa, and crack growth rate in μm/cycle)

$$da/dN = 3.2 \times 10^{-16}[\Delta\sigma_{eff}]^{4.5} \cdot a \tag{13}$$

Values of B, determined from surface corner crack specimen data and produced at maximum stresses of 350, 400, 450, and 500 MPa and R of 0.1 by Spence [*27*] on identical material, are included in Fig. 10. The end of MCG occurs at greater crack sizes in these tests, which makes definition of the CFM crack growth line more difficult. However, a reasonable agreement with 650 MPa data is apparent. It should also be noted that a curve of U ($\Delta\sigma_{eff}/\Delta\sigma$) versus R, generated from Fig. 3, was used to calculate $\Delta\sigma_{eff}$ and carries the assumption that U is independent of σ_{max}.

Equation 13 may be used to predict crack propagation lives without considering microstructure-dependent crack growth assuming that an imaginary flaw exists after the first cycle. The size of this starter flaw, a_s, is given by the exponential of constant A in Eq 11 plus the specimen slit size. Data presented in this study show scatter in a_s, suggesting that the calculated starter flaw size may be dependent on microstructure and stress [*11*].

Life Predictions

Fatigue lives may be calculated by the separate integration and then addition of expressions for MCG and CFM crack growth or simply by integration of the latter alone, assuming an initial starter flaw size. For MCG a series of expressions of the form given in Eq 8 are evaluated between an initial crack size a_0 to a_{crit} such that

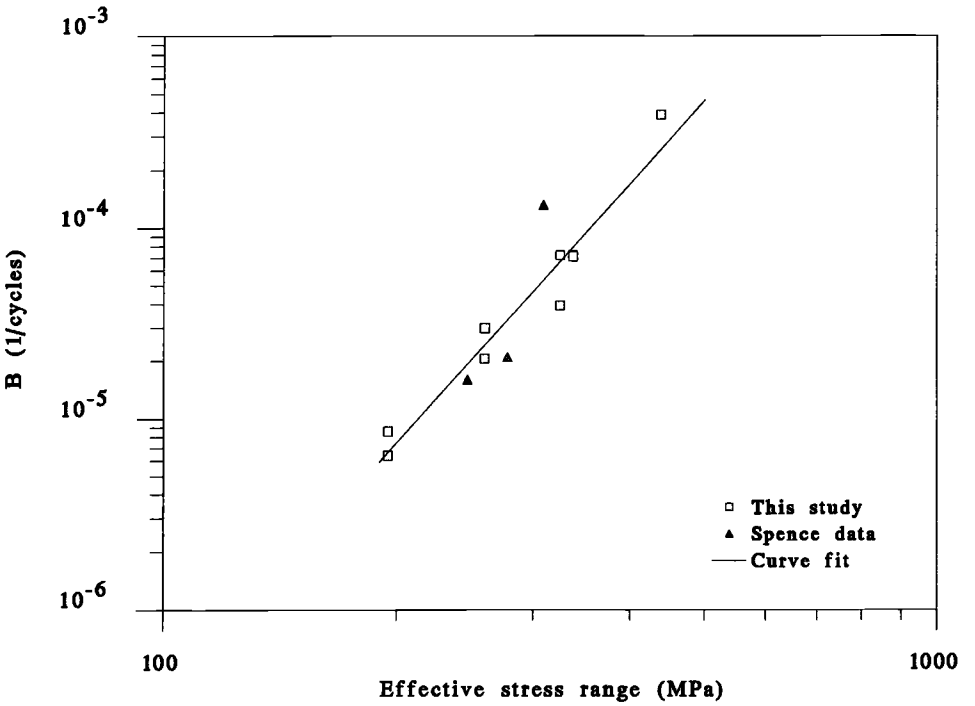

FIG. 10—*Effect of effective stress range on parameter* B.

$$N_{MCG} = \frac{1}{Q}\left(\int_{a_0}^{d_1} \frac{da}{a(d_1 - a)} + \int_{d_1}^{d_2} \frac{da}{a(d_2 - a)} \cdots + \int_{d_{i-1}}^{a_{crit}} \frac{da}{a(d_i - a)}\right) \quad (14)$$

where Q is the product $4 \times 10^{-18} \cdot \Delta\sigma_{eff}^5$. The use of a_0 assumes that crack nucleation occurs immediately after the first cycle. Its size is controlled by the engineering surface finish of the component [*28*] or the material processing route. Microcrack sources may be submicron surface discontinuities produced during machining operations or geometrical discontinuities created at the interface of slip bands and stronger matrix material on smooth polished surfaces. In polished IMI 829 specimens, cracks were found to nucleate at α-colony boundaries [*15*].

The CFM crack propagation life N_{CFM} can be determined through integration of Eq 13 between a_{crit} and the crack size, a_f, leading to burst, i.e.

$$\int_{N_{MCG}}^{N_f} dN = \frac{1}{B}\int_{a_{crit}}^{a_f} \frac{da}{a} \quad (15)$$

where B is given by Eq 12. The final crack size is dependent on stress and component design and can be measured from failed test parts. Total fatigue life is simply the sum of N_{MCG} and N_{CFM} or is calculated by the integral in Eq 15, replacing a_{crit} with a_s and N_{MCG} with N equal to 1.

Experimental crack growth rate versus crack length data are compared in Fig. 11 with curves generated from the model. An excellent correlation is observed despite the limited data in the MCG regime. The ability of the model to describe MCG would be more severely tested if cracks were inspected more frequently.

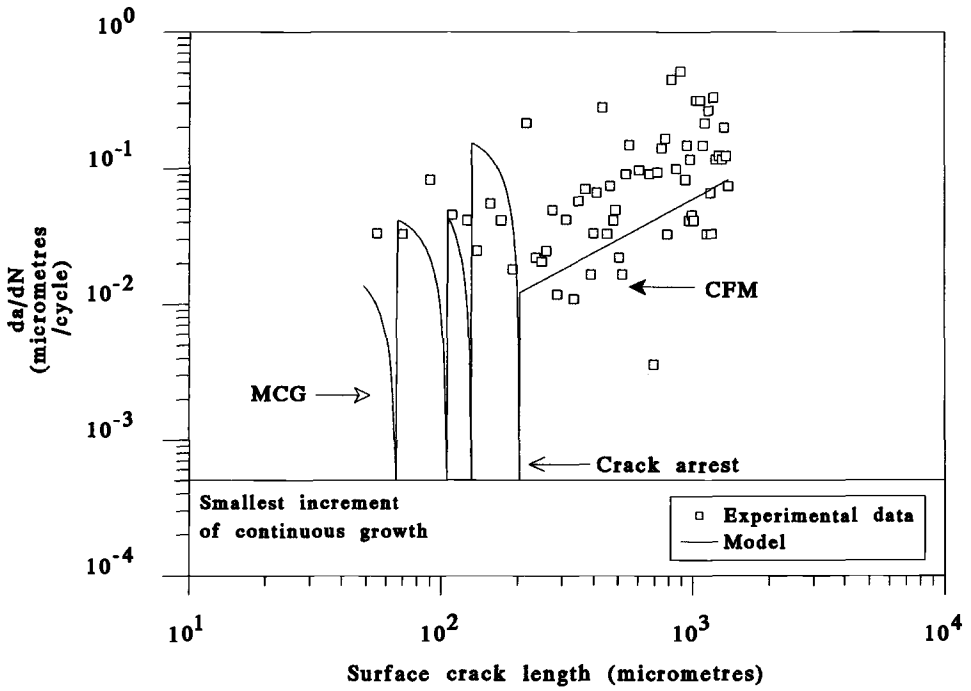

FIG. 11—*Crack growth rate* (da/dN) *versus crack length data from* R *of 0.3 test. The curve shows the short crack behavior model.*

Conclusion

Two empirical growth rate expressions describing the behavior of short fatigue cracks in a near-α titanium alloy have been formulated in terms of crack length and effective stress range. The first expression describes microstructure-dependent crack growth. The second describes the propagation of cracks under LEFM or EPFM conditions assuming continuum fracture mechanics. In generating these expressions, procedures were established to determine crack opening stress and the critical crack length above which continuum fracture mechanics apply.

References

[1] Paris, P. C., "The Fracture Mechanics Approach to Fatigue," *Fatigue—An Interdisciplinary Approach,* J. J. Burke, N. L. Reed, and V. Weiss, Eds., Plenum Press, New York, 1964, pp. 107–132.

[2] Kitagawa, K. and Takahashi, S., "Applicability of Fracture Mechanics to Very Small Cracks or the Cracks in the Early Stage," *Proceedings,* Second International Conference on Mechanical Behavior of Materials, American Society of Metals, Boston, 1976, pp. 627–631.

[3] Leis, B. N., "Discussion of the Short Crack Effect in Airframe Materials and Components," *Behavior of Short Cracks in Airframe Components, Proceedings,* the Fifty-Fifth Meeting of the AGARD Structures and Components Panel, Toronto, Canada, 1982, CP-328, AGARD, Neuilly-sur-seine, France.

[4] Harrison, G. F., "Modern Aero-Engine Disc Lifting Philosophies," RAE Technical Report TR91012, Procurement Executive, Ministry of Defence, Farnborough, UK, 1991.

[5] Knott, J. F., *Fundamentals of Fracture Mechanics,* Butterworth & Co., Ltd., London, 1973, p. 134.

[6] Lankford, J., "The Growth of Small Fatigue Cracks in 7075-T6 Aluminium," *Fatigue of Engineering Materials and Structures,* Vol. 5, No. 3, 1982, pp. 233–248.

[7] Morris, W. L., "The Noncontinuum Crack Tip Deformation Behavior of Surface Microcracks," *Metallurgical Transactions A,* Vol. 11A, July 1980, pp. 1117–1123.

[8] Neal, D. F. and Blenkinsop, P. A., "Effect of Heat Treatment on Structure and Properties of IMI 829," *Titanium '80, Science and Technology,* H. Kimura and O. Izumi, Eds., Metallurgical Society of AIME, Warrendale, PA, 1980, pp. 1287–1294.

[9] Duncan, R. M., Goosey, G. E., Jeal, R. H., and Postans, P. J., "Process Development and Evaluation of Gas Turbine Components in IMI 829," *Titanium '80, Science and Technology,* H. Kimura and O. Izumi, Eds., Metallurgical Society of AIME, Warrendale, PA, 1980, pp. 430–439.

[10] Eylon, D. and Hall, J. A., "Fatigue Behavior of Beta Processed Titanium Alloy IMI 685," *Metallurgical Transactions A,* Vol. 8A, June 1977, pp. 981–990.

[11] Hardy, M. C., "Modelling the Behaviour of Short Fatigue Cracks in a Near-Alpha Titanium Alloy at Room Temperature," DRA Technical Report TR93060, Farnborough, UK, 1993.

[12] Mom, A. J. A., "Working Document for the AGARD Cooperative Test Programme on Titanium Alloy Engine Disc Material," NLR Technical Report TR84022L, National Lucht-en Ruimtevaart Laboratum, The Netherlands, 1984.

[13] Hardy, M. C., "Low Cycle Fatigue of IMI 829 at Room and Elevated Temperature," DRA Technical Report TR91070, Farnborough, UK, 1991.

[14] Wilkinson, C., "Development of Pulsed DC Crack Propagation Equipment," Royal Aerospace Establishment Technical Memorandum TM P1159, Farnborough, UK, 1990.

[15] Hardy, M. C., "The Behaviour of Naturally Initiated Short Fatigue Cracks in a Near-α Titanium Alloy at Room Temperature," DRA Technical Report TR93046, Farnborough, UK, 1993.

[16] Brown, M. W., "Interfaces Between Short, Long and Non-Propagating Cracks," *The Behaviour of Short Fatigue Cracks,* K. J. Miller and E. R. de los Rios, Eds., Mechanical Engineering Publications, London, UK, 1986, pp. 423–439.

[17] Lankford, J., "The Influence of Microstructure on the Growth of Small Fatigue Cracks," *Fatigue and Fracture of Engineering Materials and Structures,* Vol. 8, No. 2, 1985, pp. 161–175.

[18] Larsen, J. M., Jira, J. R., and Weerasooriya, T., "Crack Opening Displacement Measurements on Small Cracks in Fatigue," *Fracture Mechanics: Eighteenth Symposium, ASTM STP 945,* D. T. Read and R. P. Reed, Eds., American Society for Testing and Materials, West Conshohocken, PA, 1988, pp. 896–912.

[19] Pickard, A. C., "Stress Intensity Factors for Cracks with Circular and Elliptical Crack Fronts

Determined by 3D Finite Element Methods," *Numerical Methods in Fracture Mechanics,* D. R. J. Owen and A. R. Luxmore, Eds., Pineridge Press, Swansea, UK, 1980, pp. 599–614.

[20] Hobson, P. D., "The Formulation of a Crack Growth Equation for Short Cracks," *Fatigue of Engineering Materials and Structures,* Vol. 5, No. 4, 1982, pp. 323–327.

[21] Hobson, P. D., Brown, M. W., and de los Rios, E. R., "Two Phases of Short Crack Growth in a Medium Carbon Steel," *The Behaviour of Short Fatigue Cracks,* K. J. Miller and E. R. de los Rios, Eds., Mechanical Engineering Publications, London, UK, 1986, pp. 441–459.

[22] Morris, W. L., James, M. R., and Buck, O., "Growth Rate Models for Short Surface Cracks in Al 2219-T851," *Metallurgical Transactions A,* Vol. 12A, January 1981, pp. 57–64.

[23] Yates, J. R. and Grabowski, L., "Fatigue Life Assessment Using a Short Crack Growth Model," *Fatigue '90,* H. Kitagawa and T. Tanaka, Eds., Materials and Component Engineering Publications Ltd., Edgbaston, UK, 1990, pp. 2369–2376.

[24] Eylon, D., Hall, J. A., Pierce, C. M., and Ruckle, D. L., "Microstructure and Mechanical Properties Relationships in the Ti-11 Alloy at Room and Elevated Temperatures," *Metallurgical Transactions A,* Vol. 7A, December 1976, pp. 1817–1826.

[25] Price, A. T. and Elder, W. J., "High Strain Fatigue and Crack Propagation in Type 316 Steel," *Journal of the Iron and Steel Institute,* Vol. 24, June 1966, pp. 594–598.

[26] Dawson, R. A. T., Elder, W. J., Hill, G. J., and Price, A. T., "High-Strain Fatigue of Austenitic Steels," *Thermal and High Strain Fatigue,* The Metals and Metallurgy Trust, London, 1967, pp. 239–269.

[27] Spence, S. H., "Small Crack Propagation in a Near Alpha Titanium Alloy, IMI 829," Ph.D thesis, University of Swansea, UK, 1990.

[28] Miller, K. J., "Initiation and Growth Rates of Short Fatigue Cracks," *Fundamentals of Deformation and Fracture,* B. A. Bilby, K. J. Miller, and J. R. Willis, Eds., Cambridge University Press, UK, 1984, pp. 477–500.

W. John Evans,[1] *Philip J. Nicholas,*[1] *and Stuart H. Spence*[1]

The Impact of Microstructural Interactions, Closure, and Temperature on Crack Propagation Based Lifing Criteria

REFERENCE: Evans, W. J., Nicholas, P. J., and Spence, S. H., **"The Impact of Microstructural Interactions, Closure, and Temperature on Crack Propagation Based Lifing Criteria,"** *Advances in Fatigue Lifetime Predictive Techniques: 3rd Volume, ASTM STP 1292,* M. R. Mitchell and R. W. Landgraf, Eds., American Society for Testing and Materials, 1996, pp. 202–219.

ABSTRACT: This paper addresses the problem of predicting crack development at a stress concentration feature from simple laboratory crack growth data. It uses a specifically designed double edge notch geometry as a test vehicle and growth rates generated on standard corner crack and compact tension specimens. A coarse-grained, near-alpha titanium alloy is employed to emphasize any microstructural interaction effects. The bulk of the work is at ambient temperature with a small amount of data obtained at 300°C. It is shown that at low stress (350 MPa), conventional fracture mechanics, without an allowance for crack closure, can correctly predict both crack shape development and cyclic life. The only significant errors occur when the crack front is retarded by prior beta or alpha colony boundaries. These tend to lead to pessimistic predictions. At 550 MPa, however, there is significant notch root plasticity that induces crack closure. An allowance for notch closure in the numerical procedures permits a more accurate prediction of crack shape and cyclic life at this stress level. To support the computer models, a detailed assessment of closure is made using potential difference (PD), strain gage, and replica techniques.

KEYWORDS: damage tolerance, database lifing, notch root closure, closure measurement, crack shapes, small crack growth, microstructural interactions, life predictions

Increasingly, fracture mechanics techniques are being used to establish service lives for critical engineering components. "Damage tolerant design" and "retirement for cause" are well-documented approaches for the aerospace industry [*1–3*]. In both cases, the number of cycles for propagation from an initial flaw to a maximum critical crack size is established using laboratory growth rate data and a knowledge of stress conditions in the component. The starting defect size, however, introduces a not insignificant level of uncertainty in the calculated lives. NDI threshold values are used, but in many cases these provide dimensions greater than the flaws typically present. Consequently, the calculations tend to be pessimistic. The database lifing [*1*], or equivalent initial flaw size approach, has been introduced to minimize this limitation. It effectively applies the fracture mechanics method retrospectively to laboratory specimen failures and component test data. Knowing the cyclic life, the flaw size responsible for the observed number of cycles can be established. By evaluating a large database, a statistical assessment of these pseudo flaws can be made, thereby allowing an appropriate maximum size for component lifing to be established.

[1]Reader and senior research assistants, respectively, IRC, Materials Engineering, University of Wales Swansea, Singleton Park, Swansea, Wales SA2 8PP, UK.

The use of specimen and component test results introduces additional difficulties. Service components largely operate under essentially elastic conditions with only limited plasticity at some stress concentration features. In contrast, laboratory tests tend to concentrate on the more highly stressed/lower life end of the *S-N* curve, while component tests are often "overstressed" to minimize the testing time. Database lifing carries the assumption that conditions are the same for the input data and the component operating in service, which clearly is not always the case. Plasticity and associated effects, for instance, do not ratio linearly with applied stress. Clearly, it is essential to quantify the scale of these differences to minimize errors. The present program was set up to address this need. The paper details some of the more significant findings.

Experimental Program

The objective of the research scheme was to use data generated on conventional crack propagation specimens to predict crack development at a notch using state-of-the-art analysis methods. It was argued that this approach should provide a realistic assessment of current technology and should highlight areas where further development is necessary.

The material selected for the exercise was the titanium alloy Ti 5331 (Ti, 5.5Al, 3.5Sn, 3Zr, 1Nb, 0.25Mo, 0.35Si).[2] It is a near-alpha alloy that has seen service applications in gas turbine engines. From the point of view of this program, it has the advantage of a coarse microstructure with a prior beta grain size of approximately 0.5 mm that facilitates the characterization of small crack growth response. The specimens were taken from barstock material that had been given a beta solution treatment at 1050°C for 30 min followed by air cooling and "aging" at 625°C for 2 h. The resultant microstructure consisted largely of basketweave alpha with some small regions of alignment. The room temperature stress-strain characteristics of the alloy are recorded in Table 1.

The base data at room temperature and 300°C were obtained from part-through cracks in corner crack (CC) specimens and through cracks in compact tension (CT) specimens. The CC design was an industry standard, as illustrated in Fig. 1. Crack growth measurements were made over a range of stresses from 450 to 600 MPa. The starter slit was 0.25 mm deep by 0.1 mm thick, and cracks were allowed to develop to a depth of 4 mm. The CT specimens were 12.5 mm thick with the overall dimensions as shown in Fig. 2. The data obtained at 20° and 300°C, respectively, are presented in Figs. 3 and 4. In both cases there are two regimes, each of which can be described by a power law relationship of the form

$$\frac{da}{dN} = C\Delta K^m \tag{1}$$

with parameters C and m recorded in Table 2.

The notch specimen was a double edge notch (DEN) configuration as shown in Fig. 5. The dimensions at the base of the notch root were the same as the CC geometry. The notch radius was 3 mm, which gives an elastic stress concentration factor, K_t, of 1.9 with respect to the net section. Although freely initiating cracks were studied, the bulk of the work involved crack growth from a machined starter flaw in a similar way to the CC specimen. The DEN was tested over a range of stresses at a frequency of 1 Hz, which is consistent with the base data. The numerical assessment, however, focused on two stress levels: 350 and 550 MPa. A finite element stress analysis based on cyclic stress-strain behavior showed that the former is essentially an elastic condition, while the latter displays substantial plasticity at

[2]Weight percentage concentrations.

TABLE 1—*Monotonic and cyclic properties for IMI829.*

Material Properties	
Elastic modulus	1.2×10^5 MPa
Monotonic yield stress	820 MPa
Monotonic yield strain	6×10^{-3}
Tensile strength	926 MPa
Cyclic yield stress	620 MPa
Cyclic yield strain	5.17×10^{-3}

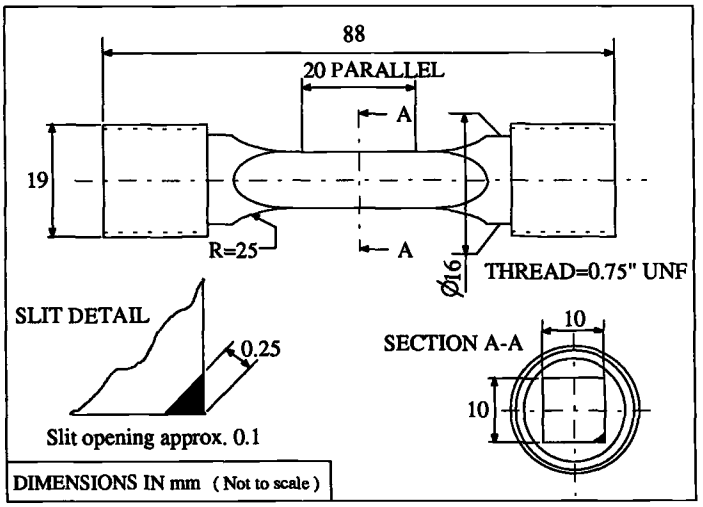

FIG. 1—*CC specimen.*

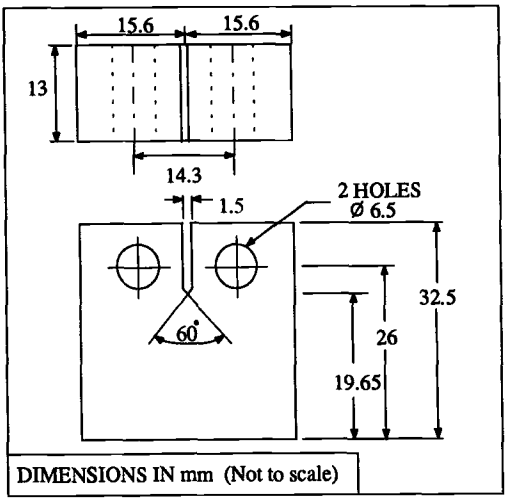

FIG. 2—*CT specimen.*

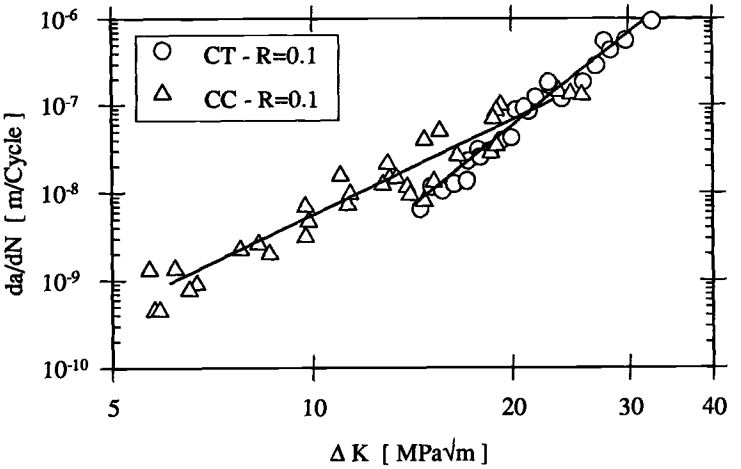

FIG. 3—*Crack growth rate data at room temperature.*

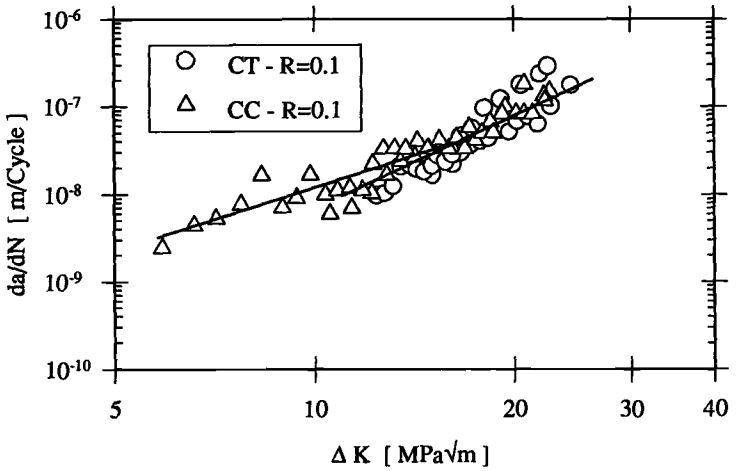

FIG. 4—*Crack growth rate data at 300°C.*

TABLE 2—*Growth rate parameters at* R = *0.1.*

Specimen	Regime, ΔK, $MNm^{-3/2}$)	m	C, MN/m	Temperature, °C
CC	$6.1 < \Delta K \leq 23$	3.6	1.4×10^{-12}	20
CT	$14.4 \leq 23\Delta K \leq 35$	6.1	6.8×10^{-16}	20
CC	$5.8 \leq \Delta K < 16$	2.4	4.8×10^{-11}	300
CC	$16 \leq \Delta K < 37$	3.5	2.2×10^{-12}	300
CT	$12.3 \leq \Delta K \leq 26.3$	3.5	2.4×10^{-12}	300

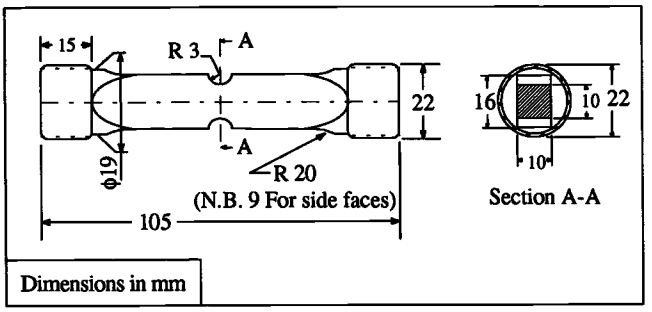

FIG. 5—*DEN specimen.*

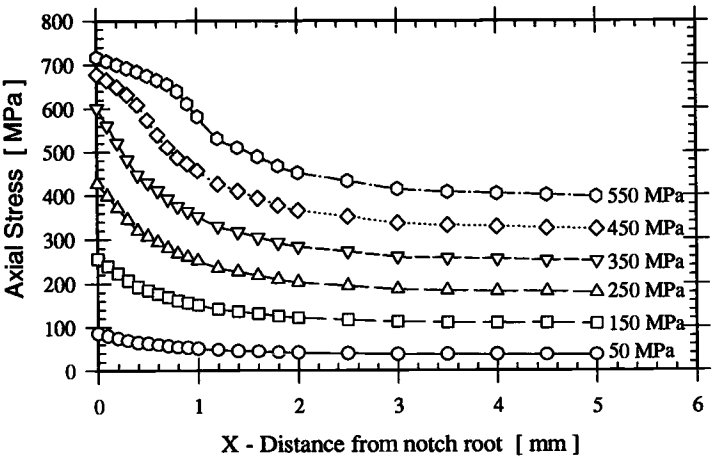

FIG. 6—*The variation of axial stress with distance in the DEN specimen from the FE analysis.*

the notch root. The difference is evident from Fig. 6, which demonstrates how the axial stress varies with distance from the root for a range of applied stresses. This demarcation is consistent with the cyclic lives for freely initiating cracks at these stress levels (Table 3).

A finite element package, which had been developed in-house, was used to analyze both uncracked and cracked double-edge notch geometries. The 3-D program is based on standard 20-noded bricks and employs reduced integration methods for plasticity. Stress-strain response is modeled using Von Mises effective stress-strain criteria and a piecewise segmentation of the material hardening curve to allow for a nonlinear hardening response. In the case of cracked geometries, meshes were set up for the individual elliptical shapes measured on tested specimens. The program then calculated J integral values by means of the surface integral suggested by Murakami and Sato [*4*]. The J integral values were used to

TABLE 3—*Cyclic response.*

Stress, MPa	Life to First Crack
350	>500 000
550	22 000

establish stress intensity values, K, around the crack fronts. The validity of this package was established by comparing its predictions for a number of standard elastic and elastic-plastic cracked geometries with known analytical solutions.

Crack growth for both CC and DEN specimens was monitored by computer-controlled optical and potential difference (PD) techniques. The PD system used a 30-A pulsed d-c supply that permitted resolution of crack length to better than 0.01 mm. A full finite element calibration of the PD facility for part-through cracks within the influence of the notch was carried out prior to the test program [5]. Characterization of the crack shapes that developed was aided by a heat-tinting technique. The typical variation in crack length along the notch root (a) with length down the side face (b) is shown for DEN tests at 350 MPa in Fig. 7. The PD system was also used to monitor crack closure. This involved the application of a single triangular waveform of 100-s duration at intervals during crack development in selected tests. For some tests, strain gages were also used to monitor closure. In a few cases, acetate replicas were applied at specific stress points during the cycle to gain a visual interpretation of the other methods.

Numerical Procedure

The computer program applied the combined small and long crack data from the CC and CT measurements to predict not only cyclic lives for the notches but also to simulate crack shape development. The algorithm used is based on the work of Pickard [6]. Provided the growth rate data are consistent with the power law relationship of Eq 1, the number of cycles for a crack to grow an increment $\Delta a = (a_2 - a_1)$ is given by

$$\Delta N = \frac{1}{CY^m F(\Delta\sigma)^m \pi^{m/2}} \left\{ \frac{a_2^{(1-m/2)} - a_1^{(1-m/2)}}{1 - m/2} \right\} \tag{2}$$

with the stress intensity factor given by

$$K = M_G M_S M_B F(\Delta\sigma)\phi(\pi a)^{1/2} \tag{3}$$

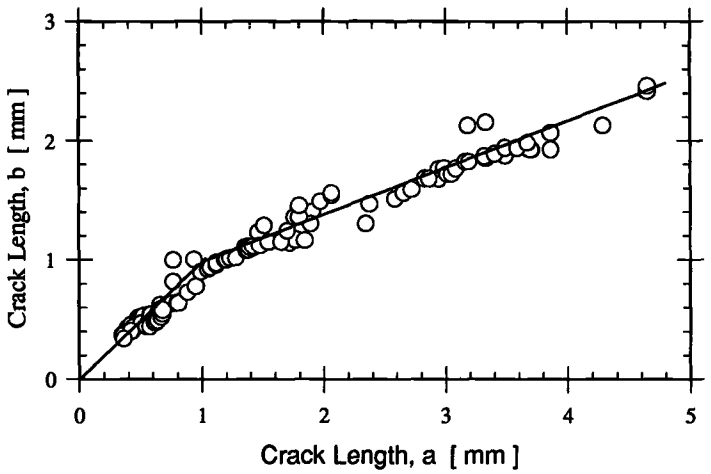

FIG. 7—*Crack shape development at 350 MPa in the DEN specimen (*a = *notch root,* b = *side face).*

where M_G, M_S, and M_B are general, side-face, and back-face corrections factors, respectively, and ϕ accounts for crack shape ellipticity. The Y factor in Eq 2 is $(M_G M_S M_B \phi)$. The stress function, $F(\Delta\sigma)$, describes how the elastic stress field changes with distance from the notch root.

In the present work, $F(\Delta\sigma)$ is a polynomial function. For an applied stress of 1 MPa, the axial stress field along the outside surface has the form

$$\sigma_y(x) = 1.712 - 1.400x + 1.121x^2 - 0.614x^3 + 0.227x^4 - 0.053x^5 + 0.007x^6 - 0.0004x^7 \quad (4)$$

where x is the distance from the notch root. It was assumed that the stress in the notch root is constant.

Predictions for Elastically Stressed Notch

The numerical procedures assume elastic behavior and should, therefore, be effective for crack development at 350 MPa. The validity of this statement has been clearly demonstrated in a number of previous publications [*7,8*]. For convenience, the main considerations are reiterated here.

A sensitive indicator of the effectiveness of the calculation method is the crack shape that develops at the notch. The optical measurements made during fatigue tests together with the heat-tinting exercise on cracked specimens provided an accurate picture for each of the stress levels considered. The pattern of behavior at 350 MPa is reproduced in Fig. 8. The lines represent the macroscopic crack front. On a finer scale, it was evident that the profile was serrated due to local microstructural interactions. These perturbations are not taken into consideration in the present work. Figures 7 and 8 demonstrate that, for this essentially elastic state, the crack fronts are strongly elliptical. Figure 8 also includes shapes predicted by the computer program. It is evident that these are consistent with the measurements. Figure 9 emphasizes that not only are the correct shapes predicted but that each is achieved at the right cyclic life. It was found that the only factor to significantly upset this correlation was a strong microstructural interaction [*7*]. These interactions involved arrests for extended periods of time, usually as a result of the crack interacting with a prior beta grain boundary, probably as a consequence of the adjacent grain being unfavorably orientated. Figure 10

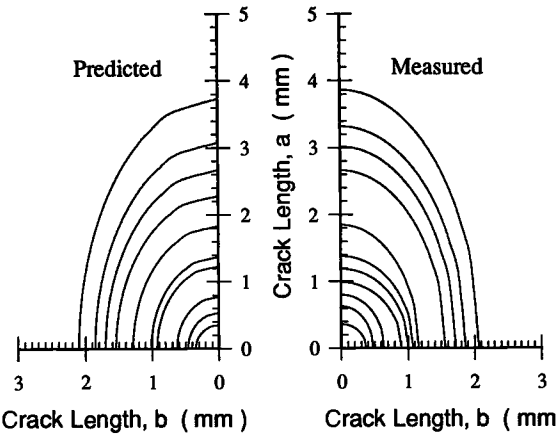

FIG. 8—*Measured and predicted crack shapes at 350 MPa in the DEN specimen.*

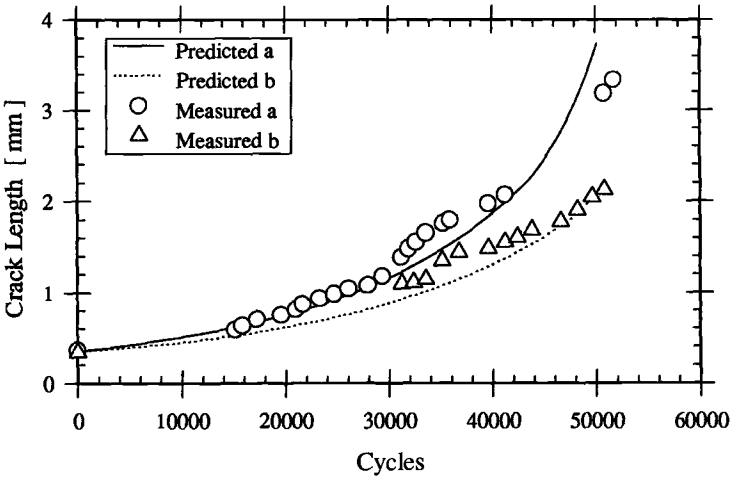

FIG. 9—*Measured and predicted growth curves at 350 MPa in the DEN specimen.*

clearly demonstrates an arrest of 16 550 cycles at one of these microstructural barriers for a crack growing along the side face of a DEN specimen.

In Fig. 11, the same analysis is applied to crack shape development at 550 MPa. Clearly, the measured crack shapes are less elliptical than those at 350 MPa (Fig. 8). This is presumably due to some restraint along the notch root. The computer program does not take the restraint into consideration and hence predicts more elliptical crack shapes. The predicted lives are also considerably shorter than the actual measurements (Fig. 12). This suggests that it is restraint along the notch and not acceleration at the side face that causes the discrepancies.

The discrepancies at 550 MPa were attributed to plasticity-induced closure at the notch root. The fact that it was not due simply to plastic redistribution of notch root stresses is testified by tests at high R (0.6) and a maximum stress of 550 MPa. The high R removes the closure influence, but the high stress maintains notch root plasticity. Consequently, the crack

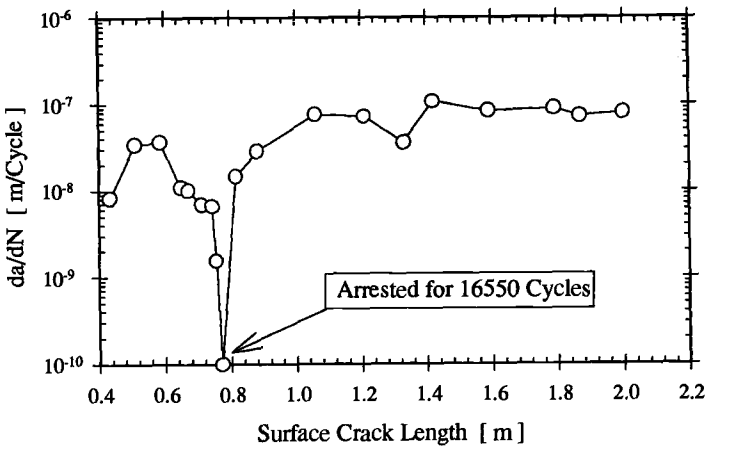

FIG. 10—*Crack arrest for side face growth in a DEN specimen.*

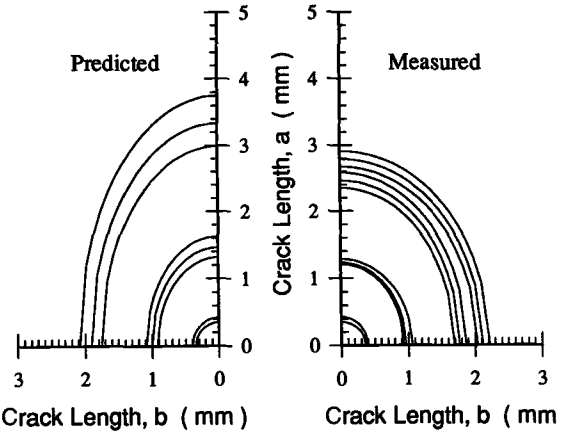

FIG. 11—*Predicted and measured shapes at 550 MPa in the DEN specimen.*

shape returns to the elliptical form observed at 350 MPa, confirming the role of closure at R = 0.1 (Fig. 13). On this basis, a detailed study was made of notch-root-induced closure, which subsequently led to modification of the numerical lifing package.

Characterization of Crack Closure

The fact that the notch response at 350 MPa can be predicted well from the base CC and CT data suggests a similar degree of crack closure in each situation. This is consistent with the essentially elastic response of the notch and with the work of McClung, who states that closure levels at notches are simply in proportion to the elastic stress magnification [*9*]. The CC tests involved stresses in the range from 450 to 600 MPa, while the peak elastic stress for the notch is 665 MPa. The contrasting response for notch tests at 550 MPa suggests a closure influence over and above the conventional crack tip effects operating in the uni-

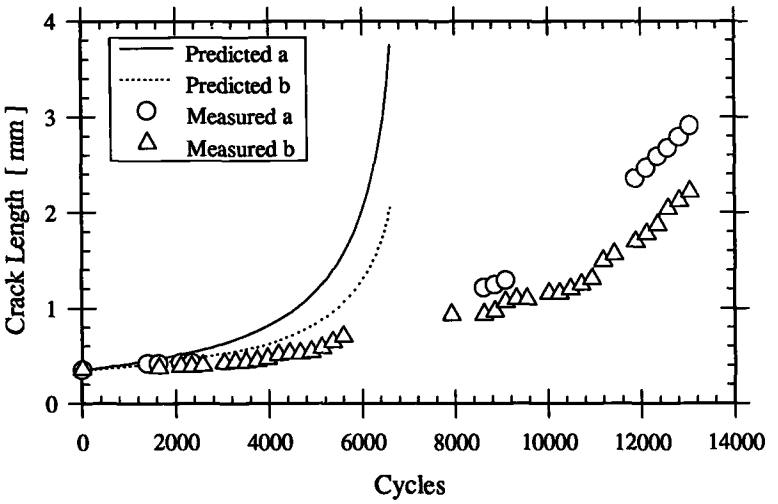

FIG. 12—*Measured and predicted growth curves for 550 MPa in the DEN specimen.*

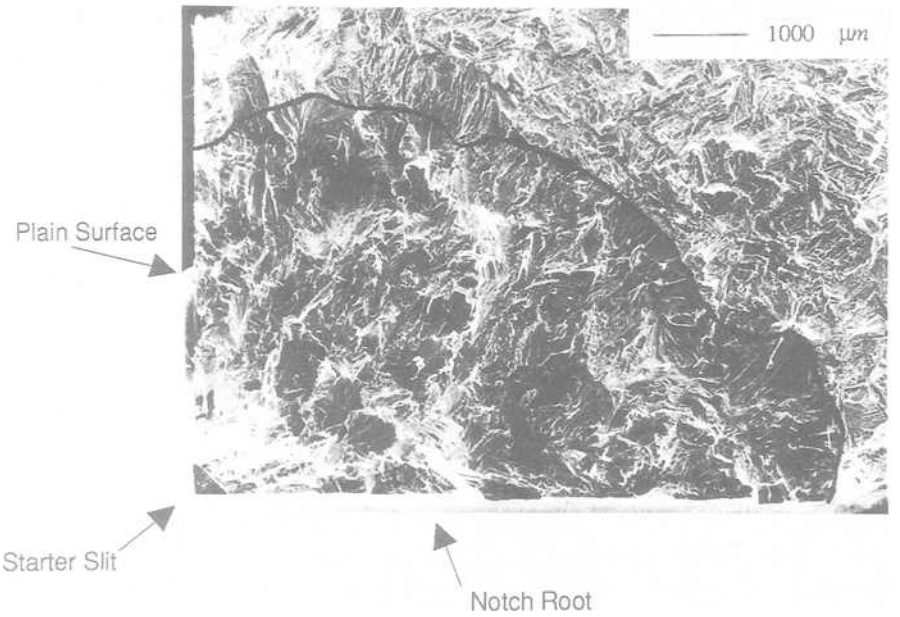

FIG. 13—*Elliptical crack shape that developed at 550 MPa and* R = *0.6.*

formly stressed CC specimens. The closure studies set out to quantify this additional contribution.

The closure investigation employed three techniques: PD monitoring, strain gages, and replicas. Each provides a slightly different view of the closure process, but these differences can be rationalized and together help to characterize the events taking place. Figures 14 and 15 compare strain gage and PD response at similar crack sizes for a given test. The strain gage is bonded at the crack tip and slightly offset from the crack path (Fig. 14). It monitors

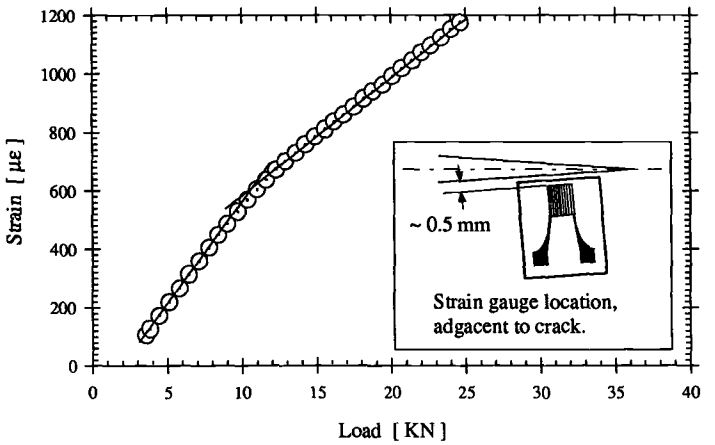

FIG. 14—*Strain gage closure curve for the plain-surface of a DEN specimen at 350 MPa. Inset illustrates the gage position.*

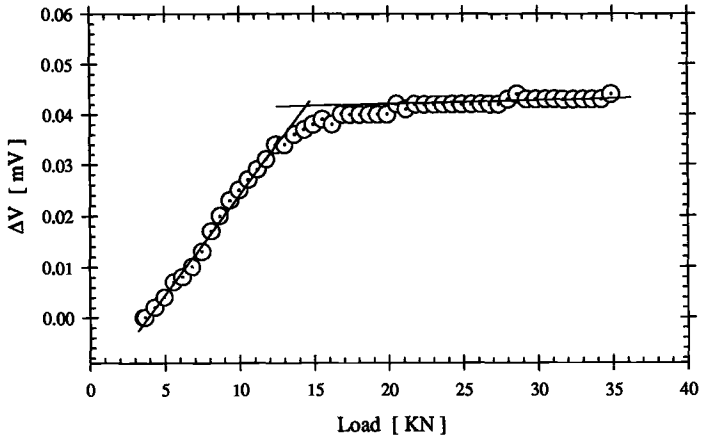

FIG. 15—*PD closure curve for DEN specimen at 350 MPa.*

changes in local deformation conditions as the degree of opening and the compliance varies. The PD variations are due to changes in resistance as the area of crack in contact alters. Both graphs can be subdivided into three regimes. At high load there is a linear region that is almost horizontal in the case of the PD signal. This gives way to an intermediate zone in which the slope changes continuously. Finally, there is a further linear region at low loads with a much higher slope than that at high load. The upper transition point from linearity for the strain gages correlates reasonably well with the lower PD transition point. This is apparent from a visual comparison of Figs. 14 and 15 and confirmed by measurements from both techniques over a range of crack lengths (see Fig. 16).

Replicas applied at fractions of the peak load provided information on the different closure conditions associated with each PD regime. During the upper linear region, the surface profile demonstrated that the crack was fully open. At the point of change to the intermediate regime, the crack tip first comes into contact. The length in contact then continues to increase until, at the onset of the lower linear regime, about 100 to 200 μm of

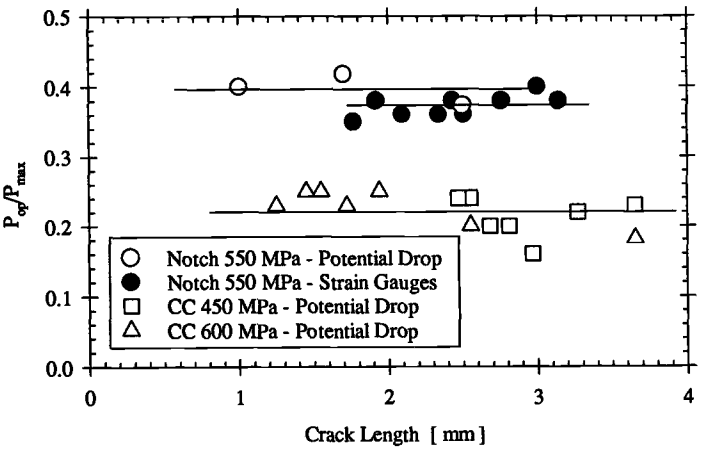

FIG. 16—P_{op}/P_{max} *against crack length for CC and DEN specimens.*

crack has closed. As the load continues to decrease, the closed region increases at a significant rate. Referring back to the strain gage record in Fig. 14, it is important to realize that the measurement is being made adjacent to the crack path and at the point when the crack tip has just passed the gage. Thus the strain gage still sees an open crack, even though the first 100 to 200 μm of crack length away from the tip has closed. In contrast, the PD signal senses this contact. This difference could account for the correlation of upper and lower transition points from the gage and PD records, respectively. It is argued, on the basis of the correlation and the information reported below, that the lower PD transition point is a valid measurement of crack closure and the most appropriate value for establishing an effective driving force. The fact that it relates to about 100 to 200 μm of closed crack suggests that an area relating to this dimension is required for the closure to become effective. It is this value that is reported below for both CC and notch specimens.

Closure in Corner Crack Specimens

The measured PD closure response for the CC specimens is summarized in Fig. 16. The graph includes data for applied stresses of 450 and 600 MPa. It plots the ratio of opening load (P_{op}) to maximum applied load (P_{max}) against crack length. It is evident that P_{op}/P_{max} is independent of both stress and crack length within the ranges studied. The line drawn through the CC results suggests an average $P_{op}/P_{max} \approx 0.22$. Figure 17 demonstrates that by using $\Delta K_{eff} = (K_{max} - K_{op})$ for this value, a good correlation is achieved between growth rate data at $R = 0.1$ and 0.6 with $m = 3.6$ and $C = 2.3 \times 10^{-12}$ (MN/m).

Closure in the Presence of Notch Plasticity

The closure response of the notch specimens is more complex, particularly at 550 MPa. The part-through cracks experience a higher level of closure at the notch root than along the side face for the larger cracks. Figure 16 presents the P_{op}/P_{max} values for PD measurements on the DEN at 550 MPa. It also includes strain gage values for the notch root. The PD and strain gage data correlate well, confirming the dominance of the notch root closure. It is evident also that the closure level along the notch root is considerably greater than that observed in CC specimens. The average P_{op}/P_{max} is approximately 0.4.

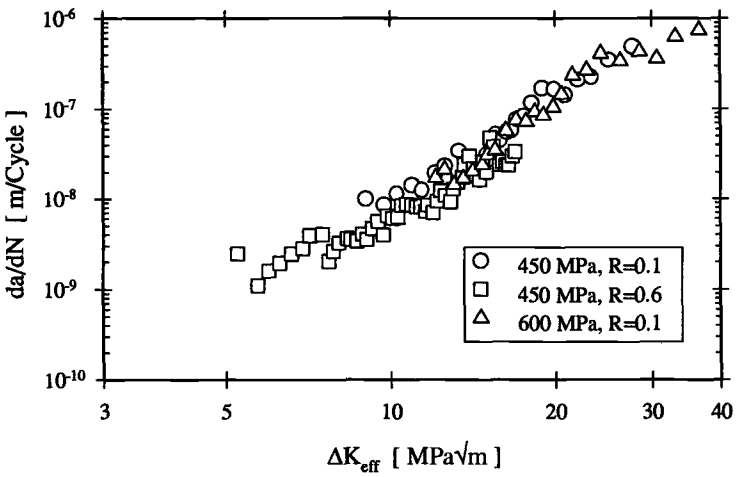

FIG. 17—*Dependence of growth rate on effective stress intensity factor for CC specimen.*

The dominance of the notch root meant that the PD method could not be used to establish closure for crack tip regions away from the root. To explore the likely variation along the side face, a 2-mm-thick version of the DEN was made in which through-thickness cracks were grown from a 0.25-mm-deep starter slit. To maintain a range of ΔK similar to the thick DEN tests, a much smaller load and hence stress was applied. The results of PD measurements on this geometry are reported in Fig. 18. The dropoff in P_{op}/P_{max} with distance from the notch root is evident. At approximately 2 mm, the values become consistent with those for the unnotched CC specimens. A more limited evaluation using strain gages on the side face of thick DEN specimens at 550 MPa confirmed this pattern of behavior.

Modeling Crack Development at Plastically Deformed Notch

On the basis of the experimental observations it was assumed that the degree of closure along the entire notch root at 550 MPa was consistent with the relationship $P_{op}/P_{max} = 0.4$. For the side face, three phases of closure were modeled. For crack lengths up to 0.75 mm from the notch root, a constant value consistent with $P_{op}/P_{max} = 0.4$ was specified. Beyond this crack length, growth is outside the influence of the notch root plastic zone. At crack lengths in excess of 2 mm, the closure level appears to fall to a value typical of plain specimens, i.e., $P_{op}/P_{max} = 0.22$. In between these extremes, it was assumed that closure decreased linearly with distance in a way similar to Fig. 18. The numerical package was modified to account for these closure values.

Confidence in the assumed notch closure levels was gained from the elastic plastic finite element analysis of the cracked specimens. The package does not model crack closure but provides information on peak stress intensity factors at any crack position. Figure 19 shows how the stress intensity factor varies with position around the crack front for a range of side face crack lengths. The crack shapes are based on the idealized forms derived from the optical measurements along the notch root and down the side face. The important positions in the present context are $\theta = 0°$ (side face) and $\theta = 90°$ (notch root). It is evident that $\theta = 0°$ and $\theta = 90°$ have similar peak stress intensity factors for the smallest crack, $a = 0.5$ mm. They then show an increasing deviation as the crack length increases to 2.5 mm. However, if the above notch closure relationships are used to determine effective stress

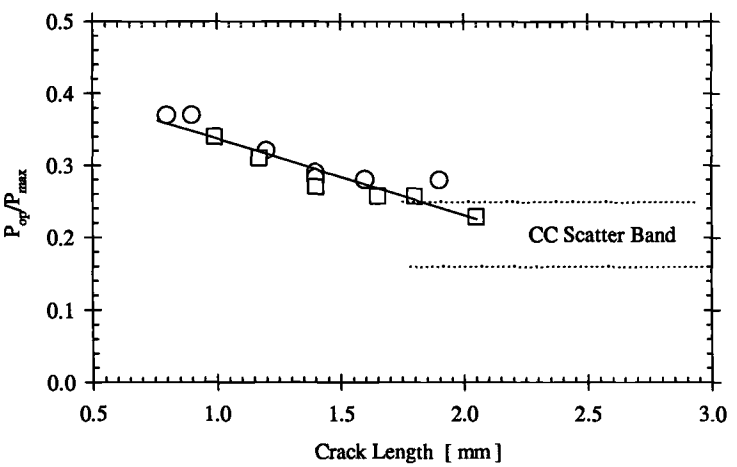

FIG. 18—P_{op}/P_{max} *for through cracks in thin DEN specimens.*

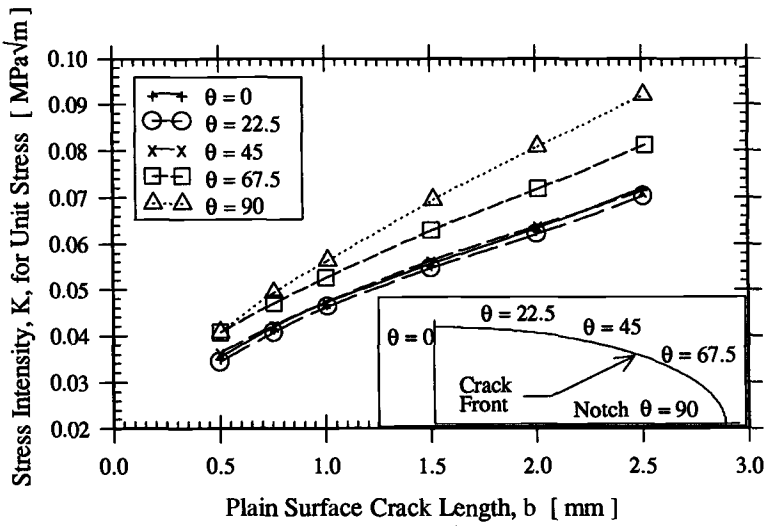

FIG. 19—*FE calculated stress intensity factors for elliptical cracks at 550 MPa in the DEN specimen. Inset defines positions along the crack front.*

intensity factors, it is found that ΔK_{eff} is virtually the same at the notch root and side face. Typical values for three crack lengths are given in Table 4.

The closure levels modeled lead to the scientifically satisfying result that the cracks are attempting to take up a shape that has a constant driving force around the crack front. Similar observations have been reported previously [*10*]. The full implications of Fig. 19 will be discussed elsewhere [*11*]. It is sufficient to point out at this stage that only the θ = 90° and θ = 67.5° positions are within the notch root plastic zone for the full range of crack lengths studied. The relatively high level of closure associated with this plasticity would account for their different response from the θ = 0°, 22.5°, and 45° positions in Fig. 19.

The results of the closure corrected modeling of crack development in the DEN at 550 MPa are presented in Figs. 20 and 21. For the calculation, the growth behavior of CC and CT specimens was re-expressed in terms of ΔK_{eff} to be consistent with the modified analysis of the DEN. Figure 20 compares the revised prediction of crack shapes with the measured values. Referring back to Fig. 11, it is evident that the degree of agreement between predicted and measured shapes has been much improved. Furthermore, Fig. 21 demonstrates

TABLE 4—*Dependence of* ΔK_{eff} *on crack front position.*

Position	K_{max},[a] MPa$\sqrt{m}$	Opening/Maximum Ratio	ΔK_{eff},[a] MPa$\sqrt{m}$	Crack Size (side face), mm
Notch root (θ = 90°)	0.041	0.4	0.024	0.5
Side face (θ = 0°)	0.035	0.4	0.021	
Notch root (θ = 90°)	0.070	0.4	0.042	1.5
Side face (θ = 0°)	0.056	0.28	0.040	
Notch root (θ = 90°)	0.092	0.4	0.055	2.5
Side face (θ = 0°)	0.072	0.22	0.056	

[a]The K values are for unit remote stress (i.e., per MPa).

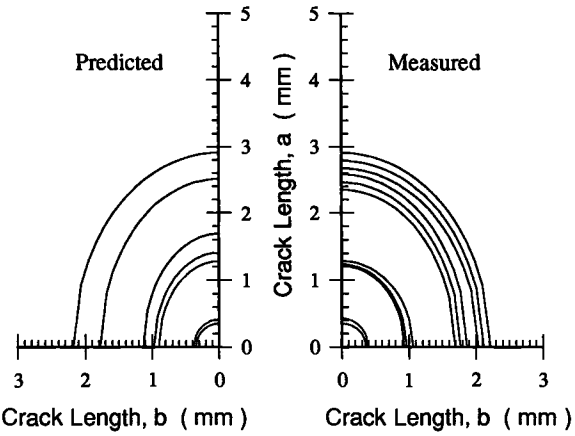

FIG. 20—*Shape prediction for the DEN at 550 MPa with closure correction.*

a much closer correlation between predicted and measured propagation lives when closure is taken into consideration, as a comparison with Fig. 12 will confirm.

Temperature Effects

The increase in temperature can introduce further difficulties with respect to predicting the life of stress concentration features. In addition to notch root plasticity and microstructural interactions, oxidation effects can affect behavior and can lead to further closure effects. Experimental difficulties also arise in attempting to measure closure loads at temperature. A detailed program is underway at Swansea to characterize these influences. Preliminary studies have focused on notch effects at stress levels where notch root plasticity is not significant, i.e., the stress/cyclic yield stress ratio, $\sigma/\sigma_{CYS} = 0.42$ to 0.53. Once again, it was found that the uncorrected data presented in Fig. 4 accurately predict both the elliptical crack shapes and notch cyclic lives at 300°C. Some typical data are presented in

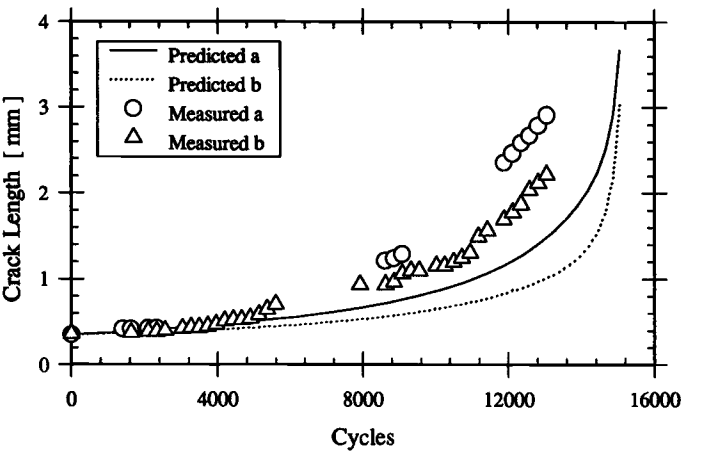

FIG. 21—*Life prediction for the DEN at 550 MPa with closure correction.*

TABLE 5—*Predicted lives at 300°C.*

Stress, MPa	*a*, mm	*b*, mm	Measured Propagation Life	Predicted Propagation Life	σ/σ_{CYS}
200	4.5	2.8	227 700	194 000	0.42
250	1.6	1.5	80 700	76 000	0.53

Table 5. To place the information in context, it is worth pointing out that σ/σ_{CYS} are 0.56 and 0.89, respectively, for the 350 and 550 MPa tests at room temperature.

Discussion

This paper has explored the effectiveness of the type of fracture mechanics analysis used in state-of-the-art component life prediction procedures. In particular, it has covered microstructural influences through the choice of a test material with a coarse unit size and has assessed the role of plasticity by evaluating a specifically designed notch over a range of stress conditions. A limited amount of data on temperature effects is also included. On the basis of this work and previously published information [*7*], it is clear that both crack shape and life to a specific crack size are well predicted provided there is not a marked microstructural influence and there is not significant notch root plasticity.

It has been reported previously [*7*] that microstructural interactions occur when the cracks address major features such as prior beta grain boundaries and alpha colony boundaries. The consequence is a retardation in growth rates leading to longer lives than the computer model predicts. In terms of establishing component lives, this might be considered acceptable albeit rather pessimistic. For the database approach, however, the retrospective use of fracture mechanics to establish starting flaw sizes might run into difficulties. The calculated maximum flaw size from a test extended by microstructural interactions could be underestimated with obvious implications for subsequent component life prediction. In practice, a large database should minimize this risk.

Plasticity has far wider reaching consequences. This influence is dominated by the resultant generation of notch root closure rather than through modification of the general stress field [*8*]. The notch root closure is in addition to closure induced by crack tip plasticity. This is evident from the modeling work at 350 MPa. For this stress, plasticity at the notch root is limited. Consequently, crack development can be predicted simply by applying laboratory data that have not been closure corrected. At 550 MPa, however, a markedly different response is evident. The cracks are less elliptical and take a larger number of cycles to grow to a given size than the simple numerical model suggests. Notch root closure is adding to the crack tip condition. Now it is essential to build closure into the numerical analysis. This again is particularly relevant for database lifing methods. These rely on laboratory tests at stresses where plasticity can be significant together with component test bed information, which is likely to be overstressed in comparison to service operating conditions. In a similar way to the microstructural interactions, failure to allow for such geometry-dependent closure will lead to pseudo flaw size values that are not appropriate for service components.

In the course of this paper it has been shown that a viable picture of closure within the DEN studied can be constructed through application of a range of experimental techniques. The PD method provides a global view of the phenomenon and has the advantage of allowing continuous monitoring. It indicates when first contact is made and provides information on when sufficient crack closure has occurred to support the compressive loads

and hence determine the effective driving force. This view contradicts earlier closure studies [*12*] that criticized the effectiveness of PD monitoring systems. Important differences here, however, are the use of corner crack specimens, the close proximity of the PD probes to the crack plane and tip, and the part-through crack geometry. The previous work tended to focus on remote monitoring of large through cracks. The replica technique is more limited from an experimental point of view but does provide information on surface effects and a visual interpretation of the PD signals. The work to date suggests that about 100 to 200 μm of surface crack length has closed at the critical P_{op} load level. The strain gage method is also dominated by surface and near-surface effects. It will, however, also be affected by the general compliance of the system and, as such, can be related directly to the PD measurements. It is argued that all three techniques are important for a full appreciation of 3-D closure, as in the case of part-through cracks at notches. The present analysis shows that it is possible to quantify this closure, although the small inaccuracies evident in the analysis suggest that our understanding is not complete. These limitations are currently being tackled by combining more specific experimental evaluations with 3-D finite element modeling.

Conclusions

1. Conventional fracture mechanics together with growth rate data from simple specimen geometries can be used to predict part-through crack development at notches without an allowance for closure provided the stress level is not sufficient to cause significant notch root plasticity (fatigue lives of 10^5 to 10^6 cycles).

2. The simple analysis has been shown to be in error if there is a major interaction between the crack front and the microstructure. Such interactions tend to result in pessimistic life predictions.

3. At stress levels where there is general yield at the notch root (lives of $<10^5$ cycles), the simple analysis predicts the wrong crack shape (too elliptical) and lives that are too short. Numerical procedures that allow for notch root closure predict the crack development correctly.

4. The 3-D crack closure at notches can be characterized by means of combined PD, strain gage, and replica techniques. At 550 MPa, $P_{op}/P_{max} = 0.4$ along the notch root. Down the side face, $P_{op}/P_{max} = 0.4$ within the notch plastic zone ($a \leq 0.75$ mm); which then decays linearly until $a = 2$ mm when it becomes constant with a value of 0.22, $P_{op}/P_{max} = 0.22$ is typical of unnotched CC specimens.

References

[*1*] Asquith, G. and Pickard, A. C., "Fatigue Testing of Gas Turbine Components," *Full-Scale Fatigue Testing of Components and Structures*, K. J. Marsh, Ed., Butterworths, London, Vol. 2, Chapter 11, 1988, pp. 210–234.

[*2*] King, T. T., Cowie, W. D., and Reimann, W. H., "Damage Tolerance Design Concepts for Military Engines," *Damage Tolerance Concepts for Critical Engine Components*, AGARD Conference Proceedings 393, AGARD, Neuilly-Sur-Seine, France, 1985.

[*3*] MIL-STD-1783, "Engine Structural Integrity Program (ENSIP)," USAF, 1984.

[*4*] Murakami, T. and Sato, T., "Three Dimensional J-Integral Calculations of Part Through Surface Crack Problems," *Computers and Structures*, 1983, Vol. 17, pp. 731–736.

[*5*] Spence, S. H., Evans, W. J., and Nicholas, P. J., "The Growth of Microstructurally Small Cracks in a Near-Alpha Titanium Alloy," *Proceedings*, Joint FEFG/ICF International Conference on Fracture of Engineering Materials and Structures, S. H. Teoh and K. H. Lee, Eds., Elsevier Science Publications, Inc., Barking, Essex, UK, 1991, pp. 673–678.

[*6*] Pickard, A. C., "The Application of 3D Finite Element Methods to Fracture Mechanics and Fatigue Life Prediction," Chapter 4, EMAS, Cradley Heath, Warley, West Mids, UK, 1986.

[*7*] Evans, W. J. and Spence, S. H., "Life Prediction Modelling for Titanium Alloys," *Theoretical*

Concepts and Numerical Analysis of Fatigue, A. F. Blom and C. J. Beevers, Eds., EMAS, Warley, UK, 1992, pp. 377–400.

[*8*] Evans, W. J. and Spence, S. H., "Modeling Fatigue Crack Growth at Notches," *Proceedings,* Conference on Processing and Properties of Materials, M. Loretto and C. J. Beevers, Ed., MCE Publications Ltd., Birmingham, UK, 1992.

[*9*] McClung, R. C., "A Simple Model for Fatigue Crack Growth Near Stress Concentrations," *Proceedings,* Innovative Approaches to Irradiation Damage and Fracture Analysis, D. L. Marriott, T. R. Mager, and W. H. Bamford, Eds., 1989 ASME Pressure Vessel and Piping Conference, Hawaii, American Society of Mechanical Engineers, New York, 1989, pp. 31–40.

[*10*] Frediani, A. and Galatdo, R., "Crack Propagation from Artificial Defects in Typical Engine Disk Materials," AGARD Report No. 769, *Damage Tolerance for Engine Structures,* AGARD, Neuilly-Sur-Seine, France, 1988, pp. 5-1 to 5-10.

[*11*] Evans, W. J. and Nicholas, P. J., to be published.

[*12*] Döker, H. and Bachmann, V., "Determination of Crack Opening Load by Use of Threshold Behavior," *Mechanisms of Fatigue Crack Closure, ASTM STP 982,* J. C. Newman and W. Elber, Eds., American Society for Testing and Materials, West Conshohocken, PA, 1988, pp. 247–259.

Jeffrey O. Bunch,[1] *Robert T. Trammell,*[1] *and Perry A. Tanouye*[1]

Structural Life Analysis Methods Used on the B-2 Bomber

REFERENCE: Bunch, J. O., Trammell, R. T., and Tanouye, P. A., **"Structural Life Analysis Methods Used on the B-2 Bomber,"** *Advances in Fatigue Lifetime Predictive Techniques: 3rd Volume, ASTM STP 1292,* M. R. Mitchell and R. W. Landgraf, Eds., American Society for Testing and Materials, 1996, pp. 220–247.

ABSTRACT: The methods used to predict crack initiation life (durability) and crack growth life (damage tolerance) of the United States Air Force/Northrop Grumman B-2 Bomber are discussed. The test matrix used to verify the methodologies is presented, followed by a discussion of each method and the results of the verification tests.

Durability analysis on the B-2 is based on a notch strain analysis method. The method uses the cyclic stress-strain properties of a material combined with the Neuber equation for strain concentration at a notch to predict crack initiation lifetimes. The method results in a design-allowable curve for durability.

Damage tolerance analyses must account for the effects of crack retardation due to overload cycles in a flight spectrum. The methods used for crack growth analysis rely on empirical parameters that are dependent on material; however, they are also often dependent on the type of spectrum. If the spectrum changes drastically, it is often necessary to recalibrate the crack growth model. A model based on phenomenon of crack closure has been developed that overcomes the need to recalibrate the model for each new spectrum. The model, referred to as the "constant closure model," was used for crack growth life prediction of metallic components in the B-2. In the constant closure model, the closure factor (CF) is the only empirical parameter. The other parameters needed to use the constant closure model are obtained from the load spectrum.

KEYWORDS: metal fatigue, aircraft fatigue, aircraft structural integrity, notch strain analysis, strain life analysis, fatigue crack growth, fatigue crack closure, constant closure model

Prediction of structural life and prevention of fatigue failures are critical to the design of new aircraft. Components subject to fatigue loading must be identified and steps taken to ensure that they are properly designed. The United States Air Force categorizes the critical parts into two categories: (1) durability critical parts—those parts whose replacement would not be economically feasible, and (2) fracture critical parts—those parts whose failure could result in the loss of the aircraft.

Durability critical parts must meet the design life of the aircraft without suffering any cracks or damage that would impair the function of the part. Fracture critical parts are designed assuming that a "rogue flaw" is present from the initial manufacture of the component. A crack growth analysis is performed using the assumed rogue flaw geometry, and this crack must not grow to failure during the life of the aircraft.

Analysis methods to predict fatigue and fracture or damage tolerance lives for metallic structures have been continuously improved with each new aircraft design. As more is

[1]Engineering specialist, senior technical specialist, and principal engineer, respectively, Northrop Grumman Corporation, B-2 Division, 8900 East Washington Boulevard, Pico Rivera, CA 90660.

understood about the basic mechanisms of fatigue crack initiation and fatigue crack growth, models have been developed that incorporate the physical processes involved. Such physical processes include the relationship of applied strain range as the important factor controlling low-cycle fatigue life and crack closure as one of the important factors influencing crack growth.

Although composite materials are used extensively on the B-2, a significant number of critical components are fabricated from metallic materials. These components include pressure bulkheads, control surface fittings, fuselage frames, and spar and rib caps. A test program was therefore performed to verify that the durability and damage tolerance methods used were accurate. The durability analysis method used was a notch strain analysis method. The damage tolerance analysis method used on the B-2 incorporated the concept of crack closure. In the following sections, the methods used to predict structural life of the metallic components on the B-2 will be presented along with experimental verification results.

Experimental Methods

An experimental program was designed to validate the durability and damage tolerance methods over a wide range of materials subjected to different loading spectra. The durability and damage tolerance methods described herein were coded into FORTRAN programs. Experimental test results were compared to the predictions of the computer codes. The experimental program involved 20 materials (various forms and heat-treat conditions of aluminum, titanium, nickel, and steel alloys). Eleven different flight spectra were employed. A previous study of the notch strain analysis method was utilized to increase the experimental database for this work [*1*]. Porter reported experimental work using F/A-18 fighter aircraft spectra. The spectra used in Ref *1* were obtained and analyzed using the current methods. These additional data increased the number of random flight spectra analyzed in the current work to 23. The experimental program permitted us to study the accuracy of the models from the following standpoints:

- Effects of materials, product form, and heat treatment.
- Effects of different notch geometries.
- Effects of different types of spectra.
- Effects of spectrum variables such as truncation.

Specimen Geometry

Figure 1 shows the nine specimen designs used to experimentally verify the durability analysis method. These specimens represent a range of side grooves and hole geometries. The load on all notch strain analysis specimens was applied uniaxially along the specimen centerline. The stress severity factors shown in Fig. 1 for each geometry are based on calculations of the elastic stress concentration factor for the notch or hole.

Crack growth specimens used to verify the constant closure model were 4-in. (102-mm)-wide panels with a central hole. A quarter elliptical flaw was initiated from one side of the hole. The procedure to introduce the flaw was to first drill a 3.2-mm (0.125-in.)-diameter hole. Using a fine tooth saw or razor knife, a corner notch was introduced on one side of the hole. The specimen was fatigue cycled until the induced flaw grew to a nominal surface length of 2.9 mm (0.113 in.) from the edge of the hole. The 3.2-mm-diameter hole was then enlarged to 6.4 mm (0.250 in.) in diameter. The end result was a sharp quarter-elliptical crack with a nominal surface length of 1.3 mm (0.050 in.) at the edge of the hole. The

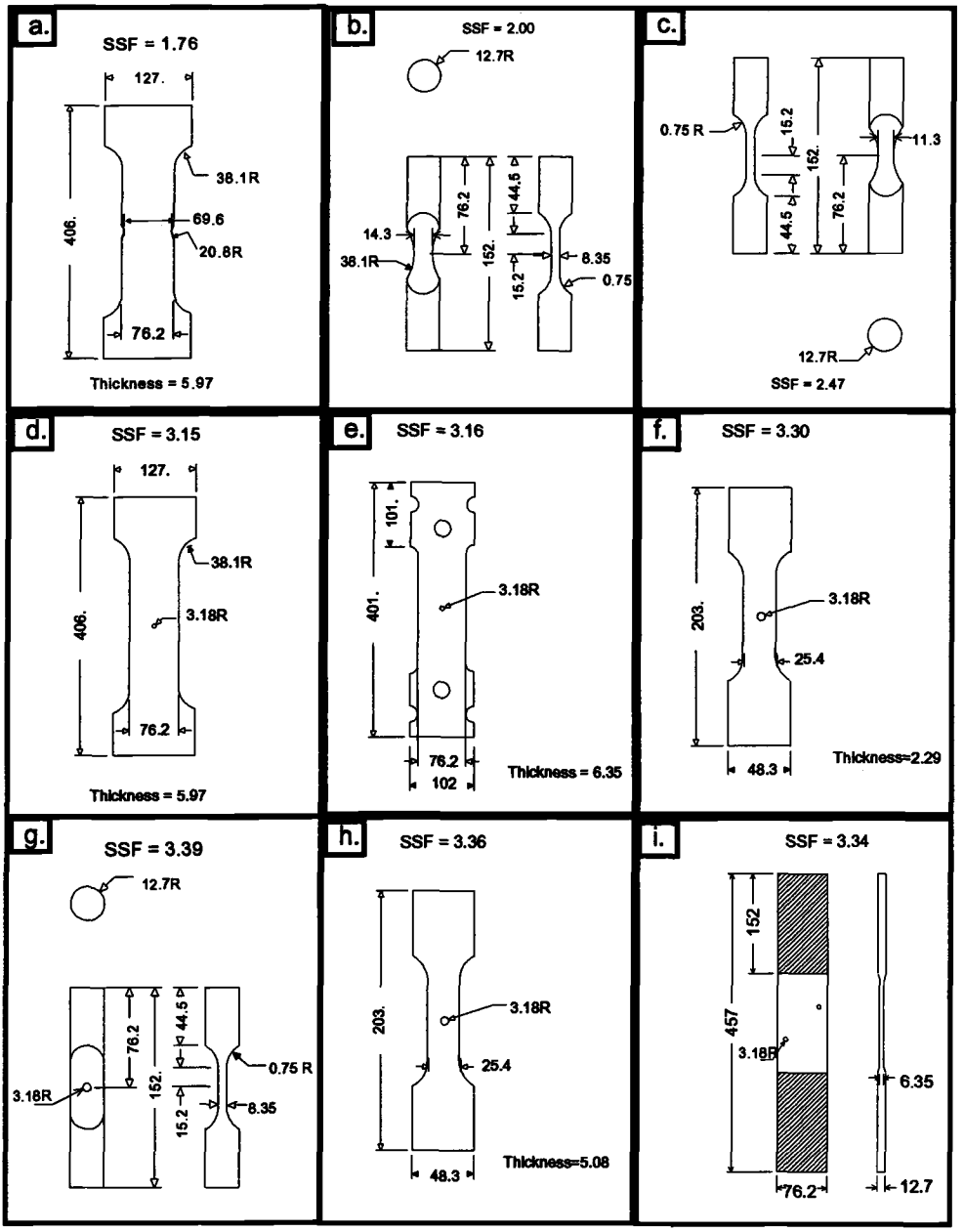

FIG. 1—*Specimens used for verification of notch strain analysis method. Specimen* i *is from Ref* 1. *(All dimensions in millimeters.)*

fatigue cycling used to precrack the specimen was a load-shedding scheme to minimize the residual plastic zone at the crack tip. Figure 2 shows the crack growth specimen geometry.

Spectra

The spectra used in the current test program are representative of flight mission profiles for long-range bomber aircraft. The spectra obtained from Ref *1* are representative of fighter/attack aircraft. The mission profiles represented stress histories at specific aircraft locations such as control surfaces, wing stations, and landing gear. Figures 3*a* to 3*e* show the exceedance curves for the bomber spectra, and Table 1 gives a description of each spectrum. Figure 4 shows airframe locations represented by the spectra.

Figure 3*a* shows a wing-bending spectrum for which the largest number of tests were performed. This spectrum is a symmetric spectrum in that it contains an equal number of compression and tension exceedances. Figure 3*b* shows the exceedance curves for five separate spectra. These spectra are also for wing bending, and all five are from the same location. The five spectra were subjected to different levels of truncation and bumping. Truncation is a technique that eliminates low-amplitude loads to reduce analysis time and to reduce test costs. Bumping refers to the "bumping up" of maximum load levels to increase fatigue damage of truncated spectra. However, it is important that the truncation and bumping levels do not affect the life calculations. Figure 3*c* shows exceedance curves for the B-2 control surfaces. Two of these spectra are dominated by tension loads and the flap spectrum shown is a constant amplitude spectrum. An engine mount spectrum is shown in Fig. 3*d* and a landing gear spectrum in Fig. 3*e*.

These spectra permit the testing of the effects of several load variables on the prediction capability of the models. The variables include spectrum truncation level, spectra dominated by positive loads ($R > 0$), and spectra with fully reversed loading ($R = -1$).

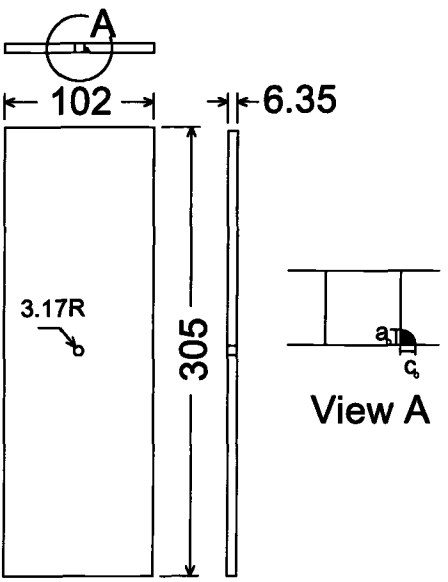

FIG. 2—*Specimen geometry used for verification of damage tolerance analysis method. (All dimensions in millimeters.)*

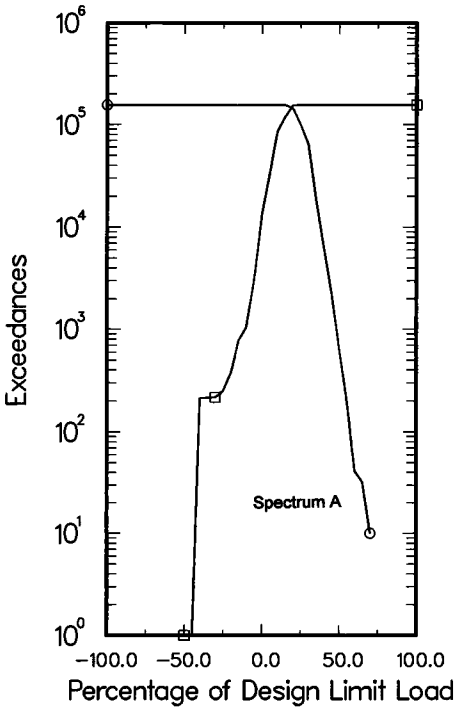

FIG. 3*a*—*Wing-bending exceedance Curve A used for spectrum fatigue test correlations.*

Material

Twenty material forms were tested. These material forms were different alloy and heat-treat conditions of aluminum, titanium, and steel. All alloys tested were commercially available products conforming to the appropriate military and commercial standards. Table 2 lists the materials tested. These materials are representative of materials commonly used for primary aircraft structures.

Test Procedures

The notch strain analysis specimens were polished to ensure a smooth initial condition. The specimen holes were deburred to ensure a smooth initial condition around the hole. Loading was applied uniaxially using a servohydraulic test system controlled by computer. The load spectrum was written to magnetic disk that the computer read as a sequence of peak and valley loads. A digital to analog converter then transferred these values to the load controller on the test system.

Tests were monitored visually using a traveling microscope. For the notch strain analysis specimens, the microscope was used to monitor the appearance of a detectable crack. This crack (or cracks) was then monitored to obtain a curve of cycles versus crack length. These data were then used to extrapolate back to a crack size of 0.762 mm (0.030 in.). The number of cycles at which the crack attained this length was used to define crack initiation life. The traveling microscope was used on the crack growth tests to continuously monitor crack length versus cycles.

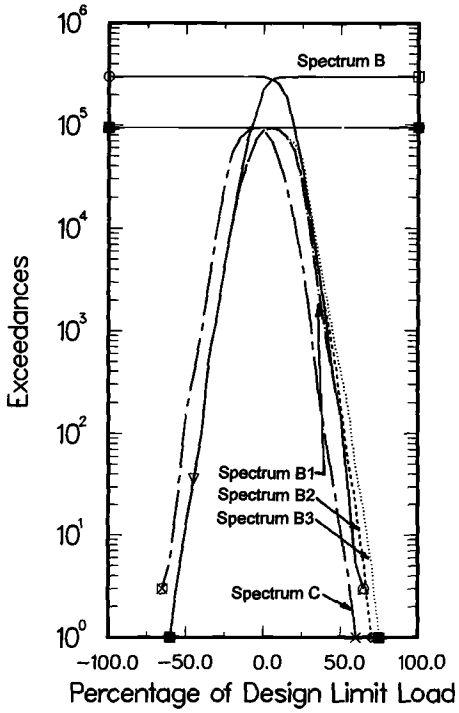

FIG. 3*b*—*Wing-bending exceedance Curve B used for determining effects of spectrum truncation and bumping on spectrum fatigue test correlations.*

All stress calculations reported herein are based on *gross* area stress. The stress reported for each test is the maximum stress for that spectrum.

Notch Strain Analysis Model

Complete reviews of the notch strain analysis methods have been presented elsewhere [*2–4*]. This discussion will only briefly summarize the important equations of the method and then will focus on the application of the method to flight spectrum analysis for the B-2. The work of Coffin [*5*] and Manson [*6*] demonstrated the relationship between applied strain and low-cycle fatigue life. The Coffin-Manson relationship relates applied strain to fatigue life. This relationship is commonly presented as the summation of two exponential expressions [*3*]

$$\frac{\Delta\epsilon}{2} = \left(\frac{\sigma_f'}{E}\right)(2N)^b + \epsilon_f'(2N)^c \tag{1}$$

where $2N$ is the life to initiate a fatigue crack, E is Young's modulus, σ_f' is the fatigue strength coefficient, ϵ_f' is the fatigue ductility coefficient, and b and c are material-dependent exponents. In addition to the Coffin-Manson relationship, the cyclic stress-strain curve is an important material parameter for notch strain analysis. Materials cycled at constant strain amplitudes demonstrate a hysteresis loop in stress and strain. Connecting the tips of hys-

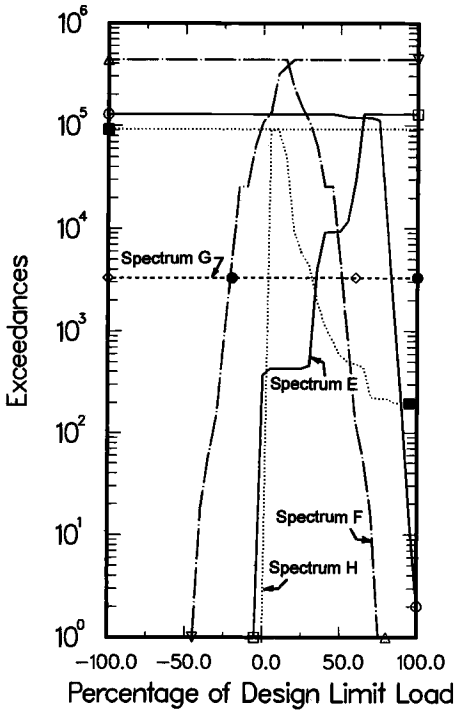

FIG. 3*c*—*Control surface exceedance curves used for correlation of* R *ratio effects on spectrum fatigue correlations.*

teresis loops for several strain amplitudes results in a cyclic stress-strain curve. A common empirical fit for this curve is [*3*]

$$\frac{\Delta\epsilon}{2} = \frac{\Delta\sigma}{2E} + \left(\frac{\Delta\sigma}{2K'}\right)^{n'} \tag{2}$$

where $\Delta\epsilon$ is the strain range, $\Delta\sigma$ is the stress range, K' is the cyclic strength coefficient, and n' is the cyclic strain-hardening exponent. Values for K' and n' are determined empirically.

The notch strain analysis methods relate the applied stresses to localized plastic strains occurring at discontinuities near notches. The applied stresses are related to the notch root strains by means of Neuber's rule. An implied assumption in the use of Neuber's rule is that the stresses and strains away from the notch *remain elastic.* For most good airframe designs this assumption is reasonable. Neuber's rule is given by

$$\frac{(SSF\Delta S)^2}{4E} = \frac{\Delta\sigma}{2}\frac{\Delta\epsilon}{2} \tag{3}$$

where SSF is the stress severity factor, ΔS is the applied stress range, $\Delta\sigma$ is the notch stress range, and $\Delta\epsilon$ is the notch strain range. Equation 3 is a hyperbola in stress-strain space as shown in Fig. 5. Application of the notch strain analysis requires a cyclic stress strain curve, and a curve of the form given by Eq 2 is also shown in Fig. 5.

As presented, the application of the Coffin-Manson Equation, the cyclic stress-strain curve, and Neuber's rule are valid for constant amplitude cycling. To apply these relation-

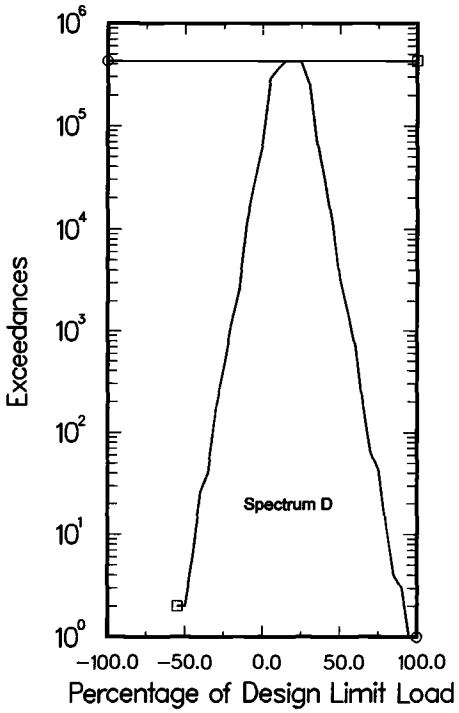

FIG. 3*d*—*Engine mount exceedance curve used for spectrum fatigue test correlations.*

ships to spectrum fatigue loading, it is necessary to convert fatigue data from multiple R ratios to a single curve at $R = -1$. This is done by using an equivalent strain formula. Several investigators have proposed equivalent strain equations. For application to the B-2, an equation similar to equations used in Ref *1* was employed

$$\left(\frac{\Delta\epsilon}{2}\right)_{eq} = [16]\begin{cases} 0, & \dfrac{2\sigma_0}{\Delta\sigma} < 1 - 2^{1/a} \\ \dfrac{\Delta\epsilon}{2}\left[2 - \left(1 - \dfrac{2\sigma_0}{\Delta\sigma}\right)^a\right], & 1 - 2^{1/a} \le \dfrac{2\sigma_0}{\Delta\sigma} < 0 \\ \dfrac{\Delta\epsilon}{2}\left(1 + \dfrac{2\sigma_0}{\Delta\sigma}\right)^a, & \dfrac{2\sigma_0}{\Delta\sigma} \ge 0 \end{cases}$$

where a is the equivalent strain exponent, $(\Delta\epsilon/2)_{eq}$ is the equivalent strain range, and σ_0 and $\Delta\sigma$ are the stabilized mean stress and the stabilized stress range for a fatigue test conducted at a strain range of $\Delta\epsilon/2$. The exponent a is determined for each material.

The cyclic stress strain curve and the Neuber hyperbola shown in Fig. 5 intersect. The Neuber hyperbola represents the state of stress and strain at the notch due to an applied stress ΔS. The cyclic stress strain curve represents the relation between stress and strain after cyclic hardening (or softening) has stabilized. The intersection of the Neuber hyperbola and the cyclic stress-strain curve represent the closure of a hysteresis loop. If it is then assumed that these hysteresis loops can be a measure of fatigue damage, the intersection of the Neuber hyperbola and the cyclic stress strain curve represents the level of fatigue damage incurred by application of a stress level ΔS. The strain levels computed by the intersection of

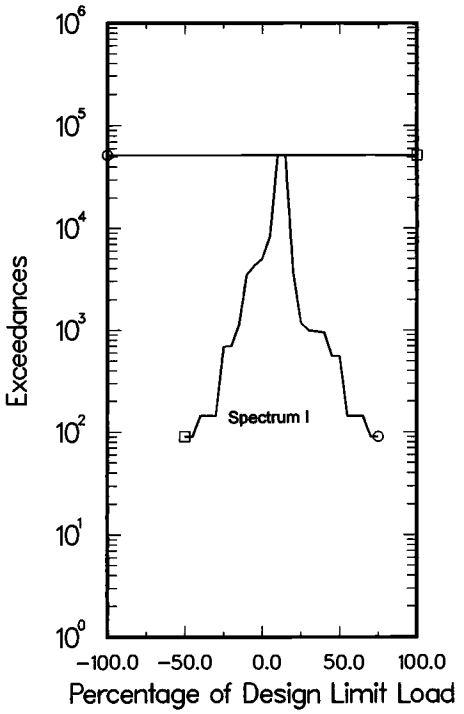

FIG. 3*e*—*Landing gear exceedance curve used for spectrum fatigue test correlations.*

TABLE 1—*Description of random flight spectra used for analysis verification.*

Spectrum I.D.	Spectrum Description
A	Wing Bending, Lower Surface, 12% Truncation
B	Wing Bending, Lower Surface, 15% Truncation
B1	Wing Bending, Lower Surface, 24% Truncation
B2	Wing Bending, Lower Surface, 24% Truncation, Bumped 6%
B3	Wing Bending, Lower Surface, 24% Truncation, Bumped 13%
C	Wing Bending, Upper Surface, 24% Truncation
D	Engine Mount Nz
E	Control Surface, Inboard Elevon Hinge Moment
F	Control Surface, GLAS Hinge Moment
G	Control Surface, Flap Hinge Moment (Constant Amplitude)
H	Control Surface, Rudder Hinge Moment
I	Landing Gear

the two curves is related to life by referring to a strain life curve. A key development in the application of the method was accurate cycle counting methods that can identify the closing of hysteresis loops [*4*]. The methods used for the B-2 incorporated cycle counting within the same computer routine used for the notch strain analysis. This permitted the calculation of fatigue damage as soon as a closed hysteresis loop was identified. The advantage of this approach is the preservation of sequence effects on fatigue life calculations.

Integral to the application of this method is the stress severity factor (SSF). The concept

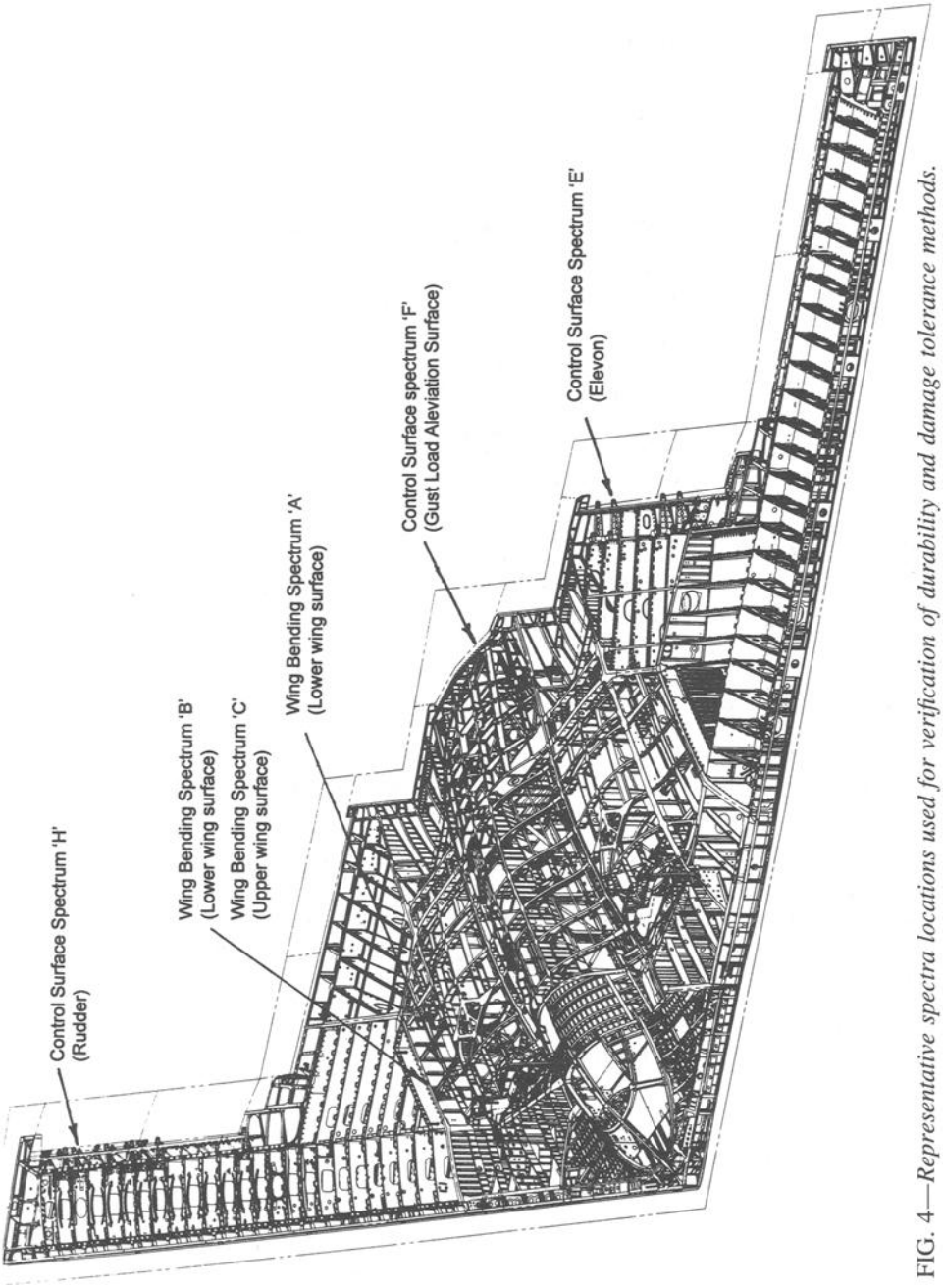

FIG. 4—*Representative spectra locations used for verification of durability and damage tolerance methods.*

TABLE 2—*Matrix of materials and load spectra tested for durability and damage tolerance verification.*

Spectrum I.D.	Spectrum Description / Material Designation	2124-T851 Plate	7049-T73511 Extrusion	7050-T74 Forging	7050-T7451 Plate	7050-T74511 Extrusion	7050-T7452 Forging	7075-T6 Bare Sheet	7075-T6 Clad Sheet	7075-T651 Plate	7075-T76 Bare Sheet	7175-T74 Forging	7475-T7351 Plate	Ti-6Al-4V ELI/RA Forging	Ti-6Al-4V ELI/RA Plate	Ti-6Al-4V MA Extrusion	Ti-6Al-4V MA Plate	Ti-10V-2Fe-3Al STA Forging	Ti-10V-2Fe-3Al STOA Forging	9Ni-4Co-0.20C Forging	Inconel 718 Forging	PH13-8Mo Forging
A	Wing Bending, Lower Surface, 12% Truncation	X			X/Y	X	X	X	X	X	X	X	X	X	X/Y	X	X	X	X			
B	Wing Bending, Lower Surface, 15% Truncation				X/Y										X/Y							
B1	Wing Bending, Lower Surface, 24% Truncation				X								X		X							
B2	Wing Bending, Lower Surface, 24% Truncation, Bumped 6%														X/Y							
B3	Wing Bending, Lower Surface, 24% Truncation, Bumped 13%				X/Y																	
C	Wing Bending, Upper Surface, 24% Truncation				X/Y										X/Y							
D	Engine Mount Nz														X/Y						X	X
E	Control Surface, Inboard Elevon Hinge Moment				X/Y										X/Y							
F	Control Surface, GLAS Hinge Moment				X/Y										X/Y							
G	Control Surface, Flap Hinge Moment (Constant Amplitude)				X										X/Y							
H	Control Surface, Rudder Hinge Moment				X/Y										X/Y							
I	Landing Gear					X									X							
	F/A-18 (Reference 1)		X	X	X		X							X			X			X		

Key: 'X' = Durability Test, 'Y' = Damage Tolerance Test

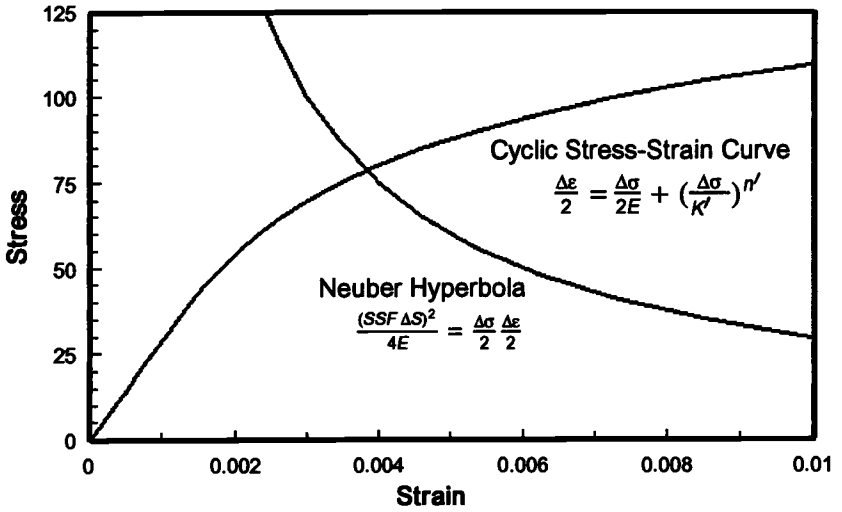

FIG. 5—*Intersection of Neuber hyperbola and cyclic stress strain curve.*

of the stress severity factor was proposed by Jarfall [*7*]. It has been discussed and refined elsewhere [*8*]. As presented by Niu [*8*], it is analogous to a fatigue notch factor. The maximum stress at a joint is the summation of the stress due to the bypass load and the stress due to the fastener load:

$$\sigma_{max} = \frac{P_{pin}}{Dt} K_{tpin} + \frac{P_{bp}}{Wt} K_{topen} \tag{4}$$

where P_{pin} is the portion of the load carried by the fastener, P_{bp} is the bypass load carried through the joint, D is the fastener diameter, W is the joint width, and t is the thickness of the component. The stress severity factor accounts for the magnification of the stress at the fastener hole (or other notch) relative to a reference stress

$$SSF = \frac{\sigma_{max}}{\sigma_{ref}} = \frac{1}{\sigma_{ref}} \left(\frac{P_{pin}}{Dt} K_{tpin} + \frac{P_{bp}}{Wt} K_{topen} \right) \tag{5}$$

In addition to notch effects, the stress concentration factors may include effects of hole countersink and adjacent hole shadow effects. The stress severity factor is also used to incorporate the effects of material processing variables on fatigue. The equation for SSF then becomes

$$SSF = \frac{F_j F_{FT}}{\sigma_{ref}} \left(\frac{P_{pin}}{Dt} K_{tpin} + \frac{P_{bp}}{Wt} K_{topen} \right) \tag{6}$$

where F_j is a factor accounting for material form, and F_{FT}, the life improvement factor, is a factor to account for beneficial processing effects such as cold working. If complete fatigue data are available for the precise material condition in question, then F_j will be set equal to 1. As an example, material data are often obtained for the long transverse (LT) grain orientation, but in some situations loading may occur in the short transverse (ST) direction.

In such cases F_j will be set to a value greater than 1 to account for the difference in product form. The life improvement factor, F_{FT}, reduces the SSF to account for the beneficial effects of certain fastening systems such as the cold working of fastener holes to improve fatigue life. The life improvement factors for certain systems are:

1. Split sleeve cold work: $F_{FT} = 0.85$.
2. Interference fit fasteners: $F_{FT} = 0.85$.
3. Hole filling solid rivets: $F_{FT} = 0.90$.

The stress severity factor concept is a value calculated by the stress analyst, and it forces the analyst to be cognizant of good fatigue design practice (i.e., large radii fillets are better than sharp radii, etc.). It provides opportunities to incorporate reasonably conservative assumptions such as the case of cold-working fastener holes. The life improvement factors noted above would reduce the stress severity factor; however, this improvement is seldom accounted for in design analysis. By setting the life improvement factor equal to 1, the analyst makes the calculations more conservative and leaves room for unexpected events such as needed repairs.

Figure 6 shows a flow chart of the notch strain analysis method as applied to the B-2. Keys features of the method are:

1. *The simplicity of the output.* Figure 7 shows a sample output fatigue allowable curve. It is presented as stress severity factor times the reference stress (SSF*σ_{ref}). The analyst can use the calculated stress to establish the life margins for a component. If a part does not meet specified life requirements, design changes are recommended. The design changes can focus on either reducing the stress or improving the fatigue notch detail and can hence reduce the stress severity factor.
2. *The accounting for sequence effects of fatigue spectrum analysis.* Rather than cycle counting the entire spectrum and setting up range-mean statistics for later damage calculations, the damage fraction is computed as soon as the cycle count identifies a closed hysteresis loop. This permits the assessment of changes in usage on the structural fatigue life, a feature that is useful when the aircraft becomes operational.
3. *The influence of geometry and processing variables on fatigue life are accounted for in the stress severity factor.* The analyst computes the stress severity factor during the life assessment of the component. Computation of the stress severity factor as part of the analysis is straightforward, yet it forces the analyst and the designer to be cognizant of good fatigue design practice.

Notch Strain Analysis Verification Results

A simple method to evaluate the accuracy of the model is to plot the test data onto an allowable curve generated by the analysis method. Such a plot is shown in Fig. 8. The B-2 was designed for four lifetimes of durability loading, i.e., all components had to be shown "good" for four times the 10 000-h design life. This is equivalent to a scatter factor of ± 4 on life. Plots such as Fig. 8 indicate a general trend that the method is accurate within this scatter factor; however, it is difficult to quantify the degree of scatter in the life data from these plots. All of the test results are plotted on Fig. 9 as predicted life versus test life. Lines representing a scatter factor of 4 are also shown, and most of the data fall within this bound.

To statistically quantify the data scatter, ratios of test life to calculated life were computed. If the prediction correlated perfectly with the test data, the value of this ratio would

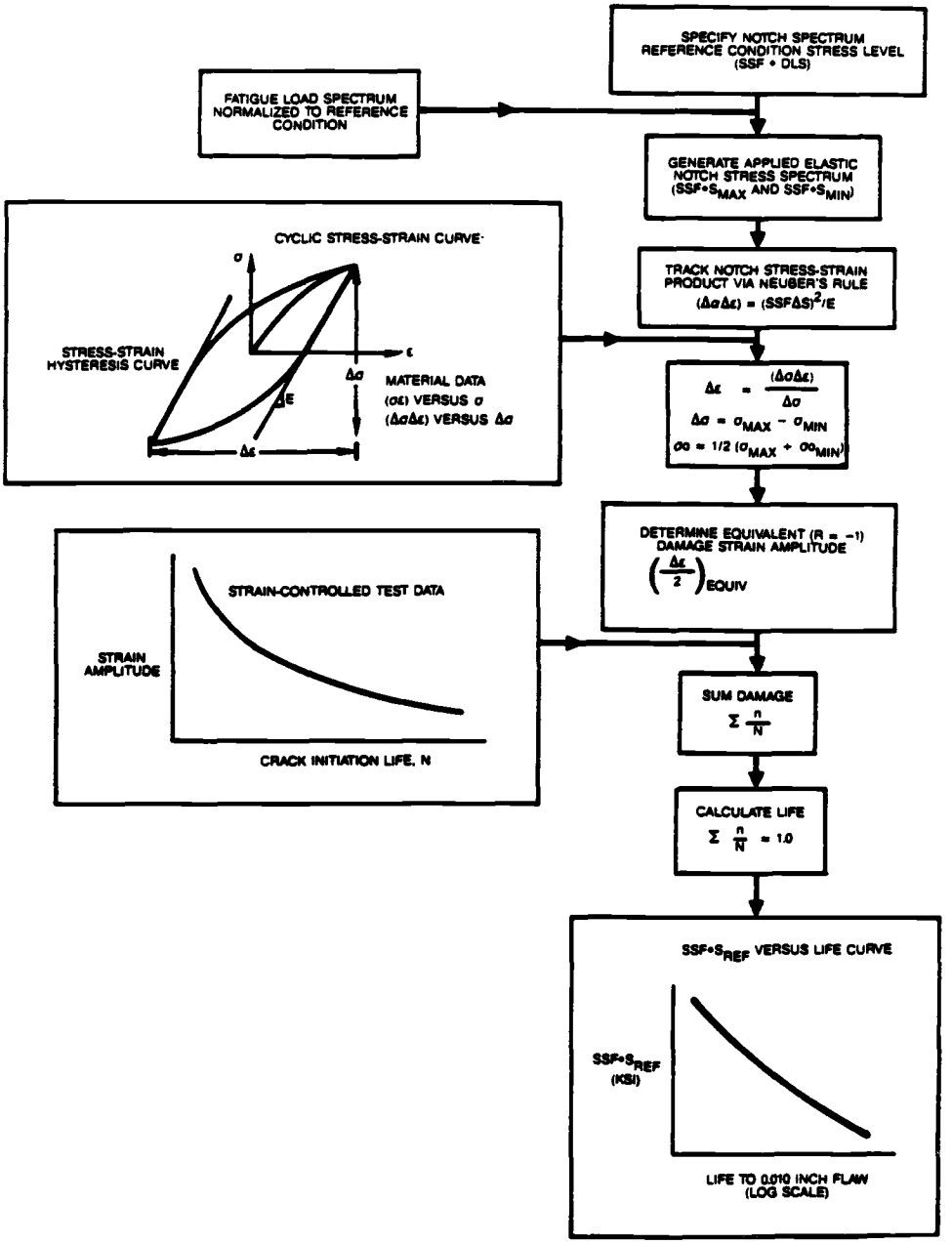

FIG. 6—*Flowchart for notch strain analysis method.*

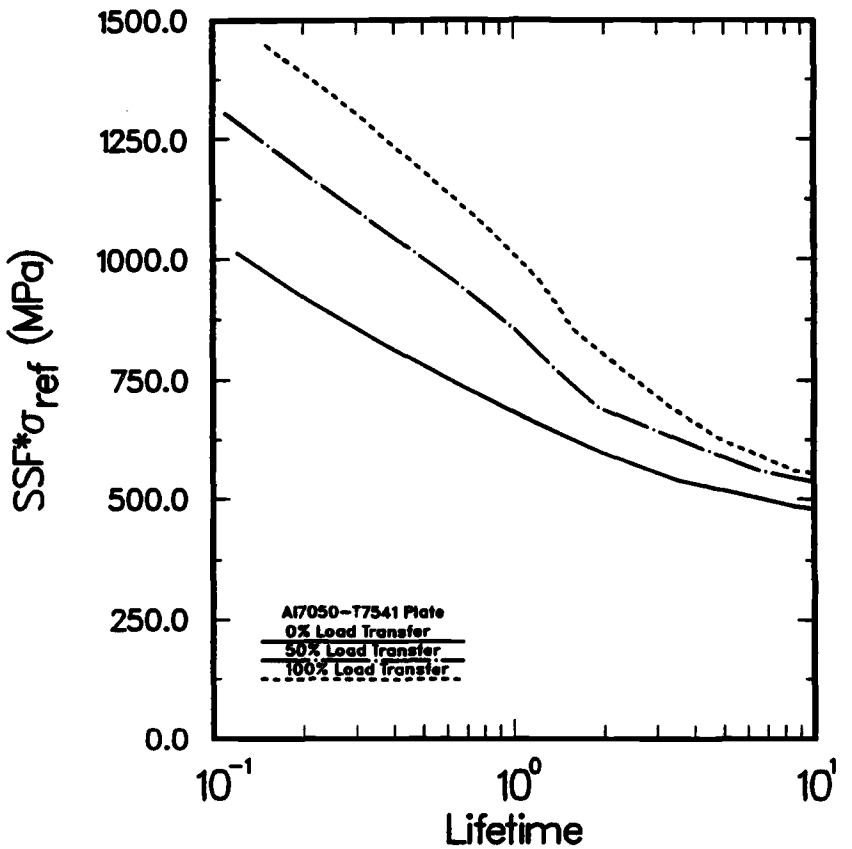

FIG. 7—*Allowable curve generated by analysis program. Curves at higher load transfer values are used for analysis of joints.*

be 1. The minimum allowable value would be 0.25 since this would represent the scatter factor of 4 applied to the design life

$$\frac{\text{test life}}{\text{calculated life}} = \frac{10\,000\text{ h}}{40\,000\text{ h}}$$

This ratio was plotted on log-normal probability coordinates to assess the correlation of the model to test data.

The log-normal probability plot for the entire population of test data is shown in Fig. 10*a*. The data correlate well with the log-normal distribution. About 79% of the tests fall within the values 0.25 to 4. Twenty percent of the test-life/calculated-life ratios were greater than 4, which is conservative. Only 1% of the tests indicated an unconservative value of less than 0.25. The 1% of unconservative results is tolerable because additional conservative assumptions would be factored into the calculation of the reference stress.

The statistical evaluations can be used to assess some of the effects of the various test parameters. Figures 10*b* through 10*d* are log-normal plots of the data plotted as functions of

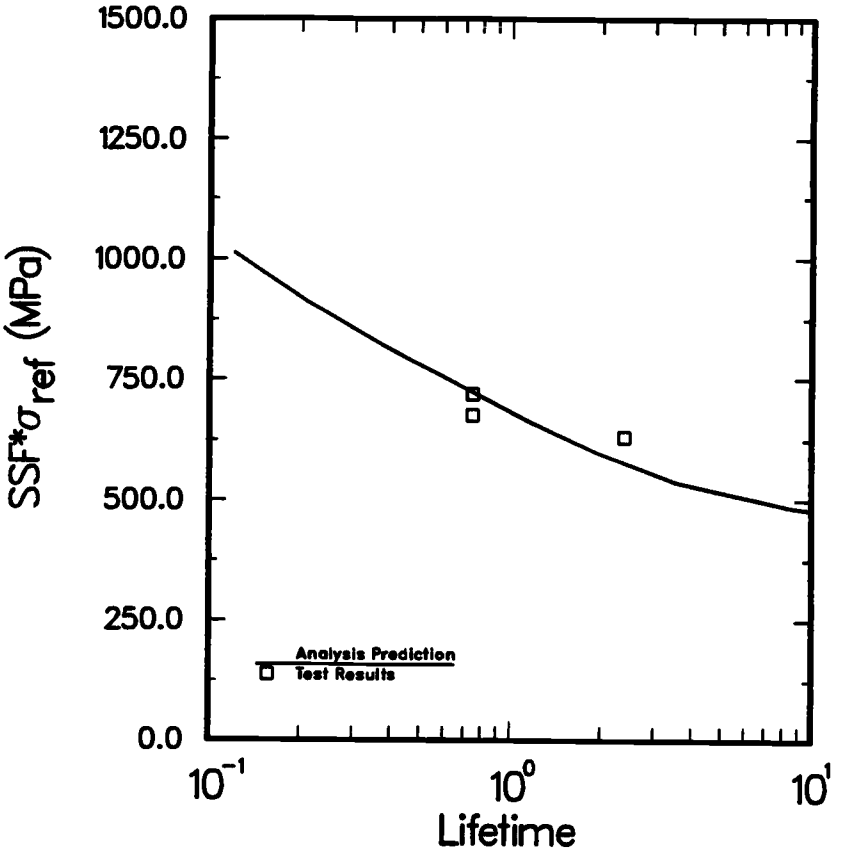

FIG. 8—*Test results for Al7050-T7451 plate shown for the Wing Bending A spectrum.*

material, spectra truncation, and specimen type. Figure 10*b* shows the correlation as a function of material type. The aluminum alloys and the PH13-8Mo steel had a narrower scatter band than did titanium, yet even the titanium was well behaved in terms of a conservative prediction on durability life. The high-strength cobalt steels were very well behaved in terms of a narrow scatter band, and the predictions were conservative for this alloy. The small amount of data for Inconel 718 or the 9Ni-4Co-0.20C steel preclude conclusive inferences.

Figure 10*c* shows the effects of spectrum manipulation on the prediction of durability life. It is notable that the spectrum with the highest level of truncation is the spectrum that had the least scatter and best correlation. As the truncation level increases, the spectrum becomes more like a constant amplitude spectrum. The other spectrum manipulations did not change the overall correlation of the model.

Figure 10*d* shows the data broken down by specimen type. Some of the specimen types demonstrated bilinear behavior when plotted in terms of the statistical log-normal model. One feature that does stand out from this data is a trend for specimens with the highest stress concentration values to have less scatter. The notch strain model assumes a high strain level, and the specimens with the low stress concentrations may not have achieved this strain.

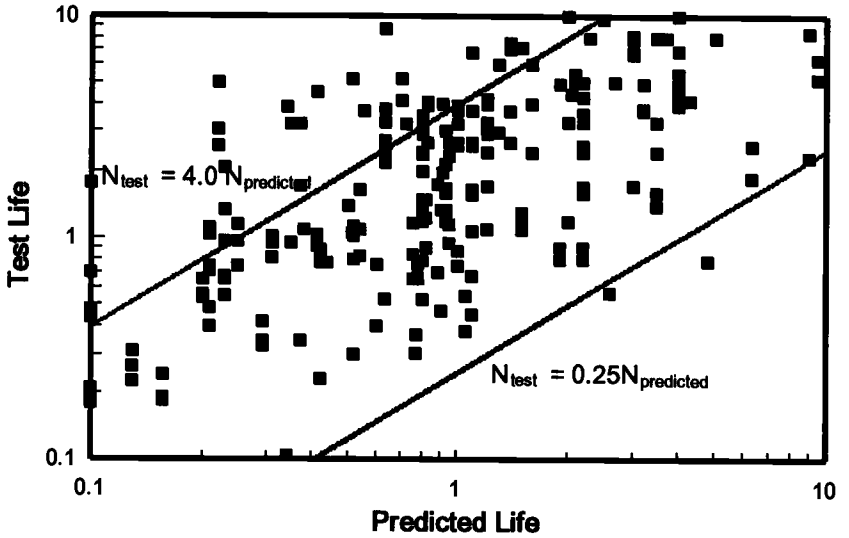

FIG. 9—*Correlation of durability tests with notch strain analysis predictions. (Note: units for life are aircraft lifetimes where 1 life = 10 000 h.)*

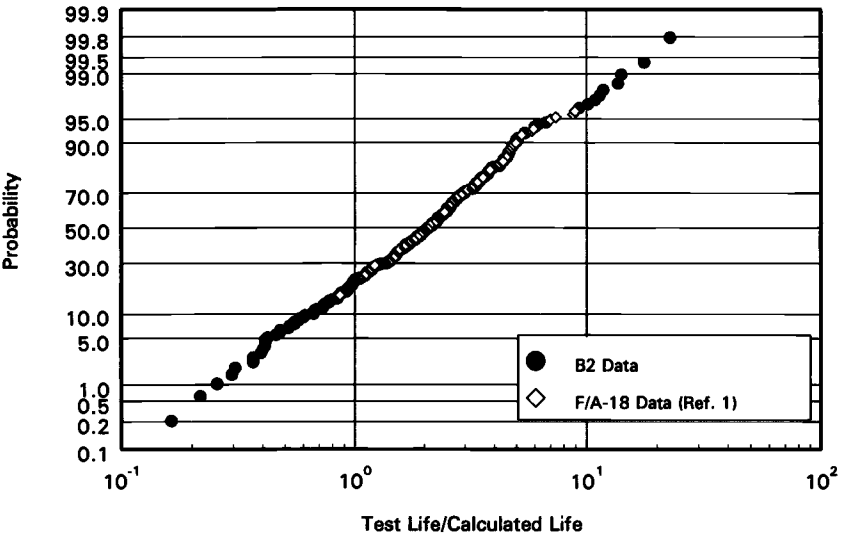

FIG. 10*a*—*Log-normal probability plot for the entire population of notch strain analysis spectrum fatigue tests.*

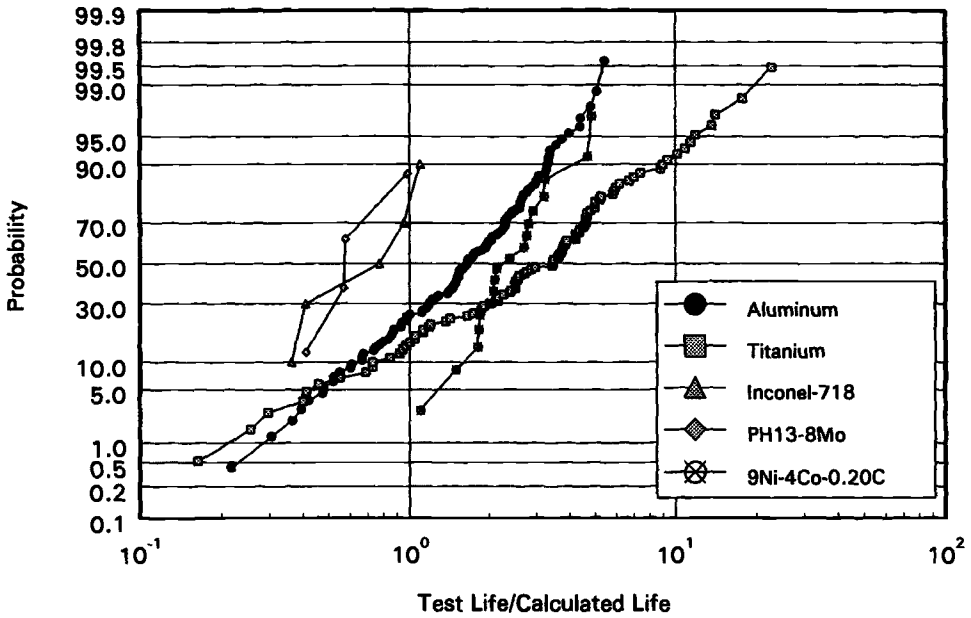

FIG. 10*b*—*Log-normal probability plot for the notch strain analysis spectrum fatigue tests separated based on alloy type.*

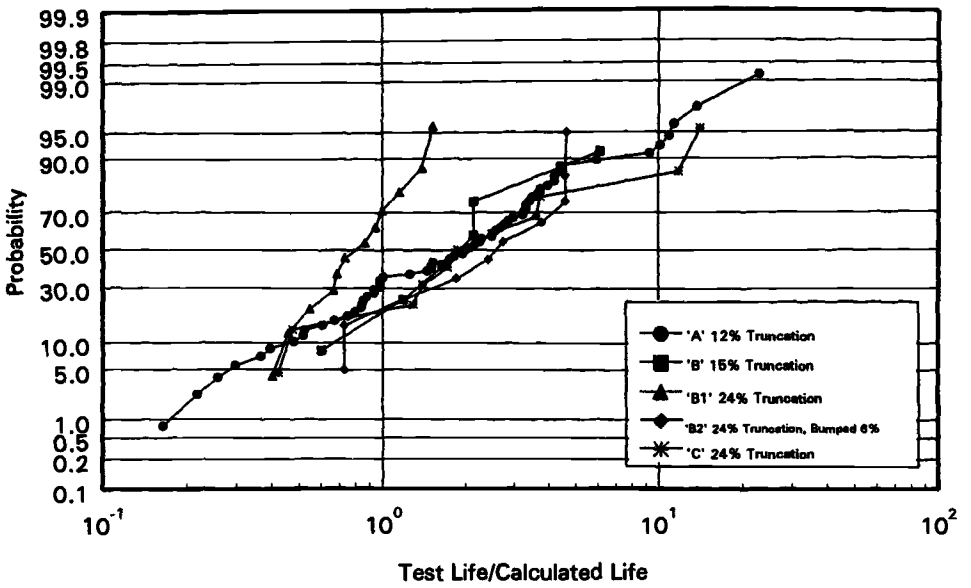

FIG. 10*c*—*Log-normal probability plot for the notch strain analysis spectrum fatigue tests separated based on spectrum type.*

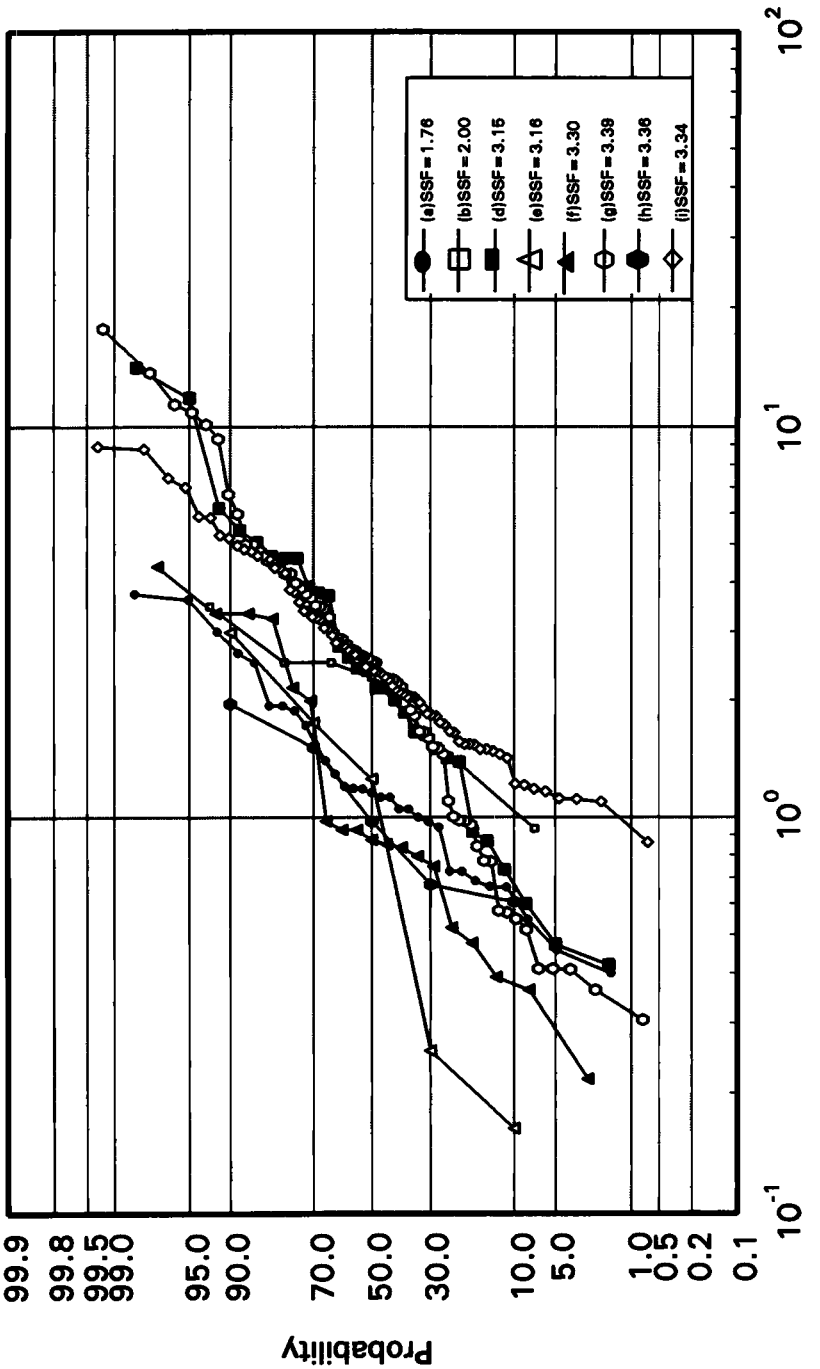

FIG. 10*d*—*Log-normal probability plot for the notch strain analysis spectrum fatigue tests separated based on coupon type.*

Fatigue analysis of airframe structures involves loaded joints that have high stress concentration factors, so this assumption of the notch strain analysis method is not a limitation.

Constant Closure Model

The purpose of crack growth calculations is to establish the safe life of structures that contain growing fatigue cracks. These safe life calculations use constant amplitude crack growth data as input; however, aircraft flight spectra seldom approach a constant amplitude. The approach of most cycle by cycle analysis methods is to perform incremental summation of a crack growth rate data. For example, a common crack growth equation is the Paris-Erdogan equation

$$\frac{da}{dN} = C\Delta K^n \tag{7}$$

where a is the crack length, N is the cycles, ΔK is the stress intensity range, and C and n are curve fit constants. For each load level of a random flight spectrum, ΔK is calculated and substituted into Eq 7

$$\delta a = C(\Delta K_{applied})^n \underbrace{(\delta N)}_{=1\ cycle}$$

Each crack growth increment δa is calculated and summed until a critical crack size is attained. Simple application of this summation to aircraft flight spectra results in life estimates that are too conservative (i.e., the structure is too heavy). This conservatism is due to the phenomenon of crack growth retardation. The occurrence of tension overload cycles is known to retard crack growth after the application of subsequent load cycles. Under some conditions, these retardation effects can be offset by compression overloads. Aircraft spectra are sequences of tension and compression overload cycles; therefore, effects of crack growth retardation and acceleration must be accounted for in order to design aircraft structures that are optimized for flight safety.

The types of models used to correlate retardation/acceleration effects tend to fall into two categories. The first category of crack growth models are yield zone models such as the models proposed by Wheeler [*9*] and Willenborg et al. [*10*]. The second type of model is crack closure such as those proposed by Bell and Creager [*11*], de Koning [*12,13*], and Newman [*14,15*]. Yield zone models assume that an overload plastic zone at the crack tip controls retardation, and as long as the crack tip remains within the overload zone, a retardation factor is applied to the crack growth rate equations. Closure models utilize the concept of crack closure to explain retardation. Elber first described plasticity-induced retardation where residual stresses in the wake of the crack tip exert closing forces on the crack [*16*]. Since Elber's work, many other closure mechanisms have been identified as summarized by McEvily [*17*].

A common feature among the referenced crack growth models is the need for a "memory." The yield zone models must track the size of plastic zones and the occurrences of overloads that increase this plastic zone size. These models must also memorize the location of the crack tip relative to the plastic zone. Likewise, closure models that have been discussed need to memorize the closure level of a prevailing overload and when the effects of that overload have decayed. The closure model proposed herein dispenses with the need for a memory by assuming a constant closure level.

The closure models derive their name from the fact that forces acting behind the crack tip

close the crack faces before the applied load reaches a zero level. Therefore, it is necessary to compute the crack opening stress level. Elber defined an effective stress intensity range, ΔK_{eff}, that defines the portion of the load cycle where the crack is open

$$\Delta K_{eff} = K_{max} - K_{open} \tag{8}$$

where K_{max} is the maximum stress intensity, and K_{open} is the stress intensity at the crack opening load. To measure the magnitude of the closure level, Elber suggested the ratio

$$U = \frac{\Delta K_{eff}}{\Delta K} = \frac{K_{max} - K_{open}}{K_{max} - K_{min}} \tag{9}$$

Experiments on constant amplitude data have shown a variation of U with the fatigue load ratio R. A number of empirical equations have been proposed to describe the functional relationship between U and R, and a number of these equations are summarized in the review by Schijve [*18*]. Typical of the equations is a second order polynomial from Schijve's work for 2024-T3 aluminum

$$U = 0.55 + 0.33R + 0.12R^2 \tag{10}$$

Elber's closure parameter U has been widely used to correlate constant amplitude data; however, for random spectra, it has been more convenient to define the closure factor as the proportionality constant between the crack opening load K_{open} and the maximum load K_{max}

$$K_{open} = CF \cdot K_{max} \tag{11}$$

Substitution of Eq 11 into Eq 9 and noting that $K_{min} = R\,K_{max}$ leads to

$$U = \frac{(1 - CF)}{(1 - R)} \tag{12}$$

and thus the factors CF and U are equivalent definitions of the closure factor. Newman has proposed equations for the closure factor that account for maximum stress level and crack tip constraint, as well as R ratio [*19*]

$$CF = A_0 + A_1R + A_2R^2 + A_3R^3 \qquad \text{for} \quad R \geq 0 \tag{13a}$$

and

$$CF = A_0 + A_1R \qquad \text{for} \quad R < 0 \tag{13b}$$

where the effects of constraint and S_{max} are accounted for in the definitions of the coefficients

$$A_0 = (0.825 - 0.34\alpha + 0.05\alpha^2)[\cos(\pi S_{max}/2\sigma_0)]^{1/\alpha}$$

$$A_1 = (0.415 - 0.071\alpha)(S_{max}/\sigma_0)$$

$$A_2 = 1 - A_0 - A_1 - A_3$$

$$A_3 = 2A_0 + A_1 - 1$$

where α is the constraint factor. For plane stress $\alpha = 1$, and for plane strain $\alpha = 3$. The term σ_0 is an allowable strength term interpreted by Newman as the average of the yield and ultimate strengths for the material.

The closure factor is used to compute the opening stress level (Eq 11). In crack growth calculations, it is assumed that the crack growth rate for a random load cycle in a spectrum is equal to the growth rate for the equivalent constant amplitude load:

$$\left.\frac{da}{dN}\right)_{\text{SPEC}} = \left.\frac{da}{dN}\right)_{\text{DATA}}$$

and since $da/dN = f(\Delta K_{\text{eff}})$ it follows that

$$\Delta K_{\text{eff SPEC}} = \Delta K_{\text{eff DATA}} \tag{14}$$

where the subscripts SPEC and DATA refer to values for the random amplitude spectrum and the constant amplitude data. Since $\Delta K_{\text{eff}} = U\Delta K$ and $U = (1 - CF)/(1 - R)$, both sides of this equality become

$$\Delta K_{\text{SPEC}} \frac{(1 - CF_{\text{SPEC}})}{(1 - R_{\text{SPEC}})} = \Delta K_{\text{DATA}} \frac{(1 - CF_{\text{DATA}})}{(1 - R_{\text{DATA}})} \tag{15}$$

and solving for ΔK_{DATA}

$$\Delta K_{\text{DATA}} = \Delta K_{\text{SPEC}} \frac{(1 - CF_{\text{SPEC}})}{(1 - R_{\text{SPEC}})} \frac{(1 - R_{\text{DATA}})}{(1 - CF_{\text{DATA}})} \tag{16}$$

The spectrum stress intensity range can be expressed in terms of the stress intensity at the peak load level

$$\Delta K_{\text{SPEC}} = K_{\text{max SPEC}}(1 - R_{\text{SPEC}}) \tag{17}$$

where K_{maxSPEC} is the peak stress intensity of the current cycle in a random amplitude spectrum. Substitution gives

$$\Delta K_{\text{DATA}} = K_{\text{max SPEC}}(1 - CF_{\text{SPEC}}) \frac{(1 - R_{\text{DATA}})}{(1 - CF_{\text{DATA}})} \tag{18}$$

or since $K_{\text{open}} = CF\ K_{\text{max}}$

$$\Delta K_{\text{DATA}} = (K_{\text{max SPEC}} - K_{\text{open SPEC}}) \frac{(1 - R_{\text{DATA}})}{(1 - CF_{\text{DATA}})} \tag{19}$$

The value of $K_{\text{open SPEC}}$ might be expected to change with each cycle. However, if it can be assumed that the closure load is constant for a spectrum or a portion of the spectrum, the calculations become much simpler. By assuming that there is a "controlling overload" that occurs often enough to keep the residual stresses in the crack tip wake constant, the equation for the constant closure model becomes

$$\Delta K_{\text{DATA}} = (K_{\text{max SPEC}} - CF_{\text{SPEC}} K_{\text{COL}}) \frac{(1 - R_{\text{DATA}})}{(1 - CF_{\text{DATA}})} \tag{20}$$

where K_{col} is the stress intensity factor at the defined "controlling overload level" for the spectrum.

The simplicity of this model is that it involves only a single parametric value, i.e., the closure factor. The assumption that the overload value and the closure factor are constant for a given spectrum simplifies this equation to a single variable quantity, $K_{maxSPEC}$. To compute crack growth rates, it is then only necessary to track the maximum stress levels. From the maximum stress level of each cycle $K_{maxSPEC}$ is computed for each cycle using an appropriate stress intensity formula. This value is then substituted into Eq 20 to compute ΔK_{DATA}. Once ΔK_{DATA} is known, the ΔK versus *da/dN* data curve for the appropriate material is referenced to obtain the growth rate for that cycle. This procedure is repeated for each maximum load level, and the crack growth increments are summed until a critical crack size is reached at which point failure occurs.

In order for the assumption of the constant closure model to be valid, it is necessary for spectrum overloads and underloads that control the residual plastic zone to be repeated periodically throughout the life of the component. The *R* ratio of the spectrum is defined by establishing a controlling value for the spectrum overload and for the underload. The *R* ratio of the spectrum is thus

$$R_{SPEC} = \frac{P_{CUL}}{P_{COL}}$$

where P_{COL} and P_{CUL} are the spectrum "controlling overload" and "controlling underload," respectively. For the B-2 these values were defined as the load levels that were exceeded 20 times during the life of the aircraft. The spectrum exceedance curve in Fig. 11 shows how these values are obtained. The value of R_{SPEC} is then used to enter a curve of *CF* versus *R* (Fig. 12) to determine CF_{SPEC}.

Closure factor data for aluminum and titanium derived from the constant closure model are plotted on Fig. 12. These points were derived by iteration. Equation 20 was used to predict the results of crack growth tests, and the value of CF_{Spec} was iterated until life predictions from the model correlated with test results. Each data point on Fig. 12 represents the correlation of *CF* with one spectrum fatigue test. The *R* ratio of the spectra were determined as shown in Fig. 11. The closure equations of Newman (Eq 13) are plotted as a comparison. The scatter shown in the *CF* data is due in part to the scatter in spectrum crack growth data and in part to the dependence of closure factor on S_{max} that the constant closure model ignores.

For damage tolerance analysis on the B-2 airframe, *CF* versus *R* curves were experimentally established for negative *R* ratios. These curves were established by linear regression of data such as that shown in Fig. 12. For positive *R* ratios, the *CF* versus *R* curves were derived from constant amplitude *da/dN* data. The end result was a closure factor curve similar in form to the curve shown in Fig. 12. These curves were established for a number of different materials and were included in the material database referenced by the FORTRAN program.

The calculation steps in the constant closure model are

1. Determine R_{SPEC} from P_{COL} and P_{CUL} that are obtained from an exceedance curve as shown in Fig. 11.
2. Enter a curve of *CF* versus *R* with the value of R_{SPEC} obtained in Step 1. Compute the corresponding value of CF_{SPEC}.
3. Determine the *R* ratio at which the available *da/dN* data was obtained. This value is R_{DATA}.
4. Use R_{DATA} to determine CF_{DATA}.

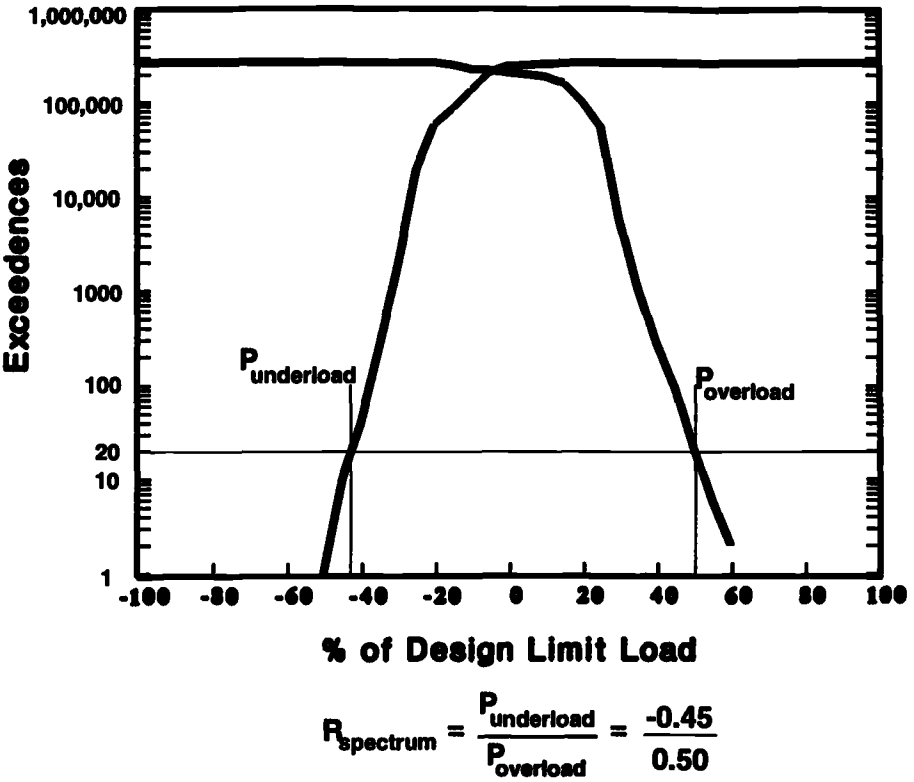

FIG. 11—*Exceedance curve demonstrating the calculation of the spectrum* R *ratio for the constant closure model.*

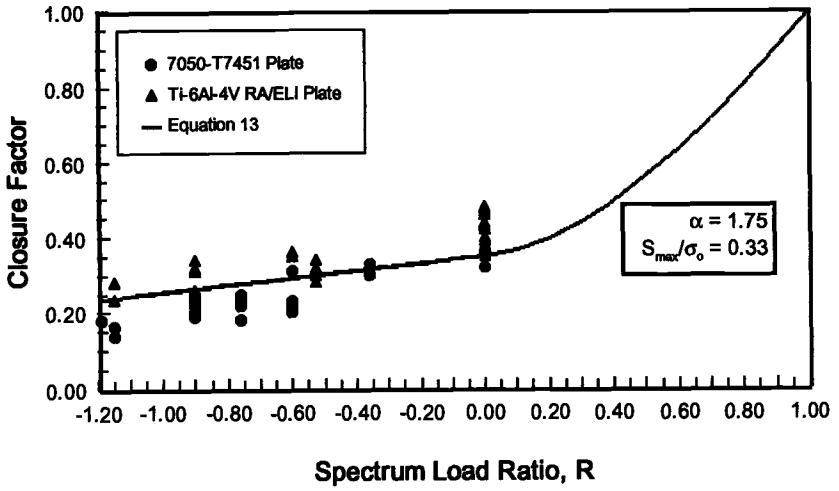

FIG. 12—*Closure factor versus* R *data. Data points are from curve fits of closure model to B-2 spectrum crack growth data.*

5. Use Eq 20 (and an appropriate stress intensity solution) to compute ΔK_{DATA} for the current load cycle.
6. Use computed value of ΔK_{DATA} to interpolate *da/dN* for the current cycle.
7. Repeat Steps 5 and 6 and sum the increments of growth until a critical crack size is attained.

The advantage of this method is fast and efficient computations. The retardation parameters are constant during life calculations, so the calculation steps required are reduced.

Constant Closure Model Verification

The damage tolerance life requirement on the B-2 was two times the design life. Figure 13 is a curve of damage tolerance allowable stress versus life for the wing bending spectrum. Shown on this plot are test data points for the same spectrum. The test data points fall within a scatter factor of 2 of the predicted lifetime. The allowable curve shown in Fig. 13 is valid for the specimen geometry shown in Fig. 2. The curve would change for different stress intensity geometries. Designs often do change significantly and therefore require the generation of a new damage tolerance allowable curve. This aspect of the design-analyze-redesign process points back to the advantage of computational efficiency for the constant closure model. The simplicity of the model allows for analysis of complex spectra with fast turnaround time for the results.

The predicted life versus test life is shown in Fig. 14 for the aluminum alloys tested. The points fall within the life factor. A limitation of many crack growth models is the requirement to recalibrate the models for each new application. This can be a costly limitation if actual usage deviates significantly from the usage assumed for the design because it would be necessary to recalibrate the retardation parameters and perform the damage tolerance analysis again.

The constant closure model assumes that the closure factor curve is valid for all types of

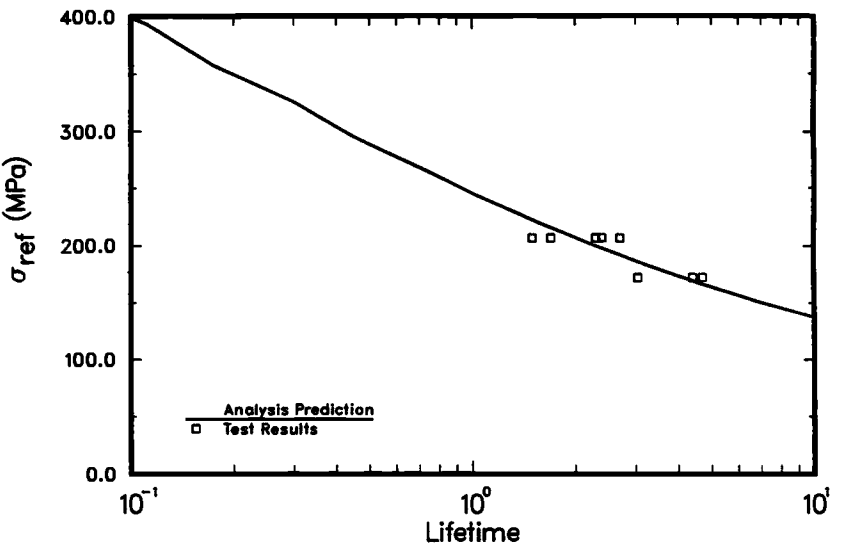

FIG. 13—*Damage tolerance allowable curve and crack growth test results for Al7050-T7451 using Wing Bending Spectrum* B.

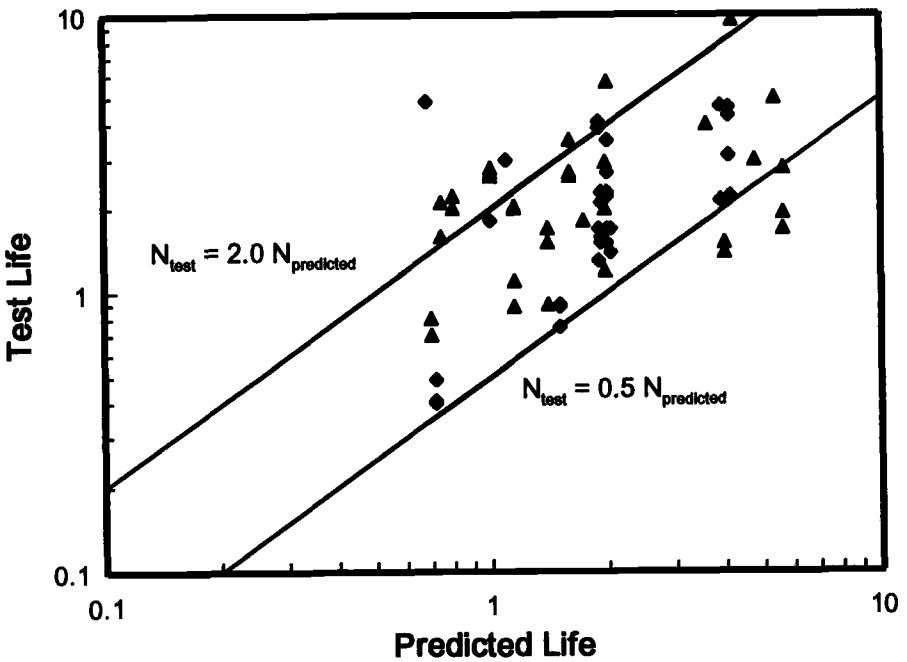

FIG. 14—*Correlation of constant closure model to test data. (Note: units for life are aircraft lifetimes where 1 life = 10 000 h.)*

spectra, assuming that a controlling overload can be properly defined. To test this assumption test, data were obtained from an F-20 fighter spectrum [*20*]. The test results and constant closure model predictions are shown in Fig. 15. The correlation of the model with these tests is quite satisfactory even though the model was not calibrated for these spectra.

Conclusions

The notch strain analysis method was used for life prediction analysis for durability critical parts on the B-2 aircraft. The constant closure model was used for life prediction analysis of fracture critical parts. Both models were subject to extensive test verification. The key advantages of these models are:

1. The notch strain analysis method decreases the redesign time by generating a geometry-independent allowable curve.
2. The constant closure model is a computationally simple model that minimizes analysis time.
3. The notch strain analysis method was reliable within the desired factor of 4 on life.
4. The constant closure model was accurate within the desired factor of 2.
5. The constant closure model keeps the retardation parameters constant for the entire analysis, which substantially reduces computation time. Although the constant closure model assumptions were developed with long-range bomber applications of the B-2 in mind, the model has been checked against fighter spectra and cargo type spectra from other test programs.

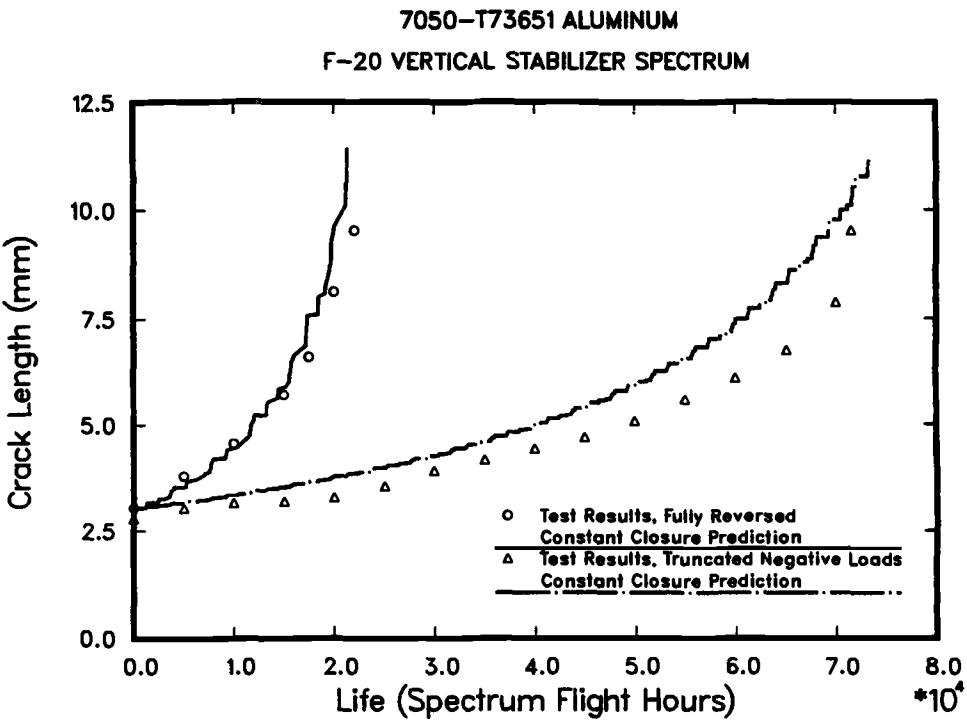

FIG. 15—*Constant closure model crack growth life predictions against test data for F-20 fighter spectrum (Ref 20).*

Acknowledgments

This work was performed under Air Force Contract F33657-81-C0087. The permission of the United States Air Force and the Northrop Grumman Corporation to publish this work is acknowledged. The authors are grateful to Mr. G. Poisal, Mr. M. McMaster, and Dr. J. Buban for their helpful discussions and insight regarding this work.

References

[1] Porter, P. G., "Development of a Rapid Method to Predict Fatigue Crack Initiation," Final Technical Report, NADC-81010-60, Naval Air Development Center, Warminster, PA, 1983.

[2] Morrow, J., "Cyclic Plastic Strain Energy and Fatigue in Metals," *Internal Friction, Damping, and Cyclic Plasticity, ASTM STP 378,* American Society for Testing and Materials, West Conshohocken, PA, 1965, pp. 45–87.

[3] *Fatigue Design Handbook AE-10,* 2nd ed., Society of Automative Engineers, Warrendale, PA, 1988.

[4] Dowling, N. E., "Fatigue Failure Predictions for Complicated Stress-Strain Histories," *Journal of Materials, JMLSA,* Vol. 7, No. 1, March 1972, pp. 71–87.

[5] Coffin, L. F., Jr., "A Study of the Effects of Cyclic Thermal Stresses on a Ductile Metal," *Transactions of ASME,* Vol. 76, 1954, pp. 931–950.

[6] Manson, S. S., "Behavior of Materials under Conditions of Thermal Stress," NACA-TN 2933, National Advisory Committee on Aeronautics, Lewis Flight Propulsion Laboratory, Cleveland, OH, 1953.

[7] Jarfall, L., "Optimum Design of Joints: The Stress Severity Factor Concepts," *Aircraft Fatigue*

Proceedings of the 5th ICAF Symposium, Melbourne, Australia, International Committee on Aeronautical Fatigue, 1979.

[8] Niu, C. Y., *Airframe Structural Design*, Conmilit Press Ltd., Hong Kong, 1988.

[9] Wheeler, O. E., "Spectrum Loading and Crack Growth," *Journal of Basic Engineering, Transactions of ASME*, Vol. 94, March 1972, pp. 181–186.

[10] Willenborg, J., Engle, R. M., and Wood, H. A., "A Crack Growth Retardation Model using an Effective Stress Concept," AFFDL-TM-71-1-FBR, Air Force Flight Dynamics Laboratory, January 1971.

[11] Bell, P. D. and Creager, M., *Crack Growth for Arbitrary Spectrum Loading*, Vol. I: *Results and Discussion*, AFFDL-TR-74-129, Air Force Flight Dynamics Laboratory, October 1974.

[12] de Koning, A. U., "A Simple Crack Closure Model for Prediction of Fatigue Crack Growth Rates Under Variable Amplitude Loading," *Fracture Mechanics: Thirteenth Conference, ASTM STP 743*, R. Roberts, Ed., American Society for Testing and Materials, West Conshohocken, PA, 1981, pp. 63–85.

[13] de Koning, A. U. and Liefting, G., "Analysis of Crack Opening Behavior by Application of a Discretized Strip Yield Model," *Mechanics of Fatigue Crack Closure, ASTM STP 982*, J. C. Newman, Jr. and W. Elber, Eds., American Society for Testing and Materials, West Conshohocken, PA, 1988, pp. 437–458.

[14] Newman, J. C., Jr., "A Crack-Closure Model for Predicting Fatigue Crack Growth under Aircraft Spectrum Loading," *Methods and Models for Predicting Fatigue Crack Growth under Random Loading, ASTM STP 748*, J. B. Chang and C. M. Hudson, Eds., American Society for Testing and Materials, West Conshohocken, PA, 1981, pp. 53–84.

[15] Newman, J. C., Jr., "FASTRAN II—A Fatigue Crack Growth Structural Analysis Program," NASA Technical Memorandum 104159, 1992.

[16] Elber, W., "The Significance of Fatigue Crack Closure," *Damage Tolerance in Aircraft Structures, ASTM STP 486*, American Society for Testing and Materials, West Conshohocken, PA, 1971, pp. 230–242.

[17] McEvily, A. J., "On Crack Closure in Fatigue Crack Growth," *Mechanics of Fatigue Crack Closure, ASTM STP 982*, J. C. Newman, Jr. and W. Elber, Eds., American Society for Testing and Materials, West Conshohocken, PA, 1988, pp. 35–43.

[18] Schijve, J., "Fatigue Crack Closure: Observations and Technical Significance," *Mechanics of Fatigue Crack Closure, ASTM STP 982*, J. C. Newman, Jr. and W. Elber, Eds., American Society for Testing and Materials, West Conshohocken, PA, 1988, pp. 5–34.

[19] Newman, J. C., Jr., "A Crack-Opening Stress Equation for Fatigue Crack Growth," *International Journal of Fracture*, Vol. 24, 1984, pp. R131–R135.

[20] Wilhem, D. P., Tanouye, P. A., and Shaw, D., "A Fracture Mechanics Evaluation of F-5G Frame Material—7050-T73651," NOR-81-114, Northrop Corporation, Aircraft Division, Hawthorne, CA, September 1981.

R. Sunder[1,2] *and Raghu V. Prakash*[2]

A Study of Fatigue Crack Growth in Lugs Under Spectrum Loading

REFERENCE: Sunder, R. and Prakash, R. V., **"A Study of Fatigue Crack Growth in Lugs Under Spectrum Loading,"** *Advances in Fatigue Lifetime Predictive Techniques: 3rd Volume, ASTM STP 1292,* M. R. Mitchell and R. W. Landgraf, Eds., American Society for Testing and Materials, 1996, pp. 248–264.

ABSTRACT: Optical fractography and special load sequencing were used to characterize the growth of naturally initiating fatigue cracks under FALSTAFF spectrum loading in lugs with bushes fitted to varying degrees of interference. The same technique was used to obtain a stress intensity calibration under constant amplitude loading. This calibration, combined with crack growth analysis using the hysteretic closure concept and the rainflow cycle count, correlated well with experimental observations of growth rate down to a crack depth of 400 μm. Available analytical stress intensity solutions do not appear to explain observed high crack growth rates, particularly as crack size diminishes to part-through dimensions.

KEYWORDS: lugs, fatigue crack growth, crack closure, spectrum loading, part-through cracks, bush-lug interference, stress intensity factor, fractography

Nomenclature

C, m	Material constants in crack growth rate expression
D	Lug hole diameter
K	Stress intensity factor, MPa$\sqrt{\text{m}}$
$\bar{K}$	K due to unit stress, MPa$\sqrt{\text{m}}$
K_c	Critical stress intensity (fracture toughness), MPa$\sqrt{\text{m}}$
K_t	Theoretical stress concentration factor
R	Stress ratio
S	Applied stress, MPa
W	Specimen width
a	Crack length, mm
da/dN	Crack growth rate, mm/cycle
da/dF	Crack growth rate, mm/flight
n_{cy}	Number of cycles in load spectrum
n_{fl}	Number of flights in load spectrum
t	Specimen thickness, mm
Δ	Prefix denoting range, as in ΔK

Subscripts

cl	Associated with the onset of crack closure (in major cycle if subscript i is absent)

[1]Presently with Biss Research, 99, 14A Cross, Malleswaram, Bangalore 560003, India.
[2]Scientist, Structural Integrity Division, National Aerospace Laboratories, Bangalore 560 017, India.

eff	Effective (as a consequence of fatigue crack closure)
i	In ith cycle
max	Maximum, as in S_{max} (highest in a sequence if without subscript i)
min	Minimum, as in S_{min} (lowest in a sequence if without subscript i)
op	Associated with crack opening (in major cycle, if without subscript i)
overscore	Indicates entity nondimensionalized with respect to maximum, e.g., $\bar{S}_{op} = S_{op}/S_{max}$, synonymous with $\bar{K}_{op} = K_{op}/K_{max}$

Lug joints are widely used in airframe structures. Their application ranges from large wing root joints down to the smaller control system linkages. Typically, airframe lug fittings are made from aluminum alloys with an interference fit steel bush. The application of fracture mechanics to assess endurance and residual strength requires the stress intensity function versus crack size and shape. While analytical techniques have been able to deliver this input for most crack geometries, this is not the case for lugs with naturally initiating part-through cracks, particularly in the presence of an interference fit bush. Analytical solutions for stress intensity have been validated against experimental data obtained on lugs with through or part-through cracks from mechanically cut crack initiators [*1–5*]. On the other hand, it has been shown that the high growth rates observed in naturally initiating part-through cracks cannot be explained by analytical solutions for stress intensity [*6,7*].

This paper describes an effort to estimate fatigue crack growth in a lug under FALSTAFF spectrum loading [*8*] using an empirically derived stress intensity calibration. A specially designed constant amplitude loading block was used for stress intensity versus crack length calibration down to a crack depth of 10 μm. Experiments were conducted to characterize the formation and growth of naturally initiating small, part-through fatigue cracks on lugs with different degrees of interference in the bush-lug interface. Spectrum load tests were performed under specially designed program loading that permitted growth rate measurements on the fracture surface using optical fractography.

Experimental Procedure

The study was performed on HE-15A ST (equivalent of L168 and 2014-T6511) Al-Cu alloy extruded bar stock, which is used to fabricate lugs for aerospace applications. Fatigue and fracture properties for the same batch of material were obtained in previous studies from tests on standard laboratory coupons [*9*].

Test coupons were cut along the extrusion direction as per the drawing shown in Fig. 1. A 1.5-mm-thick 4340 steel bush was inserted into the hole. The lug at either end of the coupon was loaded by a steel clevis-pin assembly. The clevis was in turn mounted onto the hydraulic grip on the testing machine. This method of testing essentially provides two fatigue failures for each coupon. When the first lug fails, the clevis is removed and the failed end of the coupon is sliced. The remaining end is mounted directly on the hydraulic grip, with fatigue cycling continued until failure of the other end.

Bush-Lug Interface

To examine the effect of interference fit on spectrum load fatigue, three different types of bush fit were used in the spectrum load testing: snug fit, 0.12-mm interference fit (with oversize bushes), and 0.24-mm interference fit. Further, the interference fits were made in two ways: using liquid nitrogen to ease insertion and by pressing the bush into the hole on a hydraulic press (mechanical press fit). Two specimens each were tested under a total of five different bush-lug interface conditions. This gave up to four fatigue failures per case to

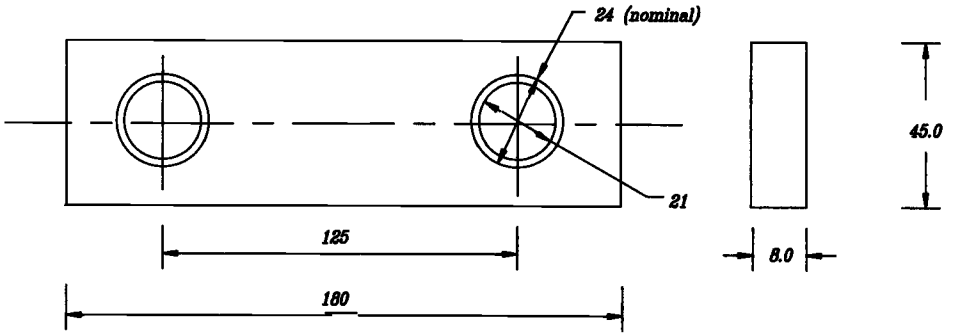

All Dimensions are in mm
Tolerance: General Machining Tolerance

FIG. 1—*Specimens used in tests. Lug bush interface was introduced by increasing bush outer diameter. Bush-pin interface was always a snug fit.*

introduce a statistical element into the study. However, some of the failures were discarded in view of damage to the fracture surface that came in the way of fractographic measurements. The calibration testing under constant amplitude loading was restricted to two coupons, both with snug fit bush-lug assembly. Thus a total of a dozen test coupons were used in the experiments.

Calibration Testing for Stress Intensity Estimates

The objective of the calibration testing was to obtain an empirical stress intensity factor (SIF) versus crack depth function for naturally initiating (part-through) fatigue cracks in the lug. The technique has been used successfully to obtain SIF calibrations for lugs [7]. The basis for the calibration is the assumption that a similar stress intensity range will produce a similar crack growth rate. Then, the SIF versus growth rate relationship estimated from laboratory testing of a standard crack geometry (for which the SIF function is known) can be used to estimate SIF for a nonstandard geometry, provided crack growth rate versus crack-size relationship for the new geometry can be obtained.

There are, however, some riders to the similarity criterion. Crack closure stress in both cases must be identical. This is a crucial requirement considering the power relationship between the crack growth rate and the effective stress intensity range. The requirement was satisfied by performing the calibration at a high stress ratio of $R = 0.7$, where crack closure is absent, particularly in thicker materials. The second requirement is that the growth rates must be desirably in the linear segment ("Paris regime") of the log da/dN versus log ΔK relationship. Threshold conditions may not be similar as there is no evidence to confirm that threshold stress intensity is constant across specimen geometries (concentrated versus distributed loading, thickness effects), crack geometry (through versus part-through cracks), and mode (the possibility of single versus multiple mode due to local crack plane orientation and constraints). Near critical conditions also may not meet similarity criteria because fracture toughness values are unlikely to be identical if material thickness is below the requirements for plane-strain fracture toughness.

The constant amplitude tests were performed under a two-step load program consisting of

ten cycles at S_{max} = 150 MPa, R = 0, followed by 1000 cycles at S_{max} = 140 MPa, R = 0.7. The stress levels listed refer to gross section at the lug (along the expected plane of fracture). It was estimated that the ten larger cycles contributed about 5% of total crack extension. They were included largely to introduce markers on the fracture surface that were required for fractographic crack growth rate estimates. The zero minimum stress in these cycles also ensured that the crack would be fully open (no fatigue crack closure) in the following 1000 cycles at a high stress ratio, which contributed to 95% of crack growth. Thus, it was assumed that applied and effective stress intensity would be similar.

Spectrum Load Testing

Tests were carried out under a modified FALSTAFF load spectrum (Fig. 2). The modifications were introduced to enable easy estimates of crack growth rate from fractography, while at the same time retaining elements of the original randomized load sequence and also the damage equivalence to the original FALSTAFF spectrum [*8*]. Reference *10* provides a detailed description of the modified FALSTAFF spectrum and the procedure for its derivation.

All the spectrum load tests were performed at a maximum gross section stress of 150 MPa, which coincides with the maximum stress in the constant amplitude calibration tests.

The testing was performed on a 100-kN computer-controlled servohydraulic load frame under ambient conditions. The computer was used to download the test load sequence onto the test controller and to monitor loading. The test frequency was 10 Hz under constant amplitude and about 15 Hz (average) under spectrum loading. Operator activity during testing was restricted to monitoring loading and specimen failure. As most failures initiated from semicircular cracks forming at the bush-lug interface, failure would occur with little or no warning by way of crack penetration to the specimen surface.

Fractography

Crack growth rates under constant amplitude as well as spectrum loading were determined through optical fractography of the fatigue fracture surface. This work was performed on an Olympus optical microscope with a digital camera attached to a personal computer. Software for image analysis assisted in sizing, including determination of striation spacing.

The first requirement was to determine the one or more origins of fatigue cracks on the fatigue fracture surface. In the present test series, there was usually one and sometimes two crack origins. Growth rate was determined for the dominant crack only on the assumption that this crack determines residual life and that its growth is not affected by the appearance of new cracks [*11*]. Crack growth rate was determined wherever possible along the depth direction perpendicular to the specimen thickness and the plane of loading. Where this was not possible, the adjacent area was chosen, assuming that growth rate at the same radius from the origin would be similar.

Results

Figures 3*a* and 3*b* show two of the fracture surfaces from the calibration tests. The origin and growth profile of the semielliptical crack is clearly visible. Figures 3*c* and 3*d* show typical enlarged optical fractographs from the constant amplitude calibration tests. The marker bands produced by the low stress ratio cycles are clearly visible. Due to the poor depth of focus associated with optical fractography, it was not possible to obtain quality photographs, particularly at the higher magnification required for smaller crack sizes. Yet

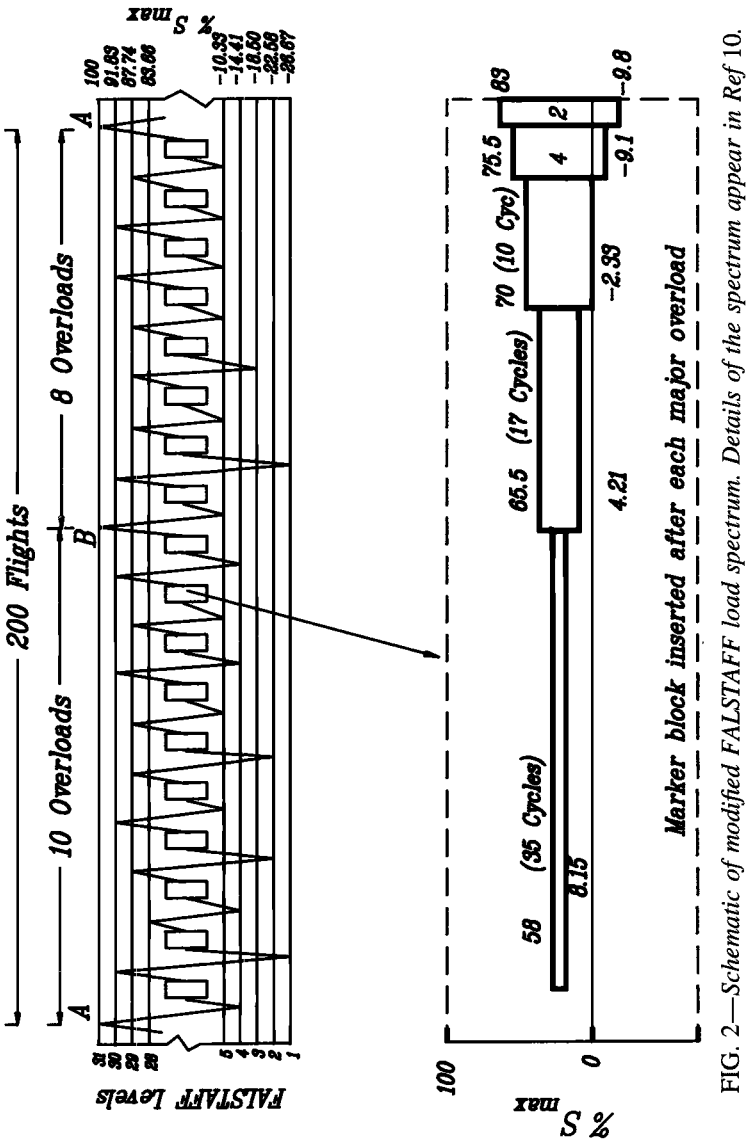

FIG. 2—*Schematic of modified FALSTAFF load spectrum. Details of the spectrum appear in Ref* 10.

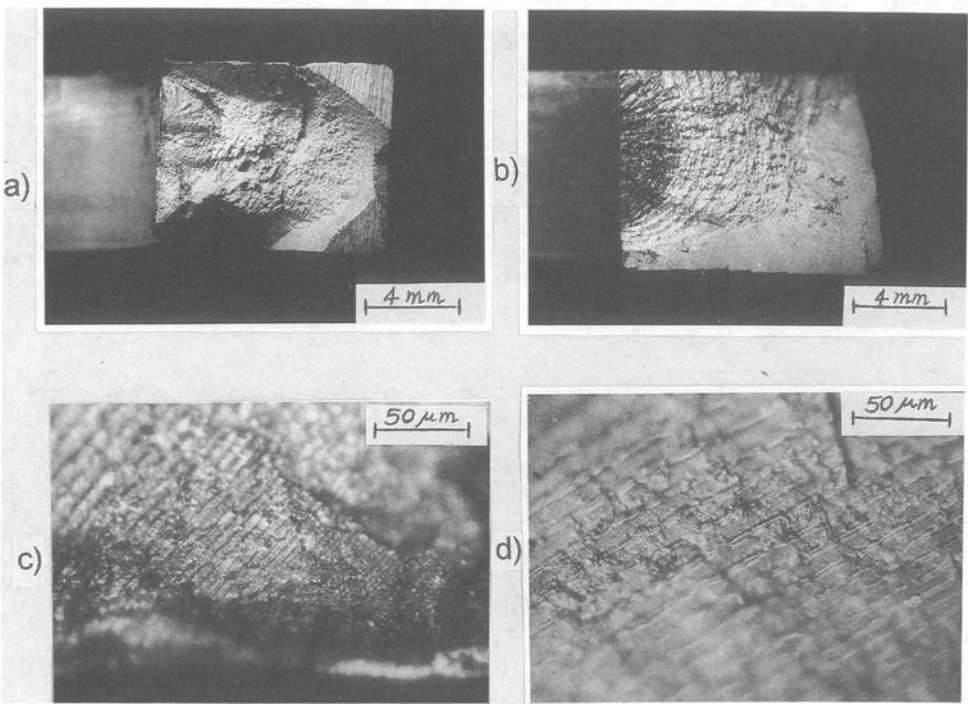

FIG. 3—*Typical fractographs from constant amplitude stress intensity calibration tests:* (a,b) *macro photograph of fracture surface;* (c,d) *optical fractographs.*

unambiguous and repeatable measurements of crack growth rate were possible down to a crack size of 20 μm. Of the four fatigue failures studied, two resulted from the formation of semicircular cracks in the interior, while the other two had origins close to the surface leading to corner cracks. Three of the failures resulted from cracking on one side of the lug with the other side failing due to static overload.

Figure 4*a* shows a quarter elliptical crack profile from the failure of a snug fit lug joint under modified FALSTAFF. Figure 4*b* shows a semicircular crack in the 0.24-mm interference mechanical press fit joint, and Fig. 4*c* shows a quarter elliptical crack in the joint with 0.24-mm interference fit made with liquid nitrogen contraction of the bush. Figure 4*d* shows a typical enlarged optical fractograph from the 0.12-mm interference fit with liquid nitrogen. "A" and "B" mark the two largest loads in the programmed FALSTAFF sequence that space the 18 steps as a combination of 10 + 8 (refer to Fig. 2). The observed striation patterns are similar to those observed in a previous study [*11*] on short cracks at notches with the same material and load spectrum. However, it was consistently observed that the interference fits produced failures with clearer patterns than in the case of snug fits. This may be attributed to the inhibition of the Mode II crack opening component (which can rub out striations) by the steel bush bearing against the lug surface.

As in the case of constant amplitude loading, there was a mix of corner and semi-elliptical cracks. Of the five fits studied under spectrum loading, the exception was the snug fit joint, where all failures were from corner crack formation. Crack depth-to-length ratio was close to 1 in most cases, with semielliptical cracks sometimes showing a ratio as low as 0.7. This effect was ignored in subsequent analysis.

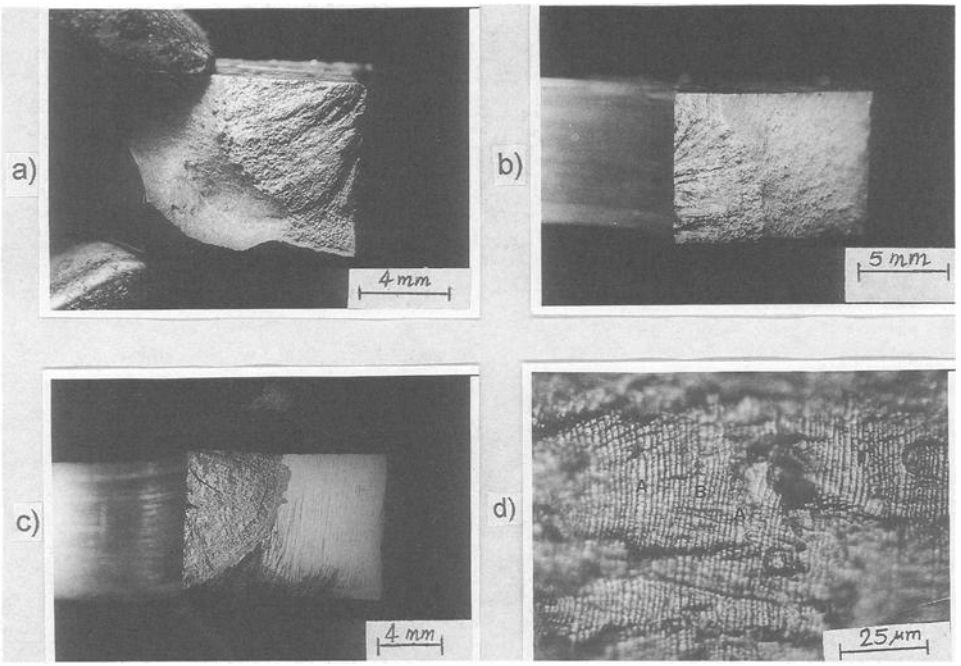

FIG. 4—*Typical fractographs from spectrum load testing:* (a) *quarter elliptical crack profile from snug-fit failure;* (b) *semicircular crack profile from a 0.24-mm mechanical interference fit failure;* (c) *quarter elliptical crack profile from a 0.24-mm interference fit made with liquid-nitrogen-cooled bush;* (d) *typical optical fractograph showing striations from modified FALSTAFF. "A" and "B" mark the two severe overloads in the sequence (see Fig. 2).*

Constant Amplitude Crack Growth Rates

Figure 5 shows a summary of all the constant amplitude crack growth rate measurements versus crack depth. While calculating growth rate to represent the action of only the high stress ratio component (1000 cycles), a block size of 1050 cycles was used on the estimate that the 10 larger cycles were equivalent to 50 small ones.

The data in Fig. 5 clearly indicate a steady and consistent increase of crack growth rate with crack depth. Crack growth rate is high even at the smallest discernible crack size of about 20 μm. Up to a crack depth of a little over 100 μm, growth rate either remains constant or increases marginally. Crack growth accelerates with further growth. Similar observations have been reported in the literature: Mann et al. [*6*] reported a steady increase in growth rate without any discernible "short crack effect" from a crack size below 15 μm in tests on lugs under constant amplitude loading. Similar observations were reported by Moon [*7*].

From the data in Fig. 5, it is difficult to observe any pattern that could be attributed to effects such as single versus double cracking and quarter versus semielliptical cracks. All the growth rates fall into a factor-of-two scatter band, which is larger than what one would observe (in the case of long crack growth) in laboratory coupons. The data in Fig. 5 served as inputs for stress intensity calibration.

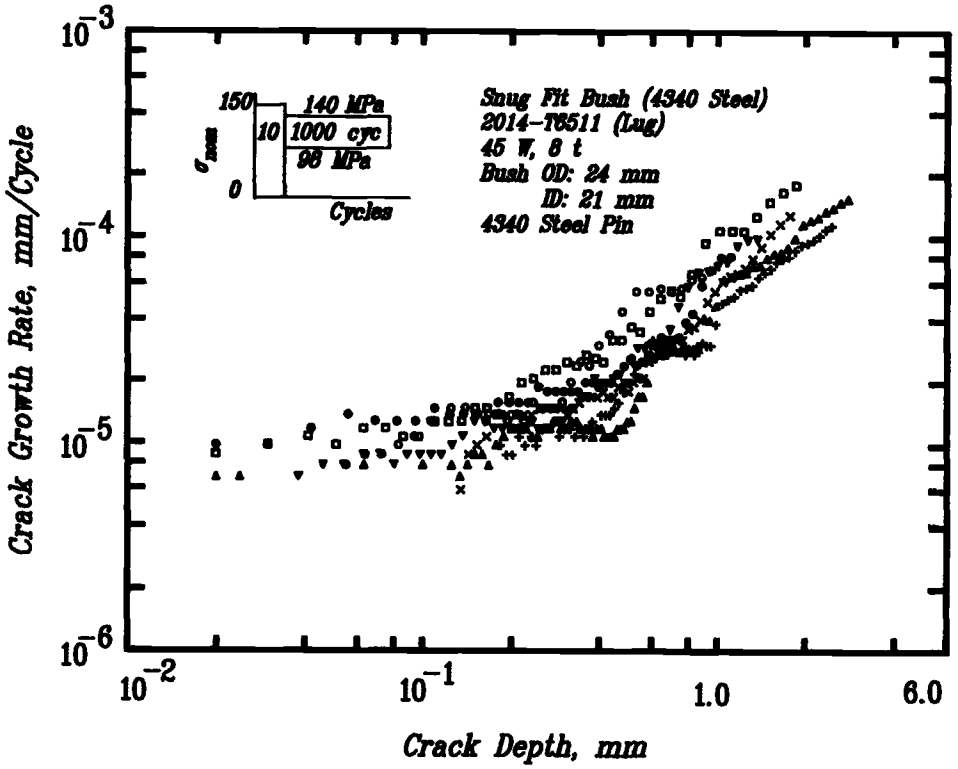

FIG. 5—*Summary of constant amplitude crack growth rate measurements versus crack depth. Different graphical symbols are used to identify data from individual fractures. These data were used to calibrate stress intensity versus crack depth.*

Stress Intensity Calibration

Previous work on the same material indicated that crack growth rate versus effective stress intensity range is described by the equation [*9*]

$$\frac{da}{dN} = C\frac{\Delta K_{\text{eff}}^{m}}{[1 - (K_{\max}/K_c)^2]} \tag{1}$$

where $C = 10^{-7}$ mm/(cycle · MPa/m), $m = 3.27$, and $K_c = 60$ MPa/m for 2014-T6511 [*9*].

The growth rate band covered by the data in Fig. 5 falls strictly into the Paris regime for this material [*9*], suggesting that the nonlinearity at the high and low end of the *da/dN* versus ΔK relationship will not affect stress intensity calibration. Also, in consideration of the high stress ratio, $R = 0.7$, a fully open crack was assumed ($\Delta K = \Delta K_{\text{eff}}$). Therefore, stress intensity due to the unit stress, $\bar{K}$, could be estimated for each data point from the expression

$$\bar{K} = \frac{1}{\Delta S}\left(\frac{da/dN}{C}\right)^{1/m} \tag{2}$$

The results of this analysis appear in Fig. 6 as the stress intensity versus crack depth calibration. An upper and lower bound fit along with a mean fit were made through least

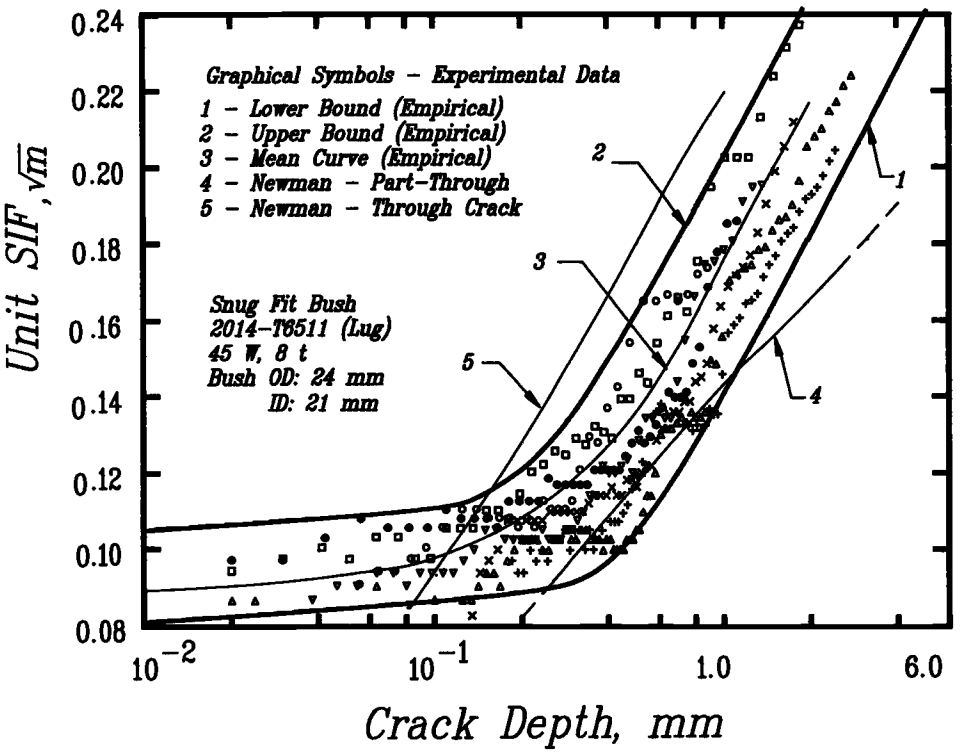

FIG. 6—*Calibrated stress intensity versus crack depth from growth rates in Fig. 5. Different graphical symbols are used to identify data from individual fractures. Also shown are the results of the approximation and analytical solution.*

square analysis using a fourth order polynomial. The three curves also appear on the figure, with very few data points falling beyond the upper and lower bound envelope.

Also shown in Fig. 6 is the Newman solution for stress intensity for a crack growing out of a hole in a lug. Below a crack size of about 100 μm, the Newman solution [*12*] underestimates crack driving force. It has been observed that other solutions from the literature also cannot explain the high growth rates of small cracks in lugs [*6,7*]. The value of the geometry correction factor given by different solutions for near zero crack length is between 5 and 8 [*5*], while the data in Fig. 6 indicate a value in excess of 15. At a crack size in excess of 100 μm, the Newman solution gives estimates closer to empirical estimates if a through crack is assumed. If a correction factor of 0.65 is imposed to reflect the constraint imposed by the part-through nature of (all) the cracks for which data are shown in Fig. 6, even lower estimates of stress intensity follow.

Spectrum Load Crack Growth Analysis

A detailed description of the procedure used for crack growth rate estimates is given in Ref *9*. Briefly, crack growth analysis is based on the Rainflow cycle count from the Modified FALSTAFF load spectrum. The minima in the spectrum were truncated for the purpose of analysis to zero load, considering that the fatigue critical area in the lug joint will

not see compressive loads. It is assumed that the largest counted cycle determines crack opening stress for small cycles embedded either on the rising or falling half of the major cycle.

It was estimated that the notch root will experience monotonic yield (but not cyclic yield), given a gross stress of 150 MPa, a net stress of 321 MPa, and $K_t = 2.4$ [*13*] (the yield stress of the material is 420 MPa). For these conditions, $S_{op} = 0.25$ and $S_{cl} = 0.47$ were determined in a previous study at $R = -0.3$ [*11*]. These values were corrected to $\bar{S}_{op} = 0.275$ and $\bar{S}_{cl} = 0.495$ in consideration of stress ratio $R = 0$ (no negative loads). The values were arrived at by interpolating with the next available data for $R = 0.1$ ($\bar{S}_{op} = 0.3$). Experimental data indicate that the slope of the S_{op} versus the R curve at negative stress ratio is much less than at a positive stress ratio in the case of aluminum alloys and other materials as well [*14*]. The two levels ($\bar{S}_{op} = 0.275$, $\bar{S}_{cl} = 0.495$) form an envelope into which crack opening stress for individual load cycles will fall. As the programmed FALSTAFF sequence is arranged in a lo-hi sequence of steps following the cyclic stress-strain response of the material, it turned out that smaller cycles are superposed on the rising half of larger cycles. Such an arrangement provides lower opening stress values and higher associated crack growth rates for smaller cycles than if the cycles were to be arranged as a hi-lo sequence. The precise value of $\bar{S}_{op,i}$ in individual cycles lying on the rising half of a major cycle follows from the hysteretic crack closure model [*9*] and is given by

$$\bar{S}_{cl,i} = \bar{S}_{op} + (\bar{S}_{cl} - \bar{S}_{op})\left(\frac{\bar{S}_{max,i} - \bar{S}_{op}}{\bar{S}_{max} - \bar{S}_{op}}\right), \qquad \bar{S}_{max,i} \geq \bar{S}_{op} \tag{3}$$

$$\bar{S}_{op,i} = \bar{S}_{cl,i} - (\bar{S}_{cl,i} - \bar{S}_{op})\left(\frac{\bar{S}_{cl,i} - \bar{S}_{min,i}}{\bar{S}_{cl,i} - \bar{S}_{min}}\right), \qquad \bar{S}_{min,i} \leq \bar{S}_{cl,i}$$

The crack growth rate over each of the Rainflow counted cycles in the spectrum is summed up assuming a stationary crack of given size. The total is divided by the number of flights in the spectrum to give an average crack growth rate per flight at the given crack size

$$\frac{da}{dF} = \frac{(S_{max} \cdot \bar{K})^m}{n_F} \sum_{i=1}^{n_{cy}} \frac{[\bar{S}_{max,i} - \max(\bar{S}_{op,i}, \bar{S}_{min,i})]^m}{[1 - (\bar{S}_{max} \cdot \bar{K} \cdot \bar{S}_{max,i}/K_c)^2]} \tag{4}$$

For modified FALSTAFF, $n_{cy} = 1242$ cycles and $n_F = 200$.

The upper-bound, lower-bound, and mean stress intensity calibrations shown in Fig. 6 were used to calculate lower bound, upper bound, and mean crack growth rate curves for spectrum loading. Integrating the inverse of these curves over a given interval of crack growth provided the crack propagation life interval. This was done over two intervals: from 10 to 100 μm and from 100 μm to failure. Failure was computed to occur at a 5-mm depth, where critical stress intensity is reached under maximum stress. The 10-μm initial crack size was chosen in consideration of observations of fatigue crack growth at that size. Similar crack size (10 to 15 μm) has been suggested as a starting point for fracture analysis in previous studies [*15*]. The 100-μm intermediate mark in the crack growth interval was selected for two reasons (refer to Fig. 5): (1) the constant amplitude growth rate data gave an indication that this mark appears to divide the crack growth curve into two qualitatively different areas, and (2) the growth rate below this size remains fairly constant or marginally increases with size.

Mil Spec 83444A [*16*] suggests an initial crack size of 125 μm for fracture mechanics analysis of lug joints. Selected 100-μm intermediate crack size is close to this value. As

shown below, spectrum load crack growth rate and associated residual life did not appear to depend greatly on the type of fit beyond this crack size.

Experimental and Calculated Crack Growth Rates

Crack growth rates under spectrum loading are consolidated in Fig. 7. Data from all the fatigue failures are included in the figure. Also shown in the figure are the upper and lower bound as well as mean crack growth rates calculated using the analysis described above. Growth rates vary by up to an order of magnitude at crack size below about 200 μm. These variations are across different levels of interference and far exceed the variation observed in the calibration tests. Interestingly, growth rates within a data set show negligible variation even over crack extension from 10 to 200 μm. This appears to underline a systematic effect rather than random scatter in data.

At a higher crack size (above 400 μm), the upper and lower bounds of calculated crack growth rates appear to almost totally encompass experimental observations. The exception to this observation are data from the 0.12-mm mechanical interference fit test, which fall well above the calculated upper bound up to a crack size of about 400 μm. The reasons for this exception are not clear, but it is possible that extensive wear (in excess of 100 μm) of the lug surface may be responsible for this observation. This is supported by the noticeably

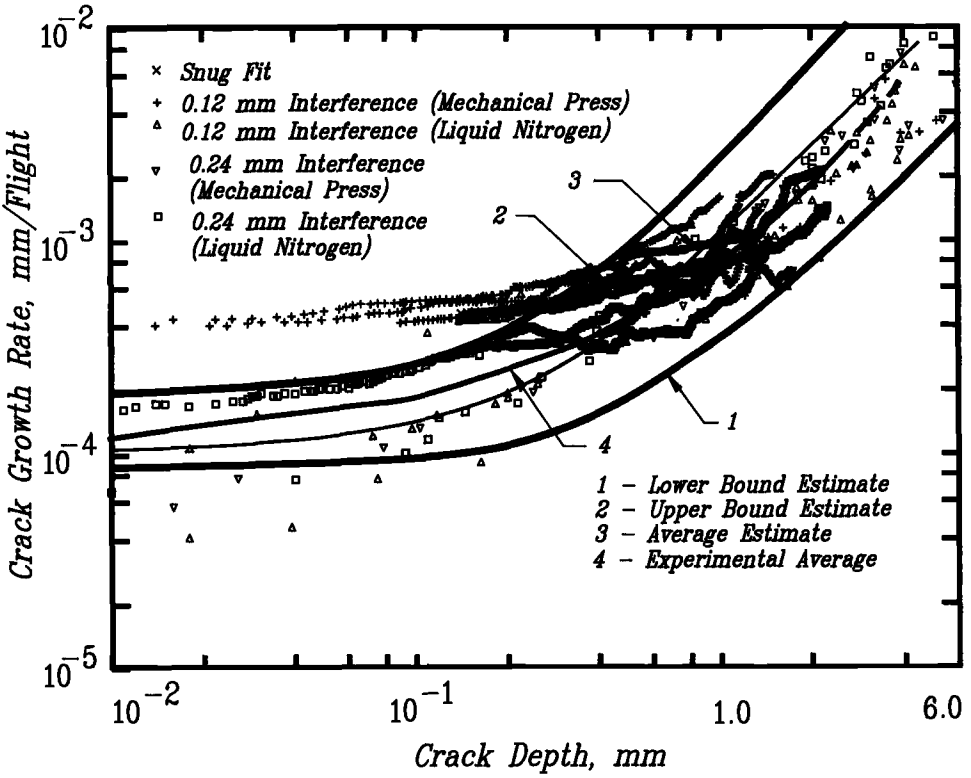

FIG. 7—*Crack growth rates under spectrum loading. Different graphical symbols are used to identify data from individual fractures. Also shown are average values, along with results of calculations based on the prediction model.*

larger life to crack formation for this particular fit (see Fig. 8) when compared to other fits, which does not tie up with high initial growth rates, suggesting that material could have been removed during as well as after crack formation, leaving evidence of higher growth rates that actually relate to a larger crack.

At a crack size exceeding 400 μm, the calculated mean growth rate curve correlates well with the mean growth rate curve fitted through empirical data. The calculated mean growth rate as well as the predicted envelope clearly demonstrate the viability of applying empirical stress intensity derivations to spectrum loading and also validate the extension of hysteretic crack closure and Rainflow-based analysis [*9*] to crack growth at lugs.

In view of the fluctuations in crack growth rate and the intersection of some growth rate curves, it was not possible to draw clear conclusions on the effects, if any, of the type of fit. In an attempt to overcome this problem, the fractographically determined crack growth rate curves were integrated to get the crack growth curve. The integration was performed over the crack growth interval from 10 μm to failure. For cases where growth data could not be obtained at certain crack lengths, interpolation/extrapolation of data was resorted to with due consideration to trends observed in other failures. This provided more relevant data for comparisons as shown by the bar charts of total life and crack growth life intervals shown in Fig. 8.

Fatigue Life Intervals

The total life to failure was recorded during the test. Integration of the growth rate curve from 10 μm to failure provided an estimate of crack propagation life. The difference between total life and this estimate gives life to formation of a 10-μm crack, which is referred to as crack initiation life. As indicated on Fig. 8, estimated crack initiation life varied between 2600 and 13 000 flights, largely depending on the type of fit.

Fatigue life estimates for the FALSTAFF load spectrum using the local stress-strain approach with Neuber conversion and the Manson-Coffin equation with mean stress correction after Morrow give an estimate of about 4500 flights for the applied stress level and K_t at the lug-bush interface [*17*]. Though this value is very close to the observed experimental average, its validity may be questioned. Low-cycle fatigue data that form the basis for calculations often refer to either life to failure or at least to 0.1 to 0.5-mm crack size (as opposed to the 10-μm size in the present case). Crack initiation in the lug joint may be fretting dominated, and the effect of interference-induced residual stresses must be considered. These possibilities are supported by the sensitivity of crack initiation life to the type of fit. In fact, of the different life intervals shown in Fig. 8, life to formation of a 10-μm crack appears to be the only component that is clearly sensitive to the type of fit and, to a large extent, contributes to variation in total fatigue life.

Crack propagation life over the interval from 10 to 100 μm varies by a factor of about 4. The 0.12-mm interference mechanical press fit and snug fit cases showed low lives of approximately 400 flights. All the others fell into the 800 to 1800 flight range, which was also predicted by analysis.

Residual life over the crack growth interval from 100 μm to failure does not appear to be influenced by the type of fit. The variation in this life interval is about a factor of 2 and largely random in nature, pointing to the insensitivity of crack growth over this interval to the type of fit.

Discussion

The fractographic technique for crack growth rate measurements used in this study had been developed earlier to study short crack growth at notches under spectrum loading [*9*].

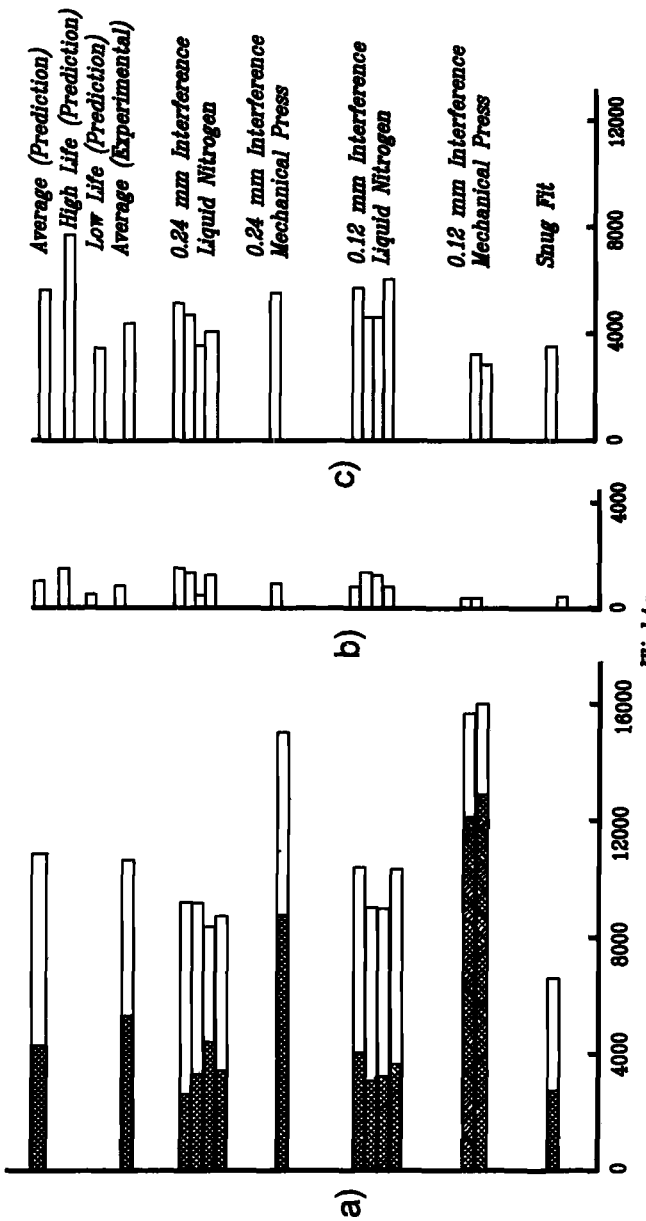

FIG. 8—*Fatigue life intervals estimated by integration of fractographic growth rate measurements:* (a) *total life to failure; hatched region indicates life to formation of a 10-μm crack;* (b) *life interval from 10 to 100 μm;* (c) *life interval from 100 μm to failure.*

Results from the present study confirm the viability of this cumbersome but reliable technique to characterize the growth of naturally initiating fatigue cracks in lugs. It has been pointed out that artificially initiated cracks from saw cuts, etc., can distort the fatigue crack growth process in lugs [*7*].

The stress intensity calibrations obtained in this study are qualitatively similar to those reported in the literature [*6,7*], indicating much higher stress intensity for small, part-through cracks than would be given by analytical solutions. Obviously, the action of fretting and high contact loads from particles, debris, and machining undulations on SIF of small part-through cracks in lugs requires further study. This effect is sustained and repeatable. However, the scatter band in the SIF versus crack depth calibration (between individual cracks) appears to be much wider than what one would see in the case of long through cracks in standard laboratory coupons. The factors that may be responsible deserve further study.

Moon has reported that stress intensity calibration may be sensitive to lug and bush material and their interaction [*7*]. However, while the calibration experiments in this study precluded the effect of crack closure by testing at a high stress ratio and by selecting a loading level to ensure all data fall within the "Paris regime," the same cannot be said of the loading conditions reported in Ref *9*. In an SIF calibration exercise, it may be important to ensure that the effect of parameters like fracture toughness, threshold stress intensity, and particularly fatigue crack closure are minimized to negligible proportions.

The crack propagation lives that were obtained fall within the bandwidth of residual life requirements for combat aircraft, indicating that the fixed maximum stress of 150 MPa used in testing was realistic. This stress caused monotonic yield at the lug-bush interface during peak loading. This would have neutralized any residual stress effects from the interference fits and may explain why crack growth life from about 100 μm to failure in all the cases falls into a single scatter band. The same observation may not remain valid under fully elastic loading conditions. On the other hand, the extent and type of interference (liquid nitrogen contraction of bush or mechanical press fit) did appear to significantly affect life to formation of a small crack. As indicated by Mann et al. [*7*] and in a recent analysis by Raju [*18*], there is an optimum interference for maximum benefit in terms of crack initiation life.

The mechanical press fits produced greater resistance to fatigue than the liquid nitrogen fits. This may be due to the "cold working" action of the forced insertion and also due to better "locking" of the two surfaces through the grooves that form in the process. The liquid nitrogen fits may in fact leave microcavities for accumulation of fretting debris. Surface finish may appear to be influential, though studies of this aspect have at best thrown up the possibility that a coarse finish may, in fact, increase fatigue resistance [*6*]. Stress analysis of interference fit joints would have to simulate details of the technological process and associated material transformations while modeling fastener response to external load.

Interestingly, the effect of interference on crack formation was noticeable even though applied stress was high. However, the effect becomes negligible once a crack even tens of microns in size is formed. Let us consider why this is so, while noting that the effect of an interference fit may extend to a larger crack size at lower applied stress levels. Figure 9*a* shows a schematic of the lug-bush interface. The crack formation process occurs through irreversible slip at the lug surface. This is schematically illustrated by the hole contour distortion along the plane of loading. The presence of considerable interference gives rise to large radial bearing load (enough to cause local yield [*19*]) from the hard bush surface that acts both as a barrier enforcing plane strain by inhibiting surface contraction/expansion across thickness) and perhaps as a corrector of slip ("ironing and trimming effects") on the lug surface (Fig. 9*b*). The radial bearing loads along the Y-axis (the axis of loading) will relax due to the high applied load causing yield along the plane of highest net stress, but the

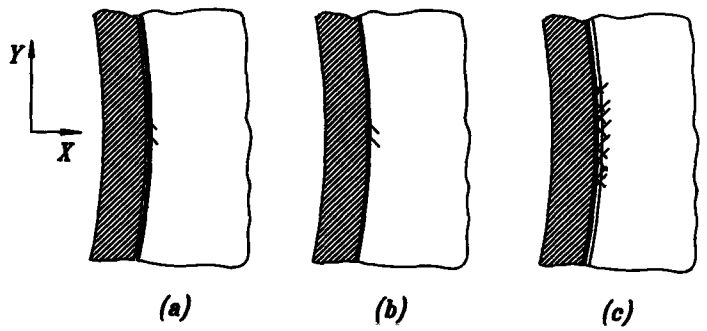

FIG. 9—*Schematic of the influence of bush-lug interference on the formation of fatigue crack through-cyclic slip band accumulation.*

bearing loads against the X-axis are unlikely to decrease. They will either obstruct crack-forming reversible slip or "clip" resulting protrusions (Fig. 9*b*). Thus, the extent and type of interference (mechanical press fit or liquid nitrogen fit) will influence the rate of accumulation of irreversible slip bands. With prolonged cycling, wear, fretting, and accumulation of irreversible slip, microcracks form on multiple planes, which intersect at some depth (Fig. 9*c*). The intersection of these cracks leads to material disintegration and debris formation that migrates either to the surface or to cavities of lower bearing stress. The hole expands in this manner (thin line along circumference), reducing interference. As a consequence, resistance to further slip-band formation is eliminated. So is resistance to Mode II fatigue crack growth. This may explain why crack growth life from 100 μm to failure in the present study was unaffected by the extent and type of interference fit.

It must be noted that data from the present study on early crack growth (up to a size of 100 to 200 μm) cannot be considered very reliable. These dimensions are of the same order as the extent of interference and dimensions of surface features due to machining and abrasion, particularly during forced mechanical interference fit. Considerable wear leading to removal of material may have distorted crack depth estimates over the small crack interval in Fig. 7. This aspect could not be verified due to a change in dimensions at fracture. The associated ambiguity in crack size estimates may not be critical as both the literature data [*6,7*] and the results from this study indicate a negligible crack size effect on growth rate over the affected interval of crack growth.

Finally, the results of this study suggest that it is possible to make predictions of lug residual life assuming an initial defect size of 0.125 mm suggested by Mil Spec 83444A on Damage Tolerance and Residual Strength for Airframes. Apart from fatigue design, the procedure is also applicable to inspection intervals and schemes for condition monitoring. There is, however, a requirement for improvements in computation of stress intensity of naturally initiating part-through cracks in lug joints with interference fit bushes. An experimental study examining this aspect is currently under progress.

Conclusions

Lugs with various interference fits were tested under a modified FALSTAFF load spectrum to characterize the growth to failure of naturally initiating (part-through) cracks. A stress intensity calibration was obtained from constant amplitude testing of a lug joint.

1. The calibrated stress intensity function differed noticeably from estimates given by available analytical solutions.

2. While the effect of type and extent of interference is sizeable in the early stage of crack formation, there appears to be no systematic effect on residual life after a size of about 100 μm. It is suggested that the resistance to slip-band formation (on the lug surface) by the bearing action of the bush may determine life to crack formation.

3. Initial crack growth rates appeared to vary by as much as an order of magnitude between different cases studied. However, the variation could not be linked to the extent or type of interference fit and appeared to diminish considerably after a crack depth of about 400 μm to fall into a narrow scatter band.

4. Calculated residual life in the presence of a 100-μm defect correlates well with experimental observations. The calibrated stress intensity function obtained under constant amplitude loading was used in predictions.

Acknowledgment

The support of the Aeronautical Development Agency towards this study is gratefully acknowledged. The authors deeply appreciate the meticulous fractography efforts of Ms. Tashina Kariappa and Mr. H. M. Girish of COMAT Services Ltd. and photography support rendered by Graphics Arts Section of NAL.

References

[*1*] Berkovits, A. and Prinz, D., "Growth of Parabolic Fatigue Cracks from Flaws at Fastener Holes," *Fracture Mechanics: Eighteenth Symposium, ASTM STP 945,* D. T. Read and R. P. Reed, Eds., American Society for Testing and Materials, West Conshohocken, PA, 1988, pp. 1050–1069.

[*2*] Friedrich, S. and Schijve, J., "Fatigue Crack Growth of Corner Cracks in Lug Specimens," Report LR-375, Delft University of Technology, Delft, 1983.

[*3*] Schijve, J. and Hoeymakers, A. H. W., "Fatigue Crack Growth in Lugs and the Stress Intensity Factor," Report LR 273, Delft University of Technology, Delft, 1978.

[*4*] Impellizzeri, L. F. and Rich, D. L., "Spectrum Fatigue Crack Growth in Lugs," *Fatigue Crack Growth Under Spectrum Loads, ASTM STP 595,* American Society for Testing and Materials, West Conshohocken, PA, 1975.

[*5*] Buch, A. and Berkovits, A., "Fatigue Crack Propagation in Al-Alloy Lugs under Constant Amplitude and Maneuver Spectrum Loading," Technical Report TAE No. 497, TECHNION Israel Institute of Technology, Haifa, 1983.

[*6*] Mann, J. Y., Revill, G. W., and Pell, R. A., "Influence of Hole Surface Finish, Cyclic Frequency and Spectrum Severity on the Fatigue Behaviour of Thick Section Aluminium Alloy Pin Joints," Aircraft Structures Report ARL-STRUC-R-430, Aeronautical Research Laboratory, Melbourne, 1987.

[*7*] Moon, J. E., "Crack Growth in Pin-Loaded Lugs," Paper 2.9, *Proceedings,* Aircraft Fatigue in the Eighties, Eleventh ICAF-Symposium, J. B. de Jonge and H. H. van der Linden, Eds., National Aerospace Laboratory, The Netherlands, 1981.

[*8*] Van Dijk, G. M. and de Jonge, J. B. in *Proceedings,* Eighth ICAF Symposium, J. Branger and F. Berger, Eds., International Committee on Aeronautical Fatigue, Lausanne, Switzerland, Swiss Federal Aircraft Establishment, Emmen, Netherlands, 1975, Paper 3.61.

[*9*] Sunder, R., Prakash, R. V., and Mitchenko, E. I., "Calculation of Spectrum Load Notch Root Crack Growth Rate Under Elastic and Inelastic Conditions," *Advances in Fatigue Lifetime Predictive Techniques: Second Volume, ASTM STP 1211,* M. R. Mitchell and R. W. Landgraf, Eds., American Society for Testing and Materials, West Conshohocken, PA, 1993, pp. 30–44.

[*10*] Mitchenko, E. I., Prakash, R. V., and Sunder, R., "Fatigue Crack Growth Under Programmed Equivalent of FALSTAFF Spectrum," NAL Project Document PDST 9233, National Aeronautical Laboratory, Bangalore, 1992.

[*11*] Sunder, R., Prakash, R. V., and Mitchenko, E. I., "Fractographic Study of Notch Fatigue Crack Closure and Growth Rates," *Fractography of Modern Engineering Materials, Composites and Metals, Second Volume, ASTM STP 1203,* J. E. Masters and L. N. Gilbertson, Eds., American Society for Testing and Materials, West Conshohocken, PA, 1993, pp. 113–131.

[*12*] Newman, J. C., Jr., "Predicting Failure of Specimens with Either Surface Cracks or Corner

Cracks at Holes," NASA TN D-8244, National Aeronautics and Space Administration, Washington, DC, June 1976.

[*13*] Rao, A. K., Dattaguru, B., and Ramamurthy, T. S., "Fatigue Behaviour of Joints," *Proceedings,* Workshop on Fracture Fatigue and Failure Analysis, National Aeronautical Laboratory, Bangalore 1979, Paper N.

[*14*] Schijve, J., "Some Formulas for the Crack Opening Stress Level," *Engineering Fracture Mechanics,* Vol. 14, 1981, pp. 101–105.

[*15*] Newman, J. C., Jr., Phillips, E. P., Swain, M. H., and Everett, R. A., Jr., "Fatigue Mechanics: An Assessment of a Unified Approach to Life Prediction," *Advances in Fatigue Lifetime Predictive Techniques, ASTM STP 1122,* M. R. Mitchell and R. W. Landgraf, Eds., American Society for Testing and Materials, West Conshohocken, PA, 1992, pp. 5–27.

[*16*] Military Specification MIL-A-83444 (USAF), "Airplane Damage Tolerance Requirements," July 1974.

[*17*] Sunder, R., "Rainflow Applications in Accelerated Cumulative Fatigue Analysis," *The Rainflow Method in Fatigue,* Y. Murakami, Ed., Butterworth-Heinemann, Oxford, 1992.

[*18*] Raju, K. N., "Fatigue Analysis of Lug Joints with Interference Fit Pins Under Constant Amplitude Loading and Elastic Conditions," NAL PDCW 9212, National Aeronautical Laboratory, Bangalore, November, 1992.

[*19*] Callinan, R. J., "Stress Analysis of a Lug Loaded by a Pin," ARL Structures Note 439, Aeronautical Research Laboratories, Melbourne, 1977.

Sheri D. Sheppard[1]

Further Refinement of a Methodology for Fatigue Life Estimation in Resistance Spot Weld Connections

REFERENCE: Sheppard, S. D., **"Further Refinement of a Methodology for Fatigue Life Estimation in Resistance Spot Weld Connections,"** *Advances in Fatigue Lifetime Predictive Techniques: 3rd Volume, ASTM STP 1292,* M. R. Mitchell and R. W. Landgraf, Eds., American Society for Testing and Materials, 1996, pp. 265–282.

ABSTRACT: The overall objective of this research is to develop a general model of fatigue crack propagation in resistance spot-welded joints. An important feature of this development is that the model and accompanying methodology should be accessible to designers evaluating fatigue response of structures containing multiple welds. This objective is achieved by examining the stress state around a resistance spot weld. A general expression for the *structural stress* around the weld is formulated that is dependent only on the loading immediately surrounding the weld; as such, it is specimen independent.

In previous work [*1*] it was found that structural stress could be successfully used to estimate life for crack initiation and growth to a length of 0.01 in. (0.254 mm) in resistance spot welds, and that this period represents less than 30% of the total life in as-welded joints. It is important to note that estimation of this period is highly dependent on fatigue-related material properties. In Ref *2* it was shown that structural stress can be related to crack propagation life through linear elastic fracture mechanics. Using the resulting relationship between structural stress and life, life estimations were made for a variety of HSLA steel specimens (e.g., tensile-shear, coach peel) in a number of conditions (e.g., as-welded, prestressed) and were compared with experimentally measured lives. Life estimations were within a factor of 3 of measured lives.

In the current work, the methodology developed in Ref *2* for estimating propagation life is extended by explicitly considering the effects of axial loading and of load ratio on life estimates. In addition, issues related to creating an appropriate finite element model are addressed, and a number of modeling guidelines are established. Total life estimations are made and compare favorably with experimentally measured lives of welds in mild steels in a variety of specimen configurations.

KEYWORDS: fatigue, resistance spot weld, structural stress, finite element analysis, life prediction

The work presented here builds upon a vast amount of fatigue-related research on resistance spot welds (RSW) that has been carried out over the last 40 years. Researchers have studied the effects of various parameters (e.g., *R*-ratio, specimen geometry, material) on fatigue performance. References *3–5* contain good summaries of many of these data. Unfortunately, until recently it has not been possible to make quantitative comparisons between most of these results because no common basis/parameter had been identified that correlates with fatigue performance. For example, it was not possible to compare alternating

[1]Associate professor, Mechanical Engineering, Design Division, Stanford University, 503 Terman, Stanford, CA 94305-4021.

load or nominal stress versus life for tensile-shear and coach peel samples. In general, it has only been possible to compare data from various researchers in a qualitative manner.

In an effort to consolidate empirical data and to develop life prediction capabilities for designers, a number of techniques have been proposed for estimating fatigue life in resistance spot-welded joints. They can be broadly classed as:

1. Techniques that characterize the intersection of the faying surface at the nugget as a crack tip and use the stress intensity factor (SIF) or J-integral range as a parameter that can be related to life. Cooper and Smith [*6*] propose relating the SIF range of a crack growing through the sheet to the crack growth rate using a Paris law relationship; they never actually make fatigue life estimations. Pook [*7*], Kurath [*8*], Swellam et al. [*9,10*], Wang and Ewing [*11*], Kardomateas [*12*], and Davidson and Imhof [*13*] have all posed relationships of a form

$$\Delta K_{\text{Imax}} = A(N)^{-b} \tag{1}$$

where ΔK_{Imax} is an equivalent Mode I SIF range *before* crack growth through the sheet, N is the number of cycles to failure (assumed to be through the sheet thickness), and A and b are material parameters. All of these approaches are based on the empirical data of Cooper and Smith [*14*] that show that the rate of crack growth through the sheet thickness is approximately constant; therefore, ΔK_{I} is approximately constant.

Various solutions (e.g., Radaj [*15*] and Pook [*16*]) have been given for the stress intensity at a spot weld. Swellam et al. [*9,10*] give relationships between the Mode I and Mode II SIFs, and the loads (Q, T, M, as defined in Fig. 1*c*) transferred through the nugget of the form

$$\Delta K_{\text{I}} = T/c + 3M/(rc) \tag{2}$$

$$\Delta K_{\text{II}} = Q/c \tag{3}$$

where $c = 2r(\pi r)^{0.5}$, and r is the nugget radius. Furthermore, they define

$$\Delta K_{\text{Imax}} = (\Delta K_{\text{I}}^2 + \beta^* \Delta K_{\text{II}}^2)^{0.5}/G \tag{4}$$

where β^* is a material parameter, and G is a geometrical correction factor; ΔK_{Imax} is then related to fatigue life through a relationship such as Eq 1.

2. Techniques that relate the forces (such as Q, T, M in Fig. 1*c*) directly to fatigue response without going through an SIF, as proposed by Okuno et al. [*17*] and Mabuchi et al. [*18*]. This approach requires an explicit mapping between a specimen of similar design and so is of limited generality.
3. Techniques that consider the faying surface at the nugget to contain a finite radius and so act as a notch. The resulting local strain range is related to life through, for example, a Smith-Watson-Topper (S-W-T) model [*19*]. Oh [*20*] and Kan [*21*] have posed strain range-life models of fatigue behavior in resistance spot welds. Strain range at the faying surface is used in these models and has been found by Kan, as well as by Tanaka et al. [*22*], to correlate well with fatigue life.

More recently, strain-based life-prediction techniques have been proposed that use finite element representations of the specimen or structure as the map between outer strain (which can be physically measured or predicted with rather crude finite element

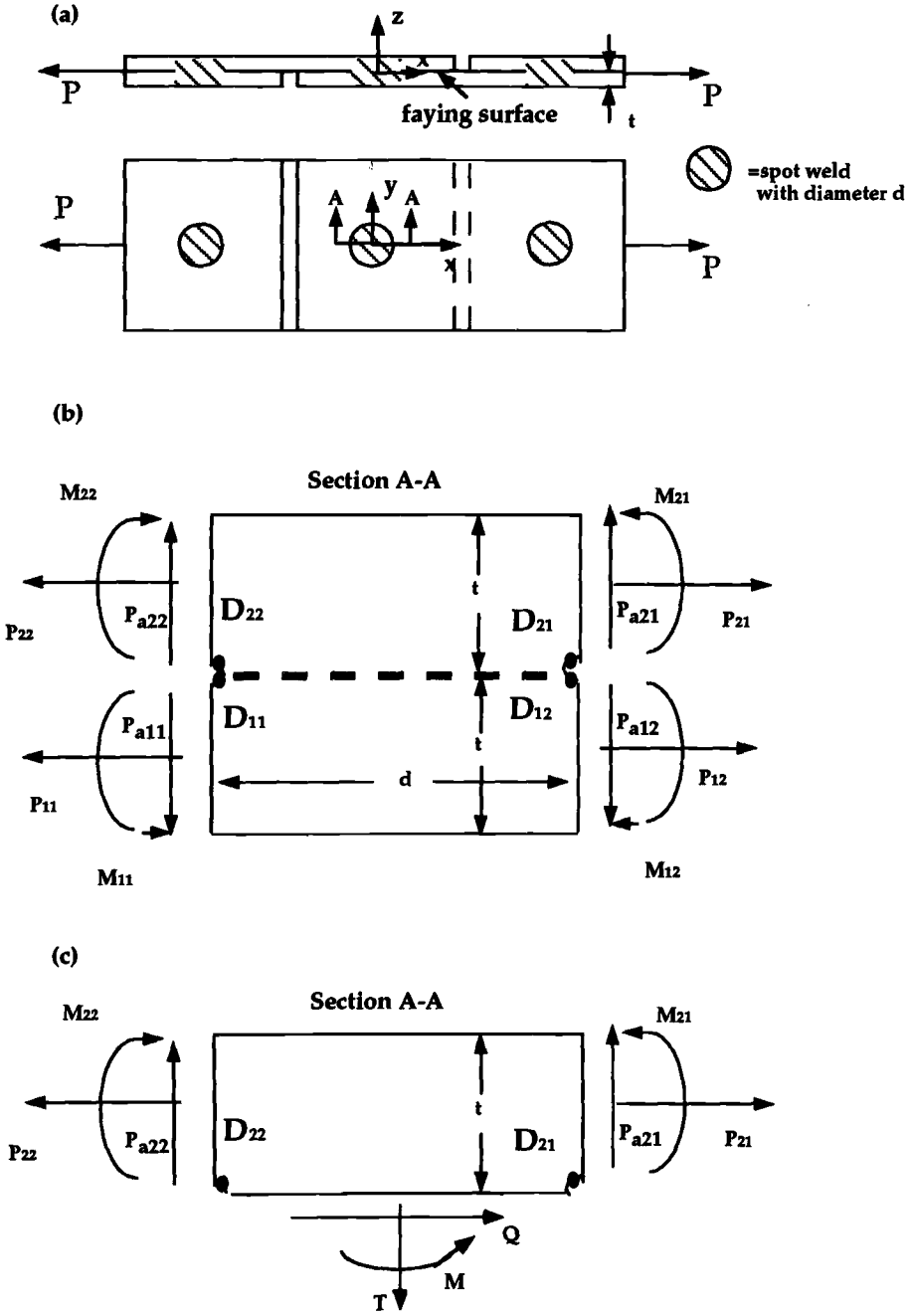

FIG. 1—*Nomenclature for weld geometry and local loads:* (a) *layout of a tensile-shear resistance spot weld specimen;* (b) *section through spot weld showing various regions;* (c) *free body diagram with faying surface cut (as shown in* (b)*);* (d) *various loading modes considered in this work.*

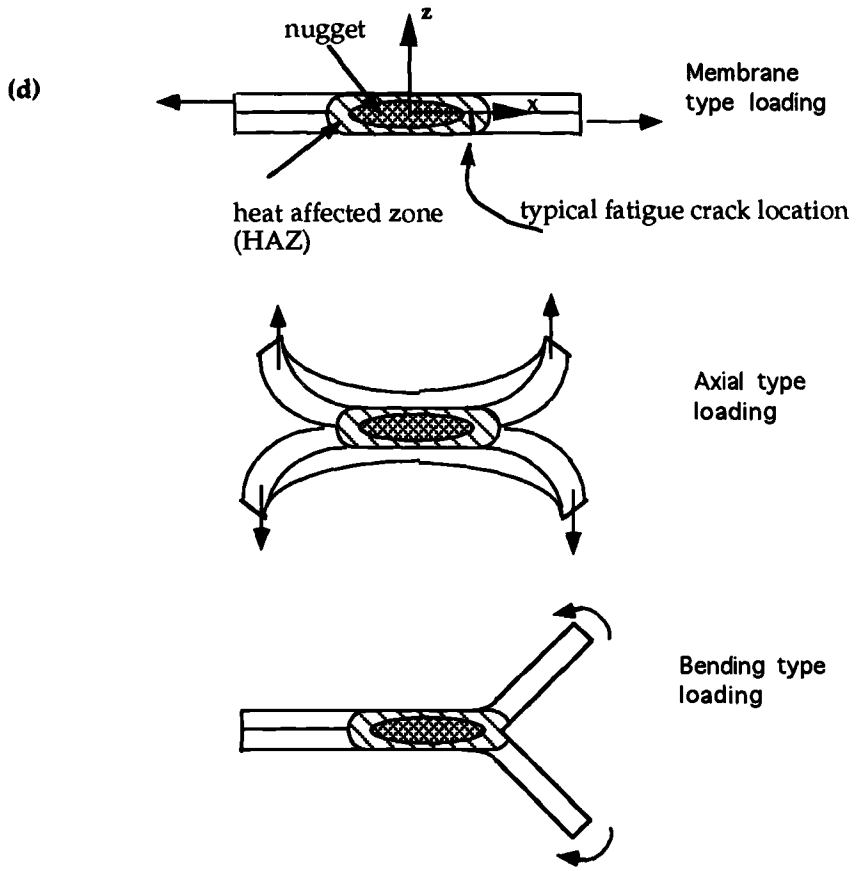

FIG. 1—*Continued.*

(FEM) representations and has been found to not correlate directly with fatigue life) and faying surface strain (which does correlate directly with fatigue life, Simon and Krause [*23*]). Examples of this approach are given in Refs *24–26*. A drawback of this general approach is that it requires a high level of detail in the finite element representation over all or part of the specimen/structure and so may be prohibitive in terms of necessary computational resources for a general structure containing multiple welds.

4. Techniques based on the idea that structural stress is an indicator of weld performance. In Refs *15* and *27* Radaj defines three relatable characterizations of the region around the nugget, namely, nominal structural stress (σ_{ns}), notch stress, and stress intensity factor. Structural stress is the stress linearly distributed over the sheet thickness, with the singularity at the spot weld edge being completely suppressed. When the nominal structural stress is multiplied by a stress concentration factor, it is equal to the notch stress. Radaj also formulates values of K_I, K_{II}, and K_{III} for the as-welded joint (i.e., no crack formation in the through sheet direction) based on structural stress and the square root of the sheet thickness.

   Using the same conceptual definition of structural stress proposed by Rahaj [*15,27*]

but with a different mathematical representation between the various loads (this point will be discussed further in the subsequent section), Sheppard and Strange [*1*] made estimates of the portion of fatigue life spent initiating and growing a fatigue crack 0.01 in. (0.254 mm) long in resistance spot-welded specimens of HSLA steel. The work used the idea of structural stress and a Smith-Watson-Topper [*20*] model of initiation. It is interesting to note that the early crack growth considered by Sheppard and Strange represents growth through approximately 40 grains (the average size of a grain in the heat-affected zone was 6 μm). They concluded that it might be appropriate to describe crack growth from a smaller crack size until it becomes visible using fracture mechanics. Sheppard developed this idea in Ref *2*, where it was shown that structural stress could be related to crack propagation life through linear elastic fracture mechanics.

In the current work, the methodology developed in Ref *2* for estimating propagation life is extended by explicitly considering the effects of axial loading and of load ratio on life estimates. In addition, issues related to creating an appropriate finite element model are addressed, and a number of modeling guidelines are established.

Structural Stress

Basic Definition of Structural Stress

The basic premise of the approach used here is that the structural stress at a distance of half the diameter of the weld nugget from the center of a weld can be related to fatigue crack propagation. This assumes that fatigue failure is via crack initiation and growth through the sheet thickness, as opposed to through the nugget (i.e., growth is in the z-direction, as shown in Fig. 1, Ref *2*, not in the x-direction). This is generally the case for fatigue of a thin sheet with welds of reasonable size, as used in the automotive industry. Structural stress is the linearly distributed stress through the sheet thickness with the stress concentration and/or notch singularity suppressed. Note that total fatigue life (N_t) in this work is defined as the sum of the number of cycles for crack initiation (N_I) and growth through the sheet thickness (N_p). N_I includes initiation and growth of a crack to a length of 5 to 10 grains. Crack growth through the width of the sheet is not included in this definition.

The structural stress range, ΔS, for the two-dimensional problem shown in Fig. 2 is derived by considering the stress developed at the edge of the weld at locations D_{ij}, $i = 1,2$, and $j = 1,2$, where i refers to the sheet (first or second) and j refers to the leg in that particular sheet. These particular locations were selected based on observed fatigue crack behavior in resistance spot welds (for example, see Fig. 1*b* from Ref *2*], or the work of Wang and Lawrence [*28*], which talks extensively about weld fatigue morphology). Nugget rotation is assumed to be negligible. The result is

$$\Delta S_{ij} = \Delta P_{ij}/(\omega t_1) + 6\Delta M^*_{ij}/(t_i^2\beta) + \Delta P_{Ai}/t_i^2; \qquad i,j = 1,2 \tag{5}$$

where ΔP_{ij} is the membrane load range at the edge of the nugget (see Fig. 2*c*), ΔM^*_{ij} is the bending moment range, as defined in Table 1, and $\Delta P_{Ai} = \Delta P_{ai1} + \Delta P_{ai2}$, as shown in Fig. 2*c*) is the axial load range in the nugget. The third term in Eq 5 represents a "cupping" deformation mode that results from a transverse load applied to the sheet; the form was suggested in Ref *29*. Note that this term represents a refinement and extension of the definition of structural stress given in Refs *1* and *2*; Eq 5 is a more general expression for

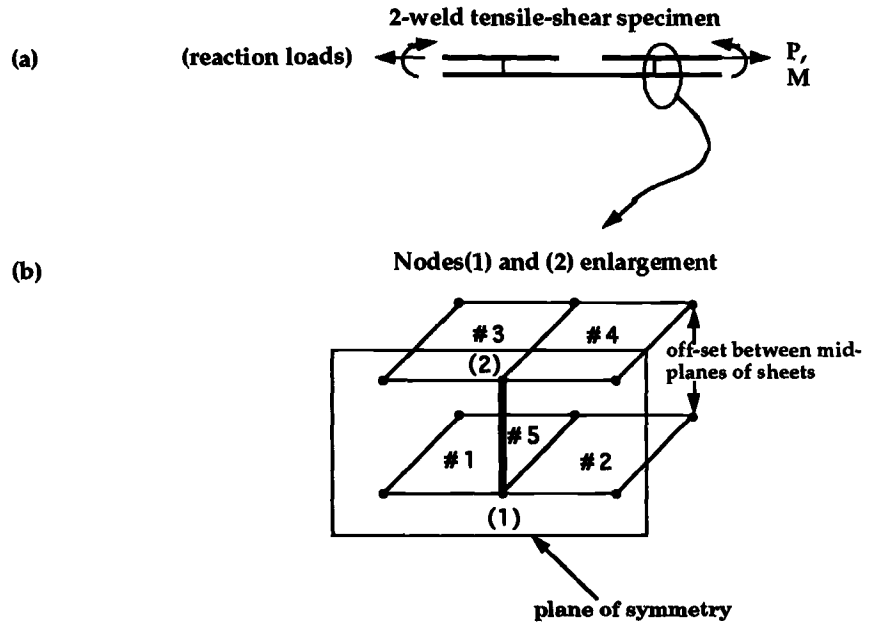

FIG. 2—*Discussion of element nodal reactions in a resistance spot weld joint:* (a) *a resistance spot weld specimen (edge view);* (b) *enlarged view of the elements around circled area in* (a)*;* (c) *schematic showing element reactions. All directions are positive as shown.*

TABLE 1—*Definition of* ΔM_{ij}^*, *as used in Eq 5.*[a]

Case	ΔP_{At}	ΔM_{i1}^*	ΔM_{i2}^*
$\Delta M_{i1} > 0$, $\Delta M_{i2} > 0$, $\Delta P_{At} > 0$			
$\Delta M_{i1} > \Delta M_{i2}$	ΔP_{Ai}	$\Delta M_{i1} - \Delta M_{i2}$	0
$\Delta M_{i1} < \Delta M_{i2}$	ΔP_{At}	0	$\Delta M_{i2} - \Delta M_{i1}$
$\Delta P_{At} > 0$ or $\Delta P_{At} < 0$			
$\Delta M_{i1} > 0$, $\Delta M_{i2} < 0$	0	ΔM_{i1}	0
$\Delta M_{i1} < 0$, $\Delta M_{i2} > 0$	0	0	ΔM_{i2}
$\Delta M_{i1} < 0$, $\Delta M_{i2} < 0$,	tbd[b]	tbd	tbd
$\Delta M_{i1} > 0$, $\Delta M_{i2} > 0$, $\Delta P_{At} < 0$	tbv[c]	tbv	tbv
	0	ΔM_{i1}	ΔM_{i2}

[a]This table is used to find values of ΔM_{i1}^* and ΔM_{i2}^* based upon the relative values of ΔM_{i1} and ΔM_{i2}, where ΔM_{i1} is the elemental moment reaction load at D_{i1}, as defined in Fig. 2*c*, and ΔM_{i2} is the elemental moment reaction load at D_{i2}, as defined in Fig. 2*c*.

[b]tbd = to be determined. This particular case has never been exhibited by any of the specimens studied to date.

[c]tbv = to be verified. This particular case has never been exhibited by any of the specimens studied to date, but the author postulated these values of loading.

structural stress. Furthermore, ω is the effective width and is defined as $\pi d/3$ based on the work of Wang and Lawrence [*28*], d is the diameter of the weld, β is the width of the piece, and t_i is the thickness of the sheet. In reality β will saturate at a finite width, as was discussed in Ref *2*. It is likely that ω will saturate for a given sheet thickness as well. The deformations resulting from the three loading modes represented in Eq 5 are shown in Fig. 1*d*.

There are a number of similarities and differences between the definition of structural stress used in the current work (and in Refs *1* and *2*) and expressions presented by Radaj [*15,27*]. Radaj gives expressions for structural stress in several specific specimen designs both in terms of the load traveling through the nugget (loads Q, T, and M in Fig. 1*c*) and in terms of the "running-through tensile force and bending moment" (here assumed to be the same as P_{ij} and M_{ij} in Fig. 2*c*). His work does not contain a general expression for structural stress (such as Eq 5) based upon the loads traveling *into* the nugget. A more complete discussion on various expressions for structural stress is contained in the Appendix.

Equation 5 is a general statement of the structural stress range at the edge of the weld in the presence of bending, axial, and membrane loadings. The application of Eq 5 to calculate structural stress is relatively straightforward if based on appropriate and accurate finite element representations of the weld joint. The appropriate results are the reaction forces in the elements surrounding the weld connection, as shown in Fig. 2*c*. The issue of accurate finite element results is discussed later in this paper.

Relationship between Structural Stress and Propagation Life

The following development describes fatigue crack growth through the sheet thickness to the point when the crack just becomes visible on the outer surface. The starting point for this development is identical to that presented in Ref *2 except* that the crack growth rate description proposed by Forman et al. [*30*] is used as it explicitly includes the effect of the load ratio, R

$$da/dN_p = A_1(\Delta K)^b/[(1 - R)K_c - \Delta K] \tag{6}$$

where

da/dN_p = the crack growth rate (change in crack length/cycle),
a = the crack depth or length, as shown in Fig. 1, Ref *2*,
N_p = the number of load cycles spent in propagating a crack,
K = the Mode I stress intensity factor,
ΔK = the stress intensity range,
R = the load ratio and is defined as P_{min}/P_{max},
P_{max} = the maximum applied load,
P_{min} = the minimum applied load,
K_c = the fracture toughness of the material under consideration, and
b and A_1 = material constants.

Note that ΔK considers only Mode I effects from membrane, axial, and bending loadings, which is reasonable when the physical evidence of fracture is considered.

If the assumptions listed in Table 2 and the assumption that ΔK strictly increases with crack depth are applied (as was done in Ref *2*) to Eq 6, the following relationship between structural stress and propagation life results

$$N_p/[(1 - R)] = A_2(\Delta S_{max})^{-b} \tag{7}$$

where $A_2 = 2a_0^{(-b+2)/2}/((b - 1)A_1\pi^{b/2})$, a_0 is the crack length at which initiation ends and crack propagation begins, N_p is the total life spent propagating the crack through the sheet thickness t, and ΔS_{max} is defined as

$$\Delta S_{max}(= \max [\Delta S_{11}, \Delta S_{12}, \Delta S_{21}, \Delta S_{22}]) \tag{8}$$

Equation 7 depicts the total propagation life, N_p, as being related to nominal stress range in a log-linear relationship.

If the assumptions listed in Table 2 and the assumption that ΔK remains constant with crack depth (as was suggested by the work of Cooper and Smith [*14*]) are applied to Eq 6, the following relationship between structural stress and propagation life results

$$N_p/[t(1 - R)] = A_3(\Delta S_{max})^{-b} \tag{9}$$

where $A_3 = A_1^{-1}a_0^{(-b/2)}$, a_0 is the crack length at which initiation ends and crack propagation begins, and N_p is the total life spent propagating the crack through the sheet thickness, t.

TABLE 2—*Basic assumptions in development of Eqs 7 and 9.*

	Assumptions
1.	Crack growth is described using linear elastic fracture mechanics and provides the basis for a relationship between structural stress and propagation life.
2.	Crack growth is through the thickness, t, and not through the nugget diameter.
3.	The crack aspect ratio is such that $0.33 < a/c < 1$.
4.	The crack length, a_0, at which initiation ends and crack propagation begins is 1 to 5 grains in size and is much less that the sheet thickness, t.
5.	No crack closure effects are considered in welds in the as-welded condition. Prestressing or stress relieving the specimens prior to fatigue testing creates some degree of crack closure.
6.	Crack growth is due to Mode I effects.
7.	Crack initiation and early growth represent a small fraction of total life, and therefore it is reasonable to assume that $N_p \approx N_t$.
8.	$K_c > \Delta K$ for materials being considered in this work (K_c is likely to be in excess of 252 $MPa(m)^{0.5}$ for the low-carbon steels under consideration, while the values of ΔK will be less than 22 $MPa(m)^{0.5}$).

Equation 9 depicts the quantity N_p/t as being related to nominal stress range in a log-linear relationship.

Modeling Issues

Sheppard and Strange [*1,2*] and Radaj [*31*] have identified some of the issues related to creating a finite element model of resistance spot-welded joints. In Refs *1* and *2*, five types of finite element models that allow for various output data about the weld joint are discussed. Furthermore, it was reported that a Type IV model (shown in Fig. 2*b*), in which plate elements are used to model the sheets and a single beam or rigid element is used to represent the weld, is generally less stiff than models where the finite footprint of the weld nugget is explicitly incorporated into the analytic model.

None of the works cited above discusses the role of *mesh density* on structural stress values. In order to address this issue, a study was undertaken that looked at the influence of mesh density on: (1) overall joint stiffness, and (2) load distribution around the weld and the value of structural stress.

The discussion below is based upon the work done with the finite element models defined in Table 3. Each model considered sheet 1.19 mm thick.

Related to Item (1)—Overall joint stiffness decreases with increasing mesh density (this is to be expected). For example, the joint stiffness of Model F-1W is approximately 26% less than that of Model C-1W. Note that the modeling approach represented by Model C-1W is more desirable from an applications standpoint because it represents less modeling effort and fewer degrees of freedom (and therefore lesser computing time).

Related to Item (2)—Consider the maximum value of structural stress calculated using Eq 5 for the models described in Table 3. For the same applied load, Model C-1W resulted in values of maximum structural stress that were 50% higher than in Model F-1W. The reason for this difference in the values of structural stress stems from how the input load travels through the weld connection, as summarized in Table 4. Model C-1W predicts that 77% of

TABLE 3—*Definition of models in mesh-refinement study.*

Model Name	Description
Model S-1W	A solid model of a tensile-shear specimen with a single weld. Attachment between the sheet is along the faying surface and reflects the entire weld nugget footprint.
Model C-1W	A plate model of a tensile-shear specimen with a single weld. The weld is modeled as a single beam. Each plate element is roughly square in layout, measuring $w/2 \times w/2$, where w is the width of the specimen. Mesh density is coarse.
Model F-1W	A plate model of a tensile-shear specimen with a single weld. The weld is modeled as a single beam. Each plate element is roughly square in layout, with dimensions that of the weld nugget radius (e.g., 3 mm). The density is approximately ten times greater than with Model C-1W. Therefore, mesh density is described as fine.
Model S-3W	A solid model of a tensile-shear specimen with three welds in series.
Model C-3W	A plate model of a tensile-shear specimen with three welds in series. Each weld is modeled as a single beam. Each plate element is roughly square in layout, measuring $w/2 \times w/2$, where w is the width of the specimen. Mesh density is coarse.
Model F-3W	A plate model of a tensile-shear specimen with three welds in series. Each weld is modeled as a single beam. Each plate element is roughly square in layout, with dimensions that of the weld nugget radius (e.g., 3 mm). The density is approximately ten times greater than with Model C-3W. Therefore, mesh density is described as fine.

TABLE 4—*Distribution of a 100-N input load through a spot weld(s).*[a]

Model	W1 (weld 1)		W2 (weld 2)		W3 (weld 3)	
	D_{11}[b] P_{11}	D_{12}[b] P_{12}	D_{11}[b] P_{11}	D_{12}[b] P_{12}	D_{11}[b] P_{11}	D_{12}[b] P_{12}
Model S-1W	+66	−33	...	...	...	...
Model C-1W	+77	−23	...	...	...	...
Model F-1W	+55	−45	...	...	...	...
Model S-3W	+49[c]	+10	+28	+7	+26	−9
Model C-3W	+58[c]	+22	+39	+12	+28	−9
Model F-3W	+25[c]	−9	+20	−10	+20	−16

[a] + means that tension is being created at that edge; − means that compression is being created at that edge.
[b] See Fig. 2*c*. Directions shown in Fig. 2*c* are all considered to be positive.
[c] Major difference in modeling.

the applied load goes through D_{11} (and therefore 23% of the input load travels as compression through D_{12}), whereas Model F-1W predicts a more even distribution at 55 and 45%, respectively. The solid model predicts that the distribution is 66 and 33%.

The results from studying a three-weld tensile shear specimen are even more enlightening (the three-welds are in series). Model C-3W resulted in values of maximum structural stress 50% higher than those in Model F-3W. Again, the reason for the differences in the values of structural stress stems from how the input load travels through the weld connection, summarized in Table 4. All three models predict that the distribution of the input load through the three-weld nuggets themselves is approximately 36, 28, and 36% (it is expected that more of the load will travel through the two end welds that are closer to the input load). This is in sharp contrast to the predicted distribution of the load P_{ij} *around* the weld, as shown in Table 4.

The major conclusions that can be drawn from the work [*1,2*] and from the results shown in Table 4 are:

1. Selective thickening allows models that represent each weld as a single beam or rigid connection (Type IV models) to attain the same overall joint stiffness as a solid representation that explicitly includes the finite footprint of each weld (from Refs *1* and *2*).
2. The amount of selective thickening necessary for attaining equivalent stiffness decreases as the number of welds in the "structure" increases. One could postulate that at some limiting number, no selective thickening may be necessary (from Refs *1* and *2*).
3. Coarse meshes (where there are only two plate elements through the specimen/flange width, and a single beam or rigid connection is used to represent each weld) adequately and accurately represent the distribution of input loads through and around the spot weld. In fact, finer meshes may incorrectly distribute the load. This is certainly an issue needing further exploration.

Estimations

Using the ideas developed above related to structural stress and crack propagation life, a procedure is now defined for estimating total fatigue life. Experimentally measured and estimated fatigue lives are then compared for a variety of specimens.

Procedure

The following steps were followed in order to determine the applicability of Eqs 7 and 9 and the definition of ΔS_{max} in Eq 8 for estimating fatigue life. Based upon the findings in Ref *2*, it is assumed that $N_p \approx N_t$:

1. A body of well-documented experimentally generated fatigue life data on resistance weld performance was gathered. Each configuration (load ratio, specimen geometry/dimensions, material, weld treatment) was considered to be a data set. Loads representing low, medium, and long fatigue lives were selected, along with the corresponding lives $(N_p)_{exp}$.
2. For each data set, a finite element representation of the weld specimen using the ideas developed in Refs *1* and *2* and in the previous section was built. Four-noded quadrilateral shell elements measuring $w/2$ by $w/2$ and a rigid connection between the sheets were used in each model. The load ranges discussed in Step 1 were applied to each model to determine values of ΔS_{max}, as defined in Eqs 5 and 8.
3. Curve fit values of ΔS_{max} data to $(N_p)_{exp}/(1 - R)$ and $(N_p)_{exp}/[t(1 - R)]$ to determine constants A_2 and b for Eq 7 and A_3 and b for Eq 9. In Ref *2*, A_2 and b were determined from material constants A_1 and b and an estimate of a_0. In general, A_1 and b are difficult to obtain for the heat-affected zone materials where crack growth occurs. Also, results are very sensitive to the value of a_0. In order to circumvent these difficulties, log-linear curve fitting was done to all empirical fatigue data.
4. Use the values of A_2 and b for Eq 7 and A_3 and b for Eq 9 determined in Step 3 to check on the quality of the fit.

Results

The ability of the procedure outlined above to estimate fatigue life in resistance spot weld specimens in mild steel is now evaluated. Tensile-shear specimen data in a variety of thicknesses and widths, as summarized in Table 5, were considered. The nominal yield strength of all of these specimens is 207 MPa (30 ksi). In addition, specimen data of mild steel with a 25% greater yield strength are summarized in Table 6. Henceforth, the data in Table 5 will be referred to as the "low-strength mild steel data" and that in Table 6 as the "medium-strength mild steel data."

Figure 3*a* shows the two bounding data sets from Table 5 for $R = 0$, plotted in terms of load range versus life. All of the other data sets in Table 5 fall in between the two limits. N_t used in this figure is defined as the total number of cycles for a fatigue crack to just appear at the outside surface. Figure 3*b* shows the consolidation of the data when plotted in terms of ΔS_{max}. The equation of the curve shown in this figure is

$$N_p/(1 - R) = A_2(\Delta S_{max})^{-3.5609}; \qquad CC = 0.83 \tag{10}$$

where N_p is in cycles, $A_2 = 5.929 \times 10^{14}$ if ΔS_{max} is given in MPa (and is equal to 6.126×10^{11} if ΔS_{max} is given in ksi) and $b = 3.5609$. Note that this value of b is in the expected range for this particular material [*32*]. If this curve is then used to estimate values of N_p, all estimated values are within a factor of 4 of experimentally measured lives. This factor is greater than for the HSLA predictions made in Ref *2*; this is to be anticipated as initiation life, N_i (which is not accounted for here), is likely to represent a greater portion of life in mild steel than in HSLA steel (as discussed in Ref *10*). The "fit" resulting from the data set

TABLE 5—*Summary of low-strength mild steel weld fatigue data.*[a]

Data Set	Researcher	R	t, mm	D, mm	β, mm	Configuration[b]
1.1	[*10*]	0	0.90	6.10	38.1	TS, as-welded
2.1	[*10*]	0	0.90	4.79	38.1	TS, as-welded
3.1	[*10*]	0	2.70	8.60	38.1	TS, as-welded
4.1	[*10*]	0	1.40	6.10	38.1	TS, as-welded
5.1	[*10*]	0	1.40	4.79	38.1	TS, as-welded
6.1	[*10*]	0	2.70	7.59	38.1	TS, as-welded
7.1	[*10*]	0.5	0.90	6.10	38.1	TS, as-welded
8.1	[*10*]	0.5	1.40	6.10	38.1	TS, as-welded
9.1	[*10*]	0.5	1.40	4.79	38.1	TS, as-welded
10.1	[*10*]	0.5	2.70	8.60	38.1	TS, as-welded
11.1	[*10*]	−0.2	0.90	6.10	38.1	TS, as-welded
12.1	[*10*]	−0.2	1.40	4.79	38.1	TS, as-welded
13.1	[*10*]	−0.2	1.40	6.10	38.1	TS, as-welded
14.1	[*10*]	0	1.40	4.79	22.	TS, as-welded
15.1	[*34*]	−1[c]	1.09	5.59	38.1	TS, as-welded
16.1	[*34*]	−1[c]	1.09	5.59	38.1	TS, prestressed[d]

[a] σ_{ys} (MPa) is approximately 207 MPa.
[b] TS is a tensile-shear specimen with a single weld.
[c] Lives reported in this work included growth through the width. As-welded lives were reduced by 30% per tensile-shear results of Swellem et al. [*10,34*].
[d] Effect of prestressed was included by reducing ΔS_{max} by the yield strength, as was done in Ref *2*.

in Table 5 based upon Eq 9 was much poorer than that obtained with Eq 7, having a correlation coefficient (*CC*) of 0.71.

Figure 4*a* shows some of the original fatigue life data for the medium-strength mild steel considered in this study, as summarized in Table 6. Specimen types have been labeled. N_t used in this figure is defined as the total number of cycles for a fatigue crack to just appear at the outside surface. Figure 4*b* shows the consolidation of the data (Data Sets 1.2 through 12.2 from Table 6 were used) when $N_p/(1 - R)$ is plotted in terms of ΔS_{max}. The equation of the curve shown in this figure is

$$N_p/(1 - R) = A_2(\Delta S_{max})^{-2.4155}; \qquad CC = 0.91 \tag{11}$$

where N_p is in cycles, $A_2 = 1.363 \times 10^{11}$ if ΔS_{max} is given in MPa (and is equal to 1.287×10^9 if ΔS_{max} is given in ksi and $b = 2.4155$. Note the excellent correlation coefficient, *CC*. If this curve is then used to estimate values of N_p, all estimated lives are within a factor of 3 of experimentally measured lives. As with the low-strength mild steel results, the correlation coefficient was significantly lower when the data were fit via Eq 9. Data from Wang and Ewing [*11*] (Data Sets 13.2 and 14.2) are shown in Fig. 4*b* but were not included in the data fit of Eq 11; the lives reported in Ref *11* for these two coach peel designs included initiation and life to propagate a crack through the sheet thickness, *plus* life for the crack to grow through the specimen width. As this later stage of life is not included in the current work, it is not possible to compare predicted lives from Eq 11 with the experimental data reported in Ref *11*.

Discussion and Conclusions

Using Forman's relationship between crack growth rate and stress intensity range, an expression between total propagation life and the structural stress range was derived. Crack growth through the sheet thickness was explicitly considered. The relationship between

TABLE 6—*Summary of medium-strength mild steel weld fatigue data.*[a]

Data Set	Researcher	R	t, mm	D, mm	β, mm	Configuration[b]
1.2	Current work	0	0.91	6.35	34.9	TS, as-welded
2.2	Current work	0	0.91	6.35	34.9	CT, as-welded
3.2	Current work	0	0.91	6.35	34.9	MCP, as-welded
4.2	Current work	0	0.91	6.35	34.9	ACP, as-welded
5.2	Current work	0	1.20	6.35	34.9	TS, as-welded
6.2	Current work	0	1.20	6.35	34.9	CT, as-welded
7.2	Current work	0	1.20	6.35	34.9	MCP, as-welded
8.2	Current work	0	1.20	6.35	34.9	ACP, as-welded
9.2	Current work	0	1.47	6.35	34.9	TS, as-welded
10.2	Current work	0	1.47	6.35	34.9	CT, as-welded
11.2	Current work	0	1.47	6.35	34.9	MCP, as-welded
12.2	Current work	0	1.47	6.35	34.9	ACP, as-welded
13.2	[*11*]	0[c]	1.27	5.84	38.1	CP, as-welded
14.2	[*11*]	0[d]	1.27	5.84	38.1	CP, as-welded

[a] σ_{ys} (MPa) is approximately 275 MPa.

[b] Where:

TS is a tensile-shear specimen with a single weld.

CP is a coach peel specimen.

MCP (modified coach peel) contains a single L piece welded to a horizontal member. The horizontal member is gripped at both ends in the tension testing machine.

ACP (angled coach peel) contains a single angled-L piece welded to a flat member. The flat member is gripped at both ends in the tension testing machine.

CT is cross-tension.

CP is coach peel.

[c] e, as defined in Ref *11*, is 16.13 mm.

[d] e, as defined in Ref *11*, is 32.26 mm.

propagation life (N_p) and the structural stress range was then used to describe fatigue in resistance spot-welded joints. In this work it was assumed that $N_p \approx N_t$ for both steels, where N_t is defined as the number of cycles to a crack to become visible.

It is necessary to determine the coefficient and exponent in Eq 7 or Eq 9 for specific materials in order to estimate propagation life. This was done by fitting a log-linear curve to

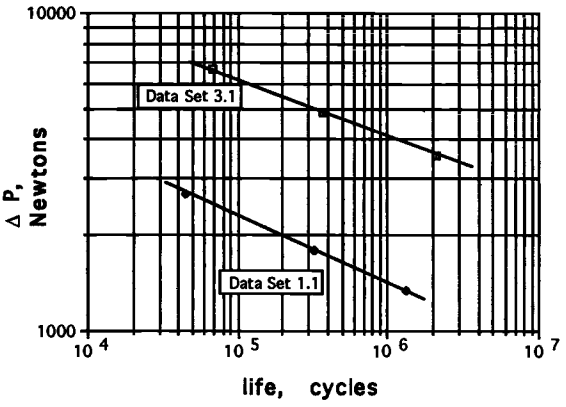

FIG. 3(*a*)—*Sample data from Table 5.*

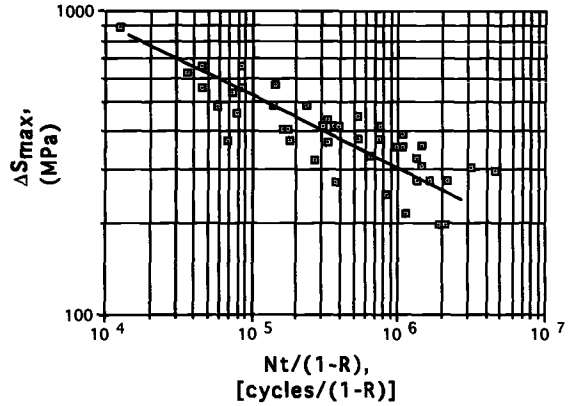

FIG. 3(*b*)—*Data from Table 5 represented in terms of structural stress.*

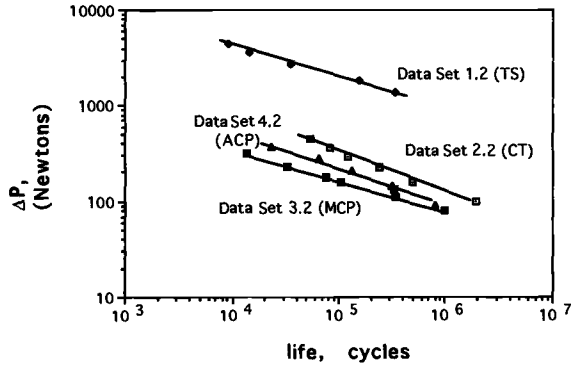

FIG. 4(*a*)—*Sample data from Table 6.*

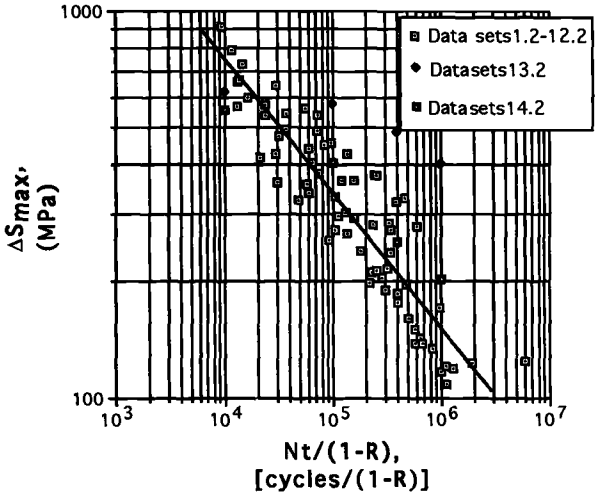

FIG. 4(*b*)—*Data from Table 6 represented in terms of structural stress.*

the experimental data listed in Table 5 for low-strength mild steel and in Table 6 for medium-strength mild steel. Note that the correlation coefficients in Eqs 10 and 11 are both very high when structural stress is related to N_p (as results from assuming that ΔK increases with crack depth); the fit is not nearly as good when made based upon N_p/t (as would be suggested by assuming that ΔK is constant with crack depth). The relationships in Eqs 10 and 11 were then used to estimate N_p. All estimated fatigue lives were within a factor 4 of experimentally measured lives.

The method developed here has several advantages over other proposed techniques. Some of these are:

1. An explicit expression for the SIF range as a function of crack depth is not needed. This is even though the method is based on the Forman relationship for crack growth (Eq 6) through the sheet thickness.
2. Fatigue life evaluation is based upon local information; the local reaction forces *into* the weld nugget are considered. Applied loads and their eccentricity relative to the weld nuggets need not be considered. This point is particularly critical when considering joints containing multiple welds, where the idea of load offset may have less meaning.
3. The weld can be represented in a simple fashion in finite element simulations of structures. This is particularly important when considering resistance spot-welded structures containing multiple welds. The current work has shown that mesh layout is an important factor in coming up with accurate estimates of the structural stress. A number of modeling guidelines have been presented.

In the near future there will be additional verification of the structural stress approach to life estimation by applying it to mixed thickness, single-weld specimens and to a T-pillar section containing multiple welds. This program is a joint experimental-analytical effort.

Acknowledgments

This work was initiated with support from the National Science Foundation under Grant DMC-8618462, General Motors Corporation, and with an ALCOA Foundation grant. Laboratory facilities were provided by the Center for Material Research at Stanford. Professor Fred Lawrence and Dr. Peter Kurath are acknowledged for their thought-provoking comments/questions during this work. Dr. Jim Widmann is gratefully acknowledged for keeping the laboratory running. The following individuals also assisted in this work: Clifton Brown, Charles Gonzales Canales, Chris Carter, Jose Armando Cervantes, Qasim S. Jami, Laura Johnson, Brian Karpiel, Tyler Phillips, Yung-Yuan Tang, and Ernest Villanueva.

APPENDIX

Expressions for Structural Stress

Summarized in Table A-1 are various expressions for structural stress as proposed by Radaj in Refs *15* and *27* (Rows 2 and 3) and by Sheppard and Strange [*1,2*] (Row 1). It is possible to compare these expressions in restricted cases. For example, compare the terms in Column C for "cross-tension" response; the form of structural stress in Box 1C is very similar in form to that posed by Radaj in Box 2C (one expression is for simply-supported boundary conditions, the other for fixed).

The structural stress expression given in Box 2A/B for the tensile-shear specimen is based

TABLE A-1—*Comparison of various expressions for structural stress.*[a]

Row	A Membrane Value of Structural Stress	A/B Tensile-Shear	B Bending Value of Structural Stress	C Axial Value of Structural Stress
Row 1 [*1,2*] (see Eq 5)	**1A.** $P_1/(\omega t)$		**1B.** $6M_1/(t^2\beta)$	**1C.** T/t^2
Row 2[b] [*15,27*]		**2A/B.** 1.27 $Q/(td)$		**2C.** $0.69T/t^2\ln(D/d)$ $1.03T/t^2\ln(D/d)$
Row 3[b] [*27*]	**3A.** 1.54 $P_1/(\beta t)$		**3B.** 9.24 $M_1/(\beta t^2)$	

[a] Q and T are defined in Fig. 1*c*. Furthermore, $P_1 = P_{21}$, $M_1 = M_{21}$. Note that in comparing Figs. 1*c* and 2*c*, $Q = p^f$, $T = P_{A2}$. D is the diameter of two disks being "pulled apart" due to pressure loading. In Ref *27* Radaj takes the ratio of D/d to be 25. In some ways D is analogous to the specimen width.

[b] The symbols to represent loads have been changed from the original works to be consistent with the current work.

on the membrane load traveling through the weld nugget (load Q in Fig. 1*c* and load p^f in Fig. 2*c*) and the assumptions that the applied load P ($= Q$ for a single spot weld) is uniformly distributed around the weld circular periphery and that there is an amplification factor of 4 caused by the presence of a bending load (see Ref *31* for the complete development). How does this expression for a tensile-shear specimen compare with structural stress as defined in Eq 5? To make this comparison, one needs to convert Eq 5 (or the sum of Boxes 1A and 1B), which is stated in terms of the loads traveling into the weld into a form based upon the loads traveling through the nugget of a tensile-shear specimen. Based upon the fact that $P_{ij} = 0.70\ Q$ (scaling factor is approximately 0.7 for a tensile-shear specimen, as shown in Table 4), $M_{ij} = P_{ij}(t/2) = 0.70\ Q(t/2)$, and T is approximately zero, it is possible to rewrite Eq 5 for structural stress, S, for a tensile-shear specimen as

$$S_{\text{tensile-shear}} = (0.7Q)/[\pi d/3t] + 6[0.70Q(t/2)/(t^2\beta)] = 2.1Q/t[(\pi d)^{-1} + (\beta)^{-1}] \qquad (12)$$

This is only the same as the expression given for structural stress by Rahaj in Box 2A/B if $\beta = 3.5\ d$. A curious feature of the expression in Box 2A/B is that it implies that the structural stress in a tensile-shear specimen is independent of width (physical evidence by Lawrence et al. [*10*] shows that fatigue response of tensile-shear specimens is affected by specimen width).

A similar comparison can be made with Eq 5 and the expressions for membrane and bending structural stress given in Boxes 3A and 3B (these were proposed by Radaj in Ref *27*; he called the force P_{ij} and moment M_{ij} the "running-through" tensile force and bending moment, respectively). In this case there is equivalence between Eq 5 and the sum of Boxes 3A and 3B only if $\beta = 3.31\ d$. A curious feature of the expression in Box 3A is that it implies that the structural stress in a tensile-shear specimen is independent of nugget diameter.

References

[*1*] Sheppard, S. D. and Strange, M. E., "Fatigue Life Estimation in Resistance Spot Welds: Initiation and Early Growth Phase," *Fatigue and Fracture of Engineering Materials and Structures*, Vol. 15, No. 6, 1992, pp. 531–549.

[*2*] Sheppard, S. D., "Estimation of Fatigue Propagation Life in Resistance Spot Welds," *Advances*

in Fatigue Lifetime Predictive Techniques: 2nd Volume, ASTM STP 1211, M. R. Mitchell and R. W. Landgraf, Eds., American Society for Testing and Materials, West Conshohocken, PA, 1993, pp. 169–185.

[3] Dickinson, D. W., *Welding in the Automotive Industry,* August 1981, Report SG81-5, Committee of Sheet Steel Producers, AISI, Washington, DC.

[4] Davidson, J. A., "A Review of the Fatigue Properties of Spot-Welded Sheet Steels," SAE paper 830033, Society of Automotive Engineers, Warrendale, PA, 1983.

[5] Reemsnyder, H. S., "Modeling of the Fatigue Resistance of Single-Lap Spot-Welded Steel Sheet," IIW Document XII-1469-92, International Institute of Welding, Dusseldorf, Germany.

[6] Cooper, J. F. and Smith, R. A., "Fatigue Crack Propagation at Spot Welds," *Metal Construction,* June 1986, pp. 383–386.

[7] Pook, L. P., "Fracture Mechanics Analysis of the Fatigue Behaviour of Spot Welds," *International Journal of Fracture,* Vol. 11, 1975, pp. 173–176.

[8] Kurath, P., "Multiaxial Fatigue Criteria for Spot Welds," SAE 920668, SAE Technical Paper Series, Society of Automotive Engineers, Warrendale, PA, 1992.

[9] Swellam, M. H., Kurath, P., and Lawrence, F. V., "Electric-Potential-Drop Studies of Fatigue Crack Development in Tensile-Shear Spot Welds," *Fatigue and Fracture Testing of Weldments, ASTM STP 1058,* J. M. Potter and H. I. McHenry, Eds., American Society for Testing and Materials, West Conshohocken, PA, 1990, pp. 47–77.

[10] Swellam, M. H., Kurath, P., and Lawrence, F. V., "Electric-Potential-Drop Studies of Fatigue Crack Development in Tensile-Shear Spot Welds," *Advances in Fatigue Lifetime Predictive Techniques, ASTM STP 1122,* M. R. Mitchell and R. W. Landgraf, Eds., American Society for Testing and Materials, West Conshohocken, PA, 1992, pp. 383–401.

[11] Wang, P. and Ewing, E., "Fracture Mechanics Analysis of Fatigue Resistance in Welded Coach-Peel Joints," *Fatigue and Fracture of Engineering Materials and Structures,* Vol. 14, No. 9, 1991, pp. 915–930.

[12] Kardomateas, G. A., "Spot Weld Failure from Buckling-Induced Stressing of Beams under Cyclic Bending and Torsion," *Engineering Fracture Mechanics,* Vol. 42, No. 3, 1992, pp. 519–530.

[13] Davidson, J. A. and Imhof, E. J., Jr., "A Fracture-Mechanics and System-Stiffness Approach to Fatigue Performance of Spot-Welded Sheet Steels," SAE Paper 830034, Society of Automotive Engineers, Warrendale, PA, 1983.

[14] Cooper, J. F. and Smith, R. A., "The Measurement of Fatigue Cracks at Spot-Welds," *International Journal of Fatigue,* Vol. 7, No. 3, 1985, pp. 137–140.

[15] Radaj, D., "Stress Singularity, Notch Stress and Structural Stress at Spot-Welded Joints," *Engineering Fracture Mechanics,* Vol. 34, No. 2, 1989, pp. 495–506.

[16] Pook, L. P., "Approximate Stress Intensity Factors for Spot and Similar Welds," NEL Report No. 588, April 1975.

[17] Okuno, S., Ohmura, K., Hatsuda, T., and Kasai, Y., "Fatigue Strength Evaluation of Spot-Welded Joints for Car Body Structures," *JSME International Journal,* Vol. 30, No. 261, 1987, pp. 394–400.

[18] Mabuchi, A., Niisawa, J., and Tomioka, N., "Fatigue Life Prediction of Spot-Welded Box-Section Beams under Repeated Torsion," SAE Paper 860603, Society of Automotive Engineers, Warrendale, PA, 1986.

[19] Smith, K. N., Watson, P., and Topper, T. H., "A Stress-Strain Function for the Fatigue of Metals," *Journal of Materials,* Vol. 5, No. 4, December 1970, pp. 767–778.

[20] Oh, H. L., "Fatigue-Life Prediction for Spotweld Using Neuber's Rule," *Design of Fatigue and Fracture Resistant Structures, ASTM STP 761,* P. R. Abelkis and C. M. Hudson, Eds., American Society for Testing and Materials, West Conshohocken, PA, 1982, pp. 296–309.

[21] Kan, Y. R., "Fatigue Resistance of Spotwelds—An Analytical Study," *Metals Engineering Quarterly,* November 1976, pp. 26–36.

[22] Tanaka, J., Kabasawa, M., Hagae, M., and Ono, M., "Fatigue Strength and Strain Behavior of Spot-Welded Joints in Steel Sheets for Automobiles," Nippon Kokan technical report, Overseas No. 47, 1986, pp. 45–50.

[23] Simon, G. and Krause, H.-J., "The Transferability of Fatigue Strength Values Determined on Single-Spot Specimens to Multi-spot Specimens and Specimens Similar to Structural Components," *Schweissen und Schneiden,* Vol. 44, No. 1, January 1992, pp. 13–17.

[24] Mizui, M., Sekine, T., Tsujimuara, A., Takishima, T., and Shimazaki, Y., "An Evaluation of Fatigue Strength for Various Kinds of Spot-Welded Test Specimens," SAE Paper 880375, Society of Automotive Engineers, Warrendale, PA, 1988.

[25] Mabuchi, A., Niisawa, J., and Tomioka, N., "Fatigue Life Prediction of Spot-Welded Box-

Section Beams under Repeated Torsion," SAE Paper 860603, Society of Automotive Engineers, Warrendale, PA, 1986.

[*26*] Rui, Y., Borsos, R. S., Gopaiakrishnan, R., Agrawal, H. N., and Rivard C., "The Fatigue Life Prediction Method for Multi-Spot-Welded Structures," SAE Paper 930571, SAE Special Publications No. 973, *Simulation and Development in Automotive Simultaneous Engineering,* Society of Automotive Engineers, Warrendale, PA, pp. 33–42.

[*27*] Radaj, D., *Design and Analysis of Fatigue Resistant Welded Structures,* Halsted Press, New York, 1990.

[*28*] Wang, P. C. and Lawrence, F. V., "A Fatigue Life Prediction Method for Tensile Shear Spot Welds," Report No. 113, College of Engineering, University of Illinois at Urbana-Champaign, October 1984.

[*29*] Roark, R. J. and Young, W. C., *Formulas for Stress and Strain,* 5th ed., McGraw-Hill Book Co., New York, 1966.

[*30*] Forman, R. G., Kearney, V. E., and Engle, R. M., "Numerical Analysis of Crack Propagation in Cyclic-Loaded Structures," *Journal of Basic Engineering, ASME Transactions,* American Society of Mechanical Engineers, New York, Vol. 89, 1967.

[*31*] Radaj, D., "Stress Singularity, Notch Stress and Structural Stress at Spot-Welded Joints," IIW-Document 111-923-88.

[*32*] Barsom, J. M., "Fatigue-Crack Propagation in Steels of Various Yield Strengths," *Journal of Industrial Engineering, ASME Transactions,* American Society of Mechanical Engineers, New York, Series B, No. 4, November 1971, p. 1190.

[*33*] Lawrence, F. V., Jr., Corten, H. T., and McMahon, J. C., "Improvement of Steel Spot Weld Fatigue Resistance," Final Report to the AISI, Washington, DC, April 1985.

Steven M. Tipton[1]

Multiaxial Plasticity and Fatigue Life Prediction in Coiled Tubing

REFERENCE: Tipton, S. M., **"Multiaxial Plasticity and Fatigue Life Prediction in Coiled Tubing,"** *Fatigue Lifetime Predictive Techniques: 3rd Volume, ASTM STP 1292,* M. R. Mitchell and R. W. Landgraf, Eds., American Society for Testing and Materials, 1996, pp. 283–304.

ABSTRACT: Coiled tubing is being used increasingly in the oil well drilling and servicing industry. Continuous steel tubing of structural dimensions (up to 89 mm or 3.5 in. in diameter) is wound onto a large-diameter reel for repeated deployment into and out of a well bore. The bending strain range associated with each wrap-unwrap cycle can exceed 3% with lives well below 100 cycles. During constant internal pressure fatigue testing, tubing has been observed to grow in diameter by as much as 30%.

This paper describes an analytical model to predict the fatigue behavior of coiled tubing subjected to variable pressure service conditions. The approach utilizes standard low-cycle fatigue data but requires additional experimental results from constant pressure fatigue testing. The algorithm is based on estimates of biaxial ratcheting from an incremental plasticity model using a hybrid associated flow rule, a modified kinematic hardening rule with multiple von Mises yield surfaces, and a specialized limit surface concept. An empirical damage parameter was formulated based on constant pressure fatigue data using mean and fluctuating von Mises equivalent strain components occurring throughout the life of a section of tubing. This parameter is used with the Palmgren-Miner definition of cumulative damage to track damage that is accumulating nonlinearly under constant or variable pressure histories. Modifications to standard incremental plasticity components and implementation assumptions used to apply the model are presented and discussed. The predictive capability of the model is demonstrated relative to data generated under constant and variable pressure histories.

KEYWORDS: cyclic plasticity, biaxial ratcheting, circumferential growth, variable amplitude, low-cycle fatigue, multiaxial fatigue, coiled tubing, fatigue life prediction

The use of coiled tubing (CT) in the oil field industry is increasing rapidly in quantity and scope [*1*]. The operational concept of CT involves running a continuous string of steel tubing into a well to perform specific operations (such as pumping, acidizing, or electric wireline logging) without disturbing existing completion tubulars or equipment. When servicing is complete, the tubing is retrieved from the well and spooled back onto its reel for transport to the next work location. Initially, tubing diameters were below 50.8 mm (2 in.), but recently tubing as large as 78.9 mm (3.5 in.) in diameter has been used for open-hole drilling operations. The use of even larger tubing is being explored. Fatigue is the single major factor controlling the working life of CT. The strain levels imposed on tubing as it is deployed and retrieved from a well are enormous, on the order of 2 to 3%. Combined with internal pressures that impose hoop stresses on the order of 60% of the material's monotonic yield stress, tubing has been observed to fail in fewer than ten bending-straightening cycles. There are essentially no other applications involving structural engineering alloys where

[1]Associate professor, Mechanical Engineering Department, The University of Tulsa, Tulsa, OK 74104.

cyclic loading of this magnitude is intentionally imposed. Thus, CT operates beyond the domain of conventional fatigue life prediction models [*2*].

In addition to the large magnitude of imposed strain, other factors complicate the analysis of CT fatigue behavior. The loading is variable amplitude and multiaxial. A "gooseneck" arch guides the tubing into an injector unit, which drives the tubing into and out of a well bore. The gooseneck radius of curvature typically differs from the radius imposed by the spool on a given section of tubing, as shown in Fig. 1*a*. Tubing is often pressurized during its use. When it is wrapped and unwrapped with an internal pressure, it grows incrementally in diameter. Growth on the order of 30% has been observed routinely during constant pressure fatigue testing. This ratcheting is caused by hoop stress levels well below 50% of the material's monotonic yield stress. Bending events imposed with high internal pressure cause fatigue damage to develop at a greater rate than cycles imposed with low internal pressure. Furthermore, the bending and pressure history of the tubing appear to be important, as damage accumulates nonlinearly. In other words, a cycle imposed on a section of tubing later in its life consumes a larger proportion of the total working life than a cycle imposed earlier in life. This is particularly important when the pressure varies from cycle to cycle, as it invariably does in field situations [*1–5*].

A number of conventional multiaxial fatigue life prediction approaches were investigated for use in describing the behavior of CT [*2,3*]. The approaches are adequate for very little or no internal pressure (essentially, a uniaxial strain-controlled situation) but cannot correlate higher pressure data points. There are three main reasons that conventional parameters fail to correlate:

1. Most parameters are based primarily on stress and/or strain *fluctuations,* which are unaffected by a static mean hoop stress.
2. Mean loading is usually accounted for with stress quantities. However, equivalent mean stresses are relatively unaffected by the hoop stress magnitude since plastic deformation is so extensive.
3. Critical plane approaches tend to ignore "noncritical" stress and strain components (such as the relatively small hoop stress). In general, no conventional approach is able

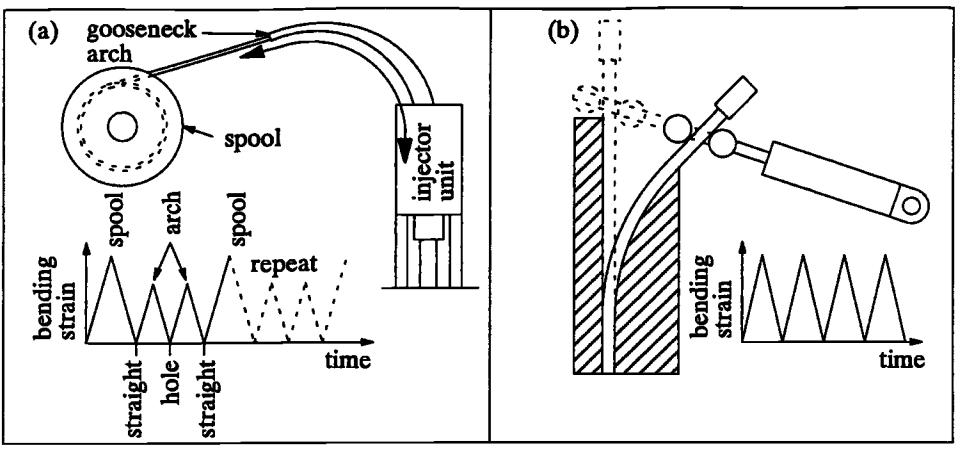

FIG. 1—*Schematic illustrations of* (a) *full-scale deployment equipment and* (b) *fatigue testing machine concept and associated bending strain histories.*

to adequately characterize the detrimental effect of circumferential ratcheting induced by hoop stress.

A life prediction algorithm designed specifically for CT is described in this paper. The approach was developed as a part of two separate projects. During the first project [*2–4*], a model was developed and validated for tubing diameters up to 44.5 mm (1.75 in.). Data were generated using full-scale deployment equipment. The second project involved the enhancement of the analytical model and its validation for diameters up to 88.9 mm (3.5 in.). Also, a CT fatigue testing concept and prototype machine, shown schematically in Fig. 1*b*, were developed as a part of this project [*6*]. A section of tubing 1.68 m (66 in.) in length was used as a specimen by sealing it at each end and alternately bending and straightening it over an arcuate and straight form, respectively. Guided rollers were used on the end of a hydraulic actuator to transfer the bending and straightening loads to the tubing, avoiding the imposition of external axial loading. In order to ensure the validity of the test machine concept, sets of data were generated for tubing of three different materials: modifed A606 steels, one normalized to a nominal yield strength of 483 and the other to 552 MPa (70 and 80 ksi, respectively) and a modified A607 steel quenched and tempered to a yield strength of 690 MPa (100 ksi). Specimen diameters ranged from 31.75 to 88.9 mm (1.25 to 3.5 in.), and wall thicknesses ranged from 2.2 to 5.2 mm (0.087 to 0.203 in.). Bending forms were used with two different radii of curvature: 1.22 and 1.83 m (48 and 72 in.). The machine data correlate well with data from full-scale tests conducted with field deployment equipment [*6*]. This confirmed that the bending-straightening cycle is the primary source of fatigue damage imposition, with other factors (e.g., contact forces from rollers or injector blocks) being negligible. Another important consideration for validation of the test machine concept pertains to the location of failure sites. From 88 tests, failure sites along the specimen length were distributed with no apparent influence from the clamping forces at the base of the tubing [*5,6*].

The CT life prediction algorithm described in the remainder of this paper is based on standard low-cycle fatigue data (generated in accordance with the ASTM Practice for Constant-Amplitude Low-Cycle Fatigue Testing (ASTM E 606) using special specimens extracted from tube walls [*2,4*]) and constant pressure data sets collected using the testing machine. The approach is based on a specialized CT fatigue damage parameter and the local multiaxial stress and strain history in the tube wall, as computed from an incremental plasticity model. This paper demonstrates the ability of the model to deal with variable bending strain amplitude loading and variable pressure history data.

Coiled Tubing Stress-Strain State

The life prediction model is based on the estimated state of stress and strain at the outer surface of the tensile side of the tubing. The stress and strain components for a section of tubing in the testing machine under constant internal pressure are depicted schematically in Fig. 2. At this location, the strain along the axis of the tubing, ϵ_x, is considered to be controlled by the amount of curvature imposed by bending (assuming plane cross sections remain plane). When straightened, the axial strain is considered to return to zero. This characterization of bending strain control in the axial direction has been supported experimentally [*4*]. The stress in the hoop direction, σ_h, is computed as the average stress according to thin-walled pressure vessel relations, and the radial stress, σ_r, is taken as zero. For the smallest diameter to wall thickness ratio examined in this study ($D/t = 11.2$), Fig. 3 shows the hoop and radial stress distributions, normalized by internal pressure, as computed from Lamé (thick-walled cylinder) relations, versus normalized through-thickness location

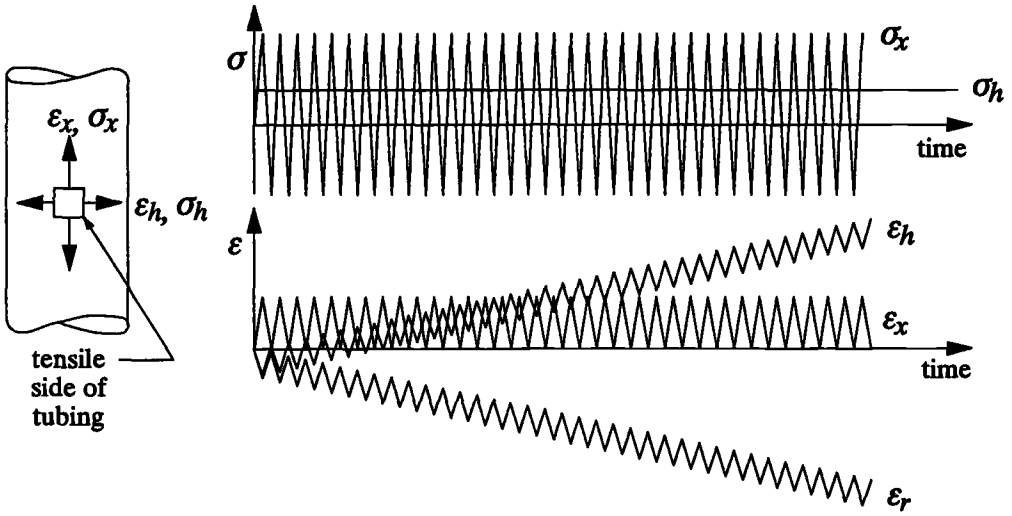

FIG. 2—*Schematic state of stress and strain in pressurized coiled tubing.*

(zero at the inner wall and one at the outer wall). The average hoop stress is shown for comparison. At the outer surface, the average hoop stress is within 10% of the Lamé hoop stress. For larger diameter to thickness ratios, up to the maximum in this study, $D/t = 18.4$, the difference is as small as 6%.

With axial strain, hoop and radial stress as input (ϵ_x, σ_h, and σ_r, respectively), the plasticity algorithm computes the corresponding axial stress, hoop, and radial strain components (σ_x, ϵ_h, and ϵ_r, respectively). The axial stress fluctuates uniformly between a tensile peak and compressive valley. The hoop and radial strains ratchet as shown in Fig. 2. This is indicative of the fact that the tubing diameter increases (ϵ_h increasing) and the wall thickness decreases (ϵ_r decreasing) at the points of maximum strain fluctuation. The rate at which this ratcheting occurs is dependent on the internal pressure and the bending strain range. Since hoop strain growth rates could not be measured during fatigue machine testing, a relation

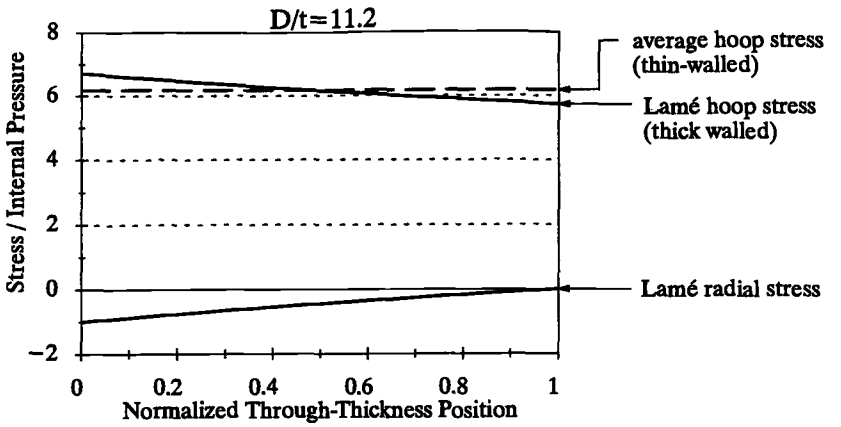

FIG. 3—*Normalized hoop and radial stress distributions through the normalized wall thickness of the tubing with the greatest* D/t *ratio used in this study.*

will be described later in this paper for approximating localized hoop strain from measurements of tubing outer dimensions. This facilitates comparison with hoop strain growth rates estimated by the incremental plasticity algorithm.

As a final note, the axial stress due to internal pressure is neglected in this approach. This decision was made since the axial pressure stress magnitude is relatively small, about 30% of the material's monotonic yield stress in the worst case. Furthermore, CT operators indicate that changes to the length of CT following routine use are not discernable, implying the absence of appreciable net axial plasticity.

Fatigue Damage Model

Fluctuating and mean equivalent strain components were used to formulate a coiled tubing fatigue damage parameter

$$\epsilon_{a,\text{eff}} = \epsilon_{a,\text{eq}}(1 + \epsilon_{m,\text{eq}})^S \tag{1}$$

where

$\epsilon_{a,\text{eff}}$ = coiled tubing fatigue damage parameter,
$\epsilon_{a,\text{eq}}$ = equivalent von Mises strain amplitude,
$\epsilon_{m,\text{eq}}$ = equivalent von Mises peak strain, and
S = coiled tubing exponent.

The CT fatigue damage parameter is considered an effective, fully reversed strain amplitude that can be used directly with the low-cycle fatigue strain-life data for the material, generated per ASTM E 606. The strain-life relation is characterized by a Manson-Coffin relation [*7–9*]

$$\epsilon_a = \frac{\sigma_f'}{E'}(2N_f)^b + \epsilon_f'(2N_f)^c \tag{2}$$

where

E' = cyclic modulus of elasticity (measured at 50% life),
σ_f' = fatigue strength coefficient,
b = fatigue strength exponent.
ϵ_f' = fatigue ductility coefficient,
c = fatigue ductility exponent,
ϵ_a = strain amplitude, and
N_f = cycles to failure.

A cycle of loading is considered complete when the tubing goes from a bent condition (a peak) to a straight condition (a valley). Damage for a cycle is computed as follows. From Eq 1, the von Mises equivalent strain amplitude, $\epsilon_{a,\text{eq}}$, is computed based on half of the range of each strain component from a peak to a valley. The values of the three strain components at the peak of the cycle are used to compute the corresponding von Mises equivalent peak strain [*7*], $\epsilon_{m,\text{eq}}$. The effective strain amplitude, $\epsilon_{a,\text{eff}}$, is taken as ϵ_a in Eq 2. The corresponding number of cycles to failure, N_f, is used to compute damage per cycle, D_i, according to a traditional Palmgren-Miner [*7–9*] approach

$$D_i = \left(\frac{1}{N_f}\right)_i \tag{3}$$

Damage is summed each cycle and failure is considered to occur when accumulated damage equals unity. However, from the hoop and radial ratcheting apparent in Fig. 2, $\epsilon_{m,eq}$ increases as cycles are applied with internal pressure. Thus, $\epsilon_{a,eff}$ will increase from Eq 1 such that a cycle applied later in life results in a greater damage estimate than a cycle applied earlier in life. In other words, damage accumulates nonlinearly.

The CT exponent, S, is identified for a particular constant pressure test result from the following procedure. A test at a particular internal pressure consists of bending and straightening a tubing specimen until it fails, defined as a loss of internal pressure from a through-thickness crack. The histories of all strain components, for the number of cycles to failure, are computed using the plasticity model with the bending strain in the axial direction and the hoop stress caused by internal pressure. Damage for each cycle is computed using Eqs 1 through 3, and S is adjusted iteratively until damage equaled unity at the cycle count corresponding to failure observed in the test. For the 483-MPa (70-ksi) yield strength material (the material for which the most data were gathered), S is plotted versus hoop stress, normalized by the cyclic yield stress, S'_y, in Fig. 4. The variation in S at low values of hoop stress is not significant. It results from scatter common to higher cycle data and the attempt of the model to fit these data. In general the value of S increases with hoop stress but, as seen in Fig. 4, the hoop stress alone cannot be used to correlate the CT exponent. Figure 5 shows the improved correlation when S is plotted against the product of the normalized yield stress and the square root of the bending strain range. A curve through the data of the form

$$S = Q\left[\frac{\sigma_h}{S'_y}\sqrt{\Delta\epsilon_x}\right]^m \tag{4}$$

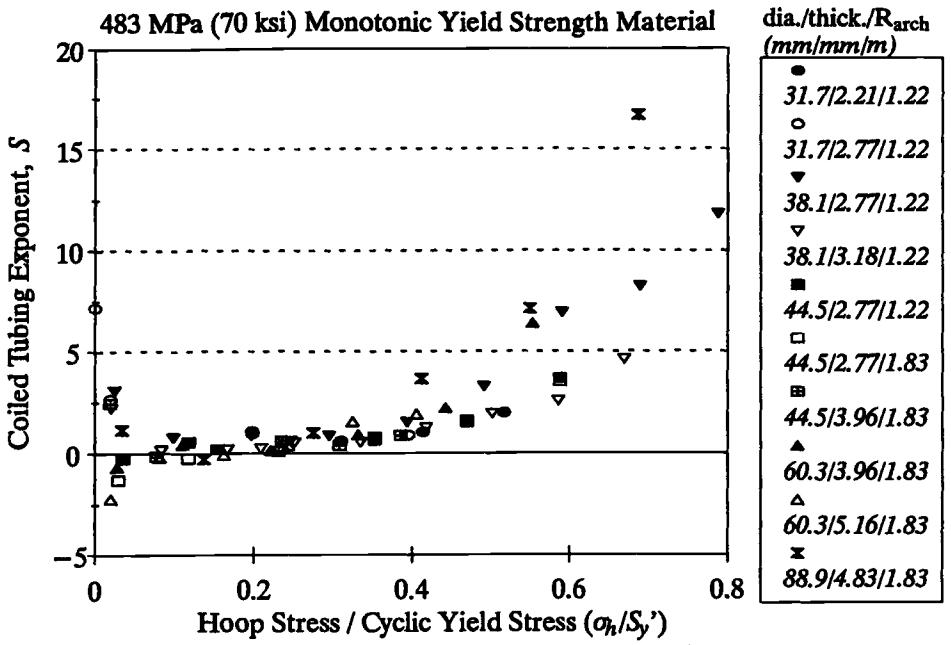

FIG. 4—*Coiled tubing exponent versus normalized hoop stress for tests on 483-MPa (70-ksi) yield strength material.*

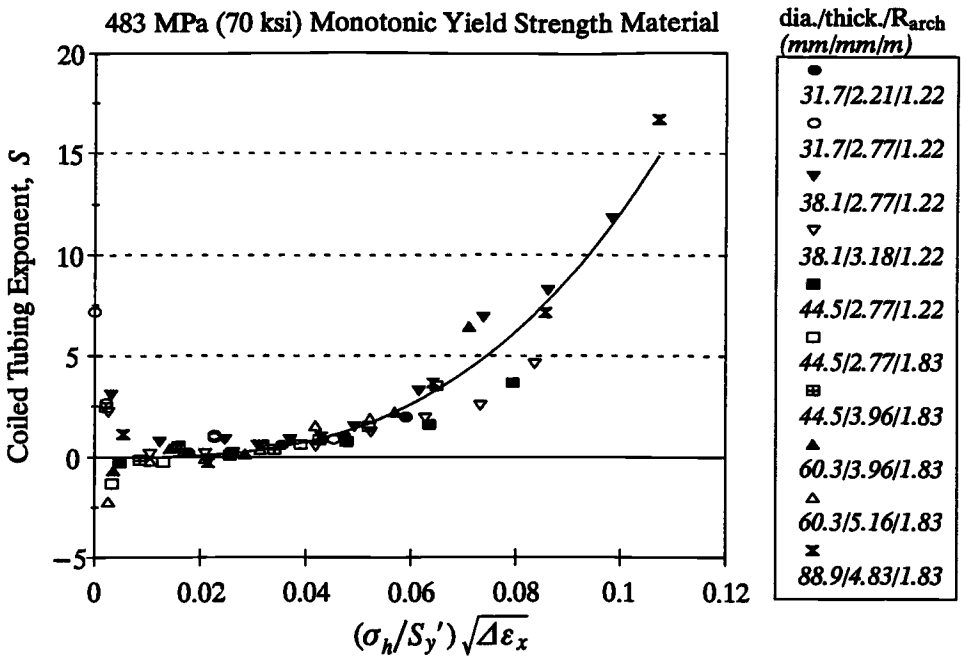

FIG. 5—*Coiled tubing exponent versus normalized hoop stress for tests on 483-MPa (70-ksi) yield strength material.*

also is shown in Fig. 5. This relation (defined by the parameters Q and m) is considered a characteristic of the material. For complex applied loading histories, Eq 4 can be used with the hoop stress and axial strain range to define the CT exponent for a particular cycle. Notice that the value of S is zero for zero hoop stress, and the coiled tubing parameter reduces to the von Mises equivalent strain amplitude.

Incremental Plasticity Model

The incremental plasticity model used in this algorithm consists of the following components:

1. The von Mises description of yielding.
2. A Mróz-type field of plastic moduli [*10*].
3. A hybrid normality flow rule [*11,12*].
4. The Garud hardening rule [*13,14*].
5. A modified supplemental hardening rule.
6. A specialized limit surface.

Additional details concerning the model are available in Refs *14–16*. Individual components are described in the remainder of this section.

Field of Plastic Moduli

Figure 6 depicts a field of eight kinematic von Mises yield surfaces on axes of axial versus hoop stress. The surfaces shown are numbered one through eight. The outermost

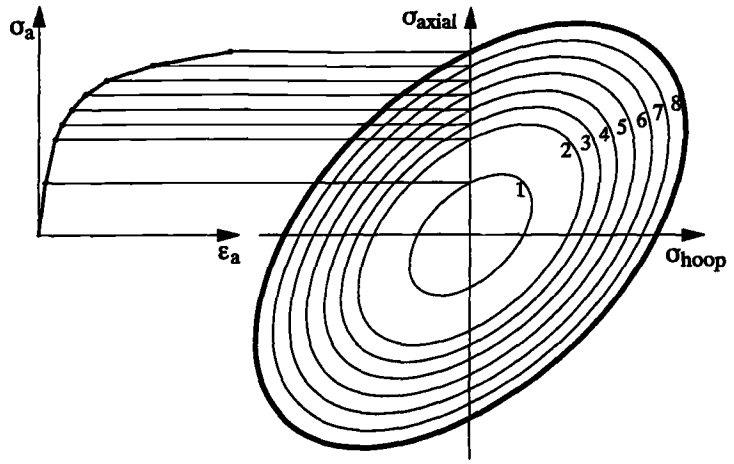

FIG. 6—*Illustration describing how the cyclic stress-strain relation is used to define the field of plastic moduli. The plastic modulus for each kinematic yield surface is associated with the slope of the linearized cyclic stress-strain curve.*

surface, Number 8, is the limit surface, described later. The size of each surface is determined from a piece-wise linearization of the cyclic stress-strain curve for the material (defined from the cyclically stable stress-amplitude versus strain-amplitude data collected during low-cycle fatigue testing and characterized by a Ramberg-Osgood relation). Because the radial stress is taken as zero, the surfaces may be considered to translate in axial-hoop stress plane. The translation of each is dictated by consistency and compatibility requirements and prescribed by hardening relations. A separate plastic modulus, (C_j, j = 1 to the number of yield surfaces) is associated with each interior yield surface and is computed based on the slope of each segment of the stress-strain curve [*14–16*].

Hybrid Normality Flow Rule

The normality flow rule, also called the Prandtl-Reuss relation [*11,12*], is based on the concept that the plastic strain increment caused by an applied stress increment is coincident with the yield surface normal at the current state of stress. Usually, this flow rule is depicted in terms of a relation between incremental strain and stress tensors. For instance, an increment of stress, $\Delta\sigma_{ij}$, is related to the total strain increment, $\Delta\epsilon_{ij}$, by the isotropic relation

$$\Delta\sigma_{ij} = 2G\left[\Delta\epsilon_{ij} + \frac{\nu}{(1-2\nu)}\Delta\epsilon_{kk}\delta_{ij} - \frac{2G}{2G + C_j}(\Delta\epsilon_{ij}n_{ij})n_{ij}\right] \tag{5}$$

where G is the elastic shear modulus, ν is Poisson's ratio, δ_{ij} is the Kronecker delta, n_{ij} is the exterior normal to the active (jth) yield surface at the current stress state, and double subscripts imply summation. In this problem, principal stress and strain can be dealt with directly since the orientation of their axes remains invariant and is assumed to intersect mutually orthogonal symmetry planes (i.e., axial, hoop, and radial directions). This facilitates the consideration of stress and strain as three-dimensional vectors

$$\underline{\sigma} = \begin{bmatrix} \sigma_x \\ \sigma_h \\ \sigma_r \end{bmatrix} \tag{5}$$

$$\underline{\epsilon} = \begin{bmatrix} \epsilon_x \\ \epsilon_h \\ \epsilon_r \end{bmatrix} \tag{6}$$

A set of closed-form equations are presented in the Appendix, expressing output increments (denoted by Δ) in terms of input increments as follows

$$\begin{bmatrix} \Delta\sigma_x \\ \Delta\epsilon_h \\ \Delta\epsilon_r \end{bmatrix} = [a_{ij}] \begin{bmatrix} \Delta\epsilon_x \\ \Delta\sigma_h \\ \Delta\sigma_r \end{bmatrix} \tag{7}$$

The 3 × 3 matrix, a_{ij}, consists of expressions based on elastic constants, the yield surface normal and the active plastic modulus. The relations are deemed "hybrid" since stress and strain increments are input with corresponding strain and stress increments as output.

In this study, the radial stress increment, $\Delta\sigma_r$, is always taken as zero since the outer surface of the tubing is being considered. However, the relations represented by Eq 7 and presented in the Appendix are suitable for use with nonzero radial stress increments. For instance, the effect of normal stress caused by internal pressure at the inner surface could be examined with these relations.

Hardening Rules

The Garud hardening rule [*13,14*] defines the yield surface translation caused by a particular stress increment. However, it is necessary to modify the hardening rule to avoid a numerical problem that will be referred to as an initial path dependency. This refers to the sequence of loading initially applied to the tubing prior to the application of alternating bending-straightening cycles.

To simulate flexural cycling under constant internal pressure, initially straight tubing must be wrapped onto a spool. Thus, a positive axial strain increment, $+\Delta\epsilon_x$, is input to the model. Next, the pressure increase must be supplied ($+\Delta\sigma_h$) to the plasticity model. This is followed by alternate applications of straightening (tubing coming off the arch, $-\Delta\epsilon_x$) and bending (tubing being rewrapped, $+\Delta\epsilon_x$). Analytically, it is possible to apply the initial wrap and pressure increase to the model, simultaneously ($+\Delta\epsilon_x$, $+\Delta\sigma_h$), referred to as "one-step" initial loading. The separate application of an initial wrap, followed by a hoop stress increase, is referred to as a "two-step" initial loading. Given the large magnitude of applied plastic straining imposed by bending ($\pm\Delta\epsilon_x$), it is unreasonable to expect that the initial path would significantly influence the ensuing plasticity behavior. However, the use of conventional hardening rules (e.g., the Garud rule used in this model or the translation rule proposed by Mróz [*10*]) result in the computation of a much higher predicted ratcheting rate following a two-step initial path relative to a one-step initial path. The reason for this is that the two-step path tends to impinge upon yield surfaces at points whose exterior normals have greater hoop direction components. Since the direction of the exterior normals dictate the plastic strain increment, more hoop strain growth results from subsequent flexural cycling. This problem became apparent whenever bending cycles followed a large pressure application that had been applied to bent tubing.

Conventional plasticity routines tend to overpredict ratcheting rates [*17*]. Therefore, to

avoid additional overprediction from the initial path effect, a modified hardening rule was developed and is invoked only when a positive hoop stress change is applied to tubing that has been wrapped (ϵ_x is positive). Yield surface translations are dictated according to limit surface image points. The image point on the limit surface corresponding to the updated stress point is used to define the exterior normal of the active yield surface. The modified hardening rule predicts ensuing hoop strain growth rates following a two-step initial loading path that are essentially identical to those predicted by the conventional hardening rules with a one-step initial loading path.

Limit Surface

The limit surface is depicted schematically in Fig. 6 as the bold, outermost yield surface. It remains stationary and centered at the stress space origin. Its purpose is to keep the equivalent stress value within a reasonable upper limit as defined asymptotically from inspection of cyclic stress-strain data. Several two-surface models from the literature have utilized limit surfaces in this manner [*18–21*]. Typically, their implementation is based on a "radial return" whereby a stress increment that attempts to exceed the limit surface is returned to the surface along a line radial to the origin of stress (of deviatoric) space. However, in this study, two of the three stress components are considered controlled inputs. Therefore, the return to the yield surface must occur along a path of constant hoop stress.

Results

The overall predictive approach is summarized in terms of an input-output flowchart in Fig. 7. An important aspect of this approach is that the same incremental plasticity program is used to identify the CT exponent relation (Q and m in Eq 4) as is used to model the behavior of the tubing in service. This is important given the difficulty of exactly modeling biaxial ratcheting behavior. It was not possible to monitor hoop strain growth rates at the tensile side of the tubing during fatigue testing. However, a technique to estimate the strain rate is presented, thus providing a comparison to the predictions from the plasticity routine. Tube walls tend to decrease in thickness at the tension and compressive sides, indicative of negative radial strain ratcheting (Fig. 2) while the horizontal and vertical dimensions of the tubing (D_x and D_y, respectively in Fig. 8) increase. These values were measured near the failure site for each specimen tested. For several tests, intermittent measurements of these dimensions indicated approximately linear growth rates. Therefore, assuming that (1) the internal and external surfaces of the tubing can be approximated by concentric ellipses, (2) the cross-sectional area of the tubing remains constant, (3) the wall thickness along the neutral axis of the tubing is unchanged from its initial dimension, t_0, and (4) the rate of thinning developed linearly over tubing life, it is possible to estimate the average rate of radial strain accumulation through the wall. It is then assumed that the hoop strain at this location is equal and opposite to the estimated radial strain based on a constant volume approximation valid for severe plastic deformation. Referring to Fig. 8, the reduced wall thickness, t', is computed from the original tubing outer diameter and wall thickness, D_0 and t_0, respectively, and the final horizontal and vertical dimensions according to the relation

$$t' = \frac{2t_0(D_0 - t_0) - D_y t_0}{D_x - 2t_0} \tag{8}$$

To assess the validity of Eq 8, several samples were sectioned and measurements were taken as presented in Table 1. The wall thickness at the tension and compression sides of the

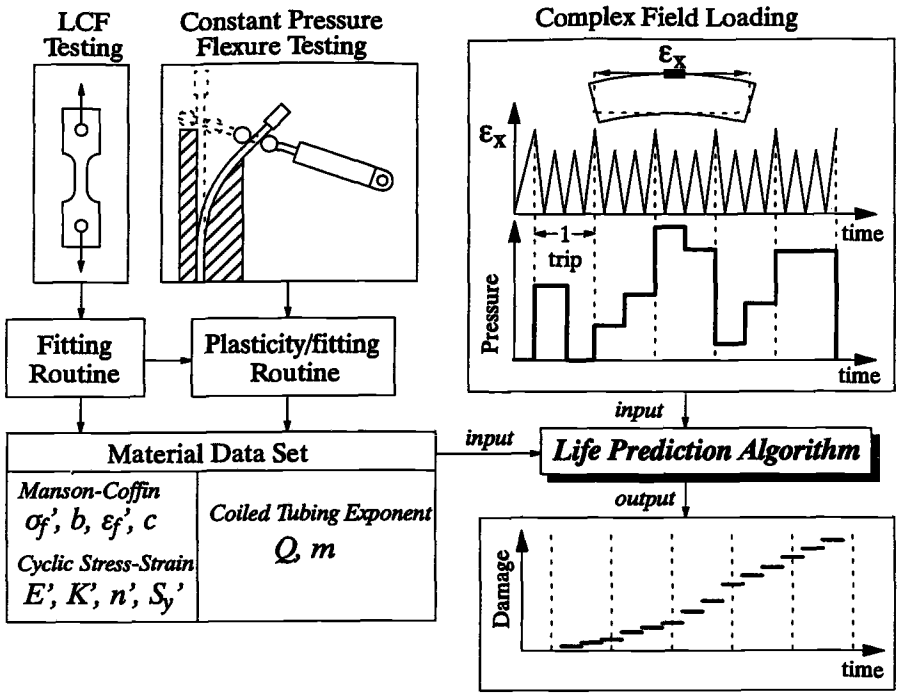

FIG. 7—*Schematic overview input-output for the coiled tubing life prediction algorithm. The plasticity routine used in the algorithm also is used to formulate the coiled tubing exponent. With the material data set, nonlinear fatigue damage can be monitored for complex field loading.*

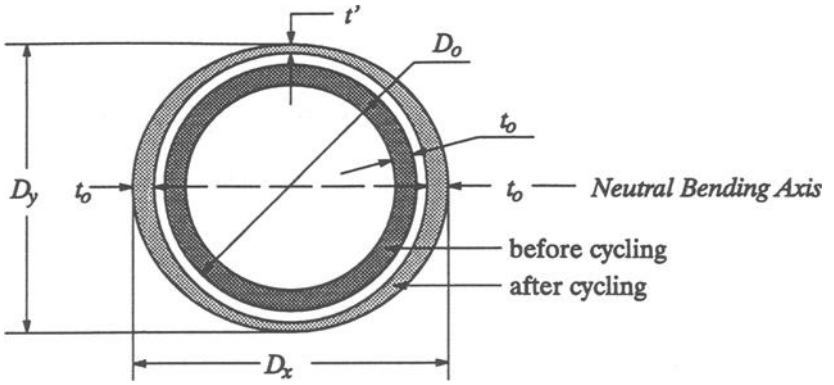

FIG. 8—*Tubing dimensions before and after loading, used to approximate the average radial and hoop strain.*

TABLE 1—*Tube growth dimensions and percentage difference between estimated thickness and average measured thickness (dimensions in millimetres).*

D_0	t_0	D_x	D_y	t'	t_{comp}	t_{tens}	t_{avg}	Difference, %
60.3	3.96	69.6	65.8	3.01	3.18	3.20	3.19	5.5
60.3	3.96	74.0	70.2	2.55	2.34	2.67	2.50	−2.1
60.3	5.16	69.1	64.1	4.05	3.89	3.96	3.92	−3.3
60.3	5.16	73.9	68.5	3.39	3.23	3.61	3.42	0.6
31.76	2.21	36.4	34.4	1.71	1.73	1.78	1.75	2.6
31.75	277	36.8	34.7	2.07	1.98	2.03	2.01	−3.0

tubing (t_{tens} and t_{comp}, respectively) were averaged (t_{avg}) for comparison to the estimated thickness. In each case the estimated wall thickness is within 5.5% of the measured thickness.

With the estimate of wall thickness, the average through-thickness hoop strain is given by

$$\epsilon_h = -\epsilon_r = \frac{t_0 - t'}{t_0} \tag{9}$$

Dividing the estimated hoop strain by the number of cycles to failure for that test provides an estimate of the hoop strain growth rate. Figure 9 shows a plot of the estimated hoop strain growth rate, normalized by the applied axial strain range versus normalized hoop stress for all of the tests conducted with normalized A606 tubing. The data are shown with estimates

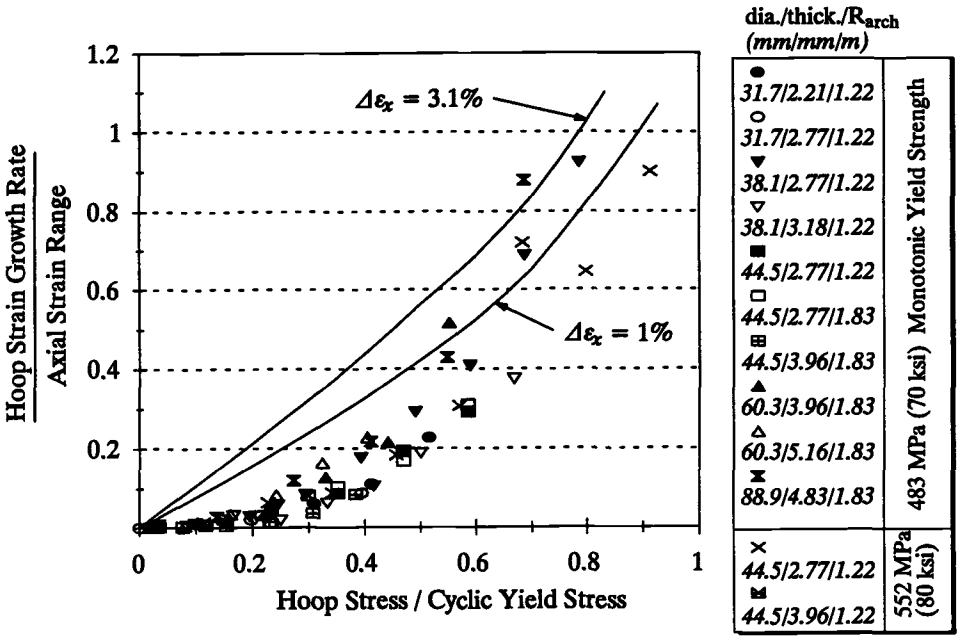

FIG. 9—*Hoop strain growth per cycle, normalized by bending strain range, versus normalized hoop stress for 483 and 552-MPa (70 and 80-ksi) yield strength material. Model predictions are shown for axial strain ranges of 1 and 3.1%.*

from the plasticity model generated with axial strain ranges of 3.1 and 1%. As previously mentioned, the hoop strain growth rates are overpredicted from the model. The model could be modified through the use of empirically determined anisotropic yield surfaces [*22*]. However, the decision was made to limit empiricism in the algorithm to the CT exponent parameters, Q and m in Eq 4. The lack of direct correlation with estimated ratcheting rates is assumed to be compensated for by using the same plasticity routine to formulate the CT parameter as is used to predict the response of the tubing to more complex loading.

Use of Low-Cycle Fatigue Data

Before comparing predictions with experimental data, a unique use of standard low-cycle fatigue data is described. "Failure" during a strain-controlled test can be defined as either the number of cycles to complete fracture or until the peak load drops a discernable amount below the cyclically stable (or half-life) value. A 10% drop in the stabilized peak stress is commonly used, as indicated in Fig. 10. This usually corresponds to the occurrence of macroscopic cracking in the gage section (cracks on the order of 1 mm in length). Therefore, a single data set could be considered to define two separate curves: one corresponding to the life to crack "initiation" and the other to "fracture." The two strain-life curves for the 483-MPa (70-ksi) yield strength material are shown in Fig. 11. The relations defining the CT exponent (Eq 4) for each material were formulated in terms of fracture properties. This was intended to account for cycles required to propagate through the wall thickness, as must occur to cause a pressure drop in the test machine. However, when the routine is implemented in the field, the initiation properties are utilized. This is done to build a reasonable

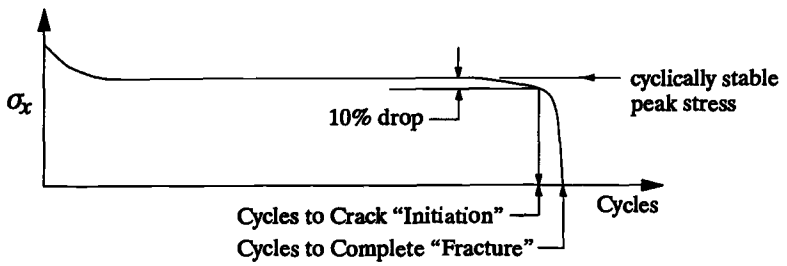

FIG. 10—*Definition of "failure" during an axial low-cycle fatigue test.*

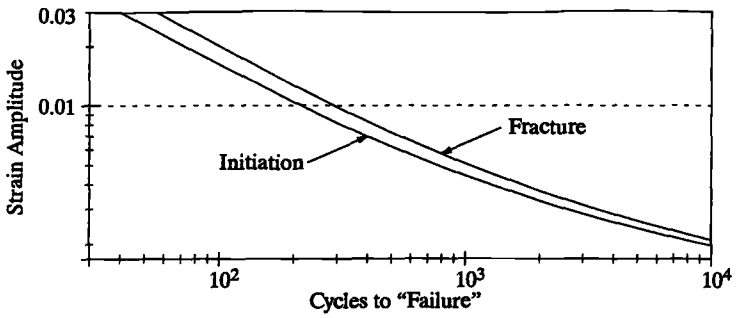

FIG. 11—*Strain amplitude versus cycles to "initiation" and cycles to "fracture" for 483-MPa (70-ksi) yield strength material.*

amount of conservatism into the approach since it would be unacceptable to operate CT after the development of macroscopic cracks.

Predictions from the model are compared to three separate data sets: (1) full-scale constant pressure test results from the initial phase of this project, (2) full-scale test results from Ref *23*, and (3) variable pressure data from the initial full-scale tests and the test machine. Full-scale tests differ from test machine results in that the bending strains vary in amplitude corresponding to the spool and gooseneck (Fig. 1). One spool cycle and two gooseneck cycles correspond to a "trip" into and out of a well for a full-scale test, with the gooseneck bending strains generally smaller than those corresponding to the spool.

Constant Pressure Data

The initial full-scale tests were conducted on 483-MPa (70-ksi) yield strength material CT of 30.6, 36.8, and 42.9 mm (1.25, 1.5, and 1.75 in.) in diameter with varying wall thicknesses, a spool diameter of 2.35 m (96 in.), gooseneck curvatures of 1.76 and 1.23 m (50 and 72 in.), and pressures from 1.7 to 34.5 MPa (250 to 5000 psi). Figure 12 is a plot of predicted life to fracture versus observed life for this data set. Points falling above the line of perfect correlation are nonconservative (failed earlier than predicted), while points below the line are conservative. Based on "life to fracture," the predictions show excellent correlation with data: over 70% of the points are predicted within 20%, and only 6 of the 22 tests are predicted nonconservatively. In Fig. 13, life to "crack initiation" predictions are compared to data. All but one of the results are predicted conservatively.

Additional full-scale test results, generated with field deployment hardware, were published in Ref *23* for 30.6 by 2.13 mm (1.25 by 0.087 in.) tubing made from 483, 552, and 690 MPa (70, 80, and 100 ksi) yield strength materials. The 483 and 690 MPa yield strength materials were identical to those used in this research. Life to "fracture" predictions correlate well with the data, as presented in Fig. 14, while the "crack initiation" predictions in Fig. 15 are excellent and slightly conservative.

Variable Pressure Data

A more severe and realistic test for an analytical model is its application to variable pressure histories. Eight such data points were generated using the test machine and two

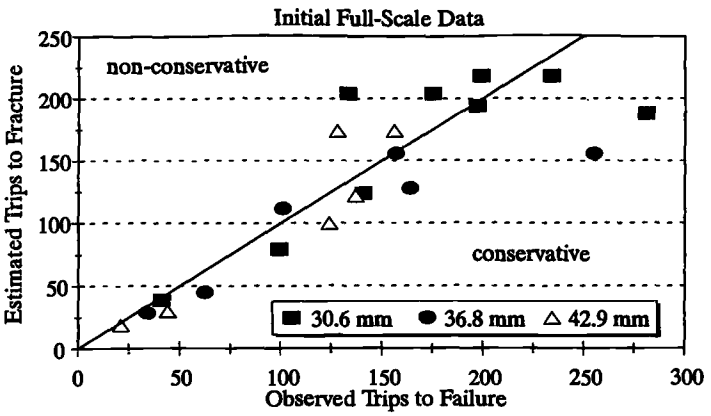

FIG. 12—*Estimated trips to "fracture" versus experimental results from initial full-scale testing using 483-MPa (70-ksi) yield strength material.*

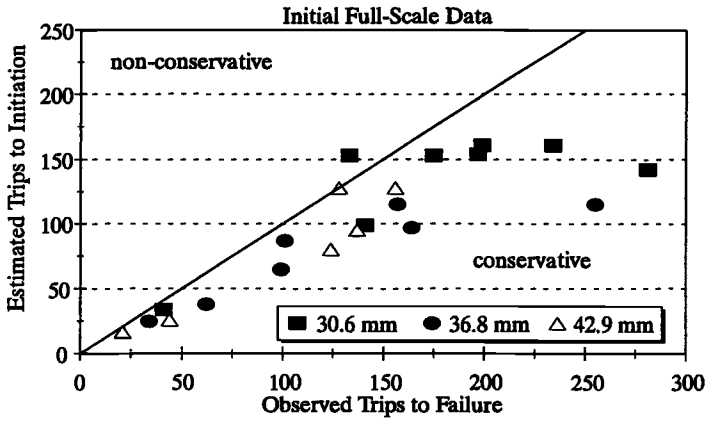

FIG. 13—*Estimated trips to "initiation" versus experimental results from initial full-scale testing using 483-MPa (70-ksi) yield strength material.*

other points during the initial full-scale tests. Figure 16 depicts the pressure profiles used. Fracture and initiation predictions from the algorithm described in this paper and predictions from a more simplistic, linear model [*23*] are presented in Fig. 17. As for the constant pressure tests, the life to fracture predictions fall on either side of the perfect correlation line with the majority of the predictions conservative. The initiation predictions are all made with a reasonable amount of conservatism. On the other hand, all but three of the predictions from the linear model are nonconservative.

It appears from Fig. 17 that a simple linear damage model (one that computes damage based only on the pressure during the cycle, independent of the previous loading history) is not adequate to characterize fatigue behavior under general, variable amplitude pressure histories. This is particularly important since variable pressure histories are routinely encountered by tubing in the field. Additional data should be generated to better understand the pressure history (load sequence) effect.

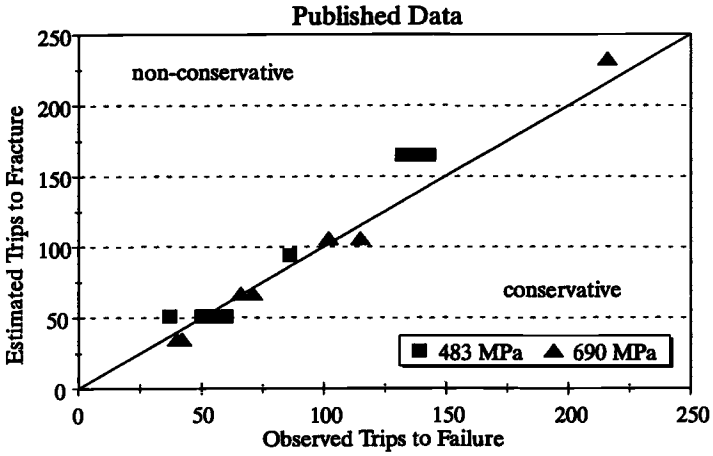

FIG. 14—*Estimated trips to "fracture" versus experimental results from Ref* 23 *full-scale testing using 483 and 690-MPa (70 and 100-ksi) yield strength materials.*

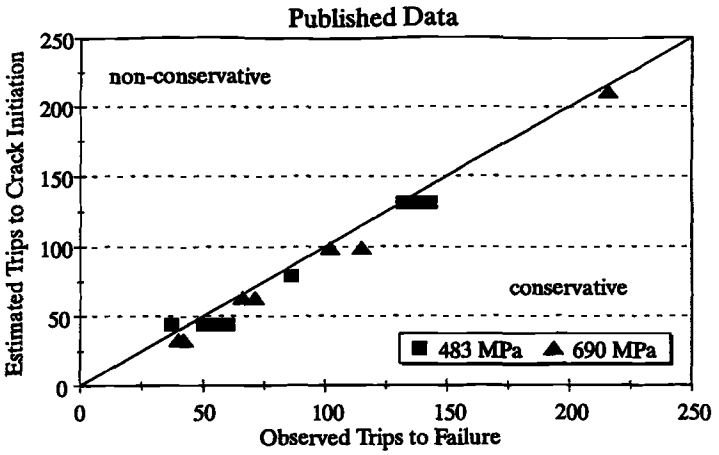

FIG. 15—*Estimated trips to "initiation" versus experimental results from Ref* 23 *full-scale testing using 483 and 690-MPa (70 and 100-ksi) yield strength materials.*

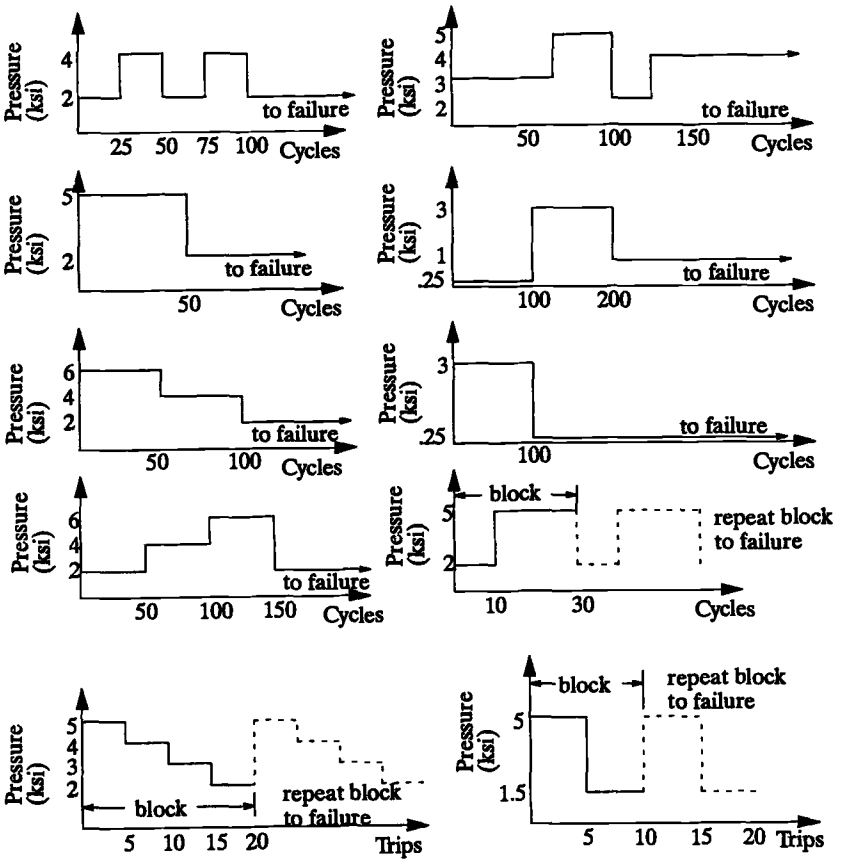

FIG. 16—*Variable pressure profiles investigated during machine (cycles) and full-scale (trips) testing.*

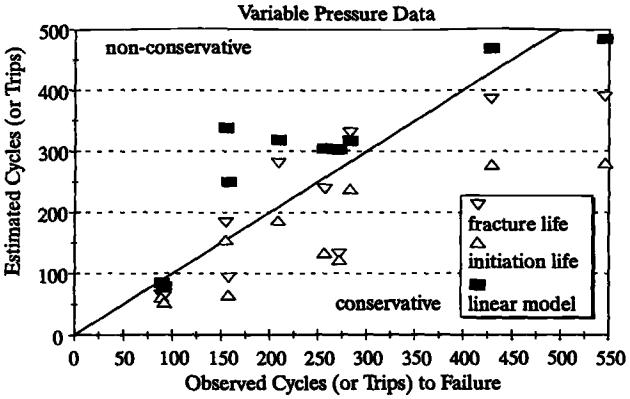

FIG. 17—*Predicted lives to crack initiation and fracture and predictions from a more simplistic linear model* [23] *versus observed life for variable pressure machine and full-scale tests.*

Discussion

A number of simplifying assumptions are required to facilitate implementation of the algorithm described in this paper. The analysis is based on the state of stress/strain at the outside wall on the tension side of the tubing. However, the majority of the failures occur at the compression side of the tubing and the majority of these initiate at the inside wall. To conduct the analysis at the compressive tube wall would involve using compressive axial strain fluctuations as input to the plasticity model instead of tensile strain increments. Some sample analyses were conducted in this manner, using average and maximum pressure-induced radial compressive stress. Slightly higher hoop and radial strain ratcheting rates are predicted by the plasticity routine for the compressive wall relative to the tensile wall. Therefore, this modification to the implementation procedure predicts greater damage on the compressive wall rather than the tensile wall. The tube wall thickness measurements in Table 1 confirm the prediction of a slightly higher rate of thinning at the compressive wall than at the tensile wall. However, the difference between the two approaches is not significant. This is confirmed by observations of broken CT specimens: in the vast majority of all specimens, cracks are visible along the tensile and compressive walls of the tubing.

Constant pressure fatigue data are required from the test machine to formulate the CT exponent. Similar data can be generated from any other test fixture capable of constant pressure cycling. The important point is to apply the plasticity algorithm to identify the CT exponent in a manner consistent with its application to general pressure loading.

Tubing ovality is not considered in this analysis. This is based on previous work [*2,4*] and on test machine results. Major and minor axes remained within 8% of each other for every specimen tested.

The fact that hoop strain growth rates are overestimated by the plasticity algorithm is assumed to be compensated for by using the same routine to both formulate the CT fatigue damage parameter and monitor damage imposed by complex pressure histories in the field. Future work should address the more precise characterization of biaxial ratcheting, as this could help to identify a less empirical damage parameter. Unfortunately, the only models capable of predicting circumferential strain development are themselves empirical in nature. Therefore, they hold only limited promise of eliminating the need for full-scale constant pressure fatigue data to supplement low-cycle fatigue data.

A more accurate plasticity model offers the additional advantage of predicting diametral

growth and localized wall thinning, which are not explicitly considered in this analysis. The original tube dimensions are used to compute input strains and stresses throughout the life of the specimen. An increase in diameter and decrease in wall thickness would result in a correspondingly greater estimated axial strain range and hoop stress, respectively, after some biaxial ratcheting had occurred. The implications of this assumption are more important academically than for CT users since tubing is typically retired if diametral growth on the order of 6% is detected.

Conclusions

An analytical model is presented to predict the fatigue behavior of coiled tubing subjected to variable pressure service conditions. The approach utilizes standard low-cycle fatigue data with additional constant-pressure, full-scale results from an experimental test fixture. The algorithm is based on estimates of circumferential and radial strain ratcheting from an incremental plasticity model using a hybrid-associated flow rule, a modified kinematic hardening rule with multiple von Mises yield surfaces, and a specialized limit surface concept. An empirical damage parameter is formulated based on constant pressure fatigue data using mean and fluctuating von Mises equivalent strain components occurring throughout the life of a section of tubing. This parameter can be used with the Palmgren-Miner approach to monitor damage that is accumulating nonlinearly under constant or variable pressure histories. Predictions from the model correlated well with constant pressure, variable bending strain range data generated with full-scale field deployment hardware, and with variable pressure data from field and fixture testing.

Acknowledgments

The author wishes to acknowledge Paul Brown and Dowell for the administration of the CoilLIFE project and the project sponsors: Agip, Arco, BP, Conoco, Dowell, Exxon, Mobil, Precision Tube Technology, Quality Tubing, and Shell. Stewart and Stevenson Services is acknowledged for developmental work on the fatigue test machine.

APPENDIX

Derivation of Hybrid Normality Flow Rule

This derivation pertains to the estimated state of stress-strain at the tension side of a section of tubing wrapped about a specific radius of curvature. At this location, the material is assumed to possess three mutually orthogonal symmetry planes, and a set of Cartesian coordinates is defined along the intersection of these planes. These axes are designated x, h, and r, (axial, hoop, and radial) as depicted in Fig. A1. In this case, stress, strain, and their increments (denoted by Δ) may be considered as three-dimensional vectors, as depicted in Eqs A1 to A4. The total strain vector, $\underline{\epsilon}$, and the total strain increment, $\Delta\underline{\epsilon}$, are considered the sum of their

$$\underline{\sigma} = \begin{bmatrix} \sigma_x \\ \sigma_h \\ \sigma_r \end{bmatrix} \quad \text{(A1)} \qquad \Delta\underline{\sigma} = \begin{bmatrix} \Delta\sigma_x \\ \Delta\sigma_h \\ \Delta\sigma_r \end{bmatrix} \quad \text{(A3)}$$

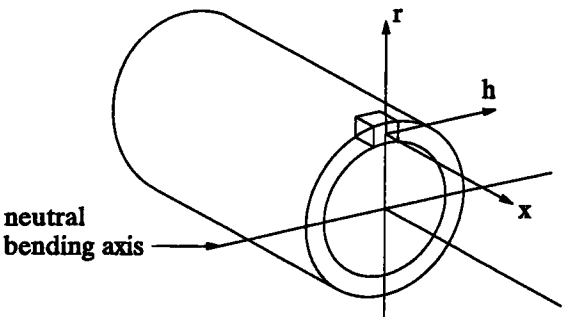

FIG. A1—*Cartesian coordinate system for coiled tubing stress element.*

$$\underline{\epsilon} = \begin{bmatrix} \epsilon_x \\ \epsilon_h \\ \epsilon_r \end{bmatrix} \quad \text{(A2)} \qquad \Delta\underline{\epsilon} = \begin{bmatrix} \Delta\epsilon_x \\ \Delta\epsilon_h \\ \Delta\epsilon_r \end{bmatrix} \quad \text{(A4)}$$

elastic and plastic components. Assuming isotropic material, the Prandtl-Reuss relation may be used to express an increment of stress in terms of a total strain increment as follows

$$\Delta\underline{\sigma} = 2G\left[\Delta\underline{\epsilon} + \frac{\nu}{(1-2\nu)}(\Delta\underline{\epsilon}\cdot\underline{I})\underline{I} - \frac{2G}{2G+C_j}(\Delta\underline{\epsilon}\cdot\underline{n})\underline{n}\right] \quad \text{(A5)}$$

where

G = elastic shear modulus,
ν = elastic Poisson's ratio,
C_j = plastic modulus of the active (jth) yield surface,

$\underline{I}$ = the identity vector, $\begin{bmatrix} 1 \\ 1 \\ 1 \end{bmatrix}$, and

$\underline{n}$ = exterior normal to the active yield surface at the current state of stress, $\begin{bmatrix} n_x \\ n_h \\ n_r \end{bmatrix}$.

Since stress and strain are three-dimensional quantities, the equations represented in A5 may be expressed as

$$\Delta\sigma_x = 2G\left[\Delta\epsilon_x + \frac{\nu}{(1-2\nu)}(\Delta\epsilon_x + \Delta\epsilon_h + \Delta\epsilon_r) - G_c(\Delta\epsilon_x n_x + \Delta\epsilon_h n_h + \Delta\epsilon_r n_r)n_x\right] \quad \text{(A6)}$$

$$\Delta\sigma_h = 2G\left[\Delta\epsilon_h + \frac{\nu}{(1-2\nu)}(\Delta\epsilon_x + \Delta\epsilon_h + \Delta\epsilon_r) - G_c(\Delta\epsilon_x n_x + \Delta\epsilon_h n_h + \Delta\epsilon_r n_r)n_h\right] \quad \text{(A7)}$$

$$\Delta\sigma_r = 2G\left[\Delta\epsilon_r + \frac{\nu}{(1-2\nu)}(\Delta\epsilon_x + \Delta\epsilon_h + \Delta\epsilon_r) - G_c(\Delta\epsilon_x n_x + \Delta\epsilon_h n_h + \Delta\epsilon_r n_r)n_r\right] \quad \text{(A8)}$$

where

$$G_c = \frac{2G}{2G + C_j} \tag{A9}$$

Omitting algebra, the three expressions in A6 to A8 may be manipulated to yield

$$-\frac{1}{2G}\Delta\sigma_x + \left(\frac{\nu}{1-2\nu} - G_c n_x n_h\right)\Delta\epsilon_h + \left(\frac{\nu}{1-2\nu} - G_c n_r n_x\right)\Delta\epsilon_r = -\left(\frac{1-\nu}{1-2\nu} - G_c n_x^2\right)\Delta\epsilon_x \tag{A10}$$

$$\left(\frac{1-\nu}{1-2\nu} - G_c n_h^2\right)\Delta\epsilon_h + \left(\frac{\nu}{1-2\nu} - G_c n_h n_r\right)\Delta\epsilon_r = -\left(\frac{\nu}{1-2\nu} - G_c n_x n_h\right)\Delta\epsilon_x + \frac{1}{2G}\Delta\sigma_h \tag{A11}$$

$$\left(\frac{\nu}{1-2\nu} - G_c n_h n_r\right)\Delta\epsilon_h + \left(\frac{1-\nu}{1-2\nu} - G_c n_r^2\right)\Delta\epsilon_r = -\left(\frac{\nu}{1-2\nu} - G_c n_r n_x\right)\Delta\epsilon_x + \frac{1}{2G}\Delta\sigma_r \tag{A12}$$

Making the following substitutions,

$$A = -\frac{1}{2G} \tag{A13}$$

$$X = \left(\frac{1-\nu}{1-2\nu} - G_c n_x^2\right) \tag{A14}$$

$$Y = \left(\frac{1-\nu}{1-2\nu} - G_c n_h^2\right) \tag{A15}$$

$$Z = \left(\frac{1-\nu}{1-2\nu} - G_c n_r^2\right) \tag{A16}$$

$$U = \left(\frac{\nu}{1-2\nu} - G_c n_x n_h\right) \tag{A17}$$

$$V = \left(\frac{\nu}{1-2\nu} - G_c n_h n_r\right) \tag{A18}$$

$$W = \left(\frac{\nu}{1-2\nu} - G_c n_r n_x\right) \tag{A19}$$

Equations A9 through A11 may be written in matrix form as

$$\begin{bmatrix} A & U & W \\ 0 & Y & V \\ 0 & V & Z \end{bmatrix} \begin{bmatrix} \Delta\sigma_x \\ \Delta\epsilon_h \\ \Delta\epsilon_r \end{bmatrix} = \begin{bmatrix} -X & 0 & 0 \\ -U & -A & 0 \\ -W & 0 & -A \end{bmatrix} \begin{bmatrix} \Delta\epsilon_x \\ \Delta\sigma_h \\ \Delta\sigma_r \end{bmatrix} \tag{A20}$$

Matrix manipulations are used to reduce Eq A20 to the following format

$$\begin{bmatrix} \Delta\sigma_x \\ \Delta\epsilon_h \\ \Delta\epsilon_r \end{bmatrix} = [a_{ij}] \begin{bmatrix} \Delta\epsilon_x \\ \Delta\sigma_h \\ \Delta\sigma_r \end{bmatrix} \tag{A21}$$

where

$$a_{11} = \frac{1}{A}\left[W\left(\frac{YW - UV}{YZ - V^2}\right) + U\left(\frac{ZU - VW}{YZ - V^2}\right) - X \right] \quad a_{12} = \left(\frac{ZU - VW}{YZ - V^2}\right) \quad a_{13} = \left(\frac{YW - UV}{YZ - V^2}\right)$$

$$a_{21} = -\left(\frac{ZU - VW}{YZ - V^2}\right) \quad a_{22} = \left(\frac{-AZ}{YZ - V^2}\right) \quad a_{23} = \left(\frac{AV}{YZ - V^2}\right)$$

$$a_{31} = -\left(\frac{YW - UV}{YZ - V^2}\right) \quad a_{32} = \left(\frac{AV}{YZ - V^2}\right) \quad a_{33} = \left(\frac{-AY}{YZ - V^2}\right)$$

With Eq A21, axial stress, hoop, and radial strain increments are computed directly from input increments of axial strain (from bending) and hoop and radial stress (from internal pressure).

References

[1] *World Oil's Coiled Tubing Handbook,* M. E. Teel, Ed., reprinted from *World Oil,* Gulf Publishing Company, Houston, TX, 1993.

[2] Tipton, S. M. and Newburn, D. A., "Plasticity and Fatigue Damage Modeling of Severely Loaded Tubing," *Advances in Fatigue Lifetime Predictive Techniques, ASTM STP 1122,* American Society for Testing and Materials, West Conshohocken, PA, 1992, pp. 369–382.

[3] Newburn, D. A. and Tipton, S. M., "Influence of a Dominant Principal Strain on Low-Cycle Multiaxial Fatigue," *Proceedings,* Fourth International Conference on Fatigue and Fatigue Thresholds, Honolulu, HI, July 1990, pp. 417–422.

[4] Newburn, D. A., "Post Yield Cyclic Strain Response of Pressurized Tubes," Master of science thesis, The University of Tulsa, Tulsa, OK, 1990.

[5] Tipton, S. M. and Brown, P. A., "Monitoring Coiled Tubing Fatigue Life," *Proceedings,* Second International Conference on Coiled Tubing Operations, Gulf Publishing Company and World Oil, Houston, TX, 28–31 March 1994.

[6] Newman, K. R. and Brown, P. A., "Development of a Standard Coiled Tubing Fatigue Test," SPE 26539, *Proceedings of the Society of Petroleum Engineers,* Fall 1993, pp. 303–309.

[7] Fuchs, H. O. and Stephens, R. I., *Metal Fatigue in Engineering,* John Wiley and Sons, New York, NY, 1980.

[8] Bannantine, J. A., Comer, J. J., and Handrock, J. H., *Fundamentals of Metal Fatigue Analysis,* Prentice Hall, Englewood Cliffs, NJ, 1990.

[9] *Fatigue Design Handbook,* Society of Automotive Engineers, Warrendale, PA, 1990.

[10] Mróz, Z., "On the Description of Anisotropic Workhardening," *Journal of the Mechanics and Physics of Solids,* Vol. 15, 1967, pp. 163–175.

[11] Prandtl, L., "Spannungsverteilung in Plastischen Doerpern," *Proceedings,* First International Congress on Applied Mechanics, Delft, Technische Boekhandel en Druckerij, J. Waltmann, Jr., 1925, pp. 43–54.

[12] Reuss, A., "Beruecksichtigung Der Elastischen Formaenderungen in der Plastizitaetstheorie," *Zeitschrift für angewandte Mathematik und Meckanik,* Vol. 10, 1930, pp. 266–274.

[13] Garud, Y. S., "Prediction of Stress-Strain Response under General Multiaxial Loading," *Mechanical Testing for Deformation Model Development, ASTM STP 765,* R. W. Rhode and J. C. Swearengen, Eds., American Society for Testing and Materials, Philadelphia, 1982, pp. 223–238.

[14] Garud, Y. S., "Multiaxial Fatigue of Metals," Ph.D. dissertation, Stanford University, Stanford, CA, 1981.

[15] Tipton, S. M., "Fatigue Behavior in the Presence of a Notch," Ph.D. dissertation, Stanford University, Stanford, CA, 1985.

[16] Tipton, S. M. and Bannantine, J. A., "Inelastic Stress-Strain Predictions for Multiaxial Fatigue Damage Evaluation," *Multiaxial Fatigue, ASTM STP 1191,* D. L. McDowell and R. Ellis, Eds., American Society for Testing and Materials, West Conshohocken, PA, 1993, pp. 273–297.

[17] Moreton, D. N., "The Ratcheting of a Cylinder Subjected to Internal Pressure and Alternating Axial Deformation," *Journal of Strain Analysis,* Vol. 28, No. 4, 1993, pp. 277–282.

[18] Dafalias, Y. F. and Popov, E. P., "A Model of Nonlinearly Hardening Materials for Complex Loading," *Acta Mechanica,* Vol. 21, 1975, pp. 173–192.

[*19*] Krieg, R. D., "A Practical Two-Surface Model for Transient Nonproportional Cyclic Plasticity," *Journal of Applied Mechanics,* September 1975, pp. 641–646.

[*20*] Lamba, H. S., "Nonproportional Cyclic Plasticity," Ph.D. dissertation, TAM Report No. 413, University of Illinois at Urbana-Champaign, 1976.

[*21*] McDowell, D. L., "A Two-Surface Model for Transient Nonproportional Cyclic Plasticity, Parts 1 and 2," *Journal of Applied Mechanics,* Vol. 52, June 1985, pp. 298–308.

[*22*] Hill, R., *The Mathematical Theory of Plasticity,* Clarendon Press, Oxford, Chapter XII, "Plastic Anisotropy," 1956.

[*23*] Avakov, V. A., Foster, J. C., and Smith, E. J., "Coiled Tubing Life Prediction," OTC 7325, Offshore Technology Conference, Houston, TX, 1993.

Vladimír Kliman,[1] *Pavol Füleky,*[1] *and Jana Jelemenská*[1]

Residual Operating Fatigue Lifetime—Estimation of Distribution Function

REFERENCE: Kliman, V., Füleky, P., and Jelemenská, J., **"Residual Operating Fatigue Lifetime—Estimation of Distribution Function,"** *Advances in Fatigue Lifetime Predictive Techniques: 3rd Volume, ASTM STP 1292,* M. R. Mitchell and R. W. Landgraf, Eds., American Society for Testing and Materials, 1996, pp. 305–327.

ABSTRACT: Engineering structures often work under operating conditions in which the character of a load undergoes permanent change (different service-loading regimes). Such an operation is very frequent for transportation equipment, earthmoving machines, airplanes, etc. Considering that the service-loading process (time history of $\sigma(t)$ stress or $\epsilon(t)$ strain) at particular operating regimes exhibits in a majority of cases the stochastic nature, the question arises as to how to estimate the fatigue resistance of the structure under such service conditions. For this reason, a method was developed to evaluate such service from the viewpoint of fatigue reliability and to estimate the resulting fatigue lifetime in terms of probability interpretation.

The result of life calculation is the distribution function (DF) of the residual fatigue lifetime for the given loading regime. This DF reflects the loading history (sequence and nature of the previous loading regimes) and the random character of the interacting material and loading parameters. The DF obtained is in a good agreement with the experimental results. Finally, illustrative examples that reflect practical applications of this theory are presented.

KEYWORDS: random loading process, fatigue life distribution function, probability, reliability, residual fatigue life, mean stress, hysteresis energy, fatigue damage accumulation hypothesis

Satisfactory resistance against fatigue still remains among the most important requirements a reliable structure should fulfill. Estimation of this property, either during the component design stage or during operation of the structure, can be formulated as the task to estimate the fatigue endurance in an assumed service or to compare the estimated fatigue life, with life under loading conditions differing from those that were considered during its design. Estimation of the fatigue life should include a whole chain of requirements that reflect the cyclic material properties, the representative loading characteristics, easy application, etc. Nevertheless, in order to estimate the reliability of the structure from the fatigue point of view, it is necessary to emphasize, first of all, the probabilistic approach, which makes it possible to estimate the fatigue resistance in terms of failure probability. In our case, this means determining the probability of premature fatigue fracture occurrence. This is of primary importance when dealing with a load of random character and with a material showing a large scatter in mechanical properties. The distribution function of life, reflecting the stochastic nature of both the loading process and the material properties, should be the result of fatigue life estimation. Such an approach to life estimation can be found in Ref *1*.

[1]Principal research scientist, senior research engineer, and research engineer, respectively, Institute of Materials and Machine Mechanics, Slovak Academy of Sciences, Račianska 75, P.O. Box 95, 830 08 Bratislava 38, Slovak Republic.

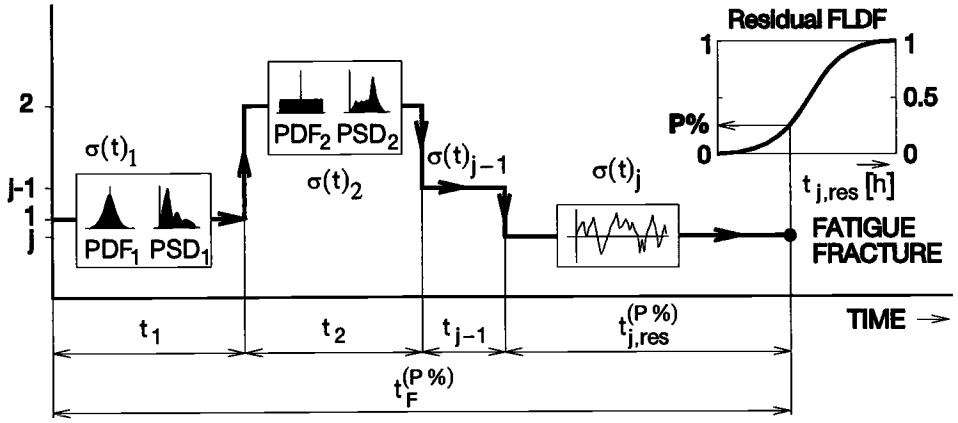

FIG. 1—*Operation under variable random load parameters.*

However, engineering structures are often subjected to severe service conditions in which the character of a load undergoes permanent change. Such an operation is very frequent in the service of transportation equipment, earth moving machines, airplanes, etc., schematically shown in Fig. 1. When considering that the service-loading process (time history of $\sigma(t)$ stress or $\in(t)$ strain) at particular operating regimes ($1 \ldots j$) exhibits in a majority of cases the stochastic nature, the question arises as to how to estimate the fatigue resistance of the structure under the described operating conditions.

In this article the major emphasis is on the above-mentioned field of concern, and a way is presented as to how to evaluate such an operation from the viewpoint of fatigue reliability and how to estimate the resulting fatigue life, t_F, in terms of probability interpretation. Finally, illustrative examples reflecting practical applications of this theory are presented.

Problem Formulation

Various formulated tasks concerning the fatigue reliability under structure loading conditions (see Fig. 1) can be characterized in general as a question of the residual life assessment regarding the previous history of loading. Let us assume that the structure is subjected to a random loading process, $\sigma(t)$, or strain-loading process, $\in(t)$, expressed by the statistical characteristics of this process, namely by: the mean value, the standard deviation, $s_{\sigma,\epsilon}$, the probability density function, PDF, and the power spectral density, PSD. Let us also assume that the service loading is alternating so that the process $\sigma(t)_1$ acts for the time t_1, the process $\sigma(t)_i$ acts for the time t_i, and the loading process $\sigma(t)_j$ will act until the fatigue fracture initiates, which corresponds with the residual life, $t_{j,\text{res}}$ (Fig. 1). It is evident that the total fatigue life, t_F, will differ from the life, $t_{f,j}$, which would correspond with only $\sigma(t)_j$, the loading process. Our goal is to estimate the residual life, $t_{j,\text{res}}$.

Life Definition

The approach to life estimation depends on the real component function. From this point of view components can be divided into two classes. The first represents components that can continue to operate even when containing an initiated fatigue crack. For this class, the fatigue life is defined by the crack length that is still acceptable from the viewpoint of a reliable component operation. Such a situation is handled by fracture mechanics, and in a

majority of cases the analysis is aimed at determining the residual life when the initial crack length (e.g., detected during in-service inspection) is known.

To the second class of components belong those for which:

1. The crack occurrence is a priori inadmissible under service conditions (components cannot be allowed to operate in-service with cracks).
2. The major part of their service life is represented by the time required to initiate the crack.
3. The service fatigue life estimation requires an analysis that is not based on crack propagation (e.g., in the design stage). These situations are analyzed by local stress-strain methods.

Our analysis is related to the second group of components. In such a case, the life will be defined as the time required to initiate a crack about 0.5 to 1 mm in length, i.e., the time required for the so-called engineering initiation of the fatigue crack. Then the life of a complex structure is expressed by the fatigue strength of the small volume of the material at critical points (the points of stress concentration).

A schematic representation of the generally accepted model for life estimation under random loading conditions for this group is given in Fig. 2. It employs an adequate hypothesis covering the fatigue damage accumulation, correlating both the material and loading characteristics resulting in the life to be found.

Residual Life Estimation

Our derivations of the respective relations stem from the so-called "energy criterion." According to this criterion, fatigue damage can be expressed by hysteresis energy, i.e., by plastic strain energy, and the fatigue fracture will occur when the material has absorbed a certain amount of hysteresis energy, W_f. The value of energy to fracture, W_f, is not a constant as originally expected, but is a function of the cyclic loading amplitude, σ_a [2]. With decreasing amplitude, i.e., with an increasing number of cycles to fracture, N_f, the W_f value increases. This dependence for the loading with σ_a = const. in logarithmic coordinates is expressed by a line (*l*) in Fig. 3*b*.

The absorbed energy increment under the random loading process, $\sigma(t)$, can be plotted in this dependence as well. It is evident from Fig. 3 that the value of energy to fracture, W_{FR}, corresponding with the random loading process, $\sigma(t)$, can be obtained also via the harmonic

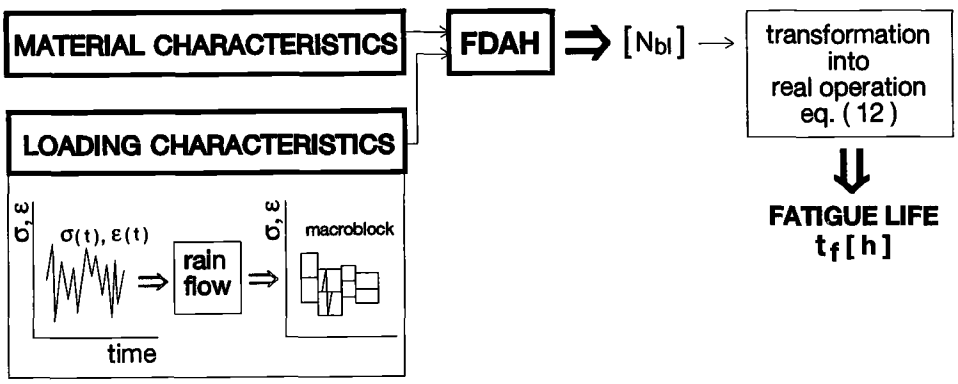

FIG. 2—*Layout of fatigue life estimation under random loading.*

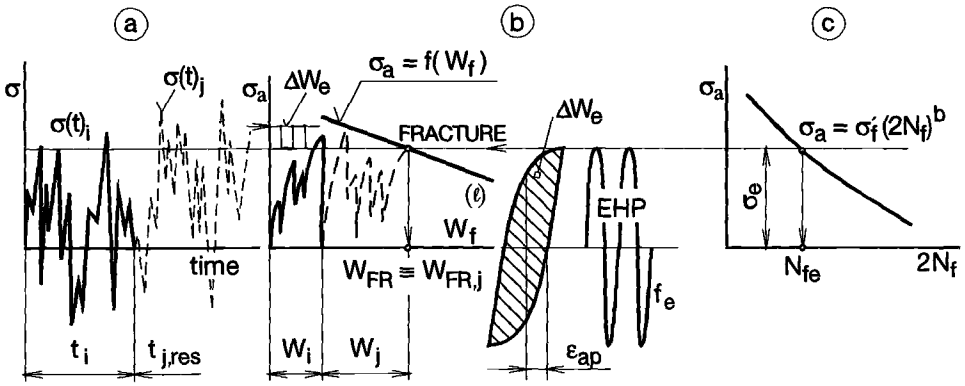

FIG. 3—*Random and equivalent harmonic processes.*

process (the equivalent harmonic process—EHP) with σ_e amplitude, i.e., $W_{FR} = \Delta W_e N_{fe}$ (where ΔW_e is the area of the hysteresis loop—the energy of the plastic strain amplitude per one cycle). In other words, the $\sigma(t)$ random process can be substituted by EHP with σ_e amplitude. However, it must oscillate with such frequency, f_e, that the energy value, W_{FR}, is attained within the same time (time to fracture t_f) as by the random loading process, $f_e = N_{fe}/t_f$. The mean value of fatigue damage induced by the $\sigma(t)$ process for 1 s is then characterized by the W_e value correlated with the W_{FR} energy.

The following relation is valid for loading only by the $\sigma(t)_j$ process

$$W_{FR,j} = \Delta W_j f_j t_{f,j} \tag{1}$$

where

$t_{f,j}$ = time to fatigue fracture initiation under loading by $\sigma(t)_j$ process, s,
f_j = EHP frequency for $\sigma(t)_j$ process, Hz,
ΔW_j = area of the hysteresis loop of the EHP, MPa, and
$W_{FR,j}$ = hysteresis energy to fracture under loading by $\sigma(t)_j$ process, MPa.

For the loading by several processes of different characteristics according to the schematic representation in Fig. 1, the following equation can be derived (see Fig. 3*b*)

$$W_{FR} = W_1 + W_2 + \cdots + W_i + W_j = W_{FR,j} \tag{2}$$

where

W_{FR} = the total hysteresis energy to fracture for the loading by $\sigma(t)_1 \ldots \sigma(t)_j$ random processes, MPa, and
W_i = the hysteresis energy absorbed by the material during $\sigma(t)_i$ process loading acting on the section i for the time t_i, MPa.

and with regard to Eq 1

$$W_{FR} = \Delta W_1 t_1 f_1 + \Delta W_2 t_2 f_2 + \cdots + \Delta W_i t_i f_i + \Delta W_j t_{j,res} f_j = W_{FR,j} \tag{3}$$

Equations 2 and 3 are valid only on the precondition that no fatigue fracture occurs during load on the segments t_1 to $t_{(j-1)}$ (Fig. 1), i.e., the limit energy value (represented by the line *l* in Fig. 3*b*) is not achieved when the processes $\sigma(t)_1$ up to $\sigma(t)_{j-1}$ are taking place. Then the total energy to fracture, W_{FR} (for the loading by the $\sigma(t)_1 \ldots \sigma(t)_j$ processes), is equal to the $W_{FR,j}$ energy (related only to the loading by the $\sigma(t)_j$ process) due to the fact, as evident in Fig. 3*b*, that the attainment of the limit curve (*l*) depends solely on the parameters of the last acting loading process, i.e., of $\sigma(t)_j$.

The following relation can be derived for the residual life based on Eqs 1 and 3

$$t_{j,\text{res}} = t_{f,j} - \frac{1}{\Delta W_j f_j} \sum_{i=1}^{i=j-1} t_i \Delta W_i f_i \tag{4}$$

and altered according to Eq 1

$$t_{j,\text{res}} = t_{f,j} \left(1 - \frac{1}{W_{FR,j}} \sum_{i=1}^{i=j-1} \frac{t_i}{t_{f,i}} W_{FR,i} \right) \tag{5}$$

where

$W_{FR,i}$ = the hysteresis energy to fracture under loading only by the $\sigma(t)_i$ process, MPa,
$t_{f,i}$ = the time to fatigue fracture under loading only by the $\sigma(t)_i$ process, s, and
t_i = the time of the $\sigma(t)_i$ process duration over the *i* section, s.

To calculate the residual life employing Eq 5, it is necessary:

1. To define the scheme of loading by the particular random processes $\sigma(t)_i$ for $i = 1 \ldots j$ in relation to Fig. 1.
2. To assess the fatigue lives, $t_{f,i}$, for the $\sigma(t)_i$ random loading processes.
3. To assess the hysteresis energies to fracture $W_{FR,i}$ for the $\sigma(t)_i$ random loading processes.

Fatigue Life Estimation Under Conditions of Random Process Loading

To estimate the life, t_f, under conditions of $\sigma(t)$ random process loading, the method referred to in Ref *1* is employed. This method modifies the generally accepted procedure to estimate the life under conditions of random loading (Fig. 2) so that the calculation results in the fatigue life distribution function (FLDF). This function takes into consideration the stochastic nature of both the loading and mechanical properties. The modification consists in such a processing of the material and loading characteristics that a set of feasible combinations of material and loading parameters represent the input to the fatigue damage accumulation hypothesis (FDAH), while a set of feasible fatigue lives serving for the distribution function (DF) calculation represent the output of the FDAH. The schematic representation of the mentioned calculation is given in Fig. 4. The following activities are necessary in order to realize the calculation of FLDF.

Processing of Loading Characteristics

Due to the stochastic nature of loading, each new implementation (realization) of the $\sigma(t)$ process would lead to a different value of the fatigue life. Hence this principle in Ref *1* was

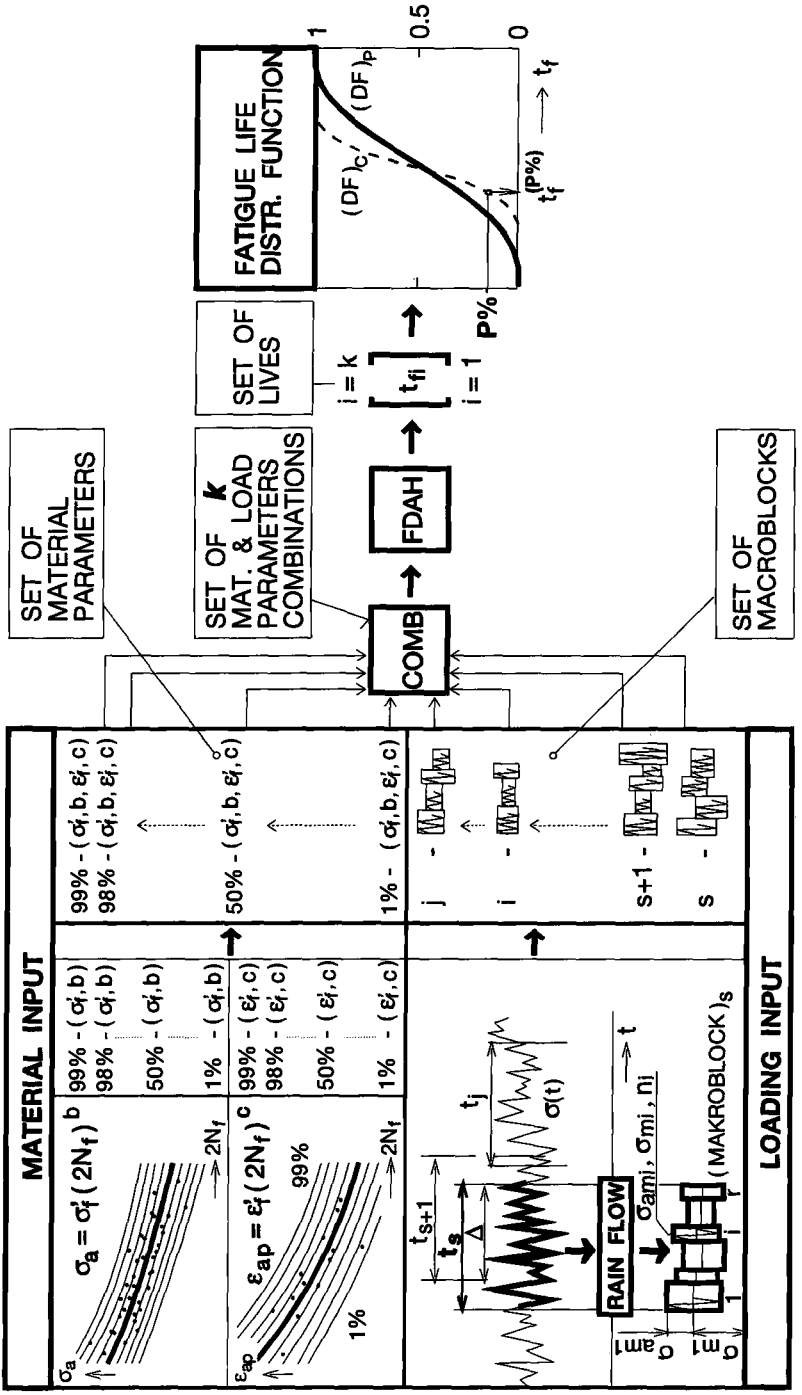

FIG. 4—*Layout of fatigue life distribution function calculation:* c(p)-*DF considering the confidence (prediction) interval for material parameters.*

substituted so that the sufficiently long and representative record of the $\sigma(t)$ random loading process was divided by appropriate means into j of mutually overlapping segments (Fig. 4). Each segment represented one realization of the $\sigma(t)$ random loading process. It should be noted here that each random loading process must have an identical time length, and the value of overlapping Δ must be kept constant. This guarantees that the $\sigma(t)$ process is uniformly represented in the life calculation, i.e., none of the process parts of the entire loading history is counted more times than the other.

The term "representative and sufficiently long" means that the process must include all significant service operations and that the record length must provide a sufficient number of segments (process realizations $\sigma(t)$) to obtain the sufficient calculated set of lives to calculate the DF. Each process segment, $\sigma(t)$, must be then transformed on a macroblock of harmonic cycles, which then enter the calculation as a loading characteristic. The macroblock consists of a set of harmonic cycles with different σ_{am} amplitudes with the appropriate mean values, σ_m—this represents a random process of t_s length equal to the segment length. The rain-flow method should be employed for transformation. The appropriate algorithm is indicated in Refs *3* and *4*. The result of the loading processing is thus a set of j macroblocks.

On actual application of this procedure, it is necessary to determine the size of the segment overlapping Δ and the minimum length of the segment required to obtain the representative calculation of the FLDF. The details are presented in Ref *1*; however, the following facts should be considered:

1. The overlapping Δ should be as large as possible (typically 95% is employed).
2. The minimum segment length had to be assessed separately for each loading process type.

To ensure these conditions, the initial length of the segment of the $\sigma(t)$ process is selected, followed by the FLDF calculations for increasing length values. The standard deviation of the calculated FLDF varies with segment length. The stabilized value of the life standard deviation determines the minimum required length of the $\sigma(t)$ process segment. The FLDF calculated for the segment length greater than its minimum value is representative for the $\sigma(t)$ process.

In this way the FLDF, respecting the stochastic nature of loading, can be obtained from one representative record of the random loading process.

Processing of Material Characteristics

The following fatigue life curves under harmonic loading conditions are considered as the representative material characteristics

$$\sigma_a = \sigma_f'(2N_f)^b \tag{6}$$

and

$$\epsilon_{ap} = \epsilon_f'(2N_f)^c \tag{7}$$

where

σ_f' = fatigue strength coefficient, MPa,
b = fatigue strength exponent,

$\in'_f$ = fatigue ductility coefficient, and
c = fatigue ductility exponent.

Inhomogeneity of the material mechanical properties is manifested in the scatter of σ'_f, b, $\in'_f$, and c values. If this scatter is omissible, it is sufficient to employ only the parameters of Eqs 6 and 7 corresponding to the regression curve to calculate the life. In such a case, the calculated FLDF represents only a random nature of loading.

Conversely, the experimental dependence of $\sigma_a = f(2N_f)$ and $\in_{ap} = f(2N_f)$ for various values of the confidence interval (CI) and the prediction interval (PI) should be evaluated. In the case of the selected constant value of interval change (it is recommended to grade the interval limit by 1%), a set of curves (interval limits) is obtained comprising the σ'_f, b, $\in'_f$, and c parameters representing the cyclic material properties for various occurrence probabilities.

Fatigue Damage Accumulation Hypothesis (FDAH)

The set of lives from which the required FLDF will be calculated (Fig. 4) is obtained by combining the material and loading parameters processed in the described procedure. The actual procedure lies in combining each evaluated macroblock with material parameters for 1 up to 99%, i.e. (j.99) combinations enter the FDAH (see also Fig. 10). The FDAH presented in Ref *5* is employed to calculate the life. According to this FDAH, the fatigue damage D (characterized by plastic strain energy) from one macroblock, i.e., induced by one segment of the $\sigma(t)$ process, is

$$D = \sum_{i=1}^{i=r} \frac{n_i}{N_{f\min}} \left(\frac{\sigma_{ai}}{\sigma_{a\max}} \right)^{\frac{b+c}{b}} \tag{8}$$

where

n_i = number of cycles at σ_{ai} amplitude (in the macroblock),
$\sigma_{a\,max}$ = maximum amplitude in the macroblock, MPa,
$N_{f\,min}$ = number of cycles to fracture under loading with $\sigma_{a\,max}$, Eq 6, and
r = number of loading levels in the macroblock (Fig. 4).

Effect of Mean Stress

Equation 8 is in this form derived for the macroblock of amplitudes showing zero mean value. In the macroblock obtained by the rain-flow method from the $\sigma(t)$ process segment, the mean value of stress σ_m is allocated to each cycle. Therefore, in the life calculation according to Eqs 8 through 12, it is necessary to proceed in such a way that each macroblock of amplitudes with the mean values will be first transformed to the macroblock of amplitudes with zero mean values in accordance with a method of considering the effect of σ_m. Equal fatigue life is considered as the transformation criterion.

In considering the effect of σ_m according to Morrow [*6*] (reduction of the σ'_f coefficient by the σ_m value), employing Eq 6, the transformation relation between the loading amplitude σ_a (at $\sigma_m = 0$) and the σ_{am} amplitude (at $\sigma_m \neq 0$) (Fig. 4) will be as follows

$$\sigma_{am} = \sigma_a \left(1 - \frac{\sigma_m}{\sigma'_f} \right) \tag{9}$$

and modified [*1*] on the basis of the energy criterion

$$\sigma_{am} = \sigma_a \left(1 - \frac{\sigma_m}{\sigma'_f}\right)^{\frac{c+1}{b+c+1}} \tag{10}$$

According to this equation, the transformation relation is also a function of the material constants b and c. It should be noted that, with the aid of the energy criterion, the other models (reviewed and compared in Ref *7*) can also be modified.

Life Calculation

Fatigue life expressed in the number of macroblocks repetition is then

$$N_{bl}D = 1 \text{ d} \qquad N_{bl} = D^{-1} \tag{11}$$

For the life transformation into time region

$$t_f = D^{-1}t_s \tag{12}$$

where

t_s = time length of the process segment $\sigma(t)$ from which the macroblock was obtained.

In this way, the life for each segment is calculated, resulting in a set of (j.99) random life values. By a statistical processing of this set, the FLDF is obtained (Fig. 4) and the result defined probabilistically.

Estimation of Hysteresis Energy to Fracture Under Conditions of Random Loading

It is evident from Fig. 3*b* that the total hysteresis energy to fracture under conditions of random loading is a random quantity (similar to the fatigue life), and it is necessary to determine its distribution function (DF) for the given type of random process.

The segmentation method applied in the FLDF calculation is also applicable to the calculation of the DF energy to fracture. The $\sigma(t)$ process processing by the segmentation method results in the set of (j.99) macroblocks with $\sigma_m = 0$. It is shown in Ref *5* that the energy to fracture under repeated loading by one macroblock of this kind can be substituted with satisfactory accuracy by the energy to fracture corresponding with the harmonic loading with $\sigma_{a\,max}$ maximum amplitude in the macroblock. The hysteresis energy to fracture under loading by one $\sigma(t)$ process realization represented by ith segment and/or ith macroblock is then determined according to the formula

$$W_{FR,i} = \Delta W_i N_{f,i} \tag{13}$$

while the energy per one cycle (with $\sigma_{a\,max}$ stress amplitude and plastic strain $\in_{ap\,max}$ amplitude) can be determined with satisfactory accuracy [*8*] according to

$$\Delta W_i = 3\sigma_{a\,max,i}\epsilon_{ap\,max,i} \tag{14}$$

considering Eqs 6 and 7, it takes the form

$$W_{\mathrm{FR},i} = \frac{3}{2} \frac{\epsilon_{\mathrm{f}}'}{\sigma_{\mathrm{f}}'^{(c+1)/b}} \sigma_{\mathrm{amax},i}^{(b+c+1)/b} \tag{15}$$

For j realizations, i.e., for j segments of the $\sigma(t)$ process (taking the scatter in material properties into consideration), this procedure ensures obtaining the set of values $\sigma_{\mathrm{a\,max},i}$ (for $i = 1$ up to $j.99$) and employing Eq 15 to obtain the set of corresponding values of energies to fracture. It is then possible to calculate the DF from this set, thus determining for the given $\sigma(t)$ process the energy to fracture, $W_{\mathrm{FR}}^{(P\%)}$, for the required probability of occurrence.

Procedure of Residual Fatigue Life Calculation

Regarding the random nature of both t_{f} fatigue life and W_{FR} energy to fracture, the $t_{j,\mathrm{res}}$ (Fig. 1) residual life is the random quantity as well, and Eq 5 will take the following form

$$t_{j,\mathrm{res}}^{(P\%)} = t_{\mathrm{f},j}^{(P\%)} \left[1 - \sum_{i=1}^{i=j} \frac{t_i}{t_{\mathrm{f},i}^{(P\%)}} \frac{W_{\mathrm{FR},i}^{(P\%)}}{W_{\mathrm{FR},j}^{(P\%)}} \right] \tag{16}$$

The variables denoted with $(P\%)$ express the values for $P\%$ occurrence probability. When evaluating the life according to Eq 16 for loading 1 to j by random processes, it is necessary to carry out calculations step by step so that the residual life is calculated gradually for each level up to the searched-for $t_{j,\mathrm{res}}^{(P\%)}$ life. The reason for this procedure lies in the possibility of finding out whether at the given order of acting random processes the fatigue life is already exhausted at a certain i level, i.e., earlier than the initiation of the $\sigma(t)_j$ loading process (Fig. 1). The above procedure enables one to judge the acceptability of particular random processes in a given operation.

In the calculation employing Eq 5, $t_{i,\mathrm{res}}$ expresses the residual life value immediately after crossing from the $(i - 1)$ level to the ith level. However, it is more convenient to define the residual life at the i level after expiration of the required, t_i time of action. For this purpose Eq 5 is modified into the form of Eq 16 so that i varies from $i = 1$ up to $i = j$.

The total life to fatigue fracture t_{F} under acting 1 up to j regimes of random loading is

$$t_{\mathrm{F}}^{(P\%)} = \sum_{i=1}^{i=j} t_i + t_{j,\mathrm{res}}^{(P\%)} \tag{17}$$

Experiment

The procedure of residual life estimation has been verified on steel specimens 15 mm in diameter subjected to loading corresponding with the scheme in Fig. 5, employing an MTS computer-controlled fatigue testing machine under a stress-controlled loading mode. The obtained experimental results of residual life are presented in Table 1.

Characteristics of the Material Examined

Material constants, parameters of Eqs 6 and 7, were obtained by statistical processing of experimental dependencies (Fig. 6) $\sigma_{\mathrm{a}} = f(2N_{\mathrm{f}})$ when $\sigma_{\mathrm{a}} = \text{const.}$ and $\in_{\mathrm{ap}} = f(2N_{\mathrm{f}})$ under strain-controlled tests employing the linear regression method. The characteristics of the applied material are given in Table 1 and Fig. 9.

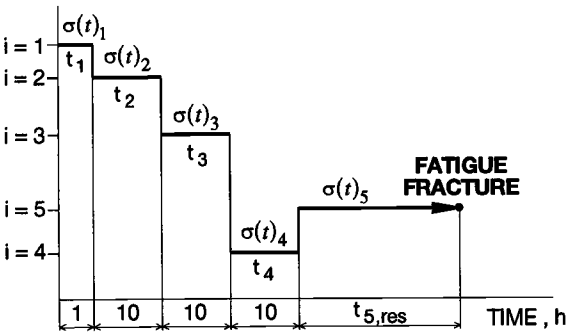

FIG. 5—*Scheme of loading by* $\sigma(t)_1 \ldots \sigma(t)_5$ *random processes (their characteristics are in Fig. 7).*

TABLE 1—*The characteristics of the test material and the result of fatigue life tests.*

Experimental residual fatigue life, h (see Fig. 5)					35.5; 42.9; 47.5; 55.5; 62.2; 82.3; 83.8		
Material parameters, regression line					$b = -0.05295$ $c = -0.52179$ $\sigma_f' = 592.34$ MPa $\epsilon_f' = 0.3448$		
	C	Cr	Ni	Mn	Si	P	S
Chemical analysis, in wt%	0.242	0.19	0.06	0.44	0.2	0.028	0.012

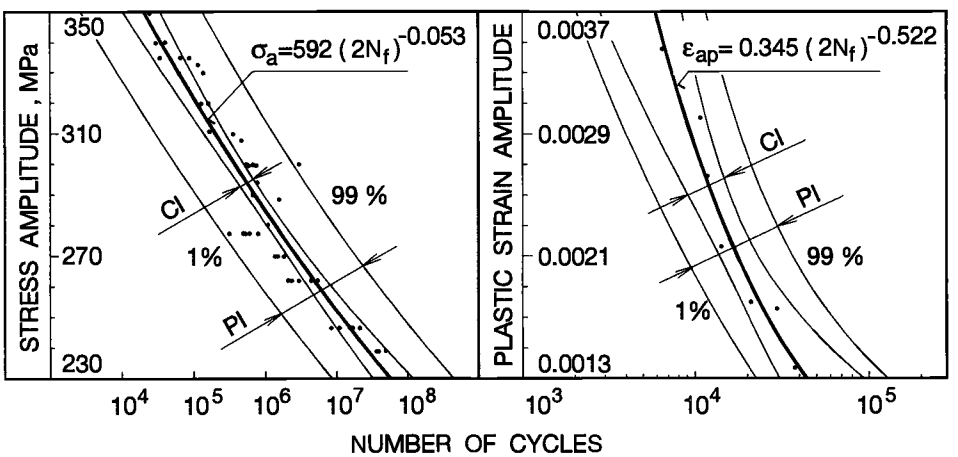

FIG. 6—*Experimental dependencies* $\sigma_a = f(2N_f)$ *and* $\in_{ap} = f(2N_f)$.

Characteristics of Applied Loading Processes

The $\sigma(t)_1 \ldots \sigma(t)_5$ processes were generated in the control computer of the pulsator, and for life calculation purposes their real courses at the output of the dynamometer of the test machine were recorded on a magnetic tape. The characteristics of proper processes evaluated for one representative segment are presented in Fig. 7. Such a $\sigma(t)$ segment exhibits a stationary course, and the σ_m, s_σ, PDF, and PSD are evaluated from the process centered to its mean value.

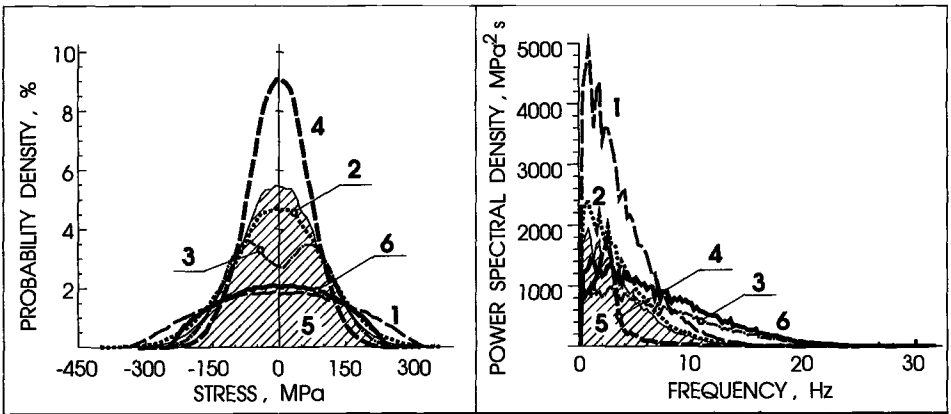

$\sigma(t)_i$	1	2	3	4	5	6
σ_m (MPa)	14.63	16.64	29.24	12.50	17.92	-22.9
s_σ (MPa)	144.19	104.14	96.46	68.21	92.13	113.84

FIG. 7—*Statistical characteristics of the applied random loading processes evaluated for one representative process segment.*

Actually, the whole process record needn't be stationary. By evaluation of these characteristics for each segment from the sufficiently long record of the $\sigma(t)$ process, a set of values (σ_m, s_σ, PDF, and PSD) can be obtained and the DF from these values calculated. It should be noted here that this procedure enables employment of the "segmentation of the process with overlapping" for the assessment of nonstationary process characteristics (random process parameters express a time function) in the form of distribution of its parameters.

Figure 8 represents the distribution of σ_m mean values and standard deviations, s_σ, calculated via the above-described procedure for $\sigma(t)_1 \ldots \sigma(t)_5$ processes. It is evident from the figure that the scatter of σ_m and s_σ in particular processes is small. It is therefore possible to treat them as stationary processes with the appropriate mean value of the whole process. It should be, however, emphasized that this is valid only in terms of engineering because these processes do not strictly meet the mathematical conditions for stationarity tests.

Estimation of the Distribution Function of $t_{5,res}^{(P\%)}$ Residual Life

To calculate the $t_{5,res}^{(P\%)}$ under loading according to Fig. 5, Eq 16 is applied, i.e., the FLDF and the DF of energy to fracture should be determined for the $\sigma(t)_1 \ldots \sigma(t)_5$ processes first.

FLDF Calculation for Loading by $\sigma(t)_i$ Processes

Processing of Material Characteristics—The experimental dependencies plotted in Fig. 6 were processed for 1 up to a 99% occurrence probability over the confidence interval of the regression line and over the prediction interval. The curves represented by Eqs 6 and 7 were put across the points corresponding with limits of confidence intervals, thus obtaining the set of 99 combinations of parameters (σ_f', b, $\in_f'$, and c). It is obvious here that σ_f' and b or $\in_f'$ and c are the random dependent variables because, in the set of curves, the $b(c)$ value is attributed to each σ_f' ($\in_f'$) value explicitly. Then the combinations (σ_f', b, $\in_f'$, c)$_i$ for $i = 1$ up

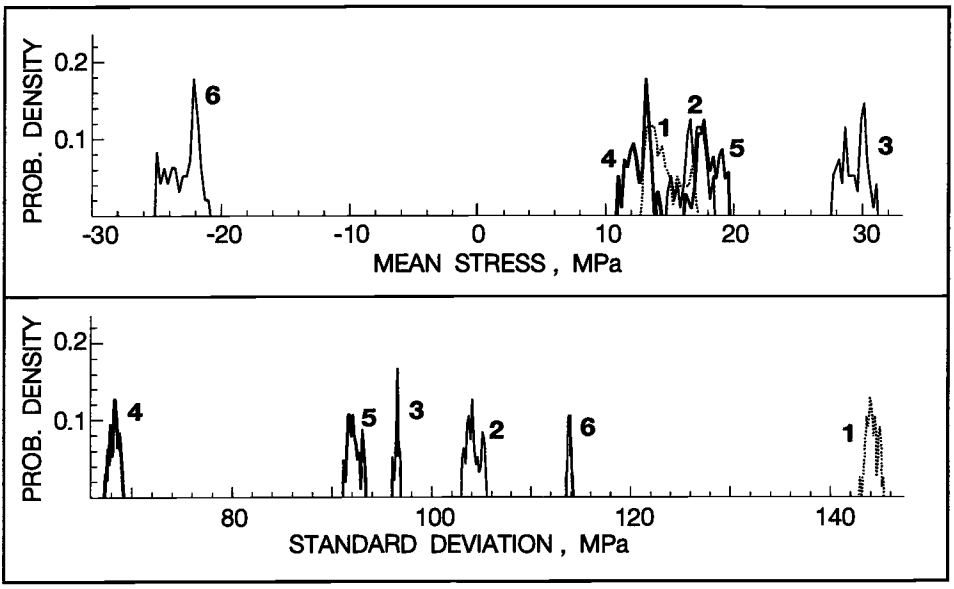

FIG. 8—*Functions of the mean stress and standard deviation of the* $\sigma(t)_i$ *probability density processes.*

to 99% were created so that the $\in_f'$, c values were allocated to the σ_f', b values for an identical percent of the confidence interval. The σ_f', b, or $\in_f'$, c values were obtained for the limits of the confidence interval with a correlation coefficient that always exceed 99%. The graphical representation of the described processing of material parameters is given in Fig. 9.

Processing of Loading Characteristics—The records of $\sigma(t)_1 \ldots \sigma(t)_5$ processes were, after spectral analysis, digitalized at the sample frequency of 256 Hz, resulting in the records of 614 000 ordinates in length (40 min). The processes were segmented at $\Delta = 95\%$ overlapping with the initial length of the segment $t_s = 3000$ of ordinates. At the segment length $t_s \equiv t_{s\,\min} = 140\,000$ of ordinates, the stabilized value of the calculated FLDF standard deviation was found out. The segment length of 170 000 of ordinates (11 min) was employed for the representative calculation of the FLDF for all processes. In this way the set of 53 segments has been obtained from the original record. Using the rain-flow method, 53 macroblocks were obtained from these 53 segments.

Calculation of $t_f^{(P\%)}$ *Life*—The effect of σ_m mean value was considered according to Eq 10, and the FDAH presented in Eq 8 was applied to calculate the life. The application of Eqs 8, 10, and 12 resulted in a set of 5247 lives after statistical processing in the obtained FLDF. The actual procedure for the FLDF calculation is shown in Fig. 10. Figure 11 shows the calculated DF lives for the individual processes. There are also the experimental results of life for the $\sigma(t)_2$ and $\sigma(t)_5$ processes.

Estimation of DF for Total Energy to Fracture under Loading by $\sigma(t)_i$ *Processes*

The procedure of DF calculation for total energy to fracture for particular processes is equal to that applied to FLDF calculation (Fig. 10) until the stage when the set of 5247 macroblocks transformed to $\sigma_m = 0$ is obtained. Then, using Eq 15, we proceed by

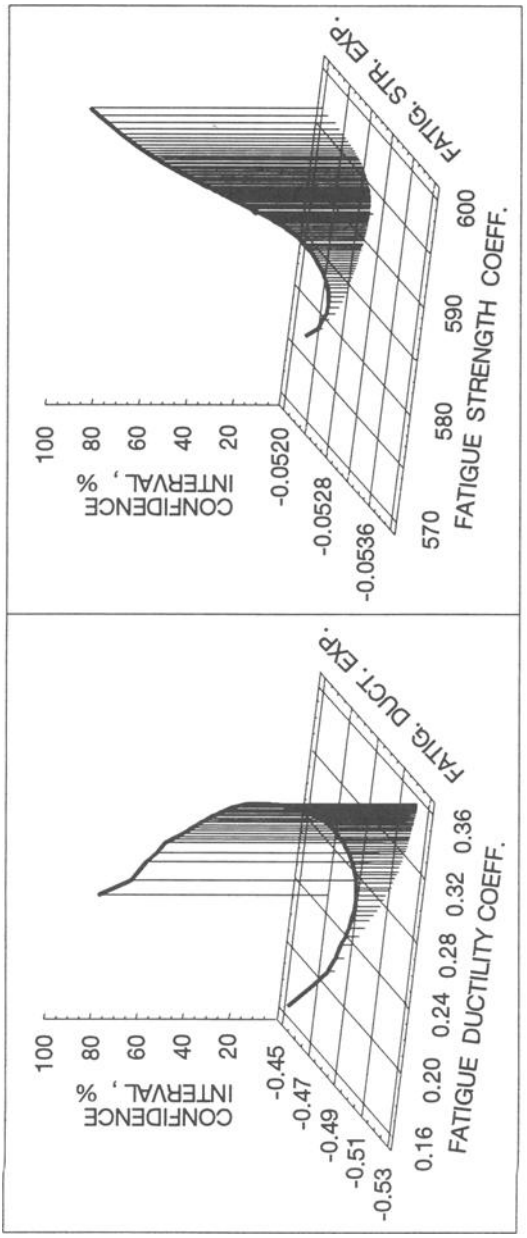

FIG. 9—*Graphical representation of the results of material parameters treatment for different probability occurrences.*

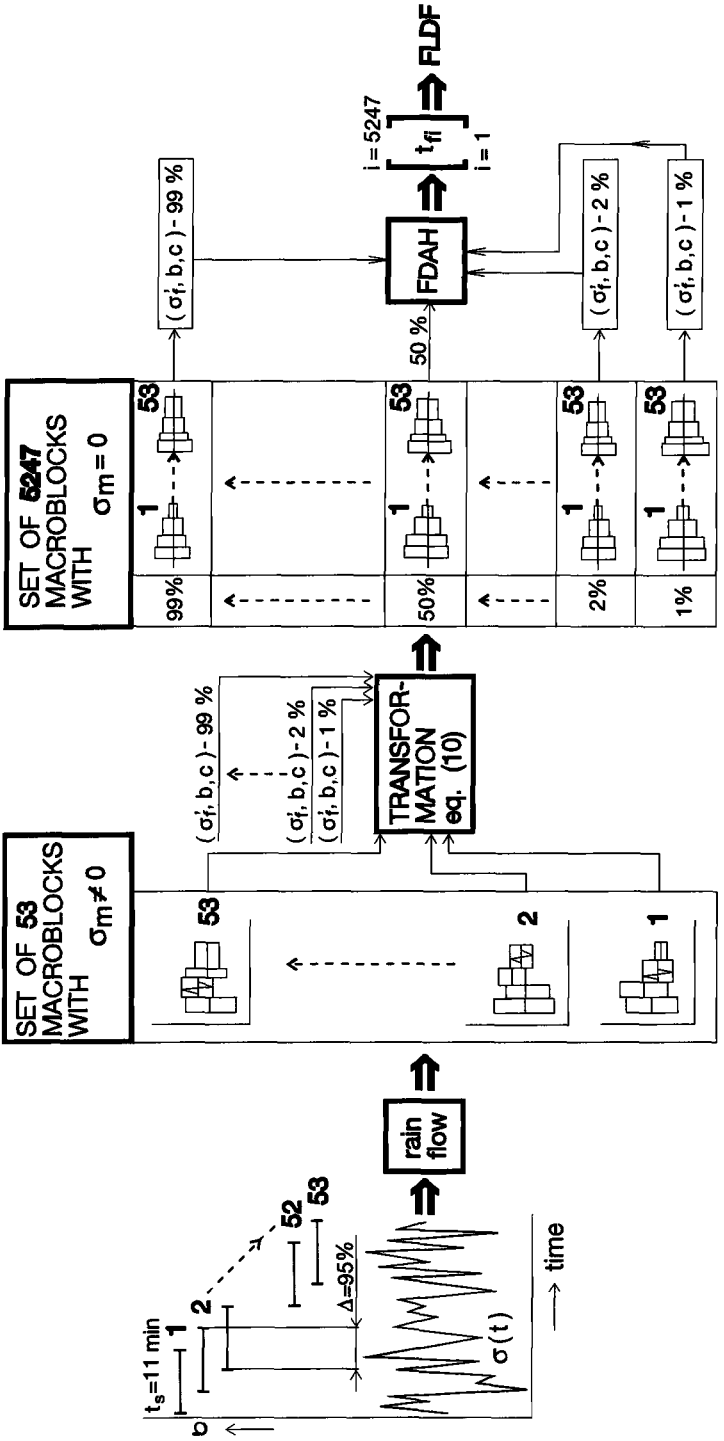

FIG. 10—*The actual procedure for the FLDF calculation.*

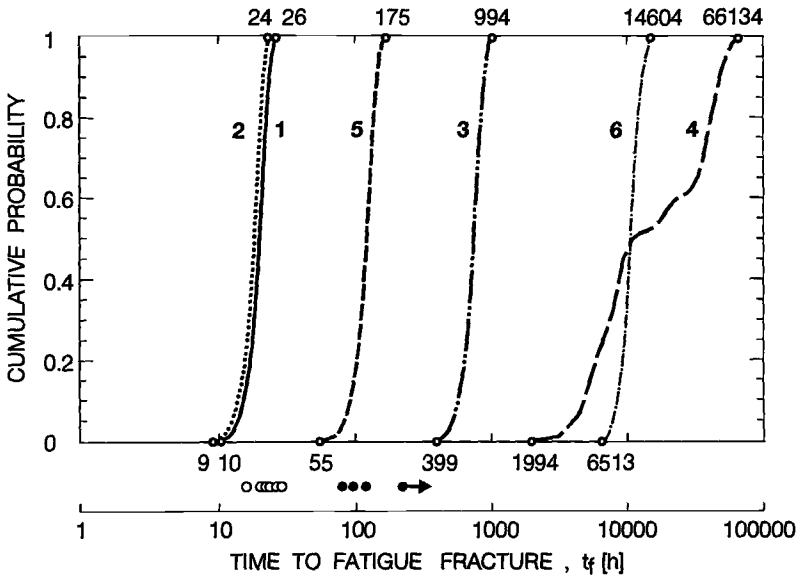

FIG. 11—*Calculated FLDFs for the* $\sigma(t)_i$ *random loading processes. Mean value: 1-19.2 h, 2-17.5 h, 3-721.7 h, 4-20 877 h, 5-116.5 h, 6-10 283 h. Standard deviation: 1-3.2 h, 2-2.8 h, 3-120.5 h, 4-17 514 h, 5-20.2 h, 6-1656 h. Experimental results under loading:* ● = $\sigma(t)_5$ *process;* ○ = $\sigma(t)_2$ *process.*

transformation of the set of 5247 maximum amplitudes obtained from the particular macroblocks into the set of 5247 energy to fracture values. After statistical processing, the required DF of energy to fracture is obtained. Figure 12 shows the calculated DFs of energy to fracture for the $\sigma(t)_1$ up to $\sigma(t)_5$ processes.

Comparison with Experiment and Analysis of Results

The DF of residual life $t_{5,res}$ calculated using Eq 16 together with obtained experimental results are shown in Fig. 13.

The calculation indicates that up to the occurrence probability value of $P = 4\%$ (for PI it is 25%), no $t_{5,res}$ life will really exist because the fatigue life is exhausted already at the $i = 2$ level (Fig. 5) during the action of the $\sigma(t)_2$ process. For example, considering 1% risk of greater damage at each level in comparison with calculation, $t_{1,res}^{(1\%)} = 10.5$ h and $t_{2,res}^{(1\%)} = -1.43$ h. The calculated -1.43 h value represents the residual life after 10 h acting of the $\sigma(t)_2$ process required and after acting of the $\sigma(t)_1$ process for 1 h. It means that exhaustion of fatigue life occurred 1.43 h prior to termination of the required 10 h action time. When we continue the calculation, $t_{3,res}^{(1\%)} = 370.28$ h; $t_{4,res}^{(1\%)} = 2159$ h, and $t_{5,res}^{(1\%)} = 25.39$ h. However, with respect to the fact that $t_{2,res}^{(1\%)} = -1.43$ h, the value of $t_{5,res}^{(1\%)} = 25.39$ h will not really exist. Consequently, the total life, considering 1% risk, will be according to Eq 17

$$t_F^{(1\%)} = (1 + 10) + (-1.43) = 9.57\,\text{h}$$

It also follows from this calculation that the $i = 2$ level is critical. By allowing the higher risk at this level ($P_2 = 5\%$ is sufficient, while for $i = 1$, 3, 4, and 5, $P = 1\%$), this level is overcome and the particular steps result in $t_{1,res}^{(1\%)} = 10.54$ h; $t_{2,res}^{(5\%)} = 0.438$ h; $t_{3,res}^{(1\%)} = 373.4$ h; $t_{4,res}^{(1\%)} = 2\,201.1$ h; and $t_{5,res}^{(1\%)} = 27.46$ h. However, the same result of $t_{5,res}^{(1\%)}$ can be obtained

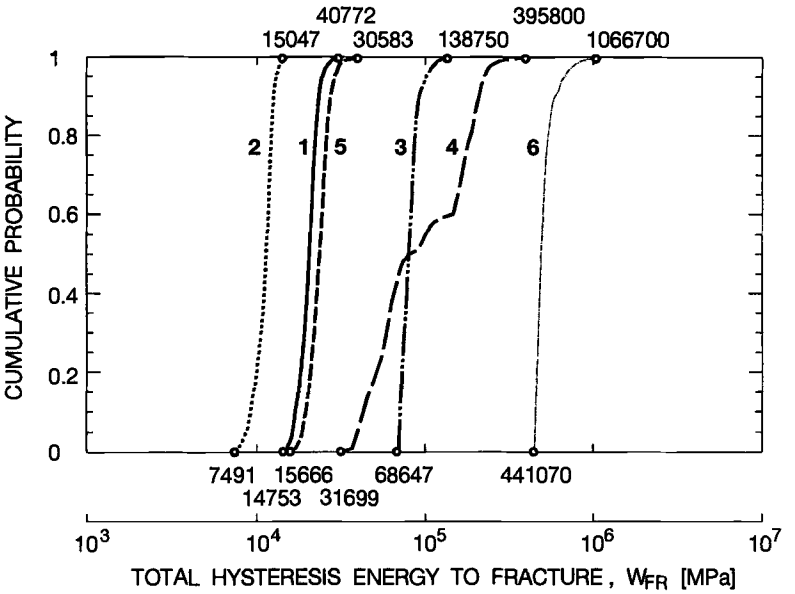

FIG. 12—*Distribution functions of total hysteresis energy to fracture for* $\sigma(t)_i$ *random loading processes. Mean value: 1-20 270 MPa, 2-11 097 MPa, 3-80 946 MPa, 4-110 030 MPa, 5-23 332 MPa, 6-508 950 MPa. Standard deviation: 1-2553 MPa, 2-1340 MPa, 3-10 785 MPa, 4-68 798 MPa, 5-3236 MPa, 6-86 325 MPa.*

by modified t_i time at particular levels, e.g., at $t_1 = 1$ h, $t_2 = 7$ h, $t_3 = 21$ h, $t_4 = 10$ h (at $P = 1\%$ at all levels) and the value of residual life will also be $t_{5,\text{res}}^{(1\%)} = 27.45$ h. Considering the risk above 4% (Fig. 13), the fatigue fracture, under acting $\sigma(t)_1 \ldots \sigma(t)_4$ processes, will not occur, and the residual life, $t_{5,\text{res}}$, is determined by the distribution function, $(KL)_c$, in Fig. 13.

This analysis also suggests the application of this theory to service fatigue life evaluation. This method easily and quickly verifies the suitability of the arbitrary service loading regime (or combinations of different operational loading regimes) with respect to the required fatigue life of structure. Such a situation can occur, e.g., in the case of considering employment of the structure in loading conditions different from those that were considered at the design stage. The above-mentioned analysis shows how to make eventual corrections in proposed loading in order to respect the requirement upon the service life of the structure (see the illustrative example based on the processes in Fig. 5).

Example of Application

The actual application of the presented method depends on the task formulation.

Example 1

The structure was designed for operation under conditions of service loading represented by the $\sigma(t)_4$ random process. The required service life is 1000 h at an allowed 5% probability of premature fatigue fracture occurrence. It is evident from the FLDF for the $\sigma(t)_4$ process in Fig. 11 and/or Fig. 14*A* that the life for $P = 5\%$ is 4100 h, i.e., the structure is

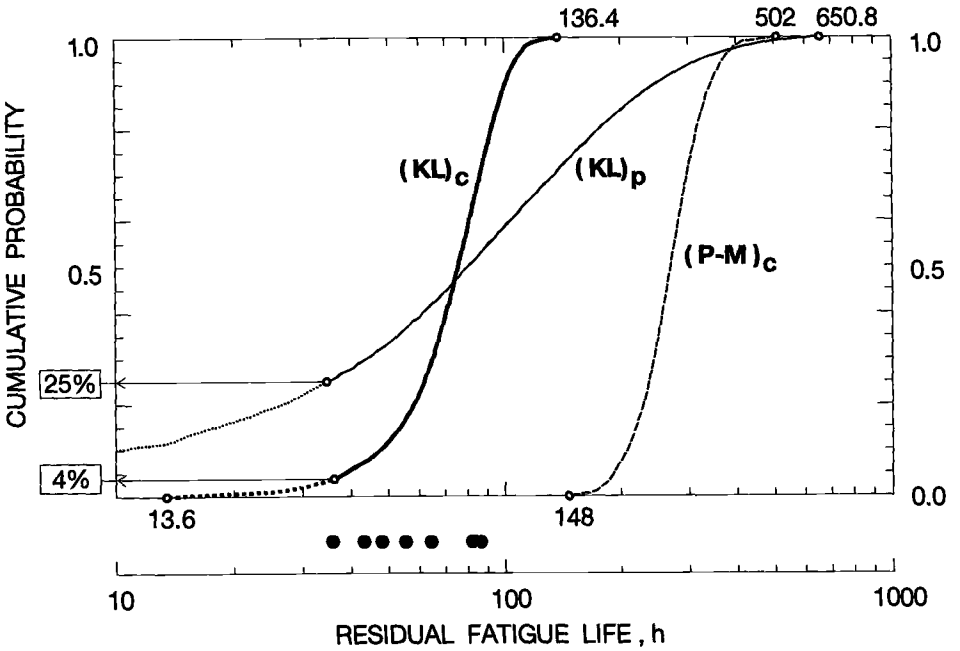

FIG. 13—*Distribution functions of residual life* $t_{5,res}$ *calculated for loading by* $\sigma(t)_i$ *processes according to scheme on Fig. 5. PM(KL)-DF calculated based on Palgren-Miner (Kliman [5]) FDAH. Mean value:* $(KL)_c = 73.8$ *h,* $(KL)_p = 101.3$ *h,* $(P\text{-}M)_c = 270.1$ *h. Standard deviation:* $(KL)_c = 21.5$ *h,* $(KL)_p = 113.2$ *h,* $(P\text{-}M)_c = 57$ *h;* ● *experimental life (Table 1);* c(p)*-for confidence (prediction) interval.*

designed with sufficient reserve with regard to the required life. However, it is necessary to judge this structure service by two users for loading during one day (cycle), as presented in Fig. 14*B* and to meet the original requirement for 1000 h total life at 5% risk of fracture occurrence.

In calculation, Eq 17 is applied for $P = 5\%$, and for the material constants due to CI of the regression line. It follows from the calculation that the total life at this loading is only $t_F^{(5\%)} = 56$ h. This would happen at the third cycle (3.c) at the second user (2.u) at the $i = 4$ level, while $t_{4,\text{res}}^{(5\%)} = -4.27$ h, i.e., at the moment of beginning of $\sigma(t)_2$ process action: (Point II). The result $t_{4,\text{res}}^{(5\%)} = -4.27$ h (at the third cycle) represents the residual life value under the condition of $\sigma(t)_2$ process acting at third cycle at the $i = 4$ level for 2 h, i.e., in Point III. Because the residual life is in absolute value higher than the time of action ($|-4.27| > 2$), the fatigue fracture would happen at the moment of beginning of the $\sigma(t)_2$ process action. It can be observed that at Point I at the $i = 3$ level (Fig. 14*B*) the residual life is at third cycle $t_{3,\text{res}}^{(5\%)} = 435.7$ h, and, at the same time, t_F, the residual life at the third cycle at Point II and at the $i = 4$ level, is $(t_{4,\text{res}}^{(5\%)} + 2\text{ h}) = -4.27 + 2 = -2.27$ h. Therefore, at repeated loading, the fracture should be classified at the moment of the beginning of the $\sigma(t)_2$ process action at the third cycle, i.e., at Point II. This situation varies with the amount of $P\%$, and the value $t_F = 56$ h is changed (i.e., at such $P\%$) when the condition $|t_{4,\text{res}}^{(P\%)}| < 2$ h is met. It is at the same time the explanation to the cases where the DFs of the total life in Fig. 14 exhibit shape showing the total life remaining unchanged with changing $P\%$. Because $t_F^{(5\%)} = 56\text{ h} < 1000$ h, the loading according to Fig. 14*B* is not acceptable.

Next we omit the operation mode at $i = 4$, i.e., the $\sigma(t)_2$ process, and the loading is

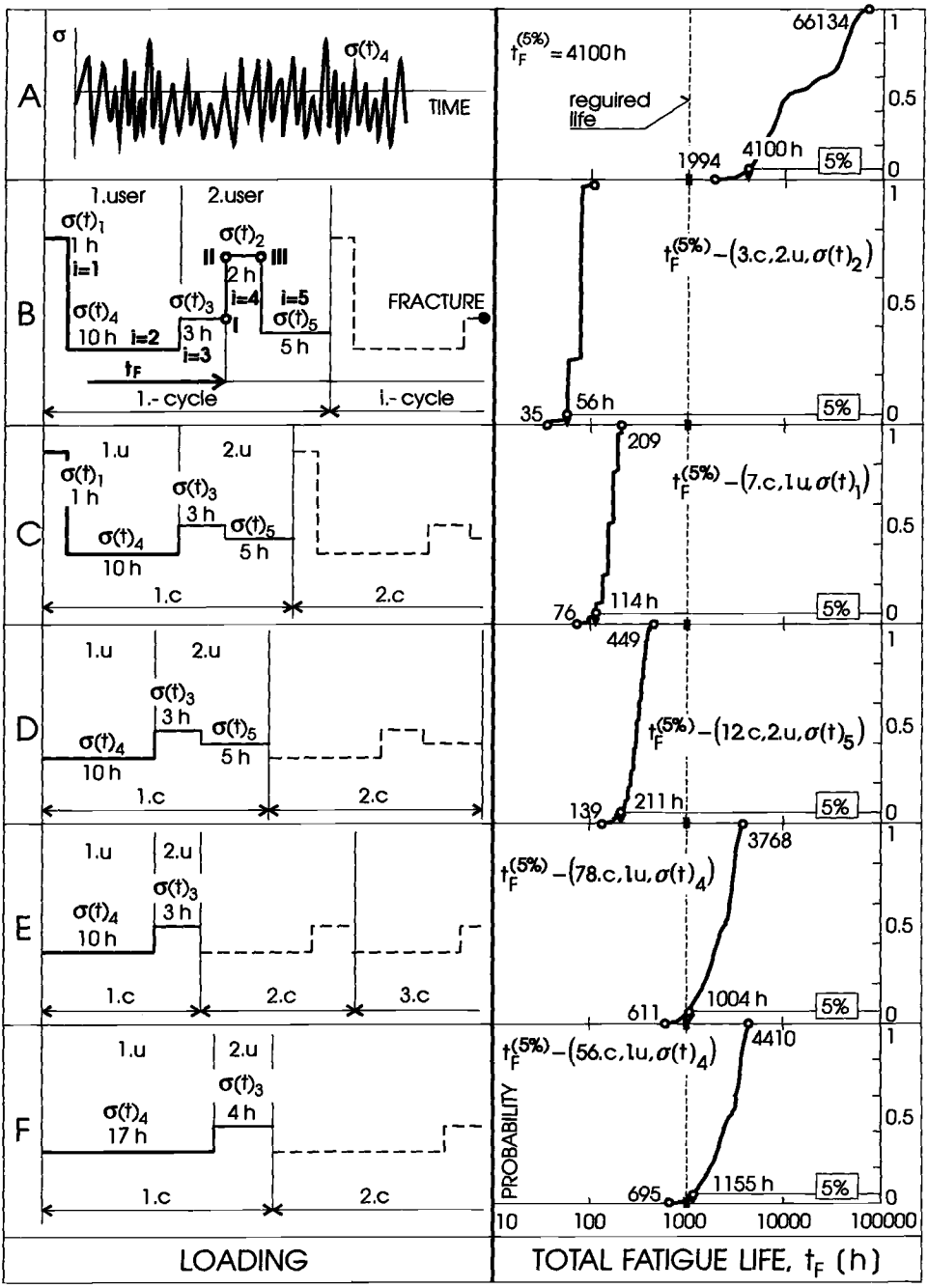

FIG. 14—*Example 1. Optimization of operational regimes with respect to the required life.*

changed to the scheme shown in Fig. 14*C*. As evident from the DF of total life, this loading does not meet the requirement of the total life $t_F^{(5\%)} = 1000$ h. In this case the mode at $i = 1$ represented by the $\sigma(t)_1$ process proved to be critical, showing $t_{1,res}^{(5\%)} = -1.7$ h at the seventh cycle.

Employing the identical procedure, i.e., the gradual omitting of "critical modes," it can be found out that only the case shown in Fig. 14*E* is acceptable. It means that, from originally five required modes in Fig. 14*B*, only the modes represented by the $\sigma(t)_4$ and $\sigma(t)_3$ processes are acceptable. An attempt to include the $\sigma(t)_5$ process for as short as 0.5 h to 2.user at $i = 3$ (Fig. 14*D*) failed because even for $P = 99\%$ at $i = 3$, the $t_F = 647.5$ h $<$ 1000 h.

In order to keep the utilization of the structure for 21 h per day, once again employing Eq 17, we find it possible to prolong the $\sigma(t)_4$ mode from 10 to 17 h; however, the $\sigma(t)_3$ mode is prolonged from only 3 to 4 h (Fig. 14*F*).

Example 2

Another example may be represented by the evaluation of the effect of loading nonstationarities or the so-called inhomogeneities in the loading process. In Fig. 15 the various waveform of the mean value is simulated, and the DF of lives of particular processes are compared. The FLDFs were calculated by considering PI when processing the material characteristics. It is evident from Fig. 15 that the effect of "nonstationarities" can be expressed by the change of probability of failure occurrence in relation to the required life value and that the presented method reflects their occurrence with sufficient sensitivity.

For instance, comparing the FLDFs shown in Figs. 15/1 and 15/5, one can conclude that the mean value loading nonstationarity in the $\sigma(t)_5$ process has practically no influence on resulting fatigue life when the period of its repetition is larger than 11A (probabilities of fatigue failure are practically the same).

In this way it is possible to assess the majority of nonstationarities occurring in real practice.

Discussion and Conclusions

Based on the compared theoretical and experimental results either in Fig. 11 or Fig. 13, it can be stated that the presented method of life estimation based on the probability approach offers good results. From a practical point of view, it is important that the DF of the life is calculated in the interval of physically possible values, i.e., there are maximum and minimum values of the set. In other words, it is possible to determine the life also for zero probability of failure, which is impossible to estimate by means of theoretical distributions. It depends on the designer or the user as to which risk of premature fracture initiation is acceptable in relation to reliable and safe service. For practical applications the DF calculated for PI should also be considered because the material properties at the critical point of the structure (notch root) can actually be represented by an arbitrary experimental point in PI.

The calculation results and thus agreement with the experiment are affected by many factors. The most important factors include the following.

Material Characteristics and Loading Mode

The following criteria should be fulfilled:

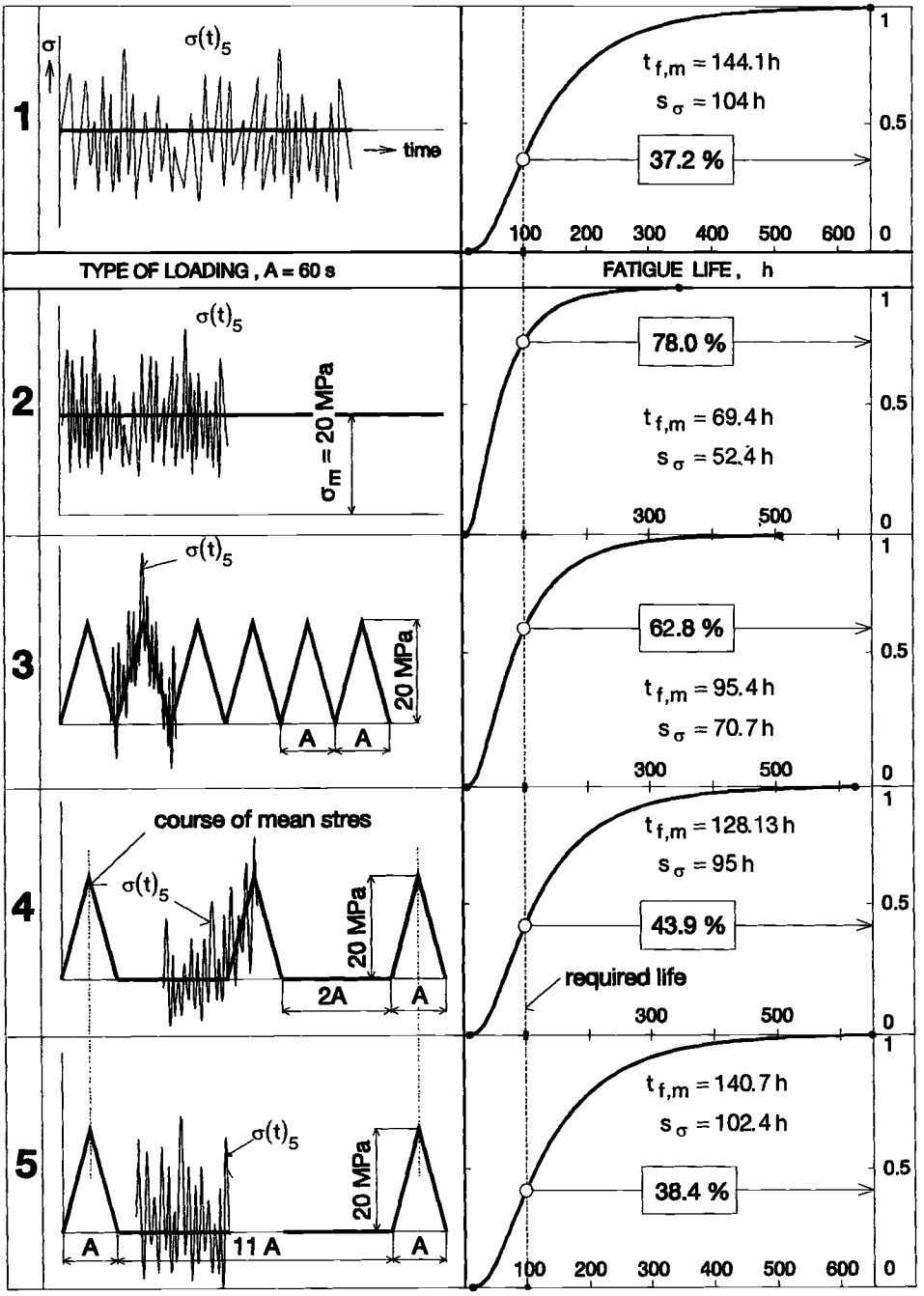

FIG. 15—*Example 2. Comparison of different loading conditions in terms of failure probability.*

1. When determining the experimental points of the dependence $\sigma_a(\in_{ap}) = f(2N_f)$, it is necessary to stop the experiment when the fatigue crack on the specimen achieves the length corresponding with the component life definition. In our case this occurs when the crack is of 1 to 2 mm in length on the specimen surface (circular specimens).
2. A sufficient number of experimental points is required (Fig. 6), and these should be uniformly distributed.
3. It is necessary to follow the mode of test control. This means that if the service process shows the nature with controlled force, then the material parameters should be obtained at this loading mode as well. If the service loading shows the nature with controlled strain, then the tests should be carried out at the mode with constant strain amplitude. Such a case can also arise when the loading process is recorded in the form $\epsilon(t)$, but obtained in the mode with controlled force. Reference *1* describes the procedure for FLDF estimation at the $\in(t)$ process, and it can also be employed for calculating the DF of residual life.

FDAH and Effect of Amplitudes Below Fatigue Limit

The results presented in Fig. 13 prove undoubtedly that the DF of residual life, $(KL)_C$, calculated on the basis of FDAH according to Eq 8 shows better correlation with experimental results than the DF calculated by the Palmgren-Miner hypothesis. Modification of Eq 8 to the form suitable for the $\in(t)$ process is given in Ref *5*.

Various considerations concerning σ_{ai} amplitudes below the fatigue limit σ_C really exist, e.g., Heuler [*9*] moves the limit of damage to 0.5 σ_C for certain cases, and in Ref *1* it is even 0.8 σ_C based on considerations of safe energy. The omitable difference between the life considering all amplitudes below σ_C and the life considering amplitudes only up to 0.8 σ_C is also outlined. The specimens were loaded by the Gaussian process with peaks of approximately 300 MPa ($\sigma_C \approx 236$ MPa), i.e., it was the case of loading with a considerably large portion of $\sigma_{ai} < \sigma_C$. Taking this into consideration we have included in the calculations all amplitudes in the macroblock, i.e., also $\sigma_{ai} < \sigma_C$. In calculations according to Eqs 8 through 12 and Eq 15, these had allocated the parameters of life curves, Eqs 6 and 7, which were prolonged below the fatigue limit. In log-log coordinates it is a line prolonged (extended) up to the zero value of the amplitude. Such a procedure leads the calculation to the right side.

Effect of Mean Stress

The method of σ_m consideration can significantly affect the results of life calculations. In our calculations, the concept by Morrow [*6*] modified into the form of Eq 10 has been accepted. Though this form includes the material parameters (σ'_f, b, c), it seems to be convenient to apply it in the following form

$$\sigma_{am} = \sigma_a \left(1 - \frac{K\sigma_m}{\sigma'_f}\right)^{(c+1)/(b+c+1)} \tag{18}$$

where the constant K would consider the individual sensitivity of material to σ_m. It was documented in the results in Fig. 16 where DFs of the residual life are calculated for loading according to Fig. 5. Equation 18 was applied in calculation for different K values. For the purpose of better visual comparison, the experimental points were approximated (despite low numbers) by theoretical DF for log-normal distribution. It is evident from Fig. 16 that the estimated DF of residual life for the material constant $K = 1.3$ nearly ideally corresponds with the experimental DF. It should be noted, however, that this result should be

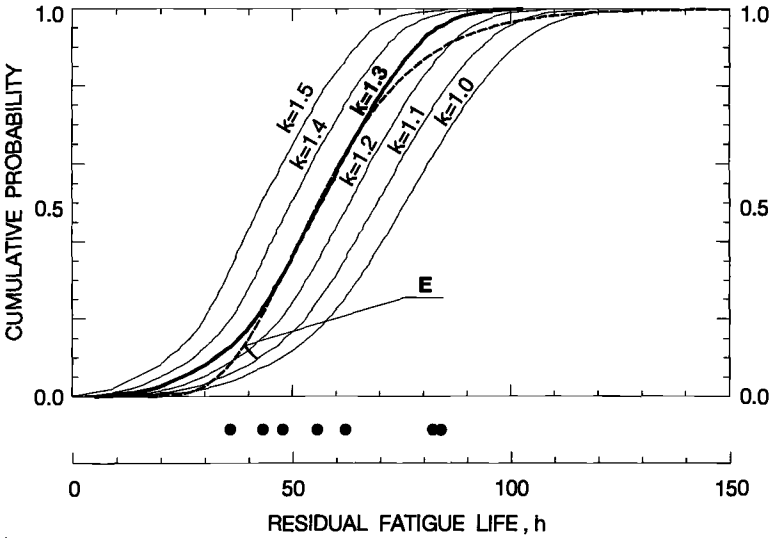

FIG. 16—*Residual fatigue life (loading according to Fig. 5) calculated for different* K *values in Eq 18. E = experimental DF.*

validated by the experimentally verified relation (Eq 18) under loading with σ_a = const. for various σ_m values.

References

[1] Kliman, V., "Prediction of the Random Load Fatigue Life Distribution," *Fatigue Design,* ESIS 16, J. Solin, G. Marquis, A. Siljander, and S. Sipilä, Eds., Mechanical Engineering Publications, London, 1993, pp. 241–255.

[2] Halford, G. R., "The Energy Required for Fatigue," *Journal of Material,* Vol. 1, No. 1, 1966, pp. 3–18.

[3] Hong, N., "A Modified Rainflow Counting Method," *International Journal of Fatigue,* Vol. 13, 1991, pp. 465–469.

[4] Downing, S. D. and Socie, D. F., "Simple Rainflow Counting Algorithms," *International Journal of Fatigue,* Vol. 4, No. 1, 1982, pp. 31–40.

[5] Kliman, V., "Fatigue Life Prediction for a Material under Programmable Loading Using the Cyclic Stress-Strain Properties," *Materials Science and Engineering,* Vol. 68, 1984, pp. 1–10.

[6] Morrow, J. D., "Fatigue Properties of Metals," *Fatigue Design Handbook,* Section 3.2, Society of Automotive Engineers, Lancaster, PA.

[7] Nihei, M., Heuler, P., Boller, C., and Seeger, T., "Evaluation of Mean Stress Effect on Fatigue Life by Use of Damage Parameters," *International Journal of Fatigue,* Vol. 8, 1986, pp. 119–126.

[8] Kliman, V. and Bílý, M., "Hysteresis Energy of Cyclic Loading," *Materials Science and Engineering,* Vol. 68, 1984, pp. 11–18.

[9] Heuler, P., "A Criterion for Omission of Variable Amplitude Loading Histories," *International Journal of Fatigue,* Vol. 8, No. 4, 1986, pp. 225–230.

Sreeramesh Kalluri,[1] *Gary R. Halford,*[2] *and Michael A. McGaw*[2]

Prestraining and Its Influence on Subsequent Fatigue Life

REFERENCE: Kalluri, S., Halford, G. R., and McGaw, M. A., **"Prestraining and Its Influence on Subsequent Fatigue Life,"** *Advances in Fatigue Lifetime Predictive Techniques: 3rd Volume, ASTM STP 1292,* M. R. Mitchell and R. W. Landgraf, Eds., American Society for Testing and Materials, 1996, pp. 328–341.

ABSTRACT: An experimental program was conducted to study the damaging effects of tensile and compressive prestrains on the fatigue life of nickel-base, Inconel 718 superalloy at room temperature. To establish baseline fatigue behavior, virgin specimens with a solid uniform gage section were fatigued to failure under fully reversed strain control. Additional specimens were prestrained to 2, 5, and 10% (engineering strains) in the tensile direction and to 2% (engineering strain) in the compressive direction under stroke control and were subsequently fatigued to failure under fully reversed strain control. Experimental results are compared with estimates of remaining fatigue lives (after prestraining) using three life prediction approaches: (1) the linear damage rule (LDR), (2) the linear strain and life fraction rule (LSLFR), and (3) the nonlinear damage curve approach (DCA). The Smith-Watson-Topper parameter was used to estimate fatigue lives in the presence of mean stresses. Among the cumulative damage rules investigated, the best remaining fatigue life predictions were obtained with the nonlinear damage curve approach.

KEYWORDS: prestraining, metal fatigue, cumulative fatigue damage, mean stress, life prediction, nickel-base superalloy

Nomenclature

a_1, a_2	Exponents in the Smith-Watson-Topper parameter-life relation
b, c	Exponents of axial elastic and inelastic strain range-life relations
e_t	Total prestrain
e_{in}	Inelastic strain offset after prestraining
n_1	Number of applied cycles at the first load level in a two-load-level fatigue test
n_2	Number of remaining cycles at the second load level in a two-load-level fatigue test
A_1, A_2	Coefficients in the Smith-Watson-Topper parameter-life relation
B, C	Coefficients of axial elastic and inelastic strain range-life relations
E	Elastic modulus
N_1	Fatigue life at the first load level in a two-load-level fatigue test
N_2	Fatigue life at the second load level in a two-load-level fatigue test
N_f	Cycles to failure
%RA	Percent reduction in area in a tensile test
Δ	Denotes range of the variable

[1]Senior research engineer, NYMA, Inc., NASA Lewis Research Center, 21000 Brookpark Rd, Mail Stop: 49-7, Cleveland, OH 44135.

[2]Senior scientific technologist and senior research engineer, respectively, NASA Lewis Research Center, 21000 Brookpark Rd, Mail Stop: 49-7, Cleveland, OH 44135. Dr. McGaw is presently at McGaw Technology, Inc., P.O. Box 26268, Fairview Park, OH 44126.

ϵ_e, ϵ_{in} Elastic and inelastic strain amplitudes
$\epsilon_{in,P}$ True inelastic strain offset after prestraining, $\ln(1 + e_{in})$
ϵ_f Ductility or true fracture strain in a tensile test, $-\ln(1 - \%RA/100)$
ϵ_t Total strain amplitude
ν Frequency
σ Stress amplitude, $(\sigma_{max} - \sigma_{min})/2$
σ_m Mean stress, $(\sigma_{max} + \sigma_{min})/2$
σ_{max} Maximum stress in a cycle
σ_{min} Minimum stress in a cycle
σ_y 0.2% offset axial yield strength
σ_u Ultimate tensile strength

Engineering components are commonly subjected to prestraining due to manufacturing processes (forming operations, straightening, etc.), unintentional overstrains (misuse, accidents, under designs, etc.), and intentional overstrains (proof testing or autofrettage). All prestraining operations can potentially damage an engineering component due to surface roughening and microcracking and thus reduce the subsequent fatigue life of the component during actual service. However, prestraining operations can be beneficial to the component and increase its subsequent fatigue life because of cold working (or hardening) within the critical regions of the component and the generation of residual stresses with a sign opposite to that of service loading. For accurate fatigue life estimation of engineering components, the damaging and beneficial effects of prestraining should be properly considered by the fatigue life prediction models.

The influence of prestraining on the fatigue behavior of the nickel-base superalloy, Inconel 718 (IN 718), was investigated by conducting fatigue tests at ambient laboratory conditions. Inconel 718 is used extensively as a structural material in the aerospace and power generation industries [*1–4*]. The baseline fatigue behavior of IN 718 was determined by performing strain-controlled fatigue tests. Fatigue tests were subsequently conducted on specimens prestrained either in tension or compression. In all the prestrained tests, development of significant mean stresses was observed. The fatigue lives of the prestrained specimens were estimated with three cumulative damage approaches, both with and without consideration of the effect of mean stress on fatigue life. For each of the six sets of life predictions, the estimated fatigue lives of the prestrained specimens were compared with those observed in the experiments.

Experimental Details

Material and Specimens

Wrought bars of IN 718 (Aerospace Material Specification 5663D) with a diameter of 31.8 mm were purchased from the vendor. The composition of the superalloy is shown in Table 1. The following heat treatment was given to the superalloy by the manufacturer: (1) solution annealing at 954°C for 1 h and water quenching, (2) aging at 718°C for 8 h followed by furnace cooling to 621°C, and (3) aging at 621°C for 10 h. The as-received material contained equiaxed grains with an average grain size of 10 μm. The microstructure and the different phases observed in the as-received material were previously reported [*5*]. IN 718 derives its strength mainly from an intermetallic phase, γ'', which precipitates coherently in the face-centered-cubic matrix with a volume fraction of about 15 to 20% [*6–8*]. Two other intermetallic phases commonly observed in IN 718 are γ' ($\approx$ 4% volume fraction) and δ [*6–9*]. The γ' phase is also a coherent phase and contributes to the strength of IN 718 [*8*].

TABLE 1—*Composition of Inconel 718.*

Element	Weight, %
S	0.002
B	0.004
P	0.006
C	0.034
Cu	0.05
Si	0.07
Mn	0.12
Co	0.39
Al	0.57
Ti	0.95
Mo	2.87
Nb+Ta	5.19
Cr	17.52
Ni	53.58
Fe	Balance

Solid, uniform gage section specimens with a diameter of 6.3 mm were manufactured from the IN 718 bars. All the specimens were polished, with the final polishing marks in the longitudinal direction. The following average room temperature tensile properties were exhibited by the as-received IN 718: (1) σ_y, 1140 MPa; (2) σ_u, 1410 MPa; and (3) %RA, 43.3 (or ϵ_f, 0.567). At room temperature, IN 718 has high strength as well as moderate ductility, and both properties contribute to the fatigue resistance of the alloy.

Test System and Procedures

All the specimens were tested at room temperature under ambient laboratory conditions. The test system consisted of a computer-controlled [*10*], servohydraulic test frame and an axial extensometer with a gage length of 12.7 mm. Baseline fatigue tests were conducted under total axial strain control. Fully reversed sinusoidal waveforms with frequencies ranging from 0.1 Hz (at higher strain ranges) to 1.0 Hz (at lower strain ranges) were used in these tests. In the baseline tests, before applying the full amplitude of the strain, a small fully reversed elastic strain cycle ($\Delta\epsilon_t$ = 0.25%) was used to obtain the elastic modulus of IN 718. The full amplitude strain was then applied beginning with the tensile direction. Cyclic data in the baseline fatigue tests were acquired at logarithmic intervals, and fatigue tests were continued until each specimen separated into two pieces.

Fully reversed fatigue tests were also conducted on specimens prestrained either in tension (to 2, 5, or 10%) or in compression (to 2%). Only the lowest prestrain level was used in compression to avoid buckling, which is possible (and was observed) at the higher magnitude prestrains in compression. Each specimen was prestrained under stroke control with a limit imposed on the strain. After reaching the required strain limit, the specimen was unloaded to zero load under stroke control and the extensometer was removed and remounted on the specimen. Before starting the fatigue portion of the test, the extensometer was zeroed to reestablish the gage length. In all the tests on prestrained specimens, cross-sectional areas of the specimens after prestraining were used to calculate stresses during the subsequent fatigue portions of the tests. Similar to the baseline fatigue tests, for all the prestrained specimens, the fatigue portion of the test was always initiated in the tensile direction. The cyclic data acquisition scheme and failure definition in these tests were the same as those employed in the baseline tests.

Fatigue Behavior

Baseline Tests

The baseline fatigue data of IN 718 obtained from the near half-life hysteresis loops are shown in Table 2. The average value of the elastic modulus, obtained from the initial elastic strain cycle data of the baseline tests, for IN 718 is 216 GPa. The total strain range in each test was separated into elastic and inelastic strain ranges by using elastic modulus and the stress range (Eq 1).

$$\begin{aligned} \Delta\epsilon_t &= \Delta\epsilon_e + \Delta\epsilon_{in} \\ \Delta\epsilon_e &= \Delta\sigma/E \\ \Delta\epsilon_{in} &= \Delta\epsilon_t - \Delta\sigma/E \end{aligned} \tag{1}$$

In all the baseline fatigue tests, IN 718 developed compressive mean stresses. However, magnitudes of these mean stresses were relatively small in comparison to the stress ranges in the baseline tests (Table 2). After the second cycle, cyclic softening was observed at all strain ranges in the baseline fatigue tests. Softening continued until failure in all the IN 718 specimens [*11*]. The observed cyclic softening was due to "mechanical scrambling" of γ'' precipitates by dislocations in the deformation bands [*5*]. Serrated flow was observed in the inelastic regions of the hysteresis loops in the high-strain range tests. The observed serrated flow in IN 718 was attributed to a repetitive mechanism in which dislocations that initially piled up at the grain boundaries were relieved by the onset of plastic flow in the neighboring grains or twins [*12*].

Basquin [*13*] and Manson-Coffin [*14,15*] types of elastic and inelastic strain range versus fatigue life relations were computed by treating the logarithms of $\Delta\epsilon_e$ and $\Delta\epsilon_{in}$, respectively, as independent variables and the logarithm of N_f as the dependent variable (Eq 2). The total strain range versus fatigue life relation was obtained by adding the elastic and inelastic life relations (Eq 3).

$$\begin{aligned} \Delta\epsilon_e &= B(N_f)^b = 0.0146\,(N_f)^{-0.0547} \\ \Delta\epsilon_{in} &= C(N_f)^c = 1.30\,(N_f)^{-0.629} \end{aligned} \tag{2}$$

$$\Delta\epsilon_t = 0.0146\,(N_f)^{-0.0547} + 1.30\,(N_f)^{-0.629} \tag{3}$$

TABLE 2—*Baseline Inconel 718 fatigue data.*

Specimen Number	ν, Hz	$\Delta\sigma$, MPa	σ_m, MPa	$\Delta\epsilon_e$, %	$\Delta\epsilon_{in}$, %	$\Delta\epsilon_t$, %	N_f
IN31	0.1	2168	−20	1.005	1.225	2.230	1 227
IN35	0.1	2122	−23	0.984	1.148	2.132	1 700
IN34	0.1	2049	−32	0.950	0.882	1.832	3 115
IN33	0.1	2000	−29	0.927	0.690	1.617	4 208
IN32	0.1	1888	−32	0.875	0.528	1.403	7 845
IN29	0.1	1888	−28	0.875	0.398	1.273	11 686
IN26	0.2	1830	−8	0.848	0.277	1.125	16 040
IN28	0.2	1757	−43	0.815	0.205	1.020	34 483
IN24	1.0	1680	−53	0.779	0.105	0.884	95 430
IN23	1.0	1627	−14	0.754	0.036	0.790	363 452

The elastic, inelastic, and total strain range versus fatigue life relations are shown in Fig. 1. The slope of the elastic life line for IN 718 (-0.0547) is very shallow when compared to that exhibited by most engineering alloys (-0.12). The fatigue life relation from the baseline tests was used to evaluate the influence of prestraining on the fatigue behavior of IN 718.

Tests on Prestrained Specimens

The prestrains imposed on the IN 718 specimens and data from the fatigue portions of the tests, obtained from near half-life hysteresis loops, are shown in Table 3. As in the case of the baseline tests, the total strain range was separated into elastic and inelastic parts by using Eq 1. All the prestrained specimens developed significant mean stresses. In general, near half-life, the specimens prestrained in tension exhibited tensile mean stresses, and the specimens prestrained in compression developed compressive mean stresses with a few exceptions. In all tests on prestrained specimens, the mean stresses persisted until failure of the specimens [*11*].

Fatigue data on the prestrained specimens and the baseline fatigue life relation are plotted in Fig. 2. Prestraining has a detrimental effect on the fatigue life of IN 718 with a few exceptions. The detrimental effect of prestraining is larger at the lowest strain range tested and progressively decreases at higher strain ranges. At the lowest strain range, tensile prestraining reduced the life substantially, whereas compressive prestraining did not significantly influence fatigue life. Since specimens prestrained in tension and compression developed different mean stresses, some of the observed differences in fatigue lives might be due to mean stress effects. The role of mean stress on fatigue life of Inconel 718 is addressed later in the paper.

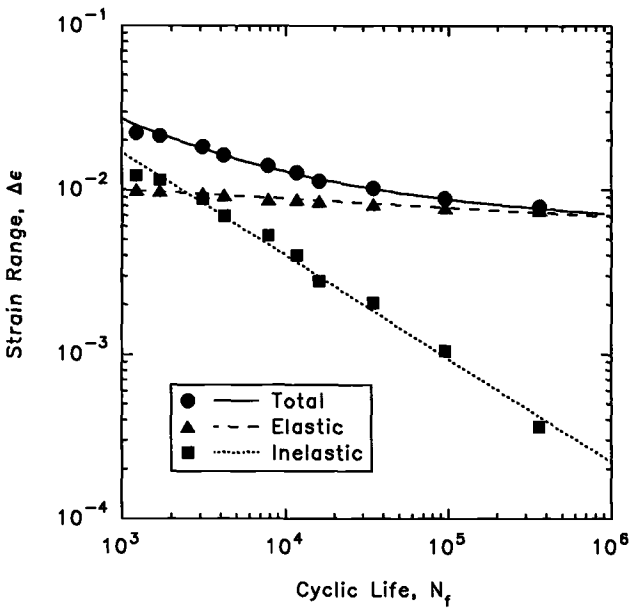

FIG. 1—*Baseline fatigue life relations for Inconel 718 superalloy.*

TABLE 3—*Inconel 718 fatigue data on prestrained specimens.*

Specimen Number	Prestrain		Fatigue						
	e_t, %	e_{in}, %	ν, Hz	$\Delta\sigma$, MPa	σ_m, MPa	$\Delta\epsilon_e$, %	$\Delta\epsilon_{in}$, %	$\Delta\epsilon_t$, %	N_f
IN43	10.01	9.111	0.1	2299	74	1.066	0.969	2.035	1 321
IN44	5.011	4.252	0.1	2308	48	1.070	0.945	2.015	1 303
IN45	2.017	1.427	0.1	2111	−9	0.979	1.037	2.016	1 776
IN52	−2.017	−1.415	0.1	2073	−53	0.961	1.096	2.057	1 632
IN39	10.01	9.209	0.1	2031	−148	0.942	0.315	1.257	14 648
IN46	10.03	9.190	0.1	2042	175	0.947	0.313	1.260	5 984
IN40	5.011	4.264	0.1	2038	72	0.945	0.340	1.285	5 644
IN41	2.011	1.379	0.1	2014	73	0.934	0.358	1.292	5 969
IN51	−1.998	−1.434	0.1	1958	−94	0.908	0.392	1.300	4 578
IN36	10.03	9.087	1.0	1427	−147	0.662	0.099	0.761	75 027
IN47	10.03	9.166	1.0	1497	93	0.694	0.082	0.776	35 145
IN37	5.029	4.222	1.0	1493	133	0.692	0.083	0.775	30 752
IN20	5.005	4.205	1.0	1452	540	0.673	0.077	0.750	20 273
IN38	2.004	1.403	1.0	1554	100	0.720	0.063	0.783	34 684
IN21	2.014	1.379	1.0	1470	274	0.682	0.052	0.734	29 600
IN50	−2.023	−1.397	1.0	1508	−217	0.699	0.077	0.776	252 363
IN59	−2.017	−1.415	1.0	1518	−427	0.704	0.071	0.775	424 538

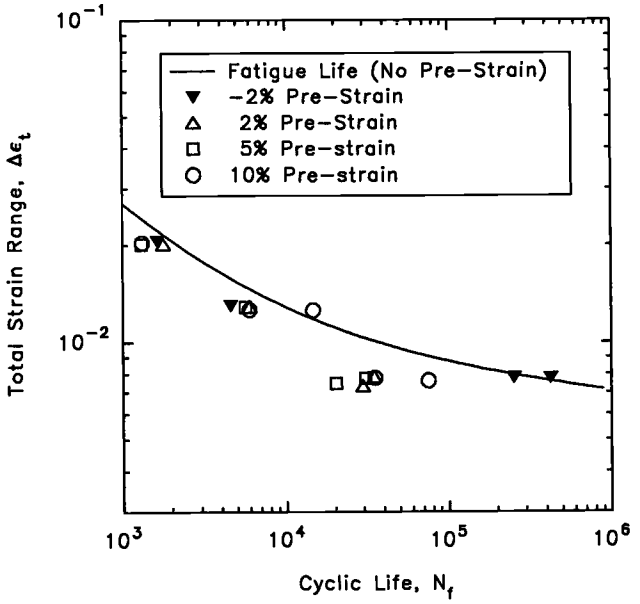

FIG. 2—*Fatigue data of prestrained Inconel 718 superalloy.*

Life Estimation

Cumulative Damage Models

Three cumulative damage models were used to estimate the fatigue lives of the prestrained specimens. They are: (1) the linear damage rule (LDR), (2) the linear strain and life fraction rule (LSLFR), and (3) the damage curve approach (DCA). The LDR of

Palmgren [*16*], Langer [*17*], and Miner [*18*] is used widely in estimating fatigue life under variable amplitude fatigue loading and assumes that fatigue failure occurs when the summation of life fractions from different loadings reaches unity. For a two load-level test, the LDR is shown in Eq 4.

$$\left(\frac{n_1}{N_1}\right) + \left(\frac{n_2}{N_2}\right) = 1 \tag{4}$$

The LSLFR is similar to the rule proposed by Burgreen [*19*] for thermal ratchetting during temperature cycling. This rule assumes that failure occurs in a prestrained specimen when the summation of the strain fraction and life fraction reaches unity (Eq 5).

$$\left(\frac{\epsilon_{in,P}}{\epsilon_f}\right) + \left(\frac{n_2}{N_2}\right) = 1 \tag{5}$$

The DCA was developed by Manson and Halford [*20,21*] to overcome the load-ordering effect commonly observed in cumulative fatigue damage tests. This rule assumes that the accumulation of fatigue damage occurs in a nonlinear fashion, and the degree of nonlinearity is a function of the ratio of fatigue lives corresponding to the lowest and the highest load levels. The DCA for a two-load-level fatigue test is shown in Eq 6.

$$\left(\frac{n_1}{N_1}\right)^{\left(\frac{N_1}{N_2}\right)^{0.4}} + \left(\frac{n_2}{N_2}\right) = 1 \tag{6}$$

All the variables in Eqs 4 through 6 are defined in the nomenclature section. Note that in Eqs 4 through 6, the accumulation of fatigue damage is completely independent from the life relation necessary to establish the fatigue life at each load level.

Fatigue Life Estimation without Mean Stress Effects

In estimating the fatigue lives of the prestrained IN 718 specimens, the effect of mean stress on the fatigue life was not initially considered. In the case of the LDR and DCA, the prestraining portion of the test was considered as a quarter cycle ($n_1 = 0.25$) with a strain range equal to twice the magnitude of the prestrain. Therefore, N_1 corresponding to this strain range was calculated with Eq 3. In the case of the LSLFR, the true inelastic strain offset after prestraining was used to compute the strain fraction in Eq 5. In all the life prediction methods, N_2 corresponding to the fatigue portion of the tests was computed from Eq 3 by using the $\Delta\epsilon_t$ values listed in Table 3. The fatigue lives of the prestrained specimens (n_2) were then estimated with Eqs 4 through 6. The results are shown in Fig. 3 for all the cumulative damage models. The fatigue lives predicted by the LDR and the LSLFR were very similar and were unconservative by up to a factor of 20 compared to the experimentally observed fatigue lives. These unconservative predictions occurred mainly at the lowest strain range in tensile prestrained specimens, most of which developed large tensile mean stresses during the subsequent fatigue loading. The fatigue lives predicted by the DCA were significantly better than those by either the LDR or the LSLFR.

Fatigue Life Estimation with Mean Stress Effects

The quantitative effect of mean stress (either tensile or compressive) on the fatigue life of the heat of IN 718 investigated in this study has, as yet, not been characterized. However, consideration of mean stress is necessary because tensile mean stress is usually detrimental to fatigue life, whereas compressive mean stress might be beneficial. Korth [*4*] investigated

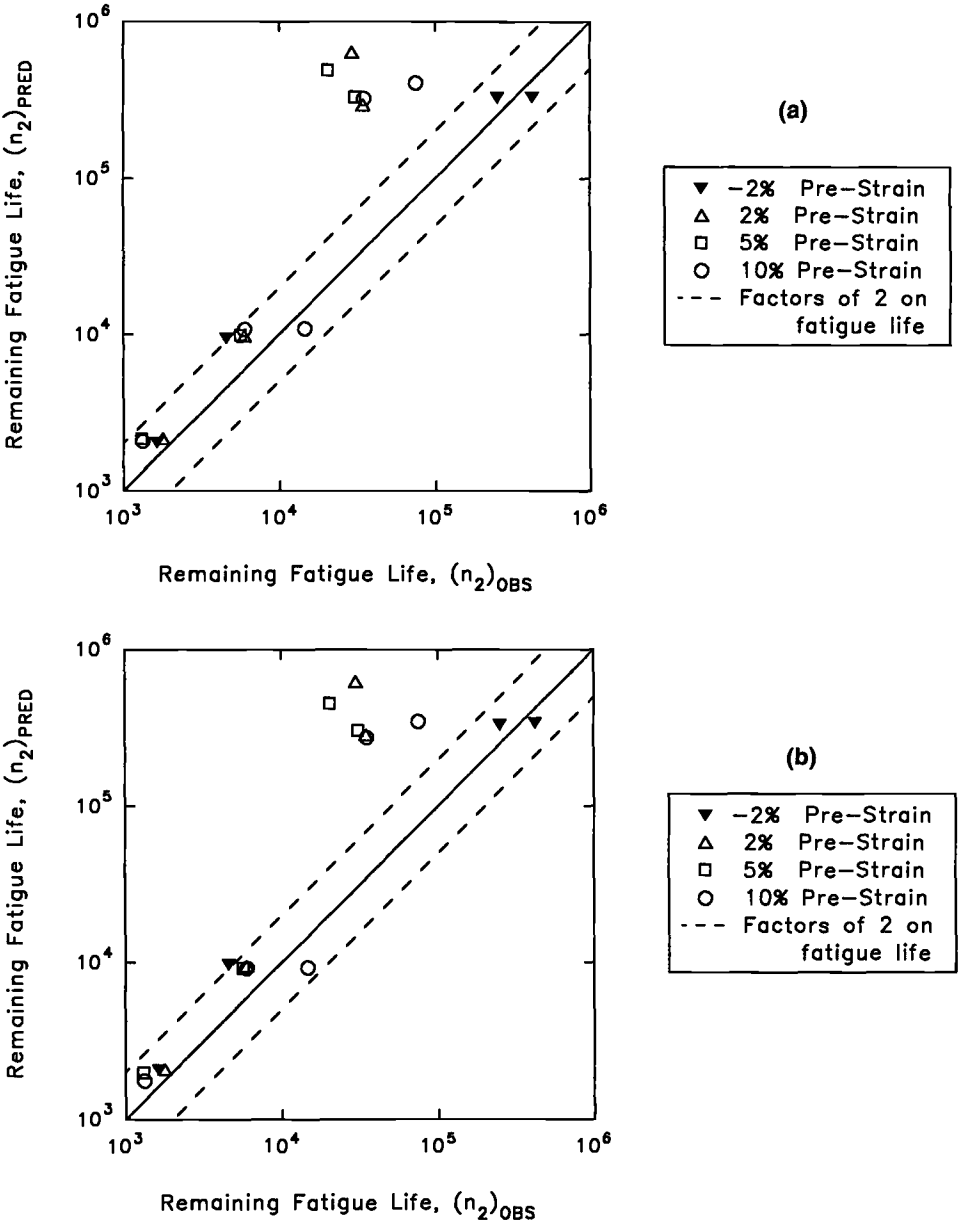

FIG. 3—*Fatigue life estimation of prestrained Inconel 718 without considering mean stress effects: (a) linear damage rule, (b) linear strain and life fraction rule, and (c) nonlinear damage curve approach.*

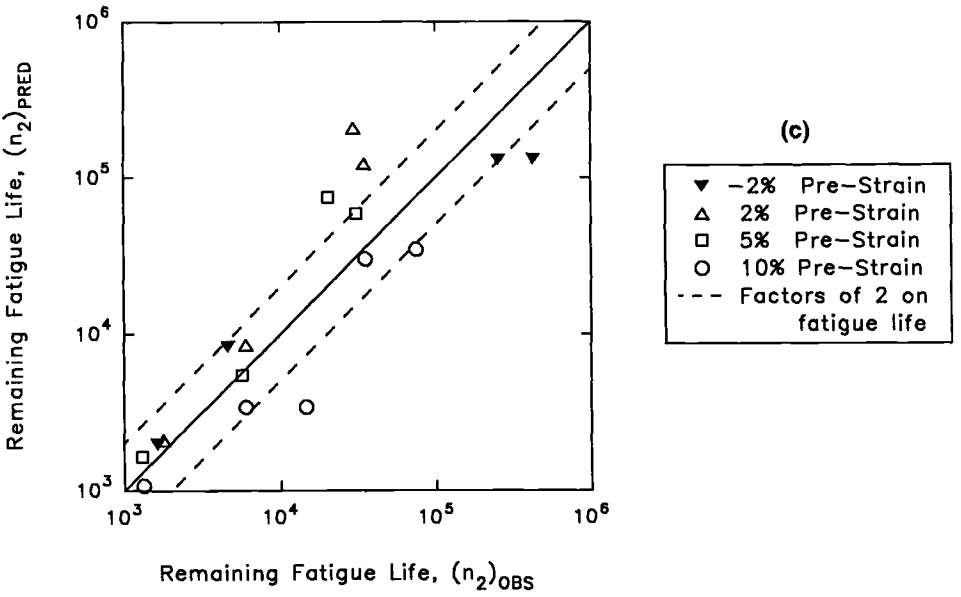

Fig. 3—*Continued.*

the applicability of three mean stress models to IN 718 and reported that the parameter proposed by Smith, Watson, and Topper [*22*] most accurately described the behavior of his alloy. Therefore, an attempt was to made to include the effect of mean stress on fatigue life with the Smith-Watson-Topper parameter (SWT). A twin power-law relation was established between SWT and N_f with the baseline fatigue data (Table 2) for IN 718 (Eq 7).

$$\sigma_{max}\epsilon_t E = A_1(N_f)^{a_1} + A_2(N_f)^{a_2}$$
$$\sigma_{max}\epsilon_t E = 2.52 \times 10^6(N_f)^{-0.114} + 2.14 \times 10^8(N_f)^{-0.683} \quad (7)$$

Equation 7 and the baseline fatigue data are shown in Fig. 4. The SWT was then employed to estimate the fatigue life, N_2, corresponding to the fatigue loading after prestraining. The computed N_2 values contain the influence of mean stresses because in SWT the mean stress effect is included through the maximum stress in the hysteresis loop (Eq 7).

Fatigue lives of the prestrained IN 718 specimens were computed with Eqs 4 through 6. For all the life prediction models, the damage from the prestraining was estimated as described earlier. Comparisons of the predicted and observed fatigue lives are shown in Fig. 5. As noted earlier, predictions by the LDR and LSLFR were very similar. At the lowest strain range, the predicted fatigue lives by these two models were unconservative by up to two orders of magnitude compared to the observed fatigue lives. All methods overestimated the fatigue lives of the lowest strain range tests on compressively prestrained specimens. Among the cumulative damage methods investigated, the best predictions were obtained with the DCA method.

Discussion

The fatigue life of IN 718 was influenced by both the magnitude and direction of prestraining (Fig. 2). In general, tensile prestraining was detrimental at all the strain ranges investigated. Compressive prestraining reduced fatigue lives marginally at the higher strain

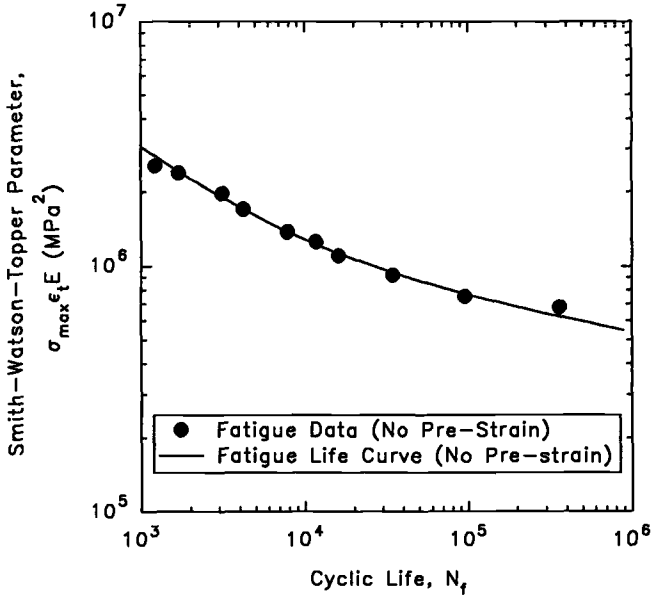

FIG. 4—*Correlation of baseline fatigue data with Smith-Watson-Topper parameter.*

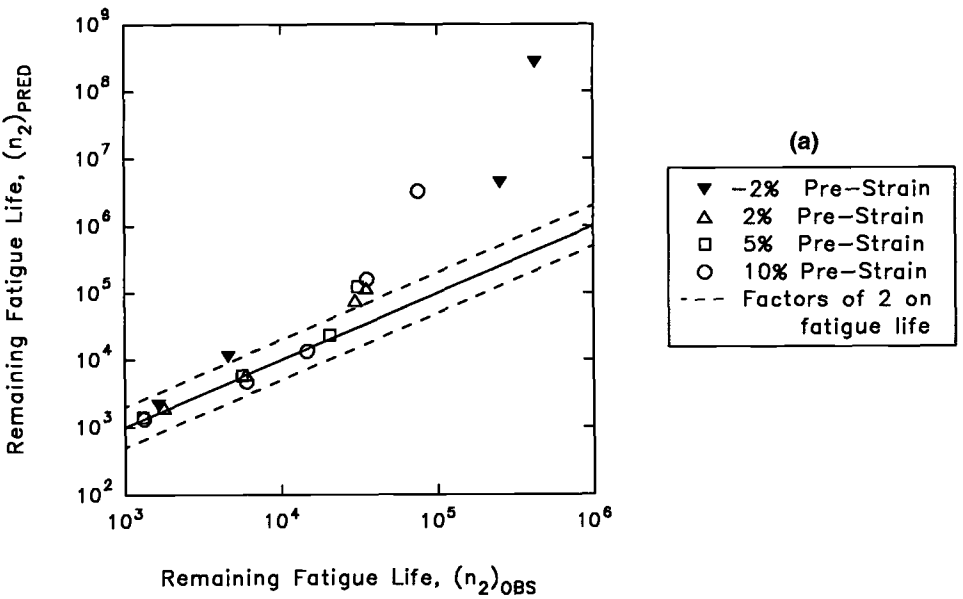

FIG. 5—*Fatigue life estimation of prestrained Inconel 718 with mean stress effects: (a) linear damage rule, (b) linear strain and life fraction rule, (c) nonlinear damage curve approach.*

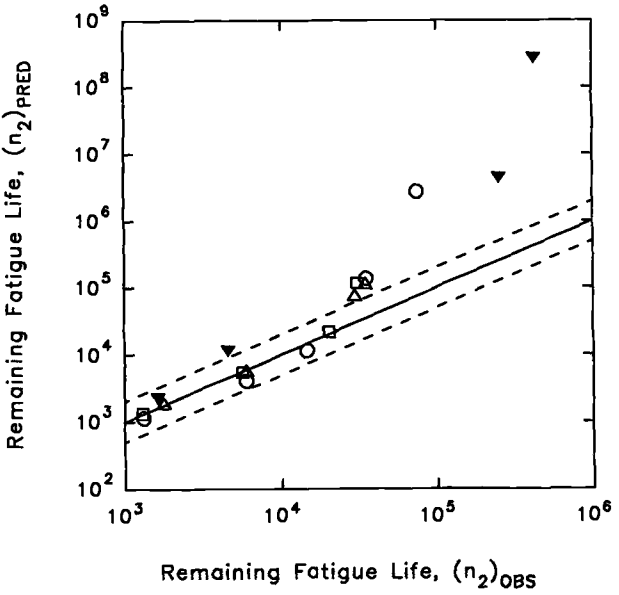

FIG. 5—*Continued.*

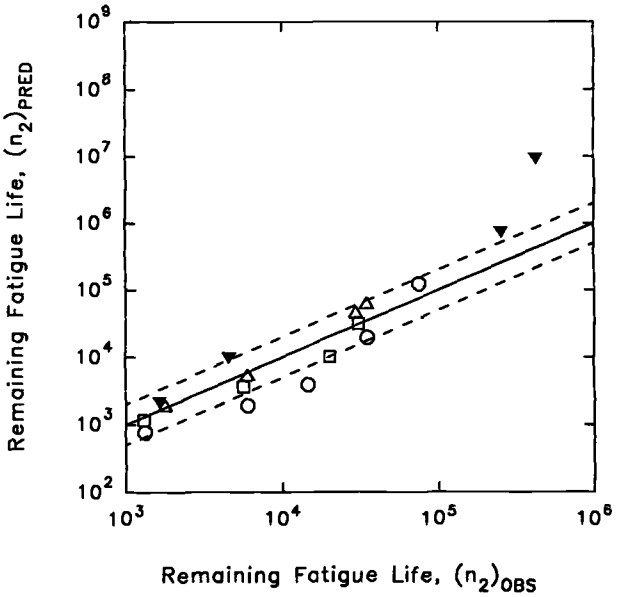

FIG. 5—*Continued.*

ranges, whereas at the lowest strain range it did not affect the fatigue life. While investigating the deformation and damage mechanisms in IN 718, Kalluri et al. [5] noted that in the 10% tensile prestrained specimen fatigued subsequently at the lowest strain range, deformation was very inhomogeneous and was confined to a few well-defined slip bands. At the lowest strain range, deformation during the fatigue loading was confined to the deformation bands activated during the tensile prestrain, whereas at the higher strain ranges additional deformation bands were activated during fatigue. The inhomogeneous deformation noted at the lowest strain range can increase stress concentration at the intersections of slip bands and grain boundaries and can lead to microcrack initiation. In addition, tensile prestraining can induce microscopic slip steps on the surface of the specimen, and these slip steps can also serve as microcrack initiation sites during the subsequent fatigue loading. Both of these mechanisms tend to lower the fatigue lives of prestrained specimens due to a reduction in the crack initiation portion of their cyclic lives. Even though the proposed mechanisms can explain the observed reduction in fatigue life due to tensile prestraining, they cannot explain the apparent lack of influence of compressive prestraining on the fatigue life at the lowest strain range. The deformation and damage mechanisms in specimens subjected to compressive prestraining followed by fatigue remain to be investigated.

The observed fatigue lives of the prestrained specimens indicated that significantly detrimental effects of tensile prestraining were experienced mainly in the low strain range, high-cycle-fatigue regime (Fig. 2). Fatigue life predictions by the nonlinear DCA, when the effect of mean stress on fatigue life was not considered, were more accurate than those by the LDR or the LSLFR, especially in the low strain range, high-cycle-fatigue regime (Fig. 3). These results suggest that the damages due to prestraining and the subsequent fatigue loading accumulate in a nonlinear manner. In the low strain range, high-cycle-fatigue regime, tensile prestraining substantially lowers the subsequent fatigue life because N_1 and N_2 in Eq 6 are significantly different in this regime. In the high strain range, low-cycle-fatigue regime, N_1 and N_2 are of the same order of magnitude, and as a result tensile prestraining does not have a significant influence on the subsequent fatigue life. At the lowest strain range, among the tensile prestrained specimens, the highest and lowest average fatigue lives were observed for the 10 and 5% tensile prestrained specimens, respectively, with the average fatigue life of 2% tensile prestrained specimens in between the highest and lowest average lives (Fig. 2). The observed ordering in the average fatigue lives of the tensile prestrained specimens cannot be predicted from cumulative damage models because they would estimate the highest and lowest fatigue lives for the 2 and 10% prestrained specimens, respectively, with lives of the 5% prestrained specimens in between the two extremes. Further investigation is needed to establish the reasons behind the observed ordering in the fatigue lives of the tensile prestrained specimens.

As mentioned earlier, all the prestrained specimens developed mean stresses of substantial magnitude. The influence of mean stresses on fatigue life is significant in the low strain range, high-cycle-fatigue regime, where the ratio of inelastic strain range to elastic strain range in the hysteresis loop is less than 0.1 [23]. As a result, mean stresses are not expected to significantly influence the fatigue lives of prestrained specimens at the highest and intermediate strain ranges (Fig. 2). However, at the lowest strain range, mean stresses can influence the fatigue lives of prestrained specimens because tensile mean stresses are usually detrimental and compressive mean stresses can be beneficial to fatigue life. The observed reduction in the fatigue lives of tensile prestrained specimens, at least to some extent, is due to the tensile mean stresses developed by most of these specimens (Table 3). For instance, in the low strain range, high-cycle-fatigue regime, the predicted fatigue lives of the tensile prestrained specimens showed improvement for all the cumulative damage models when the effect of mean stress on fatigue life was taken into consideration by the SWT parameter

(Figs. 3 and 5). However, in the same life regime, the predicted lives of the compressively prestrained specimens, which developed compressive mean stresses, deteriorated for all the models when the effect of mean stress on fatigue life was taken into consideration by the SWT parameter. This observation suggests that the SWT parameter overestimated the beneficial effect of compressive mean stress on the fatigue life of IN 718. Note also that the SWT parameter is inapplicable for fatigue life estimations when σ_{max} is negative. These results clearly indicate that it is necessary to characterize the effects of both tensile and compressive mean stresses on the fatigue life of IN 718 to facilitate accurate estimation of fatigue life under mean stress conditions.

Summary

Fatigue behavior of Inconel 718 superalloy was investigated by conducting fully reversed fatigue tests at room temperature. In addition, fatigue tests were also conducted on specimens prestrained either in tension or compression to characterize the influence of prestraining on fatigue life. Fatigue lives of the prestrained specimens were estimated by the linear damage rule, the linear strain and life fraction rule, and the nonlinear damage curve approach. The Smith-Watson-Topper parameter was used to determine the effects of mean stresses on the fatigue lives of the prestrained specimens.

In general, prestraining reduced the fatigue life of Inconel 718. The reduction in life was significant in the low strain range (or high-cycle-fatigue regime) for the specimens prestrained in tension. At the same strain range, compressive prestraining did not significantly influence the fatigue life. In general, tensile prestraining resulted in the development of tensile mean stresses during fatigue loading, which are detrimental to fatigue endurance, whereas compressive prestraining resulted in the development of compressive mean stresses, which might be beneficial to fatigue endurance.

Fatigue life predictions of the prestrained Inconel 718 by the linear damage rule and the linear strain and life fraction rule, when the effect of mean stress on fatigue life was not considered, were essentially similar and were unconservative in the high-cycle-fatigue regime by up to a factor of 20 compared to the experimentally observed fatigue lives. Life predictions by the nonlinear damage curve approach were more accurate than those by the linear damage rule and the linear strain and life fraction rule.

All the cumulative damage rules overestimated the fatigue lives of the compressively prestrained Inconel 718 specimens in the high-cycle-fatigue regime when the effect of mean stress on fatigue life was included through the Smith-Watson-Topper parameter. Fatigue lives of some of the tensile prestrained specimens were also overpredicted by the linear damage rule and the linear strain and life fraction rule.

Among the cumulative damage rules investigated, the best fatigue life predictions were obtained by using the nonlinear damage curve approach irrespective of whether the effect of mean stress on fatigue life was considered or disregarded.

This investigation indicated that it was necessary to experimentally characterize the effect of mean stress on the fatigue life of Inconel 718 for accurate fatigue life estimation under cumulative fatigue loading conditions.

Acknowledgment

The diligent efforts of Christopher S. Burke in the High Temperature Fatigue and Structures Laboratory are gratefully acknowledged.

References

[*1*] Jones, A. H., "An Overview of Alloy 718 in Large Structural Castings," *Superalloy 718—Metallurgy and Applications,* E. A. Loria, Ed., The Minerals, Metals and Materials Society, Warrendale, PA, 1989, pp. 307–318.

[2] Krueger, D. D., "The Development of Direct Age 718 for Gas Turbine Engine Disk Applications," *Superalloy 718—Metallurgy and Applications*, E. A. Loria, Ed., The Minerals, Metals and Materials Society, Warrendale, PA, 1989, pp. 279–296.

[3] Jewett, R. P. and Halchak, J. A., "The Use of Alloy 718 in the Space Shuttle Main Engine," *Superalloys 718, 625 and Various Derivatives*, E. A. Loria, Ed., The Minerals, Metals and Materials Society, Warrendale, PA, 1991, pp. 749–760.

[4] Korth, G. E., "Effects of Various Parameters on the Fatigue Life of 718," *Superalloys 718, 625 and Various Derivatives*, E. A. Loria, Ed., The Minerals, Metals and Materials Society, Warrendale, PA, 1991, pp. 457–476.

[5] Kalluri, S., Bhanu Sankara Rao, K., Halford, G. R., and McGaw, M. A., "Deformation and Damage Mechanisms in Inconel 718 Superalloy," *Superalloys 718, 625, 706 and Derivatives*, E. A. Loria, Ed., The Minerals, Metals and Materials Society, Warrendale, PA, 1994, pp. 593–606.

[6] Paulonis, D. F., Oblak, J. M., and Duvall, D. S., "Precipitation in Nickel-Base Alloy 718," *Transactions of the ASM*, Vol. 62, 1969, pp. 611–622.

[7] Oblak, J. M., Paulonis, D. F., and Duvall, D. S., "Coherency Strengthening in Ni Base Alloys Hardened by DO_{22} γ'' Precipitates," *Metallurgical Transactions*, Vol. 5, 1974, pp. 143–153.

[8] Chaturvedi, M. C. and Han, Y., "Strengthening Mechanisms in Inconel 718 Superalloy," *Metal Science*, Vol. 17, March 1983, pp. 145–149.

[9] Oradei-Basile, A. and Radavich, J. F., "A Current T-T-T Diagram for Wrought Alloy 718," *Superalloys 718, 625 and Various Derivatives*, E. A. Loria, Ed., The Minerals, Metals and Materials Society, Warrendale, PA, 1991, pp. 325–335.

[10] McGaw, M. A. and Bonacuse, P. J., "Automation Software for a Materials Testing Laboratory," *Applications of Automation Technology to Fatigue and Fracture Testing, ASTM STP 1092*, A. A. Braun, N. E. Ashbaugh, and F. M. Smith, Eds., American Society for Testing and Materials, West Conshohocken, PA, 1990, pp. 211–231.

[11] Kalluri, S., Halford, G. R., and McGaw, M. A., "Fatigue Behavior of Inconel 718 Superalloy Subjected to Tensile and Compressive Monotonic Strains," paper presented at the 1994 Conference on Advanced Earth-to-Orbit Propulsion Technology, NASA-Marshall Space Flight Center, Huntsville, Alabama, 17–19 May 1994.

[12] Bhanu Sankara Rao, K., Kalluri, S., Halford, G. R., and McGaw, M. A., "Serrated Flow and Deformation Substructure at Room Temperature in Inconel 718 Superalloy During Strain Controlled Fatigue," *Scripta Metallurgica et Materialia*, Vol. 32, No. 4, 1995, pp. 493–498.

[13] Basquin, O. H., "The Exponential Law of Endurance Tests," *Proceedings*, American Society for Testing and Materials, West Conshohocken, PA, Vol. 10, 1910, pp. 625–630.

[14] Manson, S. S., "Behavior of Materials under Conditions of Thermal Stress," *Proceedings*, Heat Transfer Symposium, University of Michigan Engineering Research Institute, 1953, pp. 9–75 (also available as NACA Technical Note 2933, 1953).

[15] Coffin, L. F., Jr., "A Study of the Effects of Cyclic Thermal Stresses on a Ductile Metal," *Transactions*, American Society of Mechanical Engineers, Vol. 76, 1954, pp. 931–950.

[16] Palmgren, A., "Die Lebensdauer von Kugellagern," *Verfahrenstechinik (Berlin)*, Vol. 68, 1924, pp. 339–341.

[17] Langer, B. F., "Fatigue Failure from Stress Cycles of Varying Amplitude," *Journal of Applied Mechanics*, Vol. 59, 1937, pp. A160–A162.

[18] Miner, M. A., "Cumulative Damage in Fatigue," *Journal of Applied Mechanics*, Vol. 67, 1945, pp. A159–A164.

[19] Burgreen, D., "Review of Thermal Ratchetting," *Fatigue at Elevated Temperatures, ASTM STP 520*, American Society for Testing and Materials, West Conshohocken, PA, 1973, pp. 535–551.

[20] Manson, S. S. and Halford, G. R., "Practical Implementation of the Double Linear Damage Rule and Damage Curve Approach for Treating Cumulative Fatigue Damage," *International Journal of Fracture*, Vol. 17, 1981, pp. 169–192.

[21] Manson, S. S. and Halford, G. R., "Re-examination of Cumulative Fatigue Damage Analysis—An Engineering Perspective," *Engineering Fracture Mechanics*, Vol. 25, Nos. 5/6, 1986, pp. 539–571.

[22] Smith, K. N., Watson, P., and Topper, T. H., "A Stress-Strain Function for the Fatigue of Metals," *Journal of Materials, JMSLA*, Vol. 5, No. 4, 1970, pp. 767–778.

[23] Halford, G. R. and Nachtigall, A. J., "Strain Range Partitioning Behavior of an Advanced Gas Turbine Disk Alloy AF2-1DA," *Journal of Aircraft*, Vol. 17, No. 8, 1980, pp. 598–604.

Author Index

Subject Index

ISBN 0-8031-2029-X